

European Federation of
Corrosion Publications
Number 48

Corrosion of metallic heritage artefacts

Investigation, conservation
and prediction for
long-term behaviour

Edited by P. Dillmann, G. Béranger, P. Piccardo
and H. Matthiesen



WP

Corrosion of metallic heritage artefacts

European Federation of Corrosion Publications
NUMBER 48

Corrosion of metallic heritage artefacts

Investigation, conservation
and prediction for long-term
behaviour

Edited by
P. Dillmann, G. Béranger, P. Piccardo and
H. Matthiesen

**Published for the European Federation of Corrosion
by Woodhead Publishing and Maney Publishing
on behalf of
The Institute of Materials, Minerals & Mining**

**CRC Press
Boca Raton Boston New York Washington, DC**

WOODHEAD PUBLISHING LIMITED
Cambridge England

Woodhead Publishing Limited and Maney Publishing Limited on behalf of
The Institute of Materials, Minerals & Mining

Published by Woodhead Publishing Limited, Abington Hall, Abington
Cambridge CB21 6AH, England
www.woodheadpublishing.com

Published in North America by CRC Press LLC, 6000 Broken Sound Parkway, NW,
Suite 300, Boca Raton, FL 33487, USA

First published 2007 by Woodhead Publishing Limited and CRC Press LLC
© 2007, Institute of Materials, Minerals & Mining
The authors have asserted their moral rights.

This book contains information obtained from authentic and highly regarded sources. Reprinted material is quoted with permission, and sources are indicated. Reasonable efforts have been made to publish reliable data and information, but the authors and the publishers cannot assume responsibility for the validity of all materials. Neither the authors nor the publishers, nor anyone else associated with this publication, shall be liable for any loss, damage or liability directly or indirectly caused or alleged to be caused by this book.

Neither this book nor any part may be reproduced or transmitted in any form or by any means, electronic or mechanical, including photocopying, microfilming and recording, or by any information storage or retrieval system, without permission in writing from the Woodhead Publishing Limited.

The consent of Woodhead Publishing Limited does not extend to copying for general distribution, for promotion, for creating new works, or for resale. Specific permission must be obtained in writing from Woodhead Publishing Limited for such copying.

Trademark notice: Product or corporate names may be trademarks or registered trademarks, and are used only for identification and explanation, without intent to infringe.

British Library Cataloguing in Publication Data
A catalogue record for this book is available from the British Library.

Library of Congress Cataloging in Publication Data
A catalog record for this book is available from the Library of Congress.

Woodhead Publishing ISBN-13: 978-1-84569-239-1 (book)
Woodhead Publishing ISBN-10: 1-84569-239-X (book)
Woodhead Publishing ISBN-13: 978-1-84569-301-5 (e-book)
Woodhead Publishing ISBN-10: 1-84569-301-9 (e-book)
CRC Press ISBN-13: 978-1-4200-5407-1
CRC Press ISBN-10: 1-4200-5407-4
CRC Press order number: WP5407
ISSN 1354-5116

The publishers' policy is to use permanent paper from mills that operate a sustainable forestry policy, and which has been manufactured from pulp which is processed using acid-free and elementary chlorine-free practices. Furthermore, the publishers ensure that the text paper and cover board used have met acceptable environmental accreditation standards.

Typeset by Replika Press Pvt Ltd, India
Printed by T J International Limited, Padstow, Cornwall, England

Contents

| | |
|--|--------------|
| <i>Contributor contact details</i> | <i>xiii</i> |
| <i>Series introduction</i> | <i>xix</i> |
| <i>Volumes in the EFC series</i> | <i>xxi</i> |
| <i>Foreword</i> | <i>xxvii</i> |
| <i>Preface</i> | <i>xxix</i> |
| 1 Examination and conservation of historical and archaeological metal artefacts: a European overview | 1 |
| C. DEGRIGNY, ICOM-CC Metal Working Group, France | |
| 1.1 Introduction | 1 |
| 1.2 How scientific examination and archaeometric studies receive most of the funding | 2 |
| 1.3 The necessity for research on conservation of historical and archaeological artefacts | 6 |
| 1.4 Training in conservation science: a chance for better recognition of the discipline? | 10 |
| 1.5 Pro-active responsibilities for conservators | 11 |
| 1.6 Networking | 12 |
| 1.7 Conclusion | 13 |
| 1.8 References | 13 |
| 2 Corrosion behaviour of low-alloy steels: from ancient past to far future | 18 |
| G. SANTARINI, Commissariat à l’Energie Atomique, France | |
| 2.1 Introduction | 18 |
| 2.2 Uniform corrosion and localized corrosion | 18 |
| 2.3 Atmospheric corrosion | 21 |
| 2.4 Corrosion in soils | 23 |

| | | |
|-----|--|----|
| vi | Contents | |
| 2.5 | Corrosion in cementitious environments | 28 |
| 2.6 | Conclusion | 28 |
| 2.7 | Acknowledgements | 29 |
| 2.8 | References | 29 |
| 3 | Archaeological metal artefacts and conservation issues: long-term corrosion studies | 31 |
| | R. BERTHOLON, Université Paris 1, Panthéon-Sorbonne, France | |
| 3.1 | Introduction | 31 |
| 3.2 | The artefact's history and its material condition | 31 |
| 3.3 | The limit of the original surface | 34 |
| 3.4 | Locating the limit of the original surface | 35 |
| 3.5 | Conclusion | 39 |
| 3.6 | References | 40 |
| 4 | Contribution of iron archaeological artefacts to the estimation of average corrosion rates and the long-term corrosion mechanisms of low-carbon steel buried in soil | 41 |
| | D. NEFF, E. VEGA, P. DILLMANN and M. DESCOSTES, Commissariat à l'Energie Atomique, France and L. BELLOT-GURLET, Université Pierre et Marie Curie Paris, France and G. BÉRANGER, Université de Technologie de Compiègne, France | |
| 4.1 | Introduction | 41 |
| 4.2 | Literature review | 42 |
| 4.3 | Characterisation of corrosion layouts and mechanisms | 43 |
| 4.4 | Average corrosion rate estimation | 59 |
| 4.5 | Conclusion | 73 |
| 4.6 | Acknowledgements | 74 |
| 4.7 | References | 74 |
| 5 | Electrochemical study of steel artefacts from World War I: Contribution of A.C. impedance spectroscopy and chronoamperometry to describe the behaviour of the corrosion layers | 77 |
| | E. PONS, C. LEMAITRE and D. DAVID, Université de Technologie de Compiègne, France and D. CRUSSET, ANDRA, France | |
| 5.1 | Introduction | 77 |
| 5.2 | Objective and experimental methods | 77 |
| 5.3 | Specific electrochemical behaviour depending on the corrosion layers | 80 |
| 5.4 | Advanced electrochemical study of the internal corrosion layer | 82 |

| | | |
|-----|--|-----|
| 5.5 | Conclusion | 90 |
| 5.6 | References | 90 |
| 6 | Species transport in the corrosion products of ferrous archaeological analogues: contribution to the modelling of long-term iron corrosion mechanisms | 92 |
| | E. VEGA, P. DILLMANN and P. BERGER, Commissariat à l’Energie Atomique, France and P. FLUZIN, Laboratoire Métallurgies et Cultures, France | |
| 6.1 | Introduction | 92 |
| 6.2 | Analysed corpus and experimental methods | 94 |
| 6.3 | Results and discussion | 96 |
| 6.4 | Corrosion rates evaluation | 100 |
| 6.5 | Conclusion | 107 |
| 6.6 | References | 107 |
| 7 | Long-term behaviour of iron embedded in concrete: from the characterisation of archaeological analogues to the verification of the oxygen reduction as the limiting step for corrosion rate | 109 |
| | W.-J. CHITTY, B. HUET, P. DILLMANN and V. L’HOSTIS, Commissariat à l’Energie Atomique, France and G. BÉRANGER, Université de Technologie de Compiègne, France and H. IDRISSE, INSA de Lyon, France | |
| 7.1 | Introduction | 109 |
| 7.2 | Characterisation of long-term corrosion layout of iron embedded in old binders | 111 |
| 7.3 | Proposition of a modelling approach for the corrosion of iron in concrete | 122 |
| 7.4 | Conclusion | 128 |
| 7.5 | Acknowledgements | 129 |
| 7.6 | References | 129 |
| 8 | Study of the atmospheric corrosion of iron by ageing historical artefacts and contemporary low-alloy steel in a climatic chamber: comparison with mechanistic modelling | 131 |
| | L. MARÉCHAL, S. PERRIN, P. DILLMANN and G. SANTARINI, Commissariat à l’Energie Atomique, France | |
| 8.1 | Introduction | 131 |
| 8.2 | Atmospheric corrosion of iron | 132 |
| 8.3 | Experimental ageing of historical artefacts | 139 |

| | | |
|------|---|-----|
| viii | Contents | |
| 8.4 | Results and discussion | 144 |
| 8.5 | Conclusion | 148 |
| 8.6 | References | 149 |
| 8.7 | Appendix: Table of symbols and values | 151 |
| 9 | The corrosion of metallic artefacts in seawater: descriptive analysis | 152 |
| | J. B. MEMET, Laboratoire Arc' Antique, France | |
| 9.1 | Introduction | 152 |
| 9.2 | Brief description of the seawater environment | 153 |
| 9.3 | Corrosion of iron-based artefacts | 156 |
| 9.4 | Marine corrosion of copper alloys | 164 |
| 9.5 | Seawater corrosion aspects of lead- and tin-based 'white' metals | 164 |
| 9.6 | Knowledge of the degradation state of metallic artefacts | 165 |
| 9.7 | Conclusion | 167 |
| 9.8 | References | 167 |
| 10 | Contribution of local and structural characterisation for studies of the corrosion mechanisms related to the presence of chlorine on archaeological ferrous artefacts | 170 |
| | S. RÉGUER and P. DILLMANN, Commissariat à l'Énergie Atomique, France and F. MIRAMBET, Laboratoire de Restauration des Monuments Historiques, France and J. SUSINI, European Synchrotron Radiation Facility, France | |
| 10.1 | Introduction | 170 |
| 10.2 | Experimental corpus of archaeological artefacts | 172 |
| 10.3 | Methodology: cross-section characterisation | 174 |
| 10.4 | Results | 176 |
| 10.5 | Discussion | 184 |
| 10.6 | Conclusion | 187 |
| 10.7 | Acknowledgements | 187 |
| 10.8 | References | 188 |
| 11 | A proposal to describe reactivated corrosion of archaeological iron objects | 190 |
| | M. A. LOEPER-ATTIA, National Institute of Heritage, France | |
| 11.1 | Introduction | 190 |
| 11.2 | Giving a name to this type of corrosion | 191 |
| 11.3 | Forms of corrosion | 192 |
| 11.4 | Diagnostics | 200 |

| | | |
|------|--|-----|
| 11.5 | Perspectives | 200 |
| 11.6 | References | 201 |
| 12 | Simulation of corrosion processes of buried archaeological bronze artefacts | 203 |
| | E. ANGELINI, F. ROSALBINO and S. GRASSINI, Politecnico di Torino, Italy and G. M. INGO and T. DE CARO, Istituto per lo Studio dei Materiali Nanostrutturati (ISMIN-CNR), Italy | |
| 12.1 | Introduction | 203 |
| 12.2 | Materials and methods | 205 |
| 12.3 | Results and discussion | 207 |
| 12.4 | Conclusions | 216 |
| 12.5 | References | 217 |
| 13 | Corrosion patina or intentional patina: contribution of non-destructive analyses to the surface study of copper-based archaeological objects | 219 |
| | F. MATHIS, J. SALOMON, S. PAGÈS-CAMAGNA, M. DUBUS, D. ROBCIS and M. AUCOUTURIER, Centre de Recherche et de Restauration des Musées de France, France and S. DESCAMPS and E. DELANGE, Louvre Museum, France | |
| 13.1 | Introduction | 219 |
| 13.2 | The objects | 220 |
| 13.3 | Instrumentations and methods for analyses | 222 |
| 13.4 | Results | 223 |
| 13.5 | Discussion | 232 |
| 13.6 | Conclusions | 235 |
| 13.7 | Acknowledgements | 236 |
| 13.8 | References | 236 |
| 14 | Tin and copper oxides in corroded archaeological bronzes | 239 |
| | P. PICCARDO, Università di Genova, Italy and B. MILLE, Centre de Recherche et de Restauration des Musées de France, France and L. ROBBIOLO, ENSCP, France | |
| 14.1 | Introduction | 239 |
| 14.2 | Materials and methods | 243 |
| 14.3 | Characterisation of the internal corrosion layers containing oxides | 244 |
| 14.4 | Discussion: tin oxide, copper oxide and 'type 2' corrosion | 254 |
| 14.5 | Conclusions | 259 |
| 14.6 | Acknowledgements | 260 |
| 14.7 | References | 260 |

| | | |
|------|--|-----|
| x | Contents | |
| 15 | Corrosion problems and reconstruction of the copper roof on Queen Anna's Summer Palace, Prague | 263 |
| | K. KREISLOVA, D. KNOTKOVA and V. CIHAL, SVUOM Ltd, Czech Republic and J. HAD, VSCHT, Czech Republic | |
| 15.1 | Introduction | 263 |
| 15.2 | Survey of corrosion products and damage to copper roofs and claddings in Prague | 263 |
| 15.3 | Corrosion damage on copper roof of Queen Anna's Summer Palace | 264 |
| 15.4 | Reconstruction of the copper roof | 265 |
| 15.5 | Artificial patinas | 267 |
| 15.6 | Study of behaviour of artificial patinas in atmospheric conditions | 268 |
| 15.7 | Conclusions | 270 |
| 15.8 | Acknowledgement | 270 |
| 15.9 | References | 271 |
| 16 | Long-term corrosion of iron at the waterlogged site of Nydam in Denmark: studies of environment, archaeological artefacts and modern analogues | 272 |
| | H. MATTHIENSEN, D. GREGORY and B. SØRENSEN, National Museum of Denmark and L. R. HILBERT, Technical University of Denmark | |
| 16.1 | Introduction | 272 |
| 16.2 | Study site | 272 |
| 16.3 | Methods | 273 |
| 16.4 | Results | 279 |
| 16.5 | Discussion | 288 |
| 16.6 | Conclusions | 290 |
| 16.7 | Acknowledgements | 291 |
| 16.8 | References | 291 |
| 17 | On-line corrosion monitoring of indoor atmospheres | 293 |
| | L. SJÖGREN, Corrosion and Metals Research Institute, Sweden and N. LE BOZEC, Institut de la Corrosion, France | |
| 17.1 | Introduction | 293 |
| 17.2 | Experimental | 293 |
| 17.3 | Results and discussion | 297 |
| 17.4 | Conclusions | 306 |
| 17.5 | Acknowledgement | 306 |
| 17.6 | References | 306 |

| | | |
|------|--|-----|
| 18 | Corrosion inhibitors for metallic artefacts: temporary protection | 308 |
| | E. ROCCA, Université Henri Poincaré, France and F. MIRAMBET, Laboratoire de Recherche des Monuments Historiques, France | |
| 18.1 | Introduction | 308 |
| 18.2 | State of the art inhibitors | 309 |
| 18.3 | New anti-corrosion formulations: sodium carboxylates | 314 |
| 18.4 | Conclusions | 331 |
| 18.5 | References | 333 |
| 19 | Surface characterisation of corrosion inhibitors on bronzes for artistic casting | 335 |
| | A. GALTAYRIES, A. MONGIATTI and P. MARCUS, Ecole Nationale Supérieure de Chimie de Paris, France and C. CHIAVARI, Università di Ferrara, Italy | |
| 19.1 | Introduction | 335 |
| 19.2 | Experimental | 336 |
| 19.3 | Results | 337 |
| 19.4 | Discussion | 346 |
| 19.5 | Conclusions | 350 |
| 19.6 | References | 350 |
| 20 | Influence of microstructure and composition on corrosion of lead-rich organ pipes | 352 |
| | C. CHIAVARI, C. DINOI, C. MARTINI, D. PRANDSTRALLER, Università di Bologna, Italy and G. POLI, Università di Modena, Italy | |
| 20.1 | Introduction | 352 |
| 20.2 | Experimental | 353 |
| 20.3 | Results | 357 |
| 20.4 | Discussion | 362 |
| 20.5 | Conclusions | 366 |
| 20.6 | Acknowledgements | 366 |
| 20.7 | References | 366 |
| | <i>Index</i> | 368 |

Contributor contact details

(* = main contact)

Editors

Philippe Dillmann
Laboratoire Pierre Süe CEA/CNRS
UMR9956 and IRAMAT CNRS
UMR5060
CEA Saclay
91191 Gif-sur-Yvette Cedex
France

E-mail: philippe.dillmann@CEA.FR

Gérard Béranger
Université de Technologie de
Compiègne
Laboratoire Roberval
Centre de Recherche de Royallieu
BP529
60205 Compiègne Cedex
France

Paolo Piccardo
DCCI
Università di Genova
via Dodecaneso 31
16146 Genova
Italy

E-mail: paolo.piccardo@gmail.com
pol@chimica.unige.i

Henning Matthiesen
National Museum of Denmark
Department of Conservation
Archaeology - In situ preservation
I.C. Modewegsvej, Brede
DK-2800 Kgs. Lyngby
Denmark

E-mail:

henning.matthiesen@natmus.dk
cons@natmus.dk

Chapter 1

Christian Degrigny
Coordinator of the ICOM-CC Metal
Working Group and co-manager of
SARL GERMOLLES Palais Ducal
en Bourgogne
Château de Germolles
Cidex 407
71640 Germolles (Mellecey)
France

E-mail: christian.degrigny@gmail.com

Chapter 2

G. Santarini
Commissariat à l'Énergie Atomique
Cabinet du Haut-commissaire
Bâtiment siège
91191 Gif-sur-Yvette Cedex
France

E-mail: gerard.santarini@cea.fr

Chapter 3

Régis Bertholon
Université Paris 1 Panthéon-
Sorbonne
Conservation and Restoration
Department
17 rue de Tolbiac
75013 Paris
France

E-mail: Regis.Bertholon@univ-paris1.fr

Chapter 4

D. Neff*, E. Vega and P. Dillmann
Laboratoire Pierre Süe CEA/CNRS
CEA Saclay
91191 Gif-sur-Yvette Cedex
France

E-mail: delphine.neff@cea.fr

L. Bellot-Gurlet
Laboratoire de Dynamique
Interactions et Réactivité (LADIR)
UMR 7075 CNRS – Université
Pierre et Marie Curie Paris VI
2 rue Henri Dunant
94320 Thiais
France

M. Descostes
DEN/DPC/SECR/L3MR
CEA Saclay
91191 Gif-sur-Yvette Cedex
France

G. Béranger
Université de Technologie de
Compiègne
Laboratoire Roberval
Centre de Recherche de Royallieu
BP529
60205 Compiègne Cedex
France

Chapter 5

E. Pons*, C. Lemaitre and D. David
Laboratoire Roberval de Mécanique
(FRE CNRS 2833)
Université de Technologie de
Compiègne
BP 20529
60205 Compiègne
France

E-mail: emmanuelle.pons@edf.fr

D. Crusset
ANDRA
Parc de la Croix Blanche
1–7 rue Jean Monnet
92298 Châtenay-Malabry
France

Chapter 6

Enrique Vega, Philippe Dillmann*
and Pascal Berger
Laboratoire Pierre Süe CEA/CNRS
UMR9956
CEA Saclay
91191 Gif-sur-Yvette Cedex
France

E-mail: philippe.dillmann@CEA.FR

Philippe Fluzin
 Laboratoire Métallurgies et Cultures
 IRAMAT CNRS UMR9956
 UTBM
 90110 Belfort Cedex
 France

Chapter 7

Walter-John Chitty* and Philippe
 Dillmann
 Laboratoire Pierre Süe CEA-CNRS
 CEA Saclay
 91191 Gif-sur-Yvette Cedex
 France

E-mail: walter-john.chitty@cea.fr

Bruno Huet and Valérie L'Hostis
 Laboratoire d'Etude du
 Comportement des Bétons et Argiles
 CEA Saclay
 91191 Gif-sur-Yvette Cedex
 France

Gérard Béranger
 Université de Technologie de
 Compiègne
 BP 60319
 60203 Compiègne Cedex
 France

Hassane Idrissi
 Laboratoire de Physico-Chimie
 Industrielle (LPCI)
 INSA de Lyon
 Bât. Léonard de Vinci
 20 av. Albert Einstein
 69621 Villeurbanne Cedex
 France

Chapter 8

L. Maréchal* and S. Perrin
 Laboratoire d'Etude de la Corrosion
 Aqueuse DEN/DPC SCCME
 CEA Saclay
 91191 Gif-sur-Yvette Cedex
 France

E-mail: steph.perrin@cea.fr

Philippe Dillmann
 Laboratoire Pierre Süe CEA-CNRS
 UMR9956
 CEA Saclay
 91191 Gif-sur-Yvette Cedex
 France

E-mail: philippe.dillmann@CEA.FR

G. Santarini
 Commissariat à l'Energie Atomique
 Cabinet du Haut commissaire
 Bâtiment siège
 91191 Gif-sur-Yvette Cedex
 France

Chapter 9

Jean-Bernard Memet
 ACORROS
 16 rue de la Madeleine
 13200 Arles
 France

E-mail: jbmemet@yahoo.fr

Chapter 10

Solenn Reguer*
 Synchrotron SOLEIL
 L'Orme des Meurisiens
 Saint Aubain BP 48
 91192 Gif-sur-Yvette Cedex
 France

Philippe Dillmann
Laboratoire Pierre Süe CEA/CNRS
CEA Saclay
91191 Gif-sur-Yvette Cedex
France

François Mirambet
LRMH
Château de Champs
29 rue de Paris
77420 Champs sur Marne
France

Jean Susini
ESRF
6 rue Jules Horowitz
BP 220
38043 Grenoble Cedex 9
France

Chapter 11

Marie-Anne Loeper-Attia
178 rue du Faubourg Saint Denis
75010 Paris
France

E-mail: loeperattia@noos.fr

Chapter 12

E. Angelini*, F. Rosalbino and S.
Grassini
Dipartimento di Scienza dei
Materiali ed Ingegneria Chimica
Politecnico di Torino
Corso Duca degli Abruzzi 24
10129 Torino
Italy

E-mail: emma.angelini@polito.it

G.M. Ingo and T. de Caro
Istituto per lo Studio dei Materiali
Nanostrutturati
ISMN CNR
Via Salaria km 29.5
00016 Monterotondo Stazione
(Roma)
Italy

Chapter 13

François Mathis*, Joseph Salomon,
Sandrine Pagès-Camagna, Michel
Dubus, Dominique Robcis, Marc
Aucouturier, Sophie Descamps and
Elisabeth Delange
Centre de Recherche et de
Restauration des Musées de France –
CNRS UMR 171 Palais du Louvre
Porte des Lions
14 quai François Mitterrand
75001 Paris
France

E-mail:
francois.mathis@culture.gouv.fr

Chapter 14

Paolo Piccardo*
DCCI
Università di Genova
via Dodecaneso 31
16146 Genova
Italy

E-mail: paolo.piccardo@gmail.com
pol@chimica.unige.it

Benoît Mille
Centre de Recherche et de
Restauration des Musées de France
Paris
France

E-mail: benoit.mille@culture.gouv.fr

Luc Robbiola
Laboratoire de Métallurgie
Structurale
ENSCP
Paris
France

E-mail: luc-robbiola@enscp.fr

Chapter 15

Katerina Kreislova*, Dagmar
Knotkova and Vladimir Cihal
SVUOM Ltd
U Mestanskeho pivovaru 934
170 00 Prague
Czech Republic

E-mail: kreislova@svuom.cz

Jiri Had
VSCHT
Technicka 5
166 28 Prague
Czech Republic

E-mail: Jiri.Had@vscht.cz

Chapter 16

Henning Matthiesen*, David
Gregory and Birgit Sørensen
National Museum of Denmark
Department of Conservation
Archaeology – In situ preservation
I.C. Modewegsvej, Brede
DK-2800 Kgs. Lyngby
Denmark

E-mail:
henning.matthiesen@natmus.dk
cons@natmus.dk

Lisbeth Rischel Hilbert
Technical University of Denmark
Department of Manufacturing
Engineering and Management
Building 204
DTU
DK-2800 Kgs. Lyngby
Denmark

E-mail: lrh@ipl.dtu.dk

Chapter 17

Lena Sjögren*
Corrosion and Metals Research
Institute
Drottning Kristinas väg 48
SE-114 28 Stockholm
Sweden

E-mail: lena.sjogren@kimab.com

Nathalie Le Bozec
Institut de la Corrosion
Technopôle de Brest Iroise
220 rue Pierre Rivoalon
29200 Brest
France

E-mail: Nathalie.lebozec@institut-
corrosion.fr

Chapter 18

E. Rocca
Laboratoire de Chimie du Solide
Minéral
Université Henri Poincaré
Nancy I BP 239
54506 Vandoeuvre Les Nancy
France

E-mail: emmanuel.rocca@lcsm.uhp-nancy.fr

F. Mirambet
Laboratoire de Recherche des
Monuments Historiques
29 rue de Paris
77420 Champs-sur-Marne
France

E-mail:
francois.mirambet@culture.gouv.fr

Chapter 19

A. Galtayries*, A. Mongiatti and P. Marcus
Laboratoire de Physico-Chimie des
Surfaces
CNRS (UMR 7045)
Ecole Nationale Supérieure de
Chimie de Paris
11 rue P. et M. Curie
75005 Paris
France

E-mail: anouk-galtayries@enscp.fr

C. Chiavari
Formerly Centro di Studi sulla
Corrosione 'A. Dacco'
Dipartimento di Chimica
Università di Ferrara
Via L. Borsari 46
44100 Ferrara
Italy

Presently at Department of Metals
Science, Electrochemistry and
Chemical Techniques
Università di Bologna
Via Risorgimento, 4
40136 Bologna
Italy

E-mail: chiavari@bomet.fci.unibo.it

Chapter 20

C. Chiavari, C. Dinoi, C. Martini*,
D. Prandstraller
Department of Metals Science,
Electrochemistry and Chemical
Techniques
Università di Bologna
Via Risorgimento, 4
40136 Bologna
Italy

E-mail: carla.martini@unibo.it

G. Poli
Dipartimento di Ingegneria dei
Materiali e dell'Ambiente
Università di Modena
Via Vignolese 905
41100 Modena
Italy

E-mail: Giorgio.poli@unimore.it

European Federation of Corrosion (EFC) publications: Series introduction

The EFC, incorporated in Belgium, was founded in 1955 with the purpose of promoting European co-operation in the fields of research into corrosion and corrosion prevention.

Membership of the EFC is based upon participation by corrosion societies and committees in technical Working Parties. Member societies appoint delegates to Working Parties, whose membership is expanded by personal corresponding membership.

The activities of the Working Parties cover corrosion topics associated with inhibition, education, reinforcement in concrete, microbial effects, hot gases and combustion products, environment sensitive fracture, marine environments, refineries, surface science, physico-chemical methods of measurement, the nuclear industry, the automotive industry, computer based information systems, coatings, tribo-corrosion and the oil and gas industry. Working Parties and Task Forces on other topics are established as required.

The Working Parties function in various ways, e.g. by preparing reports, organising symposia, conducting intensive courses and producing instructional material, including films. The activities of the Working Parties are co-ordinated, through a Science and Technology Advisory Committee, by the Scientific Secretary. The administration of the EFC is handled by three Secretariats: DECHEMA e. V. in Germany, the Société de Chimie Industrielle in France, and The Institute of Materials, Minerals and Mining in the United Kingdom. These three Secretariats meet at the Board of Administrators of the EFC. There is an annual General Assembly at which delegates from all member societies meet to determine and approve EFC policy. News of EFC activities, forthcoming conferences, courses, etc., is published in a range of accredited corrosion and certain other journals throughout Europe. More detailed descriptions of activities are given in a Newsletter prepared by the Scientific Secretary.

The output of the EFC takes various forms. Papers on particular topics, for example, reviews or results of experimental work, may be published in scientific and technical journals in one or more countries in Europe. Conference proceedings are often published by the organisation responsible for the conference.

In 1987 the, then, Institute of Metals was appointed as the official EFC publisher. Although the arrangement is non-exclusive and other routes for publication are still available, it is expected that the Working Parties of the EFC will use The Institute of Materials, Minerals and Mining for publication of reports, proceedings, etc., wherever possible.

The name of The Institute of Metals was changed to The Institute of Materials on 1 January 1992 and to The Institute of Materials, Minerals and Mining with effect from 26 June 2002. The series is now published by Woodhead Publishing and Maney Publishing on behalf of The Institute of Materials, Minerals and Mining

P. McIntyre

EFC Series Editor,

The Institute of Materials, Minerals and Mining, London, UK

EFC Secretariats are located at:

Dr B. A. Rickinson

European Federation of Corrosion, The Institute of Materials, Minerals and Mining, 1 Carlton House Terrace, London, SW1Y 5DB, UK

Dr J. P. Berge

Fédération Européenne de la Corrosion, Société de Chimie Industrielle,
28 rue Saint-Dominique, F-75007 Paris, FRANCE

Professor Dr G. Kreysa

Europäische Föderation Korrosion, DECHEMA e. V., Theodor-Heuss-Allee
25, D-60486, Frankfurt, GERMANY

Volumes in the EFC series

- 1 **Corrosion in the nuclear industry**
Prepared by the Working Party on Nuclear Corrosion
- 2 **Practical corrosion principles**
Prepared by the Working Party on Corrosion Education (out of print)
- 3 **General guidelines for corrosion testing of materials for marine applications**
Prepared by the Working Party on Marine Corrosion
- 4 **Guidelines on electrochemical corrosion measurements**
Prepared by the Working Party on Physico-Chemical Methods of Corrosion Testing
- 5 **Illustrated case histories of marine corrosion**
Prepared by the Working Party on Marine Corrosion
- 6 **Corrosion education manual**
Prepared by the Working Party on Corrosion Education
- 7 **Corrosion problems related to nuclear waste disposal**
Prepared by the Working Party on Nuclear Corrosion
- 8 **Microbial corrosion**
Prepared by the Working Party on Microbial Corrosion
- 9 **Microbiological degradation of materials – and methods of protection**
Prepared by the Working Party on Microbial Corrosion
- 10 **Marine corrosion of stainless steels: chlorination and microbial effects**
Prepared by the Working Party on Marine Corrosion
- 11 **Corrosion inhibitors**
Prepared by the Working Party on Inhibitors (out of print)

- 12 **Modifications of passive films**
Prepared by the Working Party on Surface Science and Mechanisms of Corrosion and Protection
- 13 **Predicting CO₂ corrosion in the oil and gas industry**
Prepared by the Working Party on Corrosion in Oil and Gas Production (out of print)
- 14 **Guidelines for methods of testing and research in high temperature corrosion**
Prepared by the Working Party on Corrosion by Hot Gases and Combustion Products
- 15 **Microbial corrosion (Proc. 3rd Int. EFC workshop)**
Prepared by the Working Party on Microbial Corrosion
- 16 **Guidelines on materials requirements for carbon and low alloy steels for H₂S-containing environments in oil and gas production**
Prepared by the Working Party on Corrosion in Oil and Gas Production
- 17 **Corrosion resistant alloys for oil and gas production: guidance on general requirements and test methods for H₂S service**
Prepared by the Working Party on Corrosion in Oil and Gas Production
- 18 **Stainless steel in concrete: state of the art report**
Prepared by the Working Party on Corrosion of Reinforcement in Concrete
- 19 **Sea water corrosion of stainless steels – mechanisms and experiences**
Prepared by the Working Parties on Marine Corrosion and Microbial Corrosion
- 20 **Organic and inorganic coatings for corrosion prevention – research and experiences**
Papers from EUROCORR '96
- 21 **Corrosion-deformation interactions**
CDI '96 in conjunction with EUROCORR '96
- 22 **Aspects of microbially induced corrosion**
Papers from EUROCORR '96 and the EFC Working Party on Microbial Corrosion
- 23 **CO₂ Corrosion control in oil and gas production – design considerations**
Prepared by the Working Party on Corrosion in Oil and Gas Production

- 24 **Electrochemical rehabilitation methods for reinforced concrete structures – a state of the art report**
Prepared by the Working Party on Corrosion of Reinforcement in Concrete
- 25 **Corrosion of reinforcement in concrete – monitoring, prevention and rehabilitation**
Papers from EUROCORR '97
- 26 **Advances in corrosion control and materials in oil and gas production**
Papers from EUROCORR '97 and EUROCORR '98
- 27 **Cyclic oxidation of high temperature materials**
Proceedings of an EFC Workshop, Frankfurt/Main, 1999
- 28 **Electrochemical approach to selected corrosion and corrosion control**
Papers from 50th ISE Meeting, Pavia, 1999
- 29 **Microbial corrosion (Proc. 4th Int. EFC Workshop)**
Prepared by the Working Party on Microbial Corrosion
- 30 **Survey of literature on crevice corrosion (1979–1998): mechanisms, test methods and results, practical experience, protective measures and monitoring**
Prepared by F. P. Ijsseling and the Working Party on Marine Corrosion
- 31 **Corrosion of reinforcement in concrete: corrosion mechanisms and corrosion protection**
Papers from EUROCORR '99 and the Working Party on Corrosion of Reinforcement in Concrete
- 32 **Guidelines for the compilation of corrosion cost data and for the calculation of the life cycle cost of corrosion – a working party report**
Prepared by the Working Party on Corrosion in Oil and Gas Production
- 33 **Marine corrosion of stainless steels: testing, selection, experience, protection and monitoring**
Edited by D. Féron
- 34 **Lifetime modelling of high temperature corrosion processes**
Proceedings of an EFC Workshop 2001, edited by M. Schütze, W. J. Quadackers and J. R. Nicholls
- 35 **Corrosion inhibitors for steel in concrete**
Prepared by B. Elsener with support from a Task Group of Working Party 11 on Corrosion of Reinforcement in Concrete

- 36 **Prediction of long term corrosion behaviour in nuclear waste systems**
Edited by D. Féron of Working Party 4 on Nuclear Corrosion
- 37 **Test methods for assessing the susceptibility of prestressing steels to hydrogen induced stress corrosion cracking**
Prepared by B. Isecke on behalf of Working Party 11 on Corrosion of Steel in Concrete
- 38 **Corrosion of reinforcement in concrete: mechanisms, monitoring, inhibitors and rehabilitation techniques**
Edited by M. Raupach, B. Elsener, R. Polder and J. Mietz on behalf of Working Party 11 on Corrosion of Steel in Concrete
- 39 **The use of corrosion inhibitors in oil and gas production**
Edited by J. W. Palmer, W. Hedges and J. L. Dawson
- 40 **Control of corrosion in cooling waters**
Edited by J. D. Harston and F. Ropital
- 41 **Metal dusting, carburisation and nitridation**
Edited by M. Schütze and H. Grabke
- 42 **Corrosion in refineries**
Edited by J. Harston
- 43 **The electrochemistry and characteristics of embeddable reference electrodes for concrete**
Prepared by R. Myrdal on behalf of Working Party 11 on Corrosion of Steel in Concrete
- 44 **The use of electrochemical scanning tunnelling microscopy (EC–STM) in corrosion analysis: reference material and procedural guidelines**
Prepared by R. Lindström, V. Maurice, L. H. Klein and P. Marcus on behalf of Working Party 6 on Surface Science
- 45 **Local probe techniques for corrosion research**
Edited by R. Oltra on behalf of Working Party 8 on Physico-Chemical Methods of Corrosion Testing
- 46 **Amine unit corrosion survey**
Edited by F. Ropital on behalf of Working Party 15 on Corrosion in the Refinery Industry
- 47 **Novel approaches to the improvement of high temperature corrosion resistance**
Edited by M. Schütze and W. Quadackers on behalf of Working Party 3 on Corrosion in Hot Gases and Combustion Products

- 48 Corrosion of metallic heritage artefacts: investigation, conservation and prediction of longterm behaviour**
Edited by P. Dillmann, G. Béranger, P. Piccardo and H. Matthiesen on behalf of Working Party 4 on Nuclear Corrosion
- 49 Electrochemistry in light water reactors: reference electrodes, measurement, corrosion and tribocorrosion**
Edited by R.W. Bosch, D. Féron and J.P. Cells
- 50 Corrosion behaviour and protection of copper and aluminium alloys in seawater**
Edited by D. Féron
- 51 Corrosion issues in light water reactors: stress corrosion cracking**
Edited by D. Féron and J.-M. Olive
- 52 (to come)**
- 53 Standardisation of thermal cycling exposure testing**
Edited by M. Schütze and M. Malessa

This new EFC book is the first in the EFC Series to cover the corrosion aspects of archaeological artefacts and cultural heritage. It assembles a series of papers, of which most were presented at Eurocorr 2004, Nice, 12–16, September 2004, in a session dedicated to Heritage Conservation/Corrosion of Archaeological Objects (session 19).

The aims of these papers are well described and cover a broad spectrum:

- To allow reliable prediction for very long-term corrosion processes, in particular in connection with the disposal of nuclear waste. This requires a detailed knowledge of all aspects of the corrosion mechanisms: mineralogy, electrochemistry, transport of corrosive agents and corrosion products, etc.
- To build corrosion models and mechanisms, an exhaustive description of as many archaeological artefacts as possible is needed. Here, a series both of copper-based alloys (mostly bronzes) and ferrous materials are considered. The age of ferrous artefacts here covers a range from 80 to 1800 years.
- In doing this, recognising the original surface is already a problem. This is covered in several papers, with the description of the multiple layer soil–metal or concrete–metal interfaces (including corrosion products).
- Attention is also given to the modifications due to excavation (for example when chlorides are present) and to the most adequate conservation methods (controlled atmosphere, patina, corrosion inhibitors). Some studies cover an interesting approach to *in situ* conservation.

Among the bunch of facts and data, we find interesting ideas for dating the corrosion processes of given objects. We also learn about long-term corrosion processes (for example the future of tin from bronzes, or of galvanic couples between ferrous material and bronzes). Also exciting is what we learn about ancient techniques (metallurgy, patina, welding) and living conditions.

Highly specialised techniques were used and are reported in this book, which is of great value to corrosion researchers: Energy Dispersive Spectroscopy (EDS), micro X-ray diffraction (XRD), Scanning Electron Microscopy (SEM),

Electron Probe Microanalysis (EPMA), micro Raman Spectroscopy, Electrochemistry and others.

The interest of this book is at least twofold: first, of course, there is currently an increased interest worldwide for very long-term prediction of corrosion processes and of corrosion rates, in connection with the development of projects for the storage of nuclear wastes; and second, the book is full of interesting facts and data on archaeological artefacts, witnessing ancient techniques and habits.

This book is a link between engineers and scientists responsible for one of the big challenges of modern times (storage of nuclear wastes) and archaeologists and curators who devote their lives to their interest in ancient history.

It is a general common statement that learning from history is supposed to make us cleverer and wiser. In matters concerning the conduct of the world and peace, progress can be questioned. But let us hope that with regard to such issues as the disposal of nuclear waste, the lessons from the past will be better used. The aim of this book is to support this effort.

Antoine Pourbaix

Honorary Director of CEBELCOR, Brussels

For several decades, researches have been performed on heritage artefacts (both archaeological and historical) in order to determine the ancient smelting processes and methods of thermomechanical manufacture from the ore to the final object. Moreover, these approaches have provided much information on corrosion mechanisms over long periods. The results are also interesting in the field of conservation of heritage artefacts. The main aim of such studies is on the one hand to set up efficient conservation treatments but also, on the other hand, to give tools to the restorers to retrieve information concerning the corroded artefacts, such as the ancient shape, linked to the original surface. In parallel, in many European countries and especially in France, the need to predict in a reliable way the corrosion mechanisms of metallic materials that will be used for several hundred years, and even several thousand years in specific contexts such as the storage of nuclear wastes, requires the study of archaeological artefacts considered as analogues. For this reason, the nuclear industry, and especially Working Party 4 of the EFC, have encouraged these studies to provide new and significant findings concerning the corrosion of complex systems in which the thick layers of corrosion products play an important role. Indeed, studies on archaeological analogues submitted to corrosive environments in soils, water, atmospheres, binders and concretes during multi-secular periods are the only way to control the exact role of very long time periods in corrosion kinetics. This kind of approach needs great care in comparing the new materials and their corroding environment with those of the chosen analogues. This needs knowledge of corrosion science and various parallel disciplines such as electrochemistry, characterisation techniques, soil science, archaeological science, metallurgy, etc. Thus, for several years, with the help of joint programmes related to this very interdisciplinary field, some new and interesting results have been available for both conserving heritage artefacts and predicting material degradation in the future.

This book is based on papers presented at Eurocorr'2004 during the 'Corrosion of Heritage Artefacts' workshop and the common session with the 2nd workshop on 'Prediction of Long Term Corrosion Behaviour in Nuclear Waste Systems'. It includes also other papers and reviews from specialists in

the field. It presents different corrosion studies related to heritage artefacts following the two approaches of conservation and prediction of corrosion. Its aim is to fill the gap between these two disciplines and to share the experiences and skills of the scientists coming from the two communities. Thus, in the first part of the book, general overviews present the global frames and methodologies of these two communities. Then, the second part concerns mainly the prediction studies of corrosion of ferrous alloys in different environments based on the phenomenological understanding of mechanisms. In the third part, results of studies more dedicated to alteration of archaeological artefacts are discussed, in order to improve knowledge of restoration and conservation treatments. This part presents results and reviews on artefacts produced by copper- or iron-based alloys. The last part of the book is dedicated to the monitoring of specific archaeological or museum environments and to the exposition of specific conservation and prevention techniques.

This overview of the different approaches dealing with the study of the corrosion of heritage artefacts needs to be completed in the future. We would like to thank very much the reviewers: E. Angelini, M. Aucouturier, R. Bertholon, V. Cihal, P. Cristinia, C. Degrigny, V. Fell, J.-M. Gras, R. Gübner, L. Hilbert, J.-B. Memet, A. Pourbaix, P. Refait, L. Robbiola, T. Saario, W. Sand, G. Santarini and L. Selwyn, who represent the links between the conservation and the corrosion communities, which for the first time are presented together in the same book through their case studies, reviews, methodologies and results.

We hope that this first attempt to build a common language will last and that the book will be useful to both communities and will contribute to the future promotion of new interdisciplinary and international collaborations.

Philippe Dillmann, Gérard Béranger, Henning Matthiesen, Paolo Piccardo

Damien Féron

Chairman of the Working Party on Nuclear Corrosion (EFC WP4)

Examination and conservation of historical and archaeological metal artefacts: a European overview

C. DE GRIGNY, ICOM-CC Metal Working Group, France

1.1 Introduction

The investigation of metal artefacts and their conservation has been through major improvements in the last decades. In the past large samples were required to perform an accurate investigative analysis, while today only a small amount of metal is needed. Some techniques are even non-invasive (no sample taken). As regards conservation practices, the integrity of the artefact was previously not respected when cleaning the metal surface of its corrosion layers. As a result the original surface¹ (OS) was often lost. Today, no intervention is possible without respecting the OS and preserving any archaeological or historical information that can be retrieved during the cleaning process.

Surely all professionals consider the investigation and conservation of metal artefacts as being of equal importance. But when looking at the financial support they can benefit from, it is obvious that these two disciplines do not attract the same attention. Scientific examination and archaeometric studies (for dating and provenance) are the noble tasks in conservation science and still constitute most of the labours. In comparison, the design of conservation techniques and the definition of treatment parameters have been quite neglected. Even if the situation is improving, it seems that once the artefact has appeared to reveal all possible artistic, technological and historical information, we pay less attention to the possible loss of information that could occur during the conservation treatment. We know today that confidence in conservation practices suffered serious damage from over-mechanical cleaning of artefacts, the use of improper chemical treatments and various other practices that were not sufficiently controlled.

¹ Bertholon defines the OS of an archaeological object as the surface when it was abandoned [Bertholon 2001]. For historical objects the definition is more vague and depends on the nature of the artefact (tool: last used; sculpture: original artificial patina; etc.).

However, these mistakes had positive consequences, since professionals realised that any intervention needs to be monitored thoroughly. If, in the past, artefacts were given to trained technicians, it is commonly accepted that today special skills and knowledge are required to appreciate the complexity of artefacts and to treat them in a suitable manner.

Conservation science is a multidisciplinary field. The integrity of the artefact can only be respected if all specialists (archaeologists, art historians, conservators, conservation scientists and researchers) involved contribute to the choice of the best investigation and conservation techniques. In some countries with a long history of conservation science and a solid network of research centres, the collaboration of specialists at a national level is relatively straightforward. For other European countries that had to build their skills and knowledge from almost nothing, EU funding has given them real opportunities to set up their field of expertise and put them on the map of countries acting for the preservation of cultural heritage.

1.2 How scientific examination and archaeometric studies receive most of the funding

The need to better document artefacts that are witnesses of the development of past civilisations is universally accepted. Art historians are playing a key role here since they constantly need scientific data to support their theoretical approach. The literature in the field is quite abundant and some prominent research and cultural institutions even publish their own journals dedicated specifically to these topics (*Techné*² for the Centre for Research and Conservation of French Museums – UMR 171, Paris (France), and *Technologische Studien*³ for the Kunsthistorisches Museum, Vienna (Austria)). Other journals such as *ArtMatters*⁴ in the Netherlands cover topics of national interest. These new journals clearly show the need to disseminate the outcomes of research performed on artefacts not only to conservation professionals, but also to a larger audience. The general public is indeed more and more demanding as regards the available scientific information. There is no doubt, then, that everyone strongly supports the need for research laboratories dedicated to the better understanding of museum artefacts.

Ever since the discovery of X-radiography by Roentgen, researchers working on the diagnosis of museum artefacts have always promoted the use of the most innovative tools to document artworks. X-radiography was the starting

² *Techné – La Science au service de l'histoire de l'art et des civilisations*, Réunions des Musées Nationaux, Paris (France).

³ *Technologische Studien – Konservierung – Restaurierung – Forschung – Technologie*, Kunsthistorisches Museum, Vienna (Austria).

⁴ *ArtMatters*, Netherlands Studies in Art, Waanders Publishers, Zwolle (The Netherlands).

point for the creation of research conservation laboratories all around the world [Mohen 1996] and these laboratories are still working on developing tools that respond to the needs and ethics in this field (non-invasive approaches or, if needed, sampling of the minimum required amount of materials) [Janssens and Van Grieken 2004]. The field is constantly changing as the analytical techniques get more sophisticated. It is understandable that highly specialised researchers are required to develop tools that are specially adapted to the needs of the conservation field.

The following techniques are both non-invasive and adapted to the study of metal artefacts:

- Neutron radiography [Flügel *et al.* 2004] allows structural observation that is complementary to X-radiography.
- PIXE (Proton Induced X-ray Emission) is commonly used for the analysis of bronze [Gomez-Tubio *et al.* 2000, Martinot *et al.* 2000], silver [Constantinescu *et al.* 2000] and gold [Perea *et al.* 2000, Demortier and Ruvalcaba-Sil 2000] artefacts.
- MicroXRF [Pantazis *et al.* 2002] is particularly adapted for portable elementary analysis.
- Neutron diffraction [Kockelmann *et al.* 2003] gives valuable information on phase contents and volume textures.

Other techniques are more adapted to the structural study of corrosion products:

- microRaman spectroscopy [Neff *et al.* 2004]
- microXRD [Dillmann *et al.* 2002].

These techniques often belong to exceptional research infrastructures that are primarily accessible to the national user community, but EU programmes such as the Access to Research Infrastructures (Improving the Human Research Potential and the Socio-economic Knowledge Base) have offered the possibility of finding and implementing the solutions to problems of common interest through networking activities. The Laboratories on Science and Technology for the Conservation of the European Cultural Heritage (*LabS TECH*⁵) is such a network. It aims to promote the sharing of knowledge, skills, expertise and resources in the field [Brunetti 2003]. The *LabS TECH* project is now completed and has been followed by the *ARTECH*⁶ (Access Research and Technology for the conservation of the European Cultural Heritage) project funded under the EU sixth Framework Programme (Structuring the European Research Area – Research Infrastructures) with similar aims to those of *LabS TECH*.

⁵ <http://www.chm.unipg.it/chimgen/LabS-TECH.html>

⁶ <http://becu.chm.unipg.it/euartech/HOME.htm>

The networking between major research laboratories working in conservation science is one aspect; the networking between the professionals involved is another. The EU COST (European Cooperation in the Field of Scientific and Technical Research) actions have been established to respond to the need for exchange of knowledge through the regular meeting of experts, the organisation of workshops or training schools and the mobility of researchers (through short-term scientific missions). COST Action G8⁷ (and previously G1 [Demortier and Adriaens 2000]), 'Non-destructive testing and analysis of museum objects', has played a major role in networking conservation professionals and scientists. Its main objective was to improve the synergy between art historians, archaeologists, conservators and natural scientists. This included the exchange of knowledge about the available non-destructive techniques and the requirements to perform investigations on valuable or unique objects. In addition, museums and similar institutions obtained easy access to universities and research facilities that provide such techniques.

Although the examination of artefacts and archaeometric studies correspond to a real need and constitute activities that are easily funded, research in conservation suffers terribly from lack of funds and interest from researchers. There are many reasons for this. Firstly, conservation science is a new field. Although scientists like Rathgen designed, as early as the end of the nineteenth century, conservation protocols based on scientific approaches [Gilberg 1987], these protocols were considered more as recipes than as major scientific discoveries. Their aim was to solve a 'technical problem' such as the stabilisation (extraction of aggressive species) of artefacts that were suffering from active corrosion; they were not really aiming to reveal major information from the artefacts themselves. No more funds than those required to address this technical problem were provided.

The conservation field still suffers from the problem that its outcomes are not always perceptible. What does stabilisation mean to the financial deciders? Almost nothing. The work of conservators should be promoted, since if the public can today admire all kinds of metal artefacts in museums it is often thanks to the tremendous work of these professionals assuring the long-term conservation of these artefacts. When properly informed the public get very enthusiastic about the work of conservators. However, conservation is regarded more as a skilful activity than as a field where research is required. Consequently, both conservators and conservation scientists have to disseminate in a clearer way the outcomes of their work. For instance, an exhibition such as the one organised in France in 1999 by the Musée d'Archéologie du Val d'Oise, *A la recherche du métal perdu – Les nouvelles technologies dans la restauration des métaux archéologiques*, was of particular significance. For

⁷ <http://srs.dl.ac.uk/arch/cost-g8>

the first time all innovative conservation technologies applied in the conservation of metals were presented in a didactic way to the wider public [Meyer 1999] and clearly demonstrated the recent impact of conservation science on the better understanding and preservation of metal artefacts.

Furthermore, conservation treatments are regarded as quite empirical since they do not respond exactly to the needs of each artefact. As we all know, any artefact raises specific conservation issues, but it is impossible to develop a special treatment for each of them. This is especially the case when thousands of similar artefacts have to be stabilised. Here conservators have designed protocols based on mass treatments, which require a thorough preliminary study of the whole collection. Only artefacts that have visually similar conservation problems can be treated according to the protocol defined. Although this work is performed by specialists who have learnt how to read the damage to historical and archaeological artefacts, side-effects often occur during the treatment, such as flaking and destruction of associated information (organic materials, etc.). These side-effects can be controlled, and the more experienced the conservator, the safer the applied treatments.

Conservation scientists who develop innovative conservation treatments to address specific issues or optimise the existing ones often have a difficult, yet exciting task. They need to follow up the work of conservators to understand the limits of the treatments currently used and to determine how they can be improved. The problem is that not all conservators are ready to allow someone (even a colleague) to critically assess the treatment that they apply. There is, however, no other solution than to put the problems posed by a specific treatment, or by a collection that responds badly to a treatment, on the table and to discuss them in order to find the reason for the failure. One understands, in that case, why not many conservation scientists choose to work in the conservation area. It is certainly necessary for conservation scientists to communicate very diplomatically with conservators. These professionals have gained with time a good experience of several conservation treatments that they use in their own way. To be critical, conservation scientists must not only possess a solid scientific background to understand the issues raised by conservators, but have much experience of the treatments themselves. Like a patient in front of his doctor, the conservator will easily see whether the scientist facing him knows what he or she is talking about. The discussion will be possible only if there is common respect for each other and a good mutual understanding of the issues raised.

To summarise, conservation scientists devoting their time to the conservation field do not have an easy task. The understanding of conservation issues and practices is not straightforward. Once this knowledge is acquired they must accept the development of treatments that will be used as recipes, with specifically adapted variations, by end-users. Only after some years of experience and a real and trusting relationship with conservators will some

promising applied research programmes emerge in which both the conservator and the conservation scientist involved will play a key role.

1.3 The necessity for research on conservation of historical and archaeological artefacts

We have seen in the previous section that it is often difficult to secure funding for research projects in the conservation field. We might wonder, then, whether there is really a need to perform such research activities at all. It is the objective of this section to demonstrate through case studies that not only is research in conservation absolutely required, but it is also possible to find financial support.

1.3.1 The *in-situ* conservation of artefacts: an option that has become a priority

New policies regarding the management of archaeological and historical artefacts have drastically changed our attitude towards the conservation of artefacts. If some years ago the trend was to recover all artefacts during excavations, the limited funding for conservation purposes associated with the huge amount of artefacts recovered has forced us to reconsider this approach and to set up strategies to conserve them *in situ*.

A good illustration of such a strategy is found with the Iron Age site of Nydam Mose (Denmark) discovered in 1859 [Soerensen and Gregory 1998]. Some 16,000 artefacts dating from AD 200–500 were excavated between 1989 and 1997 within a small fraction of this major waterlogged site. Due to the impossibility of raising the necessary funds to excavate properly the extremely large number of objects on the whole site and to conserve and document them, a decision was taken in 1997 to stop further excavations. To support this policy, environmental specialists set up different monitoring programmes, both on the artefacts and on the environment. Metal artefacts were also investigated and specific corrosion features (formation of siderite) were revealed through *in-situ* corrosion studies.

This research, performed by the National Museum of Denmark and its conservation division at Brede, could have been an isolated experience without the recent interest of French scientists in the long-term behaviour of iron alloys in soils in order to store nuclear wastes. Incidentally, artefacts recovered from the French archaeological site of the Glinet presented corrosion features similar to those developed at Nydam Mose. These features were used to further understand the corrosion processes developed on iron in the long term [Vega 2004] and, Danish and French teams initiated a strong collaboration through short-term scientific missions funded under COST Action G8 and its working group ‘Degradation processes, corrosion and weathering’.

Marine metal artefacts are another category of objects that have often been recovered without previously considering any appropriate post-excavation conservation strategies. Since these artefacts are highly unstable when exposed to the atmosphere, it is preferable to assure their *in-situ* conservation before a decision is taken as regards their recovery. *In-situ* conservation in this instance means monitoring the corrosion potential (E_{corr}) of the artefacts through time [Gregory 2000] and, in the case of the development of any active corrosion, protecting the artefact with sacrificial anodes [Gregory 1999]. The technique is quite simple in itself. The interpretation of the results is less so, and European professionals had to be trained by the expert in this field, Ian MacLeod [MacLeod 1989]. Today other countries such as Portugal [MacLeod and Schindelholz 2004] and France are interested in monitoring marine artefacts through the *in-situ* measurements of E_{corr} .

A similar concern applies to artefacts stored in museums or in collections that are rarely monitored. Preventive conservation strategies have been set up to monitor the environment surrounding the objects and to assure their long-term conservation. For silver artefacts that are highly sensitive to tarnishing, silvered samplers are placed inside showcases or in storage areas, in an area where the curator can easily detect the start of the alteration process [Lacoudre *et al.* 1998]. The extent of the corrosion process can easily be calculated through the thickness of the Ag_2S layer formed. The protection of silver collections from tarnishing has benefited from European funds through the EU SILPROT [Ankersmit *et al.* 2004] project of the Fourth Framework Programme – Environment and Climate (second phase: Technologies to protect and rehabilitate the European Cultural Heritage). The three research components were to develop and validate passive samplers that could be used in museums; to synthesise, characterise and test new absorbents; and to identify and evaluate suitable transparent polymer films for the long-term storage of silver.

Lead artefacts are also suffering in collections due to the evolution of aggressive organic acid vapours (acetic acid) from the wooden cabinets in which they are conserved [Degrigny and Le Gall 1999]. The same problem occurs on lead organ pipes that are currently being studied under the EU COLLAPSE project [Niklasson *et al.* 2004] funded within the Fifth Framework Programme – Energy, Environment and Sustainable Development. In that case there is no other solution than to remove the corrosive species and to stabilise the corroded artefacts.

More recently the EU PROMET project (Innovative conservation approaches for monitoring and protecting ancient and historic metals collections from the Mediterranean Basin) funded within the Sixth Framework Programme, priority INCO (specific measures in support of international cooperation), has been designed to establish and promote a conservation strategy by developing an approach to monitor and protect metal artefact collections

using state-of-the-art portable analytical techniques and new corrosion inhibitors and/or coatings that are safe and effective to use [Argyropoulos 2004]. This project started in November 2004 and should more specifically study iron-, copper- and silver-based collections. The great appeal of this project is that it involves a transfer of knowledge between EU countries and the countries of the Mediterranean basin that often do not have the resources to correctly preserve their collections.

1.3.2 Fundamental and applied research to solve conservation issues: a few success stories

Another reason why research in the conservation of metal artefacts is poorly supported might be the absence of clarity as regards the real needs of research in the field. However, these needs are known at an international level through the activity of voluntary-based organisations such as ICOM-CC (International Council of Museums – Conservation Committee). The Metal Working Group (WG) is particularly active here and its publications METAL 95, 98, 01 and 04 (MacLeod *et al.*, 1995, Mourey and Robbiola 1998, MacLeod *et al.* 2004, Ashton and Hallam 2004) are recognised worldwide. Every three years, new themes are chosen. For 2002–08 the working group is supporting research in archaeometry and conservation studies, use of electrochemical techniques in conservation, protection of metal artefacts and study/conservation of composite objects. The investigation of artefacts is not neglected since one theme deals with the development of innovative diagnostic techniques.

Some important researches have been performed on corrosion layers formed on copper or iron archaeological artefacts. They have attracted industrial funds due to the possibility of using these materials as analogues to predict the behaviour of buried structures [Dillmann 2004]. Several PhD research projects thoroughly studied the corrosion layers formed on iron artefacts using micro Raman spectroscopy and micro XRD with Synchrotron Radiation [Pons 2002, Neff 2003, Vega 2004] as well as the developed corrosion processes. These investigations have greatly modified our perception of the corrosion layers formed on archaeological iron artefacts.

These researches would not have been possible without the preliminary descriptive investigation of corrosion layers developed by Bertholon [Bertholon 2001]. When cleaning artefacts conservators are always trying to approach their original surface (OS) to make them more legible. Until recently the cleaning process was considered as highly empirical and depended on the skills and experience of conservators. Bertholon defined a model where corrosion layers are studied in detail like stratigraphic layers on excavation sites. This model also depends on markers that permit the precise location of the OS. These markers might be either specific corrosion layers (generally magnetite for iron-based alloys or cuprite for copper-based alloys), compounds

from the external environment (sand/soil) or traces of the original metal. Analytical investigation is required to identify these markers and determine their distribution in the corrosion layers. The conservator and the conservation scientist or researcher must then pool their efforts and knowledge to fully understand how the corrosion develops, shapes the corrosion layers and develops further in the future (as reactivated corrosion).

For copper-based artefacts, past efforts concentrated more on the study of corrosion layers [Robbiola *et al.* 1998]. Recent research is devoted more to the study of artificial and natural patinas that form on these materials [Robbiola *et al.* 2004, Aucouturier *et al.* 2003].

The study of corrosion layers on copper- and iron-based artefacts appears to be a French speciality. Some specific aspects that are more conservation-related are investigated in other countries such as Germany. Eggert has been examining for several years the formation of 'black spots' on copper-based artefacts [Eggert *et al.* 2004]. These efflorescences, containing both copper and sulphur, occur during the display or storage of artefacts when they are exposed to reduced sulphur gas. More intriguing are the 'brown spots' that have been observed recently on gold coins and medals of the Coin Cabinet of the Kunsthistorisches Museum, Vienna, Austria [Griesser *et al.* 2003]. Scientific investigation has shown that the spots are due to silver pollution during the manufacturing process. As regards tarnishing on silver artefacts, the formation of an adherent layer is not systematic. For some specific alloys (those containing copper), delamination of the copper sulphide layer occurs as the thickness of the layer grows [van Langh *et al.* 2004].

Beyond the understanding of corrosion processes and their effect on artefacts, a lot of specialists work on the development of innovative conservation treatments. For some years now Switzerland has been the leading country for the treatment of metallic artefacts by plasma. Research is still in progress to understand how the plasma affects corrosion layers, especially on iron artefacts [Schmidt-Ott 2004]. The optimisation of the treatment makes it possible today to work at very low temperatures (85°C) while still reducing iron corrosion products. There is no doubt that this research will contribute to the promotion of this technique, not only in Switzerland but also in other countries where it is currently used (France, Greece and Denmark).

Electrochemical techniques are used more and more in the conservation field. Although known since the end of the nineteenth century [Gilberg 1987] these techniques were considered as very dangerous until the 1980s when they were reviewed and their use became based on a really scientific approach [Lacoudre and Degriigny 1999]. These techniques are used as spot tests (measurement of E_{corr} vs. time), to monitor the behaviour of patina on outdoor bronze monuments (measurement of E_{corr} [Crespo *et al.* 2004], R_p [Bertolini *et al.* 1995] or EIS [Letardi 2004]) or on artefacts in storage [Leysens *et al.* 2004, Degriigny and Spiteri 2004], to clean encrusted marine metal artefacts

[Degrigny 2005] or tarnished silver through the reduction of Ag_2S to Ag [Degrigny *et al.* 1993], to stabilise active iron- and copper-based artefacts [Degrigny 2005], and to assess the protection applied on metals [Letardi 2004].

Another very promising field is the mechanical cleaning of metals by laser [Pini *et al.* 2000]. Very good results have been obtained on gilt bronzes [Matteini *et al.* 2003], and this technique could also bring some solutions to the issues raised by the cleaning of metallic textile threads where a dry conservation technique has to be used [Degrigny *et al.* 2003].

Due to the specificity of these techniques, conservation laboratories are working in close collaboration with research centres and universities. The number of professionals involved remains very low, however, and prevents the widespread diffusion of the acquired knowledge. As a consequence the use of innovative conservation techniques is often restricted to the laboratories where they have been developed. In France plasma is used at the Musée Archéologique Départemental du Val d'Oise [Normand-Chave *et al.* 2001] and electrolytic techniques are mainly developed at Arc'Antique [Degrigny 2005].

Apart from electrolytic techniques, these innovative conservation treatments require expensive equipment that most conservation laboratories cannot afford. Since the research centres owning such equipment have made special efforts to apply it to the conservation field, it is essential that once the techniques become established, conservators can access and make use of such equipment and feed back their experience to the research centres for further development of instruments specifically designed for practical conservation work.

1.4 Training in conservation science: a chance for better recognition of the discipline?

Training in conservation science is not the same throughout Europe. Some countries have no curriculum dedicated to conservation science. Conservation scientists usually have a natural science background and become specialised through a Masters degree or a PhD on a subject related to the heritage conservation field. The consequence is that often these scientists lack sensitivity for the artefacts and are interested only in diagnosis. The recent development of training programmes at Bachelors and Masters levels dedicated to conservation science, such as in Italy, might change the whole picture in the coming years.

Some years ago ICCROM (the International Centre for the Study of the Preservation and Restoration of Cultural Property) coordinated the EU Leonardo CURRIC (Vocational Training Curricula for Conservation Scientists) project whose aim was to design a European PhD curriculum in conservation science made up of modules that would be taught in several European universities

specialising in different disciplines [Mazzeo and Eshøj 2002]. Since then this interesting idea has been put into practice through the EPISCON project⁸ funded by the EU Marie Curie programme. Hopefully it will solve the issue of the lack of multidisciplinary among current conservation scientists.

The way conservation science is taught in conservation schools is another important issue. Chemistry and scientific investigation are considered as essential components of the programme. But one should not neglect the necessary collaboration between conservation students and conservation scientists on conservation projects in putting into practice the theoretically acquired knowledge. Another field that is often completely neglected in the curriculum of students trained in metal conservation is the proper use of electrolytic techniques. Again theoretical courses might exist on corrosion science, but the practical use of this knowledge is hardly covered. Often conservation students do not realise that good knowledge of corrosion science is essential not only to understand corrosion processes but also to design appropriate conservation treatments by immersion.

ENCoRE⁹ (European Network for Conservation/Restoration Education) has a key role to play in upgrading the level of conservation science in the education of conservation students. Giving conservators the opportunity to pursue their studies at a Masters or a PhD level should generate a community of conservation scientists with both a solid conservation and a scientific background, who would then be perfect coordinators of major conservation projects where synergy between different disciplines is required.

1.5 Pro-active responsibilities for conservators

The building of the EU and the support given to research programmes has changed the picture of how European research is funded in the field. The mentality of conservation scientists is changing slowly, but surely. They know today that they have to compete to get funds and to produce a lot of new concepts and innovative approaches to remain at the top. Old and passive conservation laboratories will disappear, but new and very active ones will emerge.

When we look at the partners involved in these EU programmes we might be surprised to find mainly members of research institutions and universities. Conservation professionals are few. We should be concerned about this, since if the trend continues it might be that in the near future research institutes that are not really involved in the conservation of cultural heritage but that are good in applying for funds will be those that receive funds to coordinate research in conservation. This is a really significant concern,

⁸ www.episcon.scienze.unibo.it

⁹ <http://www.encore-edu.org>

since there is some chance that funds would then not be used to respond to the real needs of the end-users. The positive aspect, though, is that the renewal of teams brings innovative ideas from other fields (industry) that are not directly related to the conservation field.

EU programmes are then essential to fund research projects performed at a national level. It is therefore the duty of teams in the different EU countries to define research themes that are relevant to their national needs, and to set up multidisciplinary teams comprising art historians, conservation scientists and researchers. In parallel, these different actors have to apply for funds to conduct their work. These funds can come either from the EU or from a non-EU origin.

Collaborating at EU or international levels is quite difficult and requires organisational skills that not all researchers and institutions have. Furthermore, research is normally funded for only three or four years and, since research in conservation science is often complicated, further work is always needed. Only a few institutions are really successful in obtaining regular funds to support research activities. Most of the others get some support for three years only, making the efforts that were used to build the research team unsustainable in the long term.

To summarise, managers and directors in charge of policy should consider building national teams in charge of research and giving them the possibility to apply for external funds (such as EU funds). Local resources should also be considered that are specific to the cultural heritage in each country.

1.6 Networking

The community of professionals specialising in the investigation and conservation of metal artefacts is quite well structured. Working groups exist on archaeometry and conservation topics. The French Groupe des Méthodes Pluridisciplinaires Contribuant à l'Archéologie (GMPCA¹⁰) is here particularly active. Its members meet regularly to discuss dating and provenance issues.

In conservation the most active group of professionals is, without any doubt, the ICOM-CC Metal working group. Outside the triennial interim meetings the working group has its own bulletin, the *BROMECC* (Bulletin of Research On METal Conservation), that is published every three months on the Metal homepage of the ICOM-CC website: <http://icom-cc.icom.museum/WG/Metals/>. The aim of this bulletin is to inform, on a regular basis, members of research projects in this field throughout the world. Furthermore, it gives the opportunity to conservation students to present their work. *BROMECC* also maintains the working group's dynamism between the triennial METAL conferences.

¹⁰ <http://gmpca.u-bordeaux3.fr/index.php>

Recently some sub-working groups have been set up under the Metal WG to cover topics of interest to some particularly active members. To date there are six sub-WGs: AIAE (Archaeological Iron After Excavation), BAC (Bridging Archaeometry and Conservation), EMCN (Enamels on Metals Conservation Network), ETIC (use of Electrochemical Techniques in Metal Conservation), IECO (Conservation of Industrial and Engineering Cultural Objects) and NDTMA (New Diagnostic Tools for Metal Conservation). The activities of these sub-WGs (minutes and PowerPoint presentations of meetings, news, bibliographies, etc.) can be found on the Metal homepage.

1.7 Conclusion

Experience has shown that research in the field of metal artefact conservation fluctuates. It is not healthy, but funds are not unlimited. Professionals have to consolidate the efforts made, and bring new expertise that can attract greater attention and funding.

Since the peak of activity during the Fifth Framework Programme the funding of EU projects related to the cultural field has decreased, but there is hope that the situation will improve and the community of professionals involved in metal conservation has to be prepared to respond to the availability of funds. Informing professionals of current opportunities, networking them and promoting their skills and expertise are key actions that should sustain the dynamism of these professionals.

Professionals working in the European area also have to realise the opportunities they have to apply for funds that simply do not exist in other parts of the world. The international conservation community envies us for the support we can receive to perform top-quality research. It is essential that we make the best use of these funds for the benefit of research in the conservation field.

1.8 References

- Ankersmit, H.A., Carbo, A.D. and Tennent, N.H. 2004, Tarnishing of silver: evaluation by colour measurements, in *Proceedings of the International Conference on Metals Conservation, METAL 01*, Santiago de Chile, ed. I.D. MacLeod, J.M. Theile and C. Degrieny, Western Australian Museum, Fremantle, 157–166.
- Argyropoulos, V., Angelini, E. and Degrieny, C. 2004, Innovative conservation approaches for monitoring and protecting ancient and historic metals collections from the Mediterranean basin, in *Proceedings of the International Conference on Metals Conservation, METAL 04*, Canberra, Ed. J. Ashton and D. Hallam, National Museum of Australia, Canberra, 43–52.
- Ashton, J. and Hallam, D. (ed.) 2004, *METAL04, Proceedings of the International Conference on Metal Conservation*, Canberra, National Museum of Australia, Canberra.
- Aucouturier, M., Keddam, M., Robbiola, L. and Takenouti, H. 2003, Les patines des alliages de cuivre: processus naturel ou oeuvre de l'homme, *Techné*, **18**, 86–94.

- Bertholon, R. 2001, Characterisation and location of original surface of corroded metallic archaeological objects, *Surface Engineering*, **17**, (3), 241–245.
- Bertolini, M., Colombo, B., Marabelli, M., Marano, A. and Parisi, C. 1995, Non-destructive tests for the control of ancient metallic artefacts, in *Proceedings of the International Conference on Metals Conservation, METAL 95*, Semur-en-Auxois (France), ed. I.D. MacLeod, S.L. Pennec and L. Robbiola, James & James, London, 43–49.
- Brunetti, B.G. 2003, *LabS TECH – Science and Technology for the Conservation of the European Cultural Heritage*, ed. A.M. Johansson, Programme for Improving the Human Research Potential and the Socio-Economic Knowledge Base, EU publications.
- Constantinescu, B., Bugoi, R. and Sasianu, A. 2000, Greek silver drachmae of the Roman Civil War Period (1st century BC) as reflected in external beam PIXE analysis, in *Ion Beam Study of Art and Archaeological Objects, A Contribution by Members of the COST Action G1*, ed. G. Demortier and A. Adriaens, EU 19218, 84–87.
- Crespo, M., Cicileo, G. and Rosales, B. 2004, Electrochemical characterisation of patina protectiveness evolution on outdoor bronze sculptures, in *Proceedings of the International Conference on Metals Conservation, METAL 04*, Canberra, ed. J. Ashton and D. Hallam, National Museum of Australia, Canberra, 185–194.
- Degrigny, C. 2005, Altération et conservation des objets métalliques issus de fouilles sous marines – Part II, in *Proceedings of the EU ANSER Workshop ‘Innovative Technologies and Methodologies to Study and Conserve Archaeological Artefacts’*, Livorno, Italy, 31 May–5 June 2004.
- Degrigny, C. and Le Gall, R. 1999, Conservation of ancient lead artefacts corroded in organic acid environments: electrolytic stabilisation/consolidation, *Studies in Conservation*, **44**, 157–169.
- Degrigny, C. and Spiteri, L. 2004, Electrochemical monitoring of marine iron artefacts during their storage/stabilisation in alkaline solutions, in *Proceedings of the International Conference on Metals Conservation, METAL 04*, Canberra, ed. J. Ashton and D. Hallam, National Museum of Australia, Canberra, 315–331.
- Degrigny, C., Jérôme, M. and Lacoudre, N. 1993, Surface cleaning of silvered brass wind instruments belonging to the Sax collection, *Corrosion Australasia*, **18**, (2), 16–18.
- Degrigny, C., Tanguy, E., Le Gall, R., Zafiropoulos, V. and Marakis, G. 2003, Laser cleaning of tarnished silver and copper threads in museum textiles, *Journal of Cultural Heritage*, **4**, (S1), 152–156.
- Demortier, G. and Adriaens, A. 2000, *Ion Beam Study of Art and Archaeological Objects, A Contribution by Members of the COST Action G1*, EU 19218.
- Demortier, G. and Ruvalcaba-Sil, J.L. 2000, Depth profiling of the gilding on Mesoamerican jewellery items, in *Ion Beam Study of Art and Archaeological Objects, A contribution by Members of the COST Action G1*, ed. G. Demortier and A. Adriaens, EU 19218, 105–109.
- Dillmann, P. 2004, Corrosion des objets archéologiques ferreux, *Les Techniques de l’Ingénieur*, COR 675, 20 pp.
- Dillmann, P., Neff, D., Mazaudier, F., Hoerle, S., Chevallier, P. and Béranger, G. 2002, Characterization of iron archaeological analogues using micro diffraction under synchrotron radiation. Application to the study of long term corrosion behaviour of low alloy steels, *J. Phys. IV*, France, 393–408.
- Eggert, G., Weichert, M., Euler, H. and Barbier, B. 2004, Some news about ‘Black Spots’, in *Proceedings of the International Conference on Metals Conservation, METAL 04*, Canberra, ed. J. Ashton and D. Hallam, National Museum of Australia, Canberra, 142–148.

- Flügel, C., Blumenau, E., Deschler-Erb, E., Hartmann, S. and Lehmann, E. 2004, Römische Cingulumbeschläge mit Millefiorieinlagen, *Archäologisches Korrespondenzblatt*, Römisch-Germanisches Zentralmuseum Mainz, 34/4.
- Gilberg, M. 1987, Friedrich Rathgen: the father of modern archaeological conservation, *Journal of the American Institute of Conservation*, **26** (2), 105–120.
- Gomez-Tubio, B.M., Respaldiza, M.A. and Barranco, F. 2000, Non-destructive analysis of archaeological bronzes, in *Ion Beam Study of Art and Archaeological Objects, A Contribution by Members of the COST Action G1*, ed. G. Demortier and A. Adriaens, EU 19218, 72–75.
- Gregory, D. 1999, Monitoring of the effect of sacrificial anodes on the large iron artefacts on the Duart Point wreck, *International Journal of Nautical Archaeology*, **28** (2), 164–173.
- Gregory, D. 2000, *In-situ* corrosion studies on the submarine *Resurgam*, A preliminary assessment of her state of preservation, *Conservation and Management of Archaeological Sites*, 93–100.
- Griesser, M., Denk, R., Griehl, M., Traum, R. and Winter, H. 2003, The past and the future – investigating brown spot corrosion on historic gold coins and medals to advance their preservation, in *Proceedings of Numismatics and Technology: Questions and Answers*, 25–26 April 2003, KHM, Vienna, 91–98.
- Janssens, K. and Van Grieken, R. 2004, *Non-destructive Microanalysis of Cultural Heritage Materials*, Volume XLII in the series Comprehensive Analytical Chemistry, Elsevier, Amsterdam, 800 pp.
- Kockelmann, W., Kirfel, A., Jansen, E., Linke, R., Schreiner, M., Traum, R. and Denk, R. 2003, Neutron diffraction for non-destructive texture analysis of minted and cast ‘Taler’ coins, in *Proceedings of Numismatics and Technology: Questions and Answers*, 25–26 April 2003, KHM, Vienna, 113–123.
- Lacoudre, N. and Degriigny, C. 1999, Les techniques électrolytiques, in *A la Recherche du Métal Perdu – Les Nouvelles Technologies dans la Restauration des Métaux Archéologiques*, ed. H. Meyer, Errance, Paris, 114–127.
- Lacoudre, N., Beldjoudi, T. and Dugot, J. 1998, Influence des conditions d’exposition et de protection des surfaces sur l’altération de plaquettes en laiton argenté au Musée de la Musique à Paris, in *Proceedings of the International Conference on Metals Conservation, METAL 98*, Draguignan-Figanières (France), ed. W. Mourey and L. Robbiola, James & James, London, 265–270.
- Letardi, P. 2004, Laboratory and field tests on patinas and protective coating systems for outdoor bronze monuments, in *Proceedings of the International Conference on Metals Conservation, METAL 04*, Canberra, ed. J. Ashton and D. Hallam, National Museum of Australia, Canberra, 379–387.
- Leysens, K., Adriaens, A., Pantos, E. and Degriigny, C. 2004, Study of corrosion potential measurements as a means to monitor the storage and stabilisation processes of archaeological copper artefacts, in *Proceedings of the International Conference on Metals Conservation, METAL 04*, Canberra, ed. J. Ashton and D. Hallam, National Museum of Australia, Canberra, 332–343.
- MacLeod, I.D. 1989, The application of corrosion science to the management of maritime archaeological sites, *Bulletin of the Australian Institute for Maritime Archaeology*, **32** (2), 7–16.
- MacLeod, I.D. and Schindelholz, E. 2004, Surface analysis of corroded silver coins from the wreck of the San Pedro de Alcantara (1786), in *Proceedings of the International Conference on Metals Conservation, METAL 04*, Canberra, ed. J. Ashton and D. Hallam, National Museum of Australia, Canberra, 114–125.

- MacLeod, I.D., Pennec, S. and Robbiola, L. (ed.) 1995, *METAL95, Proceedings of the International Conference on Metal Conservation*, Semur en Auxois (France), James & James, London, 1995.
- MacLeod, I.D., Theile, J.M. and Degriigny, C. (ed.) 2004, *METAL01, Proceedings of the International Conference on Metal Conservation*, Santiago de Chile, Western Australian Museum, Fremantle.
- Martinot, L., Strivay, D., Guillaume, J. and Weber, G. 2000, PIXE analysis of brass alloys, in *Ion Beam Study of Art and Archaeological Objects, A Contribution by Members of the COST Action G1*, ed. G. Demortier and A. Adriaens, EU 19218, 76–80.
- Matteini, M., Lalli, C., Tosini, I., Giusti, A. and Siano, S. 2003, Laser and chemical cleaning tests for the conservation of the Porta del Paradiso by Lorenzo Ghiberti, *Journal of Cultural Heritage*, **4** (S1), 147–151.
- Mazzeo, R. and Eshøj, B. 2002, Designing university postgraduate curricula for conservation scientists, *ICOM-CC Triennial Meeting*, Rio de Janeiro, Brazil, **1**, 137–141.
- Meyer, H. 1999, *A la Recherche du Métal Perdu – Les Nouvelles Technologies dans la Restauration des Métaux Archéologiques*, Errance, Paris, 192 pp.
- Mohen, J.-P. 1996, *L'Art et la Science. L'esprit des Chefs-d'œuvre*, Découvertes Gallimard/RMN no. 299, 160 pp.
- Mourey, W. and Robbiola, L. (ed.) 1998, *METAL98, Proceedings of the International Conference on Metal Conservation*, Draguignan-Figanières (France), James & James, London.
- Neff, D. 2003, Apport des analogues archéologiques à l'estimation des vitesses moyennes et à l'étude des mécanismes de corrosion à très long terme des aciers non alliés dans les sols, thesis, Université Technologique de Compiègne, 360 pp.
- Neff, D., Reguer, S., Bellot-Gurlet, L., Dillmann, P. and Bertholon, R. 2004, Structural characterisation of corrosion products on archaeological iron. An integrated analytical approach to establish corrosion forms, *Journal of Raman Spectrometry*, **35**, 739–745.
- Niklasson, A., Johannsson, L.G. and Svensson, J.-E. 2004, Atmospheric corrosion of historic organ pipes: influence of acetic and formic acid vapour and water leaching on lead, in *Proceedings of the International Conference on Metals Conservation, METAL 04*, Canberra, ed. J. Ashton and D. Hallam, National Museum of Australia, Canberra, 273–280.
- Normand-Chave, C., Leprince, P. and Dussère, F. 2001, Plasma treatment of artefacts, *Surface Engineering*, **17** (3), 236–240.
- Pantazis, T., Karydas, A.G., Doumas, C., Vlachopoulos, A., Nomikos, P. and Dinsmore, M. 2002, X-ray fluorescence analysis of a gold IbeX and other artefacts from Akrotiri, in *Proceedings of the 9th International Aegean Conference – Metron, Measuring the Aegean Bronze Age*, Yale University, 18–21 April, 1–7.
- Perea, A., Montero, I., Demortier, G. and Climent-Font, A. 2000, Analysis of the Guarrazar treasure by PIXE, in *Ion Beam Study of Art and Archaeological Objects, A contribution by Members of the COST Action G1*, ed. G. Demortier, and A. Adriaens, EU 19218, 99–101.
- Pini, R., Siano, S., Salimbeni, R., Pasquinucci, M. and Miccio, M. 2000, Tests of laser cleaning on archaeological metal artefacts, *Journal of Cultural Heritage*, **1** (S1), 129–137.
- Pons, E. 2002, Corrosion à long terme du fer et des aciers non ou faiblement alliés dans les sols à dominante argileuse – Caractérisation physico-chimique et étude électrochimique d'analogues archéologiques, thesis, Université Technologique de Compiègne, 239 pp.

- Robbiola, L., Pereira, N., Thaury, K., Fiaud, C. and Labbé, J.-P. 1998, Decuprification phenomenon of Cu–Sn alloys in aqueous solution in nearly neutral pH conditions, in *Proceedings of the International Conference on Metals Conservation, METAL 98*, Draguignan-Figanières (France), ed. W. Mourey and L. Robbiola, James & James, London, 136–144.
- Robbiola, L., Plowright, A. and Portier, R. 2004, A new data for improving authentication of bronze artefacts, in *Proceedings of the International Conference on Metals Conservation, METAL 01*, Santiago de Chile, ed. I.D. MacLeod, J.M. Theile and C. Degriigny, Western Australian Museum, Fremantle, 117–122.
- Schmidt-Ott, K. 2004, Plasma-reduction: its potential for use in the conservation of metals, in *Proceedings of the International Conference on Metals Conservation, METAL 04*, Canberra, ed. J. Ashton and D. Hallam, National Museum of Australia, Canberra, 235–246.
- Soerensen, B. and Gregory, D. 1998, *In-situ* preservation of artefacts in Nydam Mose, in *Proceedings of the International Conference on Metals Conservation, METAL 98*, Draguignan-Figanières (France), ed. W. Mourey and L. Robbiola, James & James, London, 94–99.
- van Langh, R., Ankersmit, H.A. and Joosten, I. 2004, The delamination of silver sulphide layers, in *Proceedings of the International Conference on Metals Conservation, METAL 04*, Canberra, ed. J. Ashton and D. Hallam, National Museum of Australia, Canberra, 137–141.
- Vega, E. 2004, Altération des objets ferreux archéologiques sur le site du Glinet (Seine-Maritime, France, XVIème siècle). Caractérisation des produits de corrosion et étude des mécanismes, doctoral thesis, UTBM, Saclay, 2004.

Corrosion behaviour of low-alloy steels: from ancient past to far future

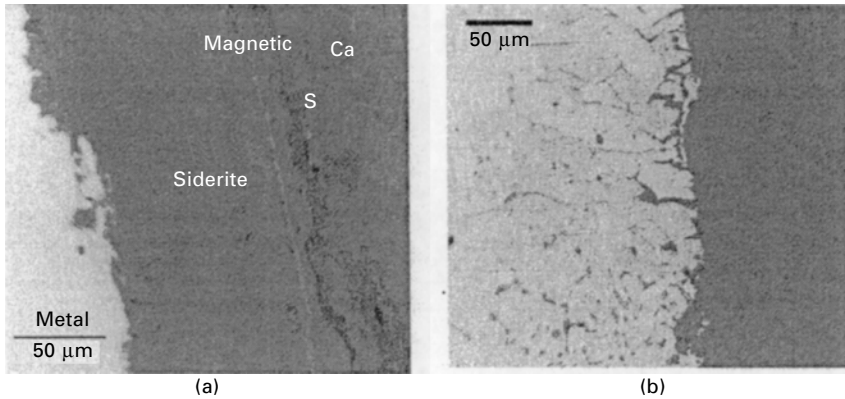
G. S A N T A R I N I, Commissariat à l'Energie Atomique, France

2.1 Introduction

The large variety of situations encountered in corrosion and the complexity of the phenomena, which involve numerous interconnected physicochemical steps, make modelling and behaviour predictions very difficult. This is probably the reason why corrosion models are still often semi-empirical, which restricts considerably the possibilities of extrapolations. With the concepts now envisaged of long-term storage and underground disposal of high-level radioactive waste, corrosion science has to face a new challenge: to obtain reliable behaviour predictions over very long periods of time, up to thousands of years [1–3]. For such durations, the development of mechanistically based models becomes an absolute necessity. Moreover, for the construction and validation of these models, laboratory tests are no longer sufficient: there is now a strong need for detailed examination of objects corroded for a long time. Archaeological analogues could provide such information, but the differences between ancient and modern materials, and also the usually poor knowledge about the initial conditions and the variation of the environmental factors with time, make the use of this information rather delicate. The aim of this chapter is to give a few examples of possible contributions of archaeological analogues to the understanding and modelling of long-term corrosion processes. The examples of modelling will be chosen among the studies performed currently in France [2, 3] to predict reliably the behaviour of metallic materials in long-term surface storage and/or underground disposal.

2.2 Uniform corrosion and localized corrosion

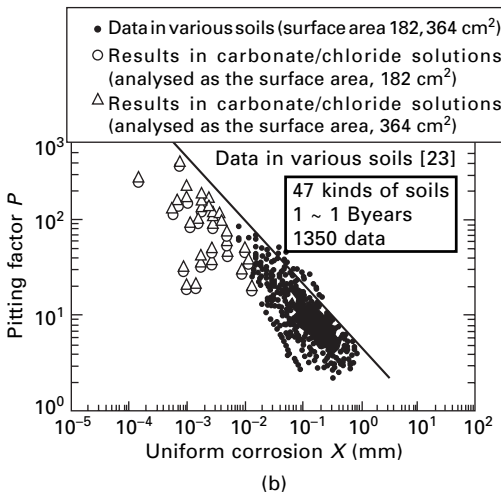
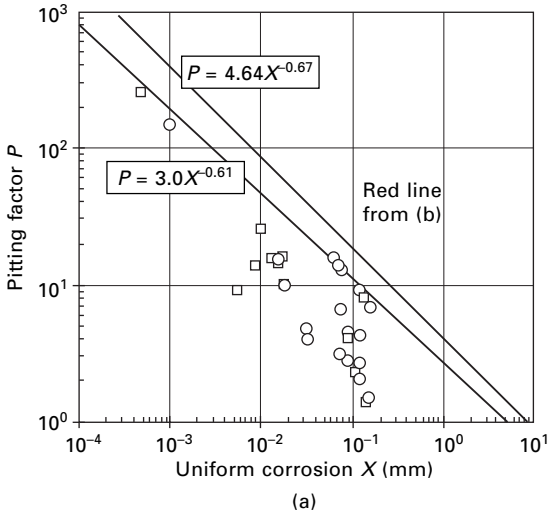
Figure 2.1 shows examples of interface morphologies observed on archaeological analogues corroded in soils. As illustrated, uniform corrosion is not the only form of corrosion liable to be encountered in the conditions of surface storage or underground disposal. Localized corrosion, such as



2.7 Examples of interface morphologies observed on archaeological analogues corroded in soils (16th and 12–13th century AD) [8–9]. In the case of (a), metallic iron is covered with a broad layer of siderite (FeCO_3 with 1–4%_{weight}Ca) surmounted by magnetite Fe_3O_4 and sulphides.

pitting, can also affect the materials, but is even more difficult to model and to predict than uniform corrosion. Since passivating alloys, such as stainless steels or nickel-based alloys, are more prone to localized corrosion than low-alloy steel, this latter material is envisaged presently in France for containers of high-level radioactive waste or spent fuel during underground disposal in deep clay geological formations. Thus, ferrous materials are expected to be used in the far future, as they were also used in the ancient past. However, though much more resistant, low-alloy steels are not completely immune to pitting. For this reason, a detailed analysis was performed of a large number of low-alloy steel or cast iron objects that were in contact with soils or water for durations up to 30 years. Laboratory results were also included in this analysis. It was shown that the evolution of both pit depth and mean corrosion depth with time could be fitted by decreasing power functions and that the pit depth decreased more rapidly than the mean corrosion depth. Therefore localized corrosion becomes, with time, less and less significant compared to uniform corrosion.

An empirical envelope law was derived [4], linking the pitting factor P (ratio of the maximal pit depth to the mean corrosion depth) to the mean corrosion depth X by a decreasing power law: as shown by Fig. 2.2, all the available results give dots lying systematically under the envelope curve. Such behaviour gives a mean for predicting the risk of pitting corrosion but this still has to be reinforced for very long durations by systematic examination of archaeological objects. Moreover, the physicochemical basis for the empirical envelope law still has to be clearly elucidated. Mechanistic modelling is currently in progress for evaluating the nature and the concentrations of



2.2 Evolution of the pitting factor as a function of the average corrosion depth. Results obtained for different carbon steels or cast iron in contact with various soils or waters [4]: (a) data compiled in ref. [4]; (b) data compiled by Japan Nuclear Cycle Development Institute, JNC [6].

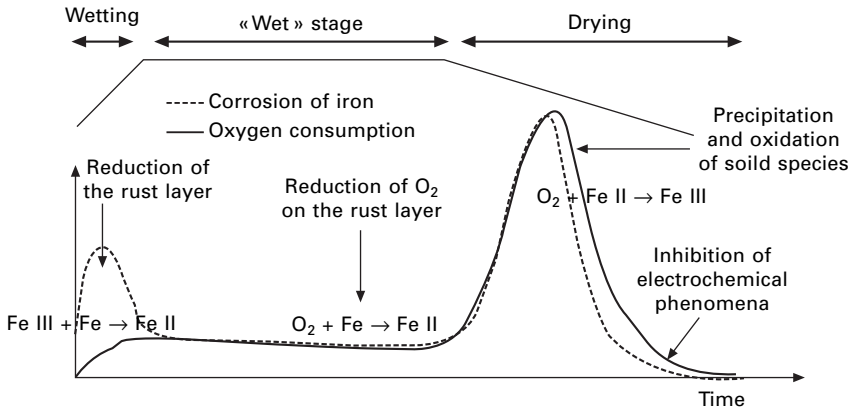
chemical species in the confined medium of a crevice in iron as a function of the geometric characteristics of the crevice and of the chemistry of the outside medium [5]. This study, which also gives access to an estimation of the propagation rate for extreme chemical conditions, could help in the theoretical validation of the empirical law.

2.3 Atmospheric corrosion

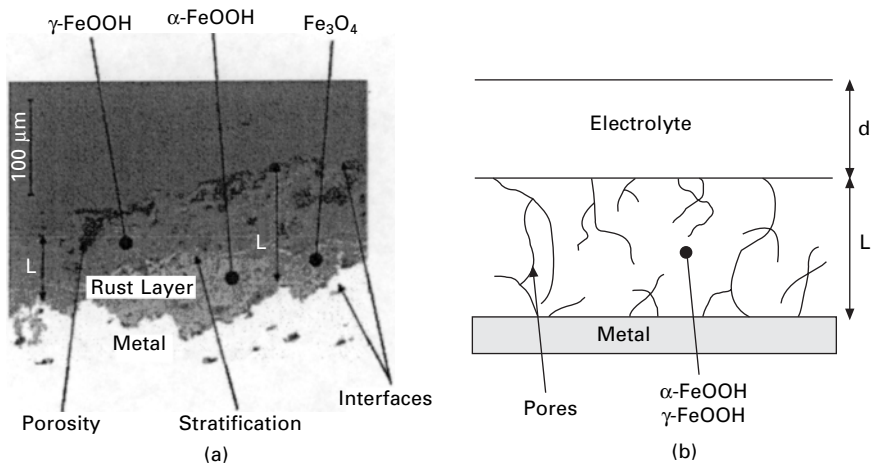
In the case of initial surface or subsurface storage before possible disposal in a deep geological formation, the nuclear heat produced by high-level waste or by spent fuel will maintain the surface of the low-alloy steel containers at a very high temperature for many years [7]. Such a situation is actually desirable, since the corrosion to which the steels are submitted in these conditions, the so-called 'dry corrosion', is, rather paradoxically, much slower than corrosion at lower temperature when water can condense at the surface of the steel. This relative slowness is due to the formation of a protective oxide film which acts as a diffusion barrier, the corrosion rate being controlled by solid-state transport of point defects. Such a process is expected to affect a metal depth of less than a few micrometres in 100 years but, unfortunately, no natural or archaeological analogue seems to be available to confirm the prediction for hundreds of years.

When the temperature at the surface of the container becomes sufficiently low for water to condense, another corrosion phenomenon will take place, usually known as 'atmospheric corrosion'. In this highly complex process, several solid corrosion products of various types and also cycles of wet oxidation followed by dry oxidation are involved. The corrosion product layers are porous and wetted by an aqueous electrolyte during the stages of aqueous oxidation. The severity of this type of corrosion is attributed to the presence of the aqueous electrolyte and also to the participation of the solid corrosion products in the corrosion reactions. Although the phenomenon has been known for many years and the damage has been well predicted by power functions of time for periods of a few tens of years, no mechanistic approach had been undertaken before a recent and original CEA work [10–14] to elaborate a complete mechanistic model aiming at reliable prediction of behaviour over many centuries.

Figure 2.3 provides a key for understanding atmospheric corrosion, at least in its general trends. It shows schematically the evolution, during a wet–dry cycle, of the rate of iron loss by oxidation and of the rate of oxygen loss by reduction. Two peaks are evident for the rate of iron consumption, one during the wetting stage and one at the end of the 'wet' stage, but only one peak is observed for the consumption of oxygen, associated with the iron peak at the end of the wet stage. This suggests that the oxidant of iron at the end of the wet stage is dissolved oxygen but that another oxidant than oxygen is involved for the oxidation of iron during the wetting stage. This other oxidant was found to be the lepidocrocite $\gamma\text{-FeOOH}$, which oxidizes metal iron to Fe^{2+} cations by reducing itself to a reduced form, $\gamma\text{-Fe.OH.OH}$. This reduced form is later reoxidized during the drying stage. Thus, lepidocrocite acts as a sort of carrier for oxygen in a cyclic oxidation–reduction process that is the main characteristic of atmospheric corrosion. The modelling work



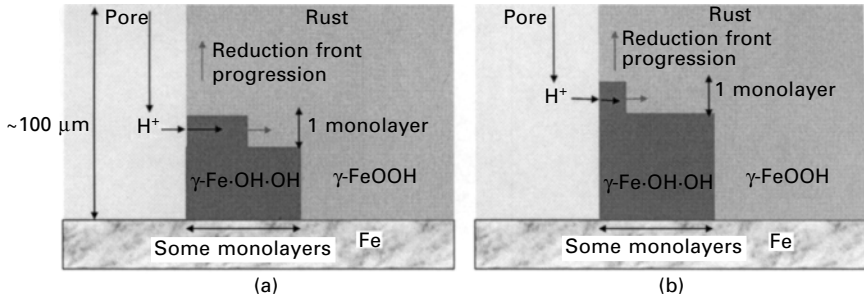
2.3 Schematic representation of a wet-dry cycle (after [15]) in atmospheric corrosion [11]. Rates of iron consumption and oxygen consumption as a function of time.



2.4 The rust layer [11]. (a) SEM micrograph of a 150-year old rust layer sample [10–12] (b) Sketch of the rust layer [11] and the electrolyte film simplified models. L and d are the rust layer and electrolyte thickness, respectively.

in progress [10–14] started from the morphological, physical and chemical analyses of the rust layers presents on archaeological analogues to propose a simplified model of a porous rust layer, composed mainly of lepidocrocite $\gamma\text{-FeOOH}$ and goethite $\alpha\text{-FeOOH}$, covered with a film of aqueous electrolyte (see Fig. 2.4).

Figure 2.5 explains schematically the way in which the reduction of $\gamma\text{-FeOOH}$ during the wetting phase is modelled. The reduced form $\gamma\text{-Fe-OH-OH}$



2.5 Sketch of the progression of the reduction front during the wetting stage in atmospheric corrosion [11]: (a) a monolayer is 'filled' from the pore wall to some monolayers deep; (b) when a plan of one monolayer thick and some monolayers deep is reduced, the plan above reduces in turn, following the same process, and thus progresses the reduction front.

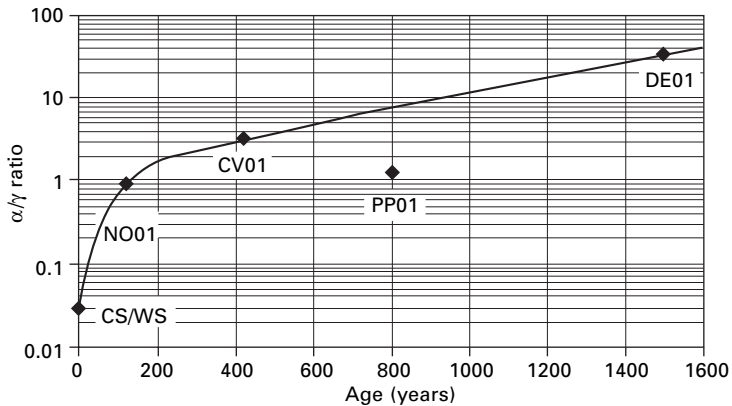
of lepidocrocite being an electronic conductor while the oxidized form γ -FeOOH is insulating, the reduction front can only move progressively along the pore walls from the iron at the inner interface to the outer interface.

The slowing down of the iron consumption rate at the end of the wetting phase is attributed to the end of the reduction of γ -FeOOH. The diffusion of oxygen dissolved in the aqueous electrolyte present in the pores of the rust layer is then involved in the corrosion process of the wet phase, and the increase in rate at the end of this stage is attributed to the decrease of the diffusion length due to the electrolyte evaporation. The following rate decrease is due to the precipitation of solid products in the pores and the transition to dry oxidation. This representation is very simplified and efforts still have to be made for a better simulation of real long-term processes.

In this search, archaeological analogues can be a useful tool since they can carry 'fingerprints' of corrosion mechanisms. An example is the evolution with time of the ratio of α -FeOOH (goethite) to γ -FeOOH (lepidocrocite) (Fig. 2.6). This ratio could be key to the understanding of long-term corrosion kinetics, which could be explained as follows. The stable form of the oxyhydroxide FeOOH is goethite, which is insulating and electrochemically inactive. Thus if, progressively over long periods of time, lepidocrocite is transformed into the stable form goethite, the cyclic corrosion process presented above, involving successive reductions and oxidations of lepidocrocite, could be inhibited, which would result in a slowing down of the global corrosion rate.

2.4 Corrosion in soils

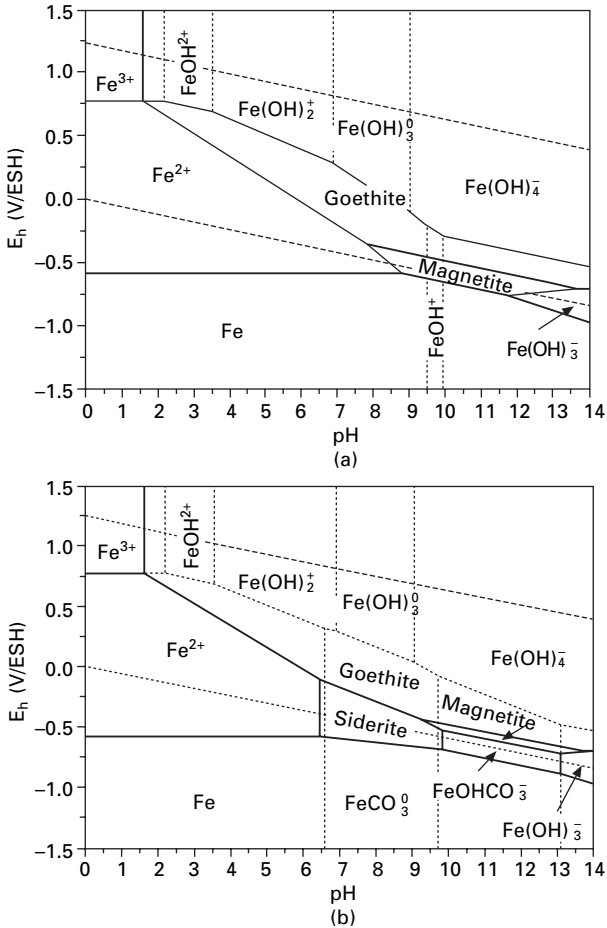
For underground disposal in a deep clay formation, steel will be in contact with the clay of the site or with the clay of an engineered barrier. In this case



2.6 Evolution of the ratio of α -FeOOH (goethite) to γ -FeOOH (lepidocrocite) in the corrosion products for indoor atmospheric corrosion [10–13]. CS/WS: results of tests in climatic chamber.

also, mechanistic modelling aims at corrosion behaviour prediction over very long periods of time. The chemistry of the medium is involved in the processes via the nature of the solid corrosion products, such as siderite or calcite, liable to be formed at the surface of the steel (see, for example Fig. 2.7). It is also involved via the solubilities of the products. The overall situation is highly complex and numerous data remain to be specified. For example, in some cases, especially at relatively high temperatures (90°C), a very thin protective (non-porous) oxide barrier seems to form, through which the transport of chemical species can occur only by solid state transport [16]. In this case, the modelling of this transport is similar to that occurring in dry oxidation. However, in other cases, at lower temperatures, the transport in liquid phase through pores in the corrosion product layers seems to be the main kinetic step involved in the corrosion process [17].

One of the main pieces of information that could be provided by archaeological analogues in this field is a rough evaluation of corrosion kinetics of ferrous materials for very long periods of time [8, 9, 18, 19]. For this objective, it is necessary to be able to calculate mean corrosion rates for similar materials exposed to similar media for different durations. When applied to modern materials in the situation of underground disposal, the results obtained with this method are only indicative, since the materials and the media are different. Moreover, since the initial dimensions of the archaeological objects are often not known, only calculations from the analysis of the corrosion products and of the soil near the object can provide an estimation of the metal loss. One of the difficulties of this method is that a given fraction of iron was possibly released far away from the metal surface and that this fraction is *a priori* not known. Attempts were made [8, 9] to calculate an upper bound for the error made in neglecting this release. In this

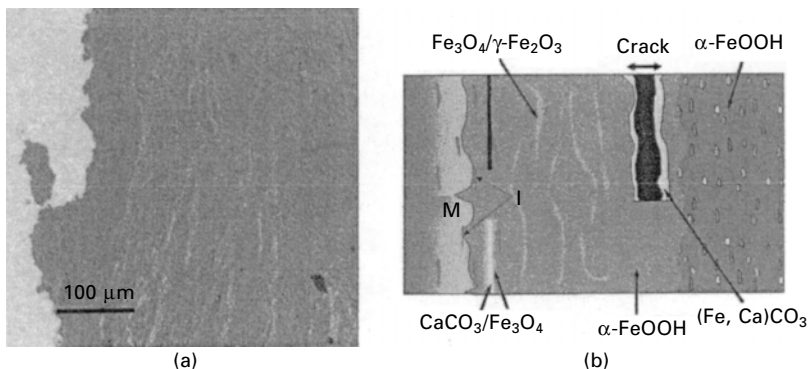


2.7 Potential-pH diagrams for the systems (a) iron-water-oxygen, $[Fe]_{total} = 10^{-5} \text{ mol.L}^{-1}$, and (b) iron-water-carbon, $[Fe]_{total} = 10^{-5} \text{ mol.L}^{-1}$, $[HCO_3^-] = 1.12 \times 10^{-2} \text{ mol.L}^{-1}$ [8, 9, 18].

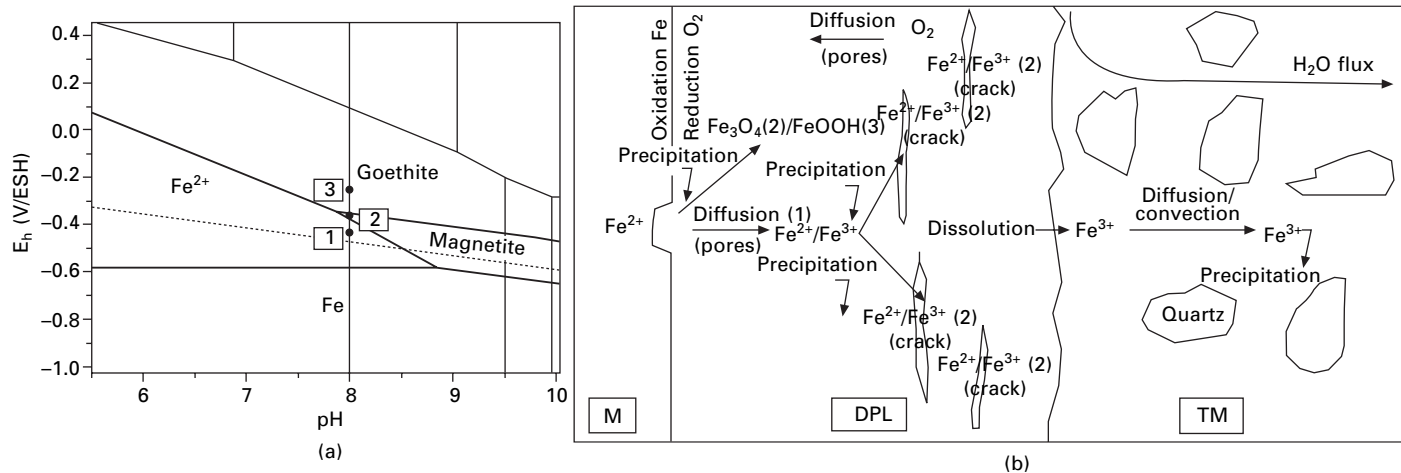
calculation, it was assumed that dissolved iron cations were released by a process of instantaneous dissolution and of rate-controlling convection, so that a maximal value of the release rate could be calculated from knowledge of solid corrosion product solubilities (from thermodynamic data) and of water flow rates in the soil. It was found that, in oxidizing conditions and in the absence of siderite (see Fig. 2.7), this error was negligible. However, the study also revealed that in reducing conditions, and even in oxidizing conditions for siderite, the error was liable to be significant. These unexpected results emphasize the need for more knowledge about corrosion in reducing conditions in soils and on the conditions of formation of siderite.

Examination of archaeological materials coupled with thermodynamic studies can provide other useful information, acting as guides for understanding corrosion mechanisms. Another example of the kind of ‘fingerprint’ mentioned above is given by the marble-like patterns often observed on sections of iron corrosion products (Fig. 2.8). Striations of magnetite–maghemite, Fe_3O_4 – γ - Fe_2O_3 , but also of calcite, CaCO_3 , and of siderite, $(\text{Fe,Ca})\text{CO}_3$, are often observed inside a goethite phase, γ - FeOOH . The presence of phases in which iron has partially valence 2 inside a phase where it is at valence 3 is *a priori* surprising, since it contradicts the classical and logical observation of a succession of a regularly increasing valence state from the iron of the inner interface to the outer interface. Figure 2.9 illustrates an attempt to explain these surprising valence inversions inside the corrosion product layer [8, 9, 18]. During the growth of this layer, the restricted transport through the porosity gives rise to concentration gradients and thus pH gradients and redox potential gradients. So, the stabilities and solubilities of the solid phases vary with distance to the interface. If, under applied or internal mechanical stresses, cracks are formed inside the layer, they can be filled with aqueous solutions liable, in the local conditions, to precipitate a new phase. Such repeated processes could be the origin of the marble-like patterns of Fig. 2.8.

Other clues for mechanisms, liable to be provided by archaeological analogues, remain to be more thoroughly examined, such as the presence in the inner layer of inclusions coming from the metal and/or the soil, that can reveal the sites of edification of the corrosion product layer. Some clues may also be obtained from the results of laboratory experiments on corroded



2.8 Marble-like patterns observed on sections of iron corrosion products [8]: (a) section of an iron archaeological object (Montbaron, Indre, France, 12th–13th century AD); (b) synthetic sketch of the morphology and composition of corrosion products in the Montbaron site.



2.9 Corrosion mechanisms of iron archaeological objects in aerated soils at pH 8 [8]: (a) variation of the electrode potential inside the dense corrosion product layer from the inner interface (1) to the outer interface (3); (b) synthetic sketch of long-term corrosion phenomena for iron in soils (numbers 1 to 3 refer to the dots in Fig. 2.8(a); M refers to metal, DPL to dense products layer and TM to transformed medium).

archaeological objects, such as oxidation in a climatic chamber or diffusion of electrolyte through the porosity of the corrosion product layers.

2.5 Corrosion in cementitious environments

In surface storage and underground disposal, some ferrous materials, such as those used for the rebars in reinforced concrete structures, will also suffer from corrosion in cementitious environments. For this type of corrosion, the mechanism begins with a stage of slow degradation during which, because of the high pH, the metal remains passive. Then, as a consequence of the alteration of concrete, due especially to carbonation by carbon dioxide, a transition occurs from the passive state to the active state: the growth rate of solid corrosion products increases. When the depth of the layer of corrosion products becomes sufficient, the mechanical stresses generated may lead to the cracking of concrete and, consequently, to the easier transport of chemical species through the concrete, leading to further enhancement of the corrosion rate.

In this type of corrosion also, as in atmospheric corrosion (Section 2.3 above), though the phenomena have been known for many years, attempts to elaborate a complete mechanistic model, aiming at reliable prediction of behaviour over many centuries, are recent [20]. The approach is based on the analysis of ancient ferrous artefacts embedded in carbonated binders [21, 22]. The model developed in ref. [20] includes two units, relating to two diffusion zones observed on the artefacts: in the first unit, reactive transport in a concrete porosity is modelled, the local thermodynamic equilibrium being assumed to be respected; in the second unit, the corrosion of iron in the presence of a thin porous layer of solid corrosion products is modelled, in a way not very far from that of ref. [11] for atmospheric corrosion (Section 2.3).

2.6 Conclusion

The brief illustrations presented in this chapter suggest that detailed investigations using archaeological analogues are able to provide useful information for the mechanistic modelling of long-term corrosion behaviour of ferrous materials, but that their use for this purpose is a very difficult task. The information is often rich and valuable but needs much care in its interpretation. Since, in ancient and modern (and future) situations, many conditions are different, only general 'fingerprints' are liable to be relevant. The main difficulty is to screen efficiently the numerous interconnected clues in order to detect what is liable to be sufficiently general to be applicable. Combinations of this approach with theoretical, especially thermodynamic, calculations and also with laboratory experiments with archaeological artefacts will probably help in this delicate but essential investigation.

2.7 Acknowledgements

Some of the studies described in this chapter were performed in the framework of a working group formed by ANDRA for defining and following its studies on the corrosion of containers in underground disposal. The other members of this group, Pierre Combrade, Didier Crusset, André Désestret, Damien Féron, François Foct, Jean-Marie Gras and Gérard Pinarid Legry, are thanked for numerous useful discussions. Thanks are also due to Philippe Dillmann, Laurent Maréchal, Delphine Neff and Stéphane Perrin for helpful contributions.

2.8 References

1. B. Kursten, E. Smailos, I. Azkarate, L. Werme, N.R. Smart, G. Marx, M.A. Cuñado, G. Santarini, 'Corrosion evaluation of metallic HLW/spent fuel disposal containers – review', *EUROCORR'2004*, Nice, France, 12–16 September 2004.
2. C. Desgranges, D. Féron, F. Mazaudier, G. Santarini, A. Terlain, 'Corrosion behavior of metallic containers during long term interim storages', *International Workshop 'Prediction of long term corrosion behaviour in nuclear waste systems'*, Cadarache, France, 26–29 November 2001, *EFC Series 36*, ed. IOM, London (2002).
3. G. Santarini, D. Crusset, F. Plas, 'Containers and overpacks for high-level radioactive waste in deep geological disposal conditions: French corrosion program', *International Workshop 'Prediction of long term corrosion behaviour in nuclear waste systems'*, Cadarache, France, 26–29 November 2001, *EFC Series 36*, ed. IOM, London (2002).
4. F. Foct, J.M. Gras, 'Semi empirical model for carbon steel corrosion in long term geological nuclear waste disposal', *International Workshop 'Prediction of long term corrosion behaviour in nuclear waste systems'*, Cadarache, France, 26–29 November 2001, *EFC Series 36*, ed. IOM, London (2002).
5. J.L. Mousson, B. Vuillemin, R. Oltra, D. Crusset, G. Santarini, P. Combrade, 'Modelling of the propagation of crevice corrosion', *EUROCORR'2004*, Nice, France, 12–16 September 2004.
6. JNC, H12 'Project to establish the scientific and technical basis for HLW disposal in Japan', *Supporting Report 2*, April 2000, p. IV–23.
7. C. Desgranges, N. Bertrand, D. Gauvain, A. Terlain, D. Monceau, D. Poquillon, 'Model for low temperature oxidation during long term interim storage', *EUROCORR'2004*, Nice, France, 12–16 September 2004.
8. D. Neff, 'Apport des analogues archéologiques à l'estimation des vitesses moyennes et à l'étude des mécanismes de corrosion à très long terme des aciers non alliés dans les sols'. Thesis, Université de Technologie de Compiègne, France, 2003.
9. D. Neff, P. Dillmann, L.B. Gurlet, G. Béranger, 'Corrosion of iron archaeological artefacts in soil: characterisation of the corrosion system', *Corrosion Science* (accepted for publication).
10. P. Dillmann, F. Mazaudier, S. Hœrlé, *Corrosion Science*, **46** (2004) 1401.
11. S. Hœrlé, F. Mazaudier, P. Dillmann, G. Santarini, *Corrosion Science*, **46** (2004) 1431.
12. P. Dillmann, V. Vigneau, F. Mazaudier, C. Blanc, S. Hœrlé, *EFC Series 36* (2002) 316.
13. P. Dillmann, D. Neff, F. Mazaudier, S. Hœrlé, P. Chevallier, G. Béranger, *Journal de Physique IV* (2002) 393.

14. H. Antony, L. Maréchal, L. Legrand, A. Chaussé, S. Perrin, P. Dillmann, 'Electrochemical study of lepidocrocite reduction and redox cycling for the mechanistic modelling of atmospheric corrosion', *EUROCORR'2004*, Nice, France, 12–16 September 2004.
15. M. Stratmann, *Metalurgia i Odlewnictwo*, **16**(1) (1990) 45.
16. C. Bataillon, J. Talandier, 'Corrosion modelling of iron based alloy in neutral media', *EUROCORR'2004*, Nice, France, 12–16 September 2004.
17. E. Pons, C. Lemaitre, D. David, D. Crusset, 'Modelling of long term corrosion behaviour of carbon steels in soils. Application to nuclear waste systems', *EUROCORR'2004*, Nice, France, 12–16 September 2004.
18. D. Neff, P. Dillmann, G. Béranger, 'Long term corrosion of archaeological iron artefacts', *EUROCORR'2003*, Budapest, Hungary, 28 September–2 October 2003.
19. E. Vega, P. Dillmann, P. Fluzin, 'A study on species transport in the corrosion products of ferrous archaeological analogues. A contribution to the modelling of iron long term corrosion behaviour', *EUROCORR'2004*, Nice, France, 12–16 September 2004.
20. B. Huet, V. L'Hostis, P. Le Bescop, H. Idrissi, 'Long-term prediction of reinforced concrete structures – Use of thermodynamic data to assess steel corrosion in carbonated concrete', *EUROCORR'2004*, Nice, France, 12–16 September 2004.
21. W.J. Chitty, P. Dillmann, V. L'Hostis, G. Béranger, 'On the characterization of the corrosion layout of ferrous archaeological analogues in binders', *EUROCORR'2004*, Nice, France, 12–16 September 2004.
22. A.W.J. Chitty, P. Dillmann, V. L'Hostis, C. Lombard, 'Long term corrosion resistance of metallic reinforcements in concretes – A study of corrosion mechanisms based on archaeological artefacts', submitted to *Corrosion Science* (2004).
23. M. Romanoff, *Underground Corrosion*, reprinted by NACE, Washington DC, 1989.

Archaeological metal artefacts and conservation issues: long-term corrosion studies

R. BERTHOLON, Université Paris 1 Panthéon-Sorbonne,
France

3.1 Introduction

Archaeological metal objects have a dual status: they are both valuable remains of cultures from the past and samples of corroded materials. As part of our cultural heritage, they constitute our main information source regarding ancient metallurgy and the corrosion behaviour of metals buried for centuries. Most often they cannot be studied right after their excavation because of their dramatic alteration during burial. Conservation aims to take care of these pieces of our heritage to allow both archaeological studies and public display. Therefore conservation and restoration treatments have to reveal the artefacts' characters such as shape, decoration and surface details, fabrication, use, etc. Of great importance for these purposes is to locate the original surface before corrosion. This chapter attempts to present an overall view of some issues related to conservation and location of the original surface of archaeological metal artefacts. Some concepts will be put forward in order to build a framework of research on these issues.

3.2 The artefact's history and its material condition

3.2.1 Periods and phases

The history of most artefacts can be divided into four main periods of time: the creation period (the object's fabrication or production), the use period, the abandonment period (with or without burial, in various environments) and the post-excavation period. This is a common framework, though some artefacts may not have gone through all these periods this way; one could have been discarded during its creation period, another may have been abandoned and later may have come back into use before being abandoned for a second time. Each period is further divided into phases, which are subdivisions of time related to particular events. Depending on the kind of events, phases can last a few seconds (as for a casting process) to several

years or even more. For example, the creation period comprises many phases from the initial conception phase to the finishing phase.

3.2.2 Artefacts as primary sources

Along with excavation data, studies of artefacts give valuable information for reconstructing an archaeological site's history. Therefore artefacts constitute part of the primary sources of a given site. Full knowledge about artefacts is based both on the materials they are made from and their functions or meanings (including, for instance, artistic style, religious purposes, etc.). Any comprehensive study of artefacts has to take into account these two approaches. But for most archaeological objects, related historical information is not available and the object's materials constitute the only source for study. Reliability of these primary sources depends on both understanding and stability of their altered conditions. Such understanding and stability are the main goals of any conservation projects.

3.2.3 The physico-chemical condition of an object

Let us now focus on what information we need in order to get a full knowledge of the physico-chemical condition of an object. Information can be sorted under three headings:

- nature and characters (properties) of the materials of the object
- the shape of the object including the shapes of all its parts (structure or internal shape)
- the surface appearance of the object.

To know the object's condition during any phase of the four periods of the object's history, we have to get information on these three points: materials, shape and surface appearance during the given phase. For example, the study of a gilded bronze head of a Roman statue of Minerve revealed six successive gildings carried out in antiquity during its use period (Oddy *et al.* 1988). Each gilding had been made during a repair phase separated by many secondary use phases. For each phase, we can try to define the materials of the bronze head, its shape and its surface appearance. An ultimate goal would be describing the physico-chemical conditions of this object related to each phase of its history.

3.2.4 Abandonment period

After the creation and use periods occurs the abandonment period. The artefact's abandonment, whether voluntary or not, is the end point of all human-induced phases of the artefact's history before its discovery. According to Jaeschke's

definition of burial, 'In this period [i.e. the abandonment period], the object is permanently lost, discarded, covered up or intentionally buried. It ceases to be actively used.' (Jaeschke 1996). Since no human-induced changes can happen until excavation or discovery, the alteration of the object depends only on physical, chemical or biological processes.

Phases of the abandonment period remain unknown most of the time but environmental archaeology studies are of great interest. Connections with corrosion history have occasionally been determined, as in the study of the 'corrosion biography' of copper artefacts found in Lake Neuchâtel in Switzerland (Schweizer 1991).

3.2.5 Informative potential of the artefact

What are archaeologists looking for? The first point is to gain knowledge of the condition of an artefact at the time of its burial, that is, at the very end of its use (and therefore anthropic) period. This is possible by first studying the changes that the materials have undergone through physical, chemical or biological degradation processes during burial in the absence of any human-induced changes. Then a conservation approach based on the present condition can give information about the abandonment phase condition.

Since no human-induced changes could have occurred during the abandonment period, knowledge of alteration mechanisms can lead to interpreting the excavation condition. Hence this research is a material science based problem and requires material degradation science studies. We must remind ourselves that conservation methodology is based on an information-oriented approach and not on trying to turn artefacts back to their abandonment condition, which is physically impossible (see for example, Fig. 3.1).

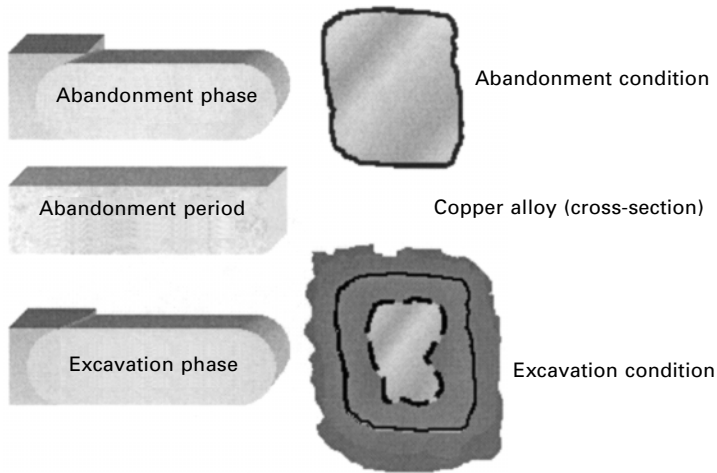
The concept of informative potential, put forward by C.A. Moberg, refers to the currently known and also still unknown characteristics or properties of artefacts that allow (or will allow) their archaeological interpretation (Moberg 1976). The informative potential of an artefact depends on its excavation condition. As a common rule, the less an artefact undergoes alteration, the better its informative potential.

Considering that the excavation phase condition of an artefact is defined by

- its excavation phase materials,
- its excavation phase shape, and
- its excavation phase surface appearance,

how can we get information about these features before the abandonment period, that is, at the abandonment phase?

Getting knowledge of abandonment phase materials requires first identifying and characterizing existing materials and then assessing how far material



3.1 Cross-section of a copper alloy artefact before and after the abandonment period. Huge changes have altered both the nature of the artefact and its appearance.

alteration has taken place. Retrieving information on either abandonment phase shape or surface appearance implies first locating the place where the abandonment phase surface lay. It is therefore possible to recognize the volume formerly defined by this surface before identifying the shape at this time. An idea of the abandonment phase surface appearance could be obtained through assessing appearance-related physical property alterations. Therefore locating the placement of the abandonment phase surface appears to be the key point in getting information on the object at that phase.

Knowing more about the abandonment phase condition of the object should reveal information about its previous condition, that is, during its use period and possibly its creation period. The condition of the abandonment phase is the starting point for studies on previous changes that had occurred during the ‘anthropological’ periods.

3.3 The limit of the original surface

This all-important abandonment phase surface is commonly referred to as the ‘original surface’ in the conservation literature in most languages (Bertholon 2000). Although the term ‘abandonment surface’, as previously proposed by Robbiola (Robbiola 1990), would have been more appropriate, the term original surface, though less precise, is already widely accepted.

If we now consider the physical entity of the original surface, defined as the surface of the artefact at the time of its abandonment, we must consider it as a superficial layer, which is a volume of a definite structure and composition and a certain thickness surrounding the artefact. We can put forward the

following definition: *‘the original surface of an artefact is its surface at the time of its abandonment.’*

How can we learn about this original surface and what can we expect to recover from it? Because of the alteration of the materials of an artefact during the abandonment period, the original surface, as a physical entity, has disappeared forever when the artefact is discovered and excavated. We cannot expect to recover this surface, whatever way we would use. Therefore what we could expect at best is to locate the limit of this surface with the environment of the artefact at the time of its abandonment phase.

We have to consider another concept, defined as follows: *‘the limit of the original surface, also termed the limitos, is the limit between the materials of the artefact and the surrounding environment at the time of the abandonment phase.’* Unlike the original surface, the *limit* of the original surface has no thickness and no volume: it is an abstract concept.

Depending on alteration mechanisms, the limitos may or may not have been retained within altered materials often arranged in several layers. Therefore what we could expect to recover, at best, is the limit of the original surface within the excavation phase surface. Locating the limit of the original surface is then a major point of any study concerning corroded artefacts. As we have previously mentioned, from the location of the limitos, it may be possible to recognize the abandonment phase shape and to assess how far materials have been altered to learn about abandonment phase materials.

3.4 Locating the limit of the original surface

Despite its utmost importance for artefact studies, the limit of the original surface (or the original surface itself) has not been the subject of many researches till now. A survey of what has been written on that topic revealed rather few references (Bertholon 2000). The idea emerged slowly from the 1950s onwards. Before those years, retrieving the original metal condition of the object by reversing the corrosion process was one of the goals of either chemists or conservators (Bertholon 2001c). Taking into account the irreversible outcomes of the corrosion process allowed a more reasonable view of what could really be done and learned from heavily corroded artefacts.

Bertholon’s survey showed that indications on the location of the limitos can be sorted into four groups:

1. Surface of interface characters still remaining within corrosion layers, such as a striking interface profile between two layers, or cleavage or parting of corrosion layers
2. Physical characters of corrosion layers such as cohesion, hardness or porosity, density to X-rays, or even colours or shine
3. Internal structure of corrosion layers such as remains of a metallurgical structure or crystalline properties

4. Composition of corrosion layers, nature of corrosion products and presence of particles coming from the environment (like sand grains) or remains of organic materials.

During this survey it was found that much of the relevant information lacked detail or explanation. Moreover, some indications are contradictory. This lack of detail hinders corrosion scientists from comparing those accounts with new findings, and hinders conservators from applying those clues when treating other artefacts. Therefore, it would be useful to develop valuable and reliable conceptual tools to deal with the problem of locating the limits:

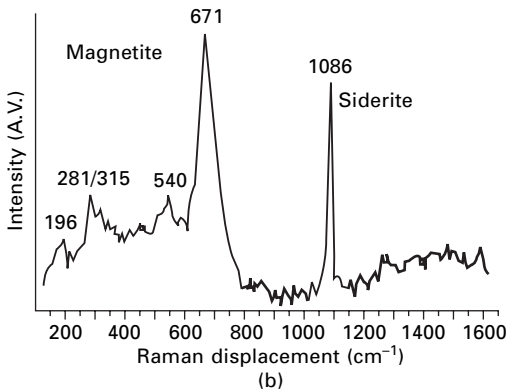
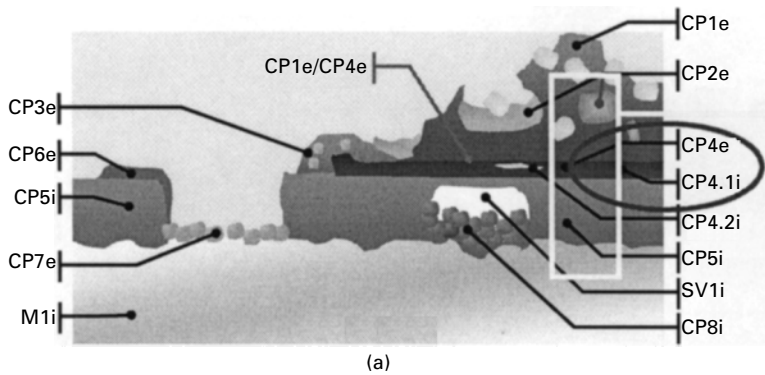
1. by perfecting a method for describing corrosion that is suitable for heavily corroded artefacts or
2. by developing a method for locating the limit of the original surface based on the physico-chemical characters of corroded materials.

3.4.1 Method for describing corrosion

The use of terms derived from the study of corrosion in industrial plants has proved to be unsuitable for heavily corroded artefacts. Both the methodology and the terms chosen are inadequate. Methodology implies describing the 'after attack' metal surface, after removing all corrosion products, which is not only inappropriate for archaeological artefacts since we expect to find information within those very corrosion products, but also impossible since in some cases there is no metal left. The chosen terms refer either to the metal surface shape (crevice corrosion, etc.) which cannot be known, for reasons just explained, or to the corrosion mechanisms (selective corrosion, etc.) which are usually unknown for heavily corroded specimens, or to the environmental conditions which are likewise unknown, due to the long history of the artefacts being studied.

A method for describing heavily corroded materials is currently being developed. This method is based on the virtual division of the materials of the artefact into different volumes called 'strata'. Each volume of materials showing the same characteristics is grouped within a stratum. Characteristics of strata and their surfaces or interfaces can be either described or measured, or both. Measurements are conducted following the commonly accepted methodology but, for many reasons, measurements are sometimes not implemented where facilities are not available or not suitable. Description is carried out according to different frames of reference; that is, a list of terms, sketches or pictures is proposed and accepted as the only choice. These frames of reference are expected to allow good and reliable communication between users of this descriptive method. Strata, interfaces and strata structure (arrangement of the strata) are encoded to allow computerized treatment of data. Strata codes refer to main constituents of strata.

Studies on archaeological artefacts conducted using this corrosion descriptive method have shown good potential for linking observations, tests and analyses carried out at various magnifications by different people (Neff *et al.* 2003). As an example, a detailed description of an iron nail dating back to the sixteenth century and published by D. Neff permitted accurate characterization of some corrosion layers (or corrosion strata) that had been seen during the macroscopic examination carried out by the conservator. In this way, information obtained at a macroscopic scale with all the physical properties and appearance of corrosion layers that can be obtained through the eyes and hands of the conservators can be linked to chemical composition, crystalline structure and microscopic properties that can be obtained through analysis and SEM examination (see Fig. 3.2).



3.2 Study of an iron nail. (a) Draft of stratigraphy drawn after macroscopic and microscopic examination. Strata are encoded and named after their nature (CP meaning corrosion products), a sequence number (starting from the present and visible surface), and a small letter referring to the stratum position ('e' meaning external stratum, i.e. in contact with the surrounding environment). (b) Raman spectroscopy graph related to the CP4e stratum composition showing the presence of magnetite and siderite.

It is not possible to describe further details of this method in this short chapter, but we can look at the expected outcomes: to describe any corroded material whatever its nature and however far the corrosion and penetration have extended, to allow connections between macroscopic and microscopic examinations and analysis, and to link these with other descriptive systems (metallurgical description, for instance).

3.4.2 Method for locating the limitos using limitos markers

In locating the limitos, as well as a method for describing corrosion we also need to establish whether some strata or interface characters can give us reliable indications. The information already gathered about the clues mentioned in the conservation literature and still in use by conservators today could be used as a basis for further researches (Bertholon 2001b). These characters can be sorted into three groups according to the type of indication they deliver:

1. Superior Limitos Marker (S.Limitos Marker). An S.Limitos marker is a strata character that indicates that the limitos is under the given strata.
2. Inferior Limitos Marker (I.Limitos Marker). An I.Limitos Marker is a strata character that indicates that the limitos is above the given strata.
3. Corresponding to the Limitos Marker (C.Limitos Marker). A C.Limitos Marker is an interface character that indicates that the limitos matches the given interface.

For example, the presence of sand grains coming from the environment within a given corrosion product stratum can be considered as an S.Limitos Marker as it implies that the limitos is under this specific stratum. However, this marker does not indicate that the limitos is directly below the given stratum; it could be deeper within the corrosion stratigraphy.

When assessing the reliability of this characteristic as an S.limitos marker, it is assumed that the sand grains from the environment surrounding the artefact were caught within the corrosion products that were formed over the original surface. On the other hand, the remains of a metallurgical structure within a corrosion product stratum, such as for instance a dendritic structure, that are still visible due either to some metal core still trapped within a corrosion product stratum or to some colour variation of the corrosion products, is a specific characteristic that can be used as an I.limitos marker, as we may consider that the corrosion replacement process has crept through the metal below the limit of the original surface.

The third type of limitos marker is specific to a strata interface. In this case the corrosion mechanism could have led to different corrosion product strata on either side of the limit of the original surface. Numerous examples

of this phenomenon have been recognized by conservators regardless of the nature of the metal, though a comprehensive explanation is still not known. Oxygen accessibility in the internal corrosion strata has often been mentioned as a main factor producing low-oxidized compounds, but recent studies tend to invalidate this hypothesis (Neff *et al.* 2004).

This phenomenon could be more related to the physico-chemical condition of the surface at the abandonment phase and to the first steps of the corrosion mechanism. In the case of the Qumran Copper Scroll buried two millennia ago near the Dead Sea, the *limitos* is still visible at the interface of two corrosion product strata of cuprous oxide. It was assumed to be due to the formation of a duplex layer of cuprous oxide showing different photochemical properties during the very beginning of the corrosion process, as it has also been observed on modern cuprous alloys specimens (Bertholon *et al.* 1998, Bertholon 2001a).

3.5 Conclusion

We may well ask, why bother with ancient metals? For archaeologists and curators they are difficult to study and even to keep from degradation and decay. Moreover, they are examples of what corrosion scientists seem to avoid at all costs: no information on metal manufacture and use, nor on the corrosive environments. The only data available is limited to the date and place of excavation, and often all that is left is a shapeless mixture of corrosion products mixed with earth, with sometimes not even a scrap of metal left. However, such archaeological artefacts provide our only available data for real-time experimentation on long-term corrosion. For that purpose and because of their profound alteration, they require specific methodology.

First, we must learn about the corrosion phenomenon that is responsible for how the materials appear to us after being thoroughly degraded during centuries of burial. These corroded materials result from complex and unfamiliar processes. That is why developing a descriptive method is so essential in dealing with complex corrosion stratigraphy.

Secondly, we have to recognize the potential of locating the limit of the original surface, or *limitos*, which is the artefact–environment interface at the time of the artefact’s abandonment and most often its burial. The location of the *limitos* should reveal more information about the corrosion rate and even the very beginning of the corrosion process, to add to any corrosion features already noted. The location of the *limitos* is also related to the cultural status of these artefacts. In this context, corrosion studies of archaeological metals help us to understand the shape and surface details of artefacts recovered from ancient civilizations. In this way modern metallurgists can get in touch with the metalworker of antiquity.

3.6 References

- Bertholon, R. 2000: La limite de la surface d'origine des objets métalliques archéologiques, caractérisation, localisation et approche des mécanismes de conservation. Doctorat en archéologie, UFR03 Art et Archéologie, Université Paris 1 Panthéon-Sorbonne, Paris, 419 pp.
- Bertholon, R. 2001a: Characterisation and location of the original surface of corroded archaeological objects. *Surface Engineering*, **17**(3), 241–245.
- Bertholon, R. 2001b: The location of the original surface, a review of the conservation literature. In: *Metal 2001*, Santiago, Chile, 2–6 April 2001, Western Australian Museum, pp. 167–179.
- Bertholon, R. 2001c: To get rid of the crust or not: emergence of the idea of original surface in the conservation of metal archaeological objects during the first half of the XXe. In: Oddy, A., Smith, S. (eds) *Past Practice–Future Prospect*. London, British Museum Press, pp. 5–11.
- Bertholon, R., Robbiola, L., Lacoudre, N. 1998: Corrosion du rouleau de cuivre de Qumrân et localisation de la surface originelle. In: *Metal 98 International Conference on Metals Conservation*, Draguignan, James & James, pp. 125–135.
- Jaeschke, R.L. 1996: When does history end? In: *Archaeological Conservation and its Consequences*, 26–30 August 1996, Copenhagen, IIC, pp. 86–88.
- Moberg, C.A. 1976: *Introduction à l'Archéologie*. Paris, François Maspéro, 260 pp.
- Neff, D., Bellot-Gurlet, L., Dillmann, P., Bertholon, R. 2003: Structural characterization of corrosion products on archaeological iron. An integrated analytical approach to establish corrosion typologies. In: *International Conference on the Application of Raman Spectroscopy in Art and Archaeology*, Ghent, 3–6 September 2003.
- Neff, D., Dillmann, P., Descostes, M. 2004: Mécanismes de corrosion à long terme des aciers non alliés – Apport des calculs de solubilité des produits de corrosion du fer à l'étude des analogues archéologiques. Commissariat à l'Energie Atomique, NT DPC/SECR 04-00 Index A.
- Oddy, A., Pearce, P., Green, L. 1988: An unusual gilding technique on some Egyptian bronzes. In: Watkins, S.C., Brown, C.E. (eds) *Conservation of Ancient Egyptian Materials*. London, UKIC Archaeology Section, pp. 35–39.
- Robbiola, L. 1990: Caractérisation de l'altération de bronzes archéologiques enfouis à partir d'un corpus d'objets de l'Age du Bronze. Mécanismes de corrosion. Doctorat es-sciences. Spécialité Métallurgie, Université Pierre et Marie Curie Paris VI, Paris, 205 pp.
- Schweizer, F. 1994: Bronze objects from lake sites: from patina to 'biography'. In: *Ancient and Historic Metals Conservation and Scientific Research*, Marina del Rey, 1991. Getty Conservation Institute, pp. 33–50.

Contribution of iron archaeological artefacts to the estimation of average corrosion rates and the long-term corrosion mechanisms of low-carbon steel buried in soil

D. NEFF, E. VEGA, P. DILLMANN and M. DESCOSTES, Commissariat à l'Énergie Atomique, France and L. BELLOT-GURLET, Université Pierre et Marie Curie Paris, France and G. BÉRANGER, Université de Technologie de Compiègne, France

4.1 Introduction

In the context of French nuclear waste storage, data on the long-term behaviour of low-carbon steel are essential. Indeed it is envisaged to store high-level radioactive waste in metallic canisters. These canisters could themselves be enclosed in a clay environment, and the whole confined deep in a geological disposal site. As the storage system has to protect against radionuclide migration for thousands of years, several approaches are needed to study the corrosion processes. The first is based on laboratory simulations whereas the second consists of modelling the long-term behaviour of iron. However, both of these phenomenological approaches need physico-chemical parameters on old corrosion products (i.e. several hundred years old). These parameters can be supplied by the study of recently excavated archaeological artefacts that are studied as analogues for long-term iron corrosion.

This chapter presents a general overview of our team's results over five years of study on archaeological artefacts. Some of these results have already been published [1, 2] but others are more recent and not previously published. Our researches have focused on the characterisation of the forms of corrosion observed on a corpus of 54 excavated iron artefacts of known antiquity. This chapter starts with a short review of previous studies dealing with the corrosion of low-carbon steel in specific conditions and of ancient iron artefacts. Then we propose a methodology to study archaeological analogues. The following part is devoted to the characterisation of the corrosion layers formed on the archaeological artefacts using specific techniques; corrosion mechanisms will then be proposed for the main observed layers. Then the chapter will focus on the determination of the average corrosion rates (CR) on the archaeological artefacts. The method proposed to evaluate the corrosion rates is based on the quantification of all the oxidised iron around the artefacts. The validity of the corrosion rates evaluated by this method will be discussed

using thermodynamic solubility calculations on the oxides constituting the corrosion layers.

4.2 Literature review

Numerous studies linked to iron or steel corrosion in aqueous solutions over short periods have been proposed. In a parallel way, for longer corrosion periods, archaeological artefacts have been studied both for purposes of cultural heritage conservation on the one hand and as analogues for long-term corrosion on the other.

Misawa *et al.* [3] established a schematic diagram showing the possible succession of phases as a function of the conditions of the aqueous solution in different aeration conditions. During the first stage of the corrosion mechanisms green rusts (Fe(II+/III+) compounds) are formed. Then, depending on the aeration conditions and the pH of the solution, different phases can form: magnetite (Fe_3O_4), maghemite ($\gamma\text{-Fe}_2\text{O}_3$), lepidocrocite ($\gamma\text{-FeOOH}$), akaganeite ($\beta\text{-FeOOH}$ containing chlorine) and goethite ($\alpha\text{-FeOOH}$). Nevertheless, as far as corrosion in soil is concerned, a more complex system must be considered [4]. Indeed, soil is a complex environment and different parameters such as geological factors (soil types, pH, electrical resistivity, etc.), hydrological factors (water flow through ground layers) and soil chemical composition play a role in the corrosion process. Specific species can play an important role: phosphate and carbonate can form a more protective layer [5] and conversely a high sulphate or chloride in soil water decreases the protectiveness of the corrosion layer [6]. Sulphides can appear in the corrosion products, due to microbial activity [7]. Moreover, specific phases such as siderite (FeCO_3) can appear in the case of very low oxygen content in the water and presence of carbonates [8, 9]. In this complex medium, the corrosion layer that forms presents a heterogeneous morphology with an inner layer less porous than the outer one [10–12].

Thermodynamic data can be very useful in understanding the influence of these different parameters on the formation of the corrosion products [13] and the appearance of peculiar phases such as siderite [8]. Moreover, for long burial periods, the corrosion mechanisms, as well as the dissolution of the corrosion products in soil, have to be considered.

Some measurements of corrosion rates (CR) on buried archaeological artefacts at least 100 years old have been published [14, 15]. These CR, measured in different aerated soils and using different methods (corrosion product thickness, electrochemical measurement, X-ray radiography), range from 0.01 to 10 $\mu\text{m}/\text{year}$. No clear influence of soil composition was evident. For shorter periods, the soil water composition seems to have a stronger influence: CR of 15 $\mu\text{m}/\text{year}$ after 500 days were measured in a sandy soil [7], while CR of 10–160 $\mu\text{m}/\text{year}$ were determined in soils with high content

of organic matter and carbonate [16]. From these experiments, it seems that organic matter and/or carbonate tend to increase the CR at the beginning of the burial period of low-carbon steels.

This short review shows that data on the long-term corrosion of iron are relatively heterogeneous and that a statistical approach is needed to better understand the mechanisms and to assess reliable CR. Moreover, soil composition on the one hand, and formation and evolution of corrosion products during burial on the other, might play a role in the corrosion mechanisms and accordingly influence the CR. Measurements of the CR are difficult to conduct on these particular samples and cannot be compared from one study to another because of the variety of the methods used, which provide a wide range of values that are difficult to interpret. The diversity of the results cannot hide the lack of statistical data on the characterisation of the forms of corrosion found during burial of archaeological iron artefacts. Long-term corrosion mechanisms are rarely evoked.

4.3 Characterisation of corrosion layouts and mechanisms

4.3.1 Experimental

Five archaeological sites (Table 4.1) where it was possible to sample iron artefacts in the embedded soil and to perform adequate environmental measurements were selected and, from those, 54 dated artefacts were collected. In most cases, pH and soil potential measurements (using a calomel saturated reference electrode, see ref. [2]) were performed *in situ* during sampling. Most of the measurements were made at the Glinet site, where P_{CO_2} values were measured at different depths in the water of the soil. The iron content in the soil water at different places was also measured by ICP-MS [17]. These *in situ* measurements were performed within the framework of the European COST ACTION G8 Short Term Scientific Mission with the help of Dr Henning Mathiessen. Complementary analyses of dried soil samples (pH and soil textures) were made later by an INRA (Institut National de la Recherche Agronomique) laboratory, specialised in soil analysis.

Table 4.1 Archaeological sites where samples were collected

| Site | Dating | Number of studied artefacts |
|-------------------|---------------|-----------------------------|
| Montreuil en Caux | 2nd c. AD | 3 |
| Cabaret | 12–13th c. AD | 15 |
| Montbaron | 12–13th c. AD | 6 |
| Avrilly | 15th c. AD | 8 |
| Glinet | 16th c. AD | 22 |

All the sampled artefacts were embedded in resin with adhering soil. They were then cut in order to obtain transverse sections of the corrosion system, and were carefully polished under ethanol using SiC paper (grade 80 to 4000) and diamond paste (3 and 1 μm).

For chemical analysis several techniques have been employed. In oxide layers, Energy Dispersive Spectrometry (EDS), directly coupled to the Scanning Electron Microscope (SEM), was used. Electron Probe Microanalysis (EPMA) was specially used to analyse minor elements in the metallic matrix and to establish the exact stoichiometry in the corrosion products in the case of the presence of carbonates that cannot be quantified by EDS.

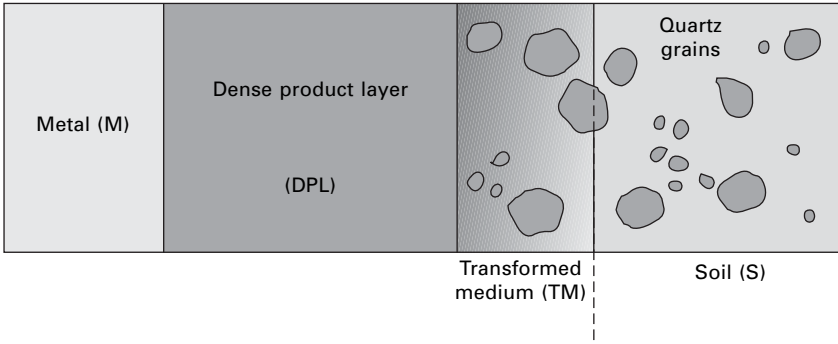
The local structure of the corrosion products at the microscopic scale was determined by two complementary methods: Micro X-Ray Diffraction (μXRD) under synchrotron radiation, and micro Raman spectroscopy (μRaman). μXRD experiments were conducted on the D15 beamline of the DCI ring at the Laboratoire pour l'Utilisation du Rayonnement Electromagnétique (LURE) at Orsay, France. The detailed set-up is described elsewhere [18–20]. A microbeam of $20 \times 20 \mu\text{m}^2$ ($\lambda = 0.08857 \text{ nm}$) was used on thin films made on cross-sections. Crystallised phases can be identified by powder diffraction and precisely located in the oxide scale; structural profiles are also obtained by this method. μRaman analyses were performed on the classical polished cross-section using a Jobin Yvon-Horiba LabRam Infinity spectrometer and an excitation at 532 nm from a frequency-doubled Nd:YAG Laser [9]. Excitation laser power on samples was adapted to each measurement and filtered at least below 0.42 mW in order to avoid the transformation of some sensitive phases under the laser irradiations.

On some samples, it was necessary to verify the valence of sulphur-containing compounds several micrometres thick. For this specific purpose, micro X-Ray Absorption Near Edge Structure (μXANES) experiments were performed at the European Synchrotron Radiation Facilities (ESRF) on the X-ray microscopy ID21 Beamline [21]. A $0.3 \times 0.3 \mu\text{m}^2$ beam was used. The energy was scanned over the Sulphur K edge from 2460 to 2530 eV. More details and the extraction procedure to obtain a normalised XANES spectra have been published elsewhere [22].

4.3.2 Terminology

All the analysed artefacts present the same general layered corrosion system. Therefore a specific terminology has been proposed to describe ferrous artefacts corroded in soil during very long periods (i.e. several hundred years). This terminology will be used for further studies on samples of this kind [23] and in Chapters 6 and 7 in this volume. We recall it briefly here (Fig. 4.1):

- **M**: metallic substrate (M)



4.1 Schematic description of the corrosion system on an archaeological iron artefact buried in soil.

- **DPL**: Dense Product Layer, from the morphological aspect (porosities) looking denser than the outer part of the corrosion products (TM)
- **TM**: transition zone between DPL and soil, containing both corrosion products and external markers characteristic of the soil (quartz grains, etc.)
- **S**: soil, where no corrosion products can be found.

The results presented below have been ordered following the analysis realised on each part of the corrosion system: the soil was first analysed from sampling on archaeological sites, and M, DPL and TM were analysed on the samples' cross-sections.

4.3.3 Soil parameters

Table 4.2 summarises the data obtained on soil samples. Soil texture varies from sandy for the Cabaret and Glinet sites to clayey in Montbaron. For the latter, pH values are the highest and can reach 8.5. The lowest pH values (5.7) were found in Montreuil en Caux. On this site, the measured potentials were between 40 and 90 mV/SHE. Moreover, on the Glinet site an average P_{CO_2} of about 0.1 atm was measured.

4.3.4 Corrosion system characterisation

Metallic substrate

The first step in studying corrosion on archaeological artefacts is to determine precisely the metallic microstructure and its influence on the corrosion behaviour of the artefact. Except on the Glinet site where two hypereutectoid steels and four cast iron samples were found (Table 4.3), all the artefacts were hypoeutectoid steels. Generally, the grains are equiaxe. Phosphorus is

Table 4.2 Soil parameters on the archaeological sites

| Site | Excavation depth (m) | Pluviometry (mm/year) ^c | pH | E (mV/SHE) | P_{CO_2} in water (atm) | [Fe] in water ^d | Fine particles clay) (%) ^b | Silt (%) ^b | Sand (%) ^b |
|-------------------|----------------------|------------------------------------|----------------------|---------------------|----------------------------------|----------------------------|---------------------------------------|-----------------------|-----------------------|
| Montreuil en Caux | 1–2 | 1200 | 5.7–6.3 ^a | 60–110 ^a | – | – | 22 | 66 | 12 |
| Cabaret | 0.4–1.7 | 742 | 8.3–8.5 ^b | – | – | – | 10 | 26 | 64 |
| Montbaron | 0.5–1 | 666 | 8–8.5 ^b | – | – | – | 32 | 47 | 19 |
| Avrilly | 0.3–2 | 611 | 7.2 ^b | – | – | – | 8 | 62 | 31 |
| Glinet | 0.5–1 | 700 | 6.7–7.8 ^b | – | 0.1–0.14 | 1.86–18.1 | 4 | 14 | 81 |

^a Analyses made during sampling

^b INRA results

^c Other data

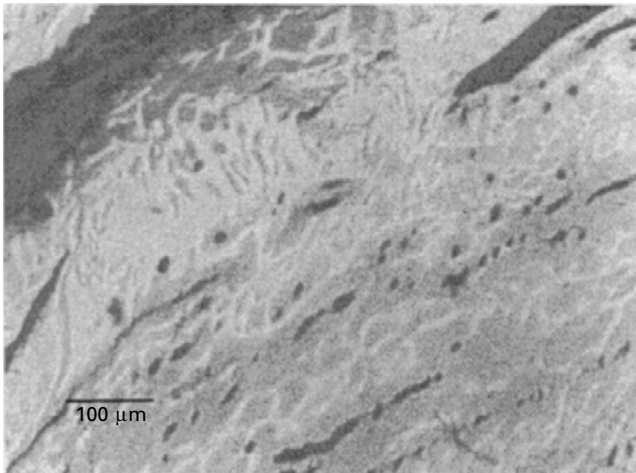
^d ICP-MS

Table 4.3 Composition and structure of the metallic substrates

| Site | Composition (mass%) | | Structure | |
|-------------------|---------------------|-------------------------|--|-------------------------------|
| | Carbon ^a | Phosphorus ^b | Grain size ^a (μm) | Inclusion number ^a |
| Montreuil en Caux | <0.02–0.4 | <0.4 | 55–180 | Average |
| Cabaret | <0.02–0.8 | <0.15 | 10–160 | High |
| Montbaron | <0.02–0.8 | <0.25 | 20–160 | Average |
| Avrilly | <0.02–0.1 | <0.46 | 17–260 | High |
| Glinet | <0.02–1.4 | <0.52 | 10–400 | Average to high |
| | 1.7–4.3 | 2–3 | – | – |

^a Quantitative metallography

^b EPMA or EDX



4.2 Phosphorus heterogeneous distribution revealed by Oberhoffer etching.

the other minor element classically detected in ancient ferrous artefacts (Table 4.3). In cast iron this element can be encountered up to 3 mass% and can be localised in iron–phosphorus precipitates; in hypoeutectoid steels it is present in solid solution in the iron. It is distributed heterogeneously in the material and follows the cold work lines also marked by the slag inclusions. (Fig. 4.2). In addition to the presence of phosphorus, the main structural difference between contemporary carbon steels and ancient iron artefacts is linked to the presence of slag inclusions, which can be much more numerous in the latter. Thus, the metallic substrates of the ancient artefacts are heterogeneous in both composition and structure. Nevertheless, this heterogeneity on the

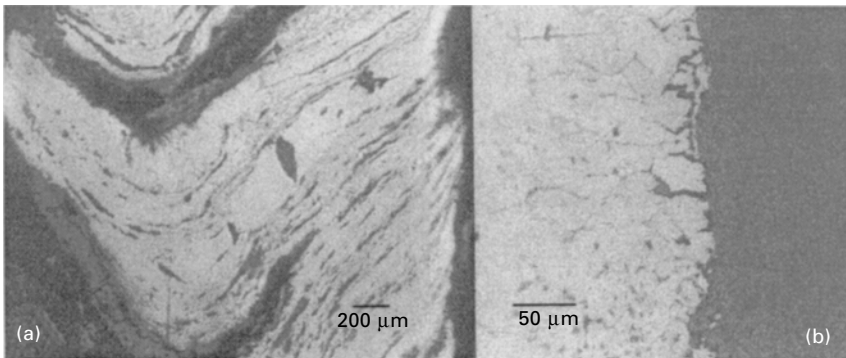
same sample allows one to study the influence of the microstructure of the metal on the corrosion behaviour in the same environment.

Corrosion products: metal/oxide interface and DPL

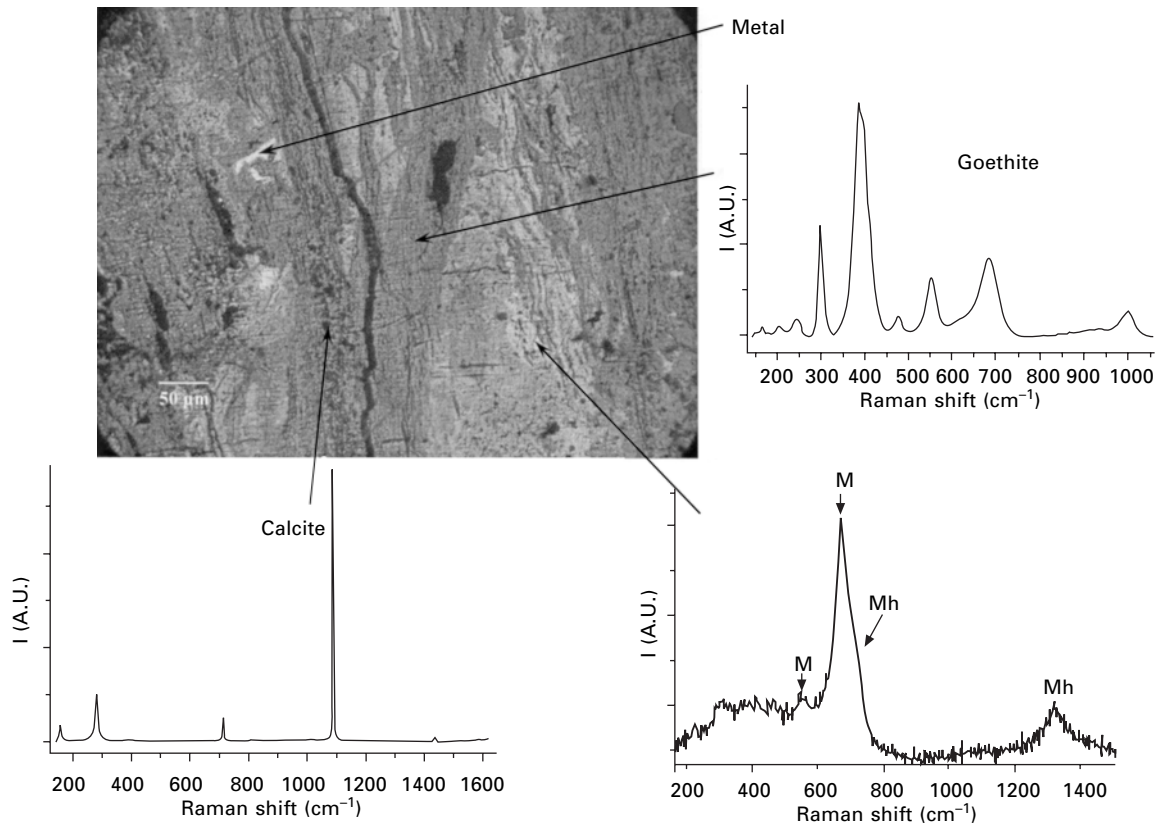
The metal/oxide interface can be relatively regular, but in most of the samples corrosion products penetrate the metallic matrix either along slag inclusions (the direction depending on their alignment) or along grain boundaries (Fig. 4.3). Observations made at the metal/oxide interface show that the local penetration of corrosion in the metallic substrate seems to be influenced by the microstructure.

Considering the DPL, the same corrosion layout was found at four of the studied sites. In this case, goethite, magnetite and maghemite are the main phases identified in the DPL. Figure 4.4 shows data from a cross-section made on a sample of the Montreuil en Caux site with three μ Raman spectra obtained at different places in this DPL. Typical light grey veins made of magnetite (sometimes of a magnetite/maghemite mix) are embedded in a goethite matrix. Raman spectra evidence the presence of magnetite linked to the 670 cm^{-1} peak. But the asymmetry of the main magnetite peak could indicate the presence of another component identified as maghemite. Pons *et al.* [12] suggested that this asymmetry could also be due to the presence of ferrihydrite which is a hydrated oxy-hydroxide. As the Raman shifts of this phase are very close to those of maghemite [24], its presence cannot be excluded. To date, no analytical method can clearly discriminate between maghemite and ferrihydrite in the case of a mixture of iron corrosion products at the microscopic scale.

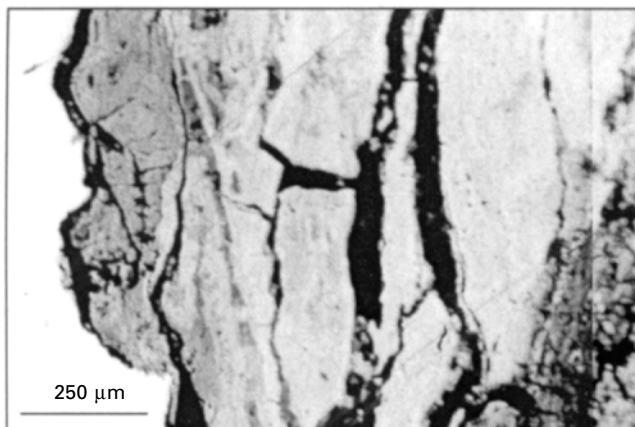
DPL always present numerous cracks several tenths of micrometres thick, easily identifiable by OM or SEM. (Fig. 4.5). These cracks are relatively



4.3 Local corrosion at the metal/DPL interface (a) along a slag inclusion (Mont 1 sample) (b) along grain boundaries (Mont 2 sample), Nital etching, optical microphotograph.



4.4 Morphology of the DPL: with marbled aspect, optical microphotograph and Raman spectra of goethite, calcite, magnetite (M) and maghemite and/or ferrihydrate (Mh), sample of Montreuil en Caux.

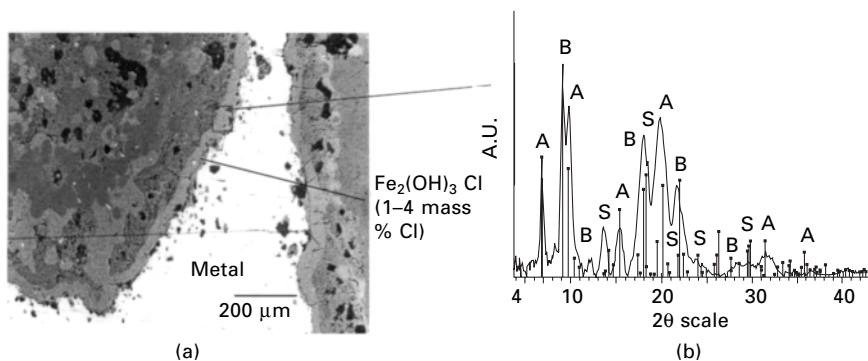


4.5 Cracks in the DPL, optical microphotograph. Archaeological sample of Montreuil en Caux.

parallel to the M/DPL interface but can sometimes be perpendicular. The fact that they often contain exogenous elements such as calcium or phosphorus (Fig. 4.5) seems to prove that they appeared not during sample preparation but during the growth of the oxide scale. In some cases, iron and/or calcium carbonates (siderite and/or calcite) can precipitate mainly along these cracks. Moreover, in very rare cases on the Avrilly site, small quantities of siderite could be identified at the M/DPL interface of a DPL made of goethite and magnetite. Lastly, in the DPL, other elements such as sulphur and silicon could be detected by EDS analysis at amounts of about 1 mass%. Lastly, on some samples from the Montreuil en Caux site, relatively important quantities of phosphorus could be detected in some parts of the DPL. At these places, the Fe/P ratio is in good agreement with vivianite ($\text{Fe}_3(\text{PO}_4)_2 \cdot 8\text{H}_2\text{O}$).

In the case of the local presence of Cl^- ions in the soil water, some specific phases can appear, such as akaganeite, which is a $\beta\text{-FeOOH}$. These phases are generally located in a delimited area at the M/DPL interface and the corresponding Cl amounts are between 3 and 20 mass%. In some artefacts, another hydroxychloride was identified by μXRD : $\beta\text{-Fe}_2(\text{OH})_3\text{Cl}$ (Fig. 4.6). For more details see Chapter 10.

Figure 4.7 (a, b and c) shows the different corrosion layouts identified on the artefacts from Montreuil en Caux, Cabaret, Montbaron and Avrilly. Despite small local variations (presence of phosphates and carbonates), the general layout presents the same feature of $\text{Fe}_3\text{O}_4/\gamma\text{-Fe}_2\text{O}_3$ strips in a non-conductive $\alpha\text{-FeOOH}$ matrix. The composition of the substrate seems not to have a significant influence on the formation of this layout, which it seems can be associated with very long-term corrosion of iron and steels in an aerated soil. The formation mechanisms will be discussed later.

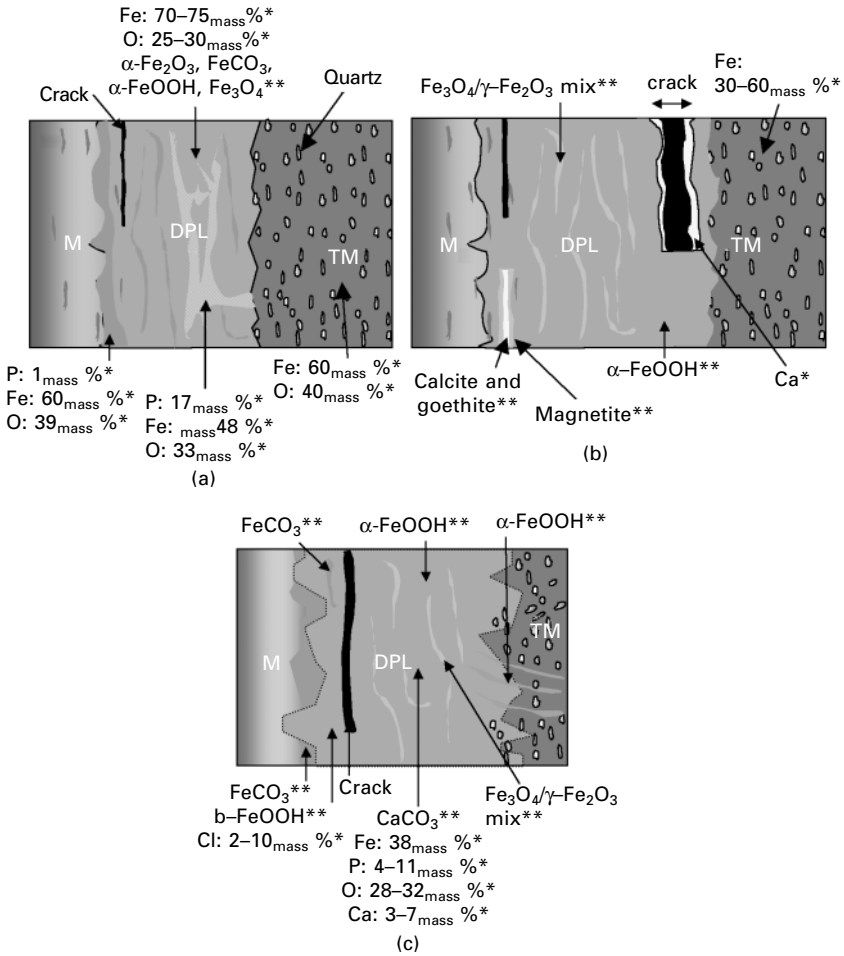


4.6 Chloride identification and localisation by μ XRD on Mont 6-2 sample: (a) Optical Microphotograph and EDS/SEM analyses. (b) μ XRD pattern obtained at the position of the open square: akaganeite, A (JCPDF 13-157), $\text{Fe}_2(\text{OH})_3\text{Cl}$, B (JCPDF 72-619) and siderite, S (JCPDF 83-1764).

Samples from Glinet are quite different and present distinctive corrosion layouts (Fig. 4.8). Indeed, on this site, siderite occurs frequently in the DPL. Four different corrosion types have been identified, as shown in Fig. 4.8. The first is very similar to the main corrosion form observed in samples from the other sites and does not contain any siderite (Fig. 4.8(a)). The other three all contain siderite. In some case, this phase can be the only component of the DPL (Fig. 4.8(d)). It can also be present with goethite and magnetite in the corrosion form (Fig. 4.8(b) and (c)). In the case of a DPL formed from a thick layer of siderite, a regular thin layer of magnetite (about 10 μm) can be observed all around the circumference of the object (Fig. 4.9). Composition analyses reveal that iron is partly substituted by 1–4 mass% Ca in siderite. At the DPL/TM interface, aggregates or strips containing high amounts of sulphur were identified. μ XANES analysis made with the $0.3 \times 0.3 \mu\text{m}^2$ beam reveal that most of these aggregates are made of sulphides (Fig. 4.9(c)), presenting a mixed (-I/-II) oxidation state.

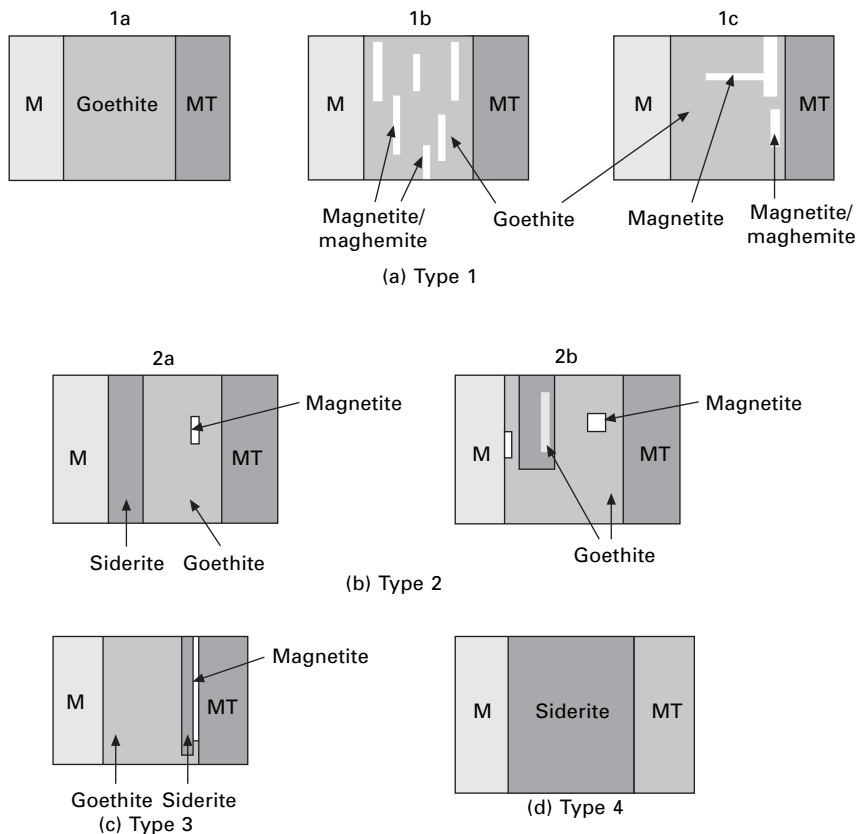
Transformed medium

The Transformed Medium can only be delimited by average EDS composition profiles made on cross-sections. On these profiles, each point represents the average composition in a rectangle of several $10 \times 100 \mu\text{m}$ strips parallel to the M/DPL interface. Figure 4.10 presents one of them collected on a sample from Montreuil en Caux. On these profiles, the average iron content shows a plateau at about 65 mass%, which corresponds to the average composition of the DPL. This amount decreases progressively until reaching a plateau corresponding to the average amount of iron in the soil. These two values



4.7 Schematic view of the DPL on (a) Montreuil en Caux, (b) Cabaret and Montbaron, (c) Avrilly. * EPMA and/or EDS, ** μ XRD and/or μ Raman.

(average iron content of the DPL and average iron content of the soil) delimit the domain of the Transformed Medium. In this domain, the decrease of the average iron content corresponds to an increase of the other exogenous elements coming from the soil. Around the remaining metal core, the TM spreads out at a distance of several millimetres. In addition to these composition analyses, local structural characterisations were performed in the TM. By μ Raman and μ XRD only Fe(III+) phases were detected and in most cases it was goethite. Moreover, by these techniques, goethite bands or peaks are weaker and broader than in the DPL (Fig. 4.11). This could be explained by a different crystallisation mode in the TM than in the DPL.



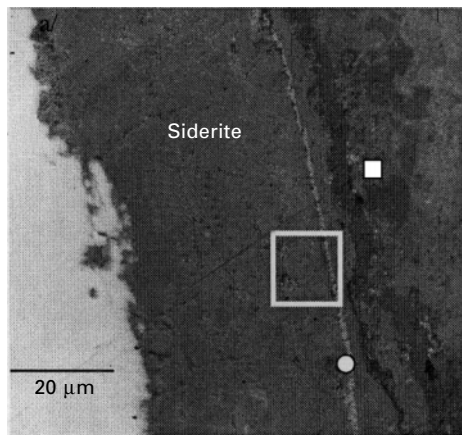
4.8 Corrosion forms observed on the samples from the Glinet site (see text), MT stands for transformed medium.

4.3.5 Corrosion mechanisms

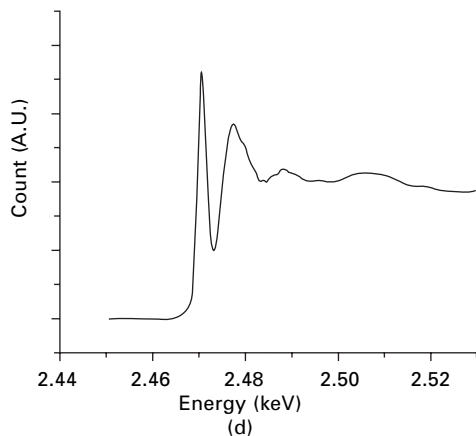
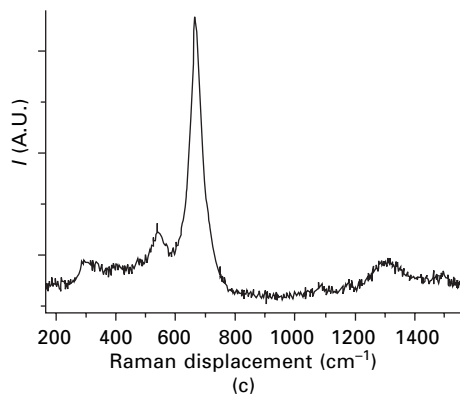
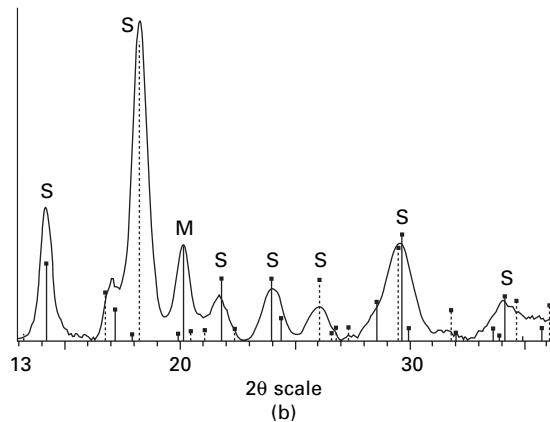
Layout observed in aerated soils

On most of the samples from the other four sites, the same layout was observed (see Fig. 4.12). It consists mainly of goethite in contact with the metallic core embedding maghemite/magnetite strips. As the metallic substrates are heterogeneous, it has been verified that these corrosion forms are not dependent on the carbon or phosphorus amount of the metallic matrix but seem to be linked to the conditions of the burial environment (Eh, pH, complex compounds, etc.). Moreover, the presence of exogenous elements (S, Si, Cl) and CaCO_3 near the metal/DPL layer shows that species transport is possible and important in the DPL and that ions can migrate in this layer.

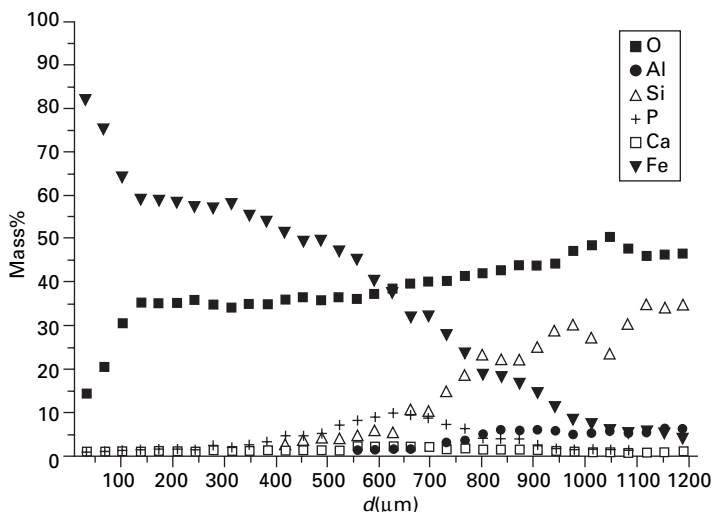
The following paragraph will propose a formation mechanism of this layout that could explain why the attempted increase of iron oxidation in the



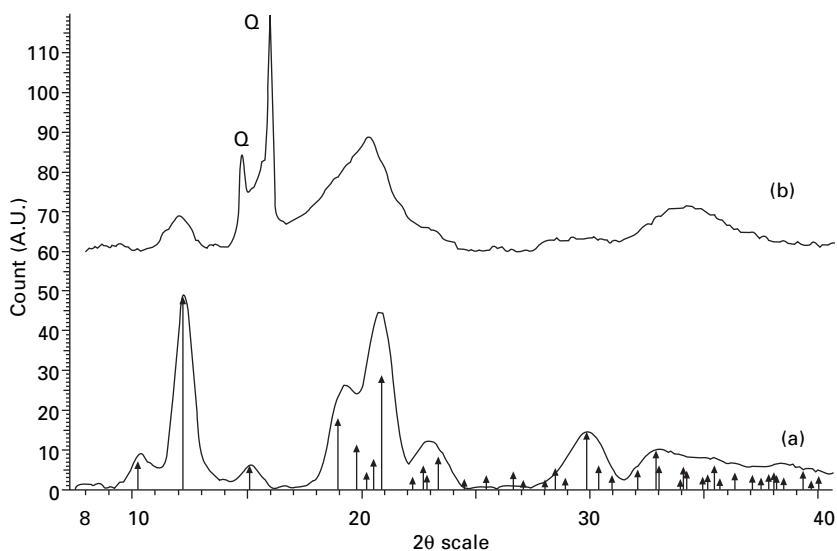
(a)



4.9 Sample from the Glinet site, (a) Optical microphotograph of DPL, (b) siderite (S)/magnetite (M) μ XRD spectra obtained at the place of the open square on (a), (c) magnetite microRaman spectra obtained at the place of the circle on (a). μ XANES spectrum at S K edge obtained in a high sulphur zone (white plain square on (a)) indicating the presence of a sulphide.

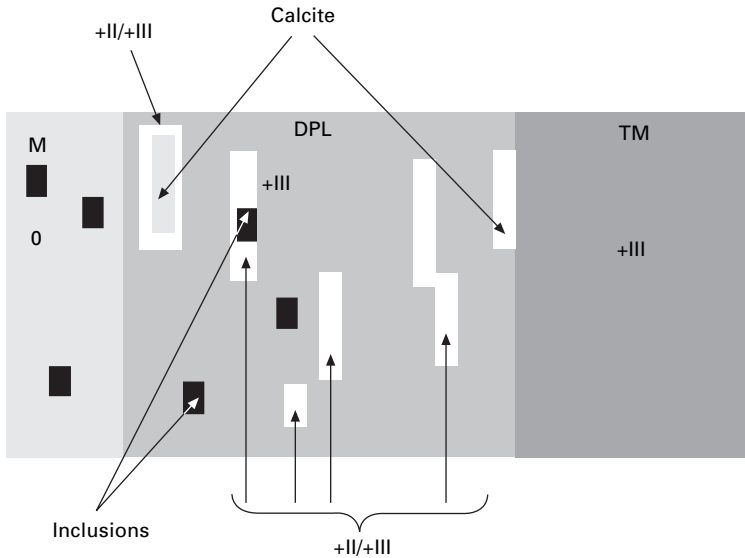


4.10 Elementary distribution profiles realised on an artefact from Montreuil en Caux. (d = distance from the metal/oxide interface).



4.11 Goethite μXRD spectra obtained from Montreuil en Caux (a) in the DPL, (b) in the TM (Q = quartz grain diffraction peaks).

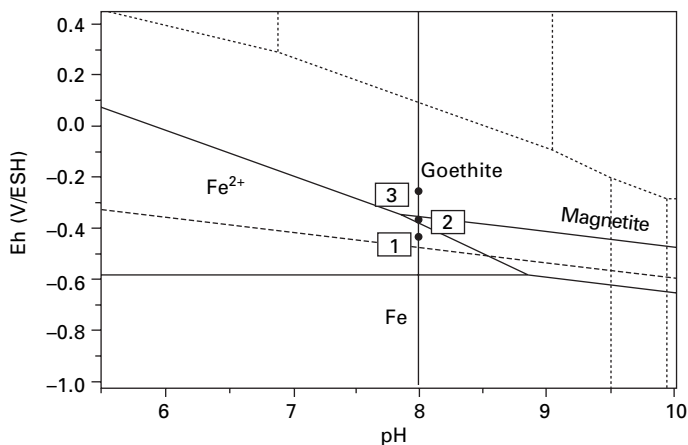
corrosion products from the metal to the soil is not observed (presence of Fe_3O_4 in the DPL). It is based on one hypothesis: because goethite is a non-conducting phase (conductivity of about $10^{-9} \Omega^{-1} \cdot \text{cm}^{-1}$ at room temperature [25]), both cathodic and anodic reactions should only occur at the metal/



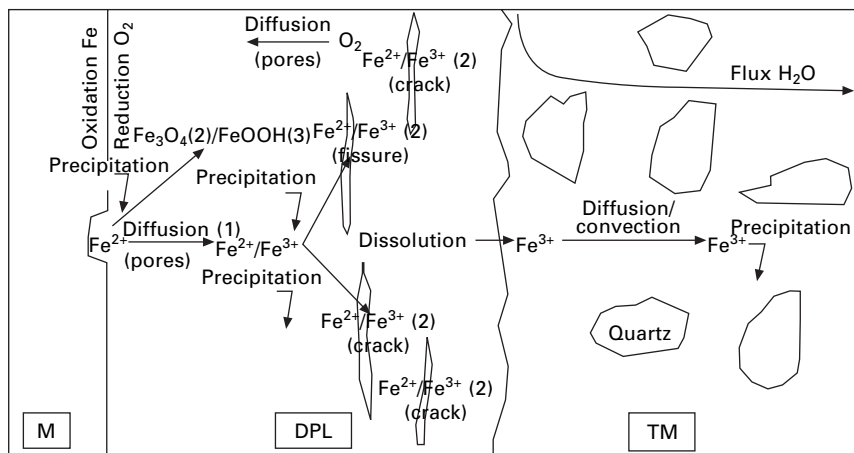
4.12 Schematic view of the distribution of iron oxidation degree in the most frequently observed DPL layout on ferrous artefacts corroded in soil.

DPL interface. For this reason, it is the oxygen diffusion in the water of the DPL pores and cracks that will control the corrosion mechanisms. Because corrosion takes place at low temperature ($<20^{\circ}\text{C}$), solid diffusion should not be considered here.

Considering these hypotheses, the only way to explain the presence of magnetite veins in goethite is through the following mechanisms. In this scenario, the pH values that will be considered are those measured in the archaeological soils, i.e. between 6 and 8.5. One should also consider that the environment is saturated with water and that, when porosities are connected to the external surface, they are also saturated with water. Moreover, to simplify, we consider that water does not contain sufficient quantities of carbonate and chlorine ions to form phases other than iron oxides and oxyhydroxides. At the beginning of the corrosion process, because high quantities of oxygen are present, mainly goethite forms (point 3 in the potential/pH diagram, Fig. 4.13). During this growth phase, cracks parallel to the metal/DPL interface can form because of the oxide expansion volume. These cracks, when they are connected with the soil, become saturated in water. At the metal/DPL interface, iron oxidation continues to generate Fe^{2+} ions. If the potential becomes relatively low, it is possible to reach a domain where neither goethite nor magnetite is stable (point 1 on Fig. 4.13). The Fe^{2+} ions can then diffuse in the DPL and reach cracks already formed. In these zones, the potential is higher because they are closer to the environment. Thus



4.13 Part of the pH/potential diagram between pH values of 5 and 10.



4.14 Schematic of long-term iron corrosion in soil mechanisms. Numbers in parentheses refer to Fig. 4.13.

magnetite can precipitate (point 2 on Fig. 4.13). In more external zones, the domain of goethite predominance is reached and this phase can form. If this hypothesis is correct, higher porosity should be observed in the internal zone of the DPL. This point will be examined in further studies.

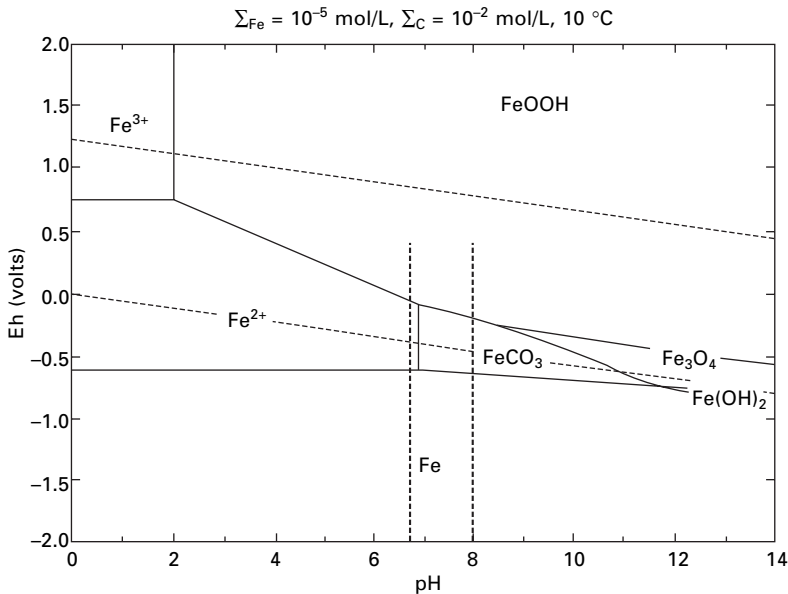
The formation of the MT could be explained by the dissolution of the phases constituting the DPL, the migration by diffusion and convection in the soil water, and the re-precipitation of solid corrosion products. These mechanisms are summarised in Fig. 4.14. The validation of these hypotheses is the subject of Chapter 6.

Corrosion mechanisms at the Glinet site

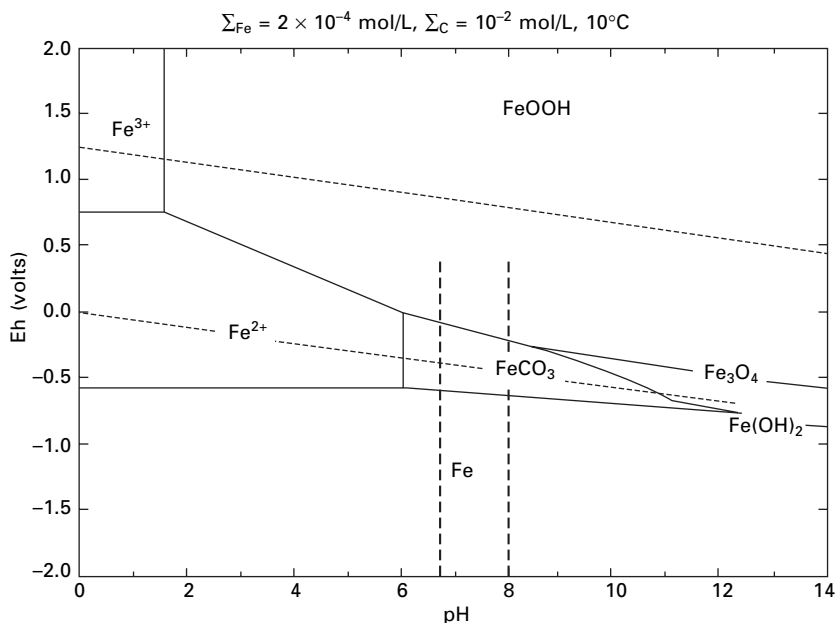
Almost all the samples observed at Glinet presented a DPL comprised of siderite. The environment at this site can be invoked to explain these particular corrosion forms. Indeed, the Glinet site was under a dam, so that for 400 years the soil was continuously saturated in water. Moreover, numerous pieces of wood were found in the soil near the ferrous artefacts, providing organic matter. The presence of this organic matter and the detection of siderite and sulphides could indicate possible biocorrosion processes, but this point needs further study and will not be developed here.

Equilibrium diagrams of the Fe–C–H₂O system have been calculated at 10°C and with the lowest and highest iron amounts in solution measured at the Glinet site (Figs 4.15 and 4.16). These diagrams show that the domain of siderite predominance varies depending on the theoretical pH, redox potential and CO₂ partial pressure. However, no variations of P_{CO_2} were measured at Glinet (all values were around 0.1 atm). Thus, the variation of this parameter cannot be invoked to explain the different corrosion types observed there.

Types 2 and 3, showing siderite and goethite, can be better understood by considering the variation of the redox potential in the corrosion layer. Indeed, the formation of a goethite layer can induce a reduction of the potential at the metal/DPL interface which favours the formation of siderite (type 2,



4.15 E–pH equilibrium diagram of the Fe–C–H₂O system at 10°C for total concentrations of dissolved iron (10^{-5} mol/L) and carbonates (10^{-2} mol/L).



4.16 E-pH equilibrium diagram of the Fe-C-H₂O system at 10°C for total concentrations of dissolved iron ($2 \times 10^{-4} \text{ mol/L}$) and carbonates (10^{-2} mol/L).

Fig. 4.8(b)). On the contrary, cracks formed in the corrosion scale perpendicular to the metal/DPL interface constitute shortcuts for the penetration of oxygen inside the corrosion layer and an increase of the local potential. Goethite can then be formed on the metal, establishing the type 3 corrosion forms (Fig. 4.8(c)).

4.4 Average corrosion rate estimation

As said in the introduction, for prediction of very long-term corrosion of future materials, the estimation of the average corrosion rates (CR) is of great importance. This part deals with this aspect of the study of corrosion of archaeological analogues. CR will be calculated using a particular method and the reliability of the results will be discussed using solubility calculations. As was previously shown, corrosion products (DPL + TM) can be delimited either by observation or by analytical methods. In order to ensure a better reliability for the prediction of iron alteration in soil, a maximal corrosion rate taking into account iron which could have come from the object in the medium is estimated. In a second step, the quantity of iron that could have migrated far from the object after solubilisation will be evaluated by thermodynamic calculation. If this quantity is too high, the CR evaluated by measuring the iron in corrosion products around the artefact is not reliable.

4.4.1 Minimal value of the corrosion rate

Corrosion rates can be obtained by dividing the iron equivalent thickness (t_{eq}) of the corrosion products by the age of the sample:

$$CR = \frac{t_{eq}}{\text{age}} \quad 4.1$$

Iron equivalent thickness is calculated from the thickness of the corrosion products (DPL and TM) corrected by the ratio of the density of the local medium and of iron as follows:

$$t_{eq_{Fe}} = \int_0^{t_{soil}} \text{mass \% Fe}(t) \times \frac{\rho(t)}{\rho_{Fe}} dt \quad 4.2$$

where t = distance from metal/corrosion products interface
 dt = elemental variation of t
 $\rho(t)$ = density of medium (metal, corrosion products, soil) at t
 ρ_{Fe} = density of iron ($7.8 \text{ g}\cdot\text{cm}^{-3}$)
 $\text{mass\%Fe}(t)$ = quantity of iron at t in mass%.

In the DPL, the density was taken as equal to that of magnetite. This phase is the densest that can be formed in iron aqueous corrosion products, thus the value obtained will be over-evaluated in the case of the other phases. For the TM, as the local density at each point of the profile is not known, it was assumed that it decreases linearly from the DPL ($\rho = 5 \text{ g}\cdot\text{cm}^{-3}$) to the soil ($\rho = 2 \text{ g}\cdot\text{cm}^{-3}$) [26]. Lastly, sample age is supplied by archaeological dating methods, so that the precision is given to the nearest 50 years. To summarise, all the adjustable parameters have been chosen in order to over-evaluate the CR.

The iron equivalent thicknesses of our samples are listed in Table 4.4 and the average CR values in Table 4.5. The maximum total CR was under $5 \mu\text{m}/\text{year}$.

As said before, because the CR are evaluated by quantifying the iron in the corrosion products around the object, it is necessary to verify if an important part of this iron has not migrated far from the artefact by dissolution

Table 4.4 Equivalent thickness of the DPL and the TM for each site (μm)

| Site | t_{eq} DPL | t_{eq} TM |
|-------------------|--------------|-------------|
| Montreuil en Caux | 60–1107 | 182 |
| Cabaret | 96–1568 | – |
| Montbaron | 30–2250 | 559 |
| Avrilly | 38–1330 | 745 |
| Glinet | 48–143 | 224 |

Table 4.5 Average corrosion rates calculated for the DPL, the TM and the sum of DPL and TM for each site ($\mu\text{m}/\text{year}$)

| Site | Age (years) | V_{DPL} | V_{TM} | V_{total} (average) | V_{total} (max) | Error |
|-------------------|-------------|------------------|-----------------|------------------------------|--------------------------|-------|
| Montreuil en Caux | 1800 | <0.1–0.3 | 0.1 | 0.3 | 0.4 | 0.1 |
| Cabaret | 800 | <0.1–2.0 | – | 0.4 ^a | 2.0 ^a | 0.4 |
| Montbaron | 800 | <0.1–2.8 | 0.7 | 1.6 | 3.5 | 0.9 |
| Avrilly | 500 | <0.1–2.7 | 1.5 | 2.2 | 3.3 | 0.8 |
| Glinet | 400 | 0.10–1.8 | 0.6 | 1.0 | 2.4 | 0.6 |

^a Values calculated without TM

and thus is not taken into account in the CR evaluation. For this purpose, evaluating the solubility of the main phases constituting the CPD, a maximal corrosion limit will be calculated.

4.4.2 Validation of the corrosion rate's maximal limit

Principle

Considering that the corrosion products formed on iron archaeological artefacts can dissolve in aqueous solutions of soil, it is possible to estimate the amount of iron that could move to the environment by this means. This quantity is given by solubility multiplied by solution volume. It is evaluated according to the following hypotheses:

- 1 Dissolution is supposed to be very rapid so that the phases are considered at equilibrium.
- 2 One considers a monophased corrosion layer (goethite, magnetite, siderite).
- 3 The surface of the corrosion products exposed to the water flux is assumed to be constant.
- 4 The medium (soil) is assumed to be constantly saturated in water.
- 5 The possible re-precipitation of phases is not taken into account.

The water volume V that flowed on the corrosion products during the whole period of burial is estimated on each site from local rainfall data. Moreover we consider that only 10% of this water arrives in contact with the buried artefacts because of the evapotranspiration phenomenon [26]. Rainfall and evapotranspiration are assumed to be constant during the burial period. Then V is given by equation (4.3):

$$V = h\%_{\text{ETP}} tS \quad 4.3$$

where h = average annual height of precipitation (mm/year)

$\%_{\text{ETP}}$ = evapotranspiration coefficient

Table 4.6 Molar weight (g/mol) and mass per unit volume (g/cm³) for goethite, siderite and magnetite

| | Molar weight | Mass per unit volume |
|---|--------------|----------------------|
| Goethite (α -FeOOH) | 88.9 | 4.30 |
| Siderite (FeCO ₃) | 115.9 | 3.96 |
| Magnetite (Fe ₃ O ₄) | 231.5 | 5.20 |

t = burial duration (years)

S = corrosion product surface in contact with the water.

Thus, the iron oxide amount Q_p (in mol) dissolved in the water volume V is obtained by multiplying V by the solubility s of the corresponding phase P. In order to compare it with the CR minimal values presented in the preceding paragraph, it was chosen to output it as a thickness of the corresponding phase T_p using the following calculation:

$$T_p = Q_p \frac{M_p}{S\rho_p} = s \frac{h\%_{ETP} t M_p}{\rho_p} \quad 4.4$$

where M_p = molar weight

ρ_p = mass per unit volume of the dissolved phase p.

Table 4.6 indicates the M_p and ρ_p values used for goethite, siderite and magnetite.

Solubility calculations

Solubilities of the main phases identified on the archaeological samples (magnetite, goethite and siderite) were calculated at thermodynamic equilibrium. Although few data are available on the aqueous solutions from the archaeological sites, solution calculations were made in order to be as close as possible to the real conditions of burial. Solubilities were calculated for a range of pH values between 1 and 14 for each phase and for different redox potential values. The solution considered were (i) pure water, (ii) water containing complex species compounds (carbonate–bicarbonate, sulphate, phosphate, nitrate and chloride). The complex compounds can lead to the formation of iron species in solution or as solid phases. The carbonate amount was calculated from the partial pressure P_{CO_2} equal to atmospheric pressure for all the phases ($P_{CO_2} = 3.16 \times 10^{-4}$ atm) except for siderite. As the solubility of this phase depends strongly on the availability of carbonate in solution, we also calculated it for higher values of P_{CO_2} (0.1 atm).

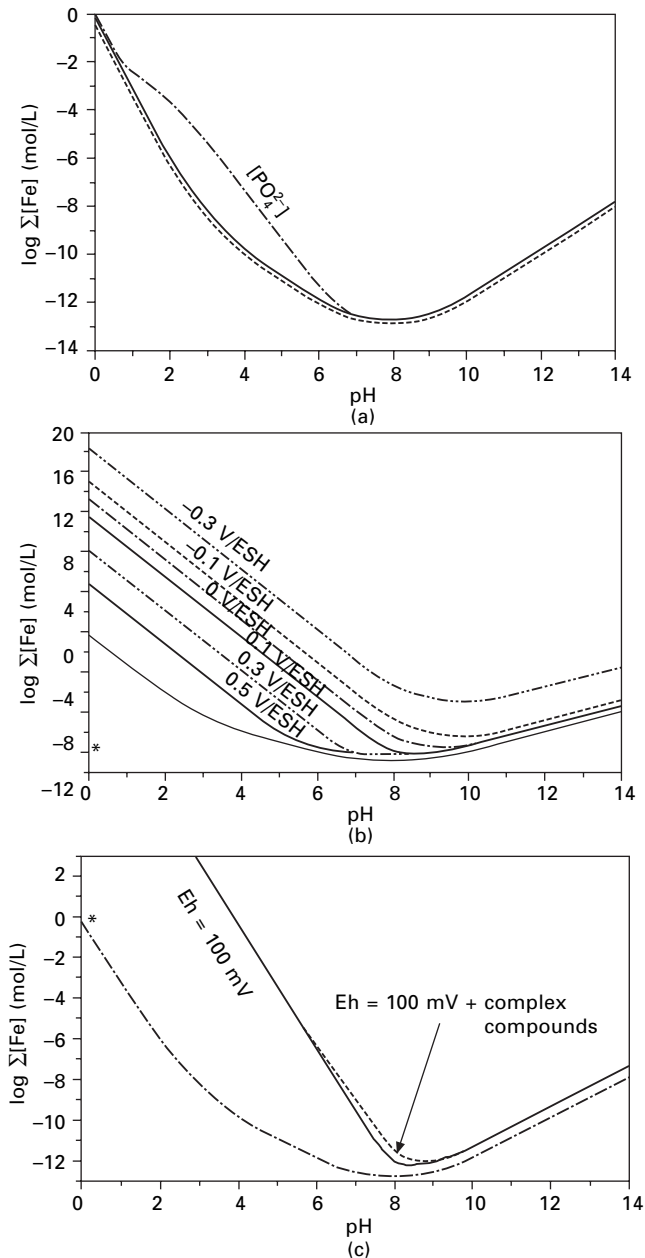
Solubility calculations were realised at 25°C, the temperature at which the thermodynamic data available are given in the literature [27, 28]. Iron

polynuclear species in solution were not taken into account because they are formed only in very acidic conditions, which is not the case for our soils. Results are presented in solubility diagrams showing the total concentration of iron versus the pH. The curves obtained for different values of redox potential are shown on the same graph.

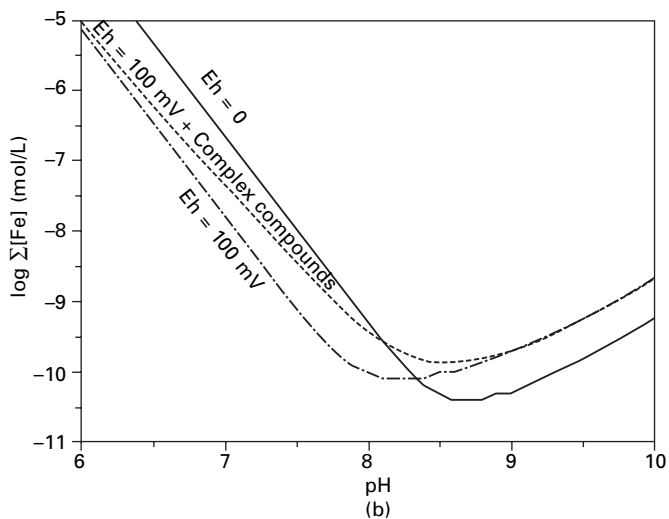
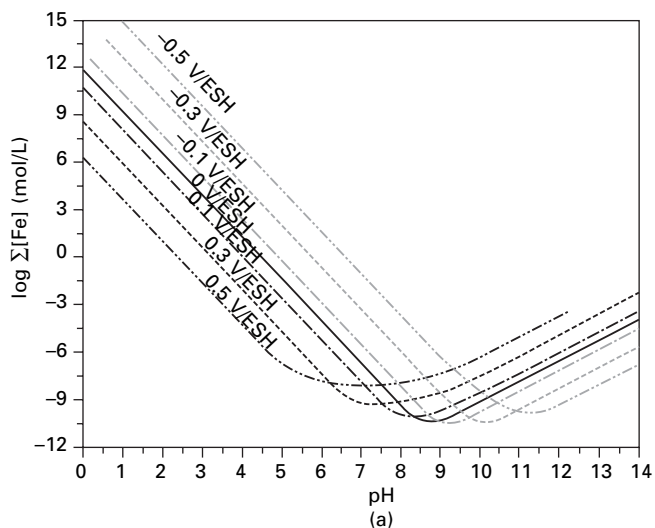
Calculations were done at thermodynamic equilibrium. The solubility diagrams obtained provide complementary information for the Eh–pH diagrams: they define the limit of the domain of stability for each phase at different iron concentrations. Parameters like pH, potential and presence of complex compounds have been taken into account, some measured on the archaeological sites (Table 4.2) and some taken from the literature when they were not available for the sites, at concentrations chosen to be close to those of river water (i.e. between 10^{-2} and 10^{-4} mol/L, depending on the complex compound).

The graphs obtained for the two main phases formed on archaeological artefacts (goethite and magnetite, Figs. 4.17 and 4.18) show that on the one hand solubilities are low in oxidising conditions, particularly for goethite whose solubility is less affected by the pH than magnetite, while on the other their solubility increases significantly for reducing conditions (under -0.3 V/SHE). Siderite, which was characterised mainly on the artefacts from Glinet, is more soluble than the two other phases, even for higher P_{CO_2} (Figs. 4.19 and 4.20). Moreover, for these three phases, among the complex compounds only the presence of phosphate increases the solubility for each phase, especially for slightly acidic pH values.

Goethite is the less soluble phase that controls iron solubility (Fig. 4.20). Regarding the estimation of dissolved iron in aqueous solution, due to goethite dissolution the iron amount in aqueous solution is the lowest. However, these calculations do not take into account the simultaneous presence of all possible iron solid phases. This can change the stability domain of each phase because of possible competition between the ionic species available in the natural medium. These species can lead to the formation of phases and complex compounds which are not taken into account when we consider solubilities independently. To assess these possible configurations, modelling using the Geochemist Workbench© software was undertaken. Average conditions were chosen for the complex compounds concentration and several Eh values were tested. The result is shown in Fig. 4.21. On this diagram, depending on the pH and the redox potential, different solid phases appear: goethite, magnetite, siderite or vivianite ($\text{Fe}_3(\text{PO}_4)_2 \cdot 8\text{H}_2\text{O}$). This last iron phosphate is liable to form, especially in oxidising conditions in the presence of phosphate complex compounds ($[\text{HPO}_4^{2-}]$ of at least 10^{-3} mol/L) and for a minimum iron species concentration at given pH and Eh. This also confirms that from a thermodynamic point of view phosphate is, with carbonate, the most complexing compound of iron in slightly acidic solutions. Nevertheless, this

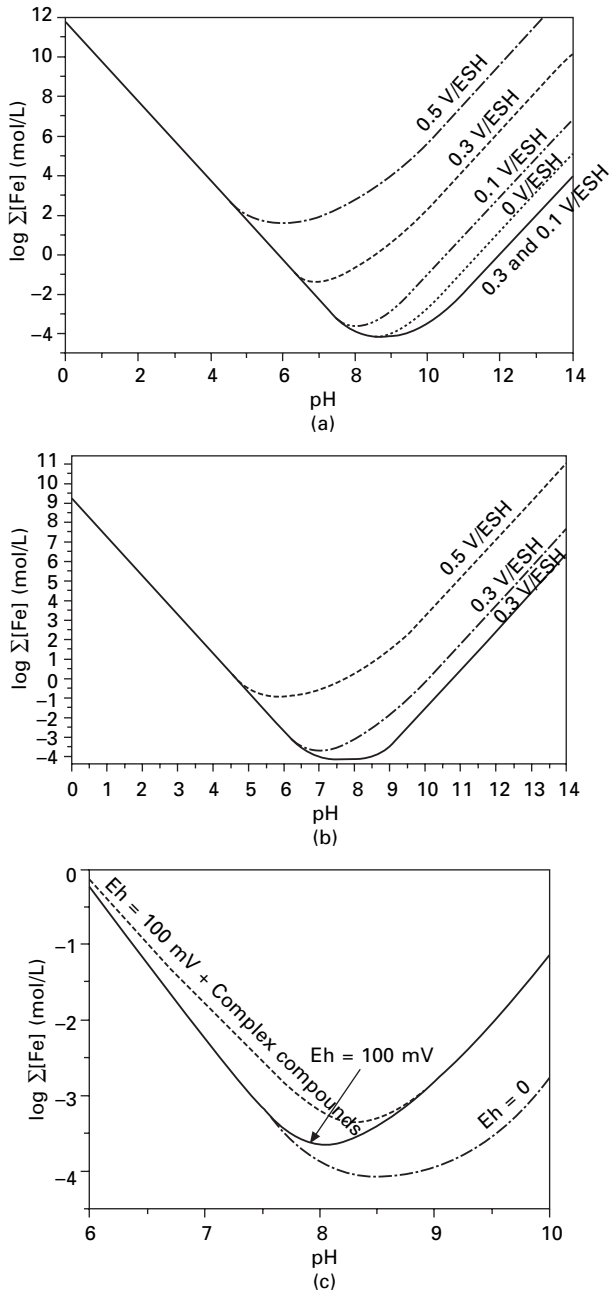


4.17 Solubility of goethite (a) in pure water and in the presence of complex compounds ($P_{\text{CO}_2} = 3.16 \times 10^{-4} \text{ atm}$; $[\text{Cl}^-] = 10^{-4} \text{ mol/L}$; $[\text{PO}_4^{2-}] = 10^{-2} \text{ mol/L}$; $[\text{SO}_4^{2-}] = 10^{-3} \text{ mol/L}$; $[\text{NO}_3^-] = 10^{-1} \text{ mol/L}$) (b) as a function of the redox potential, in pure water; and (c) in the presence of complex compounds $P_{\text{CO}_2} = 3.16 \times 10^{-4} \text{ atm}$; $[\text{Cl}^-] = 10^{-3} \text{ mol/L}$; $[\text{HPO}_4^{2-}] = 10^{-3} \text{ mol/L}$; $[\text{SO}_4^{2-}] = 10^{-3} \text{ mol/L}$; $[\text{NO}_3^-] = 10^{-3} \text{ mol/L}$; *: pure water without the potential value, i.e. $\Sigma[\text{Fe}] = \Sigma[\text{Fe}^{\text{III}}]$).

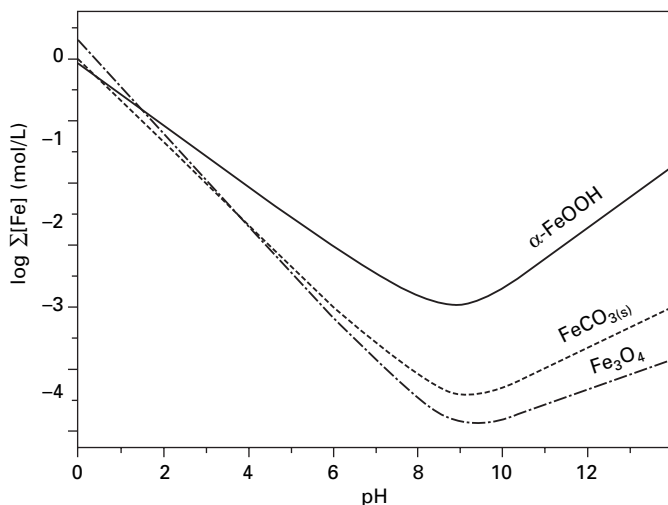


4.18 Solubility of magnetite as a function of pH (a) in pure water at various redox potentials and (b) in pure water at 0 V/SHE, at 0.1 V/SHE and in the presence of complex compounds ($P_{\text{CO}_2} = 3.16 \times 10^{-4}$ atm; $[\text{Cl}^-] = [\text{HPO}_4^{2-}] = [\text{SO}_4^{2-}] = [\text{NO}_3^-] = 10^{-3}$ mol/L).

phase is suspected only very locally in a few of the archaeological samples analysed from one site. It seems that either the conditions of the environment (pH, Eh, phosphate iron concentration species in solution) or the kinetic rates do not allow this phase to form or remain in a solid state. If Fig. 4.18 is read in terms of the precipitation of solid compounds, for a fixed concentration of complex compounds, Eh and pH, goethite precipitates for the lowest iron



4.19 Solubility of siderite as a function of pH and at various potentials in pure water: (a) $P_{\text{CO}_2} = 3.16 \times 10^{-4}$ atm; (b) $P_{\text{CO}_2} = 0.1$ atm; (c) in the presence of complex compounds for $P_{\text{CO}_2} = 3.16 \times 10^{-4}$ atm at 0 V/SHE, 0.1 V/SHE and in the presence of complex compounds ($[\text{Cl}^-] = [\text{HPO}_4^{2-}] = [\text{SO}_4^{2-}] = 10^{-3}$ mol/L).



4.20 Comparison of solubility of the different iron compounds considered in pure water as a function of pH.

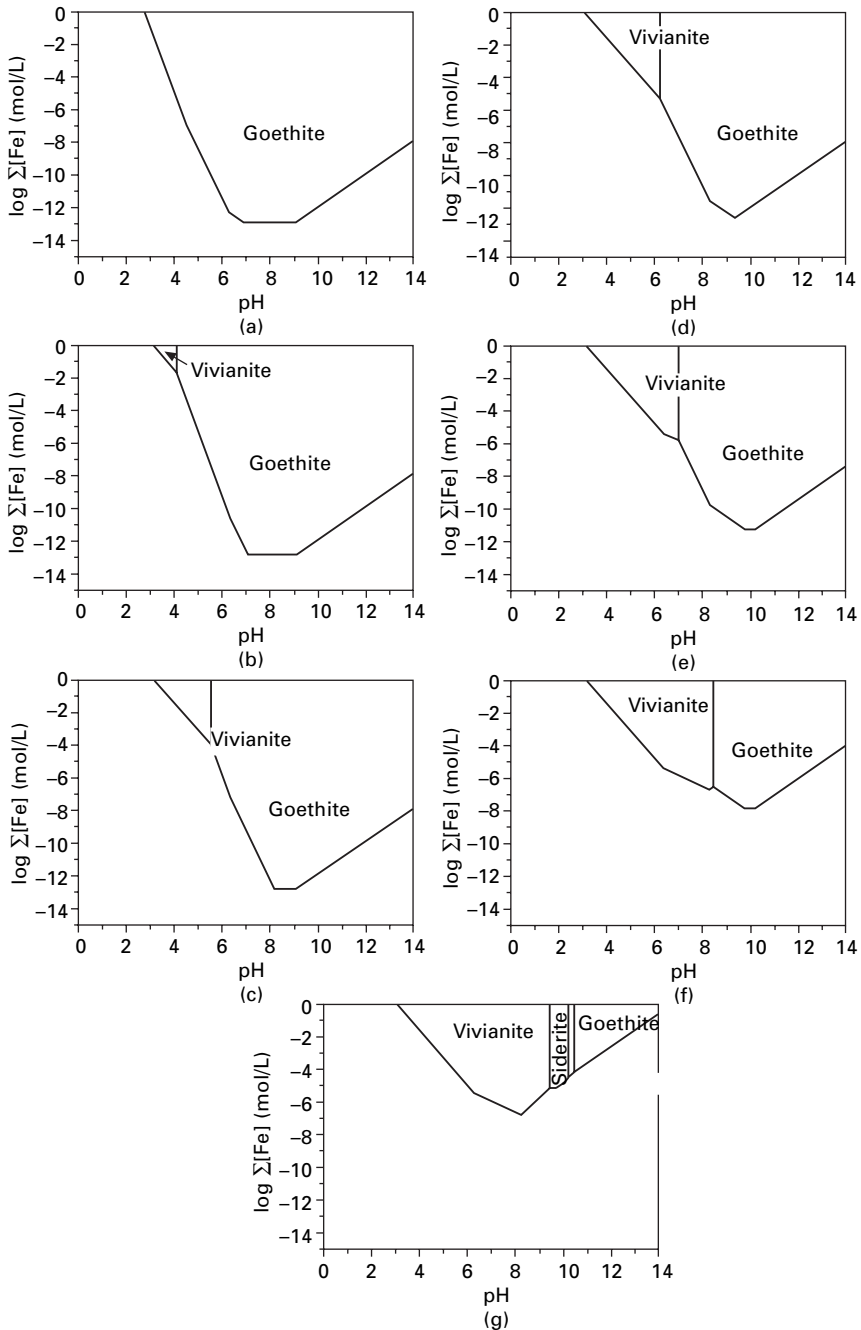
concentration. On the contrary, reading the diagram in terms of phase dissolution, at given Eh and pH, vivianite, magnetite and siderite lead to a higher concentration of iron species in solution than goethite. Together, our calculations show that magnetite and goethite solubilities are high in reducing conditions, even for pH values between 6 and 9. In these particular conditions immobilisation of iron species in soil is not favourable and can lead to their migration far from the metallic core.

In conclusion, despite the fact that the thermodynamic calculations do not take into account all the physico-chemical simultaneous equilibrium conditions that could occur in soil, i.e. competition between complex compounds and presence of cations other than iron (calcium, aluminium, sodium, etc.), such calculations make an essential contribution to this study. Keeping in mind these limitations, the values obtained have been used to calculate a maximal limit of the quantity of metal that could have been lost by dissolution of the corrosion products following the method presented in the next subsection.

CR maximal limit validation

In order not to duplicate the data, only the site of Montbaron (rainfall 666 mm/year and burial for a period of 800 years) was considered. Three pH values were used (6, 7 and 8), corresponding to that measured during the sampling, and five potential representatives of the physico-chemical conditions of soils (from -0.5 to 0.3 V/SHE) were utilised.

Graphics of thickness vs. redox potential and for the considered pH are represented in Figs 4.22 and 4.23. The horizontal line shows the thickness

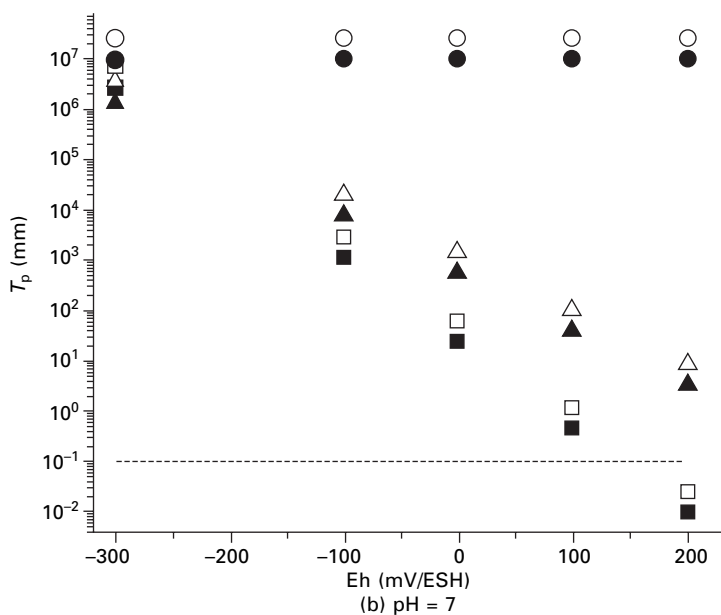
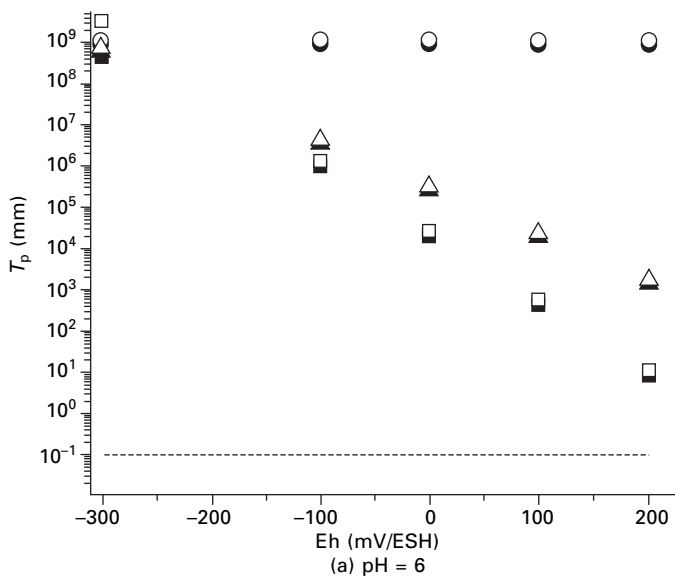


4.21 Solubility of iron considering all the studied phases:

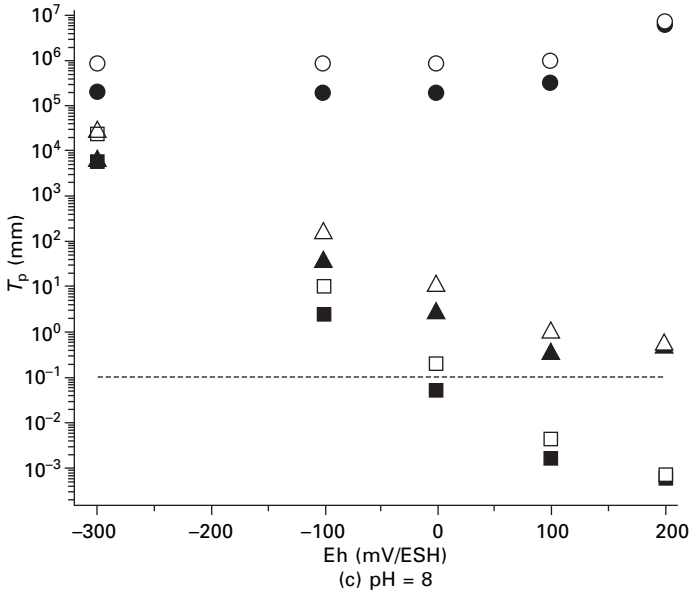
(a) 0.5 V/SHE; (b) 0.3 V/SHE; (c) 0.1 V/SHE; (d) 0 V/SHE;

(e) -0.1 V/SHE; (f) -0.3 V/SHE; (g) -0.5 V/SHE (* = magnetite;

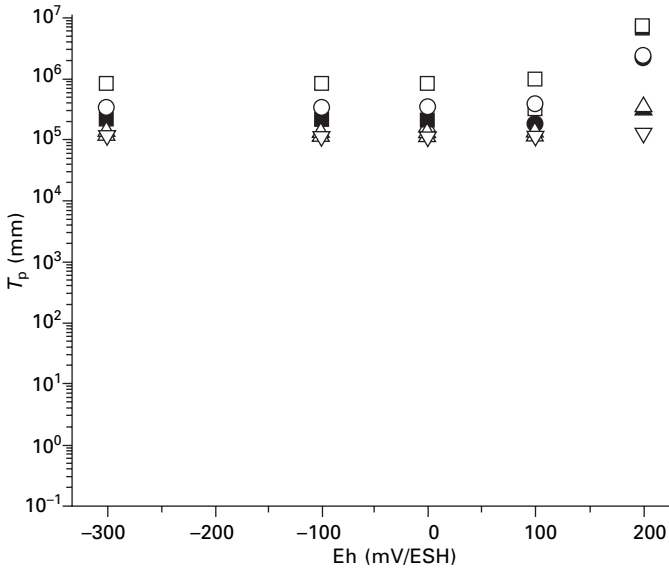
$P_{\text{CO}_2} = 3.16 \times 10^{-4}$ atm; $[\text{Cl}^-] = [\text{HPO}_4^{2-}]_{\text{tot}} = [\text{NO}_3^-] = 10^{-3}$ mol/L).



4.22 Equivalent thickness of iron corrosion product (T_p) as a function of redox potential and pH calculated from the solubility of different phases (rainfall of Montbaron) (■ α -FeOOH; ● $FeCO_3$; ▲ Fe_3O_4 ; the empty symbols correspond to the calculated thickness in the presence of complex compounds).



4.22 Continued



4.23 Equivalent thickness of siderite (T_p) as a function of redox potential and pH (pH = 8) calculated from the solubility of siderite for different values of P_{CO_2} (rainfall of Montbaron) ■ ($P_{\text{CO}_2} = P_{\text{CO}_2 \text{ atm}}$; ● $P_{\text{CO}_2} = 10^{-3}$ atm; ▲ $P_{\text{CO}_2} = 10^{-2}$ atm; ▼ $P_{\text{CO}_2} = 10^{-1}$ atm; the empty symbols correspond to the calculated thickness in the presence of complex compounds.

equivalent to 100 μm , which is in the order of magnitude of the DPL. Although these results were obtained from a simulation realised with fixed parameters, they give a general tendency concerning the behaviour of iron corrosion products in soil. For goethite and magnetite, equivalent thickness values depend on the potential. In reducing conditions (-0.3 to -0.1 V/SHE), as the phases are soluble, the calculated thicknesses are very high, but in oxidising conditions (0 – 0.3 V/SHE) they are negligible compared to the DPL thicknesses.

For siderite, identified on artefacts from Glinet, the equivalent thicknesses are very high regardless of the pH potential conditions and carbonate concentration. This implies that, if the calculation hypotheses were representative of the real burial conditions, no artefacts would remain at the site of Glinet. This paradox will be discussed in the next section.

As expected, since apparent solubilities are higher in the case of the presence of complexant, equivalent thicknesses are slightly higher than in pure water. This behaviour is more significant in reducing conditions. For example, considering goethite at pH = 6 and Eh = -0.3 V/SHE, the equivalent thickness is at most seven times higher (Fig. 4.22) than in pure water. However, this value remains lower than the thickness measured on the corrosion products.

4.4.3 Average corrosion rates

Because their initial dimensions are unknown, it is impossible to determine directly the archaeological artefacts' CR. Therefore some specific method has to be used. The one proposed here rests on the consideration of parameters that play a role in the evolution of the corrosion system during a long period of burial. This evolution affects particularly the corrosion products in contact with aqueous solutions of the burial environment. This is why solubilities of the characterised phases have been carefully considered as a function of the environment parameters. The following paragraphs discuss first the possibility of establishing a maximal CR limit, for siderite on the one hand and for goethite and magnetite on the other.

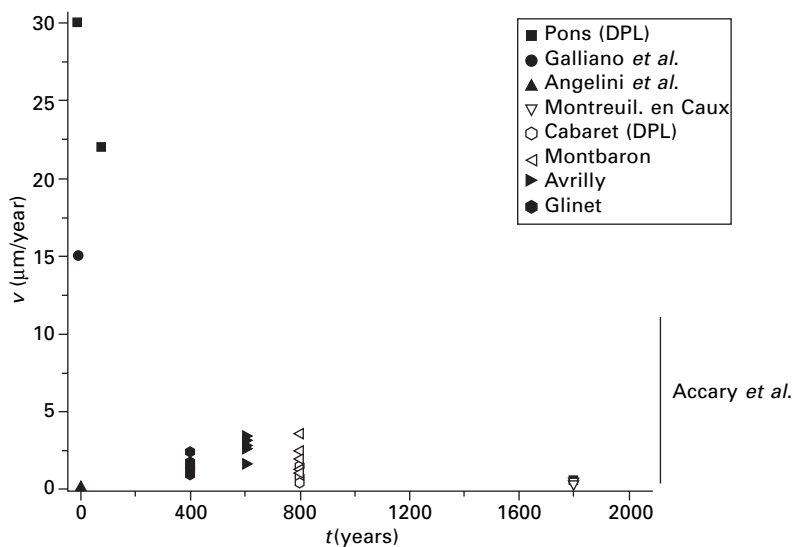
For the Glinet artefacts, the CR obtained by thickness measurements are under 3 $\mu\text{m}/\text{year}$. But the high solubility values prevent the evaluation of a reliable maximal limit of the iron quantity lost from the object by dissolution of the corrosion products. Some further measurements of water and soil compositions could allow one to determinate why siderite is detected in the corrosion products, although the thermodynamic calculations show that this phase is very soluble.

Solubility calculations show the importance of the environmental conditions and especially the redox potential. By varying these parameters, it has been demonstrated that goethite and magnetite are slightly soluble in oxidising conditions, but very soluble in reducing conditions. Generally, goethite is the less soluble phase that is characterised in the corrosion products of the

iron archaeological artefacts. For the artefacts from the four sites other than Glinet, the minimal CR values are between 0.1 and 3.5 $\mu\text{m}/\text{year}$. Moreover, in the case of the main corrosion form that contains only goethite and magnetite, for pH values in the range of 6 to 8 and potential over 0 V/SHE, maximal limit is lower than this minimal CR value, even in the presence of complex compounds. Accordingly, the iron loss due to dissolution is negligible compared to the iron quantity detected in the corrosion products. Then, in these conditions, the minimal CR values can be considered as a good evaluation of the real CR. On the contrary, in reducing conditions, the iron quantity due to the dissolution of goethite or magnetite in aqueous solutions reaches high values.

In conclusion, the minimal CR value estimated by analytical techniques is conclusive in the case of corrosion forms constituted of goethite and magnetite exposed to oxidising conditions. This particular configuration is the main one encountered on our samples. In contrast, in the case of formation of siderite or in reducing conditions, whatever the phase is, the maximal CR value is too high and does not allow any conclusions about the reliability of the minimal CR value. Among our corpus of data, only the site of Glinet is considered, but in this specific burial the conditions certainly confirm the corrosion products as slightly soluble.

Figure 4.24 shows the CR obtained in this study compared with other data collected from the literature. First one can establish that the CR values obtained for the archaeological artefacts after several centuries of burial are lower than those found in the literature for the corrosion of mild steel in soil



4.24 Comparison of the corrosion rates obtained with those gathered from the literature.

(between 35 and 68 $\mu\text{m}/\text{year}$) [29]. In the latter, it is also mentioned that experiments conducted on mild steels during nine years show a slowdown of the average CR. Comparing this result with the shape of the graph of Fig. 4.21, this tendency is confirmed by the archaeological analogues for long periods of burial. This ensures that the corrosion products formed on iron or mild steel play a protective role during the corrosion process for long periods of burial and lead to a slowdown of the metal loss. From the macroscopic point of view, they control the transport of ionic species in the corrosion system. This role needs to be studied in detail in further researches.

4.5 Conclusion

Fifty-four artefacts from five different archaeological sites were analysed in order to better understand the iron corrosion behaviour during very long periods. Samples were taken with the adhering soil in order to study the entire system composed of the metal, the corrosion products and the soil. Optical and electronic microscopic observations, combined with composition analyses by EDS coupled to SEM and EPMA, were performed to study the metallic substrates and the corrosion products. Moreover, two complementary techniques were used to investigate the local structure: μXRD under synchrotron radiation and micro Raman spectroscopy. A specific terminology, well adapted to describing corrosion on ancient artefacts, was proposed: metallic substrate (M), dense product layers (DPL), transformed medium (TM) and soil (S). It was determined that all artefacts were composed of hypoeutectoid steels except for two hypereutectoid steels and four cast iron samples from the Glinet site. Some also contain phosphorus in higher amounts than contemporary steels as well as numerous inclusions heterogeneously distributed. This heterogeneity of structure is responsible for the localised corrosion observed at the metal/corrosion product interface but does not seem to influence the generalised corrosion layer.

Corrosion products are composed mainly of a dark matrix of goethite embedding lighter veins of magnetite/maghemite, and in specific conditions (of reducing potential) siderite can be detected. This corrosion layout is independent of the local composition of the metallic matrix.

This study has revealed that species transport phenomena play an important role in the corrosion processes, i.e. the diffusion of oxygen and other species in the water of the DPL pores and cracks controls the corrosion process. Moreover, the local pH and redox potential in the corrosion scale can explain the variation of the corrosion forms obtained on samples from the same site.

During long periods of burial, corrosion systems constituted of metal, corrosion products and the environment are constantly evolving. With this in mind, a method of estimating the corrosion rate (CR) of archaeological artefacts has been set up. These CR are based on the estimation of the

quantity of iron that comes from the artefacts into the corrosion products and the environment. This method of assessment proceeds in two steps, giving a minimal and a maximal CR:

- 1 Analytical techniques were utilised to measure the thickness of the corrosion product layers: by optical microscope for DPL and by establishing average elementary distribution profiles for TM.
- 2 The maximal limit was calculated by evaluating the likely iron amount that is generated by the dissolution of the corrosion layers.

As a first conclusion, we have shown that it is possible to establish a reliable maximal CR limit for goethite and magnetite in oxidising conditions. In contrast, maximal limits are far higher than the minimal CR values for goethite and magnetite in reducing conditions and for siderite, whatever the conditions (pH, Eh, P_{CO_2}). The presence of siderite in some samples could be due to the specific burial environment: calcium in siderite, a large amount of iron in the soil, or competition between carbonate and oxygen that was not considered in the calculations. Solubility calculations need to be refined in order to get closer to the real conditions of burial: correlation of the complex compound concentrations, pH and potential with *in situ* measurements.

In conclusion, CR values measured on a corpus of 54 archaeological artefacts are under 4 $\mu\text{m}/\text{year}$. Compared with data in the literature for buried low-carbon steels, these CR values are low. Moreover, they tend to decrease with time, showing that the corrosion products themselves play a role in long-term corrosion mechanisms.

These studies are pursued further in Chapter 6 of this book.

4.6 Acknowledgements

All the archaeologists at the different sites are thanked for allowing us to cut the iron artefacts: Christophe Colliou, Danièle Aribet-Deroin, Armelle Querrien, Berengère Le Cain and Marie-Elise Gardelle. We also thank Pierre Chevallier for the μXRD experiments on the Lure D15 beamline and Nicole Metrich for the μXAS experiments on the ESRF ID21 beamline. This work was partly funded by the French ANDRA agency and the CNRS GDR Chimart.

4.7 References

1. D. Neff, P. Dillmann, M. Descostes and G. Beranger, Corrosion of iron archaeological artefacts in soil – 2: Phase solubility and average corrosion rates. *Corrosion Science*, 2006, **48**: 2947–2970.
2. D. Neff, P. Dillmann, L. Bellot-Gurlet and G. Béranger, Corrosion of iron archaeological artefacts in soil: characterisation of the corrosion system. *Corrosion Science*, 2005, **47**: 515–535.

3. T. Misawa, K. Hashimoto and S. Shimodaira, The mechanism of formation of iron oxide and oxyhydroxides in aqueous solutions at room temperature. *Corrosion Science*, 1974, **14**: 131–149.
4. B. Soerensen and D. Gregory, *In situ* preservation of artifacts in Nydam Mose. In Metal 98, Conference on Metals Conservation, 1998, Draguignan-Figanières, France: James & James, London.
5. W. Gerwin, W. Sharff and R. Baumhauer, Corrosive decay of archaeological metal finds from different soils and effects of environmental pollution. in Metal 98, Conference on Metals Conservation, 1998, Draguignan-Figanières, France: James & James, London.
6. H. Matthiesen, D. Gregory, P. Jensen and B. Sørensen, Environmental monitoring at a waterlogged site with weapon sacrifices from the Danish Iron age. I: Methodology and results from undisturbed conditions. *Journal of Wetland Archaeology*, submitted.
7. E. Angelini, E. Barberis, P. Bianco, F. Rosalbino and L. Ruatta, Effect of burial in different soils on the decay of iron artefacts: laboratory investigations. in Metal 98, Conference on Metals Conservation, 1998, Draguignan-Figanières, France: James & James, London.
8. H. Matthiesen, L.R. Hilbert and D.J. Gregory, The occurrence and stability of siderite as a corrosion product on archaeological iron from a waterlogged environment. *Studies in Conservation*, 2003, **48**(3): 183–194.
9. D. Neff, S. Reguer, L. Bellot-Gurlet, P. Dillmann, and R. Bertholon, Structural characterization of corrosion products on archaeological iron. An integrated analytical approach to establish corrosion forms. *Journal of Raman Spectrometry*, 2004, **35** (special issue on the application of Raman spectroscopy in art and archaeology): 739–745.
10. E. Pons, Corrosion à long terme du fer et des aciers non ou faiblement alliés dans les sols à dominante argileuse – Caractérisation physico-chimique et étude électrochimique d’analogues archéologiques, 2002, Université de Technologie de Compiègne, Compiègne, p. 239.
11. E. Pons, S. Joiret, A. Hugot-Le-Goff, D. David, and C. Lemaître, Approche de la corrosion d’analogues archéologiques ferreux par spectroscopie Raman et méthodes électrochimiques. *Techne*, 2003, **18**: 94–100.
12. E. Pons, L. Uran, S. Joiret, A.H.L. Goff, C. Lemaitre and D. David, Corrosion à long terme du fer dans les sols argileux: étude physico-chimique et électrochimique de vestiges de 1914–1918. *Revue de Métallurgie*, 2003, **100**(2).
13. J. Chivot, Sélection de Données Thermodynamiques Concernant le Système Fe–H₂O, 1998, CEA/FAR SCECF.
14. A. Accary and B. Haijink, La paléoméallurgie – Outil de prévision. In *Journées de Paléoméallurgie*, 1983, Université de Technologie de Compiègne, Compiègne.
15. B. Miller and N. Chapman, Postcards from the past: archaeological and industrial analogs for deep repository materials. *Radwaste Magazine*, 1995, January: 32–42.
16. W. Gerwin and R. Baumhauer, Effect of soil parameters on the corrosion of archaeological metal finds. *Geoderma*, 2000: **96**, 67–80.
17. E. Vega, Altération des objets ferreux archéologiques sur le site de Glinet (Seine-maritime, France, XVI^e siècle). Caractérisation des produits de corrosion et étude des mécanismes, 2004, Université de Technologie de Belfort Montbéliar, Belfort, p. 127.
18. P. Dillmann, P. Populus, P. Chevallier, P. Fluzin, G. Beranger and A. Firsov, Microdiffraction coupled with X ray fluorescence microprobe. Application in archaeometry. *Journal of Trace and Microprobe Techniques*, 1997, **15**(3): 251–262.

19. P. Dillmann, D. Neff, E. Vega and P. Fluzin, Etude des objets archéologiques ferreux pour la compréhension de la corrosion à très long terme. *Helvetica Archaeologica*, 2002, **131/132**: 90–99.
20. P. Dillmann, R. Balasubramaniam and G. Béranger, Characterization of protective film on ancient Indian iron using microprobe analyses. *Corrosion Science*, 2002, **44**: 2231–2242.
21. J. Susini, M. Salomé, B. Fayard, R. Ortega and B. Kaulich, The scanning X-ray microprobe at the ESRF ‘X ray microscopy’ beamline. *Surface Review and Letters*, 2002, **9**(1): 203–211.
22. M. Bonnin-Mosbah, N. Metrich, J. Susini, M. Salome, D. Massare and B. Menez, Micro X-ray absorption near edge structure at the sulfur and iron K-edge in natural silicate glasses. *Spectrochimica Acta B*, 2002, **57**: 711–725.
23. W.-J. Chitty, P. Dillmann, V. L’Hostis and C. Lombard, Long term corrosion resistance of metallic reinforcements in concrete – A study of corrosion mechanisms based on archaeological artefacts. *Corrosion Science*, 2005, **47**: 1555–1581.
24. L. Mazzetti and P.J. Thistlethwaite, Raman spectra and thermal transformations of ferrihydrite and schwertmannite. *Journal of Raman Spectrometry*, 2002, **33**: 104–111.
25. R.M. Cornell and R. Giovanoli, Acid dissolution of akaganeite and lepidocrocite: the effect on crystal morphology. *Clays and Clay Minerals*, 1988, **36**(5): 385–390.
26. P. Duchaufour, *Précis de Pédologie*, Masson et Cie, 1970, Paris, p. 481.
27. J. Chivot, *Les Diagrammes E–pH Révisés du Système Fer–H₂O en Fonction de la Température*, 1999, CEA/SCECF.
28. M. Descostes, Evaluation d’une perturbation oxydante en milieux argileux: mécanisme d’oxydation de la pyrite, 2001, Université Paris VII, Paris, p. 308.
29. L. Shreir, Ferrous metals and alloys, in *Corrosion*, Vol. I, L. Shreir, R. Jarman, and G. Burstein (eds), 1994, Oxford, p. 160.

Electrochemical study of steel artefacts from World War I: Contribution of A.C. impedance spectroscopy and chronoamperometry to describe the behaviour of the corrosion layers

E. PONS, C. LEMAITRE and D. DAVID,
Université de Technologie de Compiègne, France and
D. CRUSSET, ANDRA, France

5.1 Introduction

In order to predict the behaviour of carbon steels, which corrode over long periods in soils, six objects from a battlefield of World War I were studied. Two layers of corrosion products were observed at the interface between the residual alloy and the soil products. Microscopic observations (optical microscopy and SEM) combined with Raman-laser spectroscopy analyses revealed the same iron corrosion products in the two layers: mainly oxides and oxyhydroxides always with the presence of goethite, α -FeOOH [1], but with different physical properties between the two layers (colour, compactness). The external layer contains corrosion products mixed with soil crystals. Prior electrochemical study showed also that the corrosion process is limited by the characteristics of the internal layer. Thus, the behaviour of that internal corrosion layer was investigated by using two different electrochemical techniques – A.C. impedance spectroscopy and chronoamperometry – to propose a model which contributes to the prediction of the degradation of carbon steels in soils.

5.2 Objective and experimental methods

5.2.1 Artefacts

For these electrochemical experiments, we selected six remains made of steel from a battlefield of World War I, located in Nouvron-Vingré (Aisne, France): five pieces of shrapnel and one piece of iron wire. The artefacts were excavated with their surrounding soil, stored between two paraffin layers (5–10 mm thick), and prepared rapidly after excavation. If the lumps had to be stored for more than a few months, they were dehydrated (by freeze-drying or water/acetone exchange), before coating with a resin. The prior characterization of the samples (metallographic examination, SEM observations, Raman spectroscopy) revealed a similar metallic microstructure

Table 5.1 Measurements of the corrosion layer thickness (1914–1918 remains) [4]

| Sample | Total thickness of corrosion products (internal + external) | | | Thickness of the internal corrosion layer | | |
|---------|---|--------------------|--------------|---|--------------------|--------------|
| | Minimum value (mm) | Maximum value (mm) | Average (mm) | Minimum value (mm) | Maximum value (mm) | Average (mm) |
| NV00_01 | 1.3 | 1.9 | 1.6 | 0.5 | 1.1 | 0.8 |
| NV00_02 | 2.1 | 4.1 | 3.5 | 0.7 | 1.9 | 1.2 |
| NV00_06 | 0.2 | 2.0 | 1.0 | 0.2 | 1.9 | 0.8 |
| NV00_10 | 1.8 | 3.2 | 2.5 | 0.6 | 1.1 | 0.8 |
| NV00_19 | 0.8 | 3.5 | 2.1 | 0.5 | 1.6 | 1.1 |
| NV00_20 | 0.4 | 5.5 | 2.4 | 0.2 | 1.5 | 1 |

[2], corresponding to hypoeutectoid steels (low carbon content: under 0.1 to 0.6%). We did not detect any alloying element which could influence their corrosion behaviour, such as chromium, nickel or molybdenum. These artefacts were chosen for their relative similarity, in terms of not only the alloy but also their corrosion layers. All of them had two corrosion layers: a dark grey internal layer (in direct contact with the metallic core) and an orange-brown external layer [3]. In this external layer, soil markers, like quartz crystals, were identified among iron corrosion products. The thickness of the layers is about one millimetre. It is similar between the artefacts, and for each artefact the size is comparable between its two corrosion layers (Table 5.1). The average thickness of the internal layer was measured at between 0.8 and 1.2 mm [4].

5.2.2 Methods

The long period of burial of the artefacts had led to the formation of thick and heterogeneous corrosion layers. Among the electrochemical techniques, two are particularly well adapted to the study of such layers: electrochemical impedance spectroscopy (EIS) and chronoamperometry. EIS diagrams were recorded at the rest potential, in potentiostatic conditions. A 12 mV sinusoidal signal perturbation was chosen, with frequencies between 10^4 and 1.58×10^{-2} Hz (five frequencies per decade). The results were plotted either in the Nyquist or in the Bode representation. It was then possible to describe equivalent electrical circuits, which represent the interface behaviour.

5.2.3 Sample preparation, electrochemical cell and electrodes

To obtain reproducible results, the experiments were performed in a specially designed electrochemical cell [4]. This cell allowed us to work in the same geometric configuration (constant distance between the electrodes). The volume

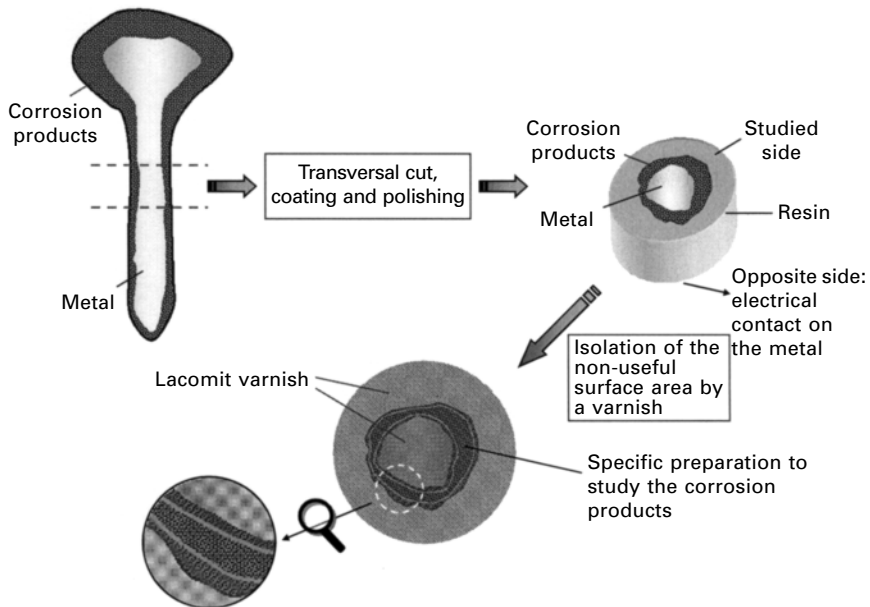
of the introduced electrolyte was 0.5 L. It was separated into two parts: the first where the solution could be de-aerated, and the second where the test was performed.

The samples had to undergo a specific preparation, which began with a transversal cut. Each cut specimen was then coated in a cylindrical form ($\text{Ø} = 25$ or 30 mm) with an epoxy resin, and polished with a silicon carbide paper, until grade 1200. The non-useful surface area was isolated by the use of a varnish (Lacomit Varnish), and the exposed surface S was calculated by surface imaging. By isolating the metal and the external layer, it was therefore possible to work only on the properties of the internal layer. Otherwise, two corrosion layers can be masked with the varnish and it was then possible to work on the residual metal. An electric contact was situated on the opposite side of the polished surface. The preparation process is illustrated in Fig. 5.1.

In the experimental cell, the coated artefact was the working electrode; we used a platinum counter electrode ($\text{Ø} = 1$ cm), and a saturated calomel electrode (SCE) for potential measurement.

5.2.4 Electrolyte

The medium for the electrochemical tests was Evian mineral water, because of its constant characteristics. The value of its conductivity in laboratory



5.1 Preparation process for the electrochemical experiments (only one corrosion layer is represented, to simplify the diagram).

conditions (ambient temperature about 20°C) was 523 μS/cm and its pH was 7.2. When better conductivity was necessary, we added 25 g/L of sodium chloride (the chloride content of pure Evian mineral water is 4.5 mg/L). In this case, the conductivity was 37,000 μS/cm, with pH 8.3. The electrolyte could be de-aerated before the test.

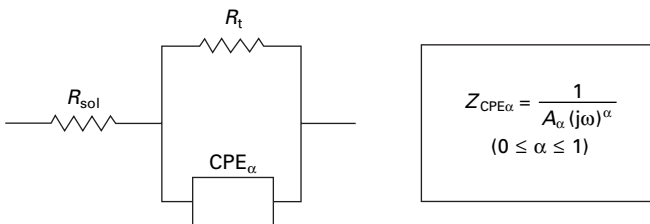
5.3 Specific electrochemical behaviour depending on the corrosion layers

Diagrams of metal samples are oblate semi-circles, beginning on the real axis (for high frequencies) at resistance R_{sol} corresponding to the electrolyte resistance. This diagram can be better simulated using a ZARC circuit than with a classical Randles circuit. This ZARC circuit (Fig. 5.2) is composed of a pseudo-capacitance, called the ‘constant phase element’ (CPE), whose impedance is given by the following relationship:

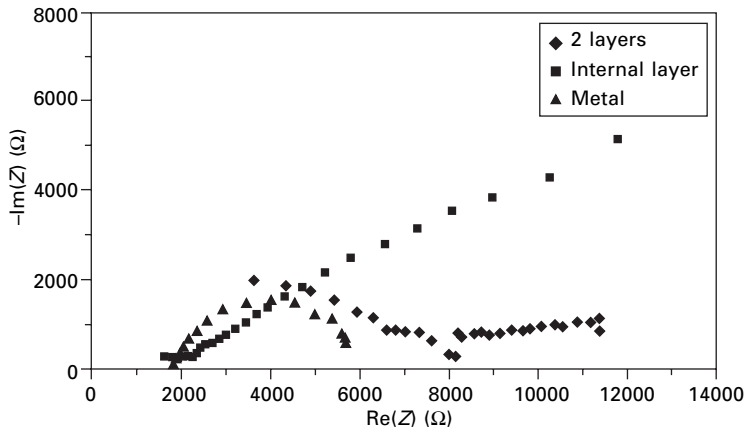
$$Z_{CPE\alpha} = \frac{1}{A_\alpha (j\omega)^\alpha} \tag{5.1}$$

with $0 \leq \alpha \leq 1$ and A_α constant. (If $\alpha = 0$, $Z_{CPE\alpha}$ is a resistance, and if $\alpha = 1$, $Z_{CPE\alpha}$ is a capacitance.) This pseudo-capacitance explains the oblate semi-circle describing the behaviour of solid electrodes [5]. A physical interpretation of this CPE can be linked to the roughness of the metal: the value of α decreases when the roughness of the metal increases [6, 7, 8]. The parameters α and A_α were determined from the experimental results; α is around 0.7 for each sample [4], which can be explained by their similar surface state (due to the preparation procedure).

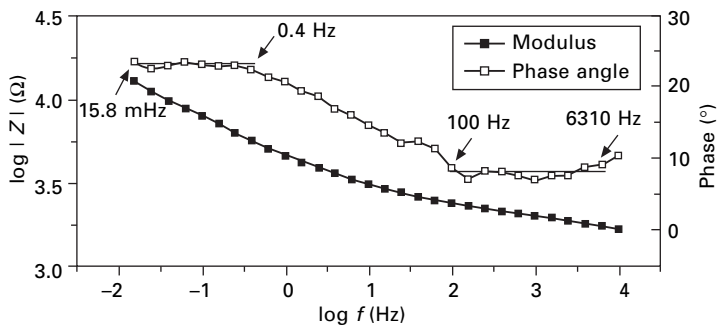
With corrosion layers, the diagram is very different. Figure 5.3 gives the Nyquist plots obtained on a piece of shrapnel with one or two corrosion layers; the plot of the metal is added for comparison. For the two-layers samples, the diagram presents three parts: a first loop at high frequencies, a second loop in the middle range of frequencies and a straight line at low frequencies, with an angle close to 6°. This result relates to the existence of three interfaces in the system: between the external layer and the electrolyte,



5.2 ZARC circuit (metal samples).



5.3 Comparison of the Nyquist diagrams in Evian mineral water with two layers of corrosion products, with the internal layer only, and for the residual metal (sample NV00_06).



5.4 Bode diagram corresponding to the presence of the internal layer (sample NV00_06).

between the internal layer and the external layer, and between the metallic core and the internal layer [3, 4].

The most interesting result concerns the diagram for the internal layer. For high frequencies (over 100 Hz), the phase angle φ is constant, close to 8° . For low frequencies, the phase angle is also constant and close to 23° (Fig. 5.4). But the characteristic angle corresponding to a pure diffusion process through a porous layer is 22.5° [6, 9, 10], as discussed later in this chapter. It therefore appeared necessary to study in more detail the internal layer according to porous electrode theory.

5.4 Advanced electrochemical study of the internal corrosion layer

5.4.1 Impedance spectroscopy

Evolution of the impedance diagram with the electrolyte conductivity

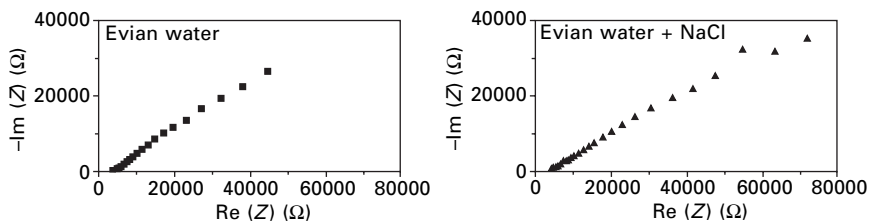
The impedance diagram established in Evian water for the internal layer shows a linear part at low frequencies with a phase angle of about 22.5° , which suggested the behaviour of a porous electrode. In the next part of this chapter, we confirm this result, referring to the De Levie theory of porous electrodes [9, 10]. Impedance diagrams were established for different immersion times in a more conductive medium: Evian water containing sodium chloride (25 g/L). The comparison of the plots in pure Evian water and in salt-containing Evian water is given in Fig. 5.5 for a representative sample (NV00_06). The main findings can be summed up as follows:

- The impedance modulus decreases by a factor of about 10 in Evian water + NaCl
- The general aspect of the diagram is not modified
- The diagram undergoes little change after two hours of immersion.

Consequently, we keep only the diagrams corresponding to an immersion time of two hours in the next part of the discussion.

Porous electrode impedance modelling

This modelling relies on the numerous studies carried out in the 1960s by De Levie on the A.C. behaviour of a porous electrode [6, 9, 10]. He established some simple formulae that relate the specific behaviour of a porous electrode to that of a corresponding flat electrode, based on the distribution of the current and potential within the pores. The main hypotheses for the mathematical modelling of De Levie theory are listed below [9, 10]:



5.5 Evolution of impedance diagram during immersion in Evian water and in Evian + NaCl (sample NV00_06A).

- The pores are identical, of uniform cross-section, of semi-infinite length and without cross-links
- The pores are homogeneously filled with inert electrolyte, present in a large amount
- The electrode material resistance can be neglected
- Any curvature of the equipotential surfaces within the pores can be neglected.

These hypotheses lead us to express the pore impedance as follows [9, 11]:

$$Z_{\text{pore}} = (R_s Z_i)^{1/2} \quad 5.2$$

where R_s = resistance of the electrolyte within the pore, per unit pore length ($\Omega \cdot \text{cm}^{-1}$)

Z_i = interfacial impedance (electrolyte–electrode interface) per unit pore length ($\Omega \cdot \text{cm}$).

Z_i , the pore wall/solution interface impedance, is also the impedance of a corresponding flat electrode [10].

The resistance of the solution within the pore was expressed by Park and Macdonald as a function of the parameters describing the porous layer [12], as represented in Fig. 5.6:

$$\rho_e L n / [(1 - \theta) S]$$

where ρ_e = resistivity of the electrolyte

L = thickness of the layer

S = surface of the layer

θ = surface coverage ratio

n = number of pores.

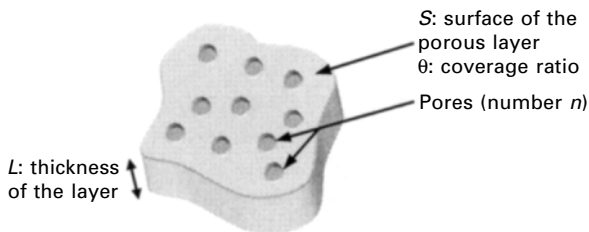
Per unit pore length, we obtain:

$$R_s = \rho_e n / [(1 - \theta) S] = \alpha \rho_e / S \quad 5.3$$

with $\alpha = n / (1 - \theta)$, an experimental constant.

From equations (5.2) and (5.3), we find:

$$Z_{\text{pore}} = (\alpha \rho_e Z_i / S)^{1/2} \quad 5.4$$



5.6 Parameters to describe a porous electrode according to Park and Macdonald [12].

Representation in the complex impedance plane

In the complex impedance plane, we have:

$$Z_i = |Z_i| e^{j\varphi}$$

in which $|Z_i|$ and φ are the modulus and the phase of the interfacial impedance. The expression for the pore impedance (5.2) becomes:

$$Z_{\text{pore}} = R_s^{1/2} |Z_i|^{1/2} e^{j\varphi/2} \quad 5.5$$

from which we deduce that the modulus of the pore impedance is $R_s^{1/2} |Z_i|^{1/2}$, whereas its phase angle is $\varphi/2$. Then, if the phase angle is $\varphi = 45^\circ$ in the case of a flat electrode with pure diffusion control, it is equal to $\varphi/2 = 22.5^\circ$ for the corresponding porous electrode. Our results showed an experimental phase angle of 23° , very close to the value of the model. This is the reason why we considered a diffusion mechanism in the presence of a porous layer. This model was completed by Park and Macdonald [12], who studied the growth of porous magnetite film on carbon steels, and had to consider the resistance of the electrode material and the interfacial impedance (metal/solution) at the base of the pore (pore of finite length).

Correction of the diagrams

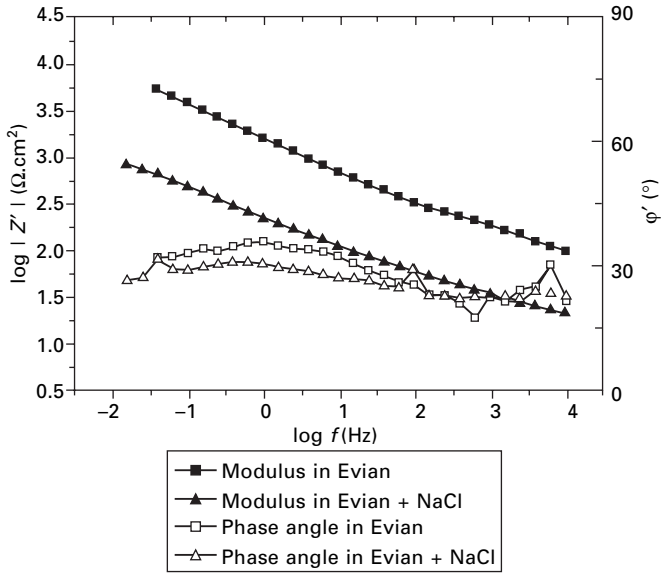
The previous impedance diagrams performed in Evian water and in salt-containing Evian water after two hours of immersion have been corrected in a two-step procedure. In the first step, we corrected the real component of the impedance from the resistance of the solution R_{sol} , obtained by a linear regression of the Nyquist plot for high frequencies. The second step consists of taking into account the surface S of the sample which is exposed to the solution. The corrected impedance is called Z' and is expressed in $\Omega \cdot \text{cm}^2$. In the complex impedance plane, its real and imaginary components are:

$$\text{Re}'(Z) = [\text{Re}(Z) - R_{\text{sol}}] \cdot S$$

and

$$-\text{Im}'(Z) = -\text{Im}(Z) \cdot S$$

In the Nyquist representation, the form of the diagram is the same, but it begins at the zero point of the complex impedance plane on the real axis and the scales are modified. To obtain the Bode diagram, the modulus and the phase angle, called $|Z'|$ and φ' , are recalculated from $\text{Re}'(Z)$ and $-\text{Im}'(Z)$. The corrected impedance diagrams in the two electrolytes are given in Fig 5.7 for the sample NV00_06A.



5.7 Corrected impedance diagram for the internal layer (sample NV00_06A).

Fitting of the impedance diagrams

From equation 5.5, the corrected impedance can be written as follows:

$$Z' = Z_{\text{pore}} S = S(\alpha \rho_e Z_i / S)^{\frac{1}{2}} = (\alpha \rho_e Z_i S)^{\frac{1}{2}} \quad 5.6$$

We then deduce the following relationship:

$$\log |Z'| = \frac{1}{2} \log \rho_e + \frac{1}{2} \log |\alpha Z_i S| \quad 5.7$$

which can be applied both to the impedance recorded in pure Evian water, and to the impedance obtained in Evian water + NaCl. It results in:

$$\log |Z'_{\text{Evian}}| - \log |Z'_{\text{Evian+NaCl}}| = \frac{1}{2} \log (\rho_{\text{Evian}} / \rho_{\text{Evian+NaCl}}) \quad 5.8$$

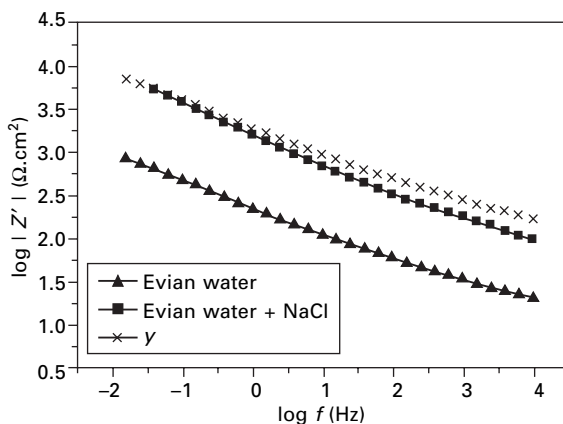
With the numerical values of the resistivity of the solutions (1910 Ω .cm for Evian water, 27 Ω .cm for salt-containing Evian), we have:

$$\log |Z'_{\text{Evian}}| - \log |Z'_{\text{Evian+NaCl}}| = \frac{1}{2} \log (\rho_{\text{Evian}} / \rho_{\text{Evian+NaCl}}) = 0.925 \quad 5.9$$

In order to verify the model, we plotted the experimental values of

$$y = \log |Z'_{\text{Evian+NaCl}}| + 0.925 \quad 5.10$$

and we compared the results with the Bode diagram in Evian water. The results are reported in Fig. 5.8 for the sample NV00_06A.



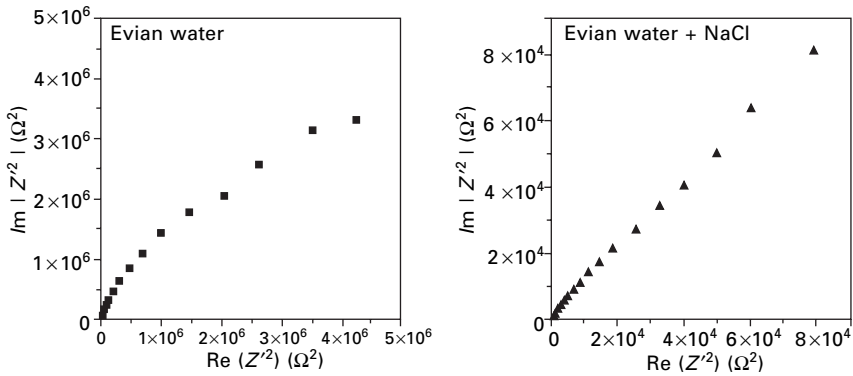
5.8 Correlations between Bode diagrams referring to the simplified De Levie theory (sample NV00_06A).

The experimental results are globally in good agreement with the proposed model. On the sample NV00_06, there is a very good correlation at low frequencies, i.e. when the signal course in the pore is longer: this result agrees with the hypothesis of semi-infinite pores considered in this simplified modelling. For high frequencies, we yet observe that $\gamma > \log |Z'_{\text{Evian}}|$. This phenomenon can be explained by a possible transport process through the internal layer – a solid phase transport process in the electrode material – whereas we considered for modelling only the diffusion process in the pores.

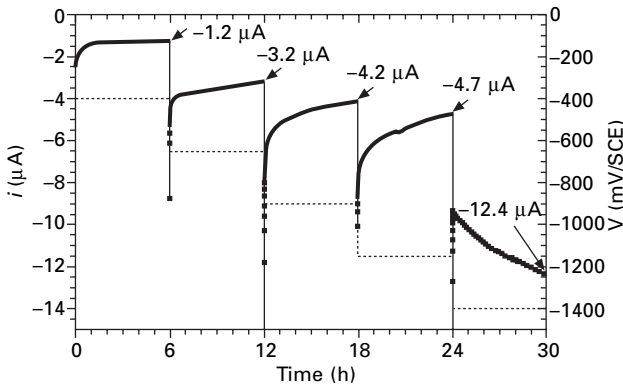
Confirmation of two transport process modes – use of the squared impedance plane

For complex porous systems, it is possible to represent the squared impedance after correction of the electrolyte resistance in the complex plane [9]. We thus obtain the impedance diagram of the corresponding flat electrode. This representation was performed from the results recorded in Evian water and in Evian water + NaCl for the sample NV00_20B (Fig. 5.9).

The squared electrode impedance diagrams are not similar in Evian water and in Evian + NaCl. In salt-containing Evian water, the diagram is very close to a straight line with a phase angle of 45° , corresponding to pure diffusion control (the average phase angle obtained on the low frequency points is 47.5°). In pure Evian water, the relationship is much less linear. This result supports the hypothesis of two distinct transport phenomena in Evian water. Because of the low conductivity of pure Evian water, it is possible to have simultaneously a diffusion process of the species in the electrolyte contained in the pores and a solid-phase transport process in the electrode material (internal layer).



5.9 Squared impedance after correction of the electrolyte resistance in Evian and in salt-containing Evian (sample NV00_20B).



5.10 Current intensity as a function of time for five cathodic potentials, sample NV00_19B (internal layer).

5.4.2 Chronoamperometry in Evian mineral water

Chronoamperometry tests were performed to investigate the steady-state behaviour of the system, when the sample is stabilized in the aqueous medium. They consisted of studying the current intensity as a function of the immersion time.

Experimental procedure

An experimental three-step procedure was followed [4]. First, the current intensity was recorded in Evian mineral water over six hours for different cathodic potentials. Figure 5.10 gives the chronoamperometry curve for the sample NV00_19B. Five cathodic potentials were chosen: $V = -400, -650,$

–900, –1150 and –1400 mV/SCE. In the second step, we could deduce from the curve the value of the steady-state current i_{stat} for each potential. It can be read on the curve after six hours at the same imposed potential. Even if the current stabilization seems not obvious, it respects the arbitrary condition which defines steady-state: the variation must be less than 40 nA/s. At potential –1400 mV/SCE, corresponding to the highest evolution, the numerical value of the current variation is 0.11 nA/s. The third stage consists of plotting the steady-state current as a function of the imposed potential to obtain the current–potential curve in steady-state conditions.

Figure 5.11 reports the curves obtained on the samples NV00_19B and NV00_01A for the cathodic branch. For each experiment, the surface of the layer exposed to the electrolyte is given.

Approximation of the cathodic curve considering the mass transport phenomena

The fifth point in the cathodic domain is not taken into account for the following development, because it corresponds to the reduction of water into hydrogen (hydrogen evolution). For the cathodic branch at high overpotential values, the curve can be modelled by the following expression for the current–overpotential, equation 5.11, which considers not only charge transfer but also mass transport phenomena [13]:

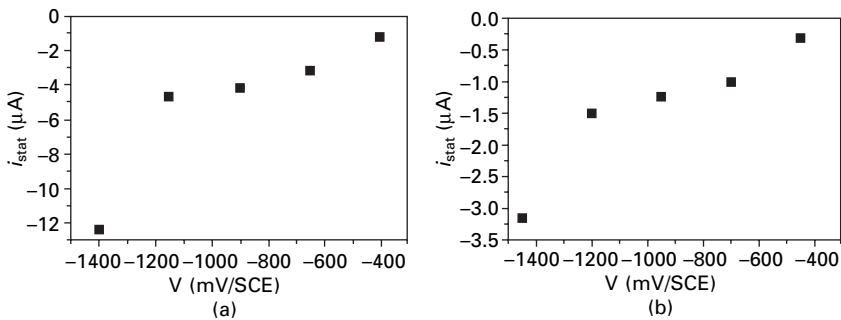
$$\frac{i}{i_o} = \left(1 - \frac{i}{i_{l,c}} \right) e^{-\alpha n f \eta} \quad 5.11$$

where i_o = exchange current

$i_{l,c}$ = cathodic limiting current

α = transfer coefficient of the cathodic reaction

n = number of electrons involved in the reaction



5.11 Current–potential curve in steady-state for two 1914–1918 remains: (a) NV00_19B, $S = 0.06 \text{ cm}^2$; (b) NV00_01A, $S = 0.02 \text{ cm}^2$.

$$f = F/RT (= 39.6 \text{ at } T = 20^\circ\text{C})$$

η = over potential.

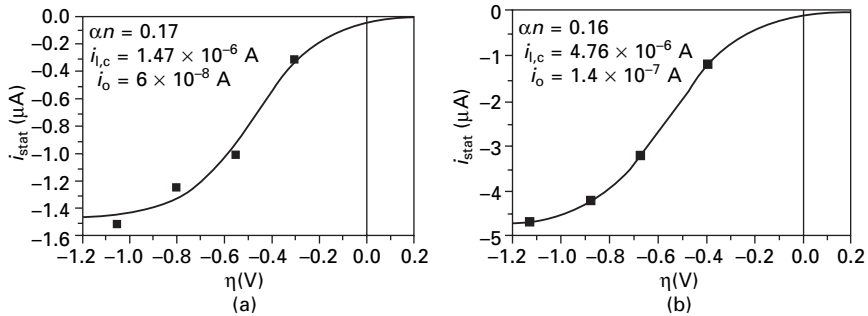
This formula is established with US conventions, i.e. with a positive cathodic current. Its solution has the following form:

$$i = \frac{e^{-\alpha n f \eta}}{\frac{e^{-\alpha n f \eta}}{i_{l,c}} + \frac{1}{i_0}} \tag{5.12}$$

The experimental curves $i_{\text{stat}} = f(\eta)$ were then modelled according to equation 5.12, using the software *Microcal Origin*. The parameters resulting from the fitting are indicated in Fig. 5.12.

Table 5.2 sums up the results obtained from this modelling. From the value of the exchange current, we could also estimate the instantaneous corrosion rate of the samples in Evian water, on the basis of Faraday’s law (considering two electrons in the reaction).

For comparison, polarization curves were performed on metal samples of the same objects. The Tafel law then provided for the metal an instantaneous corrosion rate in Evian water between 280 and 1350 $\mu\text{m}/\text{year}$ for the different remains. In spite of its porosity previously attested, the internal corrosion layer of the 1914–1918 remains led to a significant decrease of corrosion rate during burial, by a factor of 10.



5.12 Current–overpotential modelling for the cathodic branch: (a) NV00_19B; (b) NV00_01A.

Table 5.2 Results of the cathodic modelling

| Sample (internal layer) | $i_{l,c}$ (μA) | i_0 (μA) | $\alpha \cdot n$ | S (cm^2) | $J_{l,c}$ ($\mu\text{A}/\text{cm}^2$) | J_0 ($\mu\text{A}/\text{cm}^2$) | v_{cor} ($\text{cm} \cdot \text{s}^{-1}$) | v_{cor} ($\mu\text{m}/\text{an}$) |
|-------------------------|-----------------------------|-------------------------|------------------|-----------------------|---|-------------------------------------|--|--|
| NV00_19B | 1.47 | 0.06 | 0.17 | 0.06 | 80 | 2.3 | 8.45×10^{-11} | 26.7 |
| NV00_01A | 4.76 | 0.14 | 0.16 | 0.02 | 75 | 2.9 | 1.06×10^{-10} | 33.6 |

$J_{l,c}$ = the cathodic limiting current density ($i_{l,c}$) divided by the surface.
 J_0 = the exchange current density (i_0) divided by surface.
 v_{cor} = the corrosion rate.

5.5 Conclusion

Carbon steels excavated from a battlefield of World War I exhibited two thick and heterogeneous corrosion layers, formed during the subsequent long period of burial in the soil. Considering that their further corrosion was limited by the properties of the internal layer, the modelling proposed in this chapter lets us draw two distinct conclusions:

- The first series of experiments, carried out by electrochemical impedance spectroscopy, confirmed that the internal layer was porous, as was previously attested for the external one. The impedance diagrams showed that the corrosion was controlled by transport phenomena of the species through this porous internal layer. In Evian water, which has poor conductivity, it was necessary to consider simultaneously two processes: a diffusion process in the liquid medium filling the pores and a solid-phase transport process in the electrode material.
- In the second series of experiments, chronoamperometry tests revealed that the internal corrosion layer was protective, in spite of its porosity. This layer plays a significant role in hindering the further evolution of corrosion, leading to a large fall in the corrosion rate.

5.6 References

1. E. Pons, S. Joiret, A. Hugot-Le Goff, D. David and C. Lemaitre, 'Approche de la corrosion d'analogues archéologiques ferreux par spectroscopie Raman et méthodes électrochimiques', 2003, *Techné*, **18**, 95–100.
2. E. Pons, L. Uran, S. Joiret, A. Hugot-Le Goff, C. Lemaitre and D. David, 'Corrosion à long terme du fer dans les sols argileux: étude physico-chimique et électrochimique de vestiges de 1914–1918', 2003, *La Revue de Métallurgie-CIT/Science et Génie des Matériaux*, February, 223–231.
3. E. Pons, L. Uran, S. Joiret, A. Hugot-Le Goff, C. Lemaitre and D. David, 'Long term behaviour of iron in clay soils: a study of archaeological analogues', 2003, *Proceedings of International Workshop 'Prediction of long term corrosion behaviour in nuclear waste systems'*, Cadarache (France), 26–29 November 2001, D. Féron and D.D. Macdonald (eds), EFC Series, no. 36, 334–345.
4. E. Pons, 'Corrosion à long terme du fer et des aciers non ou faiblement alliés dans les sols à dominante argileuse. Caractérisation physico-chimique et étude électrochimique d'analogues archéologiques', 2002, Thesis, Université de Technologie de Compiègne, France.
5. J.R. Macdonald, *Impedance Spectroscopy, Emphasizing Solid Materials and Systems*, 1987, John Wiley & Sons, New York.
6. R. De Levie, 'The influence of surface roughness of solid electrodes on electrochemical measurements', *Electrochimica Acta*, 1965, **10**, 113–130.
7. U. Rammelt and G. Reinhard, 'On the applicability of a constant phase element (CPE) to the estimation of roughness of solid metal electrodes', *Electrochimica Acta*, 1990, **35** (6), 1045–1049.

8. F. Wenger, S. Cheriet, B. Tahli and J. Galland, 'Electrochemical impedance of pits. Influence of the pit morphology', *Corros. Sci.*, 1997, **39** (7), 1239–1252.
9. R. De Levie, 'On porous electrodes in electrolyte solutions – IV', *Electrochimica Acta*, 1964, **9**, 1231–1245.
10. R. De Levie, 'Electrochemical response of porous and rough electrodes', in: *Advances in Electrochemistry and Electrochemical Engineering*, vol. 6, 1967, P. Delahay (ed.), Interscience, New York, 329–397.
11. I. Frateur, C. Deslouis, M.E. Orazem and B. Tribollet, 'Modeling of the cast iron/drinking water system by electrochemical impedance spectroscopy', *Electrochimica Acta*, 1999, **44** (24), 4345–4356.
12. J.R. Park and D.D. Macdonald, 'Impedance studies of the growth of porous magnetite films on carbon steel in high temperature aqueous systems', *Corros. Sci.*, 1983, **23** (4), 295–315.
13. A.J. Bard and L.R. Faulkner, *Electrochemical Methods: Fundamentals and Applications*, 2nd edn, 2001, John Wiley & Sons, New York.

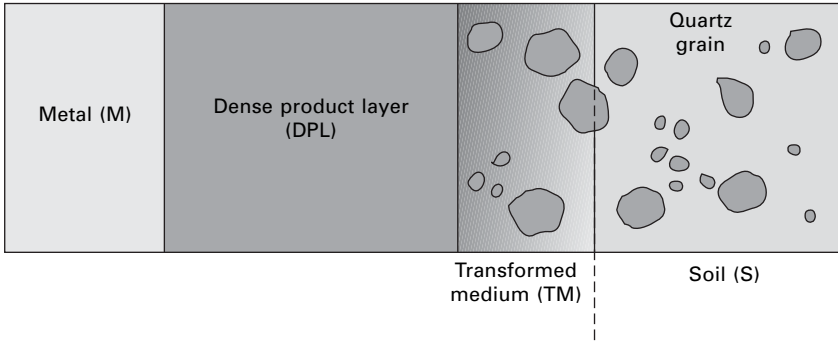
Species transport in the corrosion products of ferrous archaeological analogues: a contribution to the modelling of long-term iron corrosion mechanisms

E. VEGA, P. DILLMANN and P. BERGER,
Commissariat à l’Energie Atomique, France and
P. FLUZIN, Laboratoire Métallurgies et Cultures, France

6.1 Introduction

In French long-term storage of nuclear wastes a part of the complex multi-barrier that will separate wastes from the biosphere is a low-alloy steel over-container embedded in clay [1]. In addition to laboratory simulations and modelling, the only way to study corrosion systems formed during several centuries is to analyse archaeological ferrous artefacts buried in soil. Indeed, even if some variation in the environment of the storage concept (compacted bentonite) should occur after several tens of years, especially a decrease of the oxygen dissolved in water, it is important to understand the corrosion mechanisms of archaeological analogues in aerated conditions. Moreover, for the conservation of heritage and archaeological artefacts, these studies are of great value. Indeed, on the one hand, on particular archaeological sites, it is envisaged to conserve some important quantities of artefacts in the soil itself during the next tens of years [2, 3], while on the other hand, in order to understand the behaviour of artefacts after excavation it is fundamental to know the corrosion mechanisms that take place before this excavation. Thus, recent studies have been carried out that provide statistical information about elemental and structural characterization in artefact corrosion products called the Dense Product Layers (DPL) from different French excavation sites [4–7]. Resulting from these observations made in aerated clay soils, some assumptions of mechanisms have been proposed to explain aqueous corrosion aspects, and these need to be verified [2].

The DPL form part of a system composed of the metallic matrix (M), the transformed medium (TM) and the soil (S) (see Fig. 6.1). The TM is defined as a medium where soil markers can be observed (such as quartz grains). Inside the TM, iron migration caused by DPL dissolution, diffusion and convection, can possibly lead to iron oxyhydroxide precipitation (goethite: α -FeOOH). Considering the electrochemical aspect of the corrosion, oxidation-reduction of species can be located in both M/DPL and DPL/TM interfaces. However, because DPL is mainly constituted of goethite, an Fe (+III) non-



6.1 Schematic view of the corrosion system [4].

conductive phase, the hypothesis was made that both anodic and cathodic reactions could be located only at an M/DPL interface. For this reason, the hypothesis of corrosion control by the transport of oxygen in the water of the pores was also made. Nevertheless, the presence of non-connected marbling of magnetite (Fe_3O_4) and maghemite ($\gamma\text{-Fe}_2\text{O}_3$) in the goethite matrix seems to show that simple modelling with an oxygen gradient in a homogeneous DPL is not sufficient. Other points have to be considered such as, for example, the presence of cracks. Moreover, in several artefacts, the presence of siderite at the M/DPL interface was attested.

Consequently, it is necessary to verify all these assertions that are of great importance in modelling the long-term corrosion of iron in aerated soils but also in other aerated media as binders (see Chapter 7). The DPL porosity could be a parameter which will strongly determine how knowledge of chemical species migration is necessary to better understand the transport phenomena of chemical species through the oxide layers in order to explain the several aspects observed in buried archaeological objects and to validate or refute the control by dissolved oxygen diffusion in the water of the pores.

Thus, this study will focus on the species transport in the DPL of specimens of archaeological artefacts coming from a single site. After a short presentation of the different corrosion systems that were found on the analysed corpus, specific experiments will be made on the DPL. The aim of the first is to validate that both anodic and cathodic reactions take place at the M/DPL interface. For this purpose immersion experiments in water saturated only with an ^{18}O marker will be performed. Then, in order to verify if the corrosion kinetics are controlled by the oxygen diffusion, instantaneous corrosion rates will be determined in three different ways. The first assumes that control is effectively by dissolved oxygen diffusion, so that determination of the oxygen apparent coefficient will be made. The second method to determine an instantaneous corrosion rate will quantify the number of oxygen atoms that have reacted during the ^{18}O immersion experiment. Lastly, a third instantaneous

corrosion rate value was determined from an average corrosion rate deduced from the age of the specimen and the thickness of the corrosion products. These different values will be discussed and assessed.

6.2 Analysed corpus and experimental methods

For several years, long-term corrosion studies have been performed on artefacts from the recent excavation of an archaeological forge in a French site located in Glinet (Seine-Maritime) that is 400 years old. The corpus consists of nails, small plates or cone-shaped pieces of iron and cast iron (see Table 6.1). Transverse sections were performed on several artefacts in order to characterize the entire system from the metal to the soil. For these purposes, optical (OM) and scanning electron (SEM) microscopes were used. In order to determine the composition of the corrosion system, Energy Dispersive Spectrometry (EDS) analyses coupled to SEM were made. EDS–SEM experiments were performed with a Cambridge Instruments Stereoscan 120. The acceleration voltage used was 15 kV. The EDS detector is a Si(Li) model using a thin beryllium window. This configuration allows low detection limits for $Z > 11$ elements. For instance, major elements like Fe or Si can be detected down to 0.5 mass% in an oxide environment, with about a 1 mass% relative error. Moreover, oxygen quantification is reliable with about a 2 mass% relative error since the detector has been calibrated with reference samples representative of the corrosion products' current composition (such as Fe_2O_3 and Fe_3O_4).

The DPL structural description was obtained with both micro-diffraction under synchrotron radiation (μXRD) and micro-Raman spectroscopy. These latter measurements were performed with Dr Bellot-Gurlet in the Laboratoire

Table 6.1 Analysed samples

| Sample no. | Description | Metal |
|------------|--------------------------------------|-----------|
| GL94-102* | Rod with rectangular section (20 cm) | Iron |
| GL94-109 | Cone-shaped piece (7 cm) | Cast iron |
| GL96-107 | Rod with rectangular section (7 cm) | Steel |
| GL96-135 | Rod with square section (9 cm) | Steel |
| GL96-301 | Cone-shaped piece (9 cm) | Cast iron |
| GL96-303 | Plate ($10 \times 5 \text{ cm}^2$) | Steel |
| GL96-400 | Thick plate (10 cm) | Cast iron |
| GL02-10 | Cylinder (9 cm) | Cast iron |
| GL03-64 | Nail (2 cm) | Iron |
| GL03-65 | Nail (2 cm) | Iron |
| GL03-69 | Nail head (1 cm) | Iron |
| GL03-73 | Rod (20 cm) | Steel |
| GL03-85 | Small rod (3 cm) | Steel |
| GL03-86 | Nail (1 cm) | Iron |

*Sample used for the species transport experiments

de Dynamique, Interactions Réactivités of the French CNRS. These two methods will not be described in detail and can be found in the literature [4, 8–11].

In addition to these classical and more refined characterization studies, an iron rod was selected in the corpus in order to proceed to a specific species transport study in the corrosion layer.

The porosity of the DPL was characterized by Hg porosimetry. On a part of the rod, the soil was scraped off and three scales were sampled. According to this method, the pores have to be water free in order to let Hg enter the layers. With this intention, freeze-drying was used after liquid nitrogen freezing. During the experiment, Hg was introduced by incremental pressurization. The porosimetry diameter access is obtained through the Washburn equation [7]. Drying quality is the main parameter that determinates measurement accuracy. Nevertheless, though a drying oven is much more efficient for water elimination, freeze-drying involves less porosity damage such as cracks.

Several slices of the selected rod including all the corrosion system (i.e. metal, DPL and TM) were cut using kerdane as lubricating medium. These slices were fully cast in epoxy resin (hot cast under pressure). A cutting out, parallel to the oxide layer sequences on the TM, was then performed in order to uncover an area which will be in contact with the ^{18}O or the NaI saturated solutions. If necessary, a slight scraping can help to unblock near surface pores after cutting. Eventually, the voids due to the retracted resin were filled with Cyanolit[®] in order to avoid side-percolation.

The setup used to treat the samples in ^{18}O saturated water comprises several reactors (one per sample) filled with deaerated distilled water in equilibrium with ^{18}O (93.3% pure) at 1.2 atm. Three samples were immersed in this medium during respectively 4, 11 and 19 weeks. These durations were chosen considering corrosion rates between 1 and 10 $\mu\text{m}/\text{year}$ already measured in archaeological ferrous artefacts by various methods. Thus, after 4 weeks and considering the detection limit of the nuclear microprobe (see below) it should be possible to observe a possible variation in the ^{18}O content in the corrosion layer, with respect to a reference sample. Once exposed, samples were dried, cross-sectioned perpendicularly to the oxide layers and polished (SiC paper, grades 180–4000) under kerdane.

Local concentrations ^{18}O in corrosion layers were investigated with the nuclear microprobe of the Pierre Süe Laboratory (CEA/CNRS Saclay, France) using the $^{18}\text{O}(p, \alpha)^{15}\text{N}$ nuclear reaction. The experimental conditions were as follows: incident proton beam 0.83 MeV, beam spot size $3 \times 3 \mu\text{m}^2$, annular particle detector angle 170° without covering foil in order to collect backscattered protons. Concentration profiles of ^{18}O into the DPL were determined considering the α -emission in an energy window from 1.9 to 3.9 MeV. The proton beam was scanned by $100 \times 10 \mu\text{m}^2$ and parallel to the M/DPL interface. More details about this experiment can be found elsewhere [12].

The local concentration of ^{18}O was derived from the number of events recorded in comparison with a $\text{Ta}_2^{18}\text{O}_5$ reference sample and simulations made with the SIMNRA program. As the structure of the DPL compound had been previously identified by μRaman analyses, this number can be expressed in terms of $^{18}\text{O}/^{16}\text{O}$ ratios.

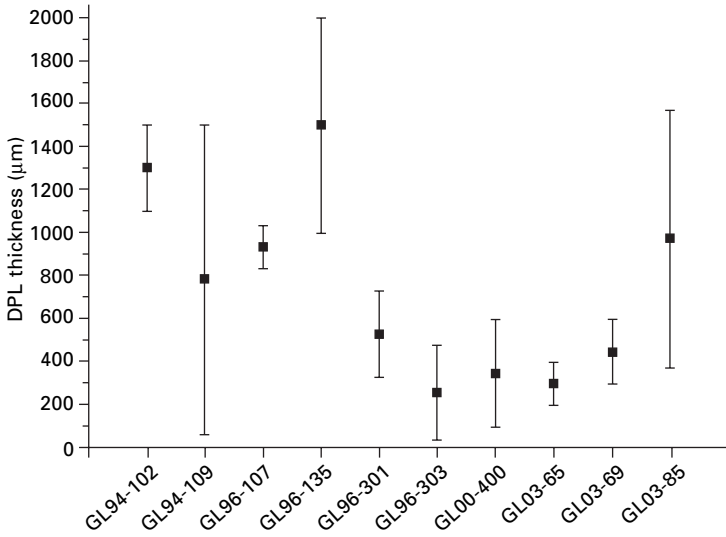
To obtain information on the transport itself, and particularly on apparent diffusion coefficients, because experiments using ^{18}O are not possible (after cutting, all the water of the pores is eliminated), iodine (NaI aqueous solution) was used. For these iodine migration experiments, all specimens were maintained in aqueous unionized solutions for a few hours so as to introduce water in the pores by convection. Then they were introduced into a NaI saturated aqueous solution for 1, 3, 7 and 168 hours. The iodide water diffusion coefficient is about $1.7 \times 10^{-9} \text{ m}^2\text{s}^{-1}$ at room temperature [13], which is comparable to that of oxygen which is $1.9 \times 10^{-9} \text{ m}^2\text{s}^{-1}$. For this reason and also because iodine is easy to detect in the DPL, a NaI saturated solution has been chosen to observe species migration. Indeed, this ionic marker is not ideal because these charged species could have a different behaviour than dissolved oxygen in the DPL. Nevertheless, up to now, it is the easiest way to obtain a first evaluation of transport species profile in the DPL. At the end of the immersion stage, a transverse section was obtained for each specimen. They were polished with silicon carbide to grade 4000 in water-free oil (kerdane).

For iodine profile collecting, EDS coupled to SEM was used. In iron oxides, the detection limit of this method is about 0.5 mass%. This limit is sufficient to obtain reliable profiles even after short immersion times.

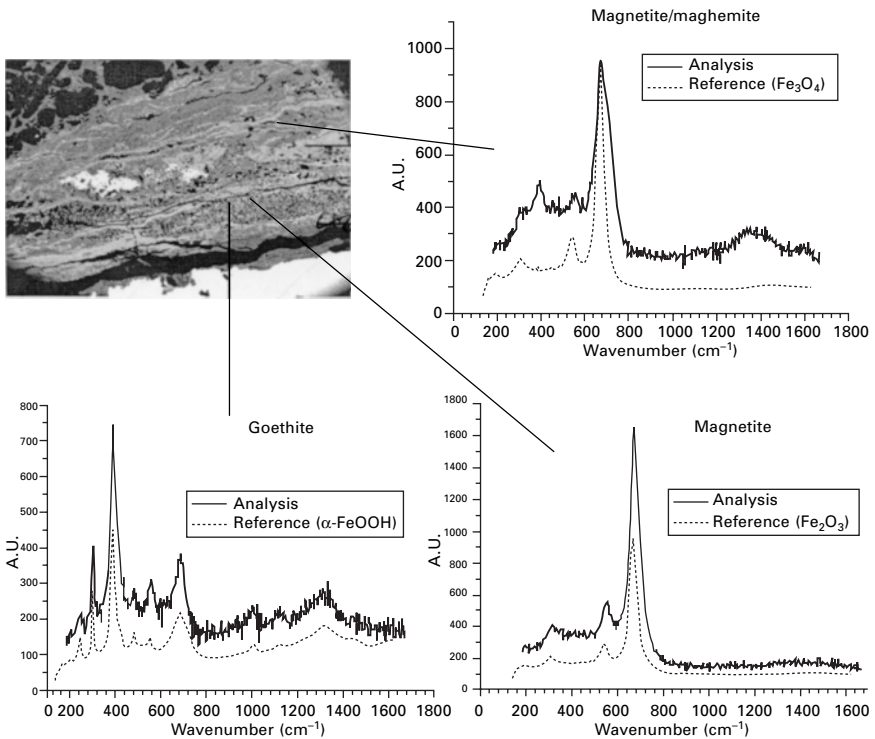
6.3 Results and discussion

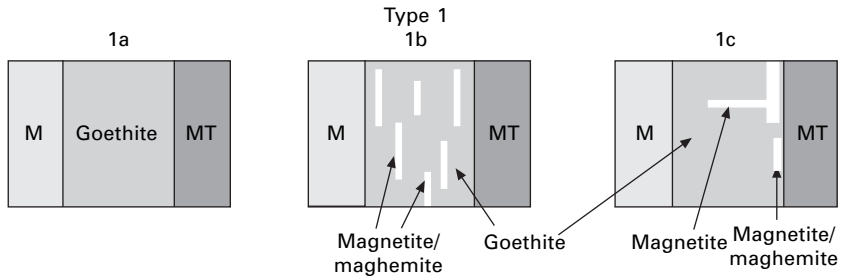
6.3.1 Corrosion system

The artefacts from the archaeological site of Glinet present two types of corrosion systems with corrosion layers of several hundred micrometres (see Figs 6.2 and 6.3). The major difference between these two systems is the presence or absence of siderite in the DPL. Soil water composition measurements that are presented elsewhere [14] indicate that the P_{CO_2} variation on the site cannot be involved to explain the presence of siderite. The pH and P_{CO_2} variation in the DPL itself are more likely to be invoked. This point will not be detailed here. The DPL of the corrosion system that does not contain siderite (Fig. 6.4) is constituted only of a goethite matrix in which marbling of magnetite/maghemite mixes can be found. Previous studies that also found this kind of profile on artefacts from other archaeological sites made the hypothesis that, because the DPL matrix is made of goethite, a non-conductive phase, and that the magnetite marbles are not connected to



6.2 Thicknesses of the DPL.

6.3 Transverse section of an archaeological sample from Glinet (GL96-303): SEM-BSE and μ Raman spectra associated with different locations.



6.4 Schematic view of the goethite/magnetite/maghemite corrosion system observed at Glinet.

the metallic substrate, both anodic and cathodic reactions (i.e. iron oxidation and oxygen dissolved in the water of the pore reduction) are located at the M/DPL interface. To verify this hypothesis, we performed some specific species transport studies on a single rod representing this corrosion system.

Optical observations made on transverse sections of the GL94-02 sample used for the species transport experiments showed that the corrosion layers range from 600 to 1200 μm .

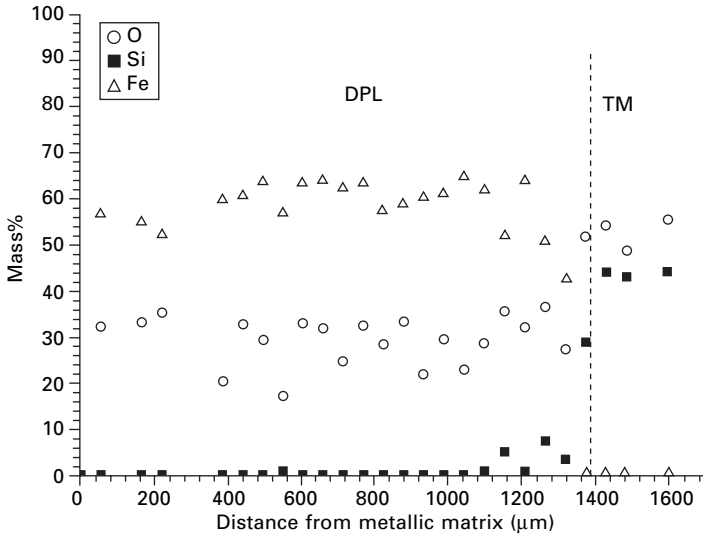
Many cracks can be seen in the DPL. Obviously, some of the macroscopic cracks come mainly from the cutting and polishing stages of the sample preparation, whereas the others could give evidence of stresses due to the growth of oxides. Such discontinuities in the corrosion layers should have important effects on species migration. Characterization studies by micro-Raman spectroscopy and μXRD showed that the DPL is made up mainly of goethite and a few magnetite zones without special location. Figure 6.5 shows a typical distribution of major elements (O, Si, Fe) into the GL 94-102 sample corrosion layers.

6.3.2 Porosity of the DPL

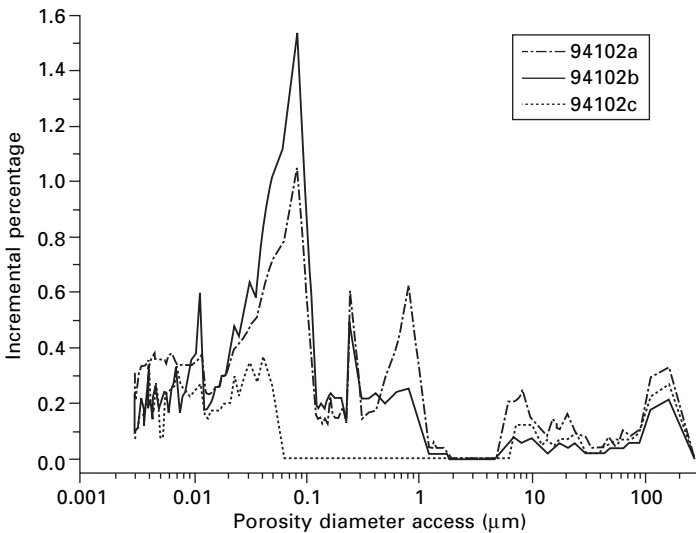
Figure 6.6 shows the results of porosity Hg measurements made on three different DPL scales of the GL94-102 sample. Two porosity families have been evidenced: microporosities (oxide layer cracks) and nanoporosities. The total porous volume is about 25%. By way of comparison, microporosities of atmospheric corrosion rust layers are about 50% [15]. This first set of observations shows that the presence of porosities allows the species transport in the DPL.

6.3.3 Location of the cathodic reaction

On each treated sample (i.e. 4, 11 and 19 weeks), an $^{18}\text{O}/^{16}\text{O}$ profile from the metal/oxide interface to the soil was obtained (see Fig. 6.7). After only 4 weeks the detection limit of the experimental setup did not allow us to

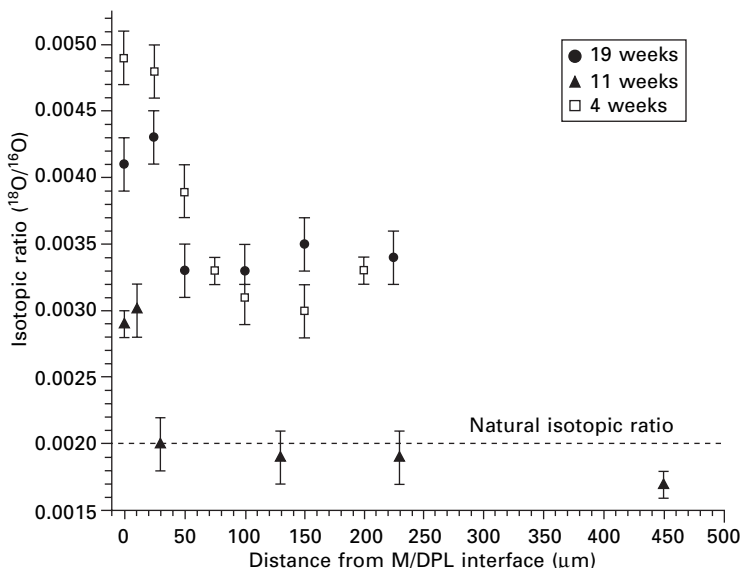


6.5 Distribution of elements in GL94-102 by EDS-SEM (spot analysis).



6.6 Porosity families in GL94-102.

observe any increase of the $^{18}\text{O}/^{16}\text{O}$ ratio in the corrosion product. Nevertheless, for the 11- and 19- week samples, a significant rise of this ratio compared to the untreated sample showed that corrosion products containing more ^{18}O than the natural ratio had precipitated during immersion. The 11-week sample shows a ratio increase only at the metal/oxide interface, revealing that the ^{18}O must have migrated through the pores of the DPL and reacted only at this



6.7 ^{18}O profiles in the CPD after several immersion tests.

location. This first evidence seems to validate the hypothesis made in previous studies on the location of the cathodic reaction of oxygen at the M/DPL interface. The high $^{18}\text{O}/^{16}\text{O}$ values also observed at this location on the 19-week sample confirm the above observations. Moreover, for this latter sample, high ratios were also observed in the rest of the DPL. This could indicate, as suggested in previous studies, a migration under the ionic form through the pore water of the corrosion products already formed at the interface and a subsequent precipitation in cracks of the DPL with the increase of the local potential [4].

The results obtained here confirm that the cathodic reaction of oxygen settles at the metal/oxide interface, i.e. that the transport of gaseous oxygen dissolved in the water of the pores of the DPL controls the mechanisms. This observation leads to a new question: does the oxygen transport in the water of the pores of the DPL control the corrosion mechanisms and subsequently, the corrosion rates? For this purpose, as said before, the instantaneous corrosion rate will be evaluated using three methods and the comparison of the different values will be discussed.

6.4 Corrosion rates evaluation

6.4.1 Hypothesis of oxygen transport control

The following hypothesis is made that the oxygen transport in the water of the DPL pores is the limiting step of the corrosion mechanisms. Then, the

corrosion rate can be evaluated using the Faraday law and taking into account the oxygen concentration gradient ΔC_{O_2} (mol/m³), the thickness of the layer x_0 (m), the iron density μ_{Fe} (g/m³), the molecular mass M (g/mol) and the apparent oxygen diffusion coefficient $D_{O_2}^*$ (m²/s):

$$v_{\text{corr}} = \frac{D_{O_2}^* \Delta C_{O_2} M}{\mu_{Fe} x_0}$$

The only value that is not known in this equation is the apparent diffusion coefficient of oxygen in the water of the pores.

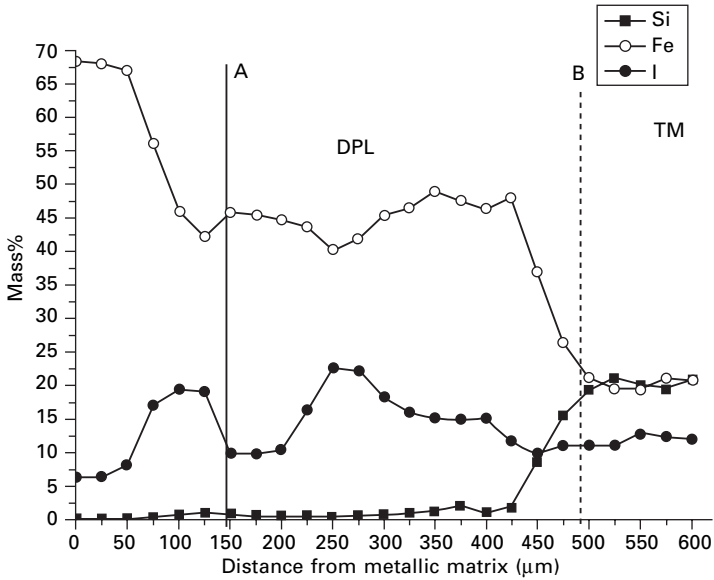
A way to determine $D_{O_2}^*$ is to observe the distribution profile of iodine in the DPL after several immersion times in NaI saturated aqueous solution. Despite the fact that Γ^- is an ionic species and also can react with the corrosion products, because the coefficient diffusion of iodine in water is very close to that of O_2 , in a first approach it will be assumed that the apparent coefficient diffusion of the two species is the same.

Concentration profiles of Na and I in the DPL have been determined using spectral mapping by EDS coupled to SEM. As each spectrum is matched to a pixel of the BSE image, spectral mapping allows one to obtain an average elemental quantification in a rectangular area in which all 'pixel-spectra' are summed. This method has been used to avoid effects of DPL heterogeneities, such as cracks, porosities and local oxide penetrations. Analysis window size was fixed at about $30 \times 900 \mu\text{m}^2$ and parallel to the M/DPL interface.

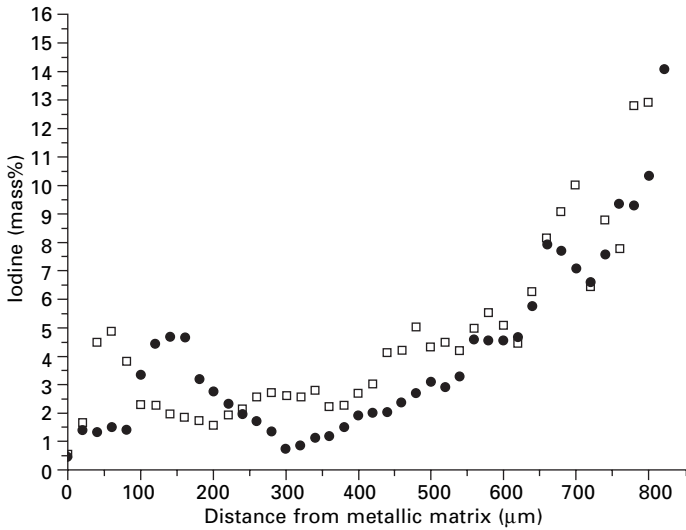
After a week's immersion, as shown in Fig. 6.8, the main result is that Γ^- ions migrated through the corrosion layers to the metallic substrate. Indeed, in this figure the DPL is located between the A and B vertical lines. The zone between the y-axis and the A vertical line should not be considered, because in the analysed window both metallic substrate and DPL are analysed, as shown by the relatively high iron content. One should assume that water of all pores is saturated by Na^+ and Γ^- . Iodine content in the layers fluctuates around a constant average maximum value of 15 mass%.

Reproducibility of measurements can be estimated by carrying out several profiles at different places on the same transverse section. Figure 6.9 shows iodine profiles at two different locations of the DPL in the same sample, indicating good reproducibility, even if one may note a slight shift of the profiles near the M/DPL interface. Indeed, this shift could be due to the irregularity of the interface.

The variation in thickness of the corrosion layers must be taken into account to compare the different immersion times. That is the reason why the origins of all the curves were relative to the DPL/TM interface which can be adjusted thanks to the Si content increase, marking the beginning of the TM. Moreover, all the iodine content values were normalized to unity at the DPL/MT interface. Figure 6.10 shows iodine content for different corrosion



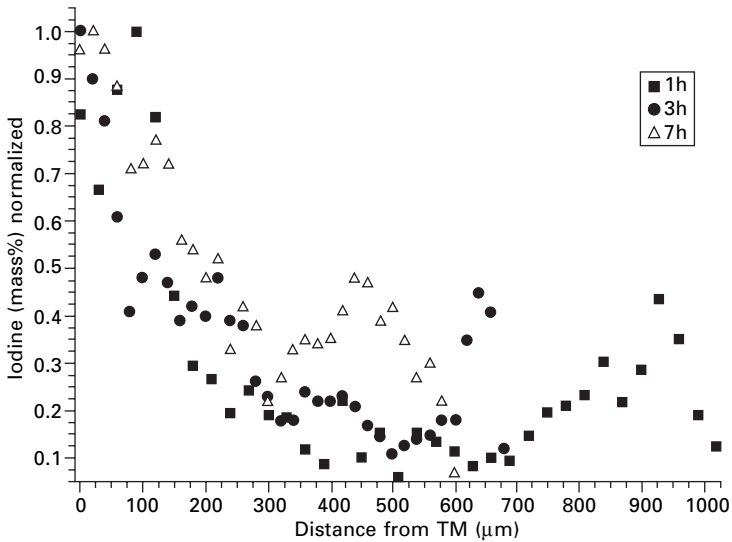
6.8 EDS-SEM profile, 1 week immersion.



6.9 Immersion test at two different locations, 3 hours (NaI saturated solution).

layers from the GL94-102 artefact. For these different samples, however, the DPL thickness was not the same: it was 900, 650 and 450 µm for samples immersed respectively for 1, 3 and 7 hours.

Except for the sample which was tested for one week, all curves have the



6.10 Iodine content profile for different immersion times.

same aspect, i.e. a similar decrease of iodine content towards the DPL/M interface. At 100 μm from this interface, the iodine content increases sharply on all samples. As said before, this is probably due to the presence of more microporosities located at the DPL/M interface. Some studies, in a marine corrosion context, have reported that the density of corrosion products decreases towards the corrosion surface [16]. But the mathematical modelling of the variation of corrosion product density in these studies, based on linear variation from the surface to the metal oxide interface, cannot be used in the present case, in which the porosity increase seems to be more localised at the M/DPL interface.

One of these iodine profiles has been mathematically modelled in order to evaluate an experimental apparent coefficient of diffusion (D_0^*) that integrates diffusion and other parameters such as DPL porosity variations, the fact that Na^+ and Γ^- are ionic species, etc. Moreover, physical and chemical adsorption by the pore surfaces should strongly influence species migration. Nevertheless, a first approximation can be made by neglecting these latter parameters and assuming Fick conditions. Even if migration experiment results do not strictly obey these conditions, they will permit a rough evaluation of the apparent diffusion coefficient value. Last but not least, because the diffusion coefficient of iodine ions in aqueous solution is the same as that of oxygen, this apparent diffusion coefficient will be used in a first approach as the oxygen apparent coefficient diffusion in the Faraday law.

For this purpose, diffusion curves based on the iodine profiles have been modelled considering that DPL is similar to a half-infinite system and that

the surface ionic concentration is constant. The 1 h immersion test has been chosen. The increase in porosity near the DPL/M interface has not been taken into account, since a constant minimal iodine content seems to be clearly observed before this location. In other words, we assume that species migration into the DPL can be considered as being driven by the Fick equation during the early immersion stage. If we consider that diffusion coefficient and concentration are not interdependent functions, a solution to the Fick equation is [14]:

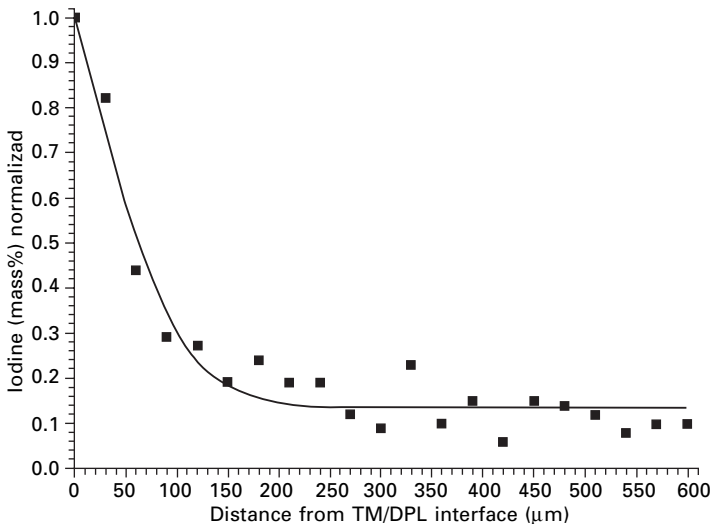
$$y = C + (1 - C) \left[1 - \operatorname{erf} \left(\frac{x}{2\sqrt{D^*t}} \right) \right]$$

where: C = iodine solubility limit (g mol^{-1})
 t = immersion time
 x = oxide layer average depth (μm).

Figure 6.11 shows the migration curve fitted with the above solution in the first 600 μm into the DPL.

The obtained apparent diffusion coefficient is $0.8 \times 10^{-12} \text{ m}^2\text{s}^{-1}$. As said before, because iodine and oxygen coefficients of diffusion in water are similar, in a first approach, one can consider this value as being an oxygen apparent diffusion coefficient and use it to evaluate a corrosion rate. Then, an instantaneous corrosion rate can be evaluated:

$$v_i = 0.07 \mu\text{m/year}$$



6.11 Fitting of 1 h migration curve.

6.4.2 Calculation of the ^{18}O quantity that precipitated into corrosion products

Another way to estimate the corrosion rate is to evaluate all the ^{18}O atoms that were reduced in the DPL by corroding the metallic core during the ^{18}O immersion experiments. By integrating the total quantity of ^{18}O atoms detected in the DPL, correcting it by subtracting the natural ^{18}O quantity in the analysed volume and assuming that the same quantity of Fe atoms was corroded, it is possible, taking into account the immersion time, to deduce a corrosion rate. This rate can be considered as ‘instantaneous’ because the immersion times are much lower than the total corrosion time in soil of the archaeological artefact. Table 6.2 gives the deduced corrosion rates for the three immersion times. The error made in the corrosion rate evaluation considering analytical errors is lower than $0.05\ \mu\text{m}/\text{year}$.

6.4.3 Deduction from the average corrosion rate

The final method for evaluating the instantaneous corrosion rate of the studied artefacts is to determine an average corrosion rate from the thickness of the corrosion products, i.e. DPL and TM. This method had already been used by Neff *et al.* [4]. DPL thicknesses are evaluated by OM measurements. An average thickness is obtained after 10 measurements. To evaluate the TM, it is necessary to determine the average EDS profile (see Section 6.2) to observe the decrease of the iron content from the DPL/TM interface to the soil. The average corrosion rate obtained using this method on the DPL of the GL94-102 sample is about $2.6\ \mu\text{m}/\text{year}$. In a first approximation, it is possible to model the corrosion by a parabolic law. This modelling does not take into account the first stages of the corrosion processes during which, because of the absence of a corrosion layer, the corrosion law is undoubtedly not parabolic and probably linear. Nevertheless, because the duration of this period is totally unknown, a simple modelling by a parabolic law was chosen. It is then possible to deduce an instantaneous corrosion rate of $1.3\ \mu\text{m}/\text{year}$.

Table 6.2 Instantaneous corrosion rates evaluated by integrating the ^{18}O atom quantity after several immersion experiments

| Immersion time (weeks) | ^{18}O atom number | Corrosion rate ($\mu\text{m}/\text{year}$) |
|------------------------|-----------------------------|--|
| 11 | 1.68×10^{17} | 0.09 |
| 19 | 1.91×10^{18} | 0.57 |
| 19 | 1.98×10^{18} | 0.59 |

Table 6.3 Instantaneous corrosion rates evaluated by different methods

| Method | Corrosion rate ($\mu\text{m}/\text{year}$) |
|---|---|
| Hypothesis of control by oxygen transport in DPL (NaI) | 0.07 |
| Evaluation of ^{18}O atom quantity | 0.09–0.59 |
| Deduced from average corrosion rate (parabolic modelling) | 1.3 |

6.4.4 Discussion

Table 6.3 sums up the different corrosion rate values obtained by the three approaches. In discussing these different values, an interesting point is that, despite the approximations, the corrosion rates determined by the hypothesis of control by the transport of oxygen dissolved in the water of the pores (NaI immersion method) are of the same order of magnitude as those evaluated by the ^{18}O atom quantity, at about 0.1–0.6 $\mu\text{m}/\text{year}$. Indeed, the latter method does not presuppose any corrosion mechanism and the fact that the two corrosion rates are of the same order of magnitude seems to validate the hypothesis of corrosion control by oxygen transport in the water of the DPL pores.

The value of 1.3 $\mu\text{m}/\text{year}$ deduced from the average corrosion rate is higher than the two more limiting instantaneous corrosion rates. Two remarks can be made. Firstly, it is not necessary to involve a more limiting hypothesis than control by oxygen transport in the pores of the DPL to obtain sufficiently low corrosion rate values. In particular, control by a barrier layer in which only solid-state diffusion could take place is not necessary. Secondly, because the 1.3 $\mu\text{m}/\text{year}$ CR value is too high, it seems that this modelling by a simple parabolic law is not adapted. Of course, the first stages of the corrosion are not taken into account and it is not yet possible to determine the exact influence of the corrosion rate (nevertheless it will surely increase). Moreover, the numerous cracks found in the DPL could play an important role in the DPL, provoking kinetic breaks in the parabolic law. This point should be taken into account in future studies.

The two immersion experiments give the instantaneous corrosion rate of the system at the time of the specimen test, when the corrosion is controlled by oxygen diffusion in the water of the pore. Nevertheless, it seems also that the kinetics cannot be modelled by a simple parabolic law but by a more complex law involving breaks, due to the appearance of cracks.

This study confirms several of the hypotheses made by Neff (see Chapter 4) during previous studies. Firstly, the fact that both anodic and cathodic reactions take place at the metal/DPL interface is validated. Secondly, despite the intrinsic limits of the different approaches that have to be corrected in

future work, it seems that the transport of dissolved oxygen in the water of the DPL pores controls the corrosion mechanisms but the appearance of cracks in the DPL could cause diffusion shortcuts and modify the kinetic law.

6.5 Conclusion

Different archaeological specimens coming from the site of Glinet (France) have been analysed to determine the corrosion system. As proposed in previous studies, this system can be described using specific terms: Metal (M), Dense Product Layer (DPL) and Transformed Medium (TM). The coupling of OM, EDS–SEM, μ XRD and μ Raman spectroscopy reveals two different corrosion systems: one contains siderite, the second only goethite and magnetite/maghemite mixes. On this second type of corrosion system, specific study of species transport using different kinds of markers was performed. Immersion of the corrosion system in a water solution saturated in ^{18}O confirms the hypothesis made in previous studies that both anodic and cathodic reactions were located at the metal/DPL interface. Then, to investigate whether the transport of dissolved oxygen in the DPL pores controls the corrosion kinetics, instantaneous corrosion rates were evaluated using different methods: (i) under the hypothesis of control by oxygen transport in the DPL pores, (ii) by evaluating the quantity of ^{18}O atoms that reacted during the immersion experiment, and (iii) by extrapolating the average corrosion rate deduced from the nature, thickness and age of the corrosion products. Comparison of the different values obtained seems to confirm the fact that the diffusion of dissolved oxygen controls the kinetics and it is not necessary to invoke a barrier layer to obtain relatively slow corrosion rates after 400 years (about 0.1–0.6 $\mu\text{m}/\text{year}$). Moreover, it seems that the corrosion kinetics cannot be modelled by a simple parabolic law, on the one hand because the first stage of the corrosion is more likely to follow a linear law and the duration of this first stage is not known, and on the other hand because the appearance of cracks in the DPL could provoke kinetic breaks that have to be taken into account in the model.

Future work will focus on a finer estimation of apparent diffusion coefficient in the DPL, by using other experimental methods such as diffusion cells and other markers. Moreover, the modelling of the corrosion kinetics will be improved by taking into account the role of cracks.

6.6 References

1. Franco, M.D., Gras, J.-M. and Moncouyoux, J.-P., Les matériaux et le stockage des déchets nucléaires. *RGN*, 1996 (3), May–June: 27–33.
2. Matthiesen, H., Hilbert, L.R. and Gregory, D.J., The occurrence and stability of

- siderite as a corrosion product on archaeological iron from a waterlogged environment. *Studies in Conservation*, 2003, 48(3): 183–194.
3. Matthiesen, H., Monitoring methods in mires and meadows: five years of studies at Nydam Mose, Denmark, in *Preserving Archaeological Sites in Situ*, 2001, London.
 4. Neff, D., *et al.*, Corrosion of iron archaeological artefacts in soil: characterisation of the corrosion system. *Corrosion Science*, 2005, 47: 515–535.
 5. Neff, D., Descostes, M. and Dillmann, P., Mécanismes de corrosion à long terme des aciers non alliés – Apport des calculs de solubilité des produits de corrosion du fer à l'étude des analogues archéologiques, 2004, CEA, Saclay, 157.
 6. Pons, E., Corrosion à long terme du fer et des aciers non ou faiblement alliés dans les sols à dominante argileuse – Caractérisation physico-chimique et étude électrochimique d'analogues archéologiques, 2002, Université de Technologie de Compiègne, Compiègne, 239.
 7. Chitty, W.-J., *et al.*, Long term corrosion resistance of metallic reinforcements in concrete – A study of corrosion mechanisms based on archaeological artefacts, *Corrosion Science*, in press.
 8. Dillmann, P., *et al.*, Characterisation of iron archaeological analogues using micro diffraction under synchrotron radiation. Application to the study of long term corrosion behaviour of low alloy steels, *J. Phys IV France*, 2002(12): 393–408.
 9. Neff, D., Dillmann, P. and Béranger, G., An analytical study of corrosion products formed on buried ferrous artefacts, in *Prediction of long term corrosion behaviour in Nuclear Wastes System*, 2003, Cadarache, France: European Federation of Corrosion.
 10. Neff, D., Dillmann, P. and Béranger, G., Long term corrosion of archaeological iron artefacts, in *Eurocorr 2003*, 2003, Budapest.
 11. Neff, D., *et al.*, Structural characterization of corrosion products on archaeological iron. An integrated analytical approach to establish corrosion forms, *Journal of Raman Spectrometry*, 2004, 35 (special issue on the application of Raman spectroscopy in art and archaeology): 739–745.
 12. Vega, E., Berger, P. and Dillmann, P., A study of transport phenomena in the corrosion products of ferrous archaeological artefacts using ^{18}O tracing and nuclear microprobe analysis, *Nuclear Instruments and Methods B*, submitted.
 13. *Handbook of Chemistry and Physics*, 1965, The Chemical Rubber Co.
 14. Vega, E., Altération des objets ferreux archéologiques sur le site de Glinet (Seine-maritime, France, XVI^e siècle). Caractérisation des produits de corrosion et étude des mécanismes, 2004, Université de Technologie de Belfort Montbéliard, Belfort, 127.
 15. Dillmann, P., Mazaudier, F. and Hoerle, S., Advances in understanding atmospheric corrosion of iron I – Rust characterisation of ancient ferrous artefacts exposed to indoor atmospheric corrosion, *Corrosion Science*, 2004, 46(6): 1401–1429.
 16. Melchers, R.E., Mathematical modelling of diffusion controlled phase in marine immersion corrosion of mild steel, *Corrosion Science*, 2003: 923–940.

Long-term behaviour of iron embedded in concrete: from the characterisation of archaeological analogues to the verification of the oxygen reduction as the limiting step for corrosion rate

W.-J. CHITTY, B. HUET, P. DILLMANN and V. L'HOSTIS Commissariat à l'Énergie Atomique, France and G. BERANGER, Université de Technologie de Compiègne, France and H. IDRISSE, INSA de Lyon, France

7.1 Introduction

Reinforced concrete is a structural material widely used in the French nuclear industry, for power plants, and for waste facilities (LLW and ILW waste disposals – MAVL and FAVL in French). Steel reinforcements are used to improve the tensile strength of concrete structures. In the case of nuclear waste storage, reinforced concrete structures have to provide not only improved mechanical properties but also the containment of radionuclides. Growth of cracks in concrete would alter its containment properties. The cracking of concrete can be caused by chemical degradation, frost/thaw cycles, wetting/drying cycles or corrosion of reinforcement.

Non-alloyed or low-alloyed steels are often used as reinforcement in these structures. Thanks to the high alkalinity of the concrete interstitial solution, reinforcement remains at a passive state. Very low corrosion rates are measured and no mechanical degradation is generated. Unfortunately, concrete is a porous material that may react with the surrounding medium. Especially, atmospheric carbon dioxide generates carbonation of concrete and leads to the alteration of its physical and chemical properties (pH decrease). Moreover, in carbonated concrete, the corrosion state of the rebar no longer remains in its passive state and high corrosion rates can be evaluated. Growing of new iron oxides at the steel–concrete interface generates tensile stresses in the carbonated concrete that may lead to cracking. Tuutti's diagram [1] schematises the time evolution of the steel–concrete interface in two time periods: the passive and active periods.

The specificity of long-term applications of the nuclear field (>100 years) limits the use of 'civil engineering' tools (minimal concrete thickness, limitation of crack dimensions, etc.) for the estimation of the lifetime of reinforced concrete structures. In this context, the CIMETAL research programme was

developed by the French Commissariat à l'Energie Atomique (CEA) for the prediction of the evolution of cement/metallic material systems in an environment representative of the storage. It deals with interactive studies dedicated to short-term experimentation (corrosion and mechanical behaviour of structures), modelling to predict the corrosion and the mechanical behaviour of objects for several hundred years, and finally validation of some hypotheses with analyses of corrosion systems on multiseular periods (ancient ferrous artefacts or archaeological analogues) [2] and mechanical behaviour of, for instance, 40-year-old pre-stressed beams (benchmark of the Rance gilder project [3]).

Three kinds of model may be used to predict long-term evolution of corrosion [4]: a material balance approach, a semi-empirical approach, or mechanistic modelling. However, only the mechanistic modelling allows long-term prediction that cannot be reached in laboratory experiments. The mechanistic models are based on the integration of elementary mechanisms in analytical or numerical models. Those models require the implementation of dissolution constants, diffusion constants and kinetic reaction constants; the latter are often not mentioned in the literature. Moreover, such models need to determine these physico-chemical parameters on artefacts corroded over the long time scales considered. The deterministic laws deduced from these models may then be compared to semi-empirical laws evaluated from laboratory tests.

Few authors have tried to model iron corrosion in degraded concrete [5, 6]. They propose to evaluate the corrosion rate with the Butler–Volmer activation law. This law permits the evaluation of corrosion rate as a function of the anodic and cathodic overpotentials and Tafel coefficient. Nevertheless, these models do not take into account either the chemistry evolution in the oxide layer at the steel–concrete interface or the aqueous transport of reactive species in the porosity of degraded concrete. These two points are of great importance because of the high thickness of these layers and the protective role they could play. Actually, the interfacial reaction kinetics may not be the controlling factor of the corrosion rate. For example, the corrosion modelling of mild steel in deep reductive clays is based on a dense corrosion layer between the metallic substrate and the clay. In this particular case, the growing of the oxide layer is limited by species motion in the solid phase: electron or point defect motion (anionic or cationic) [7, 8]. In the case of atmospheric corrosion of low-alloyed steels during storage, the wetting and drying cycles have been identified as the critical parameter to evaluate the metal loss over time. In particular, the oxygen reduction during the wet period leads to high metal loss. The reduction of oxygen has been modelled assuming the electrical conductivity of the porous oxide layers. The transport of oxygen in a thin water layer on the iron oxides is the limiting step of this system [9, 10].

Complementary to mechanistic modelling and laboratory simulations over

short periods, the only way to understand the physico-chemical properties of corrosion systems over long periods is to study ancient ferrous artefacts or archaeological analogues. This kind of study also permits the validation of some hypotheses used for modelling. In the past few years, the number of studies on the corrosion of archaeological ferrous artefacts has increased significantly. Indeed, in France, this increase is linked to more general studies dealing with the designing of nuclear waste management systems [11–13]. In this context, the use of reinforced concrete is envisaged for different applications, like low-level radioactive waste containers, and more generally nuclear infrastructures containing iron/concrete interfaces.

Thus, the aim of this chapter is to show how the fine characterisation of the corrosion systems observed on selected archaeological analogues can be used to test and develop modelling of corrosion mechanisms. It is structured in two parts. Firstly, an analytical study was performed on ferrous reinforcements embedded in binders found in ancient buildings from the Middle Ages to the beginning of the twentieth century. All the morphological and physico-chemical properties such as composition, structure and porosities of the different layers were studied with different analytical methods such as optical and electronic microscopy, EDS coupled to SEM, EPMA, mercury porosimetry, micro-Raman spectroscopy, and micro-diffraction under synchrotron radiation. Moreover, average corrosion rates were evaluated by two different methods. Secondly, the basis of a mechanistic corrosion modelling approach is proposed to simulate the evolution of the steel/concrete interface during the ‘active’ corrosion phase. Calculations emphasise the oxygen reduction mechanism.

7.2 Characterisation of long-term corrosion layout of iron embedded in old binders

7.2.1 Context and objectives

Archaeological analogue corrosion systems have been studied in detail mainly in two media: the atmosphere and soils. Indoor atmospheric corrosion on archaeological analogues has been observed [9]: apparently two layers are present, the outer made of lepidocrocite and the inner of goethite and magnetite. Several authors have studied corrosion in soils [14, 15] and a multilayer system has been noted (described later in this chapter). The corrosion products are mainly goethite, with magnetite and/or maghemite inclusions. However, to our knowledge, few published studies give detailed results on the corrosion of ancient iron artefacts in binders. The study of Duffo *et al.* [16] has to be mentioned. On a 65-year-old reinforced concrete sample, these authors observed corrosion products made mainly of magnetite close to the rebar and a mix of goethite and calcite in the external zone of these corrosion products.

Unfortunately, these authors used only macroscopic structural characterisation methods that do not confirm beyond doubt the microscopic localisation of the phases (magnetite and goethite) deduced only from SEM investigations.

Moreover, in the specific case of ancient artefacts (i.e. before the twentieth century), two binder types might be encountered: hydraulic or aerial binders. Actually, aerial binders harden by reacting with atmospheric CO_2 (for instance, air-slaked limes $\text{Ca}(\text{OH})_2$) whereas hydraulic binders (for instance, hydraulic limes [17] and cement) harden by hydration. In hydraulic binders, two corrosion states can be observed, described further in other studies [1, 5, 18]. A mortar is made by mixing lime, cement or plaster with sand, water and sometimes other materials (such as blast furnace slag). The main differences between mortars and cements are their workabilities, formulations and aggregate sizes.

In this study, classical metallographic observations using different etching reagents allow us to compare the ancient artefacts with the candidate steels that will be used to reinforce nuclear concrete structures. In a parallel way, the different parts of the corrosion system are studied in order to evaluate composition, structure and porosities. For these observations, classical methods such as optical and electronic microscopy, Energy Dispersive Spectrometry (EDS) coupled to Scanning Electron Microscopy (SEM), and Electron Probe MicroAnalysis (EPMA) are used. Moreover, less usual techniques such as micro-Raman spectroscopy and micro-diffraction under synchrotron radiation (μXRD) allow us to attempt to define the structure of the corrosion products at the microscopic scale. A general description of ancient corrosion systems and specific terminology will be given. This terminology has already been proposed in the literature to describe corrosion systems formed on archaeological artefacts in soil [15, 19] and more recently in binders [20].

7.2.2 Experimental corpus and methods

Corpus

Twenty-five artefacts from different buildings, dating from the Middle Ages to the beginning of the twentieth century, were studied (cf. Table 7.1). Indeed, even in ancient times, iron and steel clamps were sometimes used on a massive scale to reinforce the mechanical structure of buildings [21–23]. Whenever possible, the whole corrosion system (metal, rust and binder) was sampled and studied. Unfortunately, on some buildings, the entire system could not be sampled. Indeed, Qutb Minar, Conciergerie and Saudreville binders core not studied. For Tour des Latrines samples, stones were bedded with mortar in which metallic reinforcement was found, hence the corrosion medium is composed of both stone and mortar.

Table 7.1 List of the samples with their characteristics

| Building | Sample reference | Part of the system that was sampled | Age (years) |
|---|------------------|-------------------------------------|-------------|
| <i>Palais des Papes, Tour des Latrines</i> – Avignon (France) | TL02a | Rust | 660 |
| | TL02b | Rust, binder | |
| | TL02c | Binder (mortar) | |
| | TL02d | Binder (stone) | |
| | TL02f | Rust | |
| | TL06 | Metal | |
| | TL10 | | |
| <i>Qutb Minar</i> – Delhi (India) | Qu01 | Metal, rust | 650 |
| <i>Château de Vincennes, Dungeon</i> – Vincennes (France) | VIN01 | Metal, rust, binder | 630 |
| | VIN04a | Binder | |
| | VIN04b | Rust | |
| Cathedral – Rouen (France) | Re01 | Metal, rust, binder | 500 |
| <i>Conciergerie</i> Hotel – Paris (France) | Co02 | Metal, rust | 450 |
| <i>St Gervais</i> church – Paris (France) | GR01 | Metal, rust, binder | 350 |
| | GR02 | Binder | |
| | GR03 | Rust | |
| <i>Saudreville</i> Hotel – Paris (France) | SA01 | Metal, rust | 250 |
| <i>Ste Geneviève</i> Abbey – Paris (France) | GN01 | Metal, rust, binder | 250 |
| | GN02 | Binder | |
| | GN03 | Rust | |
| <i>Raincy</i> Church – Raincy (France) | RA01 | Metal, rust, binder | 80 |
| | RA02 | Binder | |
| Water tower – Saclay (France) | CEA1 | Metal, rust, binder | 50 |
| | CEA5 | Binder | |

Methodology

The first set of objects was freeze-dried to perform mercury porosimetry (Micrometrics Autopore III 9420, driven by win9400 software for pressures between 3 kPa and 412 MPa) or to be crumbled and mixed with distilled water to evaluate binder interstitial solution pH. The second set was mounted in epoxy resin. Finally, the sample was cut to obtain cross-sections. Films thinner than 50 μm were also prepared from cross-sections for μXRD experiments executed in transmission mode. Samples were polished with diamond paste (3 μm and 1 μm) for observation by optical microscope (OM). Before etching, the slag inclusion distribution in the metallic matrix was observed, giving information on the metal heterogeneity. The OM was also used to study the morphology of corrosion products around the metal. Secondly, after etching with 2% Nital, the metallographic structure of the substrate was revealed.

For the composition analysis several techniques were employed. The first was Energy Dispersive Spectroscopy (EDS), directly coupled to the Scanning Electron Microscope (accelerating voltage 15 kV). The Si(Li) detector used for these analyses was equipped with a thin beryllium window that permitted detection and quantification of oxygen with good accuracy (about 1% relative error on iron oxides standards). Electron Probe Microanalysis (EPMA) was specially used to analyse minor elements in the metallic matrix. A $2 \times 2 \mu\text{m}^2$ beam with an accelerating voltage of 15 kV (intensity 40 nA) is focused on the sample. Composition profiles could be obtained by analysing the average composition of rectangular areas that were parallel to the metal/oxide interface thanks to EDS. Considering successive areas, average composition profiles could be measured. This method was chosen in order to avoid local variations due to the presence of granulates or other local heterogeneities in the corrosion system. Indeed, the rectangular area (of several hundred μm^2) was chosen in order to obtain a constant composition value in the binder, independent of the local compound variation. Linear content profiles could also be obtained by EDS or EPMA analysing composition of several plots on a line.

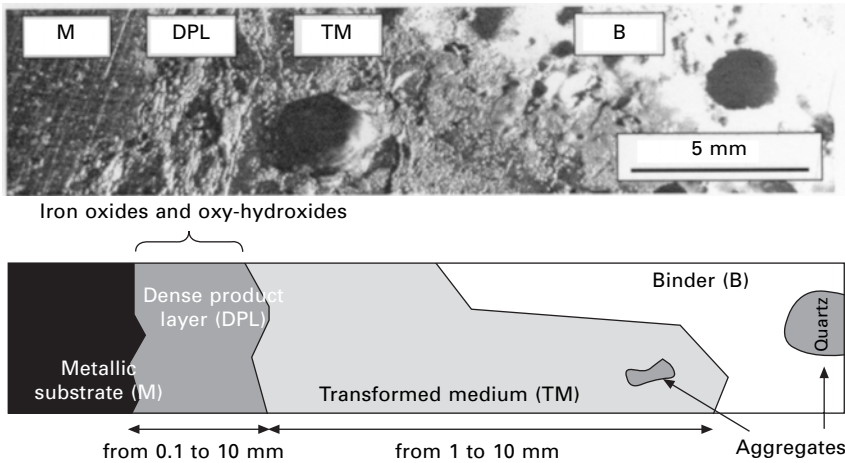
The local structure of corrosion layers was determined by two complementary methods: X-ray microdiffraction (μXRD) and micro-Raman spectroscopy (μRaman). μXRD experiments were conducted on the D15 beamline at the Laboratoire pour l'Utilisation du Rayonnement Electromagnétique (LURE) at Orsay, France. The detailed set-up is described elsewhere [24–26]. μRaman analyses were performed on the classical polished cross-section using a Jobin Yvon–Horiba LabRam Infinity spectrometer and a frequency-doubled Nd:YAG Laser at 532 nm. Spectral resolution of this set-up is about 2 cm^{-1} . It is described elsewhere [19, 27].

7.2.3 Results: corrosion layout

It seems that the general pattern encountered on archaeological corroded metallic reinforcements in binders is relatively similar to the system already observed on ancient ferrous artefacts corroded in soils [26, 28], i.e. made up of a multi-layered structure (Fig. 7.1). For this reason, the same terminology as that proposed by Neff *et al.* will be used to describe the corrosion system: the metallic substrate (M), the Dense Product Layer (DPL), the Transformed Medium (TM) and the Binder (B).

Metallic substrate

The metallic substrate (M) is the uncorroded part that remains on the original metallic object. OM observation revealed that all the structures studied on the metallic cores were made up of hypoeutectoid steels (mass% C < 0.8 – Nital etching allowed identification of ferrite and pearlite in all samples). Of



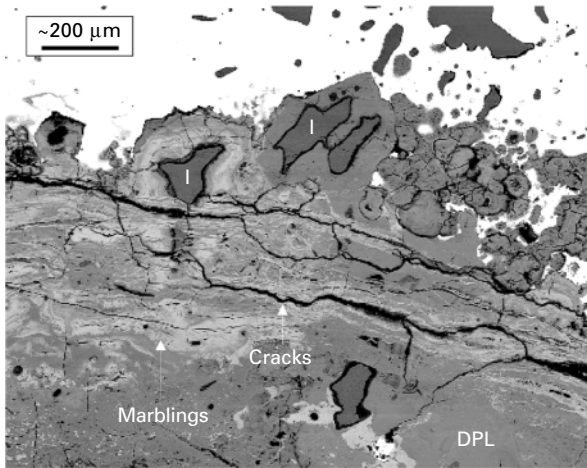
7.1 Macro-photograph of a cross-section (GR01) and schematic section of the corrosion system (M: metal; DPL: Dense Product Layer; TM: Transformed Medium; B: Binder).

particular note is the heterogeneous composition of archaeological iron (easily explained by the age of the samples and the evolution of ironmaking processes [29, 30]).

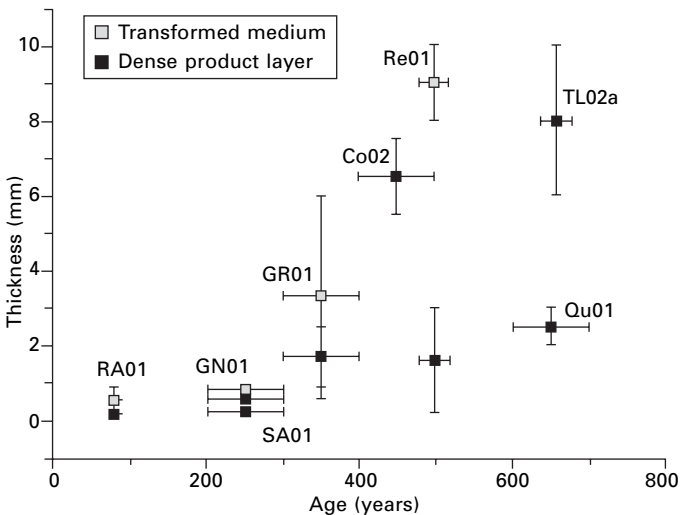
Dense Product Layer

The Dense Product Layer (DPL) appeared darker under OM compared to the metal. This zone did not contain aggregates from the binder. Typical marblings (Fig. 7.2) could be observed in the DPL of all the samples studied by OM and SEM. In general, the matrix of the Dense Product Layer appeared darker under OM than the veins, and the latter were parallel to the metallic substrate/DPL interface. However, on some samples, veins were so numerous that the DPL was formed by an interconnected network of two phases (on the TL02a and TL02b samples, for example). DPL thicknesses were measured and are represented in Fig. 7.3. Minor elements, such as calcium, silicon and sometimes chlorine, were detected in the DPL at contents under 1 mass% (samples TL02b, Re01, GR01, SA01 and RA01). These elements could have come from the binder and the fact that they were also detected in the DPL confirms that ion transport is possible inside this layer. Moreover, this layer was more compact than the more external layers (Transformed Medium and Binder) but nevertheless relatively porous and cracked (Fig. 7.2). Most cracks were parallel to the M/DPL interface and some were filled with resin. This could show that some cracks were anterior to sample moulding and permitted water displacement and mass transport in the DPL.

Mercury porosimetry was also used to evaluate the porosities (ϵ) of samples



7.2 Marblings and inclusions on the DPL (M: Metal; DPL: Dense Product Layer; I: inclusion) (GR01 sample; SEM).



7.3 Dense Product Layer and Transformed Medium thicknesses.

from Avignon (TL02f), Vincennes (VIN04b), Ste Genevieve (GN03) and St Gervais (GR03). A bimodal repartition of porosities was observed. Porosities from 300 to 6 μm access diameter are the first family that will be called microporosities. Those with access diameter from 30 to 3 nm will be called nanoporosities. DPL porosity volume was about 10% for all the analysed samples (Table 7.2). These results are in good agreement with previous data published on DPL porosities of ancient ferrous artefacts [9].

XRD analyses reveal that the Dense Product Layer consisted mainly of iron oxy-hydroxides (goethite α -FeOOH, lepidocrocite γ -FeOOH and akaganeite β -FeOOH) and iron oxides (maghemite γ -Fe₂O₃ and magnetite Fe₃O₄). The local structure of the DPL was studied by μ XRD on some samples (TL02a, GR01 and RA01). Two different phases were noticed in the diffracted volume in the RA01 sample: goethite and magnetite (and/or maghemite). Indeed, the fact that mixtures of different phases were observed can be linked to the relatively large diffracted volume ($20 \times 20 \times 50 \mu\text{m}^3$) compared to the size of the marbling observed by SEM and OM. In order to study in more detail the structure of the marbling, the microscopic laser beam of the μ Raman microscope was used. These analyses showed that veins consisted only of iron oxides, i.e. maghemite and/or magnetite, and matrices of iron oxy-hydroxides, i.e. goethite, lepidocrocite and akaganeite. The results of these different structural analyses are summarised in Table 7.2. It is noticeable that corrosion products and layouts seem not to be linked to metal or binder compositions and structures.

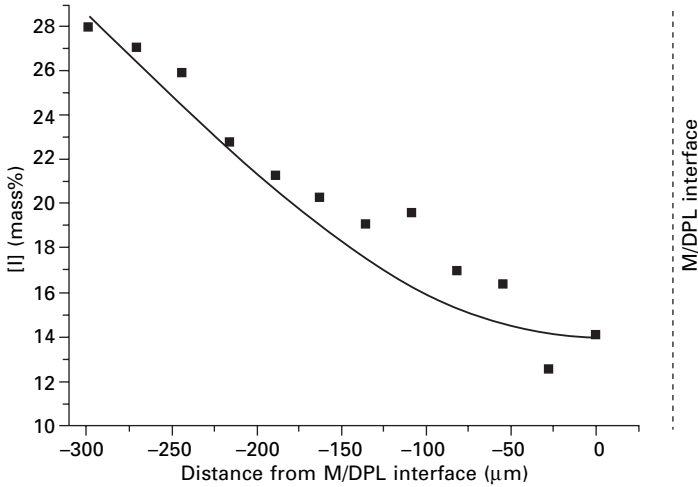
Table 7.2 DPL structural and porosity characteristics (A: akaganeite; G: goethite; L: lepidocrocite; M: maghemite and/or magnetite; Mh: maghemite; Mn: magnetite) (XRD, μ XRD, μ Raman)

| Sample | Porosity (%) | Veins number | XRD | μ XRD | | μ Raman | |
|--------|--------------|--------------|-----|-----------|--------|-------------|--------|
| | | | | Veins | Matrix | Veins | Matrix |
| TL02f | 5 | +++ | – | G | A | Mh Mn | G |
| | | | – | L | G | | |
| | | | – | M | L | | |
| Qu01 | – | +++ | – | – | – | Mn | G |
| VIN01 | 25 | + | G | G | G | Mn | G |
| | | | L | M | | | |
| Re01 | – | ++ | G | – | – | Mh | G |
| | | | L | – | – | | L |
| Co02 | – | ++ | – | – | – | Mn | G |
| GR03 | 15 | + | G | G | G | Mh Mn | G |
| | | | L | L | | | |
| | | | Mn | M | | | |
| SA01 | – | ++ | – | – | – | Mh | G |
| GN03 | 10 | + | G | – | – | Mn | G |
| | | | L | – | – | | |
| | | | Mn | – | – | | |
| RA01 | – | – | – | A | G | Mn | G |
| | – | + | – | G | | | |
| | – | – | – | M | | | |
| CEA1 | – | + | – | – | – | – | – |

Neff [19] also observed this type of Dense Product Layer in ancient ferrous artefacts corroded in soils but the only oxy-hydroxide found was goethite. Moreover, it seems that on some samples, as on TL02a, the veins are so numerous and close that it is difficult to distinguish which phase constitutes the matrix and which constitutes the veins. Finally, an important point to notice is that these iron oxide veins are not always connected to the metallic substrate (Fig. 7.2) and can be separated from it by a layer of oxy-hydroxides. A DPL formation modelling was proposed by Neff [19]. If oxide marblings and metal are not interconnected, because goethite is a non-conductive phase, anodic and cathodic reactions are located on the M/DPL interface. Moreover, corrosion studies on archaeological analogues made using ^{18}O markers (see Chapter 6) showed that new corrosion products precipitate only at the M/DPL interface. Thus, it could be the diffusion of dissolved oxygen in the water of the pores that controls the corrosion mechanisms and kinetics. This point will be discussed in Section 7.3.

Moreover, for modelling purposes, it is useful to evaluate the apparent diffusion coefficient in the DPL. Because iodide and oxygen have similar diffusion coefficients in water and because iodine is easy to detect in the DPL, the apparent diffusion coefficient of this ion in the DPL was measured. Indeed, this ionic marker is not ideal because charged species could have a different behaviour in the DPL than dissolved oxygen. Nevertheless, it is the easiest way to obtain a first evaluation of transport species profile in the DPL. Distilled water was saturated with sodium iodide to immerse DPL samples in. After a given immersion time (a sample was dried every hour for 10 hours), samples were cut and mechanically polished with water-free oil (kerdane). Iodide content profiles on the transverse section of the DPL were then obtained from EDS analyses coupled to SEM. As each spectrum is matched to a pixel of the BSE image, spectral mapping allows one to obtain an average elemental quantification in a rectangular area in which all 'pixel spectra' are summed. This method was used to avoid effects from DPL heterogeneities, such as cracks, porosities and local oxide penetrations. Analysis window size was fixed at $30 \times 900 \mu\text{m}^2$ parallel to the M/DPL interface. More details of this procedure and its limitation are discussed in Chapter 6.

Solving Fick's law, considering DPL thickness and its boundary conditions, theoretical iodide profiles were deduced and fitted to experimental results (see Fig. 7.4) in order to evaluate an experimental apparent coefficient of diffusion (D_0^*). This coefficient does not integrate parameters such as DPL porosity variations and the fact that iodide is an ionic species. Moreover, physical and chemical adsorption by the pore surfaces should strongly influence species migration. Nevertheless, a first approximation can be made by neglecting these latter parameters. The value obtained was $10^{-12} \text{ m}^2/\text{s}$.

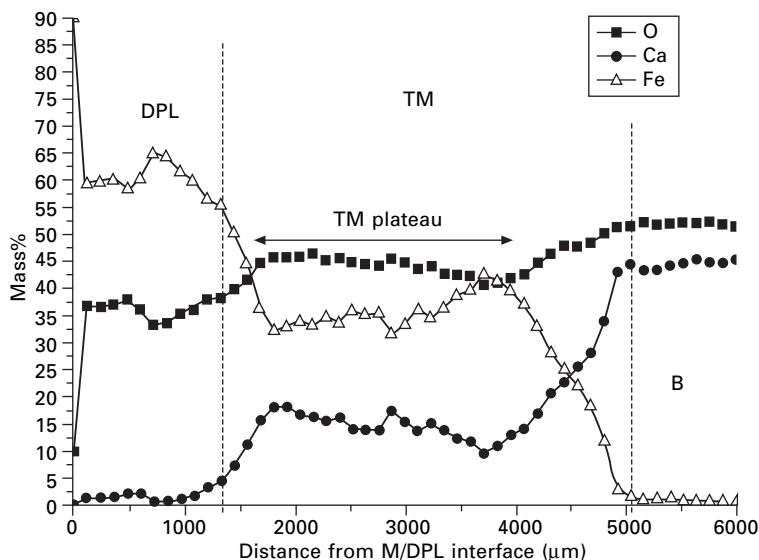


7.4 Iodide diffusion profiles in the DPL (7 hours immersion; GR01 sample).

Transformed Medium

The Transformed Medium (TM) is an interphase between the DPL and the binder that appears orange under OM polarised light. The thicknesses of these layers are represented in Fig. 7.3. The TM contains corrosion products and compounds from the binder. EDS average profiles show that, in this zone, the average iron content decreases from its value in the DPL (about 66 mass%) to its value in the binder (up to 1 mass%, depending on the binder). Moreover, $1 \times 1 \mu\text{m}^2$ composition profiles were made at the DPL/TM interface, avoiding quartz or lime grains. A typical iron content step was observed on some samples for instance on the VIN01 sample. Moreover, it seems that iron can present a plateau in a part of the TM (Fig. 7.5).

The step at the DPL/MT interface can be explained by the formation of the TM from dissolution of the CPD. Previous studies on iron oxide solubilities made by Neff [19] showed that at the pH and potential conditions attempted at the M/DPL interface (around -200 mV/S.H.E.) the solubility of iron oxides and oxy-hydroxides is very low. These calculated solubility values are too low to model the TM by dissolution of DPL and diffusion of iron in the water of the binder (Fick's law in a semi-infinite medium). Moreover, the plateau of the iron content observed on the profile of Fig. 7.5 cannot be explained by simple Fick's law modelling. The detailed formation of the TM needs to be investigated in further studies; evidently it seems that diffusion is not the only mechanism involved in TM formation.



7.5 Linear profile of major elements in VIN01 (EDS).

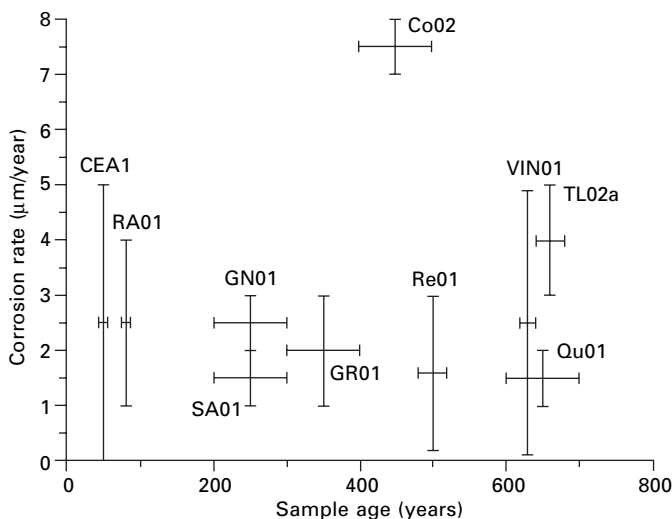
Binder

The binder (B) does not seem to be contaminated by the corrosion products from the reinforcement. Three kinds of binders could be identified on the different samples of the corpus. The most recent samples (RA01 and CEA01) are made of contemporary concretes, i.e. cement and aggregates (diameter < 200 μm). The main difference between the second kind of binder and the previous one is that it seems to be more homogeneous at the same scale. Some small aggregates (about 30 μm) containing calcium and oxygen were also identified, and quartz was detected by μXRD . Moreover, high quantities of sulphur were found on the GN01 and Re01 samples (more than 22 mass%). Sulphur is a particular case; it might be linked to gypsum ($\text{CaSO}_4 \cdot 2\text{H}_2\text{O}$) and the binder could be a plaster.

Finally, to complete the overview of the physico-chemical properties of the corrosion, system porosities (ϵ) were measured in some binders: TL02c, TL02d (Avignon, Tour des Latrines), VIN04 (Château de Vincennes), GR02 (Saint Gervais), GN02 (Sainte Genevieve) and RA02 (Raincy) samples (Table 7.3). The porosity values are between 20 and 35%. As for the Dense Product Layer, two access diameter families can be evidenced (Table 7.3): a microscopic one (about 1 μm) and a nanometric one (about 100 nm). It is important to note that even the compositional and structural analyses showed that the binders could be very different in nature depending on the sample, although the porosities were very similar.

Table 7.3 Binder (B) porosities

| | TL02c, d and f | VIN04 a and b | GN02 and GN03 | GR02 and GR03 | RA02 |
|---------------------------------|---|----------------------------|-------------------|-------------------|---|
| B porosity (%) | Mortar: 30 Stone: 25 | 35 | 35 | 25 | 20 |
| B main pore access diameters | 9 μm 0.9 μm 80 nm | 0.8 μm 80 nm | 0.8 μm | 0.8 μm | 100 μm 0.9 μm 80 nm |



7.6 Average corrosion rates of the studied sites versus sample age.

7.2.4 Results: evaluation of the average corrosion rates

In order to evaluate the average corrosion rates, the total iron quantity involved in the corrosion products can be measured by compositional analyses. Then, a density correction allows one to convert this quantity into metal loss. For this purpose, average composition profiles give access on the one hand to the evolution of the iron contents from the metal/oxide interface to the binder, and on the other hand to the thicknesses of the different layers (Dense Product Layer and Transformed Medium). A more precise description of these calculations can be found elsewhere [15, 19, 20]. Corrosion rates are lower than 10 $\mu\text{m}/\text{year}$ (Fig. 7.6). It should be noted that the CEA1 sample was unevenly corroded, with both uncorroded and corroded parts, which is why the average corrosion rate at this site varies from approximately 0 to 5 $\mu\text{m}/\text{year}$.

In order to avoid local content gradients (due to porosities and/or aggregates),

average profiles were drawn. In previous studies of iron archaeological artefacts in soils, iron content in the TM was assumed to decrease linearly from its value in the DPL (around 66 mass%) to its value in the binder (around 1 mass%) [15, 19, 20].

These studies of archaeological analogue corrosion systems reveal several characteristics that can be used to model the corrosion processes:

- Corrosion layers seem to be composed mainly of goethite and thus are isolating.
- Apparent diffusion coefficients of oxygen in the DPL are about 10–12 m²/s.
- Average corrosion rates estimated on archaeological analogues are about 2 µm/year.

In the following paragraphs, these observations and parameters will be used to propose the first step in modelling the corrosion processes.

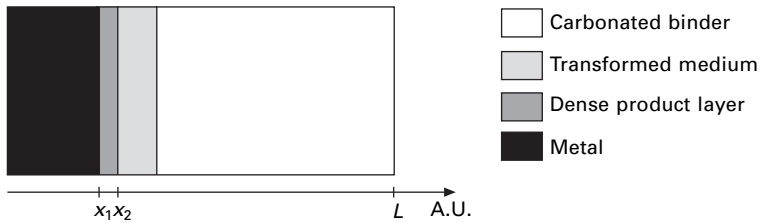
7.3 Proposition of a modelling approach for the corrosion of iron in concrete

7.3.1 Presentation of the modelling approach

This section presents the basis of a new mechanistic model for rebar corrosion in carbonated concrete, based on the analysis of ancient ferrous artefacts described in Section 7.2. As shown above, investigation of ancient ferrous artefacts embedded in carbonated binders points to a structuration of the oxides at the steel–concrete interface, this oxide being porous, even in the vicinity of the iron substrate. NaI diffusion profiles presented on pages 115–18. show how exogenous elements can diffuse through the porosity from the binder to the metal/oxide interface. Moreover, analogue analyses show a stratification of the oxides at the steel–concrete interface into two layers. The first is the Dense Product Layer (DPL), consisting of a ferric oxy-hydroxide matrix containing iron oxide marblings. The second layer is the Transformed Medium (TM), consisting of a precipitated ferric oxy-hydroxide in the porosity of concrete (see Fig. 7.1).

Following these observations, the model will be divided into two units (Fig. 7.7):

1. The first unit will describe the formation of the Transformed Medium by precipitation of the ferrous/ferric cations coupled to the transport by diffusion of aqueous species, in the carbonated concrete [31]. In this part of the model, the local chemical equilibrium of mineral phases is considered always to be respected. This approach has been presented and reported in ref. [18] and will not be detailed in the present chapter.
2. The second unit, described more precisely here, will describe the corrosion



7.7 Schematic representation of the corroding steel concrete interface.

of the iron substrate in the presence of the Dense Product Layer. In this case a local chemical disequilibrium will be assumed, thus reaction kinetics will be introduced.

The two units are coupled by fixing the boundary conditions: flow of aqueous species in both media at the DPL/binder boundary should be equal.

7.3.2 The oxygen reduction

The aim of this section is to identify the limiting step of iron corrosion in the presence of the DPL (analysed as a multi-micrometric and porous layer) when the concrete cover remains unsaturated. There are two kinds of limiting steps: reaction kinetics and aqueous species transport. Previous results show that, for carbonated concrete exposed to the atmosphere (unsaturated concrete), oxygen diffusion in concrete (binder) is not the corrosion rate-limiting step. Thus, results presented in refs [32]–[34] have shown the possibility for oxygen to diffuse in the DPL from the TM to the DPL/steel interface. Moreover, we can consider that the DPL remains water-saturated for lower relative humidity than concrete because the pore access diameter is of the order of nanometres [2]. Thus, the mechanistic modelling of reinforcing steel corrosion should take into account the redox activity within the DPL, assuming that it is a thin porous oxide diffusion barrier layer.

The purpose of this section is to evaluate of the cathodic reduction current density, in order to compare it with average corrosion rates estimated with archaeological analogues. Finally, it should be possible to validate the hypothesis of the oxygen-limiting step for the corrosion system. The following hypotheses are proposed before calculation:

- The saturation degree of concrete is below 0.9. Thus, the oxygen permeability of concrete is sufficient to maintain oxidising conditions at the DPL/concrete interface.
- The DPL is water saturated. Actually, the porosity of the oxide is in the nanometric scale and permits water condensation.
- In a first step calculation, properties of the DPL are considered to be

homogeneous in the whole layer (porosity, specific surface, effective diffusion coefficient).

- All transport mechanisms are in a stationary state.

Presentation of elementary mechanisms

Description of the system

Oxygen reduction in a porous medium can follow different mechanisms, presented and located on Fig. 7.8. Oxygen can be locally reduced at the internal interface ($x = x_1$), or in the volume of the porous medium, and the transport mechanism is diffusion in the water of the pores. The local reduction of oxygen in the vicinity of the porous DPL takes place in the case of a conductive iron oxide (magnetite). Since analyses of ancient artefacts have shown that the DPL is constituted of a goethite matrix, we will consider here that oxygen reduction in the DPL is not possible and that both anodic and cathodic reactions are located at the steel/DPL interface.

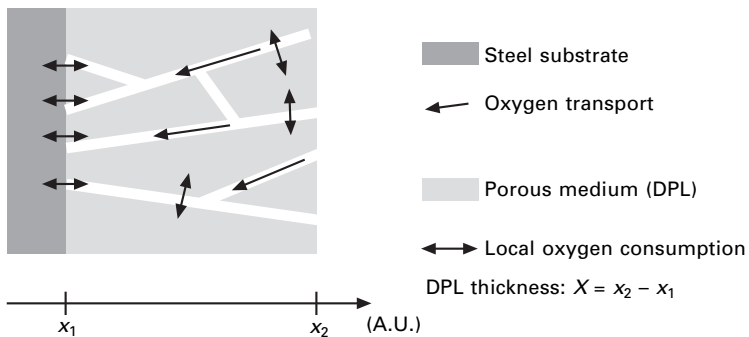
Pure reactional step

Oxygen reduction at the DPL/steel interface is assumed to follow locally a first-order reaction. The oxygen reduction rate $V(x)$ can then be written locally as:

$$V(x) = kc(x) \quad 7.1$$

where k is the kinetic constant of oxygen reduction ($\approx 10^{-5}$ m/s). The accessible concentration for the reduction, assuming the porous medium to be a homogeneous material, is:

$$c_{m,O_2} = \phi c_{O_2} \quad 7.2$$



7.8 Qualitative representation of elementary mechanisms for the oxygen reduction.

where: c_{m,O_2} = oxygen concentration related to the material volume (mol/m³)
 c_{O_2} = oxygen concentration related to the interstitial solution volume (mol/m³)
 ϕ = porosity of the porous medium.

Then, the oxygen reduction reaction at the steel/DPL interface is:

$$V(x) = k\phi c(x) \tag{7.3}$$

Equation 7.3 means that the kinetic constant for the oxygen reduction in a homogeneous porous medium is $k\phi$.

The effect of the cathodic overvoltage on the kinetic constant for the oxygen reduction is neglected because the difference between the equilibrium potentials of iron (Fe/Fe²⁺) and oxygen (O₂/OH⁻) is great (>1 V) and the iron oxidation rate is far faster than the oxygen reduction rate.

Pure diffusional step

The diffusion force is the chemical potential gradient. In the case of oxygen, this gradient is linked to the concentration gradient. First, Fick's law expresses the diffusion phenomenon, here in one dimension (1D). Moreover, it is possible to adapt the formalism to the porous medium (eqn 7.4):

$$j_{O_2} = -D_e \frac{\partial c_{O_2}}{\partial x} \tag{7.4}$$

where: j_{O_2} = oxygen flux for unit surface of the porous material
 D_e = effective diffusion coefficient of the porous medium (m²/s).

If the mass balance equation in a representative volume is combined with equation 7.4, we obtain the second Fick law:

$$\frac{\partial c_{m,O_2}}{\partial t} = D_e \frac{\partial^2 c_{O_2}}{\partial x^2} \tag{7.5}$$

And if we keep only the oxygen concentration in the interstitial solution in equation 7.5, we obtain:

$$\frac{\partial c_{O_2}}{\partial t} = \frac{D_e}{\phi} \frac{\partial^2 c_{O_2}}{\partial x^2} = D_a \frac{\partial^2 c_{O_2}}{\partial x^2} \tag{7.6}$$

where D_a = apparent diffusion coefficient of the porous medium (m²/s).

Resolution of equation 7.6 allows the calculation of the concentration profile in a porous layer (concrete or DPL), thanks to the limit conditions and the initial state. In a stationary system, the concentration profile in the porous medium is linear and the flux is constant in the entire porous layer.

The flux can be written as depending on the medium limits $c_{O_2}(x_1)$ and $c_{O_2}(x_2)$ and on the thickness (X) of the medium:

$$j_{O_2} = -D_e \frac{c_{O_2}(x_2) - c_{O_2}(x_1)}{X} = \text{const} \quad 7.7$$

Identification of limiting step

After the presentation of elementary mechanisms, the next step consists of the identification of the limiting step for the oxygen reduction for a simplified system. Oxygen is transported by diffusion in the carbonated concrete (binder) and in the DPL, which is a non-conductive oxide, and is then reduced at the steel/DPL interface.

From previous calculations, the oxygen fluxes in the DPL and binder can be written as follows:

DPL (thickness = X):

$$j_{O_2, \text{Ox}} = -D_{e, \text{Ox}} \frac{c_{O_2}(x_2) - c_{O_2}(x_1)}{X} \quad 7.8$$

Binder (thickness = L):

$$j_{O_2, \text{Bet}} = -D_{e, \text{Bet}} \frac{c_{O_2}(L + X) - c_{O_2}(X)}{L} \quad 7.9$$

Oxygen consumption rate follows first-order kinetics at the internal interface. It can be written using equation 7.3 at $x = 0$:

$$V = k\phi c_{O_2}(X) \quad 7.10$$

Different elementary steps of the reduction process are in series. If we write the mass balance for each zone, then for the whole system it is possible to establish the following relation between fluxes in a stationary system:

$$j_{O_2, \text{Bet}} = j_{O_2, \text{Ox}} = V \quad 7.11$$

Addition of equations 7.3, 7.8 and 7.9 allows the determination of the global reduction rate taking into account only elementary mechanisms:

$$j_{O_2} = \frac{c_{O_2}}{\frac{1}{k\phi} + \frac{X}{D_{e, \text{Ox}}} + \frac{L}{D_{e, \text{Bet}}}} \quad 7.12$$

We here suppose that the only variable in the system is the DPL thickness. The thickness of the concrete L is fixed. Effective diffusion coefficients of DPL are around 10^{-12} m²/s, as evaluated with NaI diffusion tests on ancient artefacts on pages 115–18. The value of the effective diffusion coefficient of concrete is between 10^{-12} m²/s for a water saturated concrete, and 10^{-8} m²/s for a non-saturated concrete, according to the literature [1].

Table 7.4 Calculation of the critical thickness and interpretation for limiting steps ($X = 100 \mu\text{m}$, $k = 10^{-5} \text{ m/s}$, $D_{e,\text{Bet}} = 10^{-12} \text{ m}^2/\text{s}$ in saturated medium and $10^{-8} \text{ m}^2/\text{s}$ in non-saturated medium, $D_{e,\text{Ox}} = 10^{-12} \text{ m}^2/\text{s}$, $\phi = 0.1$)

| Conditions | $\frac{1}{k\phi} \leq \frac{X}{D_{e,\text{Ox}}}$ | $\frac{X}{D_{e,\text{Ox}}} \leq \frac{L}{D_{e,\text{Bet}}}$ | $\frac{1}{k\phi} \leq \frac{L}{D_{e,\text{Bet}}}$ |
|--|--|---|---|
| X_c or L_c | $\sim 1 \mu\text{m}$ | Saturated concrete L (3 cm) Unsaturated concrete $L \times 10^{-4}$ (3 μm) | Saturated concrete $\sim 1 \mu\text{m}$ Unsaturated concrete $\sim 1 \text{ cm}$ |
| Limiting step | Diffusion in DPL | Diffusion in concrete Diffusion in DPL | Diffusion in concrete Mixed control diffusion/reaction |
| $i_{\text{red}} = i_{\text{corr}}$ ($\mu\text{A}\cdot\text{cm}^2$) | 9.3×10^{-2} | 3.0×10^{-4} 9.3×10^{-2} | 3.0×10^{-4} 2.3 |
| V_{corr} ($\mu\text{m}/\text{year}$) | 1 | 3.5×10^{-3} 1 | 3.5×10^{-3} 27 |

Three terms of the denominator of equation 7.12 have to be compared two by two in order to determine the limiting step of the oxygen reduction rate. Table 7.4 presents three inequalities, the calculated critical thickness value (X_c or L_c), the type of mechanism that controls the system, assuming that the DPL thickness is higher than or equal to $100 \mu\text{m}$ (GN01 or GR01 DPL thicknesses, see pages 115–18), and finally the calculated reduction current density and the average corrosion rate corresponding to each case (Faraday law).

The results presented in Table 7.4 show that, when the DPL or the concrete is water saturated, the limiting step is the oxygen diffusion. In these conditions, the oxygen reduction rate is inversely proportional to the diffusion layer thickness. Calculated corrosion rates are around $3 \text{ nm}/\text{year}$, and correspond to values of the passive corrosion state. When the concrete is not water saturated, as in ancient binders of archaeological analogues, the limiting step is also oxygen diffusion but only in the DPL. In these conditions, calculated average corrosion rates (around $1 \mu\text{m}/\text{year}$, considering DPL thicknesses of GN01 and GR01 ancient artefacts) are of the same order of magnitude as corrosion rates evaluated during the ancient artefacts analysis (V_{corr} (GN01) $\sim 2.5 \mu\text{m}/\text{year}$, V_{corr} (GR01) $\sim 2.0 \mu\text{m}/\text{year}$). A third case has to be mentioned. If the concrete is not water saturated and the DPL is thin (around $1 \mu\text{m}$), results show that the oxygen transport in the non-saturated concrete has to be taken into account. As a matter of fact, in these conditions, the reaction control is mixed. The oxygen concentration at the DPL/concrete interface is lower than that imposed by the atmosphere. In this case, corrosion rates should be around $20\text{--}30 \mu\text{m}/\text{year}$, which could correspond to corrosion rates found at the beginning of the active corrosion step.

7.4 Conclusion

This chapter is constructed in two complementary parts. The first (Section 7.2) deals with the characterisation of archaeological ferrous artefacts corroded in binders in order to better understand the corrosion system and to give some significant parameters (such as the apparent diffusion coefficient of oxygen in the water of the pores of the DPL) for phenomenological modelling of long-term iron corrosion. The second part (Section 7.3) presents the first stages of this modelling that will be developed in the French CEA in the next few years in the framework of the CIMETAL project.

Ferrous artefacts from 11 archaeological sites were studied in order to understand the corrosion system that can form in binders after long periods. The samples studied came from various areas and periods; hence material comparability with the steel considered for the nuclear waste management systems was checked. Binders are different in many ways (morphology, porosities, chemical composition, phases observed). But it was underlined that the system Metallic Substrate, Dense Product Layer, Transformed Medium and Binder is noted in all samples. These different media were characterised. In all the studied samples, the same phases were found in the DPL: mainly goethite containing magnetite and/or maghemite marblings. Other oxyhydroxides were noted on some samples (lepidocrocite and akaganeite). Because the matrix of the corrosion products is composed of a non-conductive oxyhydroxide (goethite), the hypothesis can be made that both anodic and cathodic reactions are located at the metal/DPL interface. Thus, it is probable that the oxygen diffusion in the water of the pores of the corrosion products is the limiting step of the corrosion processes. This point has to be verified in future work. In addition to those characterisations, thickness measurements coupled to a local density correction allowed the evaluation of average corrosion rate. Moreover, it was shown that several elements (calcium, chlorine, iron, etc.) could migrate in the Binder, the Transformed Medium or the Dense Product Layer. Last but not least, using an iodine marker, an apparent diffusion coefficient for oxygen in the pore water was roughly evaluated. Despite several limitations linked on the one hand to the choice of iodine and on the other to the evaluation method, this parameter is of great importance for modelling and gives an idea of the transport phenomenon kinetics that can take place in the corrosion products of archaeological artefacts.

In the second part of the chapter, a mathematical model was proposed, assuming, as demonstrated by the archaeological analogues analyses, that the corrosion product layer is not conductive and using the apparent diffusion coefficient rate that was measured in the first part. The initial results presented here show that the corrosion rate depends strongly on whether or not the binder on the one hand, and the DPL on the other, is saturated with water. When only the DPL is saturated with water, the calculated corrosion rates

are in good agreement with the average corrosion rates measured on archaeological artefacts. All these points will be refined in further studies.

7.5 Acknowledgements

The authors would like to thank the corrosionists, architects, historians and archaeologists who supplied the samples and were involved with their study, particularly Mr Maxime l'Heritier (*Université Paris I – LAMOP UMR 8589*, Paris, France), Ms Annick Texier (LRMH – Champs-sur-Marne, France) and Dr Philippe Bernardi (CNRS – LAMM UMR 6572, Aix-en-Provence, France); and Mr William Guillot (CEA Saclay – LECBA, Gif-sur-Yvette, France), Dr Ludovic Bellot-Gurlet (CNRS – LADIR UMR 7075, Thiais, France) and Dr Pierre Chevallier (LURE, Orsay, France) for their invaluable help in, respectively, μ Raman and μ XRD analyses. The authors would also like to thank Dr Gérard Santarini (CEA Paris, France) and Dr Damien Feron (CEA Saclay, SCCME, Gif-sur-Yvette, France) for their invaluable help in the model development. This study was also supported by the GDR 2114 of CNRS '*Physico-Chimie des Matériaux du Patrimoine Culturel*' (CHIMART), the CIMETAL programme (CEA France), and Electricité de France.

7.6 References

1. K. Tuutti, *Corrosion of Steel in Concrete*, Swedish Cement and Concrete Research Institute, 1982.
2. W.-J. Chitty, P. Dillmann, V. L'Hostis, C. Lombard, *Corros. Sci.* (in press).
3. S. Catinaud, V. L'Hostis, I. Petre-Lazar, O. Poupard, *Eurocorr 2004*, Nice, 2004.
4. ANDRA, *Référentiel Matériaux Tome 4. La Corrosion des Matériaux Métalliques*, ANDRA, 2001.
5. I. Petre-Lazar, Evaluation du comportement en service des ouvrages en béton armé soumis à la corrosion des aciers – Outil d'aide à la décision, Université Laval, Laval, 2000.
6. Z. P. Bazant, *Journal of the Structural Division* (1979) 1155.
7. C. Bataillon, in *International Workshop: Prediction of Long Term Corrosion Behaviour in Nuclear Waste Systems*, Cadarache, France, 2001.
8. D. D. MacDonald, *J. Electrochem. Soc.* 139 (1992) 3434.
9. P. Dillmann, F. Mazaudier, S. Hoerle, *Corros. Sci.* 46(6) (2004) 1401.
10. M. Stratmann, J. Muller, *Corros. Sci.* 36 (1994) 327.
11. M. D. Franco, J.-M. Gras, J.-P. Moncouyoux, *RGN*, May–June (3) (1996) 27.
12. C. Desgrange, F. Mazaudier, D. Gauvain, A. Terlain, D. Feron, G. Santarini, in *International workshop: Prediction of Long Term Corrosion Behaviour in Nuclear Waste Systems*, Cadarache, France, 2001, p. 49.
13. P. Dillmann, F. Mazaudier, S. Hoerle, *Corros. Sci.* (in press).
14. E. Pons, L. Uran, S. Joiret, A. H.-L. Goff, C. Lemaitre, D. David, in *International Workshop: Prediction of Long Term Corrosion Behaviour in Nuclear Waste Systems*, Cadarache, France, 2001, p. 334.

15. D. Neff, P. Dillmann, M. Descostes, G. Béranger, *Corros. Sci.* (submitted).
16. G. S. Duffo, W. Morris, I. Raspini, C. Saragovi, *Corros. Sci.* (to be published).
17. P. Bromblet, G. Martinet, *Pierre Actual 785* (2002) 66.
18. B. Huet, V. L'Hostis, P. Le Bescop, H. Idrissi, *Eurocorr 2004*, Nice, 2004, CD ROM.
19. D. Neff, Apport des analogues archéologiques à l'estimation des vitesses moyennes et à l'étude des mécanismes de corrosion à très long terme des aciers non alliés dans les sols, Université de Technologie de Compiègne, Compiègne, 2003.
20. W.-J. Chitty, P. Dillmann, V. L'Hostis, C. Lombard, *Corros. Sci.* (in press).
21. J. L. Taupin, *Monumental* 13 (1996) 18.
22. P. Dillmann, P. Bernardi, P. Fluzin, *Archaeometallurgy in Europe*, Milan, 2003, p. 199.
23. F. Amoudruz, J. Chapelot, S. Clement, Les éléments métalliques (fer et plomb) dans l'architecture du donjon du château de Vincennes. Etude préliminaire, Vincennes, 18, Equipe de Recherche sur le Château de Vincennes et la Banlieue Est, 1997.
24. P. Dillmann, P. Populus, P. Chevallier, P. Fluzin, G. Béranger, A. Firsov, *Journal of Trace and Microprobe Techniques* 15(3) (1997) 251.
25. P. Dillmann, R. Balasubramaniam, G. Béranger, *Corros. Sci.* 44 (2002) 2231.
26. P. Dillmann, D. Neff, F. Mazaudier, S. Hoerle, P. Chevallier, G. Béranger, *J. Phys. IV France* 12 (2002) 393.
27. D. Neff, S. Reguer, L. Bellot-Gurlet, P. Dillmann, R. Bertholon, *Journal of Raman Spectrometry* (Special Issue on the application of Raman spectroscopy in art and archaeology) (in press).
28. D. Neff, P. Dillmann, G. Béranger, in *International Workshop: Prediction of Long Term Corrosion Behaviour in Nuclear Waste Systems*, Cadarache, France, 2003, p. 295.
29. R. F. Tylecote, *A History of Metallurgy*, The Metals Society, London, 1979.
30. P. Dillmann, Diffraction X, Microdiffraction X et Microfluorescence X sous Rayonnement Synchrotron et analyses comparées pour la caractérisation des inclusions. Application à l'étude de l'évolution historique des procédés d'élaboration des objets ferreux (procédés direct et indirects), Université de Technologie de Compiègne, Compiègne, 1998.
31. R. Cornell, U. Schwertmann (eds), *The Iron Oxides – Structure, Properties, Occurrences and Uses*, 2nd edn, Wiley-VCH Verlag, Weinheim, 2003, p. 664.
32. E. Vega, P. Berger, P. Dillmann, *Nuclear Instruments and Methods B* (submitted).
33. E. Vega, Altération des objets ferreux archéologiques sur le site de Glinet (Seine-maritime, France, XVI^e siècle). Caractérisation des produits de corrosion et étude des mécanismes, Université de Technologie de Belfort Montbéliard, Belfort, 2004.
34. E. Vega, P. Dillmann, P. Fluzin, *Eurocorr 2004*, Nice, 2004, CD ROM.

Study of the atmospheric corrosion of iron by ageing historical artefacts and contemporary low-alloy steel in a climatic chamber: comparison with mechanistic modelling

L. MARÉCHAL, S. PERRIN, P. DILLMANN and
G. SANTARINI, Commissariat à l'Énergie Atomique, France

8.1 Introduction

Nuclear waste could be packaged in metallic containers and disposed of in very long-term interim dry storage for about 300 years. Nevertheless, in such conditions (i.e. environmental corrosion), condensation on the metallic containers, due to ambient temperature and humidity fluctuations, could not be completely prevented. The container walls, which may be made from in carbon or low-alloy steels, will then be exposed to cyclic wet and dry periods and will suffer from indoor atmospheric corrosion at room temperature.

The atmospheric corrosion behaviour of iron-based materials such as carbon or low-alloy steels has generally been well predicted for periods of a few tens of years by the well-known bilogarithmic laws [1]. However, for much longer time periods (i.e. a hundred to a few hundred years), as could be the case for some nuclear waste containers in very long-term storage, predictions are rare and almost certainly more uncertain. The most important cause of this lack of reliability is the complexity of the physico-chemical mechanisms that occur in the rust layer during atmospheric corrosion cycles, and the resulting modifications in the protective properties of the rust scale. A mechanistic modelling of these phenomena has previously been developed [2] to acquire more relevant and robust prediction of corrosion behaviour of materials. In order to get reliable experimental values of damage rates associated with a well-known wet–dry cycle, old rusted historical artefacts and low-alloy steel samples have been introduced in a climatic chamber for ageing tests. It is essential to determine such values in order to validate the modelling calculations and assumptions. Then, the experimental and calculated values are compared.

8.2 Atmospheric corrosion of iron

8.2.1 Description

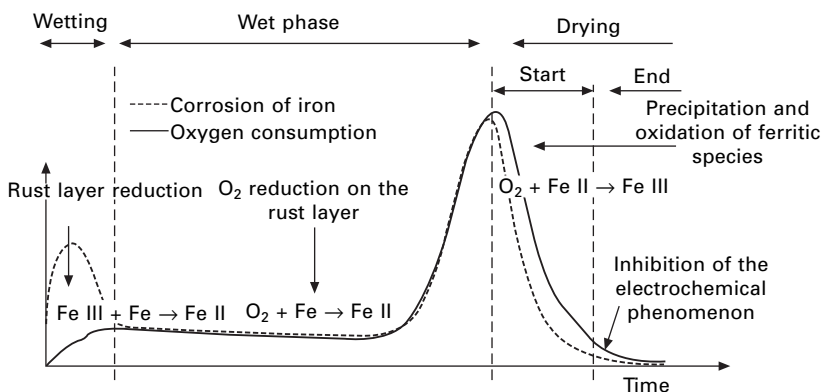
The atmospheric corrosion of iron is an electrochemical process occurring in the presence of an electrolyte. The corrosion of iron can be summarized by the following chemical equation:



The oxidation of iron by dissolved oxygen in thin electrolyte film leads to the formation of a rust layer composed of various oxides and oxy-hydroxides. By taking into account the fact that corrosion will occur away from atmospheric precipitation, the formation of the electrolyte film will be due to condensation of water from the atmosphere. This condensation depends mainly on the temperature and the relative humidity (RH) of the atmosphere. It is generally considered that corrosion phenomena start when relative humidity is higher than 60% and become more important when RH reaches 80% [3]. The variations of temperature and RH (due, for example, to the changeover between night and day) will create a succession of wet (with water condensing on the container walls) and dry cycles. Figure 8.1 shows the measurements of the variations of iron corrosion and oxygen consumption rates as experimentally measured by Stratmann [4]. Three different stages can be observed in Fig. 8.1; the wetting stage, the wet stage and the drying stage. Each of these stages is characterized by different physico-chemical mechanisms.

8.2.2 Iron atmospheric corrosion mechanistic modelling

This section presents the main lines of the physico-chemical mechanisms occurring during the atmospheric corrosion of iron (and by extension of



8.1 The wet-dry cycle. Variations of iron (dotted line) and oxygen (solid line) consumption rates as experimentally measured by Stratmann [4].

carbon and low-alloy steels). Each stage of the wet–dry cycle will be described, and damage related to a corrosion rate is calculated by using mechanistic modelling. This damage takes into account both the characteristics of the wet–dry cycles and the characteristics of the rust layer.

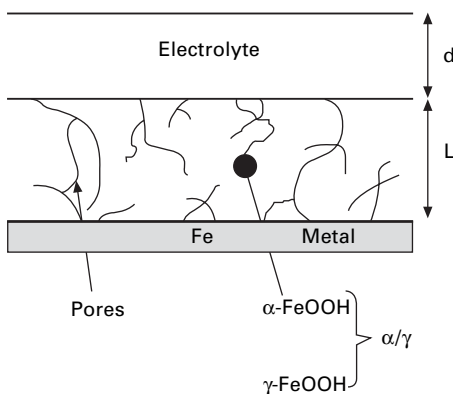
Atmospheric corrosion mechanistic modelling has already been described elsewhere in detail [2] but some modifications have since been made in order to obtain a better description of the phenomena [5, 6]. This electrochemical modelling is one of the two parts of the modelling that also includes a thermohydrodynamic module. This second module plans to describe the parameters of the wet–dry cycles as a function of the atmospheric data corresponding to the place where the containers will be disposed of in very long-term interim storage [7, 8].

Rust layer modelling

The rust layer commonly formed on low-alloy steel during atmospheric corrosion presents a complex morphology such as that presented in Fig. 8.2. A more detailed description of the rust layer and a presentation of the techniques used for its characterization are presented elsewhere [9, 10]. The description of the rust layer used in the modelling is given in Fig. 8.2. In order to simplify the rust description in the modelling, the main characteristics which have been kept are the layer thickness L , the fraction between goethite and lepidocrocite α/γ , the porosity and the specific area.

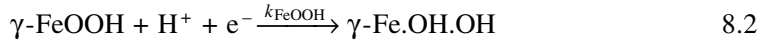
Wetting stage

During this first stage, which is characterized by an electrolyte growing at the sample surface, the anodic dissolution of iron is beginning. As it has been



8.2 Rust layer modelling.

experimentally proved [4] that there is no oxygen consumption during this stage (Fig. 8.1), the reduction of one of the active phases contained in the rust layer is the only phenomenon that can explain this anodic dissolution. As lepidocrocite (γ -FeOOH) is the only phase of the rust layer that can be reduced in these conditions, the proposed reaction for this reduction is given by [5, 11, 12]:

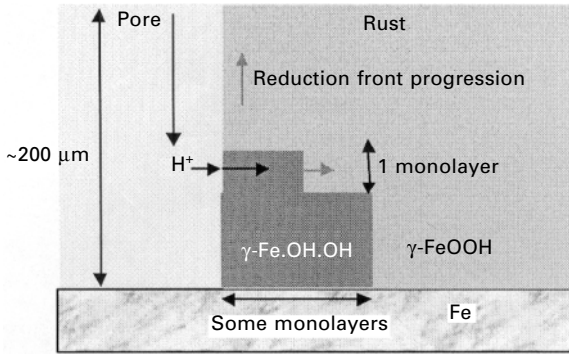


Since lepidocrocite reduction requires electrons to occur, this reduction can only take place at the metal/rust interface with the reduction front propagating through the rust layer, as γ -Fe.OH.OH is known to be an electronic conductor. At the same time, the reaction also needs H^+ ions, which are contained in the electrolyte. It is then supposed that only a few monolayers (n monolayers) of lepidocrocite will react at the porosities' surfaces in contact with the metal substrate. Reduced lepidocrocite γ -Fe.OH.OH is also an ionic conductor that also permits rather rapid movement of H^+ ions and, as the only mobile species involved are H^+ ions, this reduction reaction may also be reversible [11]. As the corrosion rate during the wetting stage is controlled by the reduction of γ -FeOOH, the amount of oxidized metal, and therefore the damage, is considered to depend only on the amounts of γ -FeOOH which can be reduced. By considering reaction 8.2 as the rate-limiting step, the expression for the reduction current is given by

$$i_\gamma = Fk_{\text{FeOOH}}[\text{H}^+]a_{\text{FeOOH}} \quad 8.3$$

where i_γ is the γ -FeOOH reduction current, k_{FeOOH} the rate constant of the electrochemical reaction, $[\text{H}^+]$ the H^+ concentration (as H^+ diffusion inside the rust layer is not considered) and a_{FeOOH} the activity of γ -FeOOH on one monolayer (expressed as the number of γ -FeOOH moles per cathodic surface unit).

As described elsewhere [12, 13], the γ -FeOOH reduction is considered to begin at the metal surface and propagates through the rust layer along the pore walls. It is also considered that the reduction front moves forward by γ -FeOOH monolayer steps on planes that are parallel to the metal (Fig. 8.3). The process stops when all the accessible amount of lepidocrocite is reduced. It is assumed that all the lepidocrocite of the rust layer is accessible to the reduction, mostly in the order of n monolayers, and that the cathodic process determines the corrosion rate. The anodic process (metal dissolution and removal of the corrosion products by diffusion) is supposed to be sufficiently fast for the cathodic reaction to impose its rate. Furthermore, it is assumed that all Fe[III] are reduced to Fe[II], without any modification of the crystallographic structure: there is a continuous path from γ -FeOOH to γ -Fe.OH.OH, without magnetite formation.



8.3 Schematic representation of the phenomena occurring during wetting.

By taking into consideration all of these assumptions, the expression for the damage p_γ associated with this stage (i.e. the consumption of metal during this stage) can be obtained by integration of the expression for the reduction current deduced from equation 8.3:

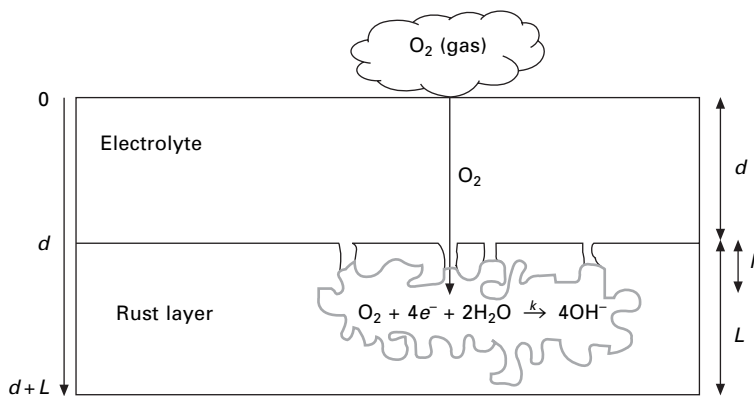
$$p_\gamma = \frac{\beta n e S}{2 V_{\text{mFeOOH}}} V_{\text{mFe}} \quad 8.4$$

where n is the number of reduced monolayers of $\gamma\text{-FeOOH}$, e is the thickness of one $\gamma\text{-FeOOH}$ layer, S is the area of the pores per surface unit, V_{mFeOOH} is the molar volume of $\gamma\text{-FeOOH}$, V_{mFe} is the molar volume of iron, and β is the molar fraction of $\gamma\text{-FeOOH}$ in the rust layer defined as the ratio

$$\beta = \frac{\gamma}{\alpha + \gamma} = \frac{1}{1 + \frac{\alpha}{\gamma}} \quad 8.5$$

Wet stage

The second stage is considered to begin when a constant thickness of electrolyte is reached at the whole surface of the rust layer. As a large part of the available $\gamma\text{-FeOOH}$ has already been reduced to the conductive $\gamma\text{-Fe.OH.OH}$, it can coat a part of the surface developed by the rust layer porosity and make a connection to the underlying metal. The reduced $\gamma\text{-Fe.OH.OH}$ on the surface of the pores can, from this point, act as a cathodic area. Oxygen will then be able to be reduced on this surface. Cathodic and anodic areas are decoupled, the iron oxidation taking place on the small metal area in contact with the electrolyte at the bottom of the pores and the reduction reaction on the large cathodic area formed by the reduced $\gamma\text{-FeOOH}$. Actually, the mechanisms of oxygen reduction are somewhat complicated and have not yet been clearly



8.4 Schematic representation of the oxygen reduction modelling. The electrolyte and the rust layer thickness are d and L respectively, and l is the oxygen average diffusion distance through the rust layer porosity. The grey tinted parts of the rust layer indicate the reduced lepidocrocite layer.

resolved in the presence of iron oxides [14]. For modelling reasons, the full mechanisms will not be considered, but only the overall reduction reaction. The modelling considers that atmospheric oxygen is dissolved at the atmosphere/electrolyte interface. Dissolved oxygen is assumed to diffuse first through the electrolyte and then through the pores in the rust layer through an average distance denoted by l in Fig. 8.4. This length is the average distance through which oxygen needs to diffuse before it can be reduced on a reduced lepidocrocite surface.

Once the oxygen has reached the reduced lepidocrocite surface, it can then be reduced following the cathodic reaction:



This reaction leads to oxygen consumption, which depletes oxygen concentration in the pores of the rust layer. The damage associated with this reduction can be calculated by considering the diffusion of dissolved oxygen, first through the electrolyte and then through the pores, only where there is an oxygen sink (the consumption of O_2 by reaction 8.6). It is assumed that the most important parameters of the rust layer, such as ϵ (porosity) or τ (tortuosity), are independent of space variables and that a stationary state is quickly reached. The expression for the damage due to the oxygen reduction on reduced γ -FeOOH surfaces in the rust layer is given by the following expression. The calculation has been made by taking into account firstly the diffusion of oxygen through the electrolyte layer to the rust layer surface (Fick's Law), secondly the diffusion of oxygen through the pores of the rust layer (Fick's Law in porous media), and thirdly the interfacial reduction of

oxygen on the previously reduced lepidocrocite layer during the wetting stage:

$$p_{\text{O}} = \frac{\varepsilon}{\tau} \cdot \frac{D_{\text{O}} C_{\text{O}}}{\frac{\varepsilon}{\tau} d + l + \lambda} \times 2V_{\text{mFe}} \left[1 - \exp\left(-\frac{L-l}{\lambda}\right) \right] \Delta t \quad 8.7$$

where D_{O} is the diffusion coefficient of oxygen, C_{O} is the oxygen concentration at the electrolyte/gas interface, V_{mFe} is the molar volume of iron, Δt is the duration of the wet stage, d is the electrolyte thickness, L is the rust layer thickness, and λ , which characterizes the mean depth of oxygen penetration inside the rust layer, is characterized by:

$$\lambda = \sqrt{\frac{\varepsilon D_{\text{O}}}{\tau \beta s_{\text{a}} k_{\text{O}_2}}} \quad 8.8$$

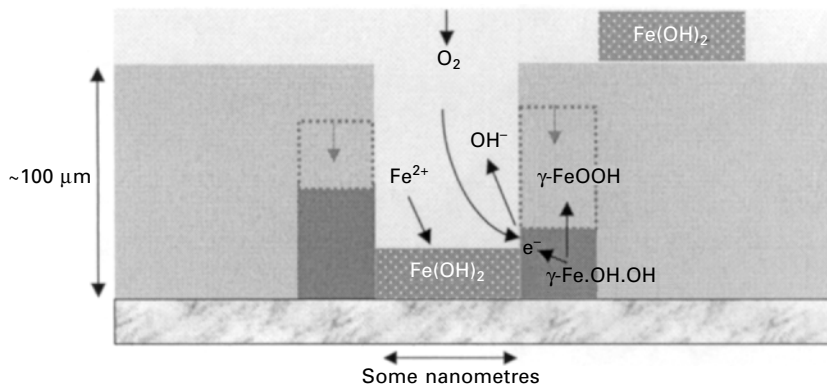
where s_{a} is the surface area of the pores per volume unit and k_{O_2} is the rate constant of the oxygen reduction reaction.

It should be noted that the first two stages – the wetting and wet stages – overlap and that the lepidocrocite reduction can continue while the electrolyte thickness has already reached its constant value and the wet stage has already begun. Furthermore, oxygen reduction on reduced lepidocrocite can occur as soon as the first amount of lepidocrocite is reduced.

Drying stage

The last stage, the drying stage, can be divided into two different stages. At the start of drying, the electrolyte thickness is decreasing at the rust layer surface and in consequence is accelerating the oxygen diffusion (and therefore the damage rate) through the film. The damage due to this film thickness reduction can be estimated by equation 8.7 in which the electrolyte thickness will not be constant. Once the electrolyte thickness has led to such an increase of the oxygen diffusion limiting current, this current is no longer the rate of the cathodic reaction. From this point it is the rate of the anodic reaction that determines the corrosion rate. This second part of the drying stage is also much more complex because the decrease of the electrolyte thickness leads to an increase of the corrosion product concentration and then to the blocking of the anodic sites. This phenomenon, which can be assimilated to a passivation, is represented by considering that the corrosion products are deposited on the anodic sites, which leads to the blocking of the dissolution sites and thus to the decrease of the oxidation current (Fig. 8.5). The anodic sites blocking process can be rendered by the following reactions:





8.5 Schematic representation of the phenomena occurring during drying.

where reaction 8.9 is the iron dissolution and reaction 8.10 reproduces the blocking of the anodic sites with a deposit of iron hydroxide. This is neither real precipitation nor adsorption, but only a model practical way to the blocking of the anodic sites when diffusion can no longer remove quickly enough the corrosion products due to a very rapid oxidation reaction (because the potential becomes very anodic during the drying) [2].

Concerning the modelling assumptions, the blocking of anodic sites by a ferrous hydroxide deposit is only a simulation of the far more complex actual process. An expression for the anodic current was determined by considering the anodic sites blocking [13]. The modelling considers only the stage of drying that comes from electrochemical reactions, i.e. that there is sufficient electrolyte at the surface. The re-oxidation of the rust layer at the end of the drying that allows the γ -FeOOH to regenerate for the next cycle is then not modelled. It is the end of the wet–dry cycle as described by the modelling.

For calculations presented in the experimental and calculated damages section, the final stages of drying have not been taken into account. This approximation does not really seem to affect the values because the damage due to the end of the drying process seems to be less important.

8.2.3 Mechanistic modelling results

A modelling code was developed on the Mathematica software in order to get damage values by integrating the three stages of the wet–dry cycle. As it has already been noted, the drying stage contribution to the damage was considered only through the damage caused by the faster diffusion of oxygen through the decreasing thickness of the electrolyte. By using data from the literature [9, 10] and from historical artefact characterizations, the code has

allowed prediction of damage values according to a well-defined wet-dry cycle. Modelling results are given, compared and discussed in the experimental section by taking into account the experimental conditions that were used in the environmental ageing tests on historical artefacts.

8.3 Experimental ageing of historical artefacts

The purpose of the experimental ageing of historical artefacts is to acquire reliable data for the atmospheric corrosion rates of steels already covered by a thick rust layer, such as those observable after several hundred years. Nevertheless, such data are very hard to obtain because the durations considered in such type of corrosion conditions are very long. Even if artefact rust thickness measurements, which can be associated with estimated damages, can give an idea of this kind of carbon and low-alloy steel damage as a function of very long durations, unfortunately this does not take into account the environmental history of the artefact and the fact that the rust layer can have been damaged during its history. Historical artefact ageing was carried out using an environmental chamber and, for comparison, contemporary low-alloy steel was also studied in the same experimental atmospheric conditions.

8.3.1 Historical artefact

The historical specimen used for this study, MAR01, is a 200-year-old rod from the framework of one of the towers of the Marly viaduct (France). The characteristics of this old rusted steel fit well with the modelling hypothesis (which considers a substantial rust layer already formed). Indeed, the rust layer thickness is about 150 μm and the sample is relatively not too old to ensure that a significant mass gain will be observed during the tests. This rust layer is of mostly constant thickness with a quite disturbed metal/rust layer interface. Quantitative powder XRD measurements were performed on rust powder scraped from the artefact (Philips diffractometer using a Co anticathode). The rust is mainly constituted of four different phases: maghemite ($\gamma\text{-Fe}_2\text{O}_3$) and/or magnetite (Fe_3O_4), goethite ($\alpha\text{-FeOOH}$) and lepidocrocite ($\gamma\text{-FeOOH}$). The presence of maghemite in the rust layer is quite controversial because the literature does not often mention this phase in rust layers formed during atmospheric corrosion but more often notes the presence of magnetite [15, 16]. In order to characterize precisely the MAR01 rust layer, and to acquire parameters that need to be included in the mechanistic modelling, sensitive techniques such as micro Raman spectrometry and XANES (X-Ray Absorption Near Edge Structure) were used to characterize the MAR01 rust layer.

In order to clearly differentiate between magnetite and maghemite,

μ -XANES was used. As the iron K edge has been heavily studied in XANES and μ -XANES [17, 18], it is now possible, by a subtle observation of the energy shift of the main absorption edge and of the pre-peak before this edge, to determine the valency and the mean coordination as considered on the analysed volume (a few μm^3). μ -XANES characterizations were made on transverse sections, on the ID21 microscopy line of the European Synchrotron Radiation Facility (ESRF, France). Goethite, lepidocrocite, maghemite and magnetite μ -XANES spectra have been realized on Alfa Aesar reference powders.

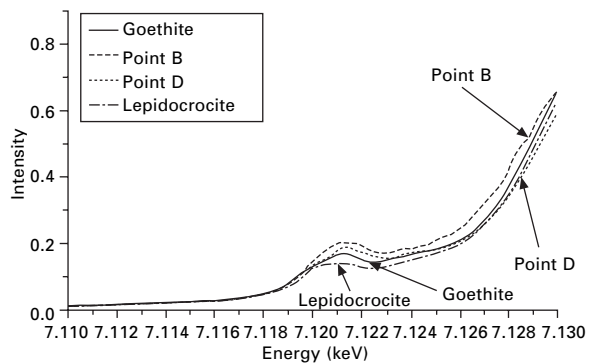
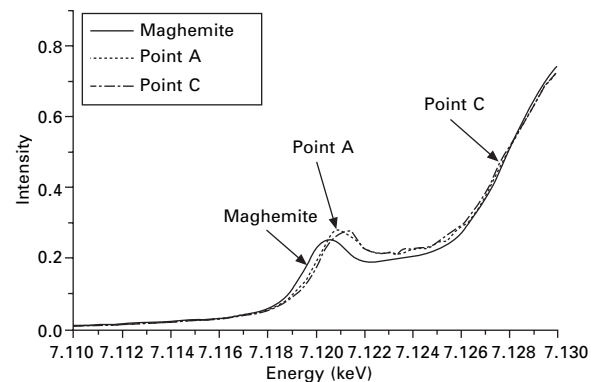
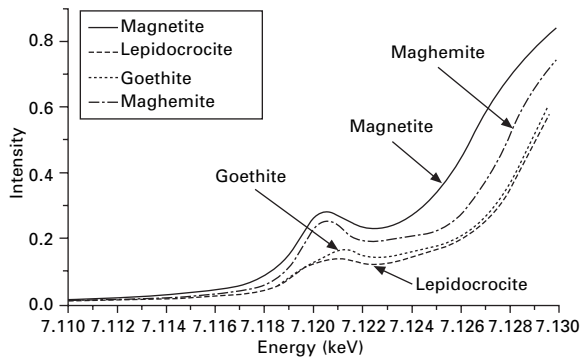
Figure 8.6 presents μ -XANES spectra obtained at different points of the MAR01 rust layer. It is very interesting to note that all the analysed points are in good agreement only with +III phases. Thus, it seems that no magnetite was observed in the rust layer, but only the presence of maghemite and oxy-hydroxides (goethite and lepidocrocite) which is compatible with the local valency indicated by this characterization technique. Actually, spectra corresponding to the more lightly rusted zones fit well with maghemite spectra and, in any case, present too high an edge position in energy in comparison with the magnetite reference spectrum.

Raman spectroscopy (performed in collaboration with Dr Bellot-Gurlet from the LADIR CNRS Laboratory) allowed differentiation of the phases contained in the rust layer such as goethite, lepidocrocite, maghemite or magnetite. By considering the complexity of the Raman spectra explanation, reference spectra were realized on several reference phases that could be present in the atmospheric corrosion rust layer, such as lepidocrocite, maghemite, magnetite and goethite. The stability of each phase was tested under Raman beam because maghemite and magnetite are, for example, likely to transform into hematite under a strong beam [19]. Raman characterizations were made with a $2 \times 2 \mu\text{m}^2$ laser beam on a LabRam Infinity with a spectral resolution of 2 cm^{-1} using a Nd:YAG laser (532 nm wavelength).

Raman maps can be obtained by choosing a significant vibration peak on the reference spectra of each studied phase. In the case of certain phases that present close peaks on the reference spectra, it is necessary to consider intensity ratios of two different peaks. These maps clearly reveal that lepidocrocite is observable mainly in the external interface of the rust layer. Maghemite is located in the more lightly rusted zones and goethite can be observed throughout the rust layer. The ratio between lepidocrocite and goethite, α/γ , was evaluated as equal to 4.

8.3.2 Contemporary low-alloy steel

A low-alloy steel (E36 steel) was also used in this study. Its chemical composition is given in Table 8.1. In order to get an initial rust layer, each



8.6 μ-XANES spectra obtained at different points of the MAR01 rust layer. Comparisons with the μ-XANES reference spectra (goethite, lepidocrocite, maghemite and magnetite).

Table 8.1 Chemical composition in wt% of the low-alloy steel E36 (Fe: base)

| | Chemical composition (wt%) | | | | | | | | | |
|-----|----------------------------|-------|-------|--------------------|-------|-------|-------|-------|-------|-------|
| | C | Mn | P | S | Si | Al | Cr | Cu | Mo | Ni |
| E36 | 0.075 | 0.511 | 0.071 | 8×10^{-4} | 0.270 | 0.034 | 0.527 | 0.282 | 0.001 | 0.124 |

E36 sample was pre-treated in a corrosion solution ($5 \times 10^{-5} \text{ mol.l}^{-1} \text{ H}_2\text{SO}_4 + 5 \times 10^{-5} \text{ mol.l}^{-1} \text{ Na}_2\text{SO}_4$) for 24 hours. Consequently, the samples can fit with the modelling conditions that consider a rust layer already formed. This kind of acid solution had already been used by other authors to reproduce the formation of a rust layer during atmospheric corrosion conditions [20–24]. The damage associated with this treatment was evaluated by successive exfoliation in a Clark bath. The rust layer formed during this pre-treatment was estimated to be about $1 \mu\text{m}$ thick.

8.3.3 Experimental procedures

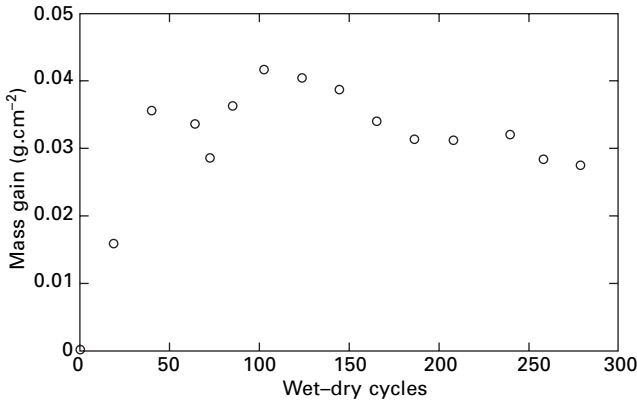
The primary MAR01 sample was a long cylinder about 20 mm in diameter. In order to obtain samples that could be aged in environmental chamber conditions, eight small cylindrical artefact samples about 20–30 mm long were cut off. The rust surface to be subjected to atmospheric corrosion in a climatic chamber was about 10 cm^2 . No cleaning of the samples was performed in order to keep the rust layer surface in its as-received state.

The metallic surfaces produced by the cutting of the original sample were first polished (to grade SiC 2400) to get a clean surface and then protected from corrosion by a non-conducting resin (COMBI SUB T-150). This resin had been aged in climatic conditions in order to confirm that it would not be the source of mass gain during the artefact ageing. Even if a small mass gain was observed during the first wet–dry cycles, the non-conducting resin finally showed no significant mass gain afterwards (Fig. 8.7).

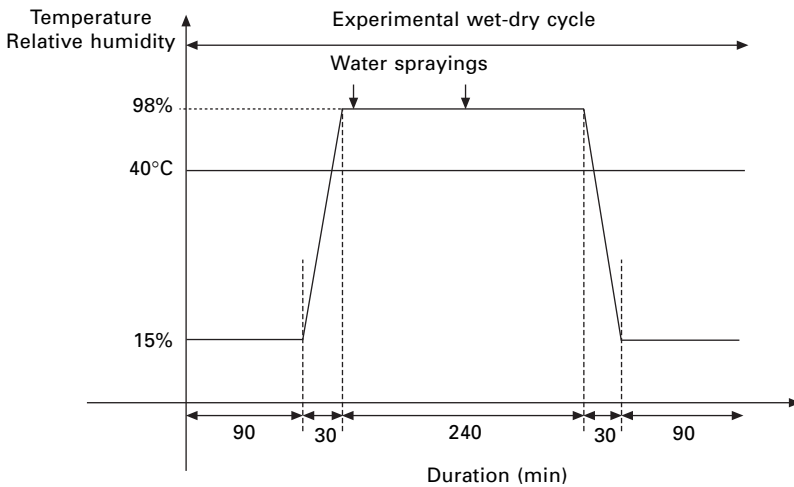
In order to check whether the protection was sufficiently good to prevent corrosion on the protected surface, cut-off surfaces were observed after 42 wet-dry cycles by scanning electron microscopy. No significant corrosion was observed.

8.3.4 Environmental conditions and corrosion rate measurements

Wet–dry cycles were programmed with the use of an environmental chamber (VC 4057) (Fig. 8.8). Experimental wet–dry cycles were characterized by a wet period of 240 minutes (98% relative humidity) and a dry period of 180 minutes (15% relative humidity). Two transition periods (wet to dry conditions)



8.7 Protecting resin behaviour during atmospheric corrosion ageing.



8.8 Experimental climatic chamber wet-dry cycle conditions.

of 30 minutes were included and water sprayings were used during these tests (two sprayings per cycle, one at the beginning of the wet period and the other after 120 minutes). The water spraying created a fog in the climatic chamber that ensured that a small water film was formed at the surface of each sample.

In order to determine the damage due to atmospheric corrosion of the samples, the mass of each sample was frequently measured (almost every 21 cycles). Samples were dried before each weighing for 10 hours at 40°C and 15% RH to ensure that they were totally dry. The damage was then estimated by considering the mass of rust formed and the proportion of the metal, that had been consumed. The hypothesis of the calculation is that the rust layer

is considered to be composed only of lepidocrocite and goethite so that its molar weight can be deduced from the average molar weight of these two phases. Damage (i.e. the quantity of metal oxidized) was then determined by the following expression:

$$p = \frac{\Delta m}{M_{\text{OOH}}} V_{\text{Fe}} \quad 8.11$$

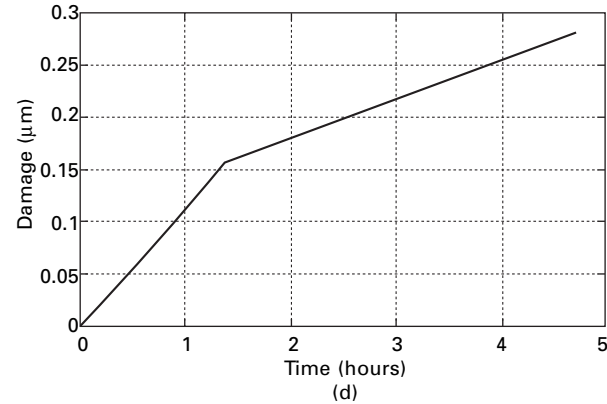
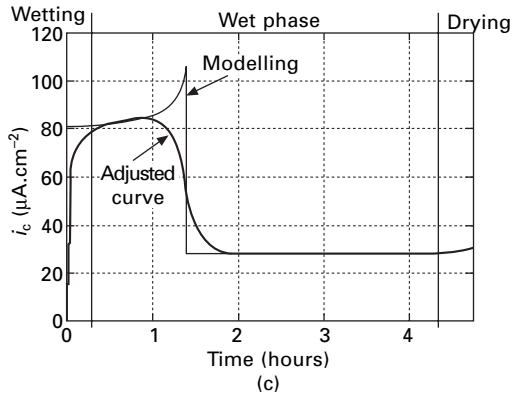
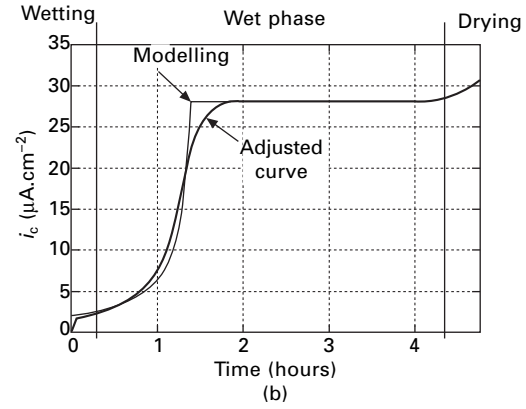
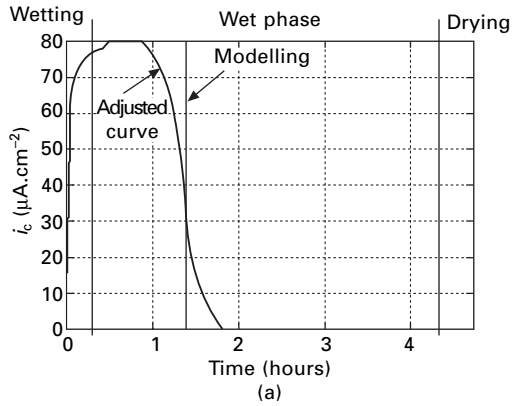
where Δm is the mass gain per surface unit, M_{OOH} is the molar weight of two moles of oxygen and one mole of hydrogen, and V_{Fe} is the molar volume of iron.

8.4 Results and discussion

8.4.1 Modelling results

The modelling code developed in Mathematica was applied to the experimental conditions used in the climatic chamber tests. Modelling allows one to obtain the variations of the current density during one cycle according to the characteristics of the MAR01 rust layer and the wet–dry cycle. The modelling takes into account variations of the rust layer, environmental parameters and conditions such as the initial rust layer thickness L , the temperature T , the oxygen partial pressure at the electrolyte/gas interface, and also the proportion of lepidocrocite contained in the rust layer. With regard to the MAR01 rust layer parameters and the wet–dry cycle conditions (durations of wetting, wet stage and drying), it was possible to calculate the current intensity during one cycle from equations 8.4 and 8.7 (Fig. 8.9). Note, however, that some of the rust layer parameters, such as the tortuosity and porosity (estimated here by mercury porosimetry), could only be estimated. Adjusted curves were determined by considering the mean of several consecutive values previously calculated by the modelling. All the characteristic values considered during the calculations are summarized in the table of symbols in the appendix to this chapter.

The values of current intensity delivered by the mechanistic modelling were of the same order as those experimentally measured by Stratmann [23], although that author worked on thinner rust layers and on steels that were a little different from those studied here. For instance, Stratmann experimentally determined current density values in the order of $200 \mu\text{A}\cdot\text{cm}^{-2}$. Furthermore, the total current intensity during one cycle was quite similar to Stratmann's. A rapid increase in current density was first observed in the early stages of the wet–dry cycle, due to the lepidocrocite reduction, and then the current density adopted a linear behaviour in accordance with the oxygen reduction during the wet stage. Finally, at the end of the cycle a short increase was observed due to the thinning of the electrolyte and the fastest diffusion of



8.9 Modelling calculations based on MAR01 rust layer parameters and experimental wet-dry cycle: (a) $\gamma\text{-FeOOH}$ reduction current intensity; (b) oxygen reduction current intensity; (c) total current intensity during one wet-dry cycle; (d) damage associated with the current intensity during one wet-dry cycle.

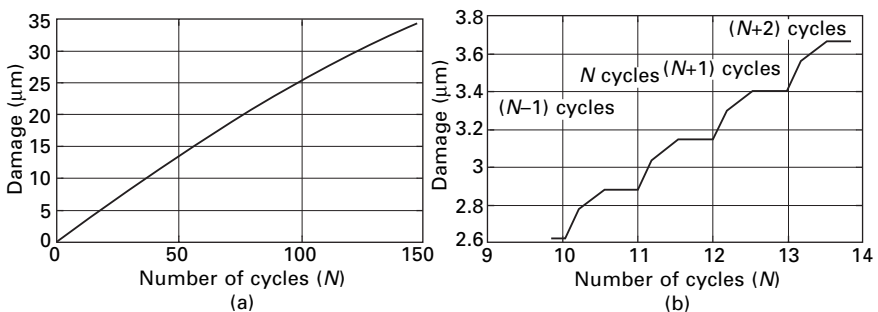
oxygen. This last stage is less important in our case because the time of drying is very short and the rust layer thickness is more important.

The estimated damage rate, corresponding to the MAR01 rust layer, was less than about $0.3 \mu\text{m}$ per cycle. This value was calculated by considering the experimental wet–dry cycle. The calculations also permit one to determine the damage due to atmospheric corrosion after N wet–dry cycles. They can take into account the evolution of sensible parameters such as the rust layer thickness, the fraction β between $\gamma\text{-FeOOH}$ and $\alpha\text{-FeOOH}$, and the evolution of the rust layer porosity as a function of the number of wet–dry cycles. An example of such a calculation is given in Fig. 8.10 where the damage during 160 cycles was determined by taking into account the evolution of the rust layer thickness. As an example, a linear evolution of β from 0.3 at the beginning to 0.1 after 150 cycles was considered. Such evolution of the $\gamma\text{-FeOOH}$ fraction is in the order of what has been experimentally observed on various historical artefacts where the protective ability index (α/γ) seems to decrease as a function of the age of the sample [9, 10].

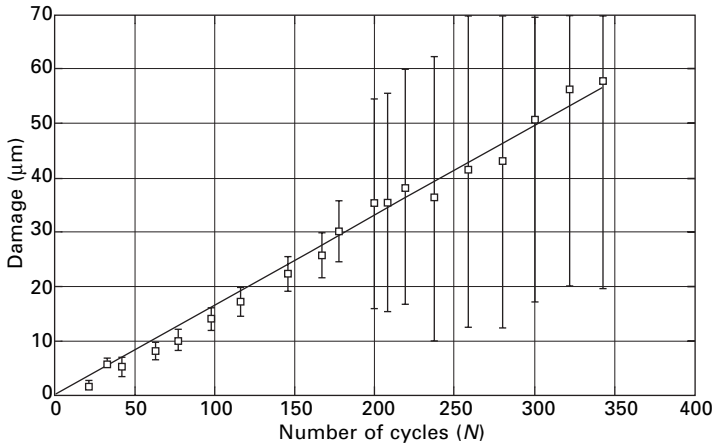
8.4.2 Experimental results

Historical MAR01 artefact samples were kept under atmospheric corrosion conditions for 350 wet–dry cycles and low-alloy steel E36 for more than 400 cycles. The damage associated with the mass gain measurements is represented as a function of the number of wet–dry cycles in Figs 8.11 and 8.12. It should be noted that the very important error bars observed in the last measurements of MAR01 damage are due to the fact that the last points were determined on fewer samples than the first points. Actually, one sample was retired from the test every 42 cycles in order to characterize the rust layer evolution as a function of the number of wet–dry cycles.

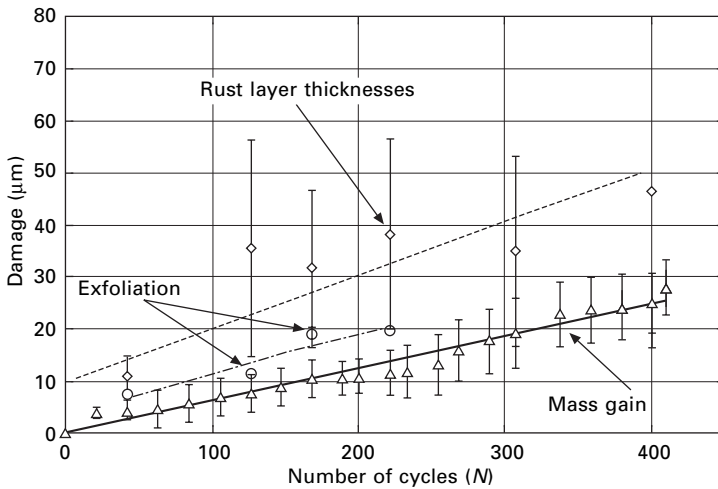
The damage rates that can be deduced from these experimental values by



8.10 Calculated damage evolution during 150 wet–dry cycles taking into account a linear evolution of the ratio β from 0.3 (first cycle) to 0.1 (last cycle): (a) full view; (b) details for five wet–dry cycles.



8.11 Historical MAR01 artefact damage deduced from the mass gain measurements during climatic chamber ageing.



8.12 Low-alloy steel E36 damage deduced from mass gain measurements during climatic chamber ageing, sample exfoliation in acid bath, and rust layer measurements.

a linear law ($a \cdot x$), are about $0.16 \mu\text{m}/\text{cycle}$ for MAR01 and $0.1 \mu\text{m}/\text{cycle}$ for E36. In the case of the E36 steel, two different methods – direct weight gain and acid solution exfoliation weight loss measurements – were used to determine the damage. The differences between the two methods that lead to more important exfoliation values can be explained by the fact that the rust layer is relatively fragile and could have been damaged during the weight gain measurement manipulations. Weight gain measurement was stopped

after 400 wet–dry cycles due to the weakness of the rust layers. The E36 samples were noticeably more rusted in the lower part, probably because of the sprayings that caused a flow of water at the surface of the sample. Furthermore, the rust layer thickness is more important in these lower parts. The rust thicknesses, which can be evaluated from the SEM observations, were in very good agreement with the values determined by weight gain (Fig. 8.12).

Concerning the evolution of the historical MAR01 rust layer during the ageing tests, significant spalling was observed on the samples after 200 wet–dry cycles without rust loss. This scaling is very interesting because it somehow demonstrates that these old rust layers could have spalled during their history and so the entire rust layer is still not fully observable. This could contribute to the fact that the damage rates deduced from the rust layer thicknesses of various historical artefacts [9, 10] are lower than those expected from the modelling. The quite good agreement with the calculations made by considering the experimental wet–dry cycle used in this study and the experimental results obtained on MAR historical artefact ageing seems to confirm this statement. However, it has to be noted that modelling calculations take into account several parameters that have not yet been well determined (or are not yet accessible), such as the tortuosity of the rust layer, the diffusion depth of oxygen to be reduced during the wet stage, and the electrolyte thickness. Moreover, the spalling that has been observed is not taken into account; this kind of phenomenon will increase the damage rate due to the creation of short-circuit oxygen diffusion paths through the rust layer.

The comparison between MAR01 damage rates and low-alloy steel damage rates is also very interesting. Actually, E36 damage rates ($0.1 \mu\text{m}$ per cycle) are lower than MAR01 damage rates ($0.16 \mu\text{m}$ per cycle). Lepidocrocite reduction during the first stage of the wet–dry cycle could explain this difference by the way in which the total amount of lepidocrocite contained in the MAR01 oxide layer is more important than in the E36 layer; Mar01 rust layer thickness is much more important than that of E36. This will result in a more pronounced effect of the wetting stage in the case of MAR01. Another explanation could be that E36 steel is low-alloy steel that is more resistant to atmospheric corrosion than the old historical steel.

8.5 Conclusion

The purpose of this study was to compare the atmospheric corrosion modelling of iron with experimental damage rate results obtained from the ageing of historical artefacts. The experimental procedure for ageing artefacts allowed us to obtain reliable data on atmospheric corrosion occurring on a low-alloy steel already covered by an old rust layer. The comparable results obtained on both old artefacts and contemporary low-alloy steel seem to confirm the

modelling, which suggests that most of the corrosion phenomena are taking place near the surface of the rust layer, where lepidocrocite has been mostly observed. Moreover, lepidocrocite reduction is certainly one of the most important parameters controlling the global corrosion rate since the amount of this phase in the rust layer governs the damage caused during the wetting stage. Another interesting fact is that significant spalling was observed after several wet–dry cycles. This spalling seems to indicate that rust layer thickness measurements of artefacts can give only a low estimation of the damage caused by the atmospheric corrosion, because part of the rust layer is already missing. Nevertheless, ageing tests on old artefacts covered with a rust layer have provided very useful information about the damage rates related to a well-defined wet–dry cycle. Such experimental results will be very valuable in providing a better understanding of the modelling of long-term iron atmospheric corrosion and will enable better comprehension and prediction of the corrosion behaviour of nuclear waste containers.

8.6 References

1. M. Pourbaix, in *Atmospheric Corrosion* (W. H. Ailor, ed.), John Wiley & Sons, New York, 1982, pp. 107–121.
2. S. Hoerlé, F. Mazaudier, P. Dillmann, G. Santarini, *Corrosion Science*, 2004, Vol. 46, 1431–1465.
3. T. E. Graedel, *Journal of the Electrochemical Society*, 1990, Vol. 137, 2385–2394.
4. M. Stratmann, *Berichte der Bunsengesellschaft für Physikalische Chemie*, 1990, Vol. 94, 629–639.
5. U. R. Evans, C. A. J. Taylor, *Corrosion Science*, 1972, Vol. 12, 227–246.
6. M. Stratmann, *Corrosion Science*, 1987, Vol. 27, 869–872.
7. F. Mazaudier, D. Feron, M. Baklouti, N. Midoux, *Journal de Physique*, 2001, Vol. 11, 259–266.
8. M. Baklouti, N. Midoux, F. Mazaudier, D. Feron, *Journal of Hazardous Materials*, 2001, Vol. B85, 273–290.
9. P. Dillmann, V. Vigneau, F. Mazaudier, C. Blanc, S. Hoerlé, *EFC Series*, 2002, Vol. 36.
10. P. Dillmann, F. Mazaudier, S. Hoerlé, *Corrosion Science*, 2004, Vol. 46, 1401–1429.
11. M. Stratmann, K. Bohnenkamp, H. J. Engell, *Corrosion Science*, 1983, Vol. 23, 969–985.
12. A. Cox, S. B. Lyon, *Corrosion Science*, 1994, Vol. 36, 1167–1176.
13. S. Hoerlé, F. Mazaudier, *EFC Series*, 2001, Vol. 36.
14. V. Jovancicevic, J. O. M. Bockris, *Journal of the Electrochemical Society*, 1986, Vol. 133, 1797–1807.
15. M. Yamashita, T. Misawa, S. J. Oh, R. Balasubramanian, D. C. Cook, *Corrosion Engineering*, 2000, Vol. 49, 133–144.
16. M. Takemura, S. Fujita, K. Morita, K. Sato, J. Sakai, *Corrosion Engineering*, 2000, Vol. 49, 111–122.
17. M. Wilke, F. Farges, P.-E. Petit, G. Brown, F. Martin, *American Mineralogist*, 2001, Vol. 86, 714–730.

18. G. Calas, J. Petiau, *Solid State communications*, 1983, Vol. 48, 625–629.
19. D. Neff, S. Reguer, L. Bellot-Gurlet, P. Dillmann, R. Bertholon, *Journal of Raman Spectroscopy*, in press.
20. A. Cox, S. B. Lyon, *Corrosion Science*, 1994, Vol. 36, 1193–1199.
21. S. H. Zhang, S. B. Lyon, *Corrosion Science*, 1993, Vol. 35, 713–718.
22. R. Bruno, *Electrochemical Methods for the Selection of Weathering Steels*, 15th Seminary Commission for Fundamental Studies and Applications, Brussels, 1974.
23. M. Stratmann, K. Bohnenkamp, T. Ramchandran, *Corrosion Science*, 1987, Vol. 27, 905–926.
24. T. Kamimura, M. Stratmann, *Corrosion Science*, 2001, Vol. 43, 429–447.
25. J.-E. Hiller, *Werkstoffe und Korrosion*, 1966, Vol. 17, 943–951.
26. M. Yamashita, H. Nagano, R. A. Oriani, *Corrosion Science*, 1998, Vol. 40, 1447–1453.

8.7 Appendix: Table of symbols and values

| | | | |
|--------------------|--|-----------------|--|
| C_0 | O ₂ concentration at atmosphere/electrolyte interface | table | 0.21 mol/m ³ |
| D_0 | O ₂ diffusion coefficient in the electrolyte | table | 3.24×10^{-9} m ² /s (40°C) |
| d | electrolyte thickness | measured | ~100 μm and >10 μm |
| e | thickness of one γ-FeOOH monolayer | table [25] | ~1 nm |
| F | Faraday constant | constant | 96 500 C/mol |
| i_c | O ₂ reduction current density | calculated | 1.2 μA/cm ² |
| i_γ | γ-FeOOH reduction current | calculated | 65 μA/cm ² |
| K | apparent rate constant of reduction γ-FeOOH | evaluated [12] | 30 s ⁻¹ |
| k_{FeOOH} | rate constant of γ-FeOOH reduction reaction | | |
| k_{O_2} | rate constant of oxygen reduction reaction | | |
| l | mean depth before oxygen reduction during wet stage | evaluated | ~10 μm |
| L | rust layer thickness | measured | ~150 μm |
| L_a | length of the pores per surface unit | calculated [6] | m ⁻¹ |
| N | number of wet-dry cycles | | |
| n | number of reduced monolayers of γ-FeOOH | evaluated | 1 |
| p | total damage from a wet-dry cycle | calculated | μm |
| p_o | damage due to O ₂ reduction | calculated | μm |
| p_γ | damage due to γ-FeOOH reduction | calculated | μm |
| S | area of the pores per surface unit | calculated [5] | 15 × 120 |
| S_a | specific area of the rust | measured | 10 m ² /g |
| s_a | surface of the pores per volume unit | calculated [26] | 7.38×10^7 m ⁻¹ |
| s_{FeOOH} | γ-FeOOH surface sites concentration | calculated | site/m ² |
| V_{Fe} | molar volume of iron | constant | 7.1×10^{-6} m ³ /mol |
| V_{FeOOH} | molar volume of γ-FeOOH | constant | 4.47×10^{-5} m ³ /mol |
| β | molar fraction of γ-FeOOH | measured | 0.2 |
| ε | porosity of the layer | measured | 10% |
| λ | depth of O ₂ penetration | calculated | 0.1 μm |
| ρ | mean α- and γ-FeOOH density | table/evaluated | 4.2×10^6 g/m ³ |
| τ | tortuosity of the rust layer | evaluated | 3 |

The corrosion of metallic artefacts in seawater: descriptive analysis

J. B. M E M E T, Laboratoire Arc' Antique, France

9.1 Introduction

As everyone knows, corrosion is the result of interactions between a metal and its environment. Seawater is a very complex medium characterized by the variety of its elements which are either chemical (water, ions, gases, etc.) or mineral (carbonates, silicates, etc.) or biological. They interact to create, on a metal surface, a very complex and corrosive medium. Because of this complex chemistry and intense biological activity, all seawater is a very corrosive environment for immersed materials [1]. Following their intrinsic physical characteristics, metallic alloys immersed in seawater take different free corrosion potentials which 'condition' the surface to its corrosion mode. These electrochemical phenomena make it possible to observe all the corrosion forms: the generalized corrosion affecting a relatively important surface, the galvanic corrosion favoured by the high conductivity of seawater, the pitting corrosion and crevice corrosion (the most localized phenomena), the corrosion induced by seawater flow, the stress corrosion, the erosion-corrosion, the fatigue corrosion and the corrosion influenced by micro-organisms.

The goal of this chapter is to evaluate, through the description of seawater parameters and through the burial chronology of heritage artefacts, the corrosion forms and hence the corrosion products that can grow on archaeological artefacts in seawater. The major corrosion products encountered on iron, copper, lead and tin alloys will be described, but, not all the details of the chronology of corrosion product formation on each metal; instead the chapter will focus on the formation and growth of corrosion products on iron-based alloys. In the first part, we will evaluate the physicochemical seawater parameters in these corrosion processes; then we will describe the kinetics of iron corrosion product formation and growth, their link with the physicochemical parameters and biological activity, and the relationship with the environmental conditions of burial. Next we will describe briefly the corrosion products observed on other metal surfaces. Finally, we will summarize

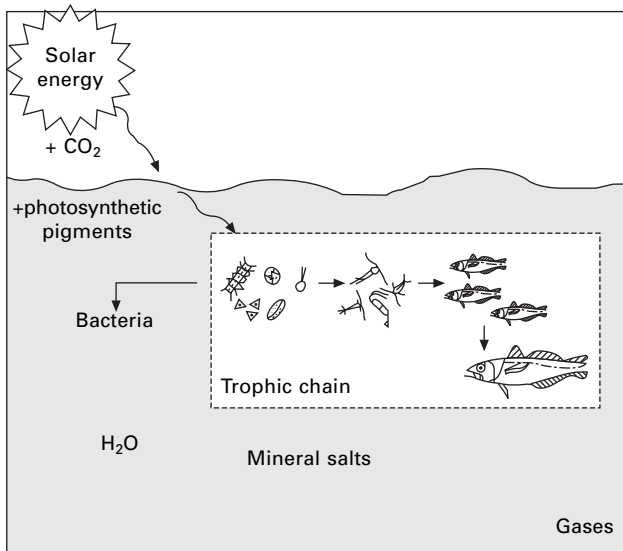
the relationship between the growth of these corrosion products and the difficulties observed in conservation and restoration laboratories.

9.2 Brief description of the seawater environment

Seawater is a very complex medium composed of pure water, mineral salts, dissolved gases, bacteria, micro- and macro-organisms participating in the food chain, matter in suspension derived from the chemical decomposition of living species, and sediments (Fig. 9.1). Highlighting the fact that this environment is chemically complex and the biological activity intense, seawater constitutes a very corrosive environment. As far as the metal's surface is concerned, this corrosivity of seawater is linked either to the chemical and electrochemical reactions of metal with the different constituents of seawater, or to the mechanical action of waves and sediments (mud, sand) or, lastly, to the biological colonization on the metal substrate which can induce some local chemical modifications. This is why the prediction of corrosion phenomena of the metal surface of archaeological artefacts requires good knowledge of the whole range of parameters of the environment in which the artefact was found. These parameters are described above.

9.2.1 Salinity and conductivity of seawater

From a theoretical point of view, since 1978 the 'practical salinity scale' has defined salinity in terms of a conductivity ratio [2]:



9.1 Schematic illustration of the complexity of seawater.

$$S = 0.0080 - 1.1692K^{0.5} + 25.3853K + 14.0941K^{1.5} - 7.0261K^2 + 2.7081K^{2.5}$$

where the practical salinity S of a sample of seawater is defined in terms of the ratio K of the electrical conductivity of the seawater sample at 15°C over the pressure of one standard atmosphere, to that of potassium chloride (KCl) solution, in which the mass fraction of KCl is 0.0324356, at the same temperature and pressure.

From a practical point of view, seawater is composed of dissolved components which are present as ion pairs or in complexes, rather than as simple ions. While the major cations are largely uncomplexed, the anions, other than chloride, are to varying degrees present in the form of complexes. One litre of seawater contains between 30 and 40 grams of dissolved salts and only about 10 mg of matter in suspension [1]. Table 9.1 gives the concentration of the most abundant ions of seawater. We note that chloride ions represent a great part of these elements and are represented mainly by NaCl and MgCl₂. This great concentration will have, as one can imagine, major consequences on the corrosion behaviour of metals in seawater. Indeed, this could lead to 'chloride containing' corrosion products in the case of generally corroded ferrous and cuprous metals and pitting of passive metals (tin, lead and aluminium based alloys).

Although the total mass of dissolved salts in seawater can vary between one ocean and another (see Table 9.2), the concentration ratio of the listed elements is stable. Thus, the concentration measurement of one component

Table 9.1 Concentrations of the most abundant ions in seawater [2]

| Cations (g/L) | | Anions (g/L) | |
|------------------|-------|-------------------------------|-------|
| Na ⁺ | 11.04 | Cl ⁻ | 19.88 |
| Mg ²⁺ | 1.30 | SO ₄ ²⁻ | 2.74 |
| Ca ²⁺ | 0.42 | HCO ₃ ⁻ | 0.18 |
| K ⁺ | 0.39 | Br ⁻ | 0.07 |
| Sr ⁺ | 0.008 | F ⁻ | 0.015 |

Table 9.2 Salinities of different seawater environments [2]

| Origin | Salinity (‰) |
|-----------------------------|--------------|
| Rivers (mean world value) | 0.1 |
| Baltic Sea | <17 |
| Black Sea | 18–22 |
| Atlantic and Pacific Oceans | 32–35 |
| Mediterranean Sea | 39–47 |
| Red Sea | 43–45 |
| Dead Sea | 276 |

can give an idea of the concentrations of the others. This great concentration of dissolved salts confers to seawater a low resistivity (around 20 to 30 $\Omega \cdot \text{cm}$) which favours considerably the electrochemical reactions between the metallic substrate and the medium. The important parameter to take into account is the fact that the salinity increases with the decrease of dissolved dioxygen concentration: practically, that means the salts concentration increases between the immersed zone and the mud zone. This could have a major effect, as one can imagine, on the chloride content of some corrosion products formed on buried artefacts.

9.2.2 Dissolved dioxygen

Seawater contains numerous dissolved gases including dioxygen O_2 and carbon dioxide CO_2 . Dissolved dioxygen is one of the most important factors affecting corrosion phenomena. It is known to be the main 'corrosion engine'. Its concentration is linked to different environmental parameters such as exchanges between sea and atmosphere, oxidation phenomena, living species respiration and photosynthesis. The dissolved dioxygen concentration varies from one geographical place to another, but even in the same geographical place it decreases with respect to depth and temperature (relatively to the seasons). Indeed, the solubility of dissolved dioxygen in seawater varies with temperature and salinity [3].

According to the corrosion phenomena, increased concentration of dissolved dioxygen induces increase in the corrosion rate of 'active' metals such as copper and iron. This could have great repercussions on the behaviour of an archaeological artefact: indeed, theoretically, without any biological consideration, the deeper the wreck, the better the conservation of metal.

9.2.3 Other parameters: pH, temperature and depth

All the physicochemical parameters of seawater are linked together. Thus, with increasing depth, the dissolved dioxygen concentration decreases, as do the temperature and pH, while the salinity increases and particularly the chloride content.

9.2.4 Biological colonization by living species

Every 'biologically non-toxic' metal in natural seawater suffers biological colonization. Following the first hours of immersion, this colonization begins with the appearance of a biofilm which is composed mainly of different bacteria consortia, of both an aerobic and an anaerobic nature. This biofilm can induce some local chemical modifications at the metal surface, leading to local differential aeration sites. These sites can locally accelerate the

corrosion rate of the metal, especially if some sulphate or thiosulphate reducing bacteria (SRB and TRB) are present. Indeed, with this type of bacteria, some pH reaching the very acid low value of 2 can be observed. Chronologically, a few days after the immersion, the metal's surface is covered by a biofilm which will attract micro-algae (white, green and red) and sediments that condition the surface to the formation, later, of a macroscopic fouling. This biological presence can affect the electrochemical reactions at the metal surface and inside the corrosion products by changing, locally, the physicochemical parameters and, more precisely, the pH and the dissolved dioxygen concentration. This biofilm and fouling are not directly responsible for the uniform corrosion phenomena but are known to play an active role in the promotion and acceleration of the local corrosion phenomena such as pitting or crevice corrosion [3–8]. From another point of view, the decrease of the dissolved dioxygen concentrations inside the corrosion products will provoke, as in the transition between the immersion and mud zones, an increase in the chloride concentration, and we wonder here whether it could play a role in the modification of the composition of corrosion products (by inserting some chloride-containing corrosion products).

To conclude this section, the corrosivity of seawater can be attributed to both general and local parameters. On the one hand, the relationships between dissolved dioxygen and salinity values with respect to depth and immersion zones allow us to determine some prediction models for the corrosion (and conservation) of metallic artefacts – such as, for example, the deeper the wreck, the better its conservation. But on the other hand, it is very difficult to predict the corrosion rates because of the interference that exists between the living species that can provoke, at the metal's surface or inside the corrosion products, a kind of 'battle of the oxygen', making the metal substrate undergo some contradictory corrosion phenomena.

Before trying to establish a link between the environmental physicochemical parameters and the chronology of burial conditions, it is necessary to describe the corrosion products' formation and growth.

9.3 Corrosion of iron-based artefacts

The mean corrosion rate of iron and iron alloys on industrial, harbour or naval immersed infrastructures is about 0.1 mm/year [2]. Depending on the thickness of an iron artefact, which can vary from a few millimetres to several centimetres, this 'modern' corrosion rate would induce the total loss of the artefact within a period of immersion varying from a few decades to several centuries. Sometimes this does occur, but often it does not, so we now consider the environmental parameters or intrinsic physical properties of the metal which provoke or prevent such total degradation of the artefact.

The large majority of the iron-based artefacts recovered from seawater are

made of wrought iron, cast iron or, for more recent objects, low carbon and stainless steels. In this section we ignore stainless steels, which are not yet considered to be included among heritage artefacts (though they will be in the near future because of their use during the Second World War). We will focus on historical artefacts and especially on the corrosion products observed on wrought and cast irons.

When an object is immersed accidentally, it undergoes, little by little, the effects of the aggressivity of seawater (infiltration in the porosities, corrosion of metals, colonization by algae, biodegradation, etc.). For a ferrous metallic artefact, the decades which follow this involuntary immersion lead, simultaneously or consequently, to the formation of a thick layer of concretions – also called ‘gange’ – made up mainly of corrosion products, micro and macro fouling and sediments. The thickness and composition of this gange remain difficult to foresee because its composition and growth depend at the same time on the physicochemical parameters of seawater, on the ‘living’ environment and/or on the geological and chemical characteristics of the sediment in which the object lies. But it is now admitted that as far as corrosion is concerned, the thickness and compactness of this gange play an essential role, acting as a barrier against the diffusion of the dissolved species towards the metal surface, and slowing down the ionic transport through the corrosion products onto the metal surface, thus notably reducing its corrosion rate [9].

In order to better predict the degradation state of the iron artefacts under this gange and, consequently, the duration of the post-excavation stabilization treatment, it is time to draw some parallels between the recent studies concerning the kinetics of corrosion at the iron surface, the evaluation of the environmental physicochemical parameters and, as far as possible, the chronology of burial conditions.

9.3.1 Theoretical formation and growth of corrosion products

From a strictly electrochemical point of view, in the few minutes following the immersion of the metallic artefact, the electrochemical mechanisms start. As we saw above, the biofilm formation starts rapidly too. Thus, a kind of competition takes place at the surface between the electrochemical reactions and the adhesion of biofilm on the surface. We now detail the different steps which lead an iron artefact to develop on the surface such a thick corrosion layer.

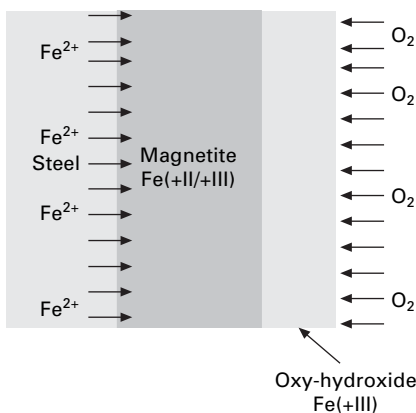
In seawater, as in near-neutral aerobic environments, iron-based alloys corrode with respect to the following anodic and cathodic reactions:

- The anodic iron oxidation reaction is $\text{Fe} \rightarrow \text{Fe}^{2+} + 2\text{e}^-$

- The cathodic reduction reaction depends on whether the iron is in aerobic or anaerobic conditions:
 - in aerobic conditions: $\text{O}_2 + 2\text{H}_2\text{O} + 4\text{e}^- \rightarrow 4\text{OH}^-$
 - in anaerobic conditions: $2\text{H}^+ + 2\text{e}^- \rightarrow \text{H}_2$.

From a thermodynamic point of view, in aerobic conditions, the iron corrosion starts instantaneously with the formation of a ferrous hydroxide $\text{Fe}(\text{OH})_2$ according to the reaction $\text{Fe}^{2+} + 2\text{OH}^- \rightarrow \text{Fe}(\text{OH})_2$. This ferrous hydroxide is unstable and its oxidation leads chronologically [3] to the formation of green rusts [10–13] (unstable), ferric hydroxides $\text{Fe}(\text{OH})_3$ (unstable) [14] and finally ferrous oxy-hydroxides like goethite $\alpha\text{-FeOOH}$ or lepidocrocite $\gamma\text{-FeOOH}$ (stable) [15]. These oxy-hydroxides are Fe^{3+} balanced and are known to be porous. This porosity has important consequences because it allows the diffusion of dissolved O_2 and its reduction onto the metal surface. Thus, a mixed balanced stable oxide ($\text{Fe}^{2+}/\text{Fe}^{3+}$) called magnetite Fe_3O_4 grows between the metallic surface and the oxy-hydroxide layer, thus creating a stratification as shown schematically in Fig. 9.2.

The rust-brown coloured external layer, constituted mainly of oxy-hydroxides, is poorly adhesive whereas the black internal layer, made mainly of magnetite, is thick and very adhesive to the substrate. At this stage, it is now well recognized that the corrosion product growth mechanisms and, moreover, the final corrosion products are chemically influenced by various parameters such as the anionic content (particularly the ferrous and chloride content) or the local pH of the solution [3, 16]. As far as the cathodic reaction is concerned, the surface rugosity also plays an active role in the dioxygen reduction mechanisms [17].



9.2 Schematic representation of the early stages of the corrosion of steel in seawater [3].

9.3.2 *In-situ* growth of corrosion products

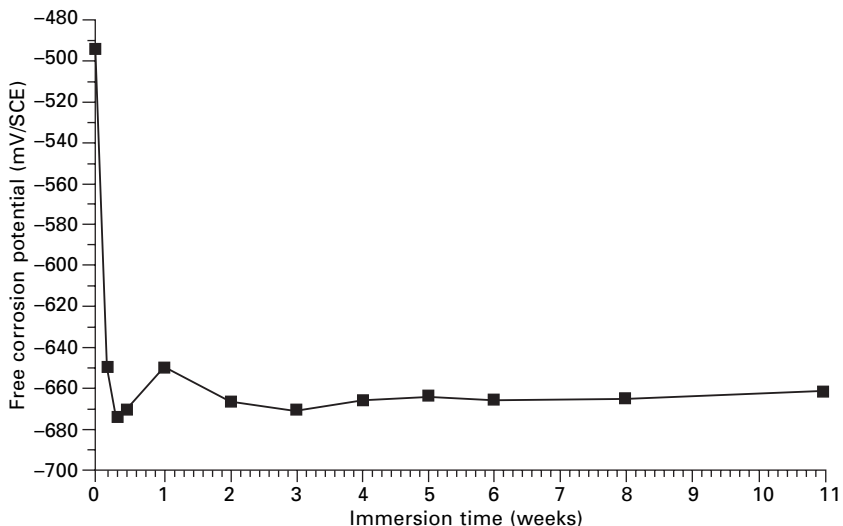
Indeed, as far as the corrosion rate already cited is concerned (about 0.1 mm/year for a low-carbon steel), it is important to mention that this is a mean value over 30 years and, obviously, is higher immediately after the immersion because of the oxygenation of the surface. Therefore, in order to understand the formation and growth of this gangue and consequently the decrease of the iron corrosion rates, we have recently studied the chemical interaction between the metal surface and the seawater environment during 21 months of immersion by either electrochemical technique or chemical analysis [3]. On the other hand, some pre-corrosion studies have more recently shown that pure iron and low-carbon steels develop approximately the same corrosion rates and stratification of their corrosion products after a few weeks of immersion in natural seawater [18]. Indeed, we are trying here to establish a link between studies realized from immersion for many decades in seawater and to compare their results with the stratified corrosion products and gangue observed on historical iron artefacts [19]. In the study mentioned above, the low-carbon steel E24 was used, whose composition is given in Table 9.3.

Three hundred plates made of this E24 steel were immersed in La Rochelle harbour for 21 months in order to follow the formation and growth mechanisms of corrosion products [20, 21]. During the first stage of the study, stationary measurements were provided, as shown for one plate in Fig. 9.3. The free corrosion potential of low-carbon steel plates, from one sample to another, remains relatively constant, between -650 and -670 mV/SCE. The important thing to notice is the rapid decrease of the free corrosion potential which could be linked to the appearance, simultaneously, of the goethite brown-rust external layer. This event is very important because it can be assimilated to a more rapid event than the biological colonization (known to be about a few days).

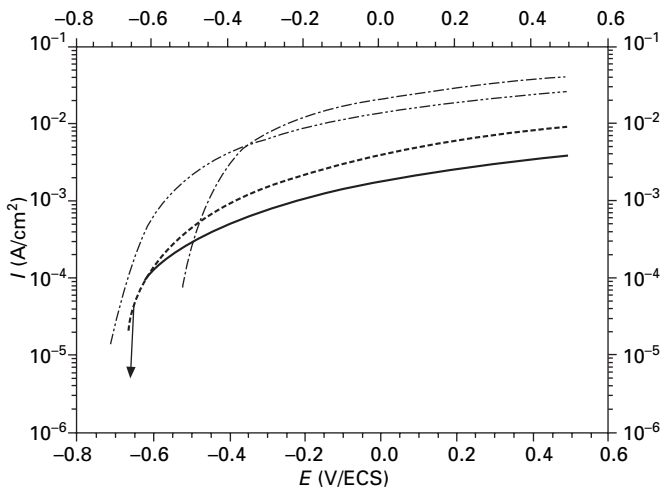
The polarization curves obtained respectively from immersion for 21 months have been simultaneously realized. The anodic representation from 0 to 6 months is presented in Fig. 9.4. This curve shows a rapid decrease of anodic current densities (also noticed on the cathodic current curves) with respect to time. This decrease was assigned to the diminution of the surface ratio between anodic and cathodic areas simultaneously with the formation and growth of

Table 9.3 Composition of the low-carbon E24 steel used: wt% of each element

| | | | |
|----|-------|----|-------|
| C | 0.122 | Cr | 0.118 |
| Si | 0.206 | Mo | 0.02 |
| Mn | 0.641 | Ni | 0.105 |
| P | 0.016 | Cu | 0.451 |
| S | 0.131 | Fe | Bal. |



9.3 Evolution with time of the free corrosion potential (mV/SCE) of a low-carbon steel plate with respect to time (weeks).

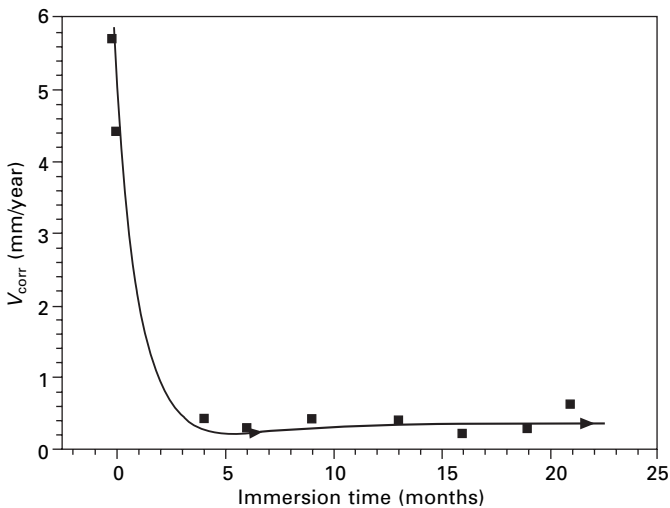


9.4 Anodic polarization curves on steel surface after 0, 12 hours, 3 and 6 months of immersion.

corrosion products. It confirms the free corrosion potential rapid decay mentioned above.

On the other hand, after the growth of a stable and adhesive corrosion layer constituted mainly of magnetite, the current density evolution with time between 6 and 21 months was more ‘chaotic’. Indeed, after 16 months of immersion, when the corrosion products are about 1 cm thick, the reduction

mechanisms are different from that observed when the surface is free of corrosion products or when the corrosion products begin to build up. Figure 9.5 shows the corrosion rates obtained during the 21 months on a low-carbon steel immersed in natural seawater [3]. This estimated curve was calculated with the polarization resistance values obtained according to the second method of Stern and Geary [3] with a low variation of 10 mV around the free corrosion potential. It shows a high corrosion rate (about 5.7 mm/year) during a short period, followed by a rapid decrease (4.4 mm/year after 12 hours, 0.2 mm/year after 4 months) which can be linked to the formation and growth of the corrosion products. These results were coupled with chemical analyses and this short period corresponds to the formation of the first oxy-hydroxide layer (composed mainly of goethite, α -FeOOH). This short period of electrochemical equilibrium was studied by polarization curves and electrochemical impedance measurements coupled to a scanning vibrating electrode [3]. Even after 10 minutes of immersion, the metal surface is active and some corrosion products begin to develop. This result is of a great importance as far as the 'battle for oxygen' is concerned: indeed, it clearly shows that electrochemical phenomena are more rapid than biological ones (first colonization after a few hours). For greater times of immersion, this study permits one to characterize the previously mentioned stratification of corrosion products, particularly on steel sheet piles immersed for more than 25 years in natural seawater. The corrosion products were scraped from the steel structure. Scanning electron microscope characterization coupled with EDS analysis revealed stratification of the thick corrosion products. Indeed,



9.5 Estimation of the corrosion rate obtained on a low-carbon steel immersed in natural seawater during the first 21 months [3].

after so many years and as a result of mechanical and/or biological stochastic events on the metal surface, several layers had formed, some alternating inorganic and chloride-containing oxy-hydroxides, others composed mainly of magnetite, near the metal surface, or composed of iron, sulphur and oxygen. Moreover, all these products contained chloride.

To conclude with the kinetics of formation and growth of corrosion products, the corrosion of iron-based alloys in seawater requires good knowledge of the iron metal/seawater system. The principal parameters are temperature, salinity (particularly chloride content) and pH. Variations of any one of these parameters can produce local physicochemical modifications and, moreover, chemical transformations of the corrosion products. Nevertheless, the dissolved dioxygen concentration is the most relevant parameter to be considered in studying the corrosion of metal artefacts. Indeed, it governs the cathodic reaction at the metal surface. If it is low, the cathodic reactions will favour the hydrogen production responsible for acidification of the medium; if it is high, cathodic reactions will produce hydroxyl ions which favour the formation of corrosion products based on oxides and oxy-hydroxides.

From a purely biological point of view, the dissolved dioxygen content is very important. Indeed, a low or zero O_2 content will favour the colonization of sulphur-producing bacteria (BSR, BTR), whereas a high O_2 content will provide an environment for ferro-oxidising bacteria.

Finally, we have shown the existence, at the metal surface, of a 'battle for oxygen' from either an electrochemical or a biological point of view. This kind of battle has major consequences on the corrosion behaviour of the metal and, moreover, on the corrosion products formed globally by stratification, or locally with 'pockets' of various types. These observations can be linked to those observed on artefacts recovered from terrestrial archaeology [22]. In the same time, some 'external' parameters can offer the opportunity for sulphate and sulphur-based corrosion products to grow, especially with the unstable state of green rust products [23].

9.3.3 Cast-iron corrosion in seawater

All iron found on wrecks prior to 1900 can be classified as either wrought iron or cast iron according to its carbon content and corrosion behaviour. We have described the kinetics of corrosion product formation on iron-based alloys with low carbon contents. Let us now describe the influence of higher carbon contents on corrosion product formation.

Marine cast-iron artefacts typically consist of an uncorroded metal core surrounded by a layer of graphitized corrosion products. Due to the different susceptibility of the various iron phases to corrosion, the division between corroded and uncorroded metal is not definite. With some objects the corrosion has even gone to completion and no metallic core remains. The graphitized

corrosion products on partially corroded cast irons typically contain goethite α -FeOOH, iron chlorides, SiO₂, Fe₃C and graphite [9]. Uncorroded or partially corroded ferrite and pearlite is present in the core metal and adjoining sections of the graphitized zone. The graphite forms a three-dimensional interlocking network which preserves the shape of the original object, including any surface markings. As graphite is an electrical conductor it also provides a pathway from electrons from the metal core to the outer artefact surface.

9.3.4 Chronological parallelism between iron corrosion products and burial conditions

The chronology of the formation of iron corrosion products, from a kinetic point of view, was discussed in the previous section. But, in order to take into account the whole range of parameters from an archaeological wreck site, the chronology of the burial conditions will be described here. We have already discussed the physicochemical parameters of seawater. Here we wish to emphasize the importance of the burial chronology in relation to the modifications induced in these physicochemical parameters. These modifications can greatly affect the chronology of the formation of corrosion products as well as the corrosion rates observed on iron-based artefacts and, furthermore, the conservation (or degradation) state of the artefact.

During the first weeks following a shipwreck, the metallic surfaces of the artefacts are not covered immediately by sediments or mud. Two environmental situations can be distinguished:

- If the depth is less than about 10 metres, the wreck is constantly subjected to wave turbulence, and the dissolved dioxygen concentration at the metal surface is maintained at a high rate (around 8 to 10 ppm). The metal surface is then very active, the corrosion products initiating rapidly, but the erosion is high due to the sand or sediments which, from time to time, abrade the surface. These events avoid the propagation of these corrosion products and the corrosion of the metal surface is maintained at a high rate.
- If the wreck is more than 10 metres deep, the metal artefacts are not affected by wave turbulence, so that the corrosion products can grow on the surface and a rapid stratification of these products occurs. The corrosion rates fall rapidly with the formation and growth of the corrosion products and, particularly, of magnetite.

After the burial period described above, mud and/or sand cover the wreck and its artefacts. The dissolved dioxygen concentration is considerably reduced; some values that have been measured near harbour infrastructures have shown a decrease from 8 ppm to around 2 ppm. Thus, the corrosion growth and moreover the corrosion rate are slowed down too. This important step leads

generally to better conservation of metal artefacts with respect to dissolved dioxygen concentration, unless the surface is reactivated by another event (such as a storm, tsunami or other dramatic climatic event). At the same time, however, anoxic sites are favoured, and consequently the presence of sulphur-reducing bacteria, which could induce some localized corrosion phenomena (some pH values as low as 2 have been observed locally within the corrosion product [3]), while also the salinity increases in this mud and/or sand layer, and consequently the chloride concentration. This increase has to be taken into account as far as the composition of the corrosion products is concerned, especially from a conservation and restoration point of view. Indeed, one can imagine that if the chloride content is higher, the composition of the corrosion products can be affected at each renewal of solution (as described previously).

9.4 Marine corrosion of copper alloys

The marine corrosion of copper alloys is linked to the same elemental correlations between the metal and its environment. Indeed, historically, pure copper and its alloys with zinc (brass) and tin (bronze) represent the large majority of copper-made artefacts recovered from the sea. The big difference between copper and iron is linked to biological activity. Indeed, copper is a perfect biologically toxic metal. Historically, it was used in naval construction to protect wooden structures against micro-fouling and especially against teredo drillings. As a result, copper-based alloys are generally found on wreck sites unconcreted or poorly concreted. The thin layer of concretion that is sometimes observed is linked to the proximity, in the burial environment, of a ferrous artefact or a ferrous part of the copper-based artefact.

The corrosion of copper in terrestrial burial sites has been studied particularly by Robbiola *et al.* [24] and is described in a previous article. The important thing to understand is the stratification that exists on copper or copper alloys. The chronology of formation of these corrosion products depends, as we have shown for iron artefacts, on the burial chronology and then on the burial conditions. Nevertheless, for copper alloys, the corrosion products are made mainly of tenorite CuO , cuprite Cu_2O , and nantokite (the chloride-containing corrosion product CuCl), and the external layer is composed of copper carbonate malachite.

9.5 Seawater corrosion aspects of lead- and tin-based 'white' metals

Lead and tin are white passivable metals. Unlike 'active' metals whose surface remains constantly in contact with its environment, 'white' passive metals develop at their surface a thin invisible oxide layer, the passive film, which

forms a barrier between the metal and the aerated medium, making the material apparently inert [25]. Lead and tin, when used in 'normal operating mode', thus continue to keep their glare. But when they are abandoned in a burial medium, terrestrial or submarine, this passive layer starts to be attacked by anions and cations, particularly chloride ions which initiate localized corrosion phenomena and the simultaneous development of corrosion products on the surface. Moreover, after years, marine lead and tin artefacts are often covered by a thick layer of concretion composed mainly of a mixture of marine seabed species and calcareous deposits from marine shells. This thick, dense layer can play the role of an oxygen barrier either during burial or after excavation during the restoration phase, hindering access of the electrolyte solutions to the metal surface. Nevertheless, tin alloys are easily recognizable from the bubbles which are the direct consequence of the pitting of tin due to chloride ions.

As far as lead and lead alloys are concerned, their corrosion products formed in either terrestrial or submarine burial sites are well known [9, 26, 27]. Lead artefacts from land sites are often covered with cerussite PbCO_3 or hydrocerussite $2\text{PbCO}_3 \cdot \text{Pb(OH)}_2$. Depending on the burial and environmental factors, varying amounts of lead oxides (PbO and PbO_2), anglesite PbSO_4 and laurionite Pb(OH)Cl are found in the lead corrosion layers. In submarine conditions, the main corrosion products found are laurionite Pb(OH)Cl and galena PbS .

The corrosion products of tin alloy artefacts such as pewters, which were the commonest alloys during the seventeenth and eighteenth centuries, are generally composed of different layers of tin minerals such as romarchite SnO , cassiterite SnO_2 and abhurite $\text{Sn}_3\text{O(OH)}_2\text{Cl}_2$. Depending on the burial conditions, possibly some other tin oxy-hydroxides and chlorides can grow in the corrosion layer. The chemical nature of these corrosion layers has been well described [26, 28] but very little is known about the environmental conditions of formation of such corrosion products. These corrosion products, based on chloride ions, are chemically and thermodynamically unstable, but museum conservators and archaeologists often consider them as 'stable' and suffering from dramatic pitting corrosion.

9.6 Knowledge of the degradation state of metallic artefacts

The aim of this last part of the chapter is to connect the information given by the environmental parameters and by the corrosion processes. Indeed, in a restoration protocol, before any mechanical intervention, restorers have to stabilize the corrosion products by dechlorinating the artefacts. In order to better evaluate the technique used, its duration and costs, restorers may obtain an extensive overview of the corrosion processes.

We have seen in previous sections that understanding the mechanisms of corrosion of metallic artefacts in seawater requires a preliminary study of the whole electrochemical system constituted of either the environmental physicochemical parameters of seawater or the nature of the substrate. From the environmental point of view, the principal parameters to consider are the temperature, pH, salinity and, most importantly, the dissolved dioxygen concentration. A sudden change in these parameters can profoundly affect the electrochemical behaviour of the metal and, moreover, its surface degradation. A better understanding of these parameters, coupled with an extensive knowledge of the corrosion mechanisms, can lead the restorer to better and/or faster restoration.

9.6.1 Air drying: a dramatic event for an archaeological metallic artefact

In the archaeological context, the discovery, excavation and conservation of an artefact provoke micro and macro changes in the physicochemical parameters surrounding the artefact. Without conservation and restoration treatments, these changes induce irreversible degradation which may lead, in many cases, to the total loss of the original surface. All metals are subject to such degradation except for white passivable metals, which are quite stable. For copper alloys the corrosion products are composed of tenorite, cuprite, and the chloride-containing corrosion products like nantokite, atacamite and paratacamite. If this corroded system is dried out, it will become coated with a green copper carbonate layer composed mainly of malachite, $\text{Cu}_2(\text{OH})_2\text{CO}_3$. But the most drastic consequences of air drying are noted on ferrous iron-based artefacts. Indeed, if marine cast iron is allowed to partially dry out in air, the iron chloride components decompose to form maghemite Fe_2O_3 , ferric chloride FeCl_3 , lepidocrocite $\gamma\text{-FeOOH}$ and hydrochloric acid HCl . This mixture of compounds provides almost ideal corrosion conditions and, in the presence of atmospheric oxygen, very rapid corrosion occurs. The overall degradation process is speeded up considerably by Cl^- ions which are present in the graphitized zone at concentrations of approximately 6–12% by weight [9]. The degradation can occur very rapidly if the cast iron artefacts are not kept continually wet. Even if no apparent damage has occurred as a result of drying, the bond between the graphitized corrosion layer and the residual metal can be seriously weakened, causing the corrosion layer to spall off during subsequent conservation treatment.

In order to avoid this irremediable and destructive degradation, some treatments are imposed on the metal in order to 'stabilize' its corrosion. The main goal of these treatments, which are based on chemical, physical or electrochemical techniques, is to dechlorinate the artefact while keeping the corrosion products which contain the historical information. This dechlorination

will lead to the stabilization of the artefact's corrosion activity and thus will help the restorer to start the restoration treatments which are based on mechanical cleaning, consolidation and finishing reversible coatings.

9.7 Conclusion

Understanding of the corrosion mechanisms observed on archaeological artefacts recovered from seawater is facilitated by taking into account the strong interactions between this aquatic environment and the metal's surface. Indeed, we have shown in this study that the formation of corrosion products starts a few minutes after immersion, eventually stabilizing the artefact's surface, even within historical or archaeological immersion times.

All the corrosion products formed on metals after many years in seawater are stratified. For generally corroded metals such as iron and copper alloys, this stratification comprises unstable products which have to be maintained in a wet state before conservation treatment starts. For passivable 'white' metals, stratification is less of a problem because the chloride-containing products are quite stable, even after excavation and even if the artefact is maintained in a dry state. These chloride-containing products are still studied because the stabilization times are still not well known, and researchers are trying to establish the link between the degradation state of the artefact and the kinetics of extraction of chloride by means of electrochemical and chemical techniques.

9.8 References

1. R. Sabot, C. Compère, J.B. Memet, Corrosion en milieu marin, in: *Corrosion des Métaux et Alliages, Mécanismes et Phénomènes* (ed. G. Beranger, C. Mazille), Hermes Science Publications, Lavoisier, Paris, 2002, pp. 353–368.
2. P.R. Roberge, Oxygen in seawater, in: *Handbook of Corrosion*, McGraw-Hill, 2000, 1140 pp.
3. J.B. Memet, La corrosion marine des structures métalliques portuaires: étude des mécanismes d'amorçage et de croissance des produits de corrosion, PhD, University of La Rochelle, 2000.
4. J. Guezennec, La biocorrosion, *Matériaux et Techniques Spécial Corrosion*, December 1990, pp. 3–8.
5. J. Guezennec, N.J.E. Dowling, J. Bullen, D.C. White, Relationship between bacterial colonization and cathodic current density associated with mild steel surfaces, *Biofouling*, Vol. 8, 1994, pp. 133–146.
6. N.J.E. Dowling, S.A. Brooks, T.J. Phelps, D.C. White, Synergistic corrosion of line pipe steel by obligately anaerobic bacteria, in: *Microbially Influenced Corrosion and Biodeterioration* (ed. N.J. Dowling, M.W. Mittleman, J.C. Danko), NACE, 1996, pp. 3.1–3.7.
7. D. Thierry, W. Sand, Microbially influenced corrosion, in: *Corrosion Mechanisms in Theory and Practice* (ed. P. Marcus, J. Oudar), Marcel Dekker, 1995, pp. 457–499.

8. D. Thierry, D. Feron, Corrosion bactérienne des métaux, in: *Meeting 'Protection des Métaux'*, Ecole Franco-Vietnamienne de Recherche, Do Son, November 1999.
9. N.A. North, I.D. MacLeod, Corrosion of metal, in: *Conservation of Marine Archaeological Objects*, Butterworths, 1987, pp. 68–98.
10. L. Simon, Réactivité des espèces du fer en milieu aqueux contenant des anions de la famille du soufre: sulfite, sulfate, thiosulfate, séléniate, thesis, Université de Nancy, 1998.
11. A.A. Olowe, P. Bauer, J.M.R. Genin, J. Guezennec, Mössbauer evidence of the existence of green rust 2 transient compound from bacterial corrosion in marine sediments, *Corrosion NACE*, Vol. 45, No. 3, 1989, pp. 229–235.
12. J.M.R. Genin, A.A. Olowe, N.D. Benbouzid-Rollet, D. Prieur, M. Confente, B. Reziac, The simultaneous presence of green rust 2 and sulfate reducing bacteria in the corrosion of steel sheet piles in a harbour area, *Hyperfine Interactions*, 69, 1991, pp. 875–878.
13. A.A. Olowe, J.M.R. Genin, J. Guezennec, Study of green rust two compound from bacterial corrosion in marine sediments by mössbauer effect; case of a wrecked ship, *Proceedings of the 11th International Corrosion Congress*, Florence, 1990, pp. 1.533–1.540.
14. NACE, *Corrosion Basics: an Introduction*, NACE Publications, Houston, TX, 1984.
15. P. Blanchard, Etude de la corrosion marine d'aciers faiblement alliés par mesure de l'impédance électrochimique, thesis, Université de Bretagne Occidentale, 1984.
16. T. Ohtsuka, H. Yamada, Effect of ferrous ion in solution on the formation of anodic oxide film on iron, *Corrosion Science*, Vol. 40, No. 7, 1998, pp. 1131–1138.
17. N. Le Bozec, Réduction de l'oxygène sur les aciers inoxydables en eau de mer naturelle. Influence du biofilm sur les processus de corrosion, Thesis, Université de Bretagne Occidentale, 2000.
18. J.B. Memet, N. Huet, M. Rakotonirainy, B. Lavedrine, Q.K. Tran, G. Chaumat, J. Duchene, Développement d'un protocole de traitement de conservation adapté aux objets archéologiques composites fer/bois gorgés d'eau, Programme National de Recherche, final report, 75 pp, October 2004.
19. C. Volfovski, Nettoyage et stabilisation de la corrosion par électrolyse, in: *La Conservation des Métaux*, CNRS Editions, 2001.
20. J.B. Memet, R. Sabot, C. Compère, C. Deslouis, Study of the formation and growth of corrosion products on low carbon steel in natural seawater, in: *Proceedings of EUROCORR'99*, 30 August–2 September 1999, Aachen, Germany, p. 208.
21. J.B. Memet, R. Sabot, C. Deslouis, C. Compère, Transport properties through oxide layers formed in marine environment, in: *Proceedings, Vol. II, EUROMAT'98*, 22–24 July 1998, Lisbon.
22. D. Neff, Apport des analogues archéologiques à l'estimation des vitesses moyennes et à l'étude des mécanismes de corrosion à très long terme des aciers non alliés dans les sols, PhD, Université Technologique de Compiègne, 2003.
23. P. Refait, J.B. Memet, C. Bon, R. Sabot, J.-M. R. Genin, Formation of Fe(II)–Fe(III) hydroxysulphate green rust during marine corrosion of steel, *Corrosion Science*, Vol. 45, 2003, pp. 833–845.
24. L. Robbiola, J.M. Blengino, C. Fiaud, Morphology and mechanisms of formation of natural patinas on archaeological Cu–Sn alloys, *Corrosion Science*, Vol. 40, No. 12, 1998, pp. 2083–2111.
25. F. Dabosi, Passivité et films passifs, in: *Corrosion des Métaux et Alliages, Mécanismes*

- et Phénomènes*, (ed. G. Beranger, C. Mazille), Hermes Science Publications, Lavoisier, Paris, 2002, pp. 161–198.
26. S. Turgoose, The corrosion of lead and tin: before and after excavation, in: *Lead and Tin: Studies in Conservation and Technology*, (ed. C.E. Miles, S.C. Pollard), UKIC, Occasional papers No. 3, London, 1985, pp. 15–26.
 27. I.D. MacLeod, R. Wozniak, Corrosion and conservation of tin and pewter from seawater, in: *Metals '95, Proceedings of the International Conference on Metals Conservation*, James & James, 1997, pp. 118–123.
 28. S. Dunkle, The mineralogy of pewter corrosion, in: *Preprints of the 6th Annual Virginia Tech Geological Sciences Student Research Symposium*, paper No. 7, 2001.

Contribution of local and structural characterisation for studies of the corrosion mechanisms related to the presence of chlorine on archaeological ferrous artefacts

S. RÉG UER and P. DILLMANN, Commissariat à l'Energie Atomique, France and F. MIRAMBET, Laboratoire de Restauration des Monuments Historiques, France and J. SUSINI, European Synchrotron Radiation Facility, France

10.1 Introduction

One of the main problems in conservation of iron artefacts after excavation is linked to the fact that some corrosion products are very reactive and that any environmental variations can disturb the corrosion layers formed on the object. Environmental changes are most pronounced when artefacts are excavated and then exposed to the atmosphere. Thus, a complete understanding of the corrosion of archaeological iron requires consideration of both the modifications that occur while the object is buried in soil and how these changes affect corrosion after excavation. During these processes, the exact role of chloride and the structure of corrosion products containing chlorine is still under discussion as shown by a recent publication [1].

Selwyn *et al.* [2] considered two stages in the corrosion processes of archaeological artefacts involving chlorides, which show the importance of environmental effects including the presence and concentration of various anions. The first consists of an accumulation of chloride in the corrosion products. These ions have high mobility and can migrate to buried iron from the surrounding soil and become trapped in crevices or pores of the corrosion products. According to Turgoose [3] the pores and cracks are then filled with an acidic iron chloride solution. The second part of the process concerns iron corrosion in air after excavation. Askey *et al.* [4] developed a model of the chloride corrosion cycle in which Cl^- ions play a direct role in the corrosion process. During this corrosion cycle, the formation of oxy-hydroxides (α -, β - or γ - FeOOH) can damage the corroded iron object by causing stresses, since the volume of these compounds is much higher than those of the previous corrosion products. To avoid this corrosion process occurring after excavation, conservators have used various treatments to remove chlorides from artefacts [3, 5, 6]. Nevertheless, the identification and optimisation of the parameters controlling the desalination process, to limit the immersion time and avoid

damage during the treatment, is an important challenge. The difficulty is due mainly to poor knowledge of the Cl-containing phases and their thermodynamic stability. Specifically, the release of Cl^- anions of the chlorinated phases found in the corrosion layers of the buried objects after excavation has to be understood.

The oxy-hydroxide akaganeite ($\beta\text{-FeOOH}$) is often identified as a corrosion product of iron in chlorine-containing environments, such as marine environments. The local high concentration of chloride combined with a low pH effectively favours the formation of akaganeite. This phase is known to form continuously after excavation even in the controlled atmosphere of a museum [3]. At the position of fractures and often located at the metal/oxide interface, some studies report the presence of an orange powder on several artefacts, which has been identified as akaganeite [2, 3, 7]. The crystal structure of akaganeite was first determined by Mackay [8] who showed that it crystallises in the tetragonal cell related to the hollandite type. In more recent work, Post and Buchwald [9] showed that the $\beta\text{-FeOOH}$ structure adopts a monoclinic symmetry ($I2/m$). It can be described as being built from an edge and corner sharing $\text{Fe}(\text{O},\text{OH})_6$ octahedral forming a one-dimensional channel. It is often assumed that tunnels, which are parallel to the c axis of the structure, can be occupied by chloride ions and water molecules. The role of halogen ions in crystallisation of akaganeite has not yet been completely elucidated. These large anions seem to induce stability of the crystal structure. However, the Cl localisation in the structure is not well determined.

The first chemical study of $\beta\text{-FeOOH}$ was performed by Weiser and Milligan in 1935 who established the formula and showed that the compound always contains chlorine, a chemical element apparently necessary for the structure stabilisation. When first precipitated, the chlorine content of akaganeite might be as high as 6–8%, but with prolonged washing it can be reduced to any desired value. For example, Keller and co-workers [10] indicate that this amount decreases from 6.5 to 3%. Rezel and Genin [11] proposed that OH^- ions can substitute for Cl^- during this repeated washing. Nevertheless, other authors assume that chlorine can be present only in the channels of the ‘hollandite-type’ structure [12]. An important part of the chlorine in akaganeite could be adsorbed on the large surface area of the $\beta\text{-FeOOH}$ akaganeite particles [1].

Thus, because of possible release of Cl^- ions the presence of this phase accelerates the corrosion processes of metallic iron artefacts. Some authors have reported that, after a long time, akaganeite lost all of the Cl^- ions and transformed into goethite. Nevertheless, none of these findings has been clearly evidenced in archaeological artefacts to date.

Ferric oxychloride (FeOCl), often found in or as corrosion products originating from marine environments, has to be taken into account. Argo [13] and North and Pearson [6] proved that this phase could be a precursor

of β -FeOOH akaganeite, because of its thermodynamic instability and capacity to release Cl^- anions. Despite its frequent presence in marine corrosion, FeOCl was apparently not mentioned in iron corrosion products of objects buried in soil. In addition, it should be noted that another compound in corrosion products, tetrahydrate ferrous hydroxychloride ($\text{FeCl}_2 \cdot 4\text{H}_2\text{O}$), which rapidly crystallises as a spherical shell, could be a precursor of akaganeite when oxidised [14].

In the particular case of low oxygen levels in the environment, relatively unstable iron(II) compounds such as $\text{Fe}(\text{OH})_2$ and the ferrous hydroxychloride β - $\text{Fe}_2(\text{OH})_3\text{Cl}$ may precipitate. Only a few works refer to the latter compound. However, Oswald and Fetknecht [15] established that the crystal structure of this hydroxychloride is hexagonal–rhombohedral, isomorphic with $\text{Co}_2(\text{OH})_3\text{Cl}$ and paratacamite $\text{Cu}_2(\text{OH})_3\text{Cl}$. Refait and Genin [16] described several oxidation mechanisms in specific conditions as values of $[\text{Cl}^-]/[\text{OH}^-] > 1$ in solutions containing large amounts of chloride (around $1\text{--}1.5 \text{ mol.l}^{-1}$). As shown first by Keller [10] and Mackay *et al.* [12] and confirmed by Misawa *et al.* [17], the akaganeite form could be obtained by the dry oxidation of this ferrous hydroxychloride, β - $\text{Fe}_2(\text{OH})_3\text{Cl}$. This mechanism implies a high chloride concentration ($2\text{--}3 \text{ mol.l}^{-1}$) and also acidic conditions, with pH values between 4 and 6. These specific conditions could be found in confined media where Cl^- ions can accumulate, such as at the interface between metal and iron oxides and fractures. Despite the frequent presence of β -FeOOH akaganeite, the possible precursor ferrous hydroxychloride β - $\text{Fe}_2(\text{OH})_3\text{Cl}$, was, to our knowledge never identified in the iron corrosion products of iron archaeological artefacts buried in soil.

Considering this short review, it appears that, despite the numerous studies on Cl-containing phases, no precise information is available on these phases and their location in the corrosion products. Moreover, in most cases, corrosion studies on Cl-containing phases formed on iron archaeological artefacts were performed using only macroscopic investigation methods. The aim of the analytical methodology presented here is to contribute to the high-resolution characterisation and location of these phases in the corrosion products. Indeed, such an understanding of the nature and distribution of corrosion products must precede any comprehensive description of the iron corrosion mechanism in soil. It is fundamental to have a good understanding of the manner in which such species as the chloride ions participate in the corrosion process.

10.2 Experimental corpus of archaeological artefacts

The historical samples available for the study represent a corpus of about 20 archaeological artefacts, buried in soil during several centuries, comprising nails or other pieces of metal. This corpus was collected from four French excavation sites, which were chosen because of their dating and soil

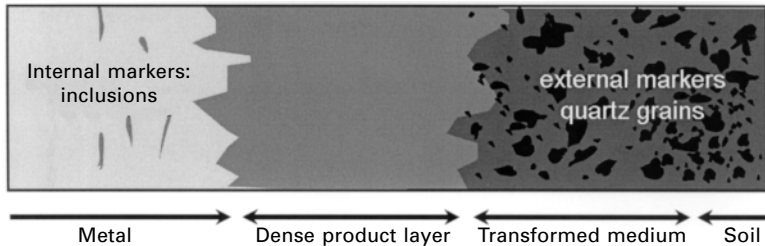
Table 10.1 Presentation of the archaeological sites: corpus of ferrous archaeological artefacts and soil characteristics

| Archaeological site and dating | Excavation date | Number and type of studied artefacts | Soil characteristics* | |
|---|-----------------|--------------------------------------|-----------------------|--|
| | | | Texture | PH |
| Avrilly, Eure et Loire France Artisanal zone, 15th century AD | May 2000 | Two nails and a piece of metal | Silty | 7.2 |
| Cabaret, Aude, France Forge, 12–13th century AD | August 2001 | Two nails and an iron plate | Sandy | 8.3–8.5 |
| Montbaron, Indre et Loire, France Seignory, 12–13th century AD | August 2000 | Two iron tools | Clayey-silty | 8–8.5 |
| Glinet, Seine-maritime, France Forge, 16th century AD | July 2003 | Eight iron plates and nails | Clayey-sandy | 7–7.3 4 < [Cl ⁻] < 14 ppm 1 < [Fe ²⁺] < 18 ppm |

*Measures obtained from Refs. [21] and [31]

characteristics (Table 10.1). Soil and water analyses were performed directly on the archaeological site at time of excavation. The pH values are noted for each site. For Glinet, P_{CO_2} was also measured. The amounts of Cl⁻ and Fe²⁺ in water sampled on the site were obtained by laboratory investigation, using ionic chromatography and ICP-MS analyses. The Cl content in the water of the soil was relatively low (4–14 ppm) compared to the published values [18].

Each specimen included the adhering soil in order to conserve the close environment. They were dried to withdraw the non-combined water from the soil and mounted in epoxy resin to ensure a good resistance between the soil and the corrosion products. Artefacts were then cut to obtain cross-sections, which were ground and polished with SiC papers. Both of the last stages were performed using kerdane or ethanol lubricant medium to avoid any new corrosion process. Cross-sections were used to obtain a local high-resolution characterisation of the corrosion products with all the techniques described below, except micro X-Ray Diffraction (μXRD). Concerning this technique, films thinner than 50 μm were prepared on transverse sections for experiments performed in transmission mode [19]. In soil, the corrosion process leads to



10.1 Schematic description of the corrosion system on an archaeological iron artefact buried in soil [20].

products (iron oxides and oxyhydroxides) distributed following a layout already described [20] (Fig. 10.1). The investigations realised in this study concern mainly the zone comprising relatively dense and homogeneous scales directly in contact with the metal and called the Dense Product Layer (DPL). This term will be used in the following to designate this specific part of the corrosion products.

10.3 Methodology: cross-section characterisation

This section presents the specific methodology adapted to the study of archaeological analogues. The main interest was the phase identification and spatial distribution determination of these phases and related oxidation states. Thus, we describe here particularly the different investigation techniques allowing high-resolution studies on the cross-sections: local determination of the morphology, composition and structure of all the corrosion products.

Firstly, the corrosion products were observed to locate possible heterogeneity. Thus, optical microscopy was used to observe the morphology and to measure the thickness of all the layers. The detailed description of this observation methodology is published elsewhere [21]. Then, composition analyses were performed by Energy Dispersive Spectrometry (EDS) coupled to a Scanning Electron Microscope (SEM), under an accelerating voltage of 15 keV. The Si(Li) detector used for such analyses is equipped with a thin beryllium window allowing good accuracy in detecting and quantifying oxygen (about 2% relative error on iron oxide standards). In addition, Electron Probe Micro Analyses (EPMA) were performed with a $2 \times 2 \mu\text{m}^2$ beam accelerated under 15 kV and 40 nA, using the SX100 microprobe from CAMECA at the Laboratoire CAMPARIS, Université Pierre et Marie Curie, Paris VI. The WDS (Wavelength Dispersive Spectroscopy) system allows one to obtain an absolute composition analysis, with detection limit about 100 ppm on an iron oxide matrix. Using these techniques, the chlorinated phases were localised in the corrosion layers and their chloride content precisely evaluated.

The size of some chlorinated phases ranges from a few micrometres to

several tenths of micrometres, making it necessary to use a micro beam. Thus, to unambiguously identify these corrosion products, some high-resolution techniques such as μ -Raman spectroscopy, and X-ray synchrotron radiation micro beam techniques such as micro X-Ray Diffraction (μ XRD) and micro X-Ray Absorption Near Edge Structure experiments (μ XANES), were used to obtain structural micro-scale information.

All synchrotron μ XRD investigations reported here were performed at the Laboratoire pour l'Utilisation du Rayonnement Electromagnetique (LURE), on the D15 beamline [22]. The X-ray beam delivered by the DCI ring is focused and monochromatised by a wide bandpass monochromator: a carbon/tungsten Bragg Fresnel Multilayer Lens (BFML). For the present experiment, photons centred around 14 keV were selected and focused down to a $20 \times 20 \mu\text{m}^2$ beam spot on the sample. The diffraction patterns $I = f(\theta)$ were obtained by circular integration of the pattern collected with a two-dimensional detector (image plate FUJI) set downstream from the sample, using the FIT2D software [23], and indexed to the JCPDF database with Diffrac+ software. Nevertheless, the D15 beamline set-up presents a specific limitation: the analyses are made with a rather large beam compared to the phase thickness of about $10 \times 10 \times 10 \mu\text{m}^3$ or less.

Complementary μ -Raman spectroscopy analyses were carried out, allowing an easier sample preparation and a sharper description of phase distribution (beam spot about $3 \mu\text{m}$ with the $100 \times$ Leitz objective of an Olympus Microscope). Micro-Raman spectroscopy measurements were performed at the Laboratoire de Dynamique Interaction et Réactivité (LADIR) with a Notch-based spectrometer LabRam Infinity (Jobin Yvon-Horiba) getting a spectral resolution of about 2 cm^{-1} for spectra recorded by Peltier-based cooling CCD, using the radiation at 532 nm of a frequency-doubled Nd:YAG laser [24]. Various reference spectra are available in the literature dealing with corrosion or mineralogy concerning iron oxides and oxyhydroxides. But as no certified database of Raman spectra exists, we also acquired with the present experimental set-up some reference spectra collected on commercial products or laboratory-synthesised samples. Thus, goethite and akaganeite powders were obtained following Schwertmann and Cornell [25] and were then verified by X-ray diffraction.

In order to check previous studies and obtain further information about the geometry of the iron sites (chemical speciation and oxidation state) in the phases constituting the iron corrosion products, the selected samples were also examined using the X-ray microscopy beamline ID 21 at ESRF [26]. The X-ray beam was focused down to a microprobe of $1 \times 1 \mu\text{m}^2$ by means of a Fresnel zone plate. Two Si $\langle 111 \rangle$ crystals provided a monochromatic beam ($\Delta E/E = 10^{-4}$). The fluorescence signal was analysed using a high energy resolution germanium solid-state detector (EDS). First, distribution maps of both major elements (Fe and Cl) were recorded in fluorescence

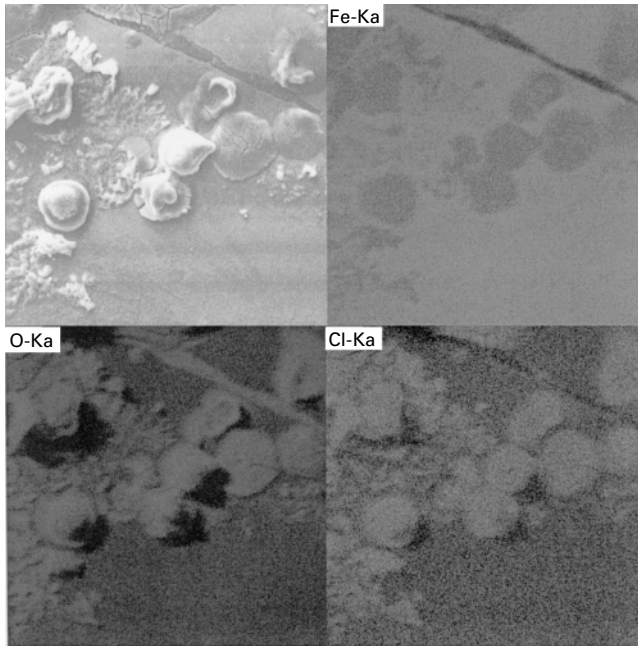
yield ($K\alpha$ X-ray lines) to precisely define the region of interest. Then, μ XANES spectra were collected in fluorescence yield at the Fe K edge by scanning the exciting energy from 7050 eV to 7350 eV. Each spectrum was normalised following the standard two-step procedure as used in the Winxas software package: background subtraction (by fitting the spectral region before the pre-edge – from 7050 to 7090 eV – using a polynomial function) and spectrum normalisation for atomic absorption (based on the average absorption coefficient of the spectral region from 7200 to 7350 eV). The energy calibration was done by defining the first derivative peak to be 7111.08 eV, which is the tabulated position of the Fe K edge.

The combination of composition analyses with the fine techniques such as μ XRD, μ XANES and μ Raman is the method best suited for analysing the iron corrosion products. As explained below, it unambiguously leads phase identification at the microscopic scale.

10.4 Results

The analysis of the DPL has revealed some new and interesting information about iron corrosion related to the presence of chlorinated phases. The first important observation deals with the appearance of specific corrosion products just after sample polishing. Indeed, even using ethanol or kerdane solution for lubrication, several spherical shells appeared on the polished surface (Fig. 10.2). As one can see on the EDS X-ray map, which shows the distribution of the main elements (Fe, O, Cl), these structures contain a significant amount of chlorine. It was even possible to observe the growth of these spherical shells under the optical microscope. It seems that this phenomenon highlights the presence of chloride ions dissolved in the water in pores and cracks at the metal/oxide interface as described in the literature [2, 3]. When this phenomenon occurred, it was necessary to re-polish the sample carefully until these structures stopped growing.

The X-ray map obtained by MEB-EDS and presented in Fig. 10.3 shows the distribution of Fe, O, Si and Cl in the DPL of the CAB5 and GL0363 samples (nails from the Cabaret and Glinet archaeological sites, respectively). As one can see, the Cl-containing phases are present mainly at the metal/oxide interface but never as a continuous layer all around the sample. The composition analyses performed in these specific zones by EPMA give the concentration profile from the metal/oxide interface in the DPL of the cross-section for the specific elements O, Si, Cl and Fe. Chlorine levels vary considerably, both from one sample to another and even in the same artefact. For example, on the CAB5 profile (Fig. 10.4(a)), two zones with different Cl content can be identified. The first shows 5–8 mass% Cl, while the other has a more important amount, about 15–20 mass% Cl. These two zones containing different amounts of chloride were present as alternate layers, while for

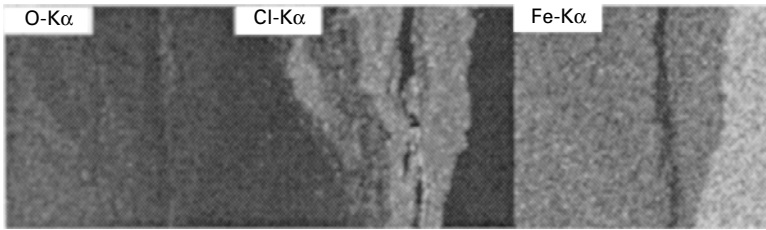


10.2 MEB-EDS X-ray map of specific corrosion products: spherical shells at the M/DPL interface.

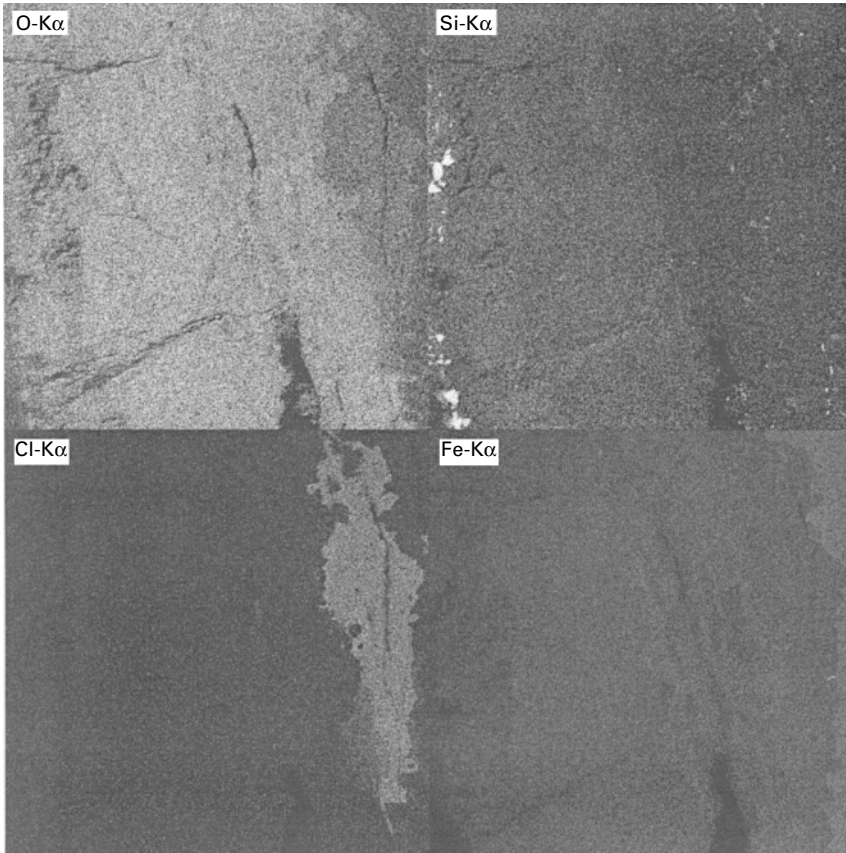
other samples the two chloride zones formed spots in DPL. However, for some other samples, only one of the two Cl contents could be detected. For example, the profile made on the GL0363 sample (Fig. 10.4(b)) shows in the DPL only one zone containing Cl content around 20%. The Cl content variation in the corrosion products is summarised in Table 10.2.

For each sample, the thickness of the chlorinated layers of all the samples analysed was measured (Table 10.2), showing that these layers were relatively thin compared to the total thickness of the DPL. In fact, the maximum thickness observed on the chloride phases was about 28% of the total thickness of the corrosion products. Thus, it could be difficult to detect the chlorinated phases by classical macroscopic XRD analyses [27] of rust powder scraped from the sample. For this reason, analyses were carried out with a micro beam on transverse sections, in order to locate and identify as well as possible, and at the micrometric scale, all the phases constituting the corrosion products.

The μ XRD analyses were carried out exactly in the two zones containing Cl and located by MEB-EDS and/or EPMA analyses. According to these experiments, the presence of the well-known β iron oxyhydroxide β -FeOOH, akaganeite, was confirmed. As one can see on Fig. 10.5, the diagram is in good agreement with the JCPDF files, numbers 80-1770 and 13-0157, relative to the respective preliminary works on akaganeite [9], [8, 12]. This phase

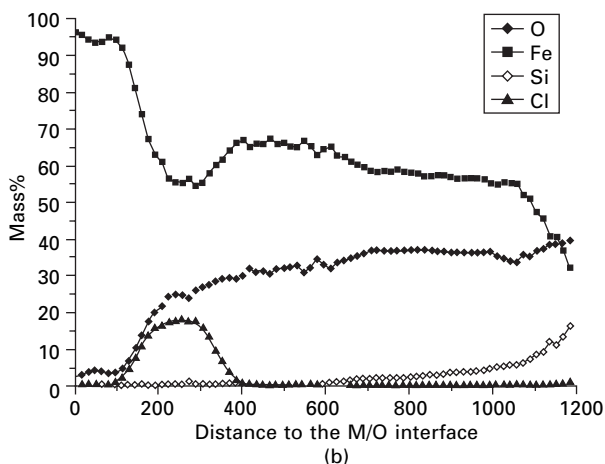
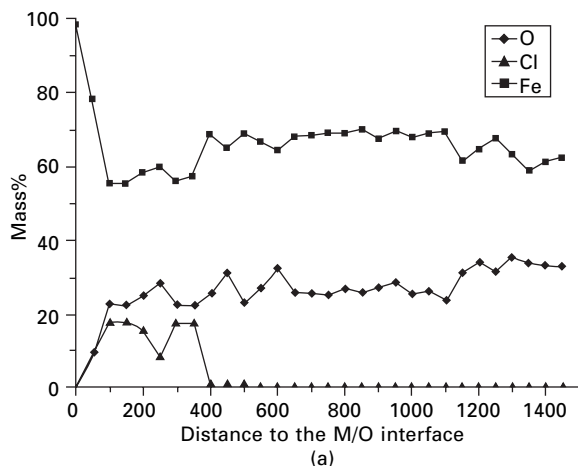


(a)



(b)

10.3 EDS X-ray map of corrosion products obtained by SEM-EDS: (a) CAB5 sample, K α lines of O, Cl and Fe; (b) GL 03 63 sample, K α lines of Fe, O, Si and Cl.



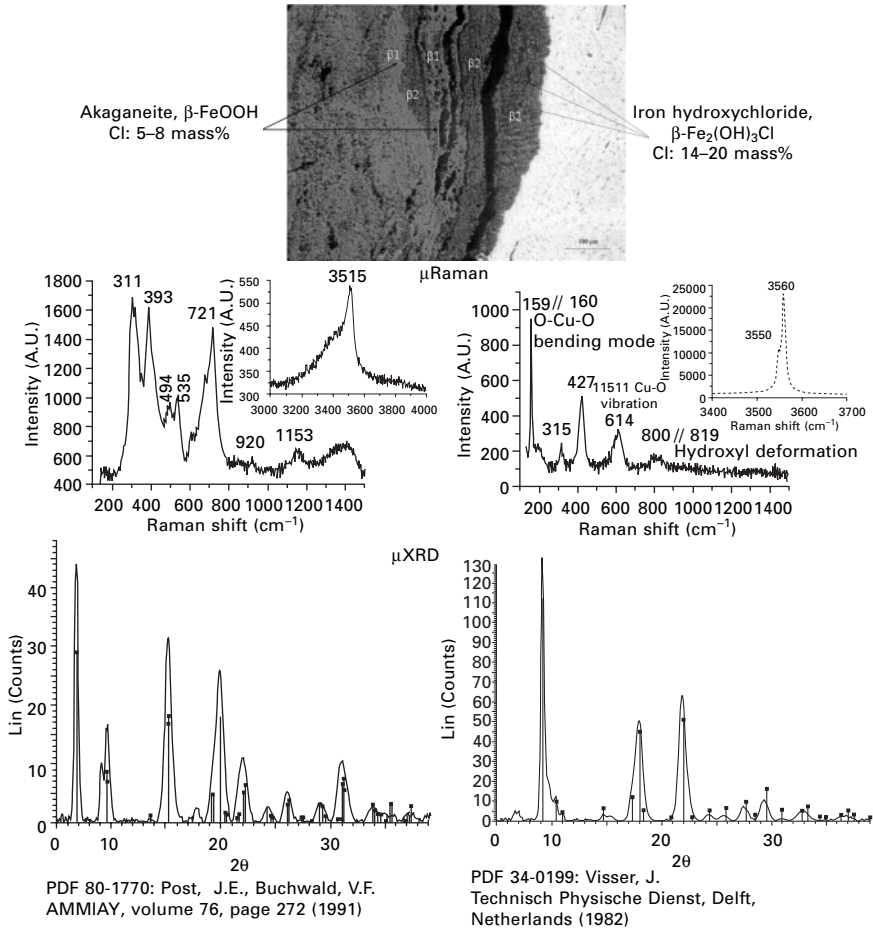
10.4 Average elementary distribution profiles obtained by SEM-EDS: (a) O, Fe and Cl in the corrosion products of the CAB5 sample; (b) O, Fe, Si and Cl in the corrosion products of the GL 03 63 sample.

was only identified in zones with a Cl content of about 5–10 mass%. In regions with a higher Cl content, another phase was found showing a μ XRD pattern in good agreement with hydroxychloride, β - $\text{Fe}_2(\text{OH})_3\text{Cl}$. The spectrum can be compared to the only existing reference known in the 2001 JCPDF database, number 34-0199 [28].

However, such analyses were made with a rather large beam ($20 \times 20 \mu\text{m}^2$), and for some samples the layers constituting the chlorinated system were thinner than the beam width. Thus, a smaller beam fit is better in order to

Table 10.2 Composition and thickness of the corrosion products

| Archaeological site | Sample reference | Zone 1 | | Zone 2 | | Total thickness of the chlorinated phases (μm) | Total thickness of the DPL (μm) |
|---------------------|------------------|------------------------|---|------------------------|--|---|--|
| | | Composition Cl (mass%) | Thickness | Composition Cl (mass%) | Thickness | | |
| Avrilly | Avri 21 | 2–3 | 75 μm | – | – | 75 | 350 |
| | Avri 3 | 5 | 3 spots about 20 μm | 17 | 4 spots 20 μm and one layer 160 μm | 300 | – |
| Cabaret | CAB5 | 5–8 | 3 layers 35 μm size spots about 80 μm | 18 | 2 layers 40 μm size | 200 | 1500 |
| | CAB16 | 8 | 80 μm | 18 | 134 | 214 | 857 |
| Montbaron | MONT5 | 5 | 190 | 16 | spots about 50 μm size | 240 | 1136 |
| | MONT6 | 2–3 | 150 | 20 | 50 | 200 | 4000 |
| Glinet | GL 03 63 x | 5–10 | 300 | – | – | 300 | 1200 |
| | GL 03 63 y | 5 | 50 | 15–20 | 200 | 250 | 600 |
| | GL 03 66 | 10 | 100 | – | – | 100 | 2500 |
| | GL 03 72 x | 8 | 2 bands 200 μm | 19 | 2 bands 250 μm | 900 | 2900 |
| | GL 03 72 y | 4 | 60 | – | – | 60 | 750 |
| | GL 03 84 | – | – | 20 | 50 | 50 | 380 |
| | GL 03 86 | 4 | 380 | – | – | 380 | 3000 |
| | GL 03 88 | 8 | 100 | – | – | 100 | 2000 |



10.5 μXRD ($20 \times 20 \mu\text{m}^2$, $\lambda = 0.08857 \text{ nm}$) and μRaman $\varnothing 3 \mu\text{m}$, $\lambda = 532 \text{ nm}$, $P = 0.4 \text{ mW}$) spectra of chlorinated phases on CAB5 sample.

clearly separate the phases and confirm the previous characterisations. Micro Raman spectroscopy analyses were precisely carried out using a $3 \mu\text{m}$ diameter beam.

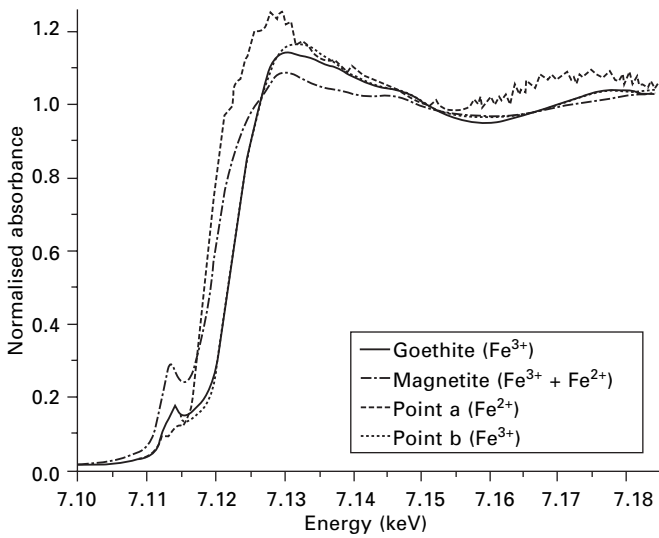
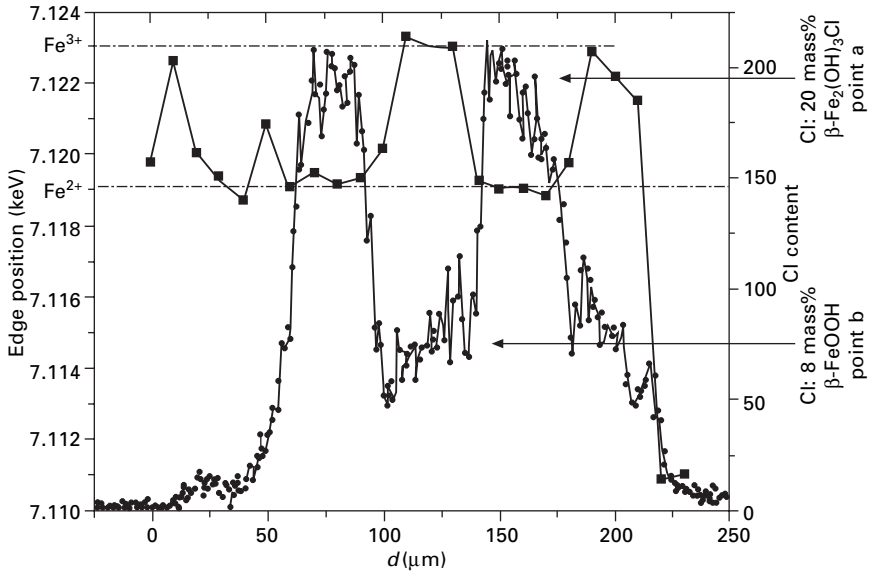
For oxides and oxyhydroxides found in iron corrosion products, the Raman spectra could be separated into two regions of interest. The first gathers the Fe–O–H bending vibration and Fe–O stretching vibration region from 200 to 1200 cm^{-1} . In this region, the first identified phase, corresponding to 5–10% Cl content, shows clearly five bands. The main ones are in good agreement with the akaganeite spectrum, as given in the literature [29] and as confirmed by a spectrum obtained on a reference powder synthesised in the laboratory.

The second phase, which contains more chlorine, showed a totally different and non-referenced spectrum. However, because of resemblance to the spectrum of the isomorphous copper chloride mineral atacamite $\text{Cu}_2(\text{OH})_3\text{Cl}$ already reported in the literature [30], it could be associated with the hydroxychloride $\text{Fe}_2(\text{OH})_3\text{Cl}$. Indeed, for this latter spectrum, particularly for the low wavenumber region, some peaks of the two spectra are relatively close to each other. For example, the most important band, which occurs at 160 cm^{-1} , can be compared to the second most intense band of atacamite observed at 150 cm^{-1} . This is assigned to the O–Cu–O bending mode. Moreover, the 427 cm^{-1} bands could correspond to the most important band of atacamite spectra, which occurs at 511 cm^{-1} . This is assigned to Cu–O stretching vibration. Between the two bands previously indicated, another analogy can be made: there is a Cu–Cl stretching vibration region. The peak, at 800 cm^{-1} , can be compared to the 819 cm^{-1} one, which is hydroxyl deformation. The second region corresponds to OH stretching vibrations. This type of line is observable from 3600 to 3000 cm^{-1} . Indeed, akaganeite presents a broad band at 3515 cm^{-1} while for the second phase there is a much more intense band with a double peak at 3550 and 3560 cm^{-1} , which certainly corresponds to a most hydrated phase.

These μRaman analyses, combined with the μXRD identification, allow conclusions to be made about the identification and location of the two phases: in addition to the presence of the well-known beta iron oxyhydroxide $\beta\text{-FeOOH}$ (akaganeite) in iron corrosion products, they highlight the presence of another important phase, the $\beta\text{-Fe}_2(\text{OH})_3\text{Cl}$ hydroxychloride.

Synchrotron-based μXANES investigations at the Fe K edge were conducted to determine the spatial variation of the predominant Fe oxidation state and corresponding crystallographic phases. Indeed, with this method, it is possible to distinguish different chemical shifts in the edge position, revealing the Fe oxidation state. In the present study, the following iron oxides and oxyhydroxides were used as reference compounds: $\alpha\text{-FeOOH}$ (goethite), $\beta\text{-FeOOH}$ (akaganeite), Fe_3O_4 (magnetite) and Fe_2O_3 (hematite). Because of the poor stability of laboratory-synthesised $\beta\text{-Fe}_2(\text{OH})_3\text{Cl}$ hydroxychloride, no reference compound of this phase was analysed. This will be performed in further studies with a specific set-up under a controlled atmosphere.

μXANES investigations were performed on the same region of interest on the same samples CAB5 and GL0363. For example, Fig. 10.6 shows the experimental results for the CAB5 sample. A fluorescence profile was first obtained on both the major elements Fe and Cl on a line across the DPL, and on the same line μXANES measurements were collected. Thus, it is possible to see the variation of the edge position, measured for each spectrum in correlation with the amount of chlorine distribution. Indeed, the edge position of the XANES spectrum is close with Fe(III) valence in the region with a low amount of Cl, as in akaganeite $\beta\text{-FeOOH}$, and shifted to the lower energy,



10.6 μ XANES experiments at the Fe K edge (7.112 keV). Correlation between the evolution of the chlorine concentration and the Fe^{2+} and Fe^{3+} distributions.

indicating Fe(II) valence and confirming the presence of $\beta\text{-Fe}_2(\text{OH})_3\text{Cl}$, in the region with a high amount of Cl.

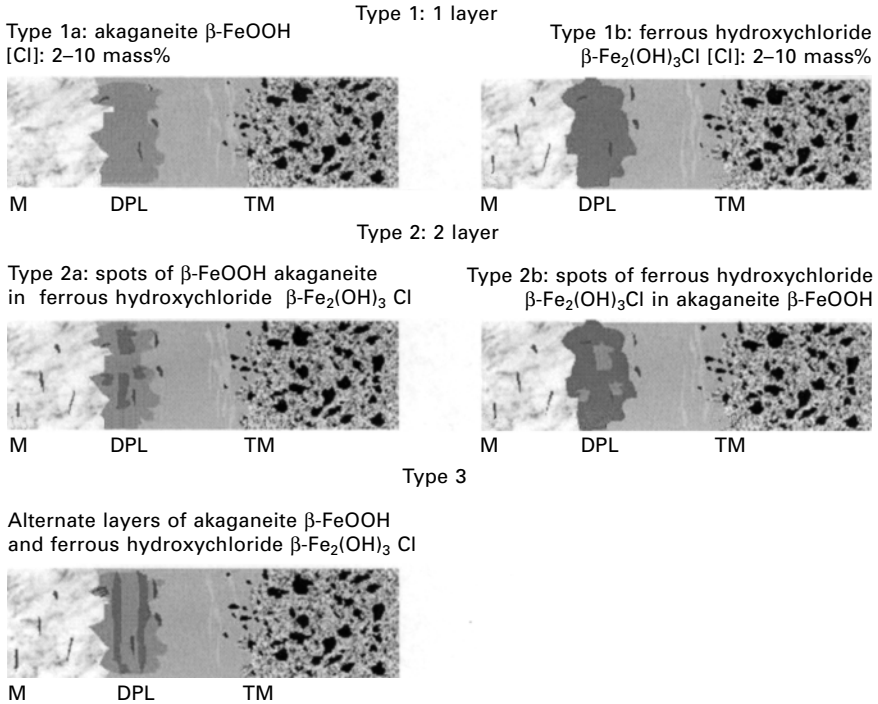
10.5 Discussion

First, it should be noted that Cl-containing phases can be formed in the corrosion products of various artefacts corroded in soil and coming from different archaeological sites. Moreover, even on sites where the Cl content is relatively low (4–14 ppm at Glinet) numerous Cl phases can form. This underlines the necessity to study the efficiency of the desalination process in the future.

According to the indications given by the compositional and structural analyses, particularly the combination of μRaman , μXRD and μXANES studies, it is possible to draw conclusions about two kinds of corrosion products that contain chlorine and can be found on archaeological artefacts. In addition to the well-known ferric oxyhydroxide akaganeite ($\beta\text{-FeOOH}$), we found a phase, not cited in previous studies on iron corrosion of archaeological artefacts, of ferrous hydroxychloride. Its chemical formula, $\beta\text{-Fe}_2(\text{OH})_3\text{Cl}$, is in agreement with the strong relative chlorine rate, about 20% found on artefacts. This phase is found surprisingly often, considering its thermodynamic instability, on the corrosion products of various samples analysed here. This result is particularly interesting because the $\beta\text{-Fe}_2(\text{OH})_3\text{Cl}$ phase has, to our knowledge, never before been identified in archaeological artefact corrosion products. On all observed artefacts, these chlorinated phases are located at the metal/oxide interface. This confirms observations made in previous studies.

Figure 10.7 and Table 10.3 sum up the structural characterisation of all the corrosion products identified on the analysed samples. The description corresponds to the successions of phases from the metal/oxide interface (M/O) to the transformed medium (TM), including the dense product layer (DPL). The various objects analysed could be classified in five different types of corrosion forms depending on the distribution of chlorinated phases. Sometimes, only a single layer was observable, which could be akaganeite ($\beta\text{-FeOOH}$) or ferrous hydroxychloride ($\beta\text{-Fe}_2(\text{OH})_3\text{Cl}$). At other times, the two phases could be distributed in alternate layers or strips composed of one phase intruding into the other: akaganeite into ferrous hydroxychloride and, conversely, spots of ferrous hydroxychloride into akaganeite.

The presence of a mix of phases in which iron has two valences, Fe(II) in $\beta\text{-Fe}_2(\text{OH})_3\text{Cl}$ and Fe(III) in $\beta\text{-FeOOH}$, contradicts the attempted observation based on the thermodynamic consideration, that is a succession of increasing valence state with increasing distance to the M/O interface linked to the increasing content of oxygen dissolved in the water of the pores of the corrosion products and coming from the environment. These observations



10.7 Schematic view of the distribution of the chlorinated phases in the DPL.

Table 10.3 Samples and corrosion types

| Archaeological site | Sample reference | Corrosion types |
|---------------------|------------------|-----------------|
| Avrilly | Avri 21 | 1a |
| | Avri 3 | 2a |
| Cabaret | CAB5 | 3 |
| | CAB16 | 2 |
| Montbaron | MONT5 | 2 |
| | MONT6 | 1b |
| Glinet | GL 03 63 x | 1b |
| | GL 03 63 y | 3 |
| | GL 03 66 | 2 |
| | GL 03 72 x | 3 |
| | GL 03 72 y | 1a |
| | GL 03 84 | 1a |
| | GL 03 86x | 1b |
| | GL 03 86y | 2 |
| GL 03 88 | 1a | |

have to be explained if the aim of precise comprehension of the relationships between all the corrosion products is to be achieved. The other part of the DPL was constituted mainly by goethite (α -FeOOH) and magnetite (Fe_3O_4) with a marbled aspect made of fine strips of one phase (magnetite) into the other (goethite). A formation mechanism has already been proposed [20]. These mechanisms involved the role of the cracks present in the DPL to explain the corrosion profile. It seems that these cracks should also be involved in explaining the alternation of Fe(+II) and Fe(+III) chlorinated phases. These points will be highlighted in future studies. However, there is a peculiar corrosion form on the objects from the archaeological site of Glinet, which show a DPL often composed of a thick layer of siderite in which a thin layer or spots of magnetite could be found. In this particular profile, the chlorinated phases are often in contact with siderite. The influence of the presence of carbonate on the stability of such phases will be investigated in the future. Moreover, previous studies [20, 31] have shown that siderite can only be stable in a more reducing environment. This kind of environment could also explain the presence of the β - $\text{Fe}_2(\text{OH})_3\text{Cl}$ phase. Last but not least, the fact that for the Glinet site only samples recently excavated contain the β - $\text{Fe}_2(\text{OH})_3\text{Cl}$ phase could be explained by an increase in oxygen content after long conservation times in the atmosphere for samples excavated earlier. This increase could have provoked the disappearance of the Fe(+II) phases (see below).

Previously, Refait and Genin [16] proved by laboratory investigations that the ferrous hydroxychloride β - $\text{Fe}_2(\text{OH})_3\text{Cl}$ may precipitate in low oxygen level conditions, i.e. in confined media where Cl can accumulate. This condition can occur when iron corrodes during burial in soil. Cl^- ions, which have a high mobility, can migrate and accumulate next to the metal, forming on the one hand concentrated Cl^- aqueous solutions in pores and cracks of the corrosion products; on the other hand, the low level of oxygen in the water of the DPL pores at the metal/oxide interface can lead to the formation of crystalline phases such as the ferrous hydroxychloride β - $\text{Fe}_2(\text{OH})_3\text{Cl}$. The oxidation of this phase may be increased by the appearance of cracks in the DPL that can play the role of diffusion shortcuts for oxygen dissolved in water and can lead to the formation of akaganeite. Such a mechanism could explain the simultaneous presence of the two phases in the DPL. Moreover, Misawa *et al.* [17] showed that the oxidation process of β - $\text{Fe}_2(\text{OH})_3\text{Cl}$ in aqueous solution gives rise before akaganeite to chlorine containing green rust 1 GR(Cl^-) compound. No trace of this phase was found in the DPL, certainly because of its instability. The following oxidation process of this compound depends essentially on the concentration of the dissolved species [16]. Particularly, the increase of the chloride content of the intermediate GR(Cl^-) compound favours the formation of akaganeite. Such a mechanism implies a high chloride concentration, at least 2 or 3 mol.l^{-1} [16]. However,

as noted in Table 10.1, the measured pH = 7 on the archaeological site is higher than the necessary acidic condition (pH values between 4 to 6). Nevertheless, this pH could change locally in the SPL and decrease at the metal/oxide interface, due to the presence of particular species.

10.6 Conclusion

The identification and location of the different phases constituting the corrosion products is a fundamental stage of any corrosion study. It is the only way to understand the long-term formation and evolution mechanism. The coupling of different techniques such as μ Raman and synchrotron-based techniques such as μ XRD and μ XANES offers great potential for investigating ancient material with a microprobe and a high resolution. In fact, it allows one to identify beyond doubt the different phases constituting the corrosion system at a microscopic scale and to propose detailed descriptions of this system. This is a necessary step before any mechanism is proposed. In the case of Cl-containing phases that appear on archaeological iron artefacts buried in soil even at low Cl levels in the water, in addition to the common oxyhydroxide containing chloride that is often mentioned in the literature (akaganeite), a ferrous hydroxychloride was also found in non-negligible amounts compared to the totality of the samples analysed. In order to set up more efficient desalination methods, the presence of these two phases in the corrosion products should be taken into account. The formation of akaganeite is a real problem because, as described above, the specific volume of these compounds is important and can cause cracks. However, to protect objects from degradation, the solution is not only to remove akaganeite but also to understand its formation in order to remove all the conditions leading to this phase. Thus, it is important to take into account also the presence of the ferrous hydroxychloride. Moreover, this unstable phase could be an important source of Cl ions after excavation of the artefact. Thus, its role at this stage, but also that of akaganeite, has to be explained in future work.

10.7 Acknowledgements

The authors are very grateful to the ID21 staff, and to P. Chevalier and E. Foy, for their assistance with the μ XANES experiments at ID21, ESRF, and with the μ XRD experiments at D15, LURE, respectively. Thanks are due to L. Bellot-Gurlet for assistance with μ Raman investigations. The authors would like also to thank the archaeologists for allowing them to work and sample the objects: M.E. Gardel (Cabaret), A. Querrien (Montbaron), B. Lecain (Avrilly) and D. Arribet-Derrouin (Glinet). This work was partly funded by the CNRS GDR CHIMART.

10.8 References

1. K. Stahl, K. Nielsen, J. Jiang, B. Lebech, J. C. Hanson, P. Norby and J. v. Lanshot, On the akaganeite crystal structure, phase transformations and possible role in post-excavational corrosion of iron artifacts. *Corrosion Science* (2003), 45: 2563–2575.
2. L. S. Selwyn, P. J. Sirois and V. Argyropoulos, The corrosion of excavated archaeological iron with details on weeping and akaganeite. *Studies in Conservation* (1999), 44: 217–232.
3. S. Turgoose, Post-excavation changes in iron antiquities. *Studies in Conservation* (1982), 27: 97–101.
4. A. Askey, S. B. Lyon, G. E. Thompson, J. B. Johnson, G. C. Wood, M. Cooke and P. Sage, The corrosion of iron and zinc by atmospheric hydrogen chloride. *Corrosion Science* (1997), 39: 539–553.
5. W. A. Oddy and M. J. Hughes, The stabilization of active bronze and iron antiquities by the use of sodium sesquicarbonate. *Studies in Conservation* (1970), 15: 183–189.
6. N. A. North and C. Pearson, Washing methods for chloride removal from marine iron artefacts. *Studies in Conservation* (1978), 23: 174–186.
7. F. Zucchi, G. Morigi and V. Bertolasi, Beta iron oxide hydroxide formation in localized active corrosion of iron artifacts. In *Corrosion and Metal Artifacts: a Dialogue between Conservators and Archaeologists and Corrosion Scientists* (1977), 479: 103–105.
8. A. L. Mackay, Beta-ferric oxyhydroxide. *Mineralogical Magazine* (1960), 32: 270–280.
9. J. E. Post and V. F. Buchwald, Crystal structure refinement of akaganeite. *American Mineralogist* (1991) 76: 272–277.
10. P. Keller, Vorkommen, Entstehung und Phasenumwandlung von beta-FeOOH in Rost. *Werkstoffe und Korrosion* (1969), 2: 102–108.
11. D. Rezel and J. M. R. Genin, The substitution of chloride ions to OH⁻ ions in the akaganeite beta ferric oxyhydroxide studied by Mössbauer effect. *Hyperfine Interactions* (1990), 57: 2067–2076.
12. A. L. Mackay, Beta-ferric oxyhydroxide, akaganeite. *Mineralogical Magazine*, (1962), 33: 270–280.
13. J. Argo, On the nature of ‘ferrous’ corrosion products on marine iron. *Studies in Conservation* (1981), 26: 42–44.
14. M. R. Gilberg and N. J. Seeley, The identity of compounds containing chloride ions in marine iron corrosion products: a critical review. *Studies in Conservation* (1981), 26: 50–56.
15. H. R. Oswald and W. Feitknecht, Über die Hydroxidhalogenide Me₂(OH)₃Cl, - Br, -J zweiwertiger Metalle (Me = Mg, Ni, Co, Cu, Fe, Mn). *Helvetica Chimica Acta* (1964), 47: 272–289.
16. P. Refait and J.-M. R. Genin, The mechanisms of oxidation of ferrous hydroxychloride β-Fe₂(OH)₃Cl in aqueous solution: the formation of akaganeite vs goethite. *Corrosion Science* (1997), 39(3): 539–553.
17. T. Misawa, K. Hashimoto and S. Shimodaira, The mechanism of formation of iron oxide and oxyhydroxides in aqueous solutions at room temperature. *Corrosion Science* (1974), 14: 131–149.
18. H. Mathiesen, D. Gregory, P. Jensen and B. Sørensen, Environmental monitoring at a waterlogged site with weapon sacrifices from the Danish Iron age. I: Methodology

- and results from undisturbed conditions. *Journal of Wetland Archaeology*, submitted.
19. P. Dillmann, D. Neff, F. Mazaudier, S. Hoerle, P. Chevallier and G. Béranger, Characterisation of iron archaeological analogues using micro diffraction under synchrotron radiation. Application to the study of long term corrosion behaviour of low alloy steels. *J. Phys. IV France* (2002) (12): 393–408.
 20. D. Neff, P. Dillmann, L. Bellot-Gurlet and G. Béranger, Corrosion of iron archaeological artefacts in soil: characterisation of the corrosion system. *Corrosion Science* (2005), 47: 515–535.
 21. D. Neff, Apport des analogues archéologiques à l'estimation des vitesses moyennes et à l'étude des mécanismes de corrosion à très long terme des aciers non alliés dans les sols. *Sciences Mécaniques pour l'Ingénieur* (2003), Université de Technologie de Compiègne: Compiègne, p. 360.
 22. P. Dillmann, P. Populus, P. Chevallier, P. Fluzin, G. Béranger and A. Firsov, Microdiffraction coupled with X ray fluorescence microprobe. Application in archaeometry. *Journal of Trace and Microprobe Techniques* (1997), 15(3): 251–262.
 23. A. P. Hammersley, *FIT2D Reference Manual*. ESRF International Report No. EXP/AH/93-02, 1993.
 24. D. Neff, S. Reguer, L. Bellot-Gurlet, P. Dillmann and R. Bertholon, Structural characterization of corrosion products on archaeological iron. An integrated analytical approach to establish corrosion forms. *Journal of Raman Spectrometry* (2004), 35 (Special Issue on the application of Raman spectroscopy in art and archaeology): 739–745.
 25. U. Schwertmann and R. M. Cornell, *Iron Oxides in the Laboratory*. (2000), Weinheim: Wiley-VCH, p. 137.
 26. J. Susini, M. Salomé, B. Fayard, R. Ortega and B. Kaulich, The scanning X-ray microprobe at the ESRF 'X ray microscopy' beamline. *Surface Review and Letters* (2002), 9(1): 203–211.
 27. A. Rinuy and F. Schweizer, Méthodes de conservation d'objets de fouilles en fer. Etude quantitative comparée de l'élimination des chlorures. *Studies in Conservation* (1981), 26: 29–41.
 28. J. Visser, *Technisch Physische Dienst*, Delft, Netherlands, 1982.
 29. S. J. Oh, D. C. Cook and H. E. Townsend, Characterization of iron oxides commonly formed as corrosion products on steel. *Hyperfine Interaction* (1998), 112: 59–65.
 30. R. L. Frost, W. Martens, J. T. Kloprogge and P. A. Williams, Raman spectroscopy of the basic copper chloride minerals atacamite and paratacamite: implications for the study of copper, brass and bronze objects of archeological significance. *Journal of Raman Spectroscopy* (2002), 33: 801–806.
 31. E. Vega, Altération des objets ferreux archéologiques sur le site de Glinet (Seine-maritime, France, XVIIe siècle). Caractérisation des produits de corrosion et étude des mécanismes (2004), Université de Technologie de Belfort Montbéliard: Belfort, p. 127.

A proposal to describe reactivated corrosion of archaeological iron objects

M. A. LOEPER - ATTIA, National Institute of
Heritage, France

11.1 Introduction

When an iron object is buried in soil, how corrosion then occurs depends on various criteria that are inherent to the soil environment and on the layer of oxide that was formed on the object when it was buried. After a certain period under soil, the object adapts to its direct environment and a dynamic balance is created. Before the object is excavated, it has reached a stable 'state' in the soil.

During excavation, the environmental parameters change. The equilibrium between the object and its environment is broken. Corrosion increases as soon as the above-mentioned parameters change significantly. Corrosion evolution can be set off after excavation or when a find is transferred to a new environment, for example when it is moved from one storage space to another one with different features. In the long run it can endanger the proper conservation of the object in a museum or in store. The main concern of conservation–restoration is to define how stable the composites and the corrosion structures are after the relic has been transferred to a new corrosive environment. In conservation–restoration this type of corrosion is often called active corrosion. This general term is used by conservators–restorers to describe different phenomena leading to rather varied corrosion facies. We know little about the reasons behind active corrosion and it can often lead in the long run to the destruction of the object, as shown in Fig. 11.1.

It is difficult to give a proper description of an object's state of conservation. There is a large gap between the methods used in corrosion studies and by conservators–restorers. The expressions used by these two branches describe corrosion phenomena in completely different terms. Before trying to improve conservation conditions for iron objects, we need to first provide a detailed description of the corrosion process in order to explain the observed phenomena. Everyone should share the same description methods aiming at a better understanding of the observed phenomena. The long-term objective should be to predict the way the object will change in the future



11.1 Iron weapon (Iron Age) totally corroded after restoration (IRRAP).

and open up possibilities for a diagnostic approach. Our study deals with this issue.

We can classify the terms used to describe this type of corrosion into three categories:

- terms referring to a certain period in the object's life: reactivated corrosion, post-excavation corrosion
- terms referring to a corrosion mechanism: cyclic corrosion, chlorination
- terms referring to the state of the object: stable/unstable object, passive/active corrosion.

11.2 Giving a name to this type of corrosion

Since the 1980s there has been a willingness in conservation–restoration to explain the encountered phenomena so that high-precision diagnosis can be achieved. This is one of the reasons why so many different expressions are used to describe this type of corrosion. More and more scientific terms are borrowed but they are often used differently in this field. Initially, the multitude of expressions shows how difficult it is to depict and explain the phenomenon. Use of the word *active* to name this type of corrosion does not mean that the speaker is not an expert in this field. The reason why this term is used so often is that for a conservator–restorer *active* is an expressive term. It is sufficiently concrete and is associated with the idea of change, of an ongoing phenomenon, which is one of the features of this type of corrosion.

We will not dwell upon the difficulties associated with most of these expressions, but rather suggest using the following terms:

- *reactivated corrosion* to refer to the process
- *stable/unstable* to refer to the object that is or is not subject to this kind of corrosion.

The term *reactivated* is commonly used in corrosion studies. Its use is not so problematic as that of the word *active* even if it has a similar etymology. In the field of metal corrosion, the word *active* should not be used to describe one single type of corrosion. Actually, every kind of corrosion is *active* by definition, because ‘the phenomenon of corrosion refers to how substances are attacked by chemical agents in their environment. Etymologically the word corrosion comes from *corrodere* (Latin), ‘to gnaw’. [1]. In addition, the term *reactivated* adds essential supplementary information concerning the archaeological find because it refers to a new factor that sets off corrosion again. Rather than talk of the object itself, then, it is thought of within a system comprised of ‘the object and its environment during or after excavation’. This kind of corrosion is described as the reaction of an object to a particular factor in the system and not as a theoretical capacity of the object to reach a more stable thermodynamic state. The same notion of dynamism is present in the terms *stable/unstable* that we can use to describe the object.

We can now define reactivated corrosion as follows. When an iron object is taken out of its environment (excavation, place of storage, etc.), it is influenced by new factors: variation in relative humidity, temperature, impact of oxygen, etc. This rapidly triggers a renewal of the corrosion process. This phenomenon occurs initially at the interface between the metal and the corrosion products such as anions, for example chloride. Corrosion then spreads to the surface of the object.

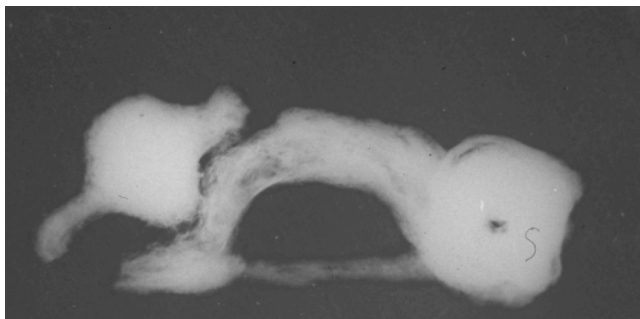
Conservation–restoration specialists treat the assessment and the description of such phenomena associated with such objects in diverse ways. Our aim is to provide a coherent description, taking into account the means and tools that the conservator–restorer has access to when he or she establishes a report on the state of an iron object. We have classified these characteristics so that we can set up a diagnosis taking into consideration that a diagnosis is based on a stable association of symptoms.

11.3 Forms of corrosion

11.3.1 Premonitory symptoms

Type of mineralisation

Mineralisation may be the preliminary sign of reactivated corrosion [2]. It is of utmost importance to measure it properly in order to assess the potential



11.2 Fibula (Iron Age; north of France) with heterogeneous metal core (IRRAP).

risk of reactivated corrosion of the object [3]. This can be determined using an X-ray image. If that is not possible, one can measure the object's density by its weight, which can help determine to what extent the find is mineralised. There are various types of mineralisation: undetectable, patchy, continuous in a part of or in the entire object; or, according to Watkinson's classification, object with a metal core, object without a metal core but retaining a core of corrosion products, object with a hollow core [4]. An example can be seen in Fig. 11.2. Watkinson assumes that a completely mineralised object contains less chloride than an object with a metal core, so the first one is less subject to renewed corrosion [2].

11.3.2 Post-corrosion symptoms

Once we have assessed the chances of finding metal in the object, several post-corrosion 'symptoms' are possible – cracking, breaking up, flaking, blistering – or specific corrosion products may be present, including orange-brown powdery composites and brown globules of liquid [5]. Some post-corrosion characteristics seem to be more typical than others. These are *major* symptoms. Nevertheless we cannot prove that any of these are pathognomonic¹ symptoms, which would mean that they are exclusively and specifically related to reactivated corrosion. Table 11.1 shows our suggested method of classification. Each of these characteristics will be discussed in the following paragraphs.

¹ Pathognomonic: typical of a disease and only of that disease (*Dictionnaire de Médecine*, Flammarion Médecine, Sciences, p. 594).

Table 11.1 Classification of characteristics related to reactivated corrosion

| Major symptoms | Minor symptoms* |
|---|-----------------|
| Pitting | |
| Cracking | Blistering |
| Flaking | Breaking up |
| Brown globules of liquid | |
| Powdery orange-brown corrosion products | |

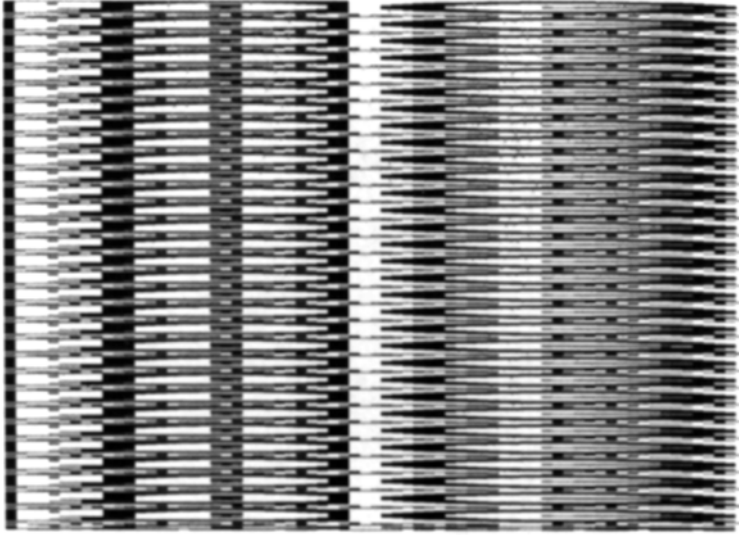
* Used in the sense 'more ambiguous' whereas major symptoms are more discriminatory

Physical changes

By physical changes we mean changes that are the source of mechanical modification of the object. The main types mentioned are pitting, cracking, flaking, blistering and breaking up. Changes of this type are almost always mentioned when we talk about reactivated corrosion, but unfortunately they are not described accurately enough. The first, quite inclusive description of these phenomena was given by Rosenberg: 'Antique iron objects undergo changes while they are exposed to atmospheric air. These are mainly chemical changes, but physical ones occur as well ... the combined corrosion layers that occur on the iron's surface represent a bigger volume than the metallic iron. On the one hand these combined layers will press on the metallic iron increasingly over time – and, on the other, they press on the hard and tight external layers composed of rust flakes of various dimensions that break off from the object' [6]. The growing internal pressure will bring about cracking, flaking or disintegration of the object [7].

Pitting

According to Shreir, pitting corrosion is the result of aggressive anionic action, mainly of chlorides [8]. Lamoureux described it as an extremely localised type of attack in which the anodic zone is limited to one point, where corrosion starts and results in deep penetration [9]. Diverse forms of pitting corrosion have been cited in the literature: narrow and profound, sub-surface, elliptic, wide and not too deep, horizontal, vertical (morphology of pitting types based on ASTM G46-76). Unfortunately this quite accurate description is not very well adapted to describing archaeological objects, because the surface layers of corrosion hide some parts of the object's metal surface. The lateral expansion of pitting leads progressively to more or less homogeneous corrosion, at least at the macroscopic level as in Fig. 11.3. Both general and local corrosion are observed [10, 11]. As a result of the geometric shape of pitting, chlorides are not easily retrieved, because they are present in large concentrations, up to 4 mol/l [12], and are deep down in



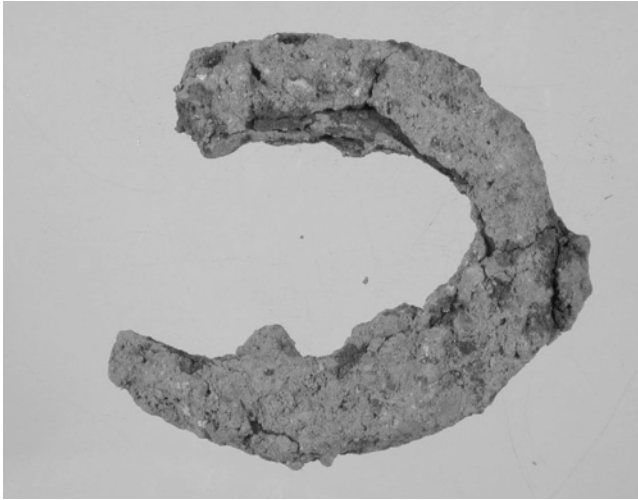
11.3 Pitting corrosion with flaking of the original surface of an iron tool (Iron Age, north of France).

the pit. Even if the term pitting is commonly used to describe this kind of alteration in chemistry, it is used only occasionally in conservation–restoration. The reason for this is clearly the great heterogeneity of an archaeological object’s surface after excavation, which makes pitting difficult to detect. However, it is the only term that is used in both fields to describe this type of corrosion. We suggest describing it as follows:

- Shape (wide or narrow)
- Quantity (affecting 0–5%, 5–25%, 25–50%, >50% of the object’s surface)
- Presence or absence of corrosion products in the inside.

Cracking

Cracking can be described as a ‘small crevice or a slight fissure’ (*Le Petit Larousse*, 1992, p. 442). It is a later stage of reactivated corrosion but seems to be triggered by the same initial phenomenon. The large volumes of corrosion products that are formed on the surface of pitting press the outside layers and lead to changes such as cracking or flaking [13] as in Fig. 11.4. Cracking is the corrosion form most often cited in the literature as well as when talking about the presence of specific corrosion products. Its distribution, the number of wedges and its spread have almost never been described or detailed in writing. We suggest describing it as follows:



11.4 Longitudinal and transverse cracking of the metal layer of a medieval horseshoe, alteration appearing just after excavation (IRRAP).

- Direction of spread (longitudinal, radial, transverse, circular²)
- Distribution (in networks³, isolated)
- Amount in proportion to the object's total surface⁴
- Localisation (on a part of or the entire surface)
- Distance between cracks (< or > 1 mm)
- Depth (whether the crack has reached the metal layer or not)
- Recent changes in the cracking⁵.

The distance between the crack's edges can be an additional means of learning whether the corrosion has just started or whether it is in its final phase. In the first case the distance between the crack's edges is not important, while in the latter the edges are far apart.

Flaking

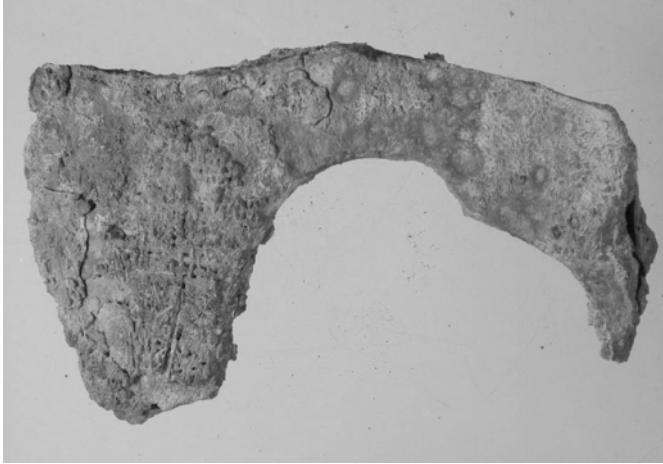
Flaking can be defined as the type of corrosion in which areas of corrosion products come off the surface of the object in small patches. Just like cracking, flaking is a later alteration (Fig. 11.5). We suggest describing it as follows:

² Phase before circular flaking.

³ Evenly distributed alteration on the object.

⁴ Measure whether the cracking is one, two or three times longer than the total length of the object.

⁵ Check whether the crack is filled with adherent corrosion products or non-adherent sediment.



11.5 Circular flaking on 5–25% on the surface (IRRAP).

- Origin (result of transverse or longitudinal network of cracking or of circular cracking)
- Quantity (affecting 0–5%, 5–25%, 25–50%, >50% of the object's surface)
- Presence or absence of corrosion products in the inside
- Depth (if loss of material).

Blistering

Blistering is characterised by a slight elevation in the object's surface layer. It can precede flaking. Nevertheless it is difficult to identify, especially on untreated archaeological finds that remain covered with outer layers of corrosion. Blistering can be due to sediments only or combined with a process of reactivated corrosion.

Breaking up

This is the final phase of the physical alterations cited above. It is often reported, especially concerning objects that have been dug up and then left unattended for a certain time (Fig. 11.6). In the case of such alteration it is essential to understand whether the object has broken up because of its inherent mechanical fragility or because it has attained the final phase of reactivated corrosion. According to Knight there are different possible reasons for an object to break up in storage. One of them is that some corrosion products can disintegrate, as a magnetite layer will due to dehydration, and this can then lead to flaking or cracking [14].



11.6 After excavation and before conservation treatment, breaking up of the extremity of a nail (Iron Age) due to corrosion (IRRAP).



11.7 Brown globules of liquid at the internal face of an iron tool (Iron Age) excavated in the north of France. The alteration appeared after restoration (IRRAP).

Chemical changes

This term refers to all the specific corrosion products that appear to be due to reactivated corrosion. We can divide them into two categories:

- Brown globules of liquid (Fig. 11.7)
- Powdery corrosion products of orange-brown or yellow-orange colour (Fig. 11.8).



11.8 Flaking in the circular flakings of an axe (Iron Age) excavated in central France. The alteration appeared after restoration (IRRAP).

We have to be very careful with the classification of these products because several of them can be responsible for corrosion at the same time. Chlorides are not the only compounds that threaten the integrity of the objects. Sulphates, for example, can also be blamed [15]. Goethite and lepidocrocite will cause physical damage: when they appear, they press on the outer layers of the object. However, they do not represent a potential danger for the object later on. They absorb only very few chlorides (0.2%) on the surface and they are very hard to remove. Akageneite can contain up to 17% chloride [13]. We suggest describing these products by the following characteristics:

- Consistency (powdery, in globules or liquid)
- Colour (brown, orange-brown)
- Location (in pits, flakes or wedges).

Brown globules of liquid

These changes are often described using the words 'sweating', 'bleeding' or 'globules of liquid' [12, 13, 15–17]. The pH of the globules is low and they contain a lot of Fe^{2+} and Cl^- . They have low relative humidity and dry up easily. Their surface crust is composed of a solid brown film (Fig. 11.9) which can be α -, β - or γ - FeOOH . Which of these three will appear depends on the level of Cl^- and the relative humidity [17].

Powdery orange-brown corrosion products

Powdery orange-brown corrosion products are iron oxide hydroxides. In fact, they are a mix of various iron oxide hydroxides at different oxidation



11.9 Flaking along the lines of cracks with powdery orange corrosion products.

levels [18, 19]. They can be seen in circular flakings (Fig. 11.8) or along cracks (Fig. 11.9).

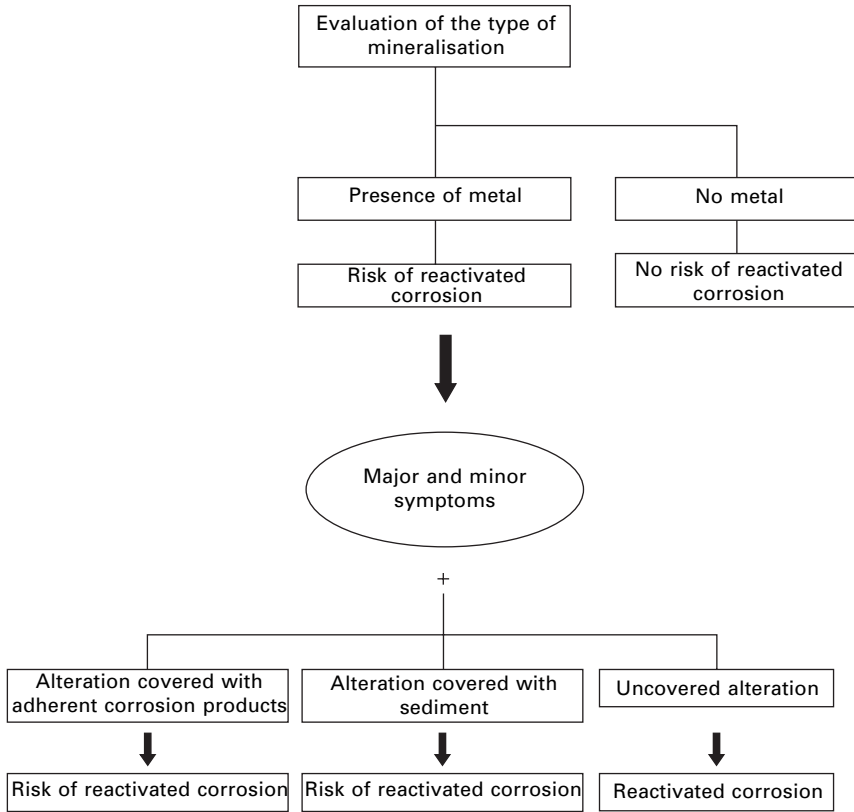
11.4 Diagnostics

Taking all the above elements into consideration, we suggest the following initial version of a diagnostic system which can be used to define the stability of an archaeological iron object [20]. For each of the presented phenomena it is essential to know whether the alteration is recent or not. If the object is covered with adherent corrosion products, we can assume that it is an old alteration. If it is covered with non-adherent sediment, we can assume that it is a recent alteration. If it is uncovered, it is new. This way we can differentiate between cases where there is a risk of reactivated corrosion (if the alteration is recent or old) and where reactivated corrosion is surely present (if the alteration is new). We sum up all of these elements in Fig. 11.10.

11.5 Perspectives

A critical bibliographical analysis of the works written on ‘active corrosion’ of iron objects has shown that we need to come to a consensus regarding the descriptive terminology that refers to the various types, forms and mechanisms of this type of corrosion. This is a *sine qua non* to establish better communication between conservation–restoration experts, corrosion specialists and art historians. Based on this effort, we have:

- suggested a general term to cover the described phenomena – reactivated corrosion;
- established an associated qualifier to describe the object – stable or unstable;



11.10 Diagnostics of reactivated corrosion for an archaeological iron object.

- enumerated various forms of associated corrosion to define their symptoms and to suggest a first classification attempt;
- opened the way to a diagnostic approach towards reactivated corrosion analysis for archaeological iron objects.

In the future, the analysis of standards such as ISO 8044 (2000) proposed by the AFNOR concerning ‘corrosion of metals and alloys: basic terms and definitions’ could be very useful.

11.6 References

1. G. Béranger, F. Dabosi, *Corrosion et Protection des Métaux, sous le Patronage du Centre Français de la Corrosion*, Editions du CNRS.
2. D. Watkinson, Degree of mineralization: its significance for the stability and treatment of excavated ironwork, *Studies in Conservation*, 28 (1983) pp. 85–90.
3. D.H.J. Wagner, M. Kropp, W.R. Fischer, H. Kars, A systematic approach to the

- evaluation of the corrosion load of archaeological metal objects, in *Metal 98, Proceedings of the International Conference on Metals Conservation*, Draguignan (1998) pp. 80–86.
4. D. Watkinson, An assessment of lithium hydroxide and sodium hydroxide treatments for archaeological ironwork, in R. W. Clarke and S. M. Blackshaw (eds) *Conservation of Iron*. Maritime Monographs and Reports no. 53, Greenwich Trustees of the National Maritime Museum (1982) pp. 28–40.
 5. F. Bertin-Bengtsson., M.-P. Lambert, M.-A. Loeper-Attia, Bilan d'efficacité des traitements de déchloruration par le sulfite alcalin pratiqués à l'IRRAP sur des objets archéologiques en fer, *Rapport IRRAP – PCR 'Fers chlorures' 1998* (2000).
 6. B.A. Rosenberg, *Antiquités en Fer et en Bronze, leur Transformation dans la Terre Contenant de l'Acide Carbonique et des Chlorures, et leur Conservation*, Copenhagen: Carlsberg Foundation (1917).
 7. R. Bertholon, Le devenir de l'objet archéologique en fer. Introduction à la corrosion et à la conservation, in *Objets en Fer et Savoir Faire*, Musée Archéologique Départemental du Val d'Oise, Guiry-en-Vexin, 1995; *AMADVO*, 1 (1992), pp. 53–70.
 8. L.L. Shreir, *Corrosion*, London: Newnes-Butterworths, 2nd edition (1976).
 9. J.J. Lamoureux, *Précis de Corrosion, Science des Matériaux*. Beauchemin: Masson (1994).
 10. M. Romanoff, *Underground Corrosion*, Washington DC: National Bureau of Standards, Circular 579 (1957).
 11. D. David, 1995, Synthèse bibliographique sur la corrosion d'objets archéologiques enfouis dans le sol, UTC, ed. ANDRA, Châtenay-Malabry (1995).
 12. S. Turgoose, Post-excavation changes in iron antiquities, *Studies in Conservation*, 27/3 (1982) pp. 97–101.
 13. A.A. Al-Zahrani, Chloride ion removal from archaeological iron and βFeOOH , PhD, University of Wales, Cardiff (1999).
 14. B. Knight, Why do some iron objects break up in store? R. W. Clarke and S. M. Blackshaw (eds) *Conservation of Iron*. Maritime Monographs and Reports no. 53, Greenwich Trustees of the National Maritime Museum (1982) pp. 50–51.
 15. R. Walker, Instability of iron sulfides on recently excavated artefacts, *Studies in Conservation*, 46/2 (2001) pp. 141–151.
 16. J.M. Cronyn, *The Elements of Archaeological Conservation*, London: Routledge (1990), pp. 175–202.
 17. B. Knight, A review of the corrosion of iron from terrestrial sites and the problem of post-excavation corrosion, *The Conservator*, 14 (1990) pp. 37–43.
 18. L.S. Selwyn, P.J. Sirois, V. Argyropoulos, The corrosion of excavated archaeological iron with details on weeping and akaganéite, *Studies in Conservation*, 44/4 (1999) pp. 217–223.
 19. S. Turgoose, The corrosion of archaeological iron during burial and treatment, *Studies in Conservation*, 30/1 (1985) pp. 13–18.
 20. M.-A. Loeper-Attia, Etude bibliographique des phénomènes de corrosion active des objets archéologiques en fer: définition du concept de corrosion active et caractérisation de ses symptômes, Mémoire de DEA Archéologie des Périodes Historiques, Université Paris I – Sorbonne (06/2002).

Simulation of corrosion processes of buried archaeological bronze artefacts

E. ANGELINI, F. ROSALBINO and S. GRASSINI,
Politecnico di Torino, Italy and G. M. INGO and
T. DE CARO Istituto per lo Studio dei Materiali
Nanostrutturati (ISMIN-CNR), Italy

12.1 Introduction

This research has been developed in the framework of a European Project, named *Efestus*, devoted to the identification of the causes of degradation of Cu-based archaeological artefacts selected as a function of the archaeological context and of the chemical composition and structure [1]. The ultimate goal of the project is to develop and apply innovative or traditional methods, anchored in local actions, for the restoration and conservation of the archaeological artefacts after validation tests carried out on Cu-based reference alloys with a microchemical structure similar to that of the ancient alloys.

As shown in Fig. 12.1 the geographical distribution of the partners involved allows the analysis of artefacts from a wide variety of archaeological contexts, from desert areas to wet environments, that have been submitted to different conservation treatments. Furthermore, the diversity of the partners involved – research institutions, archaeologists and museums – guarantees a multidisciplinary approach, whose importance and actuality is underlined by the observation that the quality of the excavated artefacts is steadily deteriorating with time. In many countries, due to the increase of environmental pollution, artefacts excavated in recent times have deteriorated more than those found in the same areas in the past [2, 3].

It is well known that during burial, the corrosion process on a bronze or copper-based alloy usually initiates with the formation of a cuprite layer, which darkens the surface successively. Depending on the nearby elements, various corrosion products of copper-II may grow, giving either a brown-black or a green colour to the surface [4, 5].

The surface layer of corrosion products is called the *patina* and its composition and thickness depend on the chemical composition of the bulk alloy and on the environmental conditions.

Several different parameters, such as geographical location, climate, land use and chemical and physical properties of the soil, may have an important influence on the deterioration of archaeological artefacts and on the corrosion



12.1 Partnership of the European Project *Efestus*: Istituto per lo Studio dei Materiali Nanostrutturati, Consiglio Nazionale delle Ricerche, Rome, Italy; Politecnico di Torino, Dipartimento di Scienza dei Materiali ed Ingegneria Chimica, Italy; Consejo Superior de Investigaciones Científicas, Centro Nacional de Investigaciones Metalúrgicas, Madrid, Spain; National Technical University of Athens, Greece; EGE University, Faculty of Letters, Turkey; Université Djillali Liabes, Algeria; Yarmouk University Institute of Archaeology Anthropology, Jordan; Jordan University of Science and Technology, Jordan; Institut National du Patrimoine, Tunisia; Institut National de Recherche, Tunisia; National Research Center, Cairo, Egypt; Egyptian Museum, Cairo, Egypt.

rate [5]. In the case of bronzes and other copper-based alloys, during burial or exposure to a museum atmosphere, the most important parameters to be considered are the moisture content, temperature, acidification and salt content. The soil water acts as an electrolyte on the buried object; a minimum value of pH is required to keep solid corrosion products stable. The position of the object in the soil, near the surface or deeply buried, needs to be considered as well as the diffusion of oxygen, one of the major agents in corrosion. The possible traces of human activity are also known to be a determining factor. It could be also necessary to take into account the presence of different anions in the soil water to explain the degradation mechanism. Chlorides and phosphates seem to have opposing effects on the corrosion rate, the former by increasing it through the destruction of the passive layer, the latter by acting as a corrosion inhibitor [6].

The corrosion process damages the alloys, as the copper required to form the corrosion products comes from the metal core [4, 5], which can considerably decrease its mass until total disappearance occurs. It is therefore crucial to find methods of protection and conservation of these metallic artefacts to prevent them from further deterioration. Sustainable preservation procedures have been carried out for years, but the currently available treatments are not

entirely satisfactory, as they cannot be applied to all artefacts and cases [6, 7] and require further investigation [8, 9].

The difficulty of establishing the connections between environmental factors and corrosion, due to the large number of parameters to be taken into account, requires the survey of a large number of artefacts and comparison of the data derived from their characterization, as foreseen in the *Efestus* project, both on excavated objects and in museum collections.

In this chapter, the description is limited to the characterization of bronze artefacts from two Italian archaeological contexts, Tharros and Sant'Antioco in Sardinia, compared with those obtained on alloys of similar chemical composition and microstructure artificially aged in soils taken from those of the excavation sites. This work will help archaeologists and curators to find the history and the evolution through time of the archaeological remains and, when feasible, to preserve, restore and protect them in order to display them in museums without causing further damage.

12.2 Materials and methods

12.2.1 Alloy production

Copper-based alloys of similar chemical composition and microstructure to the ancient alloys were produced, as cylinders 25 and 30 mm in diameter, in a laboratory furnace electrically heated in graphite crucibles under a reducing atmosphere in order to avoid the presence of oxygen. The chemical composition of the alloys, indicated in Table 12.1, was selected on the basis of the results of the characterization of more than 60 copper-based Punic artefacts [10]. A small amount of copper and iron sulphides and lead inclusions was added in order to obtain chemical features as close as possible to those of the ancient alloys. The composition of the *Aurichalcum* was determined from literature data.

12.2.2 Ageing procedures

The cylinders were cut into discs 2–3 mm thick, according to the batch of produced ingots. The samples were metallographically polished (600–100 grid) and buried in the soils coming from the selected archaeological sites, Tharros and Sant'Antioco, with addition of water in order to study the effect

Table 12.1 Chemical composition of the copper-based alloys (wt%)

| Alloy | Cu | Sn | Zn | Pb |
|--------------------------|------|-----|------|-----|
| Cu–Sn | 92.3 | 7.5 | | 0.2 |
| Cu–Zn <i>Aurichalcum</i> | 82.3 | 3.0 | 14.0 | 0.5 |
| Cu–Pb | 88.0 | 4.0 | | 8.0 |

of the soil components and properties on the corrosion mechanism. Some anions, such as phosphates, silicates and chlorides, were added as they could be of particular importance to the kinetics of the degradation mechanism and the composition of the patinas.

The alloys were buried in 60 g of soil, 30 g beneath and 30 g above, in transparent glasses of plastic and the selected solution was then added. The buried samples were submitted to an accelerated ageing test performed in a climatic chamber for 1, 4 and 7 months under the following conditions: 12 h at 10°C and 60% Relative Humidity (RH) followed by 12 h at 60°C and 90% RH. The samples were weighed every two or three days to check the amount of water or solution and then the quantity required was added to keep it almost constant during the total exposure of the samples to the ageing cycle in the climatic chamber. After increasing periods of burial (1, 4, 7 and 12 months) the aged samples were characterized with the analytical techniques listed below, which were also employed for the characterization of the artefacts. Parallel ageing tests were run directly at the archaeological sites on a set of samples buried in the areas where the artefacts had been found.

12.2.3 Artefacts and alloy characterizations

The archaeological artefacts and the alloys before and after the ageing tests were analysed from a microchemical and microstructural point of view by means of optical microscopy (OM, Leica MF4 microscope) and scanning electron microscopy (SEM-EDS, Philips 515 scanning electron microscope and EDAX 9900 energy dispersion microprobe, equipped with a W filament and a Robinson back-scattered electron detector), X-ray diffraction (XRD, automated Philips Xpert powder diffractometer) and X-ray fluorescence (XRF, Rigaku sequential X-ray fluorescence spectrometer ZSX100e/100s).

The protective effectiveness of the patina was assessed by electrochemical impedance spectroscopy (EIS). Impedance measurements, carried out with a frequency response analyser EIS300 (Gamry Instruments), were performed in aerated 0.1M NaCl solution at room temperature. Impedance spectra were recorded at the open circuit potential by applying a sinusoidal signal of 10 mV amplitude and frequency ranging from 10^5 to 10^{-2} Hz. The samples were analysed on an area ranging from 3 to 6 cm². The impedance measurements are presented as Bode diagrams. The impedance data give information about the protective effectiveness of the corrosion layers: the higher the value of the impedance, the more effective the barrier against aggressive agents.

12.2.4 Analysis of the soils

Some features of the soils from the two archaeological sites were determined by means of the following methodologies. On centrifuged aqueous extracts

of the two soils, a pH measurement was carried out with a glass electrode combined with a pH meter, while the electrical conductivity (EC) was measured with a conductimeter. The texture of the soils was determined from the particle size distribution (PSD) obtained by the pipette method. The total amounts of phosphorus and carbon were detected by elemental analysis. The fraction of carbonates was calculated by measuring the volume of carbon dioxide developed in the reaction between soil and hydrochloric acid. The percentage of carbon in the carbonates was determined using the ‘total carbonates’ method and the result was subtracted from the quantity of total carbon to obtain the percentage of organic carbon. The total silicon was quantified by means of atomic absorption spectroscopy (AAS), with the Bernas method. AAS was also utilized for the identification of the main metallic ions.

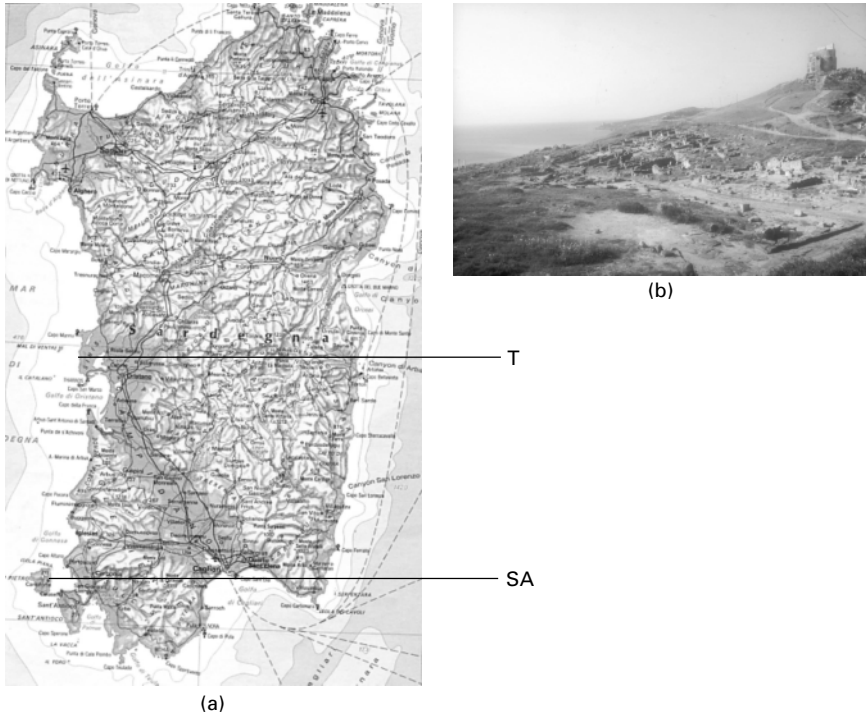
12.3 Results and discussion

One major concern of curators and archaeologists is the preservation of archaeological objects taken out of excavations and kept in museums. In the case of bronzes and other copper based alloys, the degradation phenomena occurring during burial or exposure to a museum atmosphere usually initiate with the formation of a cuprite layer, which darkens the surface, and then, depending on the environment surrounding the sample, various corrosion products of copper-II may develop, giving either a brown-black colour or a green one to the surface. This process damages the alloys, as the copper required to form the corrosion products comes from the metal core, which can then considerably decrease, and in some cases even disappear, following the corrosion rate. It is therefore crucial to find methods of protection and conservation of these metallic artefacts that prevent them from getting damaged.

12.3.1 Archaeological artefacts

The archaeological artefacts studied came from two Sardinian sites, Tharros and Sant’Antioco, Fig. 12.2. The archaeological site of Tharros is located near Oristano, on the west coast of Sardinia, and the island of Sant’Antioco is located just off the southern Sardinian coast. These sites were selected on the one hand because of the perpetual presence of different civilizations, and on the other because they were of great interest in ancient times owing to the intense smelting and metalworking activities. The metal trading was considered so important as to give to Sant’Antioco the Roman name of *Insula Plumbaria*.

Tharros and Sant’Antioco are among the most important archaeological sites in Sardinia. They were continuously inhabited by Proto-Sardinians, Nuragics, Phoenicians (who founded Tharros in the eighth century BC), Punics (from the sixth century BC), Romans (from the second century BC), and



12.2 (a) Map of Sardinia indicating the two archaeological sites, Tharros (T) and Sant' Antioco (SA), the areas of provenance of the copper-based artefacts under study; (b) panorama of the Phoenician-Punic site of Tharros.

others, and finally, during the eleventh century AD, by Saracens who destroyed Tharros. The sites were chosen for being typical of corrosive marine environments of coastal sites. The conservation conditions of their artefacts will be compared with those found recently during cleaning activities of the River Tiber in Rome in order to provide evidence of the influence of the surrounding environment on the formation of the corrosion products.

The artefacts were selected for their historical and economic value. They were produced first by casting and then by cold and hot working processes during different periods of about 600 years from the third century BC to the third century AD. They are constituted of tin leaded bronze alloys and brass (*Aurichalcum*). In Tharros, the artefacts were found both in the industrial-metallurgical area near the holy area of the *tophet* on the Muru Mannu hill at a depth of about 3 metres below ground level, and in the town situated in a room-like structure during recent near-surface inspections. In Sant' Antioco, the artefacts were found in the cemetery area (*necropolis*) at a depth of about 1–2 metres below ground level. The archaeological copper-based artefacts



12.3 Punic coins found in the archaeological excavation site of Tharros, with different degrees of conservation.

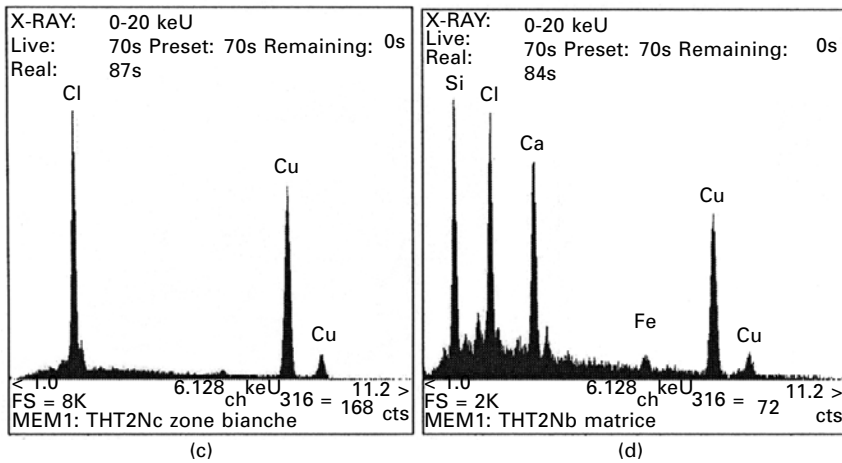
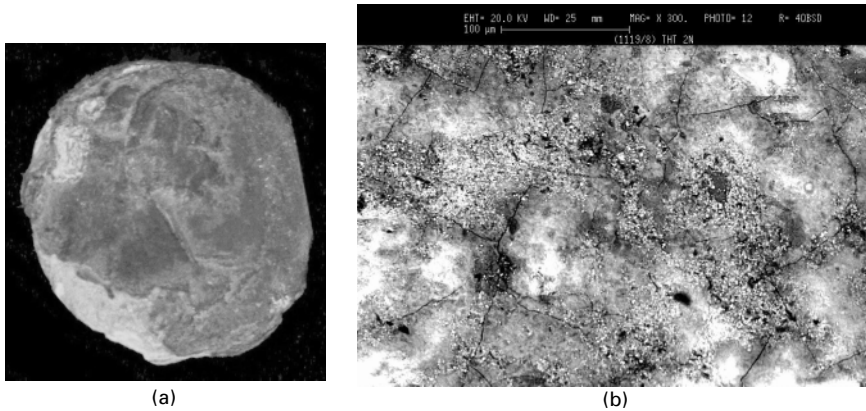
show different degrees of conservation, some suffering from extensive corrosion and degradation phenomena, generically known as bronze disease, Fig. 12.3.

As an example, the complete characterization of a Punic coin, showing a head of a Kore-Persephone on one side and a horse head on the other, found in the archaeological excavation site of Tharros, is shown in Fig. 12.4. The manufacturing process of this type of coin, minted in different Punic settlements including Sardinia from 300 to 260 BC, consisted of the hammering, between an immobile and a mobile die, of a heated bronze blank produced by casting in ceramic bivalve tier moulds. The microstructure of the blank, initially dendritic in as-cast conditions, could be transformed to a partially or fully crystallized one as a function of the thermal treatments.

As shown in Fig. 12.4, on the surface of the coin a noticeable presence of chlorine was detected and its presence was confirmed also by the X-ray diffractogram, Fig. 12.5, where the paratacamite ($\text{Cu}_2\text{Cl}(\text{OH})_3$) signals are identified together with those of brochantite, $\text{Cu}_4(\text{SO}_4)(\text{OH})_6$. The complex microstructure of the stratified corrosion products grown on the Punic coin during the long-term burial in the soil is shown in Fig. 12.6. The cross-section observed by optical microscopy in a dark field (the alloy appears black) reveals the presence of light yellow-orange copper chlorides at the interface between patina and metal. Cuprite appears as a red layer and Cu carbonates, malachite, as a thick green layer.

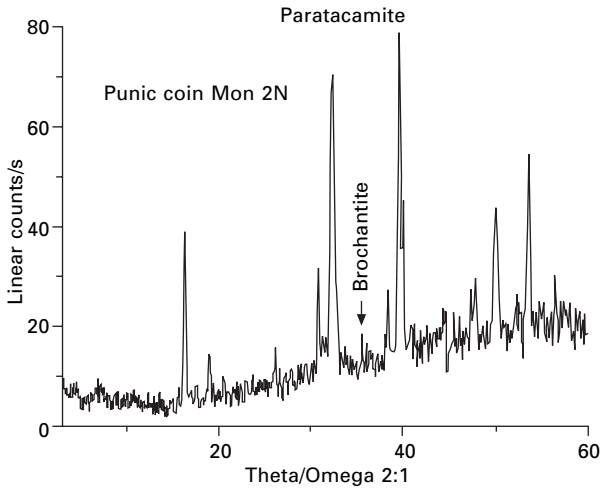
12.3.2 Soils from the archaeological sites

The aggressiveness of soils depends on different parameters, such as the amount of hygroscopic salts, humidity, gas, organic compounds, microorganisms and temperature. The water content varies over a wide range

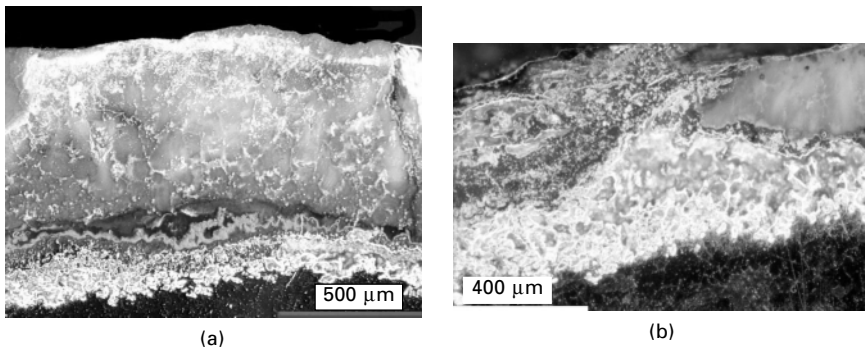


12.4 (a) Punic coin with a horse head found in Tharros; (b) SEM image of the surface with (c) the EDS spectra of the white areas and (d) that of the darker areas.

near the surface because of evaporation and absorption phenomena. Under the water-bearing layer, whose position depends on weather and geological factors, the pores are completely filled with water. Above this level the pores may contain water for capillarity; the slope is of several metres for small pores and of centimetres for large pores. Regarding the presence of oxygen, in the deeper layers oxygen diffusion takes place slowly and corrosion phenomena proceed at a reduced rate; near the surface aeration is easier, but the corrosion may be slow because of the lack of electrolyte. The most favourable conditions for corrosive attack are in regions slightly above the water-bearing layer, where both the oxygen supply and the conductivity are high enough to allow active corrosion. Soil treatments commonly carried out in agriculture ameliorate soil aeration, while the passage of vehicles increases



12.5 X-ray diffractogram of the Punic coin of Fig. 12.4.



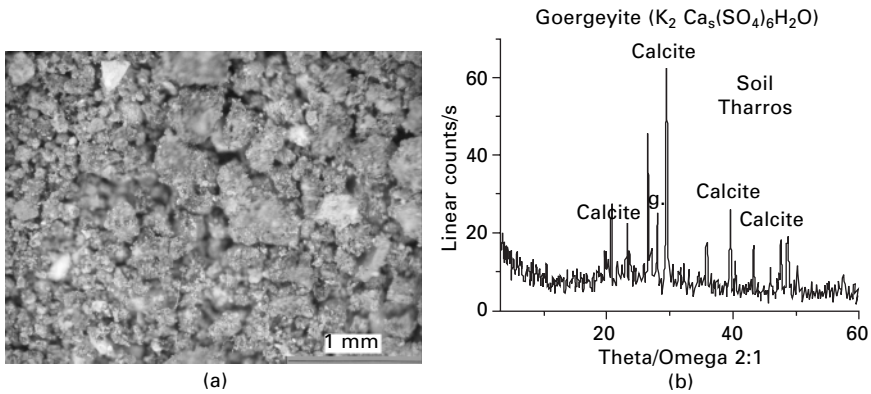
12.6 Stratification of the corrosion products grown on the Punic coin of Fig. 12.4. From top to bottom: malachite, cuprite, alloy.

compaction of the soil. In areas with different oxygen contents, corrosion phenomena may be induced by differential aeration, with microcell formation taking place. In soils with low oxygen content, sulphates may be dangerous, because in the presence of sulphate-reducing bacteria such sulphates may be broken down with the production of hydrogen sulphide, which is highly aggressive.

The pH of the soil influences to a great extent the corrosion phenomena, because the stable corrosion products may exert a protective action above certain pH values: a soil is considered not aggressive if its pH ranges from 4 to 8.5. The pH of a soil may decrease as a result of both natural and human factors.

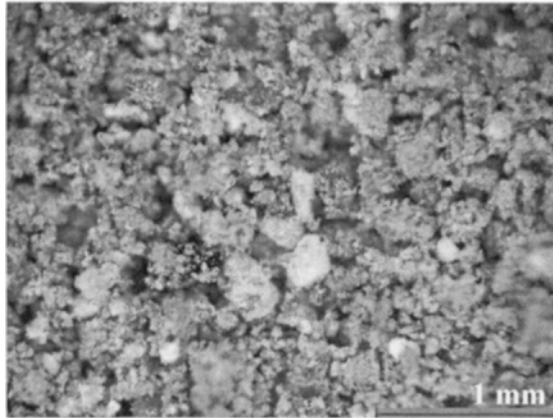
Table 12.2 Main characteristics of the soils from the selected archaeological sites

| Archaeological site | Tharros | Sant' Antioco |
|-----------------------------------|----------------|---------------|
| pH (H ₂ O) | 8.7 | 8.5 |
| EC (μS/cm) | 397 | 229 |
| wt% CaCO ₃ | 31.7 | 22.2 |
| wt% C _{CaCO₃} | 3.8 | 2.7 |
| wt% C _{organic} | 4.5 | 1.3 |
| Main metallic elements | Ca, Fe, Mg, Pb | Ca, Fe, Mg |
| wt% P _{total} | 3.2 | 1.4 |
| wt% Si _{total} | 2.65 | 4.1 |
| Texture | Sandy loam | Sandy loam |

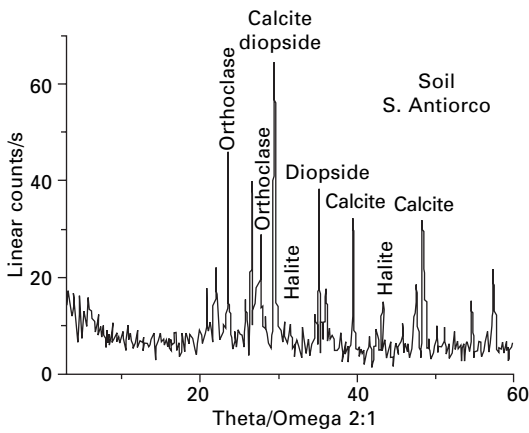
**12.7** (a) Optical image of the soil from the archaeological site of Tharros; (b) X-ray diffractogram.

With these considerations in mind, a series of characterizations were carried out on the two soils from Tharros and Sant'Antioco and are summarized in Table 12.2 and in Figs 12.7 and 12.8. Both soils are sandy loam. The optical images in Figs 12.7 and 12.8 show a similar texture; moreover, from the X-ray diffractograms, both soils appear to be constituted mainly of quartz and calcite. The pH values show both soils to be basic, thus indicating a situation that is not particularly aggressive, notwithstanding the presence of chlorides well evidenced in Fig. 12.8 in the EDS spectrum of the soil from Sant'Antioco, indicating the presence of this aggressive element.

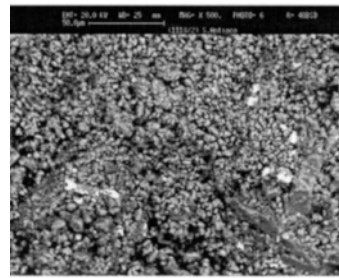
The selected Italian archaeological sites are areas where agricultural activities have never been carried out and therefore chemical compounds or fertilizers have not been added to the soil. The addition of chemical compounds induces considerable changes in the nature of the soil and therefore influences the possible conclusions drawn from the analytical investigations aimed at correlating the degradation phenomena of the buried artefacts to the soil



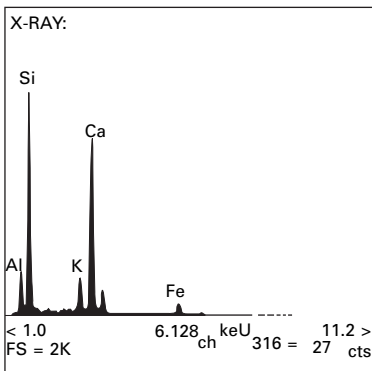
(a)



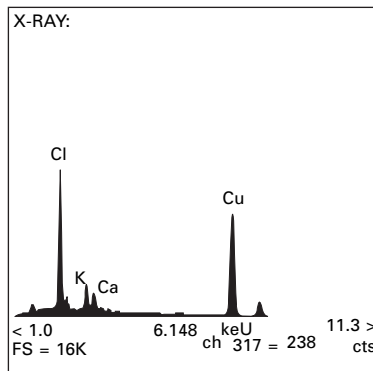
(b)



(c)



(d)



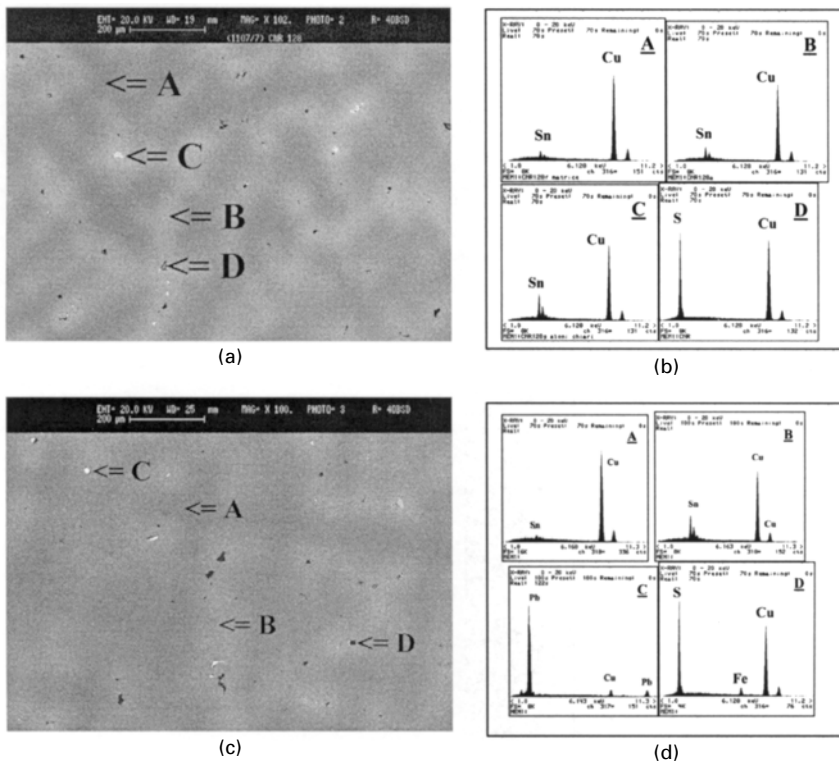
(e)

12.8 (a) Optical image of the soil from the archaeological site of Sant'Antioco, with (b) X-ray diffractogram; (c) SEM image at higher magnification together with the EDS of (d) the darker areas and (e) the white areas.

features. In these circumstances the results cannot be realistic, since today's soil conditions are so different from those experienced by the archaeological artefacts during their burial.

12.3.3 Cu-based alloys and ageing tests

All three Cu-based alloys listed in Table 12.1 show a microstructure similar to that of the archaeological artefacts examined. As an example, the comparison between an artefact and an alloy of composition 92.3 Cu, 7.5 Sn and 0.2 Pb (wt%) is shown in Fig. 12.9. The SEM images in Fig. 12.9(a) and (c) show cross-sections of the Cu–Sn alloy and the Punic coin of Fig. 12.3(b). Most of the ancient as-cast artefacts show a typical bulk structure of a copper–tin solid solution with inclusions of lead and copper sulphide scattered in a matrix where tin inverse segregation has occurred as well as the formation of δ copper–tin phases, Fig. 12.9. The SEM images show that brighter areas of



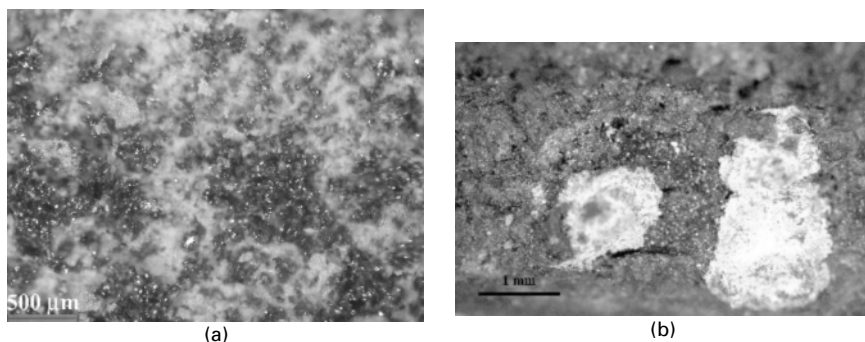
12.9 SEM images of (a) a cross-section of the Cu–Sn alloy of Table 12.1 and (c) the Punic coin of Fig. 12.3(b), with (b, d) the EDS spectra of the indicated areas.

the solid solution are richer in tin than the dark ones. The microstructures are similar, and the reference alloys may be considered suitable specimens for the ageing tests for simulation of the corrosion processes.

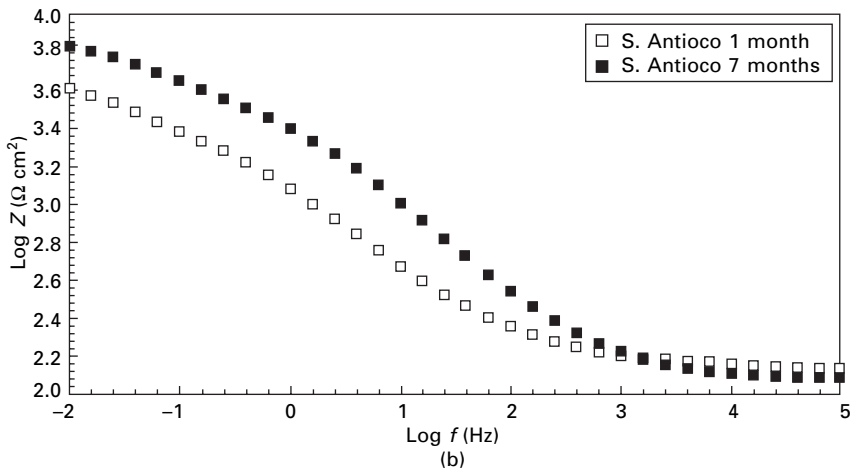
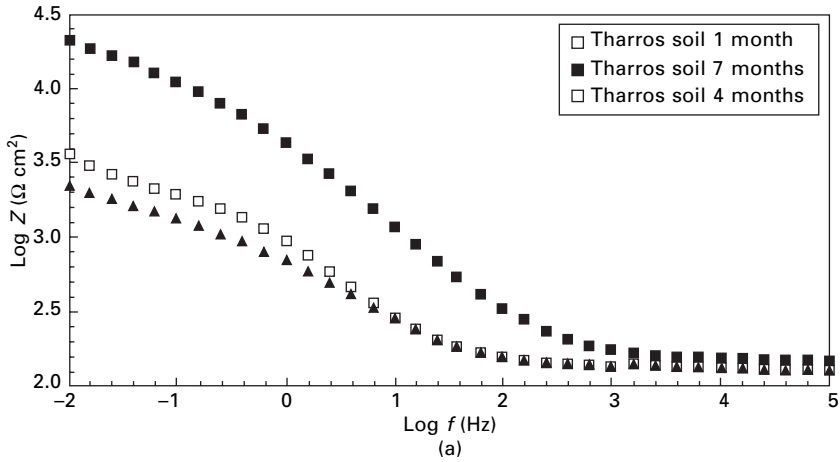
The ageing tests in the climatic chamber were carried out in the two soils from Tharros and Sant' Antioco. As expected, with increasing burial durations an increase of the thickness of the patina was observed. After 12 months of burial, on the surface of the copper-based alloys well-developed cuprite crystals were detected, like those grown on active zones of the surface of archaeological artefacts. As an example, the case of Cu–Sn alloys is shown in Fig. 12.10, together with the optical image of the Punic coin of Fig. 12.3(b). The soil typology is assumed to control the microstructure of the corrosion products more, since their formation would be governed by the interaction between the alloy components and the surrounding elements.

Electrochemical tests, in particular Electrochemical Impedance Spectroscopy (EIS) tests, were performed on aged samples in order to investigate the influence of burial time, soil typology and chemical composition on the growth and protective effectiveness of corrosion layers. For Cu–Sn alloys buried in the two different soils, Fig. 12.11 shows the Bode plots, recorded after 1 h exposure to 0.1M NaCl solution. For the first immersion period the diagrams are quite similar for the two soils; as a matter of fact, the burial time is too short to allow the development of a significantly thick layer. By increasing the ageing period in the Tharros soil to 7 months, higher values of the impedance modulus were obtained, indicating the development of a compact layer of corrosion products.

For comparison purposes, Fig. 12.12 shows the Bode plots for some archaeological artefacts: the impedance modules are of the same order of magnitude as the values recorded on the Cu-based aged alloys. The electrochemical behaviour of their patinas may be considered comparable



12.10 (a) Cuprite crystals developed on the surface of Cu–Sn alloy after 12 months of burial in the Tharros soil in the climatic chamber; (b) cuprite crystals on the Punic coin of Fig. 12.3(b).

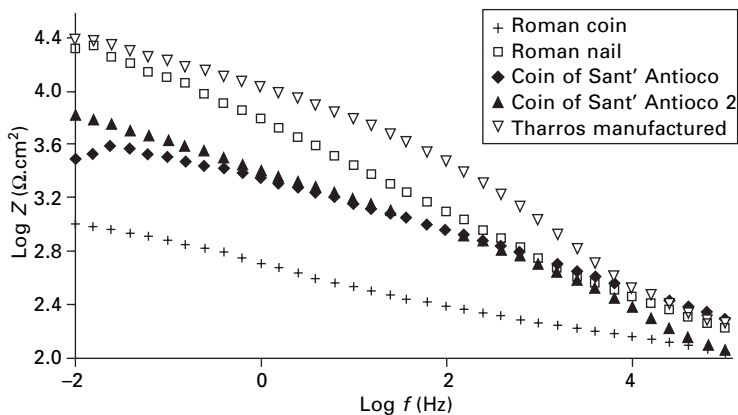


12.11 Bode plots for Cu–Sn alloy samples, buried in (a) Tharros soil and (b) Sant'Antioco soil, and aged in the climatic chamber for increasing burial times.

with those of the aged alloys even if every artefact has to be considered individually in terms of its microchemical composition, its microstructure and the soil components, because all these parameters have a noteworthy influence on the formation of the corrosion layer.

12.4 Conclusions

The simulation experiments of corrosion processes of archaeological bronze artefacts described above show that the soil composition might have a certain influence on the morphology and growth kinetics of the patinas formed on



12.12 Bode plots for archaeological artefacts found in the archaeological site of Tharros (Roman coin and Roman nail, Tharros manufactured artefact) and Sant' Antioco (coins).

copper-based alloys. The copper-based alloys with microchemical and microstructural features similar to those of the archaeological artefacts behave, for short burial times, in a similar way to the artefacts and may be reasonably proposed for a simulation study of the long-term degradation mechanisms.

The situation experienced by the archaeological artefacts is more complex than that of the reference alloys, because even if the artefacts have similar chemical composition and microstructure, they have a unique individual story and interaction with the soil. From our findings, it may be concluded that the patinas grown on copper-based artefacts in the Sardinian soils, if compact and homogeneous, show a certain degree of protective effectiveness. Long-duration burial tests are currently running both in the climatic chamber and in the archaeological sites of Tharros and Sant' Antioco in order to assess the above-mentioned results.

12.5 References

1. Incomed, Project Contract no. ICA3-CT-2002-10030, *Tailored strategies for the conservation and restoration of archaeological value Cu-based artefacts from Mediterranean countries*, Acronym: *Efestus*.
2. T.E. Graedel, K. Nassau and J.P. Franey, Copper patinas formed in the atmosphere – I. Introduction, *Corrosion Science* (1987), Vol. 27, No. 7, pp. 639–657.
3. L. Robbiola, J.M. Blengino and C. Fiaud, Morphology and mechanisms of formation of natural patinas on archaeological Cu–Sn alloys, *Corrosion Science* (1998), Vol. 40, No. 12, pp. 2083–2111.
4. W. Gerwin and R. Baumhauer, Effect of soil parameters on the corrosion of archaeological metal finds, *Geoderma* 96 (2000), pp. 63–64.
5. E. Mattson, A.G. Nord, K. Tronner, M. Fjaestad, A. Lagerlof, I. Ullen and G.C.

Borg, *Deterioration of Archaeological Material in Soil*, Stockholm: Central Board of National Antiquities, 1996.

6. O.P. Agrawal, Conservation of metals – Problems and prospects, in: *Conservation of Metals in Humid Climate: Proceedings of the Asian Regional Seminar held from 7–12 December 1987*, ed. O.P. Agrawal, Lucknow: NRLC (1987), pp. 1–17.
7. K. Huda, Protective coating in conservation of metallic antiquity, in: *Conservation of Metals in Humid Climate: Proceedings of the Asian Regional Seminar held from 7–12 December 1987*, ed. O.P. Agrawal, Lucknow: NRLC (1987), pp. 88–99.
8. R.M. Organ, The current status of the treatment of corroded metal artefacts, in: *Corrosion and Metal Artifacts. A Dialogue between Conservators and Archaeologists and Corrosion Scientists*, ed. B.F. Brown, H.C. Burnett, W.T. Chase, M. Goodway, J. Kruger and M. Pourbaix, Washington, DC: US Department of Commerce, National Bureau of Standards (1977), pp. 107–142.
9. V.C. Sharma, Corrosion inhibitors in conservation, in: *Conservation of Metals in Humid Climate: Proceedings of the Asian Regional Seminar held from 7–12 December 1987*, ed. O.P. Agrawal, Lucknow: NRLC (1987), pp. 37–40.
10. D. Attanasio, G. Bultrini and G.M. Ingo, *Archaeometry* (2001), Vol. pp. 529–547.

Corrosion patina or intentional patina: contribution of non-destructive analyses to the surface study of copper-based archaeological objects

F. MATHIS, J. SALOMON, S. PAGÈS - CAMAGNA,
M. DUBUS, D. ROBCIS and M. AUCOUTURIER,
Centre de Recherche et de Restauration des Musées de France,
France and S. DESCAMPS and E. DELANGE,
Louvre Museum, France

13.1 Introduction

Polychromy has been used by metal craftsmen from far antiquity. One may suppose that, as soon as metal alloying appeared, it was used to vary the colour of objects created by the artists. As far as copper-based alloys are concerned, it is now clear that metal artefacts fabricated in Mesopotamia as early as the third millennium BC [1], or in Egypt during the second millennium BC. [2], were intentionally made of various alloys assembled or juxtaposed in order to show a combination of colour, improving the artistic effect. Another process for controlling the colour of metal objects or parts of them is to submit the surface to intentional chemical treatments. One may for instance provoke surface composition modification by acid etching, as in the surface depletion of gold–copper alloys to give them a gilded shine [3], or the surface depletion of a lead–silver alloy to give it a silvery shine [4]; that kind of treatment will not be considered here. Other chemical treatments aim to build on the alloy surface a compound (generally oxidised) layer, with a given colour; this is usually called intentional patination. It is now known that this latter process also appeared quite early, at least in Egypt at the beginning of the second millennium BC [5].

The present chapter concerns research into this type of intentional patination on archaeological objects. Several research works have been recently published dealing with the existence of a known intentional black patination of copper alloys containing small amounts of gold and sometimes silver, on Egyptian, Minoan, Roman and Japanese objects [2, 5–9]. These black coloured alloys, called ‘black bronze’, ‘black copper’, ‘Corinthian bronze’, *shakudo*, etc., were used either for bulk objects, subsequently inlaid with other alloys, or for the inlays themselves applied on copper-base objects. Artificial black patinas using sulphur treatment have also been reported and reproduced in the laboratory, for instance on bronze objects from the wreck of the Mahdia

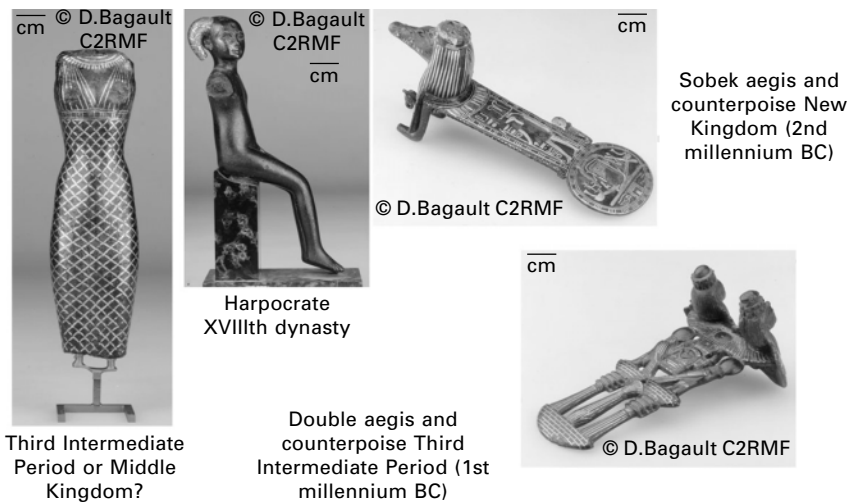
[10]. However, little is known about the ancient recipes of the craftsmen. Concerning the black copper, it is usually admitted that the copper alloys used as substrates for the patination all belong to the same family, i.e. copper–gold alloys with less than 8 wt% gold [6]. Another aim of this research is to understand why this is the only known type of intentional patination attested for the ancient world, at least from the aesthetic viewpoint. Different reasons may be given: the black patina was indeed the only one used; the other patinas have been degraded by corrosion; other patinas have not yet been detected; or the object’s surface has been cleaned too much after excavation.

Taking advantage of the availability of well-dated archaeological artefacts provided by two departments of the Louvre museum, which exhibit the occurrence of possible intentionally patinated parts, a laboratory investigation was performed in order to establish a full physico-chemical characterisation of the alloys concerned and their surface layer composition. As it was not possible to extract any sample from the surface of the objects, all the means of investigation, except the determination of the bulk alloys, had to be entirely non-destructive.

The present chapter will not discuss the historical aspects, the inlaying process or the bare metal polychromy (golden and silver inlays) described in other publications [8, 11]. We shall focus instead on the intentionally patinated parts.

13.2 The objects

The four Egyptian objects are (Fig. 13.1):



13.1 Objects from the Department of Egyptian Antiquities, Louvre Museum.

- 1 A Harpocrate figurine (inv. E 7735) today supposed to have come from the XVIIIth Dynasty, of blackish colour, with a lock of hair inlaid with golden strings on a black background.
- 2 A ritual collar counterpoise assembled to an aegis devoted to the crocodile Sobek (inv. E 11520), dated today probably from the New Kingdom period, inlaid with golden figures on a black background.
- 3 A feminine statuette (inv. E 27430) dated from the Third Intermediate Period (TIP) or perhaps from the Middle Kingdom, inlaid with golden strings on a black background.
- 4 A double aegis and its counterpoise (inv. N 4302) dated from the Third Intermediate Period, inlaid with golden figures on a black background.

The three Roman Empire objects are all dated from the first or second century AD (Fig. 13.2):

- 5 An inkpot (inv. Bj 1950), inlaid with various metals on a corroded background.
- 6 A strigil (inv. Br 1582), decorated on a corroded background by engraving and patinating.
- 7 A bistoury handle (inv. Br 2516), decorated with black and red inlays on a corroded background.

All these objects show metallic inlays and/or patinated background or inlays:

- The background of the four Egyptian objects is of a black colour, obviously intentional.
- The Roman inkpot and bistoury handle are inlaid with black inlays (the



Inkpot



© D.Bagault C2RMF
Strigil



© D.Bagault C2RMF



Bistoury handle
(with macrography)

13.2 Objects from the Department of Greek, Roman and Etruscan Antiquities, Louvre Museum (1st–2nd century AD).

himation of Venus and Adonis on the inkpot, the symmetrical decoration on the bistoury handle).

- The Roman strigil exhibits red-orange areas, presumably intentionally coloured, inside the ivy leaves and the athlete figure engraved on its handle, and on the chessboard figure strips at both ends of the handle (see Fig. 13.6 on page 232, and the accompanying discussion).

All the objects were acquired at different times by the Louvre museum departments mentioned. Their discovery and post-excavation history is generally not very precisely known. One can reasonably assess that the Egyptian artefacts were discovered during ground excavations in Egypt; the Roman inkpot was discovered in France and the bistoury was found in Tunisia. Like all museum objects they have been submitted to cleaning restoration operations, which eliminated (hopefully mechanically) the gangue containing extraneous soil products and tried to keep in place natural corrosion products as well as intentional patinas. As mentioned later in this chapter concerning the strigil decoration, these cleaning operations may sometimes have been too harsh and may have destroyed part of the decoration. The intentionally patinated regions are easily recognised, either for iconographic reasons or because they are made from specific copper alloys.

13.3 Instrumentations and methods for analyses

The analysis of the bulk metal of each object was performed on metal chips obtained by micro drilling on an invisible region, with a 1 mm drill. Each sample weighed about 10 mg, and the chips were carefully sorted under a binocular microscope to eliminate corrosion products and keep the sound metal. They were either pressed as pastilles to be analysed by PIXE (particle-induced X-ray emission, see below) or digested in acid to be analysed by ICP-AES (inductively coupled plasma-atomic emission spectroscopy [12]). The surface analyses had to be entirely non-destructive in order to keep the integrity of these valuable museum objects.

Ion beam analyses (IBA) were performed by using the external beam of the AGLAE particle accelerator of the C2RMF laboratory. This 4 MV tandem accelerator delivers a proton or alpha particle beam of high energy (up to 4 MeV for protons, up to 6 MeV for $^4\text{He}^{++}$ particles), which is extracted to free atmosphere through a 100 nm thick Si_3N_4 window [13]. The use of an external particle beam allows a non-destructive analysis directly on the object surface, without needing to remove a sample, which could evidently not be possible for these valuable museum items. A flux of helium was blown on the particle path to minimise the incident beam energy loss and straggling. The analysed spot is of 50 μm diameter, and may be scanned on a few mm^2 of area. The X-ray emission under 3 MeV proton or 6 MeV alpha particle beam allows a quantitative analysis by PIXE [13]. The backscattered particles under 3 MeV

protons or 3 or 6 MeV $^4\text{He}^{++}$ particles were used for RBS (Rutherford backscattering spectrometry) analysis, which allows an in-depth profiling of the elemental concentrations over a few micrometres [14]. The RBS spectra were interpreted in terms of successive layers, thanks to the SIMNRA code [15]. The penetration of 3 MeV protons and 6 MeV alpha particles into the samples may be estimated at respectively about 40 μm and 16 μm . This means that the 3 MeV proton PIXE analyses concern about 20 μm from the surface and the 6 MeV alpha PIXE analyses concern about 8 μm from the surface.

The determination of the nature of the crystalline compounds present on the surface was performed by X-ray diffraction (XRD) in an X-ray diffractometer equipped with focusing mirrors in order to obtain a parallel beam of 0.6 mm cross-width and to allow diffraction under controlled incidence. That arrangement allowed us to perform the XRD acquisition directly on the objects, provided they were small enough to be placed in the chamber of the diffractometer, which was case here. The incident X-ray beam is delivered by a Co K α tube (40 kV, 40 mA).

The nature of the surface compounds was also investigated by Raman micro-spectrometry, with a Jobin-Yvon Infinity equipped with CCD detector, notch filters and a horizontal issue. The horizontal objective allowed us to perform the Raman acquisition directly on the objects. The incident beam is delivered by a (Nd:Yag) laser (532 nm) and the spatial resolution is down to 2 μm . The laser power is about 5 to 12 μW .

13.4 Results

As mentioned in the introduction, the bare metal inlays (gold and silver inlays) will not be described here, and the results given concern only the corroded or patinated parts of the objects. All the results are gathered, without classification in terms of the origin and history of the objects; the historical discussion, focused on intentional patination, will be developed in the discussion section. Table 13.1 summarises the locations and procedures of the different analyses conducted on the objects.

13.4.1 Analysis of the bulk metals

Bulk metal analysis is necessary for the interpretation of patina. Results are grouped in Table 13.2. Only the main components are given (this is why they do not sum up to 100%); the values are averaged over several analyses, and are given here with a 1% absolute accuracy and reproducibility for that reason.

The bulk metals of the Egyptian objects are different from each other. Three of them contain gold and silver, and the metal of the statuette does not

Table 13.1 Location (and methods) of analyses

| Object | Analyses |
|---------------------------|---|
| Egyptian | |
| Harpocrate figurine body | Bulk metal (PIXE on sampled chips) + black background patina (IBA + XRD + Raman) |
| Harpocrate lock of hair | Black background patina (IBA) |
| Sobek counterpoise | Bulk metal (PIXE on sampled chips) + black background patina (IBA + XRD + Raman) |
| Feminine statuette | Bulk metal (PIXE on sampled chips) + black background patina on robe and décolleté (IBA+XRD+Raman) |
| Double aegis counterpoise | Bulk metal (PIXE on sampled chips) + black background patina (IBA + XRD + Raman) |
| Roman | |
| Inkpot body | Bulk metal (ICP-AES on sampled chips) + black patina on inlays + corroded background and red inlays (IBA + XRD + Raman) |
| Inkpot top | Bulk metal (ICP-AES on sampled chips) + corroded background (IBA + XRD + Raman) |
| Strigil | Bulk metal (ICP-AES on sampled chips) + corroded background + red-orange patina on ivy leaves and chessboard strips (IBA + XRD + Raman) |
| Bistoury handle | Bulk metal (ICP-AES on sampled chips) + black patina on inlays + corroded background (IBA + XRD + Raman) |

contain any of these elements. This observation is important as all these objects are patinated in black. The bulk of the Harpocrate lock of hair could not be analysed because its small size made sampling impossible. The bulk metals of the Roman objects are indicated here for information, as they are not intentionally patinated and their composition is not relevant from that viewpoint.

13.4.2 Analyses of the intentional black patinas

The black patinas observed on the objects were analysed by PIXE, RBS, X-ray diffraction under controlled incidence and Raman micro-spectrometry. Figures 13.3–13.5 below show examples of some spectra and diagrams observed and interpreted. Table 13.3 summarises the results obtained by PIXE analysis. As the penetration range of the 3 MeV proton beam is larger than the surface layer thickness, the contents obtained may in fact partly include the composition of the underlying substrates. PIXE analyses were thus also done under a 6 MeV alpha particle beam [16], whose penetration is less important. The values in Table 13.3 are given with this latter configuration when it was used.

Table 13.2 Analyses of bulk metals (main components, wt%)

| Object | Cu | Sn | Zn | Pb | As | Fe | Au | Ag |
|--|------|-----|----|-----|-----|-----|-----|-----|
| Egyptian | | | | | | | | |
| Harpocrate figurine body ^a | 76 | – | – | – | – | – | 24 | – |
| Sobek counterpoise ^a | 87 | 2 | – | – | 1 | 0.2 | 5–7 | 3 |
| Feminine statuette ^a | 86.5 | 5 | – | 5 | 2 | – | – | – |
| Double aegis counterpoise ^a | 86 | 6.4 | – | 0.3 | 2.2 | 1.3 | 0.8 | 2.8 |
| Roman | | | | | | | | |
| Inkpot body ^b | 86 | – | 14 | – | – | – | – | – |
| Inkpot top ^b | 69 | 6 | – | 25 | – | – | – | – |
| Strigil ^b | 81 | – | 19 | – | – | – | – | – |
| Bistoury handle ^b | 87 | 4 | 6 | 3 | – | – | – | – |

^a 3 MeV proton PIXE analyses on sampled chips

^b ICP-AES analyses on digested sampled chips

Table 13.3 PIXE analyses on the black patinas (averaged values, wt%)

| Object | Cu | Sn | Zn | Pb | As | Fe | Au | Ag | Cl | S |
|--|-------|-------|----|------|-----|------|-----|-----|-----|-----|
| Harpocrate figurine body ^b | 62 | – | – | – | – | – | 16 | – | 20 | 2 |
| Harpocrate lock of hair ^a | 79 | 7 | – | 4 | 2 | – | 6.7 | – | 2.9 | 2.6 |
| Sobek counterpoise ^b | 80 | 3 | – | 1.2 | 1 | 0.5 | 7.4 | 3.7 | 2 | 2 |
| Feminine statuette robe ^a | 70 | 12 | – | 15 | 3 | 0.6 | – | – | 10 | 10 |
| Double aegis counterpoise ^b | 40–70 | 10–19 | – | 4–12 | 3–5 | 5–25 | 2–3 | 3–9 | 2–5 | 1 |
| Inkpot: Venus's <i>himation</i> inlay ^b | 90 | – | – | 0.9 | 3 | – | 1 | 3 | – | – |
| Bistoury handle inlay ^a | 95 | 1.5 | – | 0.9 | 0.8 | 1.7 | – | 1 | 1 | 1 |

^a Under 3 MeV protons

^b Under 6 MeV alpha particles

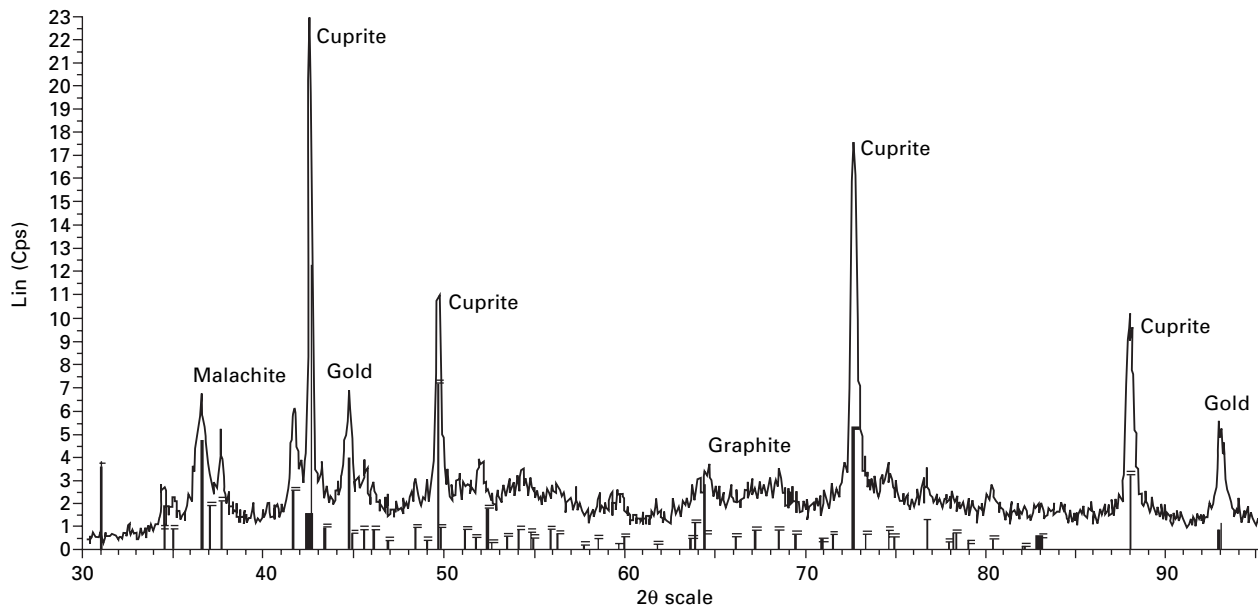
The given values are averages of several analyses, and this explains why they do not sum up to 100% for a given area. The accuracy and reproducibility are of the order of 1% for major elements and 0.1% for minor elements.

Even if one takes into account the fact that the substrate alloys are very different from one object to another, it is clear that the compositions of the patinas are also very diverse. Nearly all of them contain gold and from that point of view could be assimilated to 'black copper' or 'black bronze', but the gold and silver contents are very different, from 0.8 to 16% for gold, from 0 to 9% for silver. One of the black patinas (the statuette robe) contains neither of these elements, and one contains silver but no gold (the bistoury). The additional elements Fe, Cl and S might be residues from the burial not eliminated by the restoration. But this cannot be true for the Harpocrate body and the statuette patinas which contain high amounts of chlorine; iron in the double aegis patina may also not be a burial residue.

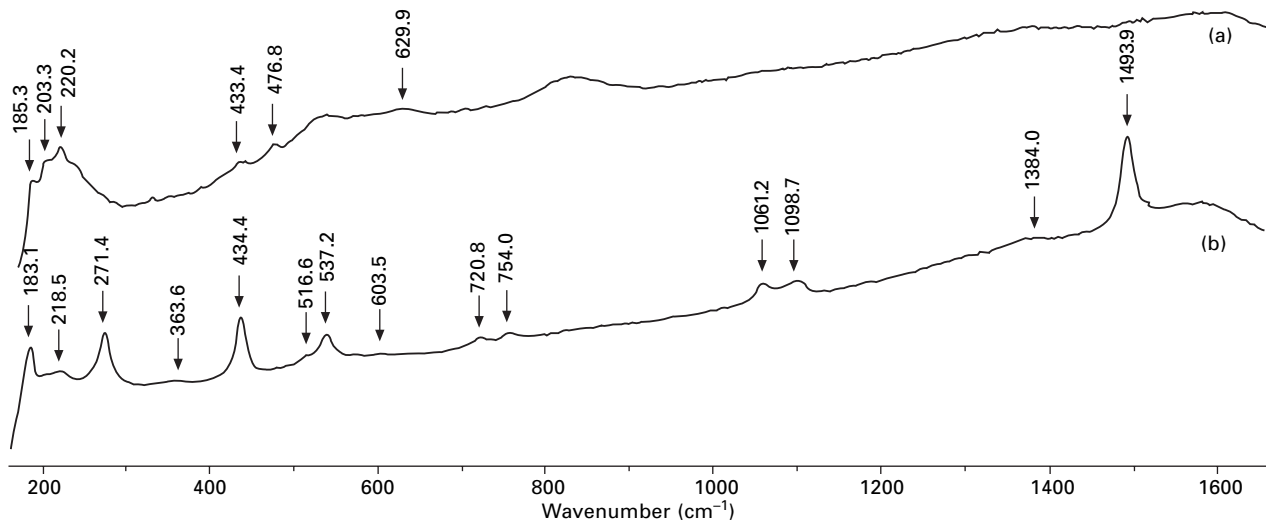
The X-ray diffraction done on all objects (except the too small Harpocrate lock of hair background) show that nearly all the patinas are constituted of cuprite, Cu_2O (see the example in Fig. 13.3). The statuette patina also contains chloride (clinoatacamite, $\text{Cu}_2\text{Cl}(\text{OH})_3$) and sulphides. The patina of the Harpocrate body is not cuprite, and is constituted mainly of chlorides (nantokite, CuCl , and clinoatacamite). These results were confirmed by Raman micro-spectrometry, which showed also that the black patina of the Venus's *himation* of the inkpot contains noticeable amounts of malachite (copper carbonate, $\text{Cu}_2\text{CO}_3(\text{OH})_2$) (Fig. 13.4).

The RBS analyses are useful in quantifying the thickness of the patina and the in-depth distribution of the elements across the surface layers. Figure 13.5 shows two examples of the RBS spectra measured and simulated by the simulation code SIMNRA [14, 15]. Table 13.4 summarises the results obtained. The thickness of the surface layers is obtained in at.cm^{-2} , which is the information given by RBS. The translation to metric thickness (μm) is done by assuming that the densities of the compounds have their theoretical value, neglecting a possible porosity or non-stoichiometry. It is seen that the thickness of the surface oxidised layer may vary greatly between objects. The RBS analyses showed moreover that for all substrates containing a small amount of gold and/or silver, the patina is always enriched with these two elements, which are present on the extreme surface (Fig. 13.5). In contrast, the surface of the patina of the Harpocrate body is nearly totally depleted of gold.

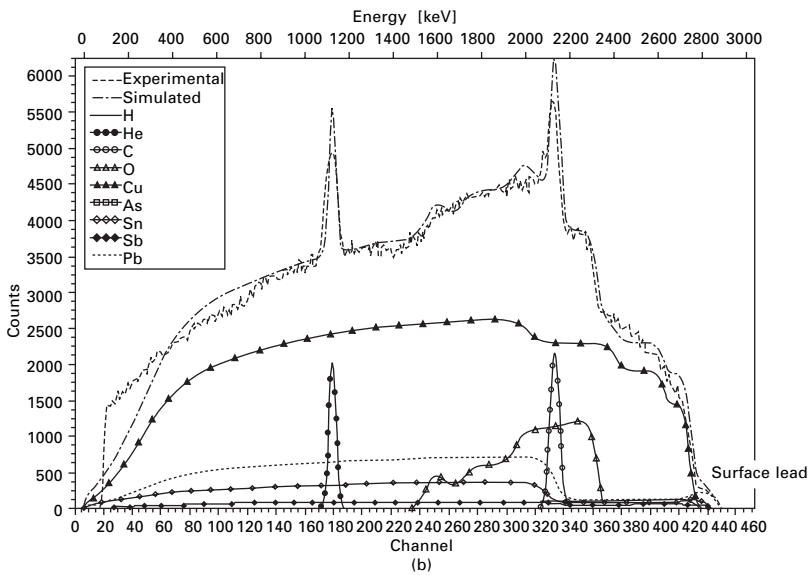
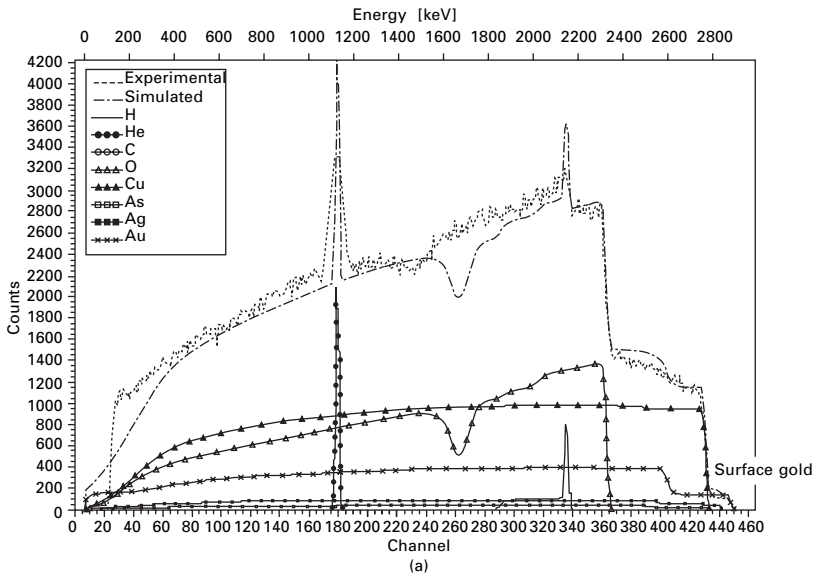
As mentioned previously concerning the elemental analyses, the presence of nantokite and clinoatacamite, well known corrosion products observed on antique bronzes buried in soil, in the patinas of the Harpocrate body and statuette robe cannot be attributed to these corrosion products remaining because chlorine (as well as sulphur) is detected in the whole thickness of the patinas by RBS. On the other hand, malachite (see Figs 13.3 and 13.4) is obviously a corrosion product, mentioned as such in Table 13.4.



13.3 Diffraction diagram for the surface of the Venus's black *himation* of the inkpot (the gold peaks may be due to overlap with neighbouring inlays). Acquisition: 0.04 degree steps, 28s per step.



13.4 Raman spectra of the black patina of the inkpot. The upper spectrum (a) corresponds to cuprite and the lower spectrum (b) corresponds to malachite. Raman vibrations at 1380 and 1580 cm⁻¹ on both spectra are characteristic of carbon black. (a) Acquisition time 500 s, four accumulations, power beam 5 μW; (b) acquisition time 50 s, five accumulations, power beam 12 μW.



13.5 RBS spectra on the surface of (a) the Eros's wing patina on the inkpot; (b) the black patina of the feminine statuette. The line --- is the experimental spectrum, others are the simulated spectra.

Concerning the non-patinated areas, the question of corrosion is irrelevant for the Egyptian objects, because the background is patinated and the inlays are made mostly of gold or silver alloys. In the case of the Roman objects,

Table 13.4 Summary of the X-ray diffraction, micro-Raman and RBS in-depth analyses

| Object | Nature of the surface layer | Thickness (at.cm ⁻²) | Estimated thickness (μm) |
|--|---|----------------------------------|--------------------------|
| Harpocrate body | Nantokite + clinoatacamite, trace of Au | 38×10^{18} | 5 |
| Harpocrate lock of hair | Cuprite + clinoatacamite (traces) + Au, Ag | $>10^{20}$ | >20 |
| Sobek counterpoise | Cuprite + Au, Ag | $>10^{20}$ | >20 |
| Statuette robe | Cuprite + chlorides (mostly clinoatacamite) + sulphides | 70×10^{18} | 9 |
| Double aegis counterpoise | Cuprite + Au, Ag | $>10^{20}$ | >20 |
| Inkpot: Venus's and Adonis's <i>himation</i> + Eros wing | Cuprite + Au, Ag + malachite (corrosion) | $>10^{20}$ | >20 |
| Bistoury handle inlay | Cuprite + Ag + malachite (corrosion) | $>10^{20}$ | >20 |

the background (and the red inlays of the inkpot) is covered with the common burial corrosion products of copper-based alloys [17], i.e. cuprite, malachite and sometimes chlorides (mostly atacamite or clinoatacamite) with the common dark-green colour. When the substrate is brass (inkpot body) or a quaternary alloy (bistoury handle), the surface is strongly depleted in zinc, due to the well-known dezincification phenomenon. When the substrate is a bronze (e.g. the inkpot top), the corrosion products are, as expected, enriched in tin and lead. The distinction between intentionally patinated areas and corroded areas is then clear.

It is interesting to mention that nantokite is not very common as a normal corrosion product. This means that the noticeable quantity of that compound found in the patina of the Harpocrate body is not the result of corrosion but more probably due to the intentional patination process.

13.4.3 Analyses of other surface layers

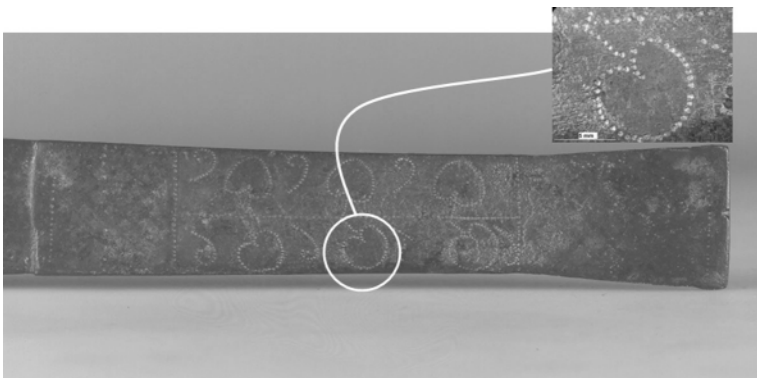
The Roman objects are corroded and an identification of the corrosion layers has been attempted. The corrosion layers of the Cu–Zn surfaces (inkpot body on non-inlaid regions, strigil on non-patinated region, and bistoury on non-inlaid regions) are in fact constituted of common corrosion products usually found on copper alloys: cuprite, malachite and chlorides, without special zinc enrichment. PIXE analysis shows that the surface layers are on the contrary depleted in zinc compared to the bulk alloy. This is a consequence

of the dezincification during the burial time. The other corroded parts, such as the inkpot top and the pure copper inlays present on the inkpot body (boxes, Venus throne, column, etc.), are also covered by a mixture of cuprite and malachite with traces of chloride (clinoatacamite).

One important exception is found on the carved decoration of the strigil handle (Fig. 13.6). The inside of the ivy leaves (and of the athlete figure engraved on the back) exhibits obviously a red-orange and smooth surface aspect, different from the rougher neighbouring regions. Similarly, the lines of the chessboard decoration appearing at both ends of the handle have the same smooth red-orange aspect. X-ray diffraction and micro-Raman investigation show that these regions are covered with cuprite. RBS spectra are characteristic of a cuprite layer of 35×10^{18} at.cm⁻² (i.e. about 4.5 μm) thickness. The areas outside the decoration are covered with normal corrosion products of this kind of alloy, i.e. mainly cuprite plus malachite.

13.5 Discussion

This investigation has shown the extreme variability between several intentionally patinated artefacts recovered from two ancient civilisations. From a first analysis, the majority of them could be considered as belonging to the family of ‘black bronze’ or ‘black copper’ described in the literature. The term ‘black bronze’ may refer at the same time either to a particular surface chemical treatment, the oldest presently known, of copper–gold alloys, or to the particular alloys used as substrate for that treatment. The interest of most research works on those patinas is based on the fact that that process, attested since ancient Egypt of the XVIIIth dynasty (and even much earlier, as early as the Middle Kingdom [5]), appeared also in the Minoan and Mycenaean civilisations during the second millennium BC. It was then successively attested in the Roman world under the name ‘Corinthian bronze’



13.6 The strigil handle.

(*Corinthium aes*) (first to fourth centuries AD), and from the fourteenth century onward in Japan where it is still practised to colour in black sword hilts or inlays of art objects made in *shakudo* (a copper–gold alloy containing 1–4% gold) [6, 18]. Some authors [e.g. 9] even point out the existence of such black patinated copper–gold alloys in India during the first millennium BC, and in China during the first millennium AD.

As far as Egypt is concerned, the difficulty of transcribing the hieroglyphic signs which describe this type of process has led to an evolution of their interpretation. First read as *Bia*, the word was later understood and read as *Hsmn-Km* (literally black bronze); today a third hypothesis is proposed in the light of the new analyses: *Hmty-Km*, literally ‘the black copper’ [7].

Amongst all that world family of ‘black bronze’ or ‘black copper’, the composition of the bulk alloys, copper-based and always containing gold as an addition, may vary: more or less gold content, presence or absence of tin, silver or arsenic intentionally added. One should then more likely speak not of a single recipe on a single alloy, but of a set of recipes on various alloys. The recent analyses of ‘Mycenaean daggers’, probably of Minoan origin [19], tend to prove that some ‘true’ bronzes (containing tin) have been alloyed with gold in order to be patinated in dark brown. Moreover, recent comments from a translation of the Zosimos manuscript, the Panopolis alchemist, preserved in the University Library in Cambridge, mention that as early as the third century AD, several chemical treatment recipes were known, at least for darkening Corinthian bronze [20, 21]. This variety is not surprising if one takes into account the varieties of periods and civilisations, and the present investigation is a full demonstration of that concept. In all cases, however, the black patina of ‘black bronze’ or ‘black copper’ has been described, when it has been analysed, as constituted of pure cuprite [6]. All authors agree on the fact that the cuprite contains gold.

This procedure of intentional patination has to be clearly distinguished from the modern (post-Renaissance) colouring recipes described in several books and publications. Although chemicals are used in both cases, the procedure is entirely different. As explained in the introduction, ancient craftsmen were aiming to polychrome decoration by using different metals and alloys and probably a limited number of chemical patination recipes, whereas modern founders usually use one bulk alloy and various recipes.

The four Egyptian objects analysed here all exhibit black patination, always on the background, but they are done with different alloys (Table 13.1): a copper–tin–gold–silver alloy for the Sobek counterpoise and for the double aegis counterpoise, but with different alloying element concentrations; a lead bronze without gold and silver addition for the feminine statuette; a copper–gold alloy with a high gold content for the Harpocrate figurine body; and probably (because only analysed across the patina) an 8% tin bronze with small gold addition for the Harpocrate lock of hair. The composition

and structure of the different patinas are also quite different: all are constituted mainly of cuprite, except for the Harpocrate body patina which is very different. This last patina is made of chloride, and is strongly depleted in gold compared to its substrate. The statuette patina does not contain any gold or silver.

So, at least the patinas of the Harpocrate body and of the feminine statuette are entirely different from what is usually described as *hmty-km*. One may compare the problem of the Harpocrate body patina with what has been recently observed on another famous Egyptian artwork, the statue of Karomama [8, 22]. On that statue, it was observed that some black patinated inlays are also made of a gold-rich copper–gold alloy. This is the first mention in the literature. The results of that extensive study are detailed in a forthcoming publication [22]. A gold-rich black patinated inlay was found and analysed on the robe of the statue.

The feminine statuette studied here belongs to a category also not mentioned in the literature to our knowledge. The bulk metal does not contain gold, but it is still patinated in black.

The black patinated inlays of the Roman inkpot seem to be more ‘common’, and should be considered as belonging to the *Corinthium aes* family. But when one compares the patinas of the Roman objects, it must be noted that one (the Venus’s *himation* and Eros’s wing patina of the inkpot) contains more silver than gold and no tin, whereas the other (the bistoury handle inlay) contains tin, no gold and a small amount of silver. The background is never intentionally patinated. All those patinas are moreover much thicker (5 μm to more than 20 μm) than the later Japanese *shakudo* patina, which is known to be as thin as 1 to 2 μm [18].

In addition, a new kind of intentional patination was found on the Roman strigil handle decoration. This kind of red-orange patina has never been mentioned to our knowledge in the literature. At the present state of investigation, it is not possible to speculate on the recipe used to achieve this coloration. From the physico-chemical viewpoint, the non-patinated areas are not very different from the patinated ones; it is the surface roughness which is the key criterion of distinction. These important observations are discussed in a forthcoming publication [23].

Table 13.5 summarises the main conclusions of this study. It is thus clear that the antique metalworkers were using various chemical recipes and various alloys to obtain coloured effects on the surfaces of their bronze works of art. A surprising observation is that, in spite of being buried for such long periods, those patinas have been preserved from corrosion degradation. One possible explanation, proposed by some authors [24] and confirmed by one sentence in the recent translation of the ancient manuscript of Zosimos [20], is that the black patination of copper–gold alloys may spontaneously reappear after mechanical destruction. Another explanation could be an exceptional resistance

Table 13.5 Summary of the results

| | | |
|-------------------------------|---------------------------|--|
| 'Common' dark patina | | |
| <i>Egyptian:</i> background | Harpocrate lock of hair | Cuprite + Au + Ag |
| | Sobek counterpoise | Cuprite + Au + Ag |
| | Double aegis counterpoise | Cuprite + Au + Ag |
| | <i>Roman:</i> inlays | Cuprite + Au + Ag |
| | Inkpot inlays | Cuprite + Au + Ag |
| | Bistoury handle inlay | Cuprite + Ag |
| 'Uncommon' dark patina | | |
| <i>Egyptian:</i> background | Harpocrate body | Nantokite + clinoatacamite |
| | Feminine statuette | Cuprite + chlorides + sulphide (no Ag, Au) |
| 'Uncommon' red patina | | |
| <i>Roman:</i> direct patina | Strigil handle | Cuprite |

to the environment, a passivating effect with the modern significance of that word. The interpretation of this surprising stability has yet to be found, and further laboratory experiments would be of great help for this interpretation.

13.6 Conclusions

This comprehensive study of the patinated surface found on various objects of different origins and periods, from ancient Egypt to the Roman Empire, has shown that it is possible by laboratory non-destructive investigations to obtain a precise physico-chemical description of the surface layers intentionally elaborated for the purpose of coloration.

The distinction between intentional patina and pure corrosion products remains a challenge in the general case. The present investigation has been greatly facilitated from that viewpoint by the active collaboration between the authors in charge of the physico-chemical analyses and those (museum curators, conservation–restoration experts) who brought the iconographic, historical and archaeological insights. The result of that collaboration is that intentional patination and burial corrosion products could be clearly distinguished. But it must be kept in mind that the present study does not bring any universal recipe to identify without doubt all intentional patina. Other kinds of intentional patina could have been present on archaeological objects and have been degraded or even entirely destroyed by corrosion during burial. Further investigation is necessary to continue to list the possible criteria for tracing human intervention on ancient copper alloy artefacts.

The results show that the often black coloration on copper-base alloys is obtained by various chemical treatments, some only oxidising, some bringing other compounds as chlorides and sulphides, applied to various copper alloys.

The base substrates may range from simple copper–gold binary alloys with a low gold content to leaded bronze containing no gold. A black intentional patina has been observed on a copper–gold alloy containing a high gold content, but the oxide layer is depleted in gold, in contrast to what is observed for Egyptian *hnty-km*, Roman *Corinthium aes* and also Japanese *shakudo* patinas. Another variable is the thickness, ranging from 1 μm for *shakudo* patina to more than 20 μm for most of the patinas investigated here.

An intentional patination with a red-orange coloration has been observed and analysed for the first time on a Roman object. This observation proves that chemical recipes other than ‘black copper’ were known by the antique craftsmen, at least at the Roman Empire period.

One may suppose that many other occurrences of intentional metal coloration in the ancient world will be reported in the future. The present observations and investigations should encourage research into intentional chemical treatments on archaeological objects.

It is desirable to conduct more laboratory experiments in order to attempt to reproduce the observed surface effects on various alloys. Such experiments are also necessary to understand the physical mechanisms of the observed colours and the reason for their surprisingly good conservation over very long periods of burial.

13.7 Acknowledgements

This study forms part of the Doctorate thesis of one of the authors (FM). The authors wish to thank the Louvre Museum for providing the objects, Benoît Mille (C2RMF) for alloy sampling and analyses, the C2RMF photographer Dominique Bagault and radiologist Thierry Borel, and the technical team of the AGLAE accelerator.

13.8 References

1. Piebald Babylonian bull, Department of Oriental Antiquities, Louvre Museum, inv. AO 2151.
2. J.D. Cooney, On the meaning of *Hsmn-Km*, *Zeitschrift für Ägyptische Sprache und Altertumskunde*, 93 (1966), 43–47.
3. W. Bray, Techniques of gilding and surface-enrichment in pre-Hispanic American metallurgy, in: *Metal Plating and Patination*, ed. S. La Niece, P. Craddock, Butterworth, London (1993), pp. 182–192.
4. B. Mille, P. Callet, A. Zimla, A. Benoit, Une gueule d’argent en plomb, métallurgie expérimentale et virtuelle pour découvrir un procédé d’argenture antique, *Alliage*, no. 53–54 (2004), 124–134.
5. A. Giumlia-Mair, Das Krokodil und Amenemhat III aus el-Faiyum, *Antike Welt*, 27 (1996), 313–321.
6. P. Craddock, A. Giumlia-Mair, *Hsmn-Km*, Corinthian bronze, *Shakudo*: black-patinated

- bronze in the ancient world, in: *Metal plating and patination*, ed. S. La Niece, P. Craddock, Butterworth, London (1993), pp. 101–127.
7. A. Giunla-Mair, S. Quirke, Black copper in bronze age Egypt, *Revue d'égyptologie*, 48 (1997), 95–108.
 8. M. Aucouturier, E. Delange, M.-E. Meyohas, Karomama, Divine Adoratrice d'Amon; son histoire, sa restauration, l'étude en laboratoire, *Techné*, no. 19 (2004), 7–16.
 9. A. Giunla-Mair, P. Craddock, *Corinthium Aes, das schwarzen Gold des Alchimisten*, Von Zabern, Mainz (1993).
 10. F. Willer, Fragen zur intentionellen Schwarzpatina an den Madhia Bronzen, in: *Cat. expo. Das Wrack. Die antike Schiffsfund von Madhia*, Rheinland-Verlag GmbH, Köln (1994).
 11. F. Mathis, S. Descamps, D. Robcis, M. Aucouturier, Laboratory investigation of inlays and surface treatments for the decoration of copper-base alloy objects from the Imperial Roman period, *Int. Conf. Archaeometry 2004*, Zaragoza, May 2004, to be published.
 12. D. Bougarit, B. Mille, The elemental analysis of ancient copper-based artefacts by ICP-AES: an optimised methodology reveals some secrets of the Vix crater, *Meas. Sci. and Technol.*, 14 (2003), 1538–1555.
 13. J.-C. Dran, T. Calligaro, J. Salomon, Particle-induced X-ray emission, in: *Modern Analytical Methods in Art and Archaeology*, ed. E. Ciliberto, G. Spoto, Wiley, Chichester (2000), p. 135.
 14. E. Ioannidou, D. Bourgarit, T. Calligaro, J.-C. Dran, M. Dubus, J. Salomon, P. Walter, RBS and NRA with external beams for archaeometric applications, *Nuclear Instruments and Methods in Physics Research B*, 161–163 (2000), 730–736.
 15. M. Mayer, SIMNRA © Max-Planck-Institut für Metallphysik, www.rzg.mpg.de/~mam/ (1997–1998).
 16. F. Mathis, L. Pichon, B. Moignard, O. Dubreuil, J. Salomon, Particle detection at high retrodiffusion angle in external beam mode: a new experimental device with annular particle detector and application to a 6MeV $^4\text{He}^{2+}$ beam in coupled PIXE and RBS, *Int. Conf. ECAART 2004*, Paris, September, 2004.
 17. L. Robbiola, J.-M. Blengino, C. Fiaud, Morphology and mechanisms of formation of natural patinas on archaeological Cu–Sn alloys, *Corrosion Science*, 40 (1998), 2083–2111.
 18. R. Murakami, Japanese traditional alloys, in: *Metal plating and patination*, ed. S. La Niece, P. Craddock, Butterworth, London (1993), pp. 85–94.
 19. K. Demakopoulo, E. Mangou, R.E. Jones, E. Photos-Jones, Mycenaean and black inlaid metalware in the National Archaeological Museum, Athens. A technical examination, *Annual of the British School of Athens*, 90 (1995), 137–153.
 20. E.C.D. Hunter, Beautiful black bronzes: 'Zosimos' treatises in Cam. Mm 6.29, in: *I Bronzi Antichi, Atti del XV Congresso Internazionale*, Università di Udine, 22–26 May 2001, pp. 655–660.
 21. A. Giunla-Mair, Zosimos the alchemist-manuscript 6.29, Cambridge, metallurgical interpretation, in: *I Bronzi Antichi, Atti del XV Congresso Internazionale*, Università di Udine, 22–26 May 2001, pp. 317–323.
 22. E. Delange, M.-E. Meyohas, M. Aucouturier, The statue of Karomama, a testimony of the skill of Egyptian metallurgists in polychrome bronze statuary, *J. Cultural Heritage*, to be published (2005).
 23. F. Mathis, S. Descamps, M. Aucouturier, D. Robcis, An original surface treatment of copper alloy in ancient Roman Empire: chemical patination on a Roman strigil, *18th*

Int. Conf. on Surface Modification Technologies, SMT 18, Dijon, France, November 2004, *Surface Engineering*, to be published (2005).

24. A. Giunlia-Mair, M. Lehr, Experimental reproduction of artificially patined alloys, identified in ancient Egyptian, Palestinian, Mycenaean and Roman objects, in: *Archeologie Sperimentali, Atti del Convegno*, Trento (Italy), September 2001, pp. 291–302.

Tin and copper oxides in corroded archaeological bronzes

P. PICCARDO, Università di Genova, Italy and B. MILLE, Centre de Recherche et de Restauration des Musées de France, and L. ROBBIOLO, ENSCP, France

14.1 Introduction

Tin bronzes have been materials in common use since archaeological times. From the 'Bronze Age' (beginning of the second millennium BC in Western Europe) to the present day they have been one of the most utilised metallic alloys [1]. For many years, characterisation of their corrosion products has been conducted in order to define conservation strategies and to improve restoration procedures. Many factors, such as the composition and microstructure of bronzes and the corrosive environment features of the burial context, can influence the chemical and structural nature of patinas. In general, the corrosion compounds have been roughly identified by X-ray diffraction (performed on the surface directly or on powder produced from the patina). In contrast, modelling the corrosion mechanisms of ancient bronzes is a more recent research topic. Investigation at the microscopic level is in fact required, since bronze corrosion exhibits complex and heterogeneous structures. Nevertheless, it is now established that patinas of ancient bronze objects reveal numerous common morphological features such as the presence of tin-enriched corrosion layers. Furthermore, the formation process of bronze patinas in natural environments is mainly related to a selective dissolution of copper as suggested in refs [2–7]; this decuprification phenomenon is connected to an internal oxidation of the alloys [8–10]. For ancient and historical metals this was evidenced more than 50 years ago [2, 8, 11, 12] and, more recently, for synthetic bronzes artificially corroded in aqueous solutions [9, 10, 13, 14].

The understanding of bronze patinas is most often based on two types of corrosion structures, according to the presence or absence of an original surface preserving the original shape of the artefact. This will be introduced and detailed in the first part of this chapter. For both types, an internal tin-enriched layer, often linked to a remnant metallurgical structure of the alloy, is usually evidenced, mainly connected to the presence of oxide compounds containing tin and copper. Models describing the structure and mechanisms

of bronze alteration have been set up mainly using optical microscopy combined with SEM-EDX microanalysis on metallographic sections [2, 5, 15]. However, the corrosion compounds are never fully identified and these models need to be refined. A major challenge, amongst those currently existing, is to characterise the compounds where both Sn and Cu are present. Determining whether they are separate tin oxides (or hydroxides) mixed with copper compounds or combined copper–tin products is not a simple task using these characterisation techniques. Therefore, one of the main goals of this study will be to obtain a structural characterisation of the nature of the corrosion compounds of internal tin-enriched corrosion layers in the case of ‘type 2’ patinas. In addition to the classical approaches (optical and electron microscopy, elemental analysis), we will also use Raman microspectroscopy and X-ray microdiffraction in order to get a structural analysis of the compounds with a lateral resolution at the microscopic level. The results achieved will be discussed in the frame of a better understanding of bronze corrosion mechanisms.

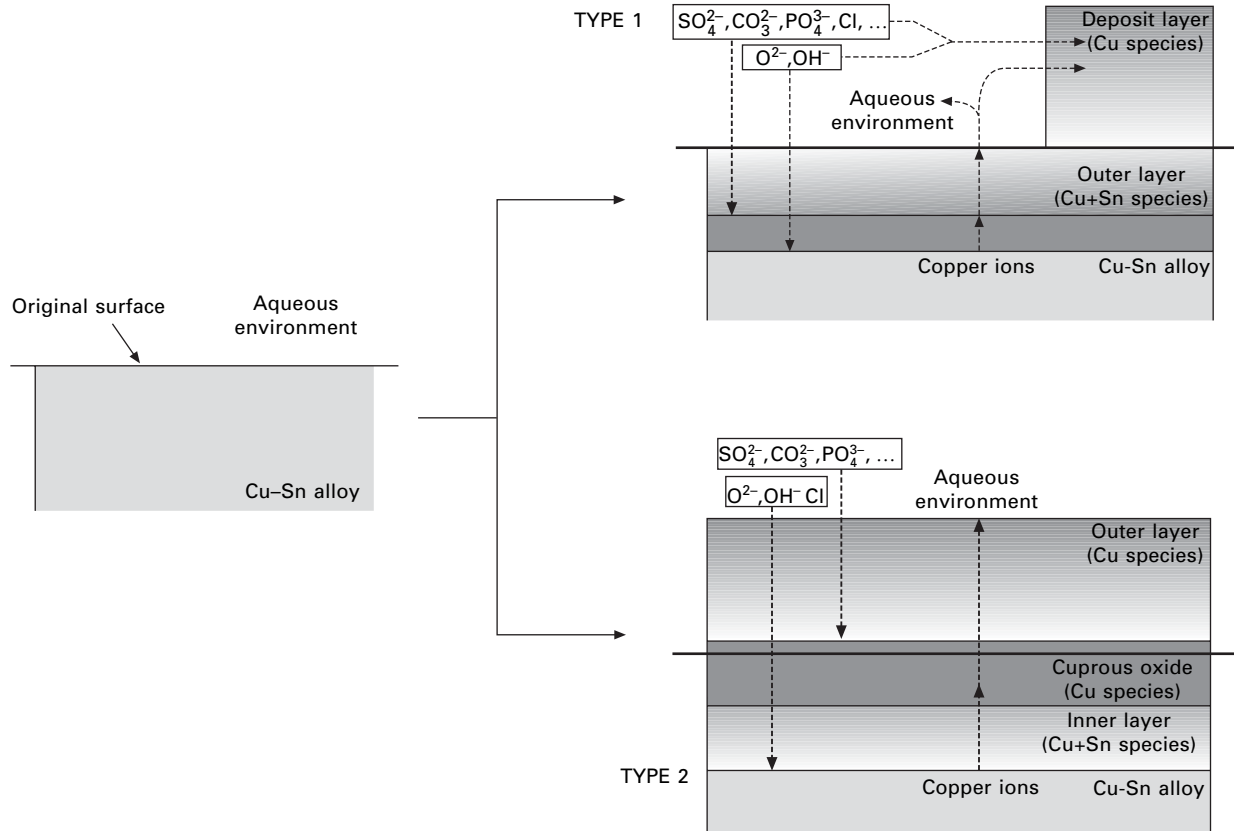
14.1.1 Bronze corrosion structures – general presentation

As previously mentioned, the description of tin-bronze patinas is most often based on two main types of corrosion structures, according to the presence or absence of an original surface (marker layer) preserving the original shape of the artefact [8, 16]. They are schematically depicted in Fig. 14.1.

In the first type (type 1), the original surface is visible or simply concealed by copper-containing deposits. The patinas are characterised by tin-enriched corrosion layers due to copper depletion. Usually two layers can be distinguished: (1) an outer layer containing tin species and copper(II) hydrated and/or hydroxyl compounds such as hydroxycarbonate, hydroxysilicate or hydroxysulphate according to the nature of the corrosive environment, and (2) an inner layer, characterised by a lower Sn/Cu ratio than the outer one and containing mainly copper hydroxyl and oxide compounds.

For the second type of structure (type 2), when the original surface has been destroyed or deformed by severe corrosive attacks (e.g. pits, crevices, lamellar corrosion, etc.), a much more complex and thicker structure than the previous one is observed. It can be described by a three-layer structure characterised by (1) a layer of copper-containing compounds in the external part (cupric species), (2) a cuprous oxide beneath, and (3) an inner layer. This last layer usually reveals metallic ghost structures, and is characterised both by a selective depletion of copper, due to a decuprification process, and by a relative enrichment in Cl content at the alloy/corrosion interface.

The first type, also previously described as the ‘standard nature’ of bronze patina [17], corresponds to a ‘noble’ patina [18] with or without deposits on it. It has some remarkable protective properties [19] and is equivalent to a



14.1 Schematic representation of the two main types of corrosion features found on archaeological bronzes.

thick passive layer (typically from 10 to 100 μm). Type 2, which exhibits 'coarse' surfaces, is close to the 'vile' patina described by Gettens [18]. It corresponds to a barrier layer due to localised or non-uniform generalised corrosion.

From a practical point of view, both structural types are usually observed on the same artefact with amplitudes which may vary from one area to another. Several variations (deviations) from these models can often be found. They have been detailed in ref. [8] and will be mentioned only briefly here. For type 1, the inner layer can be very thin or discontinuous – as often observed for dendritic structures of cast alloys – or, conversely, can cover some extensive areas due to either localised extension or internal mechanical breakdown. For type 2, the first case of deviation affects the copper-containing layers which can exhibit a complex stratified corrosion as described by Scott [20] for Egyptian artefacts or by Robbiola *et al.* [21] for Bronze Age objects. A second case of deviation is related to a local transformation of type 1 in type 2 structure, leading to a shift of the initial tin-enriched layer up in the outer copper-containing layer. Another case is the fragmentation of the cuprous layer which may appear disrupted and not continuous, often in connection with the presence of cuprous chloride in the inner layer. Finally, intensified corrosion can lead to an intensive and thick inner layer leading to zoning or to an important inter- or transgranular corrosion. This last case of deviation is of particular interest as the phenomena observed on bronze are in fact over-expressed and the tin and copper corrosion compounds can be more easily investigated.

Even though these structural types exhibit different features, both involve migration processes through the corrosion layers, with anions migrating inward and cations outward. In both types also selective dissolution of copper (i.e. decuprification) is evidenced while tin compounds always remain acting as a stabilising structural agent of the patinas. Applying the fact that corrosion is a physico-chemical response of the material to the environment solicitations, the amount of released copper ions is related to the corrosiveness of the context (e.g. soil, atmosphere, and so on). For example, in moderately aggressive media (i.e. soil, urban atmosphere, lake water, etc.), it is found that, in the outer layer, the remaining copper content is only about 6% of the total copper atoms initially present in the α -bronze [8]. It is expected that the more severe the corrosive conditions are, the more the copper is dissolved and, consequently, the higher is the Sn/Cu ratio in the patina.

Until now these results have not often been mentioned in the literature as tin compounds are poorly crystallised or amorphous and cannot be evidenced by the usual methods of characterisation such as X-ray diffraction or infrared spectroscopy. One wonders whether the presence of tin compounds contributes to the corrosion resistance of the bronzes. Work has been proceeding on the corrosion phenomena on these alloys and several conclusions have been

found which sometimes are contradictory. On ancient Chinese mirrors, some authors have identified a particularly stable form of a mixed tin–copper oxide ($\text{Sn}_{1-x}\text{Cu}_x$, where $x =$ about 0.16 [4, page 101] or $\text{Sn}_{1-x}(\text{CuFePbSi})_x\text{O}_2$ with cassiterite structure [22]). Others [8, 17, 23] suggested that only insoluble tin oxide ($\text{SnO}_2 \cdot x\text{H}_2\text{O}$) which could be mixed with Cu-containing compounds is responsible for the corrosion resistance of these alloys. However, in both cases, a clear and precise identification of the corrosion compounds of tin–copper alloys is missing and their relationship with the corrosion structure must also be investigated.

14.2 Materials and methods

The investigations were performed on three fragments of Etruscan bronze artefacts (5th–3rd centuries BC):

- a chip sampled from the wall of a fragmented kyathos vase (K4), located where the handle was soldered, and a sample from the edge of a metallic mirror (MIR1), both found in the archaeological site of Musarna (Viterbo, Italy) [24] by the Ecole Française de Rome;
- a fragment from the handle of a kyathos from the archaeological museum of Monterenzio [25] (KM).

The K4 and MIR1 archaeological specimens were prepared according to the common metallographic procedure and polished up to a diamond suspension of 0.25 μm . By cutting and polishing the previous enrobed samples, thin cross-sections of about 30 μm thickness were also obtained for microdiffraction. The KM specimen (completely mineralised) was fractured in order to obtain two fragments, one to be used for the fractographic characterisation (mainly by SEM-EDXS) and the other to produce powders (once the external greenish compounds were eliminated) for XRD investigation.

The following instrumentations were used. Optical microscope: Leica MEF4 Dark-Field equipped (DF-OM); Scanning Electron Microscope: Cambridge Stereoscan 200 coupled with an Energy-Dispersive X-ray microprobe Link Pentafet sensitive to elements with atomic weight $>\text{Be}$ (SEM-EDX); X-ray diffractometer (Bragg Brentano type): Philips X'pert with Cu $K\alpha_1$ wavelength; Raman microspectrograph: Jobin-Yvon Infinity; synchrotron X-ray microdiffraction conducted on the D15 beamline at LURE (14 keV photons focused down to a $20 \times 20 \mu\text{m}$ beam). The quantitative EDXS analyses were performed using pure Cu, pure Sn and O from Al_2O_3 as reference standards.

The use of DFOM, as explained in ref. [26], allows one to differentiate the main corrosion products of copper alloys by their colour, with a sensitivity higher than using the more classical light source. The DF observation is especially useful to select the areas to be analysed through other analytical

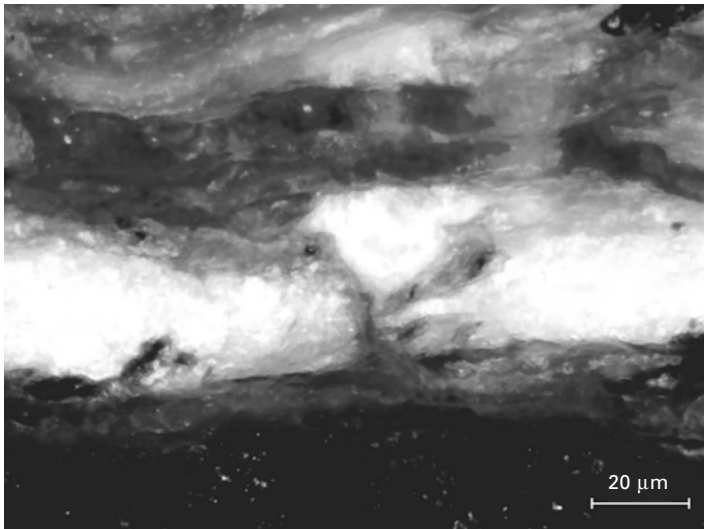
techniques such as Raman microspectroscopy or synchrotron X-ray microdiffraction.

Prior to the Raman characterisation of the corrosion products, Raman spectra were collected from reference synthesis compounds [27] representing the most common tin and copper products encountered in bronze corrosion [12]. The reference Raman spectra obtained showed good agreement with those published following similar ongoing projects on copper alloys corrosion [28–30]. Spectra obtained here will be presented without any baseline subtraction, as fluorescence appeared to provide valuable information for cuprous oxide.

14.3 Characterisation of the internal corrosion layers containing oxides

14.3.1 General presentation of the studied specimens

The three fragments studied exhibit corrosion structures coherent with the type 2 model previously described (Fig. 14.1), but with different amplitudes of corrosion. They are covered by greenish products, mainly carbonates and silicates relative to the archaeological environment. In the case of the K4 and KM samples, whitish areas due to the corrosion of the solders are also visible on the surface. K4, in particular, shows a stratification where dark and white compounds alternate with each other (Fig. 14.2). The white compounds from the KM fresh fracture were powdery and therefore a small

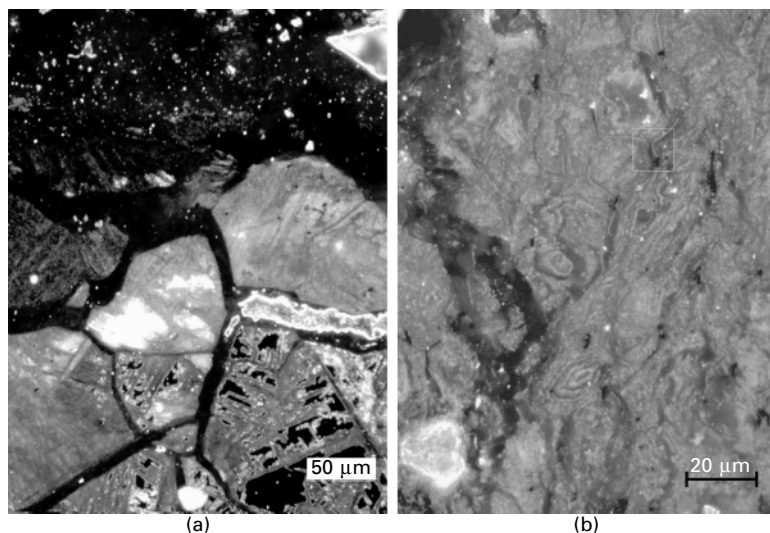


14.2 DFOM, sample K4. Red products (top of the micrograph) are Cu(I) oxides, white parts are Sn(IV) oxides and brown areas (bottom of the micrograph) are Sn(II) oxides.

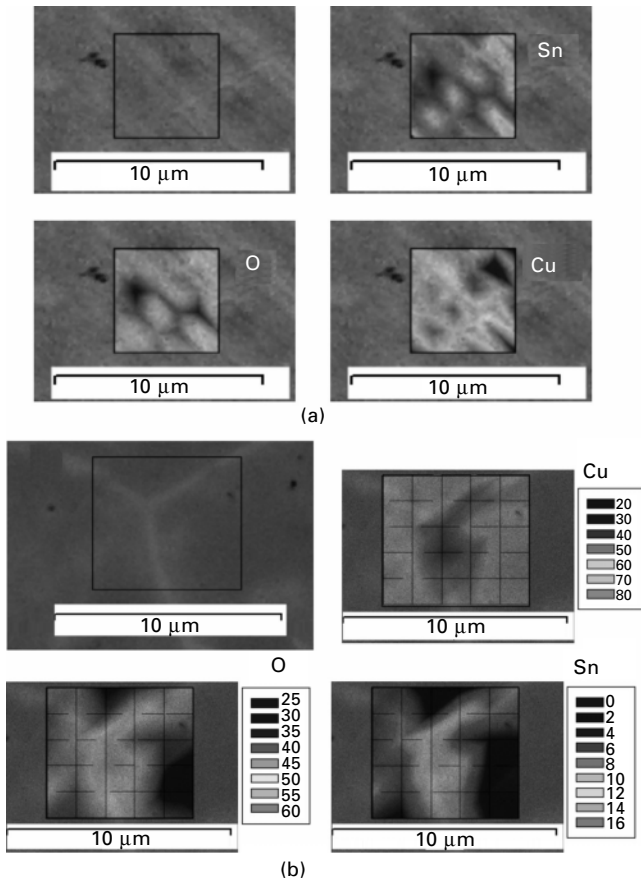
quantity was collected to be studied separately by Raman spectroscopy and EDXS. Under the outer layer a strongly disrupted cuprous oxide layer, was observed on the mineralised metallic matrix (inner layer). The inner layer is composed mainly of oxides which exhibit different colours: from red to orange and yellow (Fig. 14.3).

Sound metal areas remained on the MIR1 sample only: it is a high-tin α -bronze, 15 wt%, which is characterised by a microstructure typical of homogeneously cold-deformed material after recrystallisation annealing. The K4 original alloy, analysed by EDXS on a non-mineralised part of the vase, is an α -bronze containing 10–11 wt% of Sn, slightly and inhomogeneously cold-hardened after annealing (see Fig. 14.4). Both artefacts also contain copper sulphide inclusions, probably a heritage from the original copper ores. The microstructural information from the studied KM fragment, completely mineralised, was achieved by the ghost microstructure only.

As often observed in archaeological Cu–Sn artefacts showing type 2 corroded areas [31], K4, despite its complete mineralisation, and MIR1 within corroded areas, exhibited ghost microstructures maintaining the microstructural features of the original alloys. As shown in Fig. 14.3(a) and (b), decuprification appears to start on the grain boundaries, which have a higher reactivity than the metallic matrix of the grains [32]. Then, it extends to the grains following the mechanical twins edges and the thermal twins borders (Fig. 14.4(a)). In this way the original microstructure is revealed and, in the absence of secondary corrosion processes such as mechanical breakdown or internal evolution due to chlorides, it remains fossilised. The effect of a residual microsegregation

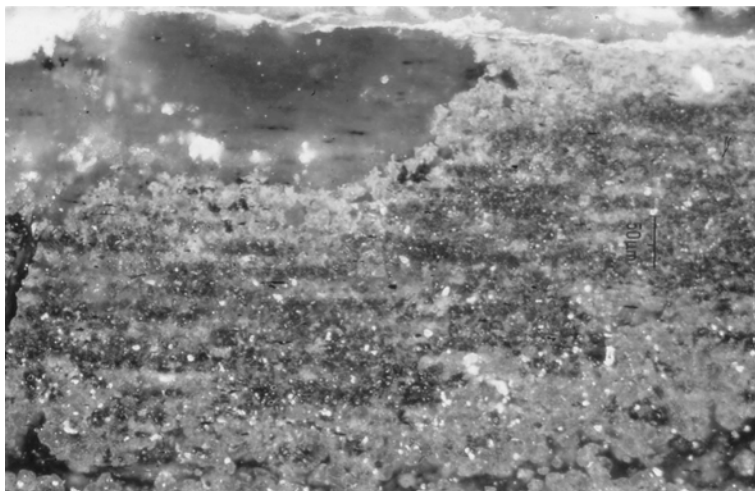


14.3 DFOM: (a) sample MIR1; (b) sample K4 (dark areas are coloured red; grey areas are coloured orange/yellow).



14.4 Quantitative maps of distribution of the elements achieved by EDX spectrometry (at%) on corroded areas presenting ghost microstructures: (a) corresponding to MIR1 (detail of Fig. 14.3(a)); (b) corresponding to K4 (detail of Fig. 14.3(b)).

of Sn is sometimes evidenced by DFOM on the internal corrosion layers, as in the example presented in Fig. 14.5. Here, the residual heterogeneity of the solid solution due to the initial primary segregation of tin reduced and distorted (assuming the typical band shape) during the thermomechanical deformation of the bronze, is revealed by the presence of colour shades (dark orange and yellow). This sensitivity of the corrosive attack to a gradient in tin content has often been observed in as-cast materials (where the heterogeneity is at the highest degree) but more rarely in wrought bronzes in which the tin gradient can be detected only by tint etching [33] and not by SEM-BSE observation.



14.5 DFOM. Cross-section of a mineralised bronze sheet sampled from a Celtic situla. The blue area (top left corner) shows carbonates containing copper sulphide inclusions (black lines), the rest of the micrograph shows alternate shades of colour showing a linear distribution between dark yellow-orange and brown colours. It corresponds to the fossilised residual solid solution heterogeneity of the original metallic matrix, and is coherent with the direction of the mechanical deformation of the metal.

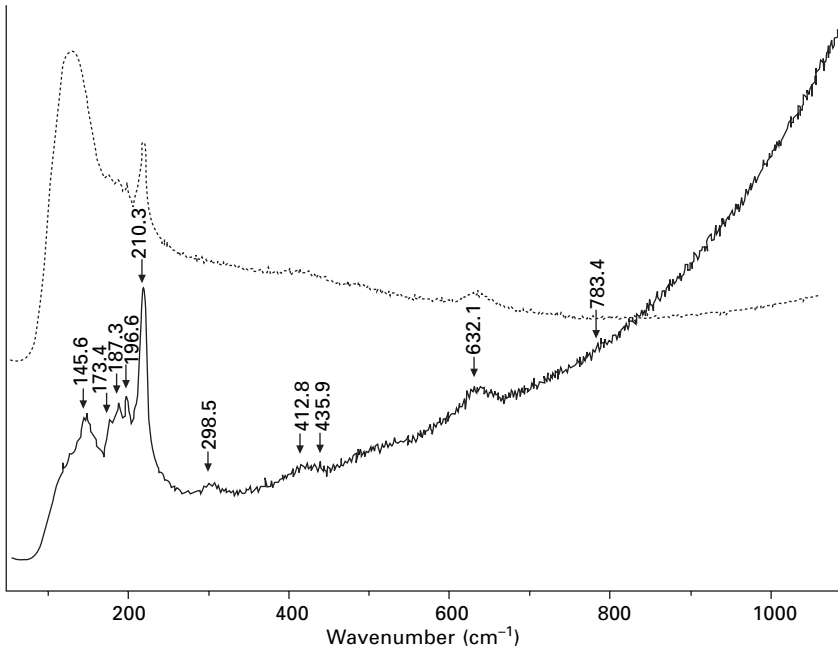
14.3.2 Copper oxides

The red-coloured, stiff and dense compounds found in the metallographic cross-sections (as shown in Figs 14.2 and 14.3) correspond to Cu(I) oxide, the main product found in corroded ancient bronzes [12]. Raman spectroscopy (Fig. 14.6) confirmed this result, despite the variation of the oxygen content measured by EDXS which ranges between 30 and 37 at%. When the measured stoichiometry corresponds to cuprous oxide, the colour observed by DFOM darkens and the crystal becomes translucent. The cuprous oxide can assume its typical cubic morphology [34, 35] when it crystallises in a hollow space such as cavitations or porosities, as shown in Figure 14.7.

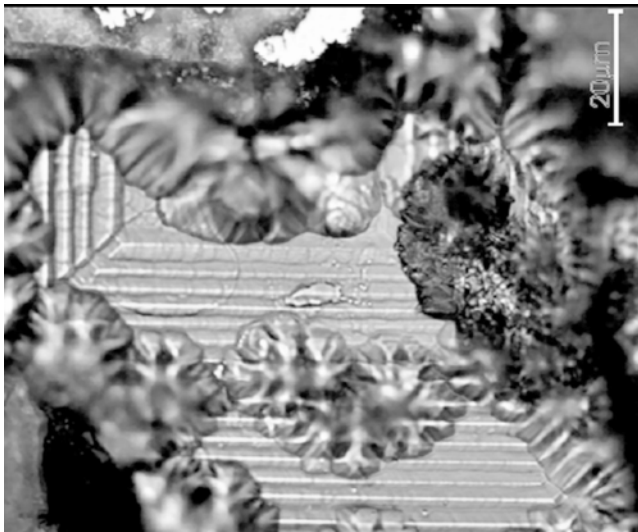
Small amounts of Sn (<2 at %) could be measured by EDXS, and might be attributed to a low solubility of Sn cations in Cu oxide. It is known [34–36] that Cu(I) oxide can receive in its lattice other cations, maintaining its crystallographic structure.

14.3.3 Tin oxides

The K4 and KM samples exhibited on their surface the rest of the tin-soldering alloy (with traces of Pb for K4), completely mineralised. In the



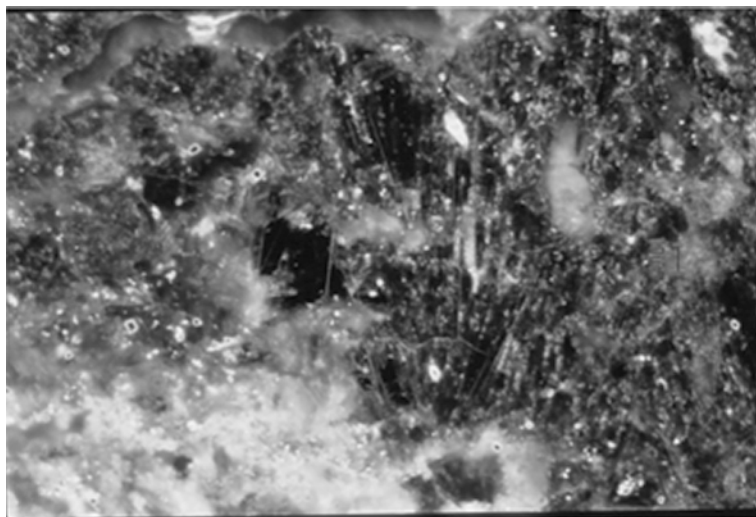
14.6 Raman spectrum typical of cuprous oxide (WL exciting line: 633 nm). Dotted line: red translucent crystal from MIR1 sample. Black line: synthesis cuprous oxide (Prolabo).



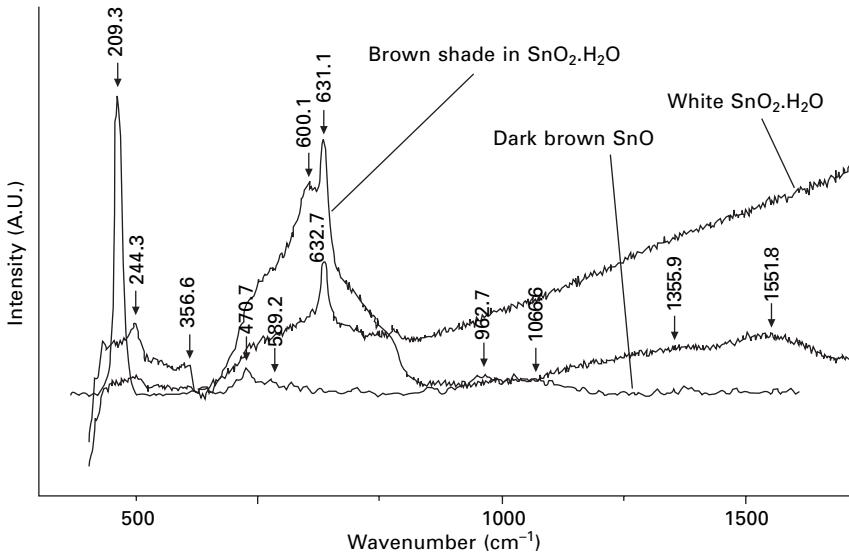
14.7 DFOM. A grain of cuprous oxide slightly etched. The lines correspond to the 100 planes.

solder, in particular, alteration compounds containing tin without copper were found and studied. The tin oxides found in these two specimens are either dark brown or white (Fig. 14.2):

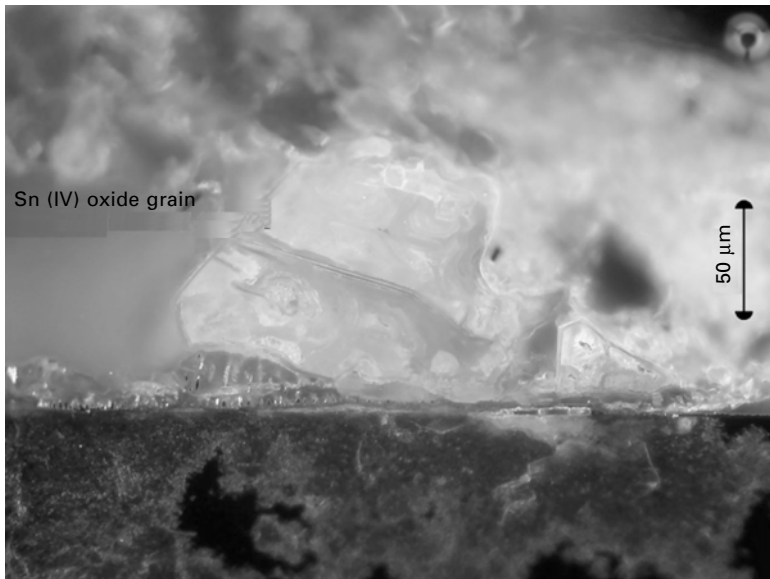
- Dark brown products, mainly observed in the K4 sample, presented a well-defined ghost microstructure (Fig. 14.8) and surround or infiltrate the lacteous white areas. These compounds were identified as Sn(II) oxide by Raman spectroscopy (Fig. 14.9) and elemental composition. It is known that this compound is unstable at high temperatures [37] and, under the excitation of laser power, reacted to a more stable form, up to Sn(IV) oxide in some cases. Using reduced acquiring time and adequate filters, it was possible to overcome the difficulties on the single phase layers (spectra from archaeological and synthetic products). Nevertheless, when spectra were acquired from the brown veins in Sn(IV) oxides the results were of uneasy interpretation [38]. The resulting spectrum, reported in Fig. 14.9(a), shows a predominant presence of Sn(IV) oxide, but some supplementary weak peaks, only partially resolved, are to be noted. Given the fact that tin and oxygen are the only elements detected by EDXS, these brown zones probably also include an unidentified tin compound in addition to the Sn(IV) oxide.
- White zones could be either well-formed crystals (Fig. 14.10) having a polygonal shape coherent with the crystal lattice (found mainly in the KM specimen) or aggregates of crystals too fine to be observed (Fig. 14.2).



14.8 DFOM. Detail of the stannous oxide area showing a ghost microstructure. Orange compounds (grey coloured areas in the micrograph) contain both Cu and Sn and are immersed in a white stannic oxide matrix.



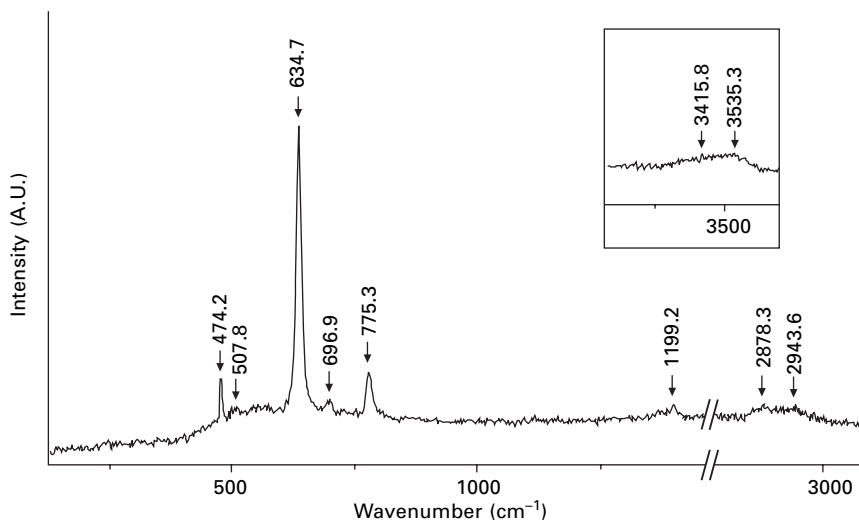
14.9 Raman spectra acquired in the white, dark brown and brown shades of Fig. 14.2. WL exciting line 532 nm.



14.10 DFOM. An example of a macro crystal of stannic oxide in the solder zone. The lower part is the bronze matrix showing its typical corrosion.

They correspond to stannic oxide and give Raman spectra which always show the typical peak around 632 cm^{-1} (Fig. 14.9). However, several factors seem to affect the Raman spectra of the stannic oxide, such as polarisation or surface effect, crystal size and shape, and hydration [38–40]. It was possible to observe two large peaks (Fig. 14.11): the first is at $2800\text{--}3000\text{ cm}^{-1}$, always present, and should correspond to crystallisation water [41]; the second, around 3500 cm^{-1} , was found only on some specimens and might be correlated to the hydrophilic behaviour of stannic oxide [41, 42]. These observations are also supported by the oxygen content measured by EDXS: if the analyses are performed on well-formed grains (Fig. 14.10), it is close to the atomic ratio Sn/O, i.e. 1:2; if aggregated areas are taken into account (Fig. 14.2) there is an increase in the O content (until Sn/O = 1.3) due to the contribution of water of crystallisation. Such a compound could therefore be written as $\text{SnO}_2\cdot\text{H}_2\text{O}$.

Very small amounts of Cu (i.e. $<2\%$) were found in areas close to the bronze matrix. According to the literature [43] this could be explained by the solubility of few Cu^{2+} ions into the Sn(IV) oxide lattice by substitution of Sn ion sites, since the ionic radius for Sn^{4+} (0.71 \AA) is very close to that of Cu^{2+} (0.72 \AA) [44]. Cu amounts above 7 at% will form some Cu oxide crystals mixed up in the SnO_2 lattice [43, 45].

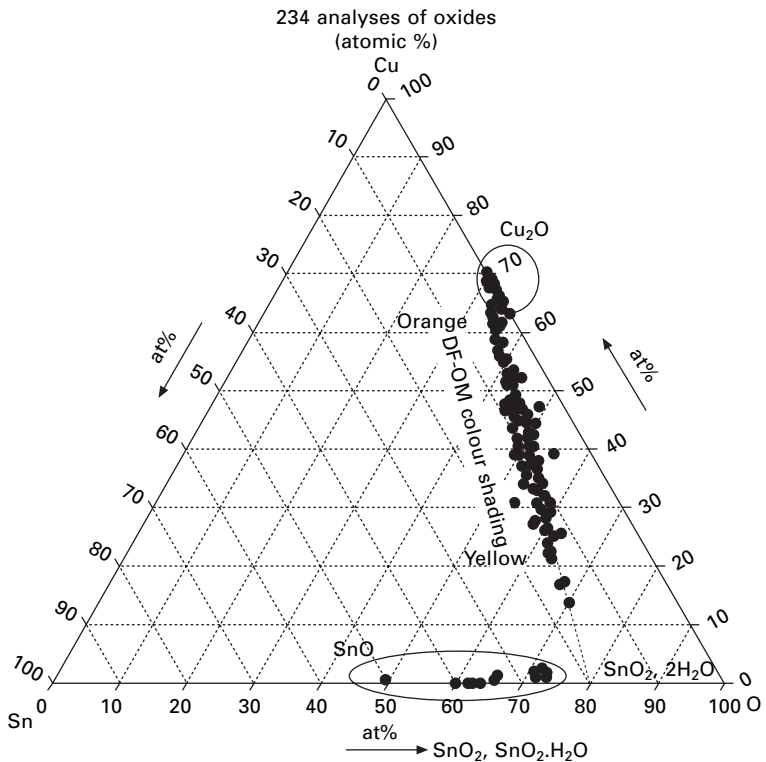


14.11 Raman spectrum of the hydrated stannic oxide (SnIV). WL exciting line 633 nm. Peaks in the $2800\text{--}3000\text{ cm}^{-1}$ region, always present, should correspond to crystallisation water, whereas a large peak around 3500 cm^{-1} found only on some specimens might correspond to the hydrophilic behaviour of stannic oxide.

14.3.4 Oxide areas containing both copper and tin

In this section, we will focus on the inner layers of the type 2 corrosion structure which correspond to areas exhibiting colours and shading from bright red (corresponding to Cu_2O border) to orange, then orange to yellow (Fig. 14.3). More than 200 EDXS analyses were performed on these areas, which appeared to be composed of oxides containing both Cu and Sn, as will be discussed. The main aims were: (1) to understand the reasons for the important variations in elemental composition observed; and (2) to decide between the interpretation as a single oxide containing both Cu and Sn or a finely mixed binary system of two different oxides respectively containing Sn or Cu.

Figure 14.12 plots all the available analyses in a ternary diagram where the O, Cu and Sn amounts are the coordinates expressed as atomic percentages. This graph also incorporates the previous results achieved on copper oxides

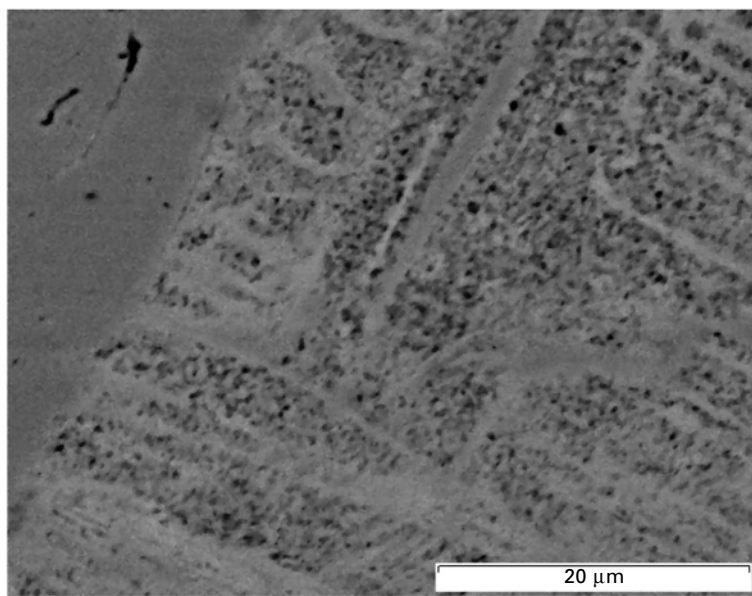


14.12 Graphical representation of the EDXS analyses acquired on the oxides of specimens K4 and MIR1. The microprobe was calibrated on an Al_2O_3 certified sample, in order to reduce to less than 10% the uncertainty in the oxygen content. Red cluster: cuprous oxides (Section 14.3.2). Black cluster: tin oxides (Section 14.3.3). Orange to yellow zone: binary mix of cuprous oxide and tin oxide, $\text{SnO}_2 \cdot 2\text{H}_2\text{O}$.

(Section 14.3.2) and tin oxides of the soldering zone (Section 14.3.3). On the Cu side of Fig. 14.12, a cluster is observable corresponding to the bright red areas, composed mostly of Cu(I) oxide (Section 14.3.2). On the Sn side a cluster of dots is visible around the Sn(IV) hydrated oxide, corresponding to the white compounds of the soldering zone of sample K4, already characterised in Section 14.3.3. This corresponds not to the bronze corrosion but to the tin-alloys corrosion, and is considered outside the present discussion.

The largest cluster of dots, spreading all along the line joining cuprous oxide and dihydrated stannic oxide compositions, contains all the analyses achieved from the orange and yellow areas. Colour is clearly correlated with composition: as the Cu/Sn ratio decreases, the colour changes from red (Cu_2O only) to orange, and then to yellow (i.e. the zones richest in tin). SEM-BSE observations in these orange and yellow areas revealed aggregates of fine products of submicrometric size (Fig. 14.13 as a detail of Fig. 14.3(a)).

The decuprification phenomenon is clearly visible at the grain boundary on the quantitative map of Fig. 14.4(b). A colour zoning (Fig. 14.3(b)) affects the grains, characterising their corrosion as a probable isotropic corrosion phenomenon (see the discussion in Section 14.4). In contrast Figs 14.3(a) and 14.4(a) show evidence of a higher decuprification rate: the amount of dissolved copper in the grain is so high that cuprous oxide precipitates along the grain boundaries and the mechanical twins edges.



14.13 SEM-BSE. Detail of Fig. 14.3(a). The left side of the picture shows a grain boundary filled by cuprous oxide (red in DFOM). The remaining part of the micrograph corresponds to the orange area of the grain, where a ghost microstructure is visible.

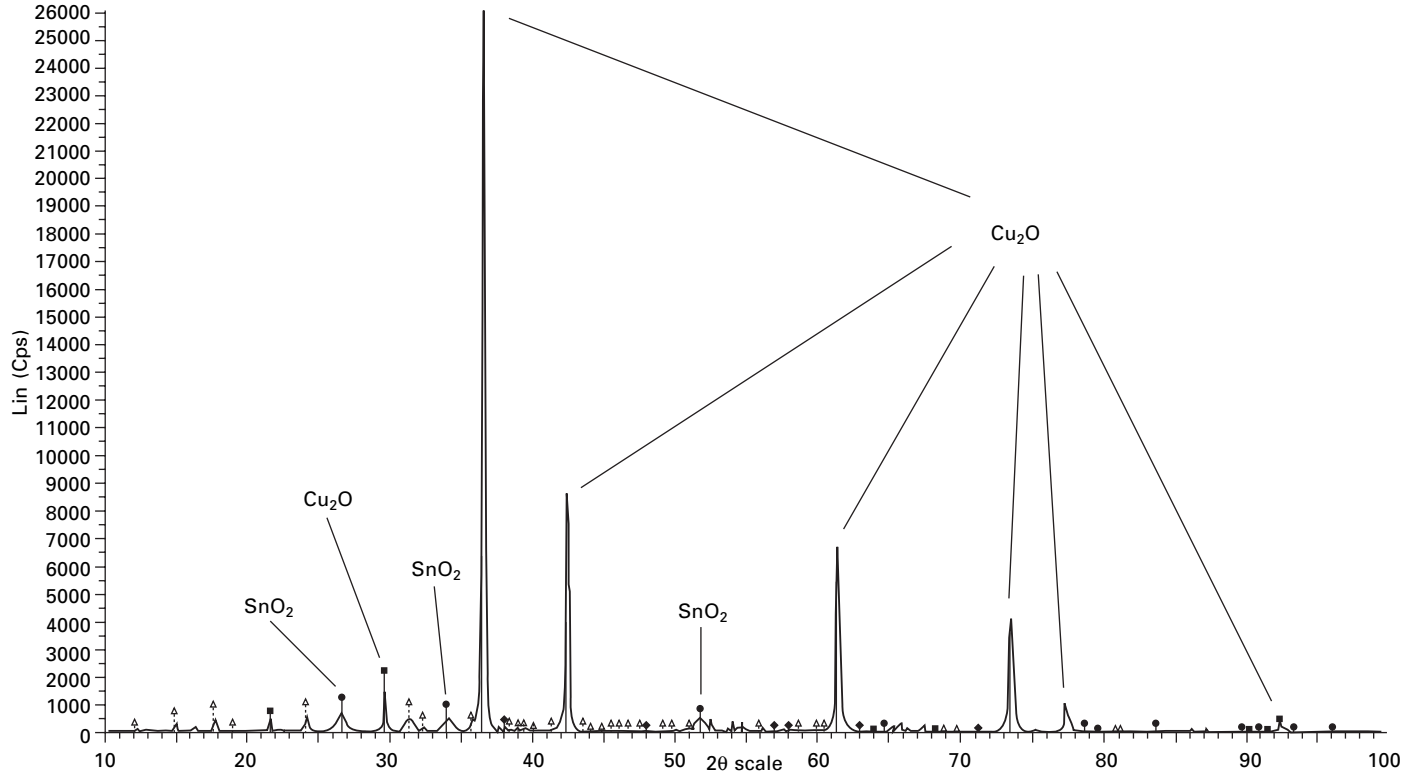
X-ray diffraction of powders obtained by grinding a portion of the KM fragment showed up and confirmed the presence of Cu(I) oxide as the main compound mixed with Sn(IV) oxide (Fig. 14.14). The microdiffraction paths acquired on orange and red areas of K4 allowed us to ensure that SnO₂ is present only in the orange areas (Fig. 14.15). Red areas are therefore composed only of cuprous oxide; in the orange ones it is mixed with stannic oxide. Although these last zones have a high tin content (atomic ratio Sn/Cu > 1:3), it should be noted that the stannic oxide diffraction pattern remains very weak.

Raman microspectroscopy performed on the yellow areas (i.e. those where the Sn content is highest) gave spectra of critical interpretation; the most intense peak of Sn(IV) oxide at 632 cm⁻¹ is completely interfered with by the typical peak at 629 cm⁻¹ of the Cu(I) oxide (Fig. 14.16). This increases the difficulty of detecting the presence of stannic oxide under standard Raman acquisition conditions when Cu(I) oxide is present as the main compound. A promising improvement was the selection of different laser wavelengths for the excitation. This was tested using several exciting lines on a Dilor XY Raman spectrograph on mechanically mixed synthesis compounds: a laser wavelength in the red region attenuates the Cu(I) oxide contribution more strongly than that of the Sn(IV) oxide (Fig. 14.17). At the same time, we experienced difficulties in detecting hydrated Sn(IV) oxide even in the soldering zones from the K4 sample; this signal weakness is also reported in the literature – see ref. [46] for an example from some Chinese black mirrors. It is known, in fact, that Sn(IV) oxide gives Raman spectra differing in quality and intensity as a function of factors such as the crystallisation degree, or the crystal size and shape [38–40, 47]. Therefore a very small crystal size and/or the presence of amorphous dihydrated stannic oxide could explain why the use of an excitation line in the red region did not lead to the expected answer once applied to corrosion on bronzes.

However, even though the spectra in the orange and yellow zones show the dominance of cuprous oxide peaks, there are some significant changes (Fig. 14.18): the typical fluorescence above 800 cm⁻¹, characteristic of the Cu₂O Raman spectrum, is completely absent; a large peak between 480 and 560 cm⁻¹ appears; whereas the typical peak at 632 cm⁻¹, common to the two oxides and supposed to be the sum of both spectra, is significantly enlarged (between 560 and 660 cm⁻¹) and the peak maximum is displaced towards lower wavenumbers.

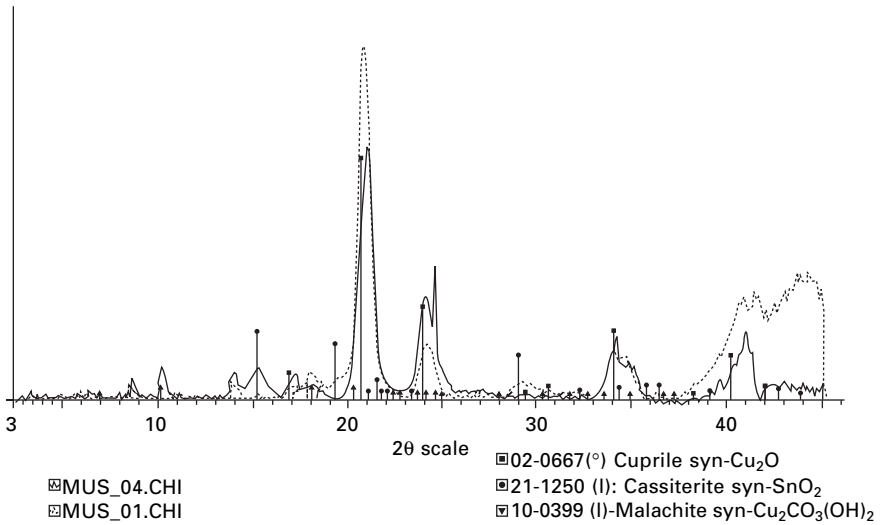
14.4 Discussion: tin oxide, copper oxide and 'type 2' corrosion

Despite our intensive efforts to precisely identify tin compounds in the inner layer of 'type 2' corroded bronzes, the structural data seem, at first sight, difficult to obtain with certainty. Even in the yellow zones, corresponding to

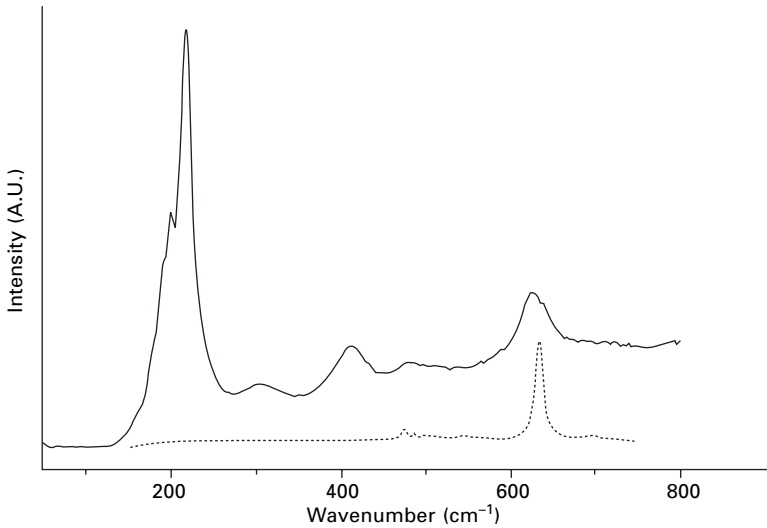


WinFit converted file. This file was converted by WinFit, krumm@geol.uni-erlangen.de-File: oxmix.raw-Type: 2Th/Th locked-Start: 10.000°-End: 100.000°-Step: 0.020°-Step time: 1. s-
 05-0667 (*)-Cuprite syn-Cu₂O-Y: 87.50%-d × by: 1. - WL: 1.54056-0-
 21-1250 (I)-Cassiterite syn-SnO₂-Y: 4.17%-d × by: 1.-WL: 1.54056-0-
 10-0399 (I)-Malachite syn-Cu₂CO₃(OH)₂-Y: 4.17%-d × by: 1.-WL: 1.54056-0-
 27-0605 (I)-Silicon Oxide-SiO₂-Y: 2.08%-d × by: 1.-WL: 1.54056-0-

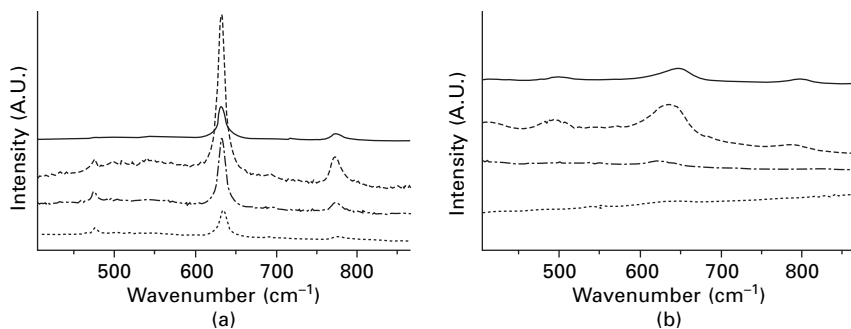
14.14 Powder X-ray diffraction on a ground sample (KM).



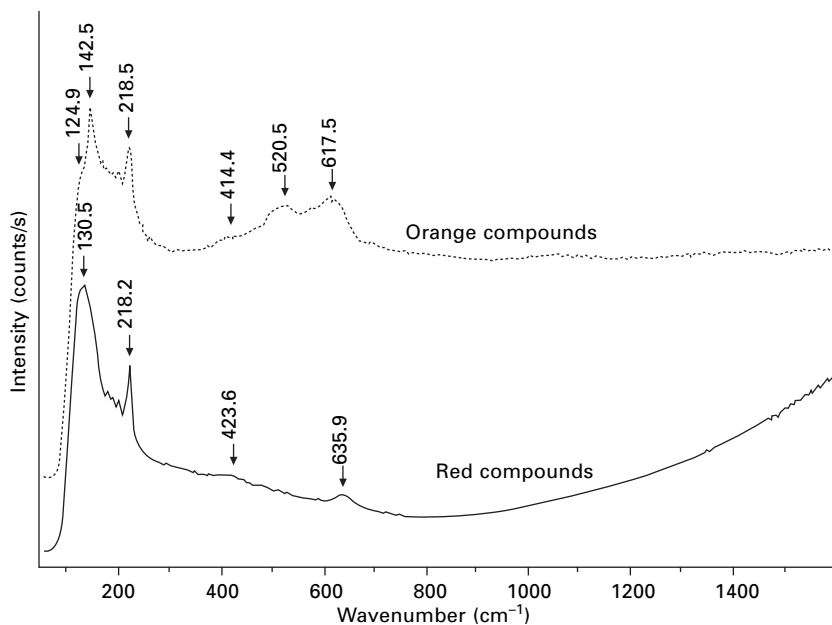
14.15 Microdiffractions acquired on red and orange (dotted line) zones of the K4 sample. The comparison highlights the presence of stannic oxide in the orange areas.



14.16 Superposed reference Raman spectra of Cu(I) oxide (black line) and Sn(IV) oxide (dotted line). Acquisitions performed on synthesis compounds using the common 532 nm laser wavelength (Nd-Yag). The strongest stannic oxide peak (632 cm⁻¹) is fully interfered with by the 629 cm⁻¹ cuprous oxide peak.



14.17 Raman spectra using several laser wavelengths exciting line on a Dilor XY spectrograph: — 647.1 nm, --- 568.2 nm, - . - . 488.0 nm, 457.9 nm; other acquiring parameters unchanged. (a) Stannic oxide; (b) Cuprous oxide. A strong attenuation is achieved for the Cu(I) oxide signal when using the 647.1 nm exciting line.



14.18 Two spectra from the cuprous oxide (red) and the oxide containing Cu and Sn (orange) of the MIR1 sample (WL exciting line: 633 nm). Orange spectrum: the typical fluorescence of Cu(I) oxide disappears, a new large peak between 480 and 560 cm^{-1} is visible, and the peak around 630 cm^{-1} is slightly modified.

a Sn/Cu ratio from 1:1 to 1:3, Raman microspectroscopy is unable to clearly identify stannic oxides and the spectra are of uneasy interpretation. The tin oxide path is revealed by microdiffraction but remains very weak if compared with cuprous oxide. Nevertheless, the ternary diagram plotting the

Cu–Sn–O contents shows undoubtedly that the orange and yellow zones are the result of a binary mixture of cuprous oxide and dihydrated stannic oxide. For these reasons, the combined use of DFOM and EDXS still represents the easiest and most efficient way to differentiate areas of oxides as a function of their relative Sn and Cu contents, and especially to recognise the areas containing tin oxide.

For Raman microspectroscopy, these difficulties cannot be attributed only to the spectral interference of Cu(I) oxide on the Sn(IV) highest peak. The peak shape enlargement in the 600 cm^{-1} region should also result from the probable nanoscopic size of the stannic oxide in the corrosion layers (widely discussed in the literature [46]), combined with its possible incomplete crystallisation. The signal weakness of the stannic oxide in diffracted patterns from the same zones also supports this interpretation. A more precise identification of the tin oxide features (e.g. particle size, crystallisation degree, polarisation surface effect [48]) will require TEM investigations.

Sn(IV) oxide is nowadays mainly known and used as a semi-conductor, since it exhibits interesting properties for many applications (e.g. gas sensors, protective coatings, photodetectors) [49]. Numerous attempts have been made to prepare Sn(IV) ceramics by sintering. According to the literature, sintering Sn(IV) is really difficult and small quantities of CuO are suggested as the best way to produce these ceramics [49]. The effect of copper monoxide is to produce a sort of macrostructure surrounding and compacting stannic oxide particles of nanometric size. Quoting ref. [49], cupric oxide (CuII) reduces to cuprous oxide (CuI) during sintering, and forms the stiff matrix around stannic oxide particles. As for tin corrosion in archaeological bronzes, copper and tin oxides do not react with each other to form some copper–tin oxides. This approach, although based on high-temperature phenomena, leads to similar compounds and microstructural features very close to those observed in oxidised layers of archaeological bronzes.

It is important to note that the areas containing tin compounds (soldering and orange-yellow zones) are the only ones to be concerned by ghost microstructures. In the case of Cu/Sn oxide mixtures, the colour shading observed by Dark Field optical microscopy is clearly correlated to changes in composition. Grain boundaries, mechanical twins and solid solution heterogeneities are underlined by changes in the $\text{Cu}_2\text{O}/\text{SnO}_2 \cdot 2\text{H}_2\text{O}$ ratio, drawing a ghost microstructure visible in the corrosion patina. Different kinds of mineralised metallic microstructures are observed, probably depending on the corrosiveness of the environment (i.e. amount and type of incoming anion species) and on the initial microstructural features of the α -bronze alloy. During a soft alteration of a material in equilibrium (e.g. after a complete recrystallisation annealing), each grain suffers an isotropic attack, leading typically to zoned grains as observed in Fig. 14.3(b). On the contrary, on stressed bronzes (i.e. with microstructures characterised by mechanical twins

and slip bands) or on recrystallised metallic matrices in more aggressive conditions, each metallurgical defect acts as a potential short-circuit for diffusion [32], and the complete heritage of the metallurgical features is reported as shown in Fig. 14.3(a).

This interpretation, based on the idea that tin compounds are responsible for the ghost microstructures, is of fundamental importance for a better understanding of corrosion mechanisms of Sn bronzes. It is probably the best evidence that tin does not diffuse in the corrosion layers, but it is oxidised at its initial position in the metallic matrix. This result confirms previous findings [3] in which studies carried out on two Bronze Age objects by wet chemical analyses stated that the absolute tin content of bronze remains unchanged during corrosion. The decuprification involved in the corrosion processes of Sn bronzes as developed in Refs. [8] and [10] appears to be reliable in explaining the complex migrations of ionic species. During this process, it is also clearly evidenced that hydrated tin oxide plays an important role as a stabilising agent of the corrosion structure.

14.5 Conclusions

The joint use of Dark-Field optical microscopy, scanning electron microscopy (equipped with backscattered electron detector), Raman microspectroscopy and X-ray microdiffraction allowed the successful investigation of the oxidation products of Cu–Sn alloys at the microscopic level. The oxides present in the corroded layers were characterised and described, providing information on their nature and improving the study of the corrosion mechanisms.

It was shown that the internal tin-enriched layer of type 2 patinas is a binary mixture of dihydrated Sn(IV) oxide and Cu(I) oxide. The colour of the corrosion layers, ranging from red to yellow, is related to the relative proportion of copper and tin oxides. Cu and Sn oxides form an agglomerate in which dihydrated stannic oxides seem to be finely dispersed in a cuprous oxide matrix. This last result is supported by X-ray microdiffraction. The Raman spectra acquired in mixed oxide areas show that Cu(I) oxide is always easily identified whilst the presence of dihydrated stannic oxide is often dubious or elusive. This last point can be explained only by its nanometric size and its tendency to form amorphous phases. TEM examination is now required for more precise characterisation of the hydrated Sn(IV) oxides.

It was also shown that tin oxides play a major role in the corrosion resistance of bronze, acting as a structural stabilising agent of the patinas. The systematic presence of dihydrated Sn(IV) oxides in ghost microstructures supports convincingly the idea that tin oxidises in its initial position, and does not diffuse through corrosion layers, giving also indirect proof that bronze corrosion can be described essentially as a decuprification phenomenon involving complex migration processes.

14.6 Acknowledgements

We are particularly grateful to Dr Philippe Dillmann (CNRS, UMR 5060) who gave us access to the LURE facility and mastered the microdiffraction measurements. Special acknowledgement must be made to the staff of the Ecole Française de Rome (EFR) and the Archaeological Museum of Monterenzio (Bologna, Italy) who allowed us to sample and study recent archaeological findings. The authors would also like to thank Prof. M.G. Ienco, Dr A. Ubaldini and Dr M. Carnasciali from the University of Genoa, Dr D Bourgarit and Dr S. Pagès-Camagna from C2RMF, Paris, and Dr R. Bertholon from the University of Paris I.

14.7 References

1. AA. VV., *Le Métal, Techné*, 18 (2003), éd. Réunion des Musées Nationaux – C2RMF, Paris.
2. R. J. Gettens, *J. Chem. Educ.*, February (1951), 67–71.
3. W. Geilmann, *Angewandte Chemie*, 68 (1956), 201–212.
4. T. W. Chase, Chinese bronzes: casting, finishing, patination, and corrosion, in *Ancient and Historic Metals: Conservation and Technology*, D. A. Scott, J. Podany and B. Considine (eds), Getty Conservation Institute, Los Angeles, 1994, 85–117.
5. P. Piccardo, M.R. Pinasco, E. Stagno, M.G. Ienco, E. Ciliberto, G. Spoto, G.C. Allen, C.M. Younes, R. Maggi, *British Corrosion Journal*, 35(1) (2000), 43–47.
6. I. De Ryck, A. Adriaens, E. Pantos, F. Adams, *Analyst*, 128(2003), 1104–1109.
7. C. Wang, B. Lu, J. Zuo, S. Zhang, S. Tan, M. Suzuki, W. T. Chase, *Nanostruct. Mater.*, 5 (1995), 489.
8. L. Robbiola, J.-M. Blengino, C. Fiaud, *Corrosion Science*, 40 (1998), 2083–2111.
9. I. Mabilille, A. Bertrand, E.M.M. Sutter, C. Fiaud, *Corrosion Science*, 45 (2003), 855–866.
10. L. Robbiola, N. Pereira, K. Thaury, C. Fiaud, J.-P. Labbé, in *Metal 98*, W. Mourey and L. Robbiola (eds), James & James, London (1998), 136–144.
11. F. Schweizer, Bronze objects from lake sites: from patina to biography, in *Ancient and Historic Metals: Conservation and Technology*, D. A. Scott, J. Podany and B. Considine (eds), Getty Conservation Institute, Los Angeles, 1994, 33–50.
12. D.A. Scott, *Copper and Bronze in Art, Corrosion, Colorants, Conservation*, Getty Publications (2002).
13. C. Debiemme-Chouvy, F. Ammeloot, E.M.-M. Sutter, *Appl. Surf. Sci.*, 174 (2001), 55–61.
14. L. Tommesani, G. Brunoro, G. L. Garagnani, R. Montanari, R. Volterri, *Revue d'Archéométrie*, 21 (1997), 131–139.
15. L. Robbiola, C. Fiaud, S. Pennec, *Proc. 10th ICOM Meeting*, Washington, August, vol. II (1993), 796–802.
16. R. Bertholon, *Proc. Eurocorr 2004*, Nice, 12–16 September 2004, session 19, paper 19-KN-574, p. 14.
17. L. Robbiola, L.-P. Hurtel, in: *Metal 95*, I. MacLeod, S. Pennec and L. Robbiola (eds), James & James, London (1997), 109–117.
18. R. J. Gettens, in: *Art and Technology – a Symposium on Classical Bronzes*, S.

- Doeringer, D. G. Mitten and A. Steinberg (eds), MIT Press, Cambridge, MA, 1970, 57–72.
19. L. Soto, J. P. Franey, T. E. Graedel, G. W. Kammlott, *Corrosion Science*, 23 (1983), 241–250.
 20. D. A. Scott, *Studies in Conservation*, 30 (1985), 49–56.
 21. L. Robbiola, I. Queixalos, L.-P. Hurtel, M. Pernot, C. Volfovsky, *Studies in Conservation*, 33 (1988), 205–215.
 22. H. Strandberg, L.-G. Johansson, G. Lindqvist, *Materials and Corrosion*, 48 (1997), 721–730.
 23. C. Wang, B. Lu, J. Juo, S. Zhang, S. Tan, M. Suzuki, W. T. Chase, *Nanostruct. Mater.*, 5 (1995), 489–496.
 24. P. Piccardo, M. Pernot, *Les bains tardo-républicains de Musarna in Collection EFR*, V. Jolivet and H. Broise (eds), Editions EFR, Rome, in press.
 25. M. Esposito, M.G. Ienco, P. Piccardo, E. Poggio, E. Stagno, D. Vitali, *Proc. Archaeometallurgy in Europe, International Conference*, AIM, Milan, 2, 2003, Milan, 24–26 September 2003, 147–156.
 26. P. Piccardo, *Microscopy and Analysis*, no. 63 (2000), 13–15.
 27. J. Solard, *Etablissement d'une base de spectres Raman de référence sur les produits de corrosion du bronze*, rapport de stage d'IUT Mesures Physiques d'Orsay sous la direction de B. Mille, 2002.
 28. V. Hayez, J. Guillaume, A. Hubin, H. Terryn, *J. Raman Spectrosc.*, 35 (2004), 732–738.
 29. M. Bouchard-Abouchacra, PhD thesis, Museum d'Histoire Naturelle (2001).
 30. I. De Ryck, E. Van Biezen, K. Leysens, A. Adriaens, P. Storme, F. Adams, *Journal of Cultural Heritage*, 5 (2004), 189–195.
 31. P. Piccardo, M.R. Pinasco, E. Stagno, *Paléoméallurgie des Cuivres*, Collection Monographies Instrumentum, ed. M. Mergoïl, Montagnac (France), no. 5 (1998), 185–190.
 32. P.E. Flewitt, R.K. Wild, *Grain Boundaries: Their Microstructure and Chemistry*, John Wiley and Sons, 2001.
 33. E. Poggio, P. Piccardo, *Microscopy and Analysis*, 18(3) (May 2004), 5–7.
 34. G. Zhou, J.C. Yang, *Applied Surface Science*, 210 (2003), 165–170.
 35. A. Martínez-Ruiz, M. Guadalupe Moreno, N. Takeuchi, *Solid State Sciences*, 5 (2003), 291–295.
 36. D.P. Norton, *Materials Science and Engineering*, 43 (2004), 139–247.
 37. Y.-S. Choe, J.-H. Chung, D.-S. Kim, G.-H. Kim, H. Koo Baik, *Materials Research Bulletin*, 34(9) (July 1999), 1473–1479.
 38. B. X. Huang, P. Tornatore, Y.-S. Li, *Electrochimica Acta*, 46 (2000), 671–679.
 39. M. Ocaña, C.J. Serna, J.V. Garcia-Ramos, E. Matijević, *Solid State Ionics*, 63 (1993), 170–177.
 40. J. Zou, C. Xu, X. Liu, C. Wang, *J. Appl. Phys.*, 75 (1994), 1835.
 41. D.F. Cox, G.B. Hoflund, H.A. Laitinen, *Applications of Surface Science*, 20(1–2) (1984), Elsevier Science B.V.
 42. S. Lenaerts, J. Roggen, G. Maes, *Spectrochimica Acta*, 51A(5) (1995), 883–894.
 43. M. Galdikas, V. Jasutis, S. Kaciulis, G. Mattogno, A. Mironas, V. Olevano, D. Senulienė, A. Setkus, *Sensors and Actuators B*, 43 (1997), 140–146.
 44. J.A. Yang Li, J. Larea, E. Baggio-Saitovitch, G.C. Che, Z.X. Zhao, G.H. Cao, Z.X. Xu., *Physica C*, 312 1999, 283–288.

45. R.B. Vasiliev, M.N. Rumyantseva, N.V. Yakovlev, A.M. Gaskov, *Sensors and Actuators B*, 50 (1998), 186–193.
46. C. Wang, B. Lu, J. Zuo, S. Zhang, S. Tan, *Nanostruct. Mater.*, 5(4) (1995), 489–496.
47. M. Ocaña, C.J. Serna, *Spectrochim. Acta*, 47A (1991), 765–774.
48. V.M. Jimenez, A. Caballero, A. Fernandez, J.P. Espinos, M. Ocaña, A.R. Gonzalez-Elipe, *Solid State Ionics*, 116 (1999), 117–127.
49. J. Lalande, R. Ollitrault-Fichet, P. Boch, *Journal of the European Ceramic Society*, 20 (2000), 2415–2420.

Corrosion problems and reconstruction of the copper roof on Queen Anna's Summer Palace, Prague

K. KREISLOVA, D. KNOTKOVA and V. CIHAL,
SVUOM Ltd, Czech Republic and J. HAD, VSCHT,
Czech Republic

15.1 Introduction

Copper is an important metal for architectural purposes. Copper sheets and metalwork elements were used in the past for roofing and on other parts of important buildings (churches, palaces) only. These applications rely on a number of properties of copper, such as high resistance to atmospheric corrosion, or its ability to form characteristic layers of corrosion products (patina), which not only protect objects but usually make copper objects visually more attractive too. A high resistance of copper corrosion products makes the objects highly stable in the atmospheric environment. Long-term experience proves that the long-term corrosion rates for copper are 0.1–1.0 $\mu\text{m}/\text{year}$ in moderately polluted urban atmospheres and 1.0–3.0 $\mu\text{m}/\text{year}$ in heavily polluted urban atmospheres. Objects and elements made of these materials survive for centuries. Copper construction parts (roofs, cladding) are affected by the atmospheric environment. Its effect, especially during long-term exposure, causes gradual changes. The surfaces of these objects become covered with corrosion products, dirt, biological contamination, etc.

15.2 Survey of corrosion products and damage to copper roofs and claddings in Prague

Surface corrosion layers, including the protective patina on copper, do not have a simple composition, not even an unambiguous crystalline structure. Metallographic cuts show a two- or three-layer construction of patina in most cases; in some cases also foreign matter can be seen in the top green layer. The thickness of green patina (green top sub-layer) formed in an open atmosphere over a long period of time is between 40–50 and 75 μm . The thickness of the black, red or dark sub-layer is approximately 10 μm . An overview of phases determined repeatedly in surface corrosion layers on copper objects in the Czech Republic is shown in Table 15.1 (57 samples of

Table 15.1 Composition of patina layers [1]

| Composition | Abundance |
|--|-----------|
| Antlerite | 18 |
| Brochantite | 43 |
| Cuprite | 16 |
| Atacamite, paratacamite | 3 |
| (NH ₄) ₂ Cu(SO ₄) ₂ ·6H ₂ O | 4 |
| Quartz | 33 |
| Gypsum | 2 |
| Calcite | 3 |
| Entirely amorphous | 1 |

Table 15.2 Types of defects on copper and bronze objects in Prague

| Age of object (years) | Type of object (number) | | Defect (occurrence) | | |
|-----------------------|-------------------------|----------------------------|------------------------|------------------------|-------------------------|
| | Roof, cladding (copper) | Sculpture (bronze, copper) | Aesthetic ^a | Corrosion ^b | Mechanical ^c |
| 450–240 | 1 | 5 | 3 | 3 | 2 |
| 150–110 | – | 4 | 2 | 1 | 1 |
| 100–80 | 3 | 28 | 25 | 21 | 4 |
| 75–60 | 3 | 17 | 13 | 13 | 6 |
| 50–15 | 1 | 39 | 24 | 24 | 6 |
| <15 | 2 | 4 | 3 | 5 | 1 |
| total | 10 | 97 | 70 | 66 | 20 |

^a Non-uniform patina, differences in colour

^b Pitting, crusts, etc.

^c Holes, damaged joints and supporting constructions

statues and copper roofs in central Prague, investigation in 1994) [1]. Table 15.2 lists defects found on copper roofs or claddings.

There are four main causes of defects and damage to copper roofs and metalwork elements – mechanical damage, corrosion impact of the outdoor environment, and corrosion impacts derived from the construction design of a building or its indoor regime. The degree of stress caused by individual factors may differ, though the causes are often combined.

15.3 Corrosion damage on copper roof of Queen Anna's Summer Palace

Queen Anna's Summer Palace was built in 1558–64 and some parts were replaced over the centuries. For many years, it was exposed to an environment of corrosivity category C3-C4-C3 [2]. Extensive measurements were performed on copper sheets applied from the sixteenth to the twentieth centuries in

Table 15.3 X-ray analysis of surface layer^{a,b}

| Area of removal of samples | Appearance of layer | Composition |
|----------------------------|---------------------|--------------------------------|
| 1 Cover of window | Middle green | Brochantite |
| 2 Sheets on east side | Yellow-and-green | Brochantite, quartz, gypsum |
| 3 Area with black spots | Black | Cuprite |

^a The samples were analysed by system XRD 3000 P, radiation CoK_α, graphite monochromator; results were compared with database PDF 2

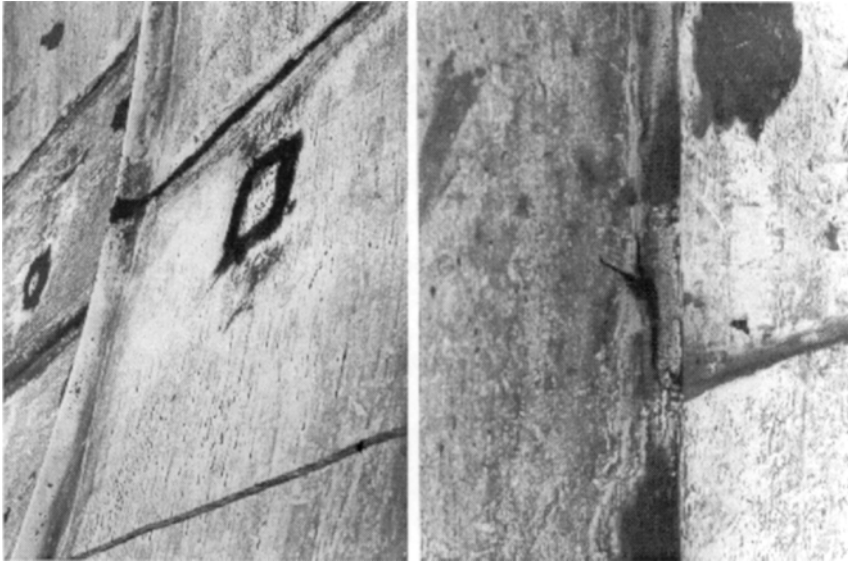
^b Microprobe analysis of spots: high amount of Fe

different parts of the roof. The original thickness was about 0.8 mm. The residual thickness of the sixteenth century copper sheets decreased to 0.35–0.50 mm with a minimum of 0.3 mm on the most affected eastern ridge part. The residual thickness of other, less affected parts decreased to about 0.6 mm in the sixteenth century or later applied copper sheets. The reason for replacement of some of the sheets in the nineteenth and twentieth centuries was mechanical damage following fires and other disturbances. Corrosion rates of copper determined from these measurements correspond to those derived from long-term testing (e.g. ISO 9224) [3]. A variety of colours and compositions patina correspond to the shape arrangement of a long-term exposed object (mainly brochantite, locally cuprite, sporadically antlerite) – see Table 15.3 [4, 5, 10]. Compared to new objects, brown surface layers of impurities (quartz, calcite) are more marked.

Local corrosion effects are very rare and usually connected with either microclimatic corrosion factors or, more often, technological factors. They are mostly situated near the joints. Flat pits 50 μm deep were observed. There were a lot of defects, e.g. cracks and perforations on the sheets with minimal thickness, with occurrence of black spots on the sheets (Fig. 15.1). The formation of mechanical and corrosive cracks is also caused by insufficient fixation of the sheets. These defects limit the serviceability of the roof.

15.4 Reconstruction of the copper roof

The Summer Palace of Queen Anna in Prague represents a very important cultural heritage and it was necessary to elaborate a plan of reconstruction in such a way that it would prolong the lifetime of the roof to a level comparable to the whole building, with the urge to sustain the character of this historical building, whilst not changing its public perception. It was recommended to replace the eastern part of the roof by a new copper roofing material and also to use the new material only on parts of heavily damaged areas of the western side. Some undamaged dismantled parts from the old roofing were also reused during the reconstruction (Fig. 15.2).



15.1 Defects on the copper roof.



15.2 Reconstruction of the copper roof.

The formation of a natural patina in the contemporary low-polluted atmospheric environment in Prague is going to be very different from the patina that had formed in the past. At the same time it was impossible to wait for the natural green patina layer to form. Therefore it was decided to patinate the new roofing material using modern industrial technology. Recommendations were based on laboratory and atmospheric site testing of copper, and of copper with various surface treatments.

The reconstruction was carried out during 2000–03 and involved the replacement of damaged sheets by new copper sheets and also the application of artificial green patina on the replaced sheets (Fig. 15.3). The replacement of copper sheets was carried out in several steps during the summer season.



15.3 New patina layer after four years' exposure (a) eastern and (b) western sides).

During the following winter a natural dark layer formed and the year after that a special solution was applied by a form roller in two layers. After the application of each layer a fixing solution was sprayed over it. The second layer was applied the next day after the previous layer had fully dried out.

15.5 Artificial patinas

The formation of natural patina is a long-term process, which goes through a number of stages. Because the natural patina takes a long time to form, there is a need to create patina artificially. Artificial patination is an important step in the process of creation and restoration of historical copper objects and *objets d'art*. Artificial patination is used mainly when a desired appearance of a surface needs to be reached quickly. Protective properties or resistance to corrosion of created layers vary; in most cases they are not known or considered.

Natural and artificial patinations are processes that differ in principle and therefore need to be understood and evaluated. The possibility of using an artificial patina needs to be assessed case by case (taking into consideration the size and shape of objects, aesthetic requirements, applicability, etc.).

There are a number of formulae for patination, which contain various components. Artificial patinas vary in composition and the components they contain depend on the composition of patination solutions or pastes used. Most of them are complex procedures and their success is conditioned by experience and practice. The effects of chemical components are completed by other procedures that mechanically remove unadhesive portions of patina, mechanically increase homogeneity of remaining layers or cause secondary reactions at higher temperatures. Artificial patinas are more porous and less compact than natural patinas. Layers of artificial patina cannot be sufficiently bound to the copper base of an object. That is reached gradually by repeated impact of climatic conditions, especially precipitation and dry-out. Uneven

impact of the outdoor environment also creates colour tones that are typical of natural patina.

Artificially created green patinas on restored historical objects have a number of disadvantages:

- Insufficient adhesion
- Partial wash-out by precipitation (artificial patinas contain more water-soluble components)
- Undesired changes of appearance during the process of transformation of the artificial patina into a patina with a composition that is closer to the natural patina.

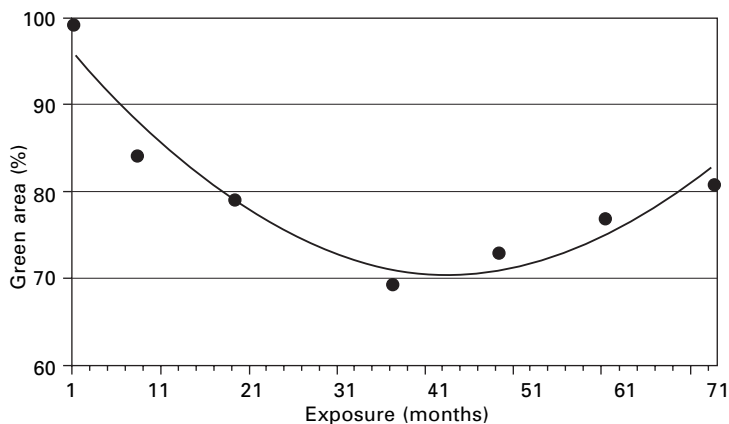
15.6 Study of behaviour of artificial patinas in atmospheric conditions

Manufacturers of copper sheets also offer sheets with a layer of artificial patination – dark and green. Patinas are made continually on a production line by a mechanical–chemical heat process or by the application of a gel, which contains copper nitrate and basic sulphates or copper chlorides. Extensive changes of patina composition can be expected to occur during its ageing. The biggest problems occur in cases of patination of parts of objects after their repair, after the exchange of damaged parts, etc. Even if the colour of artificial patina is the same as the colour of natural patina, the new layer becomes visible due to the transformation of artificial patina.

In the Czech Republic copper sheets with artificial patina have been used on the roofing of Queen Anna's Summer Palace. The application of commercially produced copper sheets with a layer of artificial patination was not possible due to technological reasons. After six months of natural weathering the replaced parts were provided with the artificial patina system Nordic Green. Nordic Green solution is a water suspension of copper nitrate and hydroxide, basic copper salts and other components [6–8]. For the fixation of the patina layer a water glass solution was applied by spraying.

Sheets of copper with the same artificial patina were exposed over a long period of time at atmospheric test sites (1999–2004) and changes in the patina layer were observed. The samples were exposed at 45° on racks (in accordance with ISO 8565 [9]), at 5° to the open atmosphere and at 90° in a sheltered position. A gradual wash-out occurred during the exposure, but after approximately four years the green surface began to spread again. The sheltered position was the worst in terms of visual evaluation, the slightly adherent patina layer flaking off. This exposure situation prevented the surface from being wet enough to form a natural patina. The surfaces were regularly photo-documented.

There is a gradual formation of natural patina, which grows through the



15.4 Changes of layer of artificial green patina Nordic Green expressed as ratio of green to black areas.

Table 15.4 X-ray diffraction analysis of patina layers^a

| Sample | 1 year | 2 ¹ / ₂ years | 3 ¹ / ₂ years | 5 years |
|--------|-------------------------|-------------------------------------|-------------------------------------|----------------------------------|
| A | Brochantite | Brochantite, posnjakite, cuprite | Cuprite, Brochantite, posnjakite | Posnjakite, cuprite, brochantite |
| B | Posnjakite, brochantite | Posnjakite, brochantite, cuprite | Cuprite, posnjakite, brochantite | Posnjakite, brochantite, cuprite |

^a The samples were analysed by system XRD 3000 P, radiation CoK_α, graphite monochromator; results were compared with database PDF 2

layer of artificial patina. Computer picture analysis (LUCIA 4.11 software by Laboratory Imagine Ltd) was used to evaluate these changes; allows this precise objective evaluation of a decreasing portion of the surface covered with green patina, and the expression of gradual changes by numerical values (Fig. 15.4). A transformation of the patina layer was observed at the same time (Table 15.4). After exposure at a test site in Prague the samples of patina layer were removed to be analysed by an X-ray diffraction method.

Posnjakite was determined as the main component in the patina suspension and in the newly prepared layer on copper samples. During the exposure only cuprite, brochantite and posnjakite formed a patina layer. The dominance of the components changed slightly. The occurrence of brochantite and cuprite shows the transformation of an artificial patina layer to one with the characteristics of a natural patina.

Visual assessment and photo-documentation of the industrial application on the roof have been periodically performed ever since the time of reconstruction:

- After one year of exposure the green layer was homogeneous, with good adhesion to the copper surface, but was relatively thin and did not cover the surface completely. There were sporadic, relatively small spots on sheets with more intense washing-up of patina. The appearance of the patina, especially its colour, was slightly different. After a year of exposure the layer of green patina was darker than the newly applied layer.
- After two years of exposure the layer of patina was darker due to the existing washing-up. The appearance of artificial patina layers (density of green parts, green spots) was slightly influenced by the type of copper sheets (folds).
- After three years the colour differences between the artificial patina Nordic Green and the natural patina formed over centuries had increased but were still acceptable.

Basic analyses of the characteristics of surface layers were performed for the test site exposed samples only.

15.7 Conclusions

The reconstruction project of the copper roof on the Summer Palace of Queen Anna in Prague is based on a systematic evaluation of corrosion and corrosion-mechanical manifestations, including measurements of the thickness of local residues on the copper sheets and analyses of surface layers from different exposure areas [1]. Recommendations of a suitable technology for the repair and patination are supported by extensive laboratory and field testing. Good results were acquired through cooperation with the Czech monument care institutions and the restoration workshop. Results of long-term testing prove that artificial patinas (produced in workshops or industrially) are transformed into natural patinas which are in balance with the surrounding environment. The rate and degree of transformation depend on the type of atmosphere, its corrosivity and its impact on the patina in particular outdoor environments [4, 5]. Periodic inspections of artificial patina on a historic roof proved the suitability of the aim of the restoration.

15.8 Acknowledgement

The authors express their gratitude to the Ministry of Education CR (Project VZ MSM 2579478701) for its financial support.

15.9 References

1. Knotkova D., Kreislova K., Vlckova J. and Had J., Effect of atmospheric environments on copper and bronze cultural monuments, COPAL I–VI, SVUOM technical reports to project EU 316 EUROCARE COPAL, 1994–1999.
2. ISO 9223 Corrosion of metals and alloys – Corrosivity of atmospheres – Classification.
3. ISO 9224 Corrosion of metals and alloys – Corrosivity of atmospheres – Guiding values for the corrosivity categories.
4. Knotkova D., Vlckova J., Kreislova K. and Had J., Atmospheric corrosion of bronze and copper statues, roofs and cladding on Prague's monuments, *Proc. Art '96*, Budapest, October 1996.
5. Kreislova K., Knotkova D. and Had J., Database of corrosion damage of copper and bronze monuments in Prague, *Proc. 5th International Congress on Restoration of Architectural Heritage*, Florence, Italy, 17–24 October 2000.
6. British patent 940,764, 11.2.1960, *Method and Composition for the Artificial Green Patination of Surfaces*.
7. Mattson E. and Holm R., Properties and applications of pre-patinated copper sheet, *Institute of Sheet Metal Engineering*, 1967, pp. 1–5.
8. Nordic Green. Outokumpu Poricopper Oy, Finland, www.outokumpu.com.
9. ISO 8565 Metals and alloys – Atmospheric corrosion testing – general requirements for field tests.
10. Knotkova D., Had J. and Kreislova K., Restoration of copper and bronze monuments in Prague in metal restoration, *Arbeitshefte des Bayerischen Landesamtes für Denkmalpflege*, Vol. 94, p. 70, Munich, 1998.

Long-term corrosion of iron at the waterlogged site of Nydam in Denmark: studies of environment, archaeological artefacts, and modern analogues

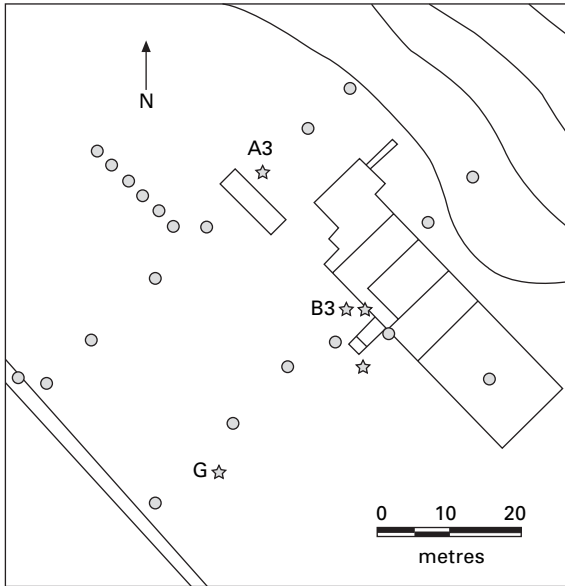
H. MATTHIESEN, D. GREGORY and
B. SØRENSEN, National Museum of Denmark and
L. R. HILBERT, Technical University of Denmark

16.1 Introduction

In situ preservation has become a common practice in the management of archaeological sites during the last decade: there are only limited resources for excavation and conservation, and at the same time there is a wish to preserve unexcavated sites for future generations of archaeologists asking new questions of the material. From this there follows the need to make feasibility studies, i.e. to investigate under which conditions different archaeological materials can actually be preserved in the soil for our descendants. Studies of corrosion processes are necessary to evaluate whether there are any threats to unexcavated iron artefacts and also to explain how the artefacts have survived until today. However, understanding the corrosion of archaeological iron is also relevant in order to model the long-term behaviour of modern iron, for instance in relation to the storage of radioactive waste (see Chapter 2). It is thus interesting how well the corrosion of modern iron actually reflects the corrosion of archaeological artefacts and vice versa. In this chapter we compare the behaviour of archaeological and modern iron in a waterlogged soil. The text also summarises all our studies on iron corrosion at the archaeological site of Nydam.

16.2 Study site

Nydam is an 11-hectare water meadow located in Southern Jutland, Denmark. During the Danish Iron Age it was a shallow freshwater lake into which sacrificial offerings of military equipment from defeated enemies were deposited on at least five different occasions in the period from approximately 200 to 500 AD. Excavations have taken place on several occasions since 1859, and the latest campaign, from 1989 to 1997 [1], yielded more than 16,000 archaeological artefacts within an area of only 600 m². Due to the volume of finds it was decided in 1997 to stop further excavation campaigns and preserve the site *in situ* [2]. Since then the National



16.1 Excavation areas and position of monitoring equipment at Nydam. Circles: dipwell alone. Stars: dipwell and probe for electrochemical impedance spectroscopy (EIS) and electrical resistance (ER) measurements. Coupons for weight loss and measurement of corrosion potentials are distributed throughout the area (not shown). Straight lines show the position of the excavations from 1989 to 1999, curves in the upper right corner are 1 m contour lines, the double line in the lower left corner is a small brook. Results from A3, B3, and G are discussed in some detail below.

Museum of Denmark has conducted an extensive monitoring scheme at the site (Fig. 16.1).

The archaeological remains are found approximately 0.80–1.25 m below the surface. The uppermost finds are lying in peat, whereas the deeper finds are in a carbonate-rich organic mud (*gyttja*). Wood and iron are the most abundant materials in Nydam, but also artefacts of bone, leather, amber, glass, bronze and precious metals are found. This chapter will focus solely on the preservation of iron (Fig. 16.2).

16.3 Methods

The corrosion of archaeological metal artefacts in soil is a broad research area, but a good overview is given by Selwyn [3, 4]. Some studies have focused on the state of preservation of the artefacts [5, 6] while others have been looking at the corrosion products [7, 8], trying in some cases to evaluate the corrosion history from the minerals present [9]. Modern metal samples have been used in some studies to evaluate the corrosion processes [10, 11],

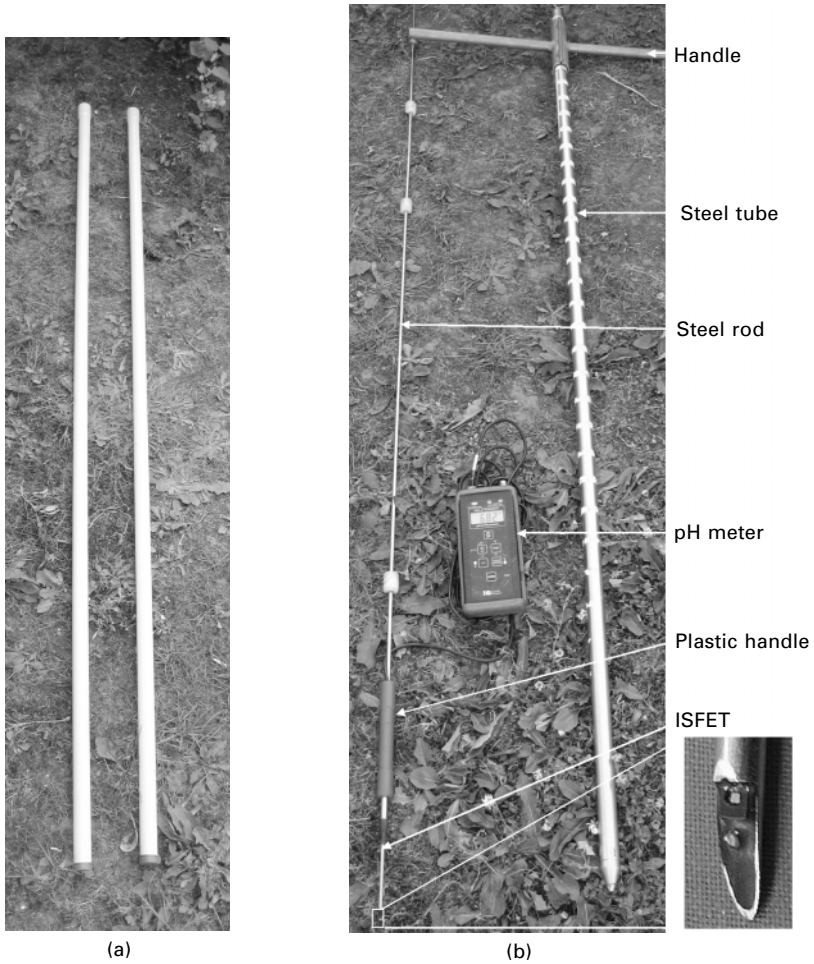


16.2 Excavation of an axe head still on its shaft. The state of preservation of artefacts is very variable. The axe in the picture still contains metallic iron, but important surface details have been lost through corrosion. The corrosion products had a light yellow-brownish colour that was observed on many artefacts.

while others have focused on the environmental conditions at the archaeological sites [12, 13]. At Nydam we have tried to combine these different approaches in order to get a better overview of the whole soil–metal system and to develop and test different theories for the corrosion processes. A similar ‘multi-approach’ study was done in Germany [14] studying iron corrosion in unsaturated soil, and another is ongoing in England [15] monitoring the effects of rewatering a drained archaeological site.

16.3.1 Environmental monitoring

The methodology for environmental monitoring at Nydam has been optimised during the seven-year study period. A cornerstone is a system of dipwells (Figs 16.1 and 16.3(a)) that allows the measurement of water level in the area either manually or by automatic data loggers. The dipwells are also used for sampling of soil pore water for chemical analysis; the samples are filtered and analysed for different components either in the field or back in the laboratory. A major drawback of this system is that it is very difficult to extract water samples without changing the concentration of some of its components. In order to avoid some of the problems related to sampling, a system has recently been developed that allows measurement of different parameters directly in the soil (Fig. 16.3(b)). So far, this system is being used for the measurement of oxygen, pH, carbon dioxide and temperature. The different monitoring methods are described and evaluated in detail in refs [16–18].

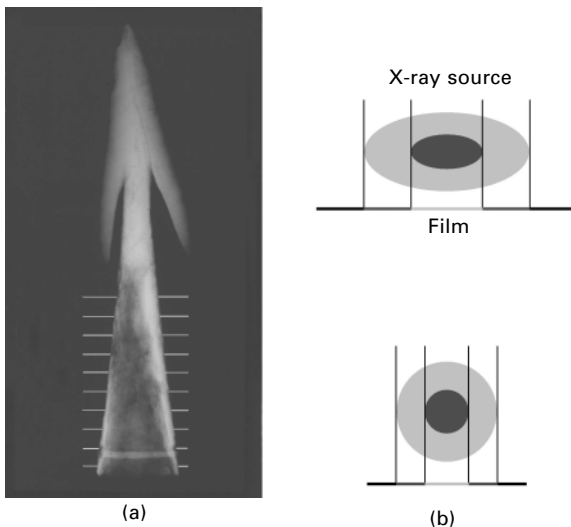


16.3 Equipment used in the environmental monitoring. Dipwells (a) are long plastic tubes that are installed in the soil by means of a hand probe and remain permanently at the site. The tubes are perforated at the lower end to allow the entrance of soil pore water. The dipwells are used for taking water samples and for measuring the water table. The system for measuring directly in the soil (b) consists of a long hollow steel tube that is pressed down at intervals through the different soil layers. At each depth different electrodes are led through the tip of the steel tube to take measurements directly in the undisturbed soil (the inset shows an ISFET pH electrode as an example). This system is used for spot measurements only and is not left at the site.

16.3.2 State of preservation of artefacts

To evaluate the state of preservation of iron artefacts in Nydam on a sound statistical basis, a large number of uniform objects were required. Lance- and spearheads were chosen because they are present in large numbers, they are spread throughout the find, and the round shape of their socket is well suited for measuring corrosion depth by the selected technique (X-ray radiography). More than 1000 lance- and spearheads have been found during the different excavation campaigns in Nydam until now. Of these, 151 were X-rayed in order to measure the corrosion depth.

The artefacts had all been conserved and exterior corrosion products removed. Consequently, the radiographs show the contours of the original surface and below that, in a lighter colour, the contours of the preserved iron core (Fig. 16.4). The corrosion depth was measured in 10–15 positions in 5 mm increments on each side of the picture using a precision scaled magnifier. This method was shown to be independent of the operator and the exact measuring position, and with 20 measurements on each artefact the relative standard deviation of the mean value was approximately 11%. Details of the

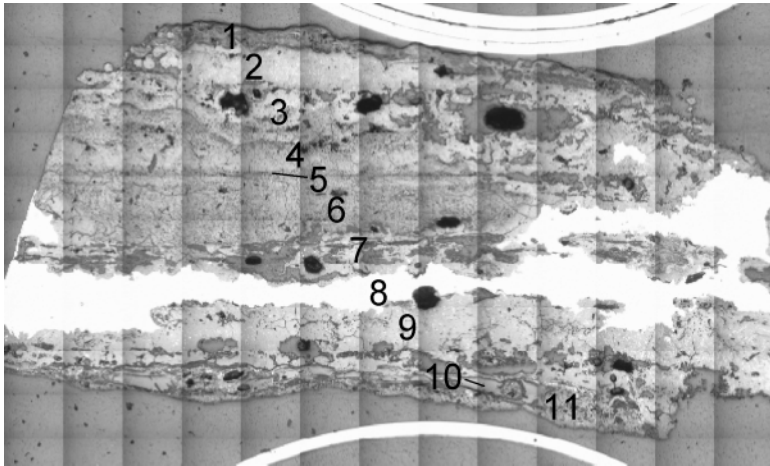


16.4 (a) X-ray photo of a spearhead. Corrosion depth is measured in 10–15 positions on each side of the socket, indicated by white lines. Photo: Birthe Gottlieb. (b) Idealised drawing demonstrating the advantage of using round artefacts for measuring corrosion depth on X-ray photos. Dark grey indicates iron core, light grey indicates corrosion product; for simplicity the round socket is drawn without a hole in the middle. The measured corrosion depth of the socket (lower) is independent of the exact orientation of the spearhead, whereas the measured corrosion depth of the flat point (upper) depends strongly on the orientation. From ref. [19].

evaluation method are given in ref. [19]. If the whole socket, or part of it, was fully converted to corrosion products, a default value of 1.755 mm for ‘totally corroded’ was used, corresponding to the average material thickness measured on the socket of 11 well-preserved spearheads.

16.3.3 Corrosion products

A small excavation was carried out in July 1999 in order to obtain ‘fresh’ archaeological objects for studies of the preservation conditions. Three lanceheads from AD 200–400 were found and immediately transferred to a container with 99.9% ethanol and subsequently kept at 4°C until analysis. Corrosion products from different places on the lances were scraped off and analysed by Attenuated Total Reflection Fourier Transform Infra-red spectrometry (ATR-FTIR) for a preliminary evaluation of the composition, as well as by transmission FTIR on pressed CsI tablets. The results were checked by X-ray diffractometry (XRD) analysis of the surface of one of the lances. In order to investigate a possible layering of different corrosion products with depth, the socket of one of the lances was sectioned and a small piece was cast in epoxy and examined with Scanning Electron Microscopy/Energy Dispersive Spectrometry (SEM-EDS) and microprobe



16.5 Cross-section of a small piece of a lance socket that has been analysed by microprobe ATR-FTIR. Based on the visual differences in porosity, a total of 11 layers or areas have been identified. Each layer was analysed at two or three points with the microprobe. Layer 1 at the top of the picture is the outer corrosion layer, and layer 11 is the innermost part of the socket, where the lance shaft is placed. Layer 8 (white) is the remaining metallic iron. Total width of picture is approximately 4 mm. From ref. [20].

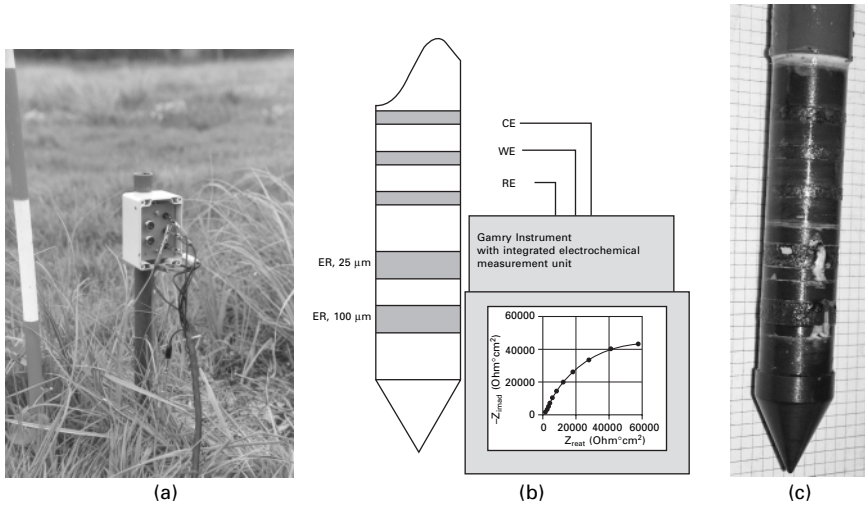
ATR-FTIR (Fig. 16.5). Corrosion products were also analysed on a few modern samples. Details of the methodology are given in ref. [20]. More recently, the three lances along with a cross-section of a sword from Nydam have been investigated by micro-Raman spectroscopy, using the same methodology and equipment as described by Neff *et al.* [8].

16.3.4 Modern samples

Modern iron samples were used to evaluate the corrosion rate under the present environmental conditions. Four types of measurements were made: weight loss, corrosion potential, electrical resistance (ER) and electrochemical impedance spectroscopy (EIS). The modern samples were made from unalloyed carbon steel (C 0.031, Si < 0.001, Mn 0.25, P 0.004, S 0.011, Mo 0.02, Ni 0.01, Al 0.003, N 0.004, Fe 99.6%) except for the ER probes that were made instead of pure iron foil (99.9% Fe), since sufficiently thin carbon steel foils were not available. In order to reduce the number of variables we did not attempt to simulate the heterogeneous composition of archaeological iron [21].

For weight loss measurement pre-weighed and ethanol-cleaned coupons of $10 \times 60 \times 0.5$ mm carbon steel plate were placed at different depths in the peat and *gyttja* layers of Nydam. In order to have minimal disturbance of the soil conditions no holes were dug for the installation of the coupons. Instead the coupons were placed in the soil through a hollow steel tube that was pressed down through the peat layers to the selected depth. After insertion of the coupon the steel tube was withdrawn and the coupons were connected to the surface only by a thin polyamide thread. After approximately two years in the soil the coupons were retrieved and immediately transferred to sample containers with 99.9% ethanol. Back in the laboratory the coupons were cleaned of exterior corrosion products (using a soft brush and 10% hydrochloric acid with 0.1% hexamethylene tetramine) and reweighed.

Some of the coupons were fixed to the end of a plastic tube and connected to the surface through a cable to allow potential measurements. The plastic tube was necessary to seal the connection between the cable and coupon from the environment, and only 10×35 mm of the coupon was exposed. Potential measurements were carried out at intervals against a Cu/CuSO₄ reference electrode. After two years the coupons were retrieved in order to compare the potentials with weight loss of the coupons. Other probes were used for longer series of potential measurements, consisting of large carbon steel rings ($\varnothing = 30$ mm, height 20 mm) that were slid onto a central, thick walled polyethylene pipe at 50, 100 and 150 cm depth and separated by spacers (see Fig. 16.12 on page 286). An insulated copper wire was soldered to the inner surface of the rings and led through the pipe to the top, where it was protected by a close-fitting polyethylene cap.



16.6 Pictures of equipment for EIS and ER measurements: (a) terminal box above ground for connection of measurement unit; (b) drawing of EIS and ER probes placed at 1 m depth; (c) picture of probe after two years in the soil. The three uppermost rings on (b) and (c) are counter (CE), working (WE), and reference (RE) electrodes for EIS measurements; the two lower rings are 25 and 100 μm ER probes.

Similar probes were used for EIS measurements. These had three concentric rings ($\text{O} = 30$ mm, height 5 mm) at 10 mm spacings that were pushed to 1 m depth in the soil (Fig. 16.6(b), (c)). The rings were electrically connected to a terminal box above ground (Fig. 16.6(a)). The middle ring was used as working electrode, while the top was used as counter electrode and the bottom one as reference electrode. EIS measurements were conducted on a Gamry potentiostat PC4/300 mounted in a portable PC. An amplitude of 10 mV rms (root mean square) was applied in the frequency range of 1000 kHz to 1 mHz. A separate reference electrode (SCE or Cu/CuSO_4) was mounted in the top of the soil for measurement of corrosion potentials.

Electrical Resistance (ER) iron foil probes of 25 and 100 μm thickness were mounted on the same tube as the EIS probes (Fig. 16.6(b), (c)). The increase in resistance is directly proportional to the thickness reduction of the iron foil, whereby an average corrosion rate can be obtained. The foil can be used until approximately half the original thickness is left.

16.4 Results

16.4.1 Environment

The water table is one of the most important parameters when it comes to the preservation of archaeological artefacts in Nydam. It varies somewhat with

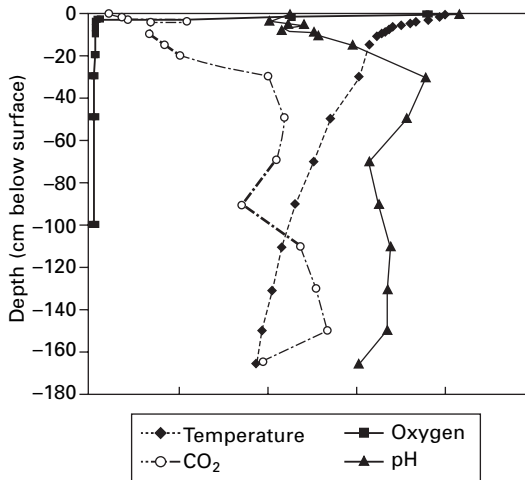
Table 16.1 Measured concentrations in filtered water samples from dipwells from the period 1997 to 2003. CI: confidence interval; *n*: number of samples; from ref. [16]

| | Min. | Max. | Mean | 95% CI of mean | <i>n</i> |
|-----------------------------------|-------|------|------|-------------------|----------|
| pH | 5.99 | 7.02 | 6.50 | 6.47–6.54 | 140 |
| Sulphate (mg SO ₄ /L) | <10 | 200 | 21 | 16–27 | 101 |
| Sulphide (mg S(-II)/L) | <0.03 | 2.22 | 0.18 | 0.12–0.23 | 116 |
| Nitrate (mg NO ₃ /L) | <2 | 37.0 | 7.8 | 6.8–8.8 | 109 |
| Nitrite (mg NO ₂ /L) | 0.02 | 0.43 | 0.13 | 0.10–0.16 | 50 |
| Ammonium (mg NH ₄ /L) | 1 | 300 | 12 | 6–18 | 109 |
| Phosphate (mg PO ₄ /L) | <0.2 | 135 | 6 | 3–9 | 99 |
| Iron (mg Fe/L) | 2 | 48 | 12 | 10–14 | 76 |
| Manganese (mg Mn/L) | <0.5 | 4.1 | 1.5 | 1.2–1.8 | 61 |
| Chloride (mg Cl/L) | 22 | 62 | 37 | 33–41 | 24 |
| Potassium (mg K/L) | 0.8 | 31.0 | 7.5 | 5.3–9.6 | 45 |
| Alkalinity (meq/L) | 2.4 | 7.9 | 4.6 | 3.9–5.3 | 21 |
| Conductivity (µS/cm) | 225 | 2100 | 686 | 651–722 | 139 |

the season, the area being turned into a small lake during winter. The lowest groundwater level measured during a dry summer is approximately 30 cm below the soil surface, excluding periods with archaeological excavations where pumping lowers the water table around the excavation pit [18].

The concentrations of dissolved species in water samples from dipwells are shown in Table 16.1. An example of measurements directly in the soil with different electrodes is demonstrated in Fig. 16.7. In brief the analyses show that the conditions are anoxic, slightly acidic (pH 6–7), with relatively high concentrations of dissolved iron compared to dissolved sulphide [16]. Detailed pH profiles were measured directly in the soil twice a year through the period 2001–04, showing no significant temporal variation and only a modest vertical variation [17]. Detailed oxygen profiles were measured directly in the soil on a few occasions, showing the absence of oxygen below the water table (values below or near the detection limit of ca 0.1 mg O₂/L) but installation of an automated oxygen logger is considered in order to study oxygen penetration depths, e.g. during heavy rainfall.

Apart from the current environment, it is of interest to discuss the former conditions in Nydam from the Iron Age until today, in order to understand the deterioration patterns observed on the artefacts. It will never be possible to know the former environment in all details, but we can at least have a general idea of it from different proxy indicators in the archaeological material. Analysis of the wooden artefacts shows no collapse, even though their physical strength is very limited – this tells us that there has been no prolonged drainage of the find layers in modern times [22]. The peat layers right above the finds are well preserved and have a light brown colour [23] – this indicates that the oxygen access has been limited. The survival of calcareous shells

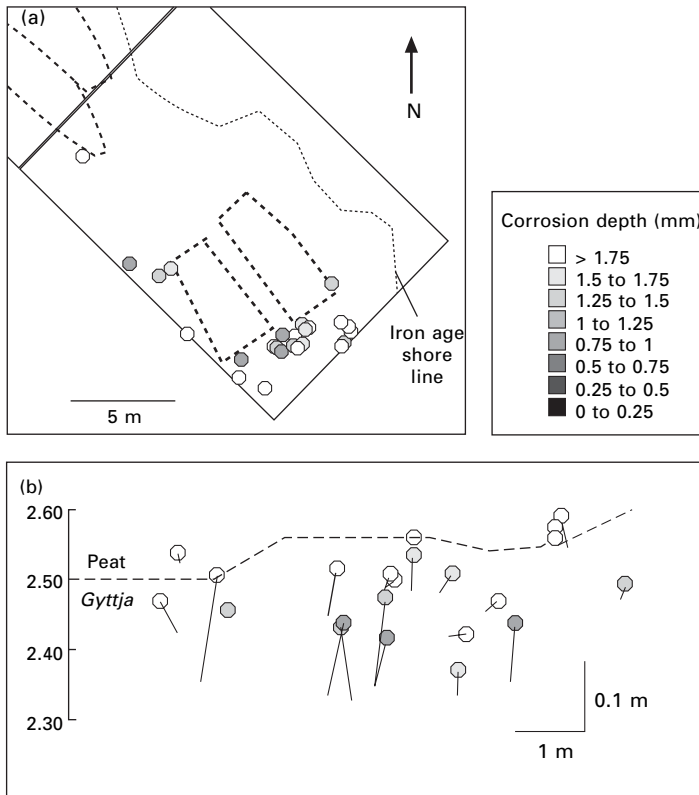


16.7 Example of data measured directly in the soil with a recently developed system (16.3(b)). Full scale on the x-axis is: temperature 0–25°C, oxygen 0–100% saturation, carbon dioxide pressure 0–1 atm, and pH 5–7. Data are from July 2003, when the water level was a few centimetres below the soil surface. From ref. [16].

and bone in the find layers [24, p. 44] indicates that the conditions have never been highly acidic. Overall, this indicates environmental conditions not too different from the ones we observe today. The most substantial environmental change is probably that the artefacts have become overgrown with still increasing layers of organic matter (peat), so that artefacts sacrificed on the mire surface in the Iron Age are today found approximately 1 m below the present surface. It should be possible to achieve more detailed information about the former environment by a comparison between the state of preservation of the different materials and their exact find location, but until now this has been done only for iron artefacts.

16.4.2 State of preservation of artefacts

The state of preservation of lance- and spearheads, as measured on X-radiographs, showed a very varying picture, with some objects being completely converted into corrosion products, and others with a corrosion depth of less than 0.1 mm. Already during the excavation it was noted that well-preserved and heavily deteriorated objects on some occasions were lying just a few centimetres from each other. In order to evaluate this further, the measured corrosion depths were correlated to the exact find position using a Geographical Information System (Fig. 16.8). The results are discussed in detail in ref. [19], but very briefly they indicate that the deterioration pattern observed today is to some extent a function of the first few years after deposition. It



16.8 Corrosion depth of a group of lance- and spearheads excavated in 1994. (a) plan view, where solid lines indicate modern excavations and dashed lines show excavations during the nineteenth century; (b) vertical profile (seen from SE) where dashed line indicates interface between peat and *gyttja*. Solid line at each point represent a projection of the spearhead to the vertical view plane, so long steep lines indicate artefacts deposited in a steep angle. Numbers to the left are metres above sea level. From ref. [19].

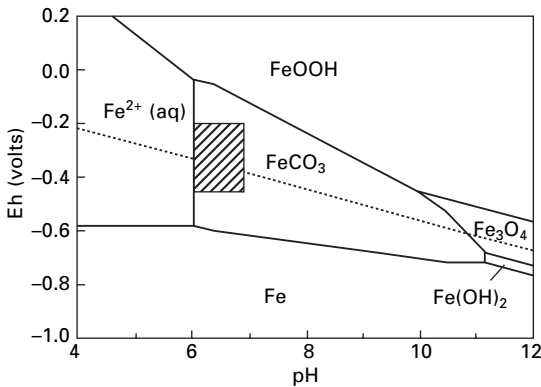
thus seems that artefacts that have been thrust down into the anoxic peat layers have deteriorated less than artefacts that have been sacrificed on the mire surface. The latter have lain exposed in an oxygen-rich environment for a period of time before being finally overgrown and embedded in an anoxic environment, and these differences from 1500–1800 years ago are still observable today.

16.4.3 Corrosion products

XRD studies on the surface of a lancehead showed that the corrosion product consisted of siderite (FeCO_3) with only a minor amount of other crystalline

minerals. Analysis by different FTIR methods of corrosion products scraped from several artefacts, as well as a cross-section of a lance, indicated that also the subsurface corrosion layers consisted of almost pure siderite (Fig. 16.5). However, later analysis by micro Raman spectroscopy also revealed some magnetite (Fe_3O_4) and/or maghemite ($\gamma\text{-Fe}_2\text{O}_3$) especially in the innermost corrosion scales close to the metallic iron. Both oxides are very difficult to determine by the FTIR methods used in this study and further comparison between micro Raman and FTIR methods is necessary to evaluate the quantitative content of the different corrosion products. Importantly, SEM-EDS showed only very low contents of sulphur, indicating that corrosion by sulphate-reducing bacteria is not a problem at this site. Siderite was also found on modern iron samples that had been exposed for a few years in the soil at Nydam (Figs 16.6 and 16.12). The siderite layer on the modern samples and the analysed artefacts was black to light grey; however, well-crystallised siderite can also be light yellow-brownish [25], similar to the crystals observed on some artefacts during excavation (Fig. 16.2).

The occurrence and stability of siderite is discussed in ref. [20], along with an evaluation of its protective properties. A Pourbaix diagram based on the actual soil conditions at Nydam is shown in Fig. 16.9. Examination by micro Raman spectroscopy and thus the discovery of magnetite/maghemite in the corrosion layers was made after publication of ref. [20] and their occurrence is therefore not discussed in that paper. Their implications for the corrosion system in Nydam has not yet been fully evaluated, but similar observations are described and discussed in chapter 2 of this book.

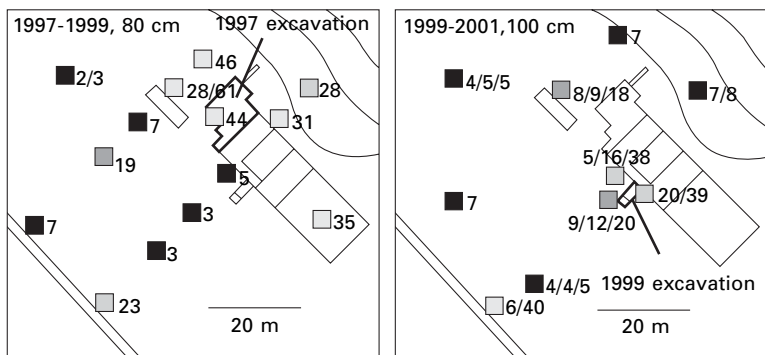


16.9 Pourbaix diagram for iron in an environment with 10^{-2} M carbonate, and 2×10^{-4} M dissolved iron at a temperature of 10°C , which is similar to the conditions measured in Nydam (Table 16.1). The thermodynamic data for the diagram are taken from ref. [27], including stability data for siderite from ref. [28]. Hatched area shows the pH values and corrosion potentials measured *in situ* at Nydam. Dotted line shows the stability limit for water. Updated from ref. [20].

Siderite is a common mineral in mires where it is formed through microbiological reduction of iron oxides in the environment [25, 26]. This mechanism may explain its occurrence on artefacts that have lain exposed on the mire surface for a period of time: they will quickly have become covered by a layer of iron oxides that was subsequently reduced to siderite after the artefact was overgrown and embedded in an anoxic environment. However, for other artefacts (and modern samples) that have been placed directly under anoxic conditions the siderite must have formed directly from the metallic iron; the exact formation mechanism is still unclear but here the oxidation of iron may involve the reduction of H^+ or HCO_3^- [20]. The hatched area in the Pourbaix diagram demonstrates that the pH values found at Nydam are close to the lower limit for siderite stability, so the soil pH is monitored intensively to be sure that no acidification takes place [17].

16.4.4 Modern samples

Weight loss was measured for more than 40 iron coupons, each being exposed for $1\frac{1}{2}$ –2 years in the waterlogged peat and *gyttja* layers in Nydam. The results have demonstrated a close correlation between archaeological excavations in the area and measured corrosion rates (Fig. 16.10). Apart from two coupons placed near the brook (lower left corner), the highest rates were all found near the archaeological excavation trenches where the water level had been lowered by pumping during the excavations. In these areas temporary changes in the water chemistry were also measured, such as an increased concentration of nutrients and sulphate, and a slight lowering of the pH [18]. It must be emphasised that the coupons on both occasions were

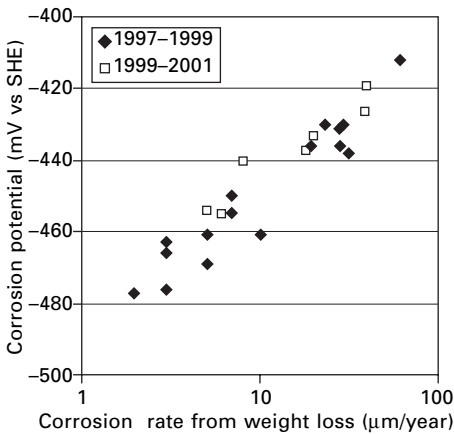


16.10 Corrosion rates on modern iron coupons. One set of coupons was buried in October 1997 at 80 cm depth and retrieved in May 1999. The other set was buried in November 1999 at 100 cm depth and retrieved in June and October 2001. All numbers are in $\mu\text{m}/\text{year}$: ■: 0–10, ▒: 10–20, ▒: 20–30, ▒: 30–40, □: >40 $\mu\text{m}/\text{year}$.

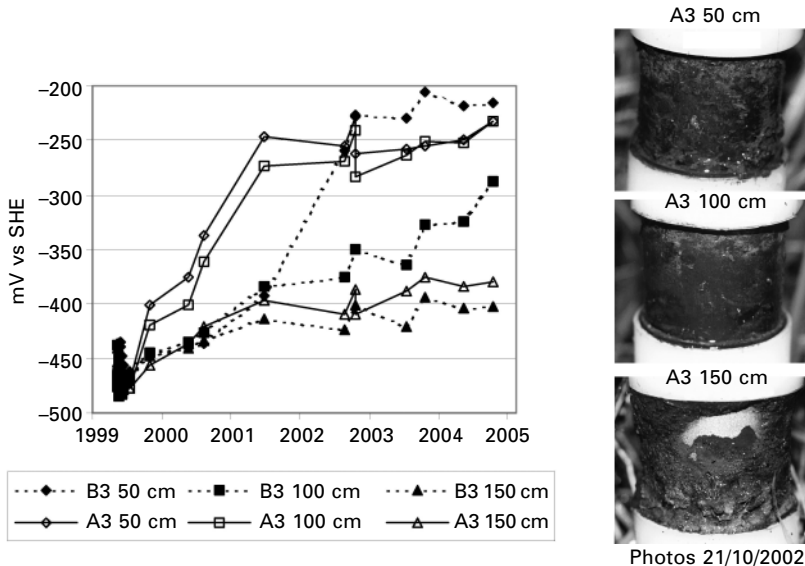
placed in the soil several months after the excavations in 1997 and 1999 had been finished, and all coupons have constantly been below the water table.

Corrosion potentials were measured at intervals on some of the weight loss coupons in Fig. 16.10. Right after installation of the coupons the potentials varied between -580 and -450 mV/SHE, showing no clear system, but for all coupons the potential increased during the two years in the soil. Figure 16.11 shows the close correlation between the weight loss and the 'final' potential of the coupons (i.e. the last potential measured before the coupons were retrieved). This may have at least two explanations. It may show that the coupons act more 'noble' as they are covered by corrosion products, and the coupons with the highest corrosion rates obviously have the thickest corrosion layer after two years. In this context it must be emphasised that the corrosion rates in Fig. 16.11 are the *average* rates during the two years the coupons were left in the soil and not necessarily the *actual* rates. Another explanation for the correlation would be that the more positive corrosion potentials in Fig. 16.11 are simply due to an increased cathodic reaction. In this case the more positive potentials are warning signals indicating an acceleration of corrosion.

Long-term measurements of corrosion potentials were made on steel rings (Fig. 16.12). The results show an interesting pattern, with increasing potentials for two or more years from a start level of -480 to -430 mV/SHE. It is noted that the fastest increase is found with the upper electrodes at 50 and 100 cm depth, first at position A3 and afterwards at position B3, before the potentials appear to become stable at a level of -250 to -200 mV. The deepest electrodes at 150 cm depth have increased to only -400 mV after five years in the soil.



16.11 Comparison between corrosion rate and 'final' corrosion potential measured just before the iron coupons were retrieved after approximately two years in the soil. Note logarithmic x-axis. Data from two groups of coupons are presented (see text to Fig. 16.10).



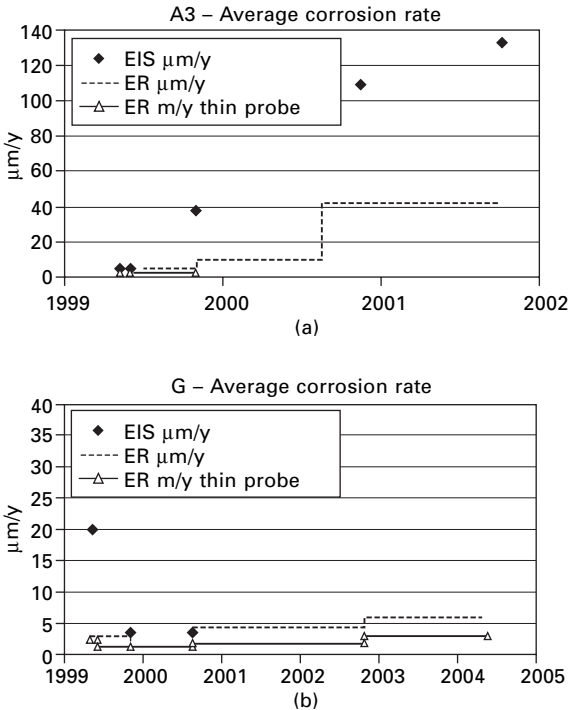
16.12 Five years of measurements of corrosion potential for permanently buried carbon steel rings at 50, 100 and 150 cm depth at two sites in Nydam. The photos to the right show the probe at A3 that was briefly retrieved from the soil, rinsed and photographed, before it was reintroduced at exactly the same position. Tiny samples of the corrosion products were taken for later analysis in the laboratory; the products seemed dense and were difficult to scrape off. The thick deposits on the lower ring (at 150 cm depth) are not corrosion products but soil material (this ring is situated in *gyttja*, which is sticky and cannot be removed by rinsing alone).

Corrosion potentials measured on the weight loss coupons (for two years only) and EIS probes have followed a pattern similar to the deep probes, and none of them have yet ‘jumped’ up to a level of -200 mV (not shown).

Again there are two possible explanations for the increasing potential: either a layer of corrosion products on the rings has made them appear more inert or ‘noble’ (for comparison, the redox potential measured in the soil by inert gold electrodes is very stable around -200 mV during the same period [16]), or it is due to an increased cathodic reaction. We are more in favour of the first explanation as the environmental monitoring has not indicated that the soil conditions have become more aggressive since 1999. Furthermore the probe at A3 was inspected in October 2001, when the two upper probes had corrosion potentials around -250 mV and the lower ring had a potential of -400 mV. This inspection showed that the two upper probes were covered by a dense layer of corrosion product while the lowest ring still showed areas with bare iron (or badly adhered corrosion product falling off during the inspection) – see Fig. 16.12. The corrosion product on all rings was analysed

by ATR-FTIR showing the presence of siderite and possibly some quartz from the environment. The rings have not been analysed by XRD or micro Raman spectroscopy, and the presence of other corrosion products invisible by ATR-FTIR cannot be excluded. The passivating properties of siderite are still unclear [20] but it is assumed that a dense layer may function as a diffusion barrier and decrease the corrosion rate.

EIS and ER data from two probes are shown in Fig. 16.13. EIS data have been fitted to equivalent circuits initially indicating a simple corroding metal and with longer exposure time a circuit indicating film covered and diffusion limited metal. Corrosion rate has been calculated from the fitted charge transfer resistance as for a simple activation-controlled system. EIS measurements were carried out on five occasions from 1999 to 2002 and ER measurements on five occasions up to 2004. All ER probes except at position G have now failed, probably because the iron foil has corroded all the way through at some point.



16.13 Corrosion rates at 100 cm depth as measured by EIS and ER techniques. For comparison the average corrosion rate measured by weight loss was 12 $\mu\text{m}/\text{year}$ at A3, and 4 $\mu\text{m}/\text{year}$ at G, both based on three coupons buried from November 1999 to June/October 2001. Three EIS and ER probes placed next to the excavation pit in 1999 showed similar patterns to the probe at A3.

Overall, the EIS and ER probes give a picture similar to the weight loss coupons, with the highest corrosion rates near the excavation pits (position A3, Fig. 16.13(a), and three probes placed near the 1999 excavation) and a lower rate in an undisturbed area (position G, Fig. 16.13(b)). According to the results from both methods, the corrosion rates near the excavation pits start at a low level but then increase as if the environment gets more aggressive or some kind of auto-catalysis takes place (Fig. 16.13(a)). This is worrying, as there are no signs of passivation of the probes in these data and the calculated corrosion rates are very high. An increasing corrosion rate is difficult to understand, as the environmental effects from the excavations were most prominent during and immediately after the excavation, so a few comments on the reliability of the EIS and ER methods in this environment are necessary. The equivalent circuits of the EIS measurements indicated a high degree of film formation, which makes it difficult to make certain rate calculations. For EIS measurements in environments with a high biological activity, it has earlier been observed that the formation of thick corrosion scales and biofilms greatly increases the capacitance of the system which may lead to a gross (10 or 100 fold) overestimation of the actual corrosion rate [29]. In the actual data the capacitance also increases dramatically with time and it is therefore possible that the estimated corrosion rates are unrealistically high. ER measurements are not normally recommended at sites with local corrosion, and some pitting was actually observed on the ER probe retrieved after two years in the soil (Fig. 16.6). Furthermore it is possible that the ER probes with a thickness of only 25 and 100 μm are simply too thin to allow the formation of a protective corrosion layer.

Measurements at G show a low and fairly constant corrosion rate by both methods. The high initial rate for the EIS measurement is possibly due to disturbance of the environment (e.g. carry-down of oxygen), as the measurement was carried out immediately after installation of the probe.

16.5 Discussion

The purpose of the present study is twofold: to evaluate the feasibility of preserving the remaining archaeological artefacts *in situ* at Nydam, and to compare the corrosion pattern observed for modern and archaeological iron.

Analyses of the archaeological artefacts have shown that the state of preservation observed today is highly variable, but also that to some degree it is a function of the first few years after sacrifice (Fig. 16.8). Some artefacts have been lying for a period exposed in an oxic environment on the mire surface before being overgrown and incorporated in an anoxic environment. This change of environment has given a complex corrosion pattern, where most deterioration has taken place during the first few years, and where the later history has probably included a transformation of corrosion products

from iron(III) oxides into iron(II) carbonate. Other artefacts have been thrust down into the anoxic peat layers right away and have experienced more constant environmental conditions.

Especially in the first case, the corrosion rate has been all but constant so it is questionable to state an ‘average corrosion rate’ for an artefact. Still, it may be illustrative. Measurements on 151 lances have demonstrated corrosion depths as low as 50 µm (average of 20 measurements on a lance). With 1700 years of age this corresponds to an average corrosion rate of 0.03 µm/year (or even lower, if the volumetric expansion of the corrosion products is taken into account). The average corrosion depth for the 151 lances was 300 µm or 0.2 µm/year. The *upper* limit for the corrosion rate of archaeological artefacts is by its nature more difficult to estimate: some artefacts are completely converted into corrosion products (or may have disappeared entirely) and it is not possible to say when this conversion was complete. Axes with no metal left at all have been found in Nydam and with an estimated original thickness of 2 cm they have had an average corrosion rate of at least 5 µm/year, i.e. more than 100 times higher than the best-preserved artefacts. These corrosion rates are comparable with the literature values compiled by Neff *et al.* [30].

Turning to the modern samples, the estimated corrosion rates are compiled in Table 16.2. All these probes have been ‘thrust down’ into anoxic conditions right away, but still there are differences in the corrosion rates. Most markedly the corrosion rates near the excavations are higher than in undisturbed areas (such as position G). This explains some of the variation but there are also individual coupons with high corrosion rates where the explanation is less obvious (Fig. 16.10).

Even at the most undisturbed places the corrosion rates for modern iron are higher than those is observed for the best-preserved archaeological artefacts. Of course this could be due to the current environment being more aggressive than the ‘average’ environment during the last 1700 years; however, apart

Table 16.2 Comparison of corrosion rates as measured on archaeological and modern samples

| Corrosion rate (µm/year) | Max. | Min. | Comments |
|--------------------------|------|------|---|
| Archaeological artefacts | >5 | 0.03 | Max. corrosion rate is unknown |
| Weight loss | 61 | 2 | Max. values near excavation pits |
| ER | 50 | 1 | Max. values near excavation and at A3; low values at position G |
| EIS | 130 | 3 | Max. values near excavation and at A3; low values at position G |

from the effects of archaeological excavations in the area we have no proof of such an environmental change. Another explanation would be that the corrosion rate decreases as the iron samples get covered by a layer of corrosion products. The question then is how long a time it takes before the modern samples become comparable to the archaeological artefacts. Based on Fig. 16.12 we hypothesise that it takes *at least* two years before the modern iron becomes 'stable' in this environment and even then we cannot be certain that these coupons are passivated or still corroding. It thus takes quite a long time before we can expect the modern samples to be comparable or representative of the archaeological artefacts in the soil, making it difficult to obtain a fast answer regarding the preservation conditions in the soil. This is in accordance with the findings of Scharff *et al.* [14], studying the effects of agricultural practice on archaeological iron artefacts in unsaturated soil. They also used modern samples for their studies, but had to conclude that a period of 500 days was not enough to demonstrate, e.g. effects from different fertilisers, probably because it takes a long time before the modern samples are covered by a representative corrosion layer. We have tried to precondition modern coupons with a siderite layer in the laboratory to allow a faster 'realistic' response in the field, but the method needs further development [31]. Also we have initiated a long-term experiment where sufficient weight loss coupons have been placed at the same site in Nydam to allow retrieval at intervals for the next 100 years, in order to study both the variability and possible passivation of the coupons.

16.6 Conclusions

Work will continue to interpret and supplement the data in this chapter. Hitherto it has been found that the use of modern samples is very efficient in demonstrating the great variability within this environment. Also it has been demonstrated that major environmental changes such as temporary drainage are clearly reflected by increased corrosion rates on the modern iron. It remains to be shown whether the high corrosion rates near the excavation pits also affect the archaeological artefacts. Also it remains to be shown whether the modern samples actually do become stable or corrode continuously.

The 'multi-approach' used in the monitoring programme has turned out to be useful, reducing the number of unknowns and giving more confidence to the conclusions. When combining data from the environment, the artefacts and the modern samples, as well as information from archaeologists and geologists working at the site, it is actually possible to evaluate not only the current environment and preservation conditions, but also to some extent the former conditions and corrosion history at the site.

The work at Nydam has focused solely on the preservation of the archaeological artefacts. However, it should be possible to use the same data,

samples and artefacts to discuss the long-term corrosion of modern iron, for instance in relation to the storage of radioactive waste. Sacrificial sites like Nydam may be especially suited for that purpose as it is possible to have at least some information about the burial conditions of the artefacts from the Iron Age until today.

16.7 Acknowledgements

We wish to thank Lars Vendelbo Nielsen, MetriCorr, for his work on ER probes, as well as Ludovic Bellot-Gurlet from Université Pierre et Marie Curie, Paris, and Philippe Dillmann from CEA, Saclay, for micro Raman analysis, revealing that our corrosion products did not consist of pure siderite. This paper is also presented in the 'Science and Technology series' published by the French Agency for Nuclear Waste Management (ANDRA), in a special issue with the EUROCORR 2004 proceedings concerning long-term corrosion behaviour.

16.8 References

1. F. Rieck, *The Spoils of Victory. The North in the Shadow of the Roman Empire* (L. Jørgensen, B. Storgaard and L. G. Thomsen, eds). National Museum of Denmark, 2003, 296–309.
2. B. Sørensen and D. Gregory, *Proc. Metal '98 Conf.* (W. Mourey and L. Robbiola, eds). James & James, 1998, 94–98.
3. L.S. Selwyn, in *ASM Handbook, Volume 13C, Corrosion: Environments and Industries* (S.D. Cramer and B.S. Covino, eds.) ASM (American Society for Metals), 2006, 306–322.
4. L.S. Selwyn, in *Proc. Metal '04 Conf.* (J. Ashton and D. Hallam, eds). National Museum of Australia, 2004, 294–306.
5. M. Fjaestad, A.G. Ullén, K. Tronner, G.C. Borg and M. Sandberg, *Proc. Metal '98 Conf.* (W. Mourey and L. Robbiola, eds). James & James, 1998, 71–79.
6. H.B. Madsen, J.H. Andersen and L.B. Andersen, *Proc. Preserving Archaeological Remains in situ? 2nd Conf. 2001* (T. Nixon, ed.). Museum of London Archaeology Service, 2004, 50–57.
7. V. Fell and M. Ward, *Proc. Metal '98 Conf.* (W. Mourey and L. Robbiola, eds). James & James, 1998, 111–115.
8. D. Neff, S. Reguer, L. Bellot-Gurlet, P. Dillmann and R. Bertholon, *J. Raman Spectroscopy*, 2004, 35, 739–745.
9. F. Schweizer, *Proc. Ancient and Historic Metals. Conservation and Scientific Research*. The Getty Conservation Institute, 1994, 33–50.
10. A.M. Pollard, L. Wilson, A.S. Wilson, A.J. Hall and R. Shiel, *Conservation and Management of Archaeological Sites*, 2004, 6, 363–376.
11. E. Angelini, E. Barberis, P. Bianco, F. Rosalbino and L. Ruatta, *Proc. Metal '98 Conf.* (W. Mourey and L. Robbiola, eds). James & James, 1998, 106–110.
12. C. Caple and D. Dungworth, *Waterlogged anoxic archaeological burial environments*, English Heritage, 1998, report 22/98.

13. A. Smit, *Proc. Preserving Archaeological Remains in situ? 2nd Conf. 2001* (T. Nixon, ed.). Museum of London Archaeology Service, 2004, 168–172.
14. W. Scharff, C. Arnold, W. Gerwin, I. Huesmann, K. Menzel, A. Pötzsch, E. Tolksdorf-Lienemann and A. Tröller-Reimer, *Schutz archäologischer Funde aus Metall vor immissionsbedingter Schädigung*. Konrad Theiss Verlag, Stuttgart, 2000.
15. V. Fell and J. Williams, in *Proc. Metal '04 Conf.* (J. Ashton and D. Hallam, eds). National Museum of Australia, 2004, 17–27.
16. H. Matthiesen, D. Gregory, P. Jensen and B. Sørensen, *J. Wetland Archaeology*, 2004, 4, 55–74.
17. H. Matthiesen, *J. Archaeological Science*, 2004, 31, 1373–1381.
18. H. Matthiesen, D. Gregory, B. Sørensen, T. Alstrøm and P. Jensen, *Proc. Preserving Archaeological Remains in situ? 2nd Conf. 2001* (T. Nixon, ed.). Museum of London Archaeology Service, 2004, 91–97.
19. H. Matthiesen, E. Salomonsen and B. Sørensen, *J. Archaeological Science*, 2004, 31, 1451–1461.
20. H. Matthiesen, L.R. Hilbert and D. Gregory, *Studies in Conservation*, 2003, 48, 183–194.
21. V.F. Buchwald and H. Wivel, *Materials Characterization*, 1998, 40, 73–96.
22. D. Gregory and P. Jensen, *J. Wetland Archaeology*, 2006, 6, 65–81.
23. C. Christensen, *Nydam Mose: Bassinets geologiske udvikling i relation til offerfundene*, National Museum of Denmark, 1995, NNU-report 11.
24. G. Bemann and J. Bemann, *Der Opferplatz von Nydam: Die Funde aus den älteren grabungen: Nydam-I und Nydam-II*, vol. 1-2. Wachholtz Verlag, Neumünster, 1998.
25. D. Postma, *Chemical Geology*, 1981, 31, 244.
26. M.L. Coleman, D.B. Hedrick, D.R. Lovley, D.C. White and K. Pye, *Nature*, 1993, 361, 436–438.
27. J. Chivot, *Thermodynamique des produits de corrosion*, ANDRA, 2004, report 236.
28. J. Bruno, P. Wersin and W. Stumm, *Geochim. Cosmochim. Acta*, 1992, 56, 1149–1155.
29. L.R. Hilbert, PhD Thesis, Technical University of Denmark, 2000.
30. D. Neff, P. Dillmann and G. Beranger, *Proc. Prediction of Long Term Corrosion Behaviour in Nuclear Waste Systems* (D. Féron and D.M. Digby, eds). European Federation of Corrosion, 2002, vol. 36, 295–315.
31. M. Henningsen and B. Bertelsen, BSc. Report, Technical University of Denmark, 2002.

On-line corrosion monitoring of indoor atmospheres

L. SJÖGREN, Corrosion and Metals Research Institute,
Stockholm, Sweden and
N. LEBOZEC, Institut de la Corrosion, Brest, France

17.1 Introduction

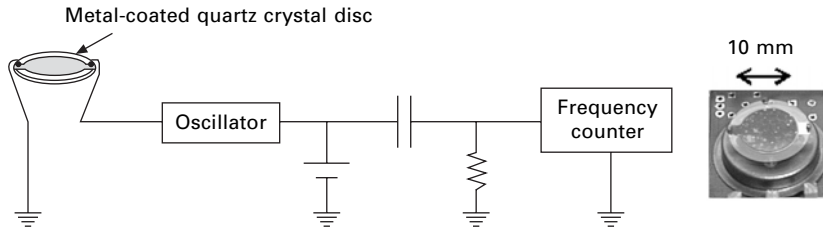
Investigations have shown that risks of indoor corrosion are more easily and more reliably estimated by exposing metals, as compared with analysing climatic conditions and air pollutant concentrations [1]. Such methods are employed for environmental classification, as described by international [2] and business [3, 4] standards. Methods stated in the standards referred to are not for continuous monitoring. Resistance sensors and the quartz crystal microbalance (QCM) are commercially available methods used for on-line measurements in process industry control rooms and in museums. The use of resistance sensors in control and storage rooms has been described by Johansson and Leygraf [5]. Use of the quartz crystal microbalance for monitoring corrosivity under mild atmospheric conditions has been described by Zakipour and Leygraf [6] and its use for environmental characterisation of control rooms by Forslund *et al.* [7].

The aim of this investigation was to evaluate the performance of commercially available corrosion monitoring instruments and sensors. A second aim was the development of a small battery-operated corrosion logger suitable for permanent or temporary use at various indoor locations.

17.2 Experimental

17.2.1 Quartz crystal microbalance (QCM)

A quartz crystal microbalance measures corrosion as changes in resonance frequency of a piezo-electric quartz crystal with a metal coating, the resonance frequency being a function of the mass of the crystal; see Fig. 17.1. Most crystals used for this application are of the so-called AT-cut, the disc being cut at an angle of $+35^{\circ}15'$ relative to the crystallographic Z-axis of the original single crystal. This results in a shear deformation of the crystal with a stable and sharp resonance frequency. The temperature dependence of the



17.1 Principle of the quartz crystal microbalance and photo of a copper-coated crystal disc after exposure.

resonance frequency is slight at about 25°C, which is convenient for indoor applications. Crystals for corrosion measurements are coated by the metal of interest, usually by physical vapour deposition.

The frequency response from changes in mass follows the Sauerbrey equation (17.1):

$$\Delta f = - \left(\frac{f_0^2}{\rho_q N} \right) \Delta m \quad 17.1$$

where: Δf = change in frequency

f_0 = resonance frequency

ρ_q = density (2.648 g/cm³ for quartz)

N = frequency constant (1670 kHz mm for a transverse wave in AT-cut quartz)

Δm = mass change/area, assuming film growth on one side of the crystal.

A frequency change of 1 Hz for a 5 MHz crystal (readily measurable) corresponds to 18 ng/cm², giving a film thickness resolution of 2 Å for a Cu₂S film [6, 8]. A disadvantage of the quartz crystal method is that it is equally sensitive to dust and other contaminants as to corrosion products formed. Further, water is adsorbed on the surface, adding to the mass of the crystal and to sensor response. The amount of water depends on relative humidity, metal coating, surface roughness and surface films present [9, 10].

Commercial instruments with 6 MHz quartz crystal sensors, coated with 4000–5000 Å copper or silver, were used in this investigation. The instruments measure resonance frequency, and the results obtained are reported as film growth, assuming corrosion films of copper and silver sulphide (Cu₂S and Ag₂S) respectively.

17.2.2 Electrical resistance sensors

With this method, resistance of a thin track of metal was measured. Corrosion, reducing the metal thickness, causes resistance to increase. The method

requires the sensing metal to corrode uniformly; metals prone to pitting, crevice or grain boundary corrosion, under the conditions to be monitored, are not usable. The sensors employed in this investigation consisted of serpentine copper or silver tracks, deposited on a glass substrate; see Fig. 17.2. By measuring relative to a corrosion-protected track of the same metal and at the same temperature, the temperature dependence of the metal resistivity was compensated for. The corrosion rate is calculated according to equation 17.2:

$$\text{Corrosion depth} = t_i \left(1 - \frac{R_{\text{ref}}}{R_s} \cdot \frac{R_{i,s}}{R_{i,\text{ref}}} \right) \quad 17.2$$

where: t_i = initial metal track thickness (assumed equal for the reference and sensor tracks)

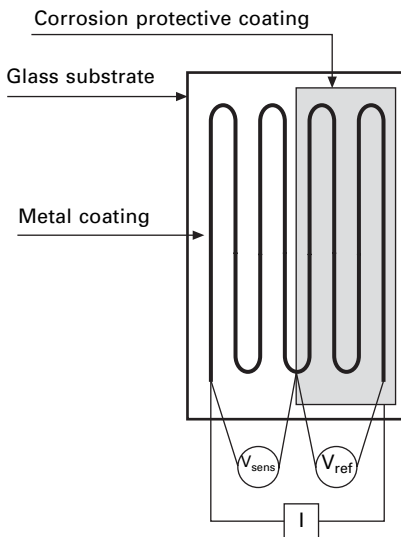
R_s = resistance of the sensor track

R_{ref} = resistance of the reference track

$R_{i,s}$, $R_{i,\text{ref}}$ = initial resistance of sensor- and reference track respectively.

Besides the accuracy of the resistance meter, sensitivity is governed by metal track length, width and thickness. It is thus possible to produce sensors with a sensitivity and life adapted to the specific requirements.

Measurements were performed using a logging instrument storing results for up to four resistance sensors, connected via cables. Additional measurements were performed manually, using a resistance bridge or a microohmmeter. In both cases, measurement current was less than 1 mA and current pulses were



17.2 Principle of the electrical resistance sensor.

used for thermo potential compensation. Properties of commercially available resistance sensors with 2 mm wide and 5000–6000 Å copper or silver tracks, and of laboratory-manufactured sensors (Acreo, Norrköping, Sweden) with 1 mm wide, 4300 Å thick sputtered copper tracks or 3900 Å thick evaporated silver tracks, were evaluated.

17.2.3 Prototype corrosion logger

A small battery-operated corrosion logger was developed for enabling measurements to be made in confined spaces or where electricity is unavailable, e.g. in display cases, in cabinets intended for storage of sensitive objects or inside transport packages. The logger, shown in Fig. 17.3, employs the electrical resistance technique. It has been evaluated with laboratory-manufactured sensors with copper and silver tracks.

17.2.4 Reference methods

For field exposures and some laboratory exposures, reference coupons of silver and copper were employed. The coupons were degreased and ground with 1200 P (600 grit) SiC paper. The coupons were weighed relative to a reference weight before and after exposure; approximate weighing accuracy is $\pm 0,15 \mu\text{g}/\text{cm}^2$. In some cases, besides mass gain, mass loss was determined for copper coupons after removal of the corrosion products in 5 wt% sulphamic acid, $\text{H}_2\text{NSO}_3\text{H}$. For silver, coulometric reduction was employed, following the method described by Krumbein *et al.* [11].



17.3 Taking readings from a prototype corrosion logger.

17.2.5 Laboratory exposures

Sensors and metal coupons were exposed in a climatic cabinet under varying temperature and humidity conditions, with and without corrosive gases. Sulphur dioxide, hydrogen sulphide and/or nitrogen dioxide in low concentrations, e.g. from a few ppb to 100 ppb, were used as corrosive gases.

17.2.6 Field exposures

Three different exposure sites were employed, all at pulp and paper plants. At the first site, sensors were mounted inside ventilation shafts, one before and one after a carbon filter cassette for incoming air. At the second site, sensors were positioned on top of a cabinet, directly exposed to incoming purified air, inside a room for a distribution plant of a cardboard mill. The third site was inside a pump room in a building located beside a sewage plant, the sensors being positioned approximately 1 m above the floor.

17.3 Results and discussion

For exposures including both quartz crystals and resistance sensors, measurement results for the different sensors and metal coupons were transformed to film growth, as measured from the start of each exposure. The film thickness is calculated according to equation 17.3:

$$\begin{aligned} \text{Thickness of corrosion film} = & \text{Corrosion depth} \times \frac{\rho(\text{metal})}{\rho(\text{film})} \\ & \times \frac{1}{n(\text{metal/film})} \times \frac{\text{Mw}(\text{film})}{\text{Mw}(\text{metal})} \end{aligned} \quad 17.3$$

where: ρ = density (of corrosion film or metal)
 n (metal/film) = metal equivalents per film equivalent (e.g. 2 for Cu_2S)
 Mw = molecular weight.

For calculating film thickness, films on copper are assumed to consist of copper sulphide Cu_2S and films on silver of silver sulphide Ag_2S , in accordance with the presentation of the quartz crystal sensor results – see paragraph 17.2.1. Since corrosion products formed under benign conditions are normally not sulphides, this assumption will result in incorrect film growth results. As an example, if the dominant constituent of the corrosion film is $\text{Cu}_4\text{SO}_4 \cdot (\text{OH})_6$, measuring corrosion as mass loss or via changes in electrical resistance and assuming that the film is Cu_2S will result in a calculated film thickness of half its true value – see Table 17.1.

Table 17.1 Film thickness calculations from corrosion depth

| Copper corrosion product | Film thickness (Å) for a corrosion depth of 1Å | Silver corrosion product | Film thickness (Å) for a corrosion depth of 1Å |
|--|--|---------------------------------|--|
| Cu ₂ S | 2.0 | Ag ₂ S | 1.7 |
| CuS | 2.9 | AgCl | 2.5 |
| Cu ₂ O | 1.7 | Ag ₂ O | 1.6 |
| CuO | 1.7 | Ag ₂ SO ₄ | 2.8 |
| Cu ₄ SO ₄ *(OH) ₆ | 4.0 | | |

Note: Under indoor conditions mixtures of different carboxylate salts are reported to be formed on copper surfaces, i.e. even larger molecules than used in the examples of the table. On silver, Ag₂S is common [12].

Table 17.2 Corrosion depth calculations from mass gain

| Copper corrosion product | Corrosion depth (Å) for 1 mg/m ² mass gain | Silver corrosion product | Corrosion depth (Å) for 1 mg/m ² mass gain |
|--|---|---------------------------------|---|
| Cu ₂ S | 4.4 | Ag ₂ S | 6.4 |
| CuS | 2.2 | AgCl | 2.9 |
| Cu ₂ O | 8.9 | Ag ₂ O | 12.8 |
| CuO | 4.5 | Ag ₂ SO ₄ | 2.1 |
| Cu ₄ SO ₄ *(OH) ₆ | 1.4 | | |

Measuring mass gain, corrosion depth can be calculated according to equation 17.4:

$$\text{Corrosion depth} = \text{Mass gain} \times \frac{1}{\rho(\text{metal})} \times \frac{\text{Mw}(\text{metal}) \times n(\text{metal/film})}{\text{Mw}(\text{film}) - \text{Mw}(\text{metal}) \times n(\text{metal/film})} \quad 17.4$$

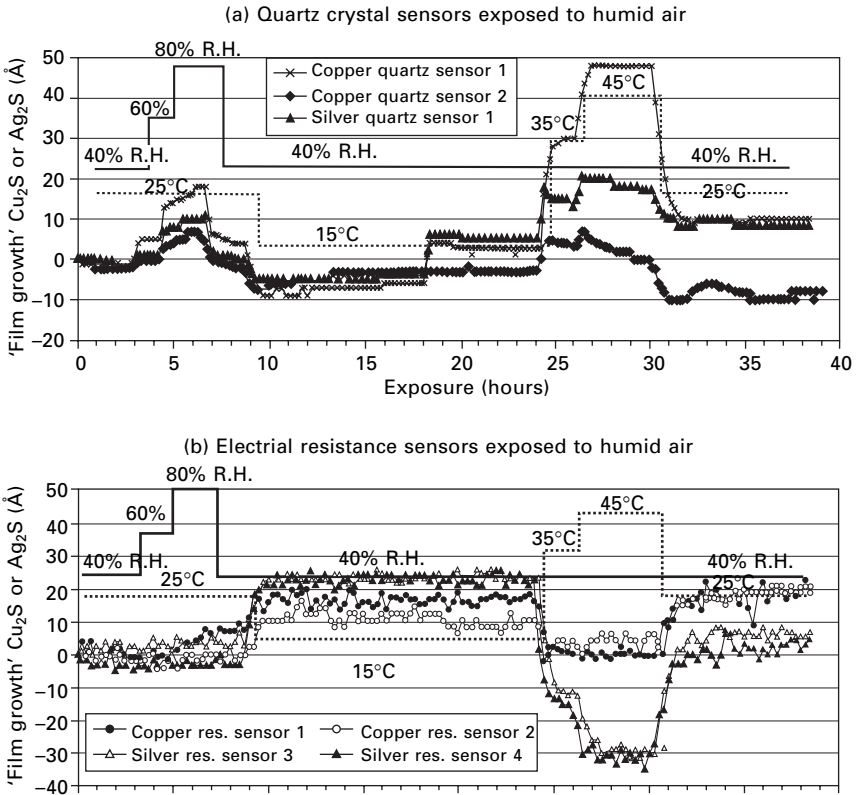
Examples are given in Table 17.2. If mass gain from growth of a Cu₄SO₄*(OH)₆ film is measured using the QCM and is presented as film thickness assuming Cu₂S, this would correspond to overestimating the corrosion depth by a factor of 3.

17.3.1 Laboratory exposures, commercial instruments and sensors

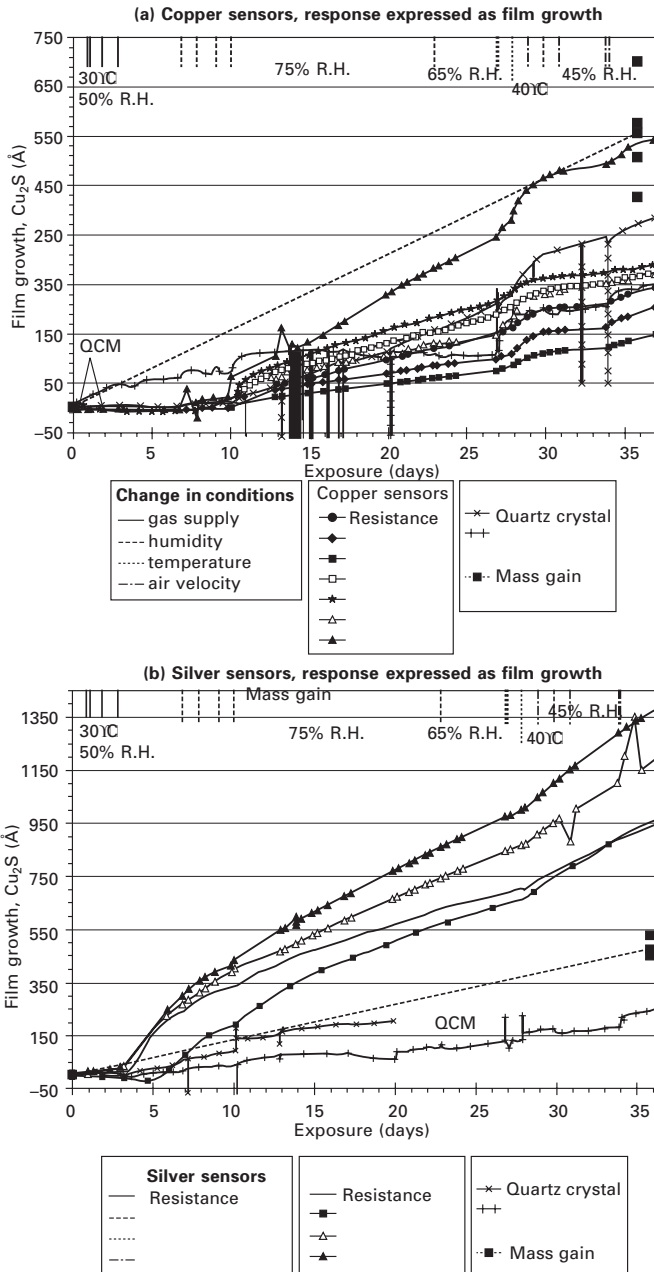
As expected, readings from the quartz crystal sensors are affected by both humidity and temperature, with individual differences in magnitude:

Fig. 17.4 (a). Readings from electrical resistance sensors have shown no humidity dependency but effects of temperature, despite the use of a reference for temperature compensation. As shown in Fig. 17.4 (b), the temperature effects differ between individual sensors and between metals used, silver showing the most pronounced effects.

Examples of results from laboratory exposures in humid air, with corrosive gases added, are presented in Fig. 17.5. Differences in slopes of the individual graphs reflect the spread in sensor response. The ability to indicate changes in test conditions is shown as changes in the slope of the graphs. Even if individual differences are large, all sensors reveal changes in exposure conditions. Differences in behaviour of the two metals are evident, copper showing higher sensitivity to humidity and temperature changes while silver is more affected by the addition of corrosive gases. For copper, corrosion rate increases when humidity increases, while silver corrosion is indicated



17.4 (a) Quartz crystal, and (b) commercial electrical resistance sensors, temperature and humidity effects. Readings are expressed as film growth – corresponding Cu_2S or Ag_2S film thickness as if the readings were due to corrosion.



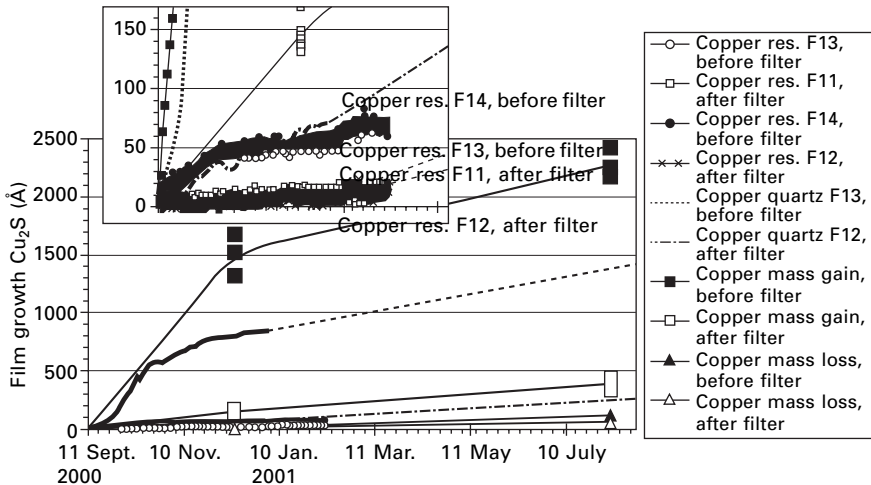
17.5 Exposure of (a) copper and (b) silver sensors in humid air, 65–75% R.H., 30–40°C with low concentrations of NO₂, SO₂ and H₂S (approx. 50 ppb SO₂ and NO₂, 2–3 ppb H₂S, gases added one by one during the first three days). Curve symbols mark manual measurements while curves without symbols show results from logging data every 15 minutes.

also at lower humidity. Measurement disturbances do occur for both types of sensors, as also shown in Fig. 17.5.

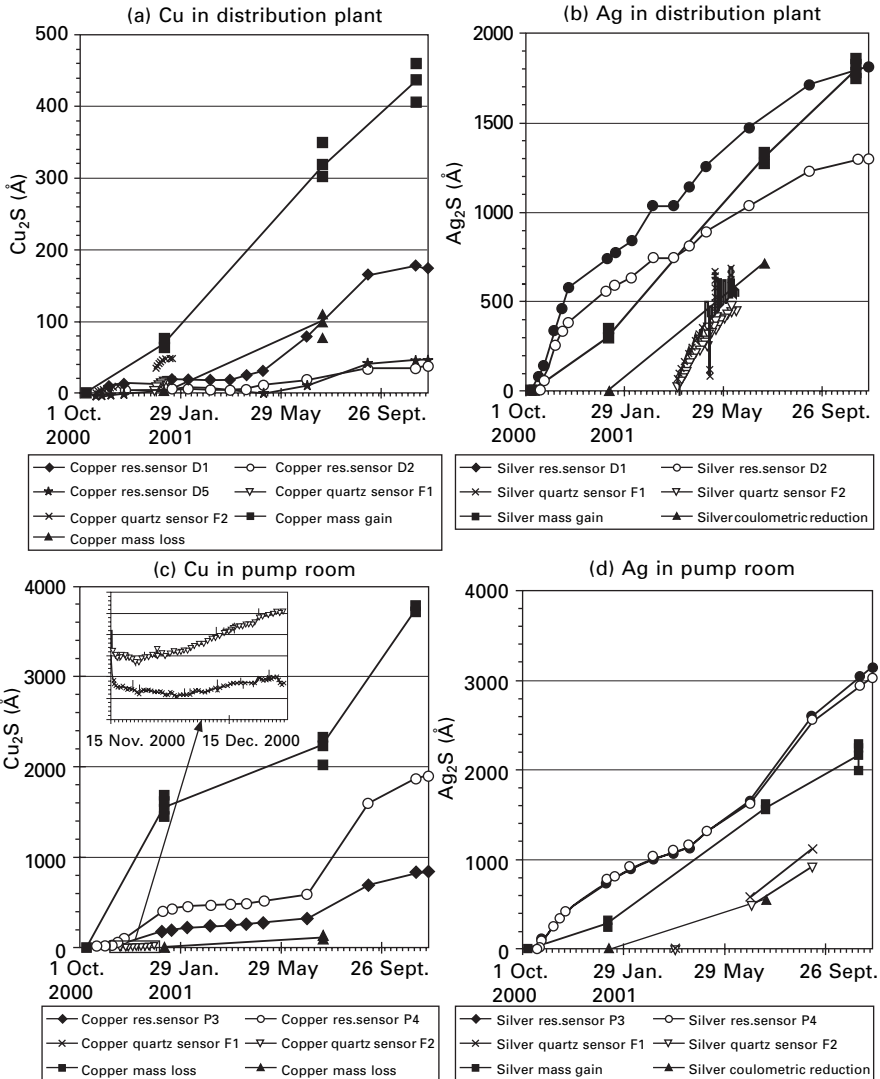
17.3.2 Field exposures, commercial instruments and sensors

In dusty environments, such as before the carbon filter in a ventilation shaft, Fig. 17.6, effects of dust are far greater than effects of corrosion. Quartz crystal sensors are thus not very useful under such circumstances. The resistance sensors show that corrosivity is indeed lower after the carbon filter. It is evident from mass gain and quartz crystal results that the amount of dust is much lower after the filter, through it still seems too high for the quartz sensor to give useful results. Based on electrical resistance sensor and mass loss results, corrosivity is estimated as low (G1 according to ISA-S71.04-1985 [3], a corrosivity classification system for electronic equipment) both before and after the carbon filter.

Results from sensors exposed in a distribution plant and in a pump room, at both a pulp and a paper plant, are shown in Fig. 17.7. The relation between the different types of sensors is similar to the laboratory exposure with low concentrations of corrosive gases, Fig. 17.5. Compared to resistance sensors, relatively higher copper corrosion rates are indicated by mass gain. A reason may be that corrosion products with larger, thus heavier, molecules than Cu_2S , the substance assumed for the film thickness calculations, are formed



17.6 Exposure of copper sensors in ventilation shafts before and after a carbon filter. Mass gain curve symbols indicate the metal coupon being exchanged. The resistance sensors were removed after half the exposure period.



17.7 Exposure of copper and silver sensors in the distribution plant and pump room. Measurement results are expressed as film growth. Mass gain curve symbols indicate the metal coupon being exchanged. The quartz crystal sensors were alternately exposed in the two rooms.

in the low gas concentration test and in the field (Cu_2S is expected to form under more corrosive conditions).

In the exposures of Fig. 17.7, the quartz crystal sensors and instrument were moved between the two locations, a procedure that seems to affect readings. Moving the copper quartz sensors from the distribution plant to the pump room resulted in a diversion between the two individual sensors. When

moved back to the distribution plant, the two sensors follow the same path, but are now parallel. The copper quartz sensors were later exchanged for silver ones. Due to an instrumental problem, however, it was only possible to obtain information on average film growth rate for silver sensors in the pump room; these results, for silver quartz sensors F1 and F2, are presented as broken lines in Fig. 17.7 (d). Employing the broken line as quartz crystal results, the three methods for measuring silver corrosion (compare the slopes of the curves) show much better agreement when compared to the copper sensor results.

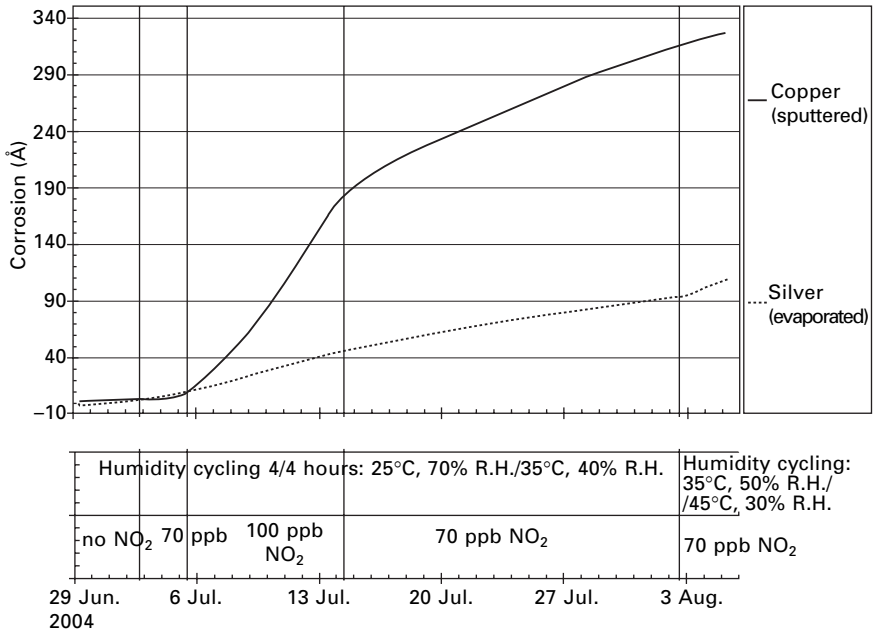
From Fig. 17.7 it is obvious that corrosivity is higher in the pump room than in the distribution plant, copper showing the largest difference. A higher corrosion rate is further indicated during the summer period in the pump room; this may be due to higher summer temperatures or to variations in wind direction, the windows of the room facing a sewage plant. The increase in corrosivity in the distribution plant registered by the resistance sensors in the spring may be due to activities preparing for a planned shutdown, activities involving open doors, and the making of a hole in the floor.

Based on copper sensor and mass gain results, corrosivity is estimated as low in the distribution plant, e.g. G1 according to ISA-S71.04-1985 [3]. Silver corrosivity is higher, entailing risks for deteriorated silver-plated connectors, for example. In the pump room, copper corrosivity is low to moderate, e.g. G1-G2 corrosivity category, which can be regarded as a borderline case for electronic equipment. Silver corrosivity is equivalent to that measured in the distribution plant.

17.3.3 Laboratory exposure, prototype logger, laboratory manufactured sensors

Results from a laboratory exposure to cyclic humidity, including low concentrations of NO_2 , are shown in Fig. 17.8, illustrating differences between the two metals in reacting to changes in environmental conditions. Copper sensors appear more sensitive to changes in NO_2 concentration while silver sensors show stronger reactions to temperature variations. With the prototype corrosion logger and the approximately 4000 Å copper and silver sensors, measurement sensitivity is estimated at a few angstroms reduction in thickness, which should be sufficient for corrosion rate measurements under benign indoor atmospheric conditions.

Figure 17.9 shows results from several copper and silver sensors exposed in parallel, including both logger readings and manual readings. For the manual silver sensor readings, average corrosion rate was calculated for two exposure periods and is presented in the diagram. A standard deviation of 26% and 13% was obtained for the two exposure periods respectively. This variation in sensor response is considered acceptable for corrosivity

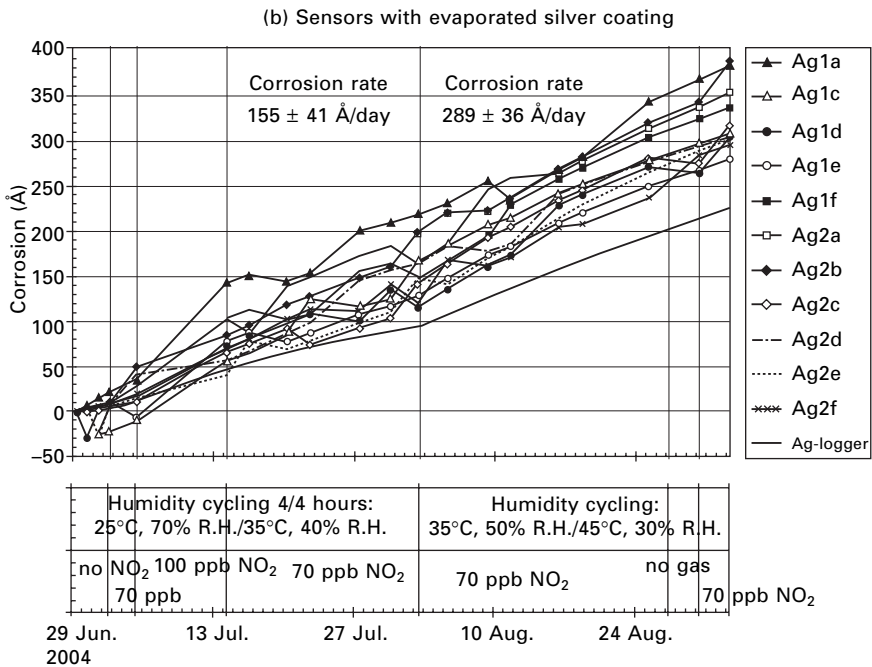
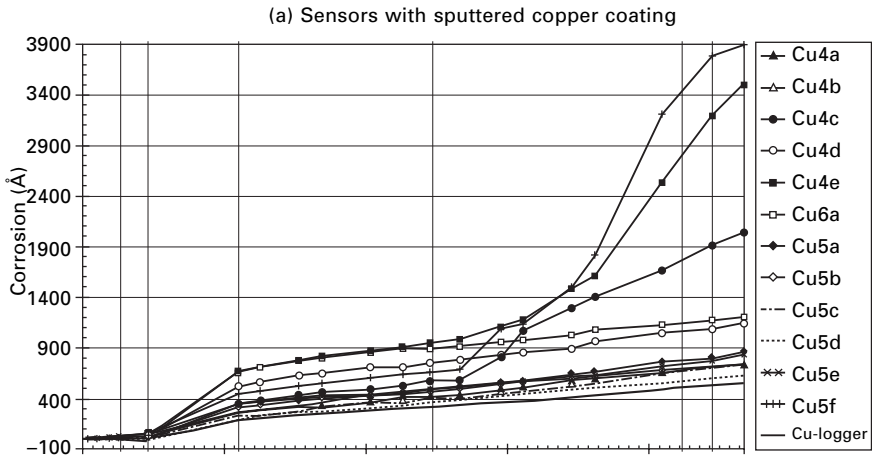


17.8 Corrosion logger results presented as corrosion depth, for copper and silver sensors exposed to humidity and temperature cycling and low concentrations of NO₂. If films of Cu₂S and Ag₂S are assumed to be formed, the corrosion film thickness (in Å) would be approximately twice the corrosion depth (see Table 17.1).

classification purposes, even if variations in response from mass gain measurements are generally smaller – compare Fig. 17.7.

Since a couple of copper sensors showed substantially deviant behaviour, no statistical evaluation of the copper sensors has been performed. The deviant behaviour, characterised by sudden large increases in measured corrosion rate, is explained by local attack. Protruding corrosion products are clearly visible at 10× magnification; the attack resulted in a substantial reduction in metal thickness across a small part of the copper track. The attack is believed to have been initiated by dust particles which, being hygroscopic, would be more corrosive to copper than to silver, thus explaining why this effect was observed only for copper.

As shown in Fig. 17.9, the logger readings were lower than the manual readings, for both metals. A likely explanation for this behaviour is differences in voltage instrument response between the sensor and reference tracks, a problem not relevant for the manual measurements where the same instrument circuitry was used for both tracks. This problem should be easily corrected in future developments of the logger.



17.9 (a) Copper and (b) silver sensor results presented as corrosion depth. The sensors were exposed to humidity and temperature cycling in presence of low concentrations of NO₂. If films of Cu₂S and Ag₂S are assumed to be formed, the corrosion film thickness (in Å) would be approximately twice the corrosion depth (see Table 17.1).

17.4 Conclusions

The monitoring methods evaluated, quartz crystal microbalance and electrical resistance sensors, are both found to be useful for monitoring changes in environmental conditions and to be sufficiently sensitive for use under indoor atmospheric conditions. Both sensor types can be used for measuring corrosion rates of different metals, provided corrosion is uniform.

Electrical resistance sensors measure corrosion, i.e. metal loss, directly and can be adapted for use under various corrosivity conditions. These sensors are not directly affected by particles, water films, etc., and are thus considered most suited for general use. With approximately 4000 Å thick copper or silver tracks, it has been possible to achieve a measurement sensitivity of 1–2 Å corrosion (reduction in thickness). The reproducibility of sensor response is considered acceptable for the silver sensors with <30% standard deviation for corrosion rate measurements during laboratory exposures. The copper sensors require further development, optimising track dimension, in order to reduce effects of local attack, e.g. caused by dust particles.

The small battery-operated corrosion logger that has been developed, working with resistance sensors, offers sufficiently high measurement sensitivity for detecting changes and differences in corrosion rate under indoor conditions, with the advantage of giving on-line information. The logger is thus suited for comparing conditions at different locations and is small enough for monitoring corrosive conditions, e.g. inside packages during transport.

17.5 Acknowledgement

The authors wish to express their thanks to Conseil Régional de Bretagne for supporting the development of the prototype corrosion logger.

17.6 References

1. E. Johansson, B. Rendahl, V. Kucera, *Corrosion* 98, San Diego, paper 359.
2. ISO 9223, 'Corrosion of metals and alloys – Corrosivity of atmospheres – Classification', International Organization for Standardization, Geneva (1992).
3. ISA-S71.04-1985, 'Standard. Environmental conditions for process measurements and control systems: Airborne contaminants', Instrument Society of America, Research Triangle Park, NC (1985).
4. SSG 4251E, 'Electrical operations rooms. Air treatment plants. Project engineering instructions', Pulp and Paper Industries' Engineering Co. (1994).
5. E. Johansson, C. Leygraf, *British Corrosion Journal*, vol. 34, no. 1 (1999), p. 27.
6. S. Zaki pour, C. Leygraf, *British Corrosion Journal*, vol. 27, no. 4 (1992) p. 295.
7. M. Forslund, J. Majoros, C. Leygraf, *Journal of the Electrochemical Society*, vol. 144, no. 8 (1997) p. 2637.
8. T. Aastrup, C. Leygraf, *Journal of the Electrochemical Society*, vol. 44, no. 9 (1997) p. 2986.

9. M. Forslund, C. Leygraf, *Journal of the Electrochemical Society*, vol. 44, no. 1 (1997) p. 113.
10. T. Aastrup, 'In situ investigations of the metal/atmosphere interface', Doctoral Thesis, Department of Materials Science and Engineering, Division of Corrosion Science, Royal Institute of Technology, S-100 44 Stockholm, Sweden (1999).
11. S.J. Krumbein, B. Newell, V. Pascucci, *Journal of Testing and Evaluation*, vol. 17 (1989), p. 357.
12. D. Persson, C. Leygraf, *Journal of the Electrochemical Society*, vol. 142, no. 5 (1995), p. 1468.

Corrosion inhibitors for metallic artefacts: temporary protection

E. ROCCA, Université Henri Poincaré, France and
F. MIRAMBET, Laboratoire de Recherche des
Monuments Historiques, France

18.1 Introduction

The environment is the main cause of the decay of metallic elements from the cultural heritage. Art curators with the support of analytical science attempt to intervene to stop the deterioration. In many cases, the conservation efforts cannot stop the deterioration process or reverse the ensuing damage, but they can help slow the rate of degradation to ensure a longer existence for artefacts.

The interactions between the metal and its environment are responsible for the electrochemical reactions leading to corrosion. To avoid further degradation and in general the appearance of corrosion products, a more or less insulating barrier must be created on the metallic surface between the object and the atmosphere. Different barrier coatings have been developed, such as anodic oxides, ceramic and inorganic coatings as corrosion inhibitors, organic coatings and conversion coatings. Most of them were first developed for industrial applications. They generally require the removal of the corrosion products, and their application leads to important changes in the visual appearance of the metallic surface. These treatments have also been applied for the outdoor protection of large structures that are part of the cultural heritage, like bridges or buildings protected by French legislation. But for a large proportion of works belonging to the cultural heritage, such as patinated artefacts or sculptures and archaeological artefacts, these protection systems cannot be applied.

For the application of these protective systems in the restoration domain, the selection of an anti-corrosion treatment should be based on the evaluation of different specific criteria:

- Storage conditions of the artefact (outdoor, indoor, controlled or uncontrolled environmental conditions)
- Presence or absence of corrosion products on the surface which can decrease the efficiency of the treatment

- Final visual appearance of the treated object surface which should not be altered
- Reversibility of the protective system. Indeed, the removal of the protective system should be easy, to allow future treatments on the object.

Three other criteria are nowadays important to evaluate the replacement of the protection:

- The temporary character of some treatments which have to be applied two or three times per year to be efficient
- The toxicity of the chemical substance responsible for the inhibition properties
- The price of the protection system.

In the first part of this chapter, we present a brief review of the protection systems, except painting systems, currently used for conservation purposes. In the second part, recent researches on a new corrosion inhibitor family will be developed.

18.2 State of the art inhibitors

Because of their weak influence on the modification of the surface appearance, lacquers (varnishes), waxes and corrosion inhibitors are the most common protection systems used in the context of restoration works [1]. Since the 1960s, many studies have been carried out to evaluate their efficiency for the protection of different metallic elements of the cultural heritage. Because various factors such as preparation of the metal surface, adhesion and impermeability of the film may influence the effectiveness of these coatings, a clear evaluation of these protection systems is not always easy to perform.

18.2.1 Varnish

For artefacts conserved in museums under controlled environmental conditions, varnishes are generally applied as a final protection system. Three polymer-based materials are currently employed in restoration: cellulose nitrate, acrylic and vinylic polymer. The nitrocellulose varnishes were introduced in the 1960s and were used in museums for coating bronze, brass and silver alloys. However, due to the rapid degradation of cellulose nitrate under moisture and UV radiation exposure, this kind of varnish is applied mainly in the case of indoor conservation. Nevertheless, the weak performance of this varnish class does not allow its use in uncontrolled storage conditions [1]. Thus, such varnishes have gradually been replaced by acrylic-based lacquers.

For acrylic systems, Paraloid B72, a copolymer of ethyl methacrylate and methyl methacrylate, has been used extensively for more than 20 years in metal conservation work, as both an adhesive and a protective coating [2].

Incralac is another acrylic varnish employed mainly by conservators that contains an ethyl methacrylate–butyl acrylate copolymer (named B44) and a small amount of benzotriazol acting as a corrosion inhibitor, according to the supplier. This coating has been widely applied for outdoor applications, especially for bronze sculptures [3]. In the case of outdoor artefacts, the high molecular weight of the acrylic-based polymer provides good resistance, according to many conservators. However, some studies realised over long periods have shown that Incralac could have good barrier properties for outdoor bronze for two years' duration, but for a longer exposition time this protection system breaks down and becomes insoluble [4, 5]. This fact can be correlated to the important water permeability of the acrylic polymer which is well known in the industrial domain. Moreover, some authors have reported that the weak adhesion between Incralac and bronze may allow the development of corrosion at the interface beneath the varnish layer [6]. Several experiments realised on bare metal surfaces showed that with Incralac a topcoat of wax has to be applied to provide sufficient protection [7]. The Incralac/wax duplex system seems to allow the association of the acrylic polymer barrier property with the hydrophobicity of the wax.

Vinyl systems like Rhodopas M and Pioloform have also been used for archaeological artefacts, and their performance was tested on different metallic surfaces by Mourey *et al.* [8]. However, the results obtained do not allow the determination of a clear evaluation of these different coatings because their performance seems to be correlated with the metal/coating system.

Epoxy polymer systems are seldom used in restoration, although the best performances are observed with these coatings. Indeed, the epoxy base is generally known as the most impermeable organic coating for industrial applications. Nevertheless, their insolubility in water and organic solvents leads to poor reversibility of this kind of coating, which prevents its use on a large scale in conservation restoration.

In conclusion, varnishes are generally considered by conservators as temporary protection systems that provide good barrier performance only for short ageing times. But the very limited visual changes observed after their application allow their use on a wide range of metallic surfaces. Nevertheless, this kind of organic coating can induce, in some cases, local corrosion phenomena at the metal/coating interface due to weak adhesion between the polymer and the substrate. In addition, the re-treatment of the objects often demands complex procedures using organic solvents in the restoration workshop.

18.2.2 Waxes

Because wax-based coatings fulfil the main conditions of application (reversibility and transparency) laid down by conservation ethics, their use

is advocated by professionals involved in the conservation of the cultural heritage. Waxes are intensively used for outdoor sculpture and ornamentation. They can be applied hot or cold, with or without pigment on the metallic surface. In the past, a variety of waxes, both natural and synthetic, have been used, but the ageing of natural waxes in contact with moisture is known to produce some organic acids that can interact with the metal. For this reason, the application of synthetic waxes is nowadays rather recommended. Many types or combinations of synthetic microcrystalline or polyethylene waxes are used for the protection of both outdoor monuments and indoor metal artefacts. These coatings, which were developed for industrial applications, have not been refined specifically for the protection of metallic cultural heritage artefacts. Therefore, several studies have been devoted to the measurement of the efficiency of commercial waxes on different metals of metallic artefacts.

Electrochemical studies such as impedance measurements and climatic chamber tests have generally been performed on both uncorroded and corroded bronze samples treated with commercial waxes. In general, the chemical composition of commercial waxes used commonly by conservators in a specific country is not perfectly known, and it is difficult to compare their results.

Price *et al.* [9] have studied two categories of waxes – commercial microcrystalline and polyethylene waxes – on bronze plates, by using both surface analysis and electrochemical impedance spectroscopy (EIS). Scanning electron spectroscopy showed that the film morphology is directly correlated to the method of application that induces changes in the performance of the coating. These authors reported also that EIS measurements carried out on wax-coated bronze plates in NaCl can provide some quantitative data about the wax failure. According to their results, BeSq 195, a microcrystalline wax, outperforms the other waxes. Other EIS experiments have been performed on five different commercial waxy coatings to evaluate their performance in comparison with the BeSq 195 wax for long-term protection of outdoor bronze sculptures [10]. The EIS data obtained in a NaCl corrosive medium suggest that Dinitrol 4010 and Cor-Tol 450 coatings provide better corrosion resistance than BeSq 195.

According to some restoration works in which multilayer systems were applied on outdoor sculptures, many studies have been devoted to the evaluation of the efficiency of duplex coatings composed of Inralac and waxes. By using EIS (in a corrosive medium composed of $(\text{NH}_4)_2\text{SO}_4$ and NaCl), Ellingson *et al.* [7] evaluated the performance of three specific coatings applied on bare bronze plate: a microcrystalline wax, Inralac and an acrylic/urethane topcoat often used by conservators in the United States. The different data obtained by EIS experiments show that the better performance is observed for a system composed of three parts: acrylic + acrylic/urethane + wax.

In most restoration work, the waxes and the varnishes are not applied on

fresh stripped metal surfaces. Thus, the efficiency of these coatings on corroded surfaces is also very important, though it has been studied by only some authors. Otieno-Alego *et al.* [11] performed EIS measurements to evaluate the performance of wax coatings on bronze artefacts that were artificially patinated by three different chemical solutions. The conclusion of this work is that each kind of bronze patina needs a specific wax to have good corrosion behaviour.

Among the large number of wax-based coatings tested in those different studies, some authors consider this kind of protection as a low-maintenance system. Nevertheless, these coatings systems have only limited long-term stability and require considerable maintenance to provide good protection properties for long duration, and some authors have reported that regular application of waxes must be done two or three times per year [12]. To increase the time between applications, a new class of materials, lacquers containing organic–inorganic copolymers named Ormocer, developed by the Fraunhofer Institute, have been used for bronze conservation. The base material of this coating is siloxane molecules in water or water/solvent solution. After hydrolysis, these molecules are transformed in insoluble organic–inorganic structures on the surface. Various Ormocer coatings were tested by Pilz and Römich [13] and compared to reference coatings such as microcrystalline wax or Incralac. In these tests, the Ormocer system applied in a bilayer showed no loss of performance after the ageing process. This seems very promising, but the reversibility of these coatings is open to doubt because their removal in many cases requires hard mechanical methods. Moreover, after application of Ormocer, an important darkening of the treated patina has been observed, which is a limiting factor for the application of this system in the conservation domain.

18.2.3 Inhibitor compounds

The use of corrosion inhibitors in the context of metal conservation has also attracted a large amount of interest [14]. Some studies have been carried out on some organic inhibitors in the case of acid cleaning [15]. They have evaluated the effect of different corrosion inhibitors such as benzotriazole and thiourea in the case of stripping solution for brass, copper or iron artefacts. The ability of corrosion inhibitors to form insoluble compounds at the metal surface which can provide better corrosion resistance is also of great interest for the conservation of metallic elements of the cultural heritage. The application of inhibitor compounds allows the formation of a thin passive layer which can retard the anodic and/or cathodic reactions responsible for corrosion.

The most widely used inhibitor compound is benzotriazole (BTA) in the case of copper alloys for protection purposes, or with the addition of some stripping solutions to decrease the kinetics of metal dissolution [16]. This

inhibitor compound was employed for the first time in 1967 for the treatment of antiquities of copper and copper alloys [17]. Since then, many conservators have used this protection system as a preventive treatment for the conservation of archaeological copper alloys because of its ability to form complexes of Cu(I) and Cu(II). The effectiveness of BTA has clearly been proved for clean copper surfaces. But few researchers have studied BTA application for corroded copper alloys. Brostoff [18] reported that a copper–benzotriazole complex can form on various copper corrosion layers containing several corrosion products, the Cu–benzotriazole film morphology depending on the heterogeneity of the corrosion layers. In general, the treated artefacts are immersed in a 3 wt% solution of BTA in alcohol at room temperature for 24 hours. A topcoat composed of Paraloid B72 is commonly applied to increase the protective capacity. But the effectiveness of this corrosion inhibitor on corroded archaeological artefacts is still controversial, especially for artefacts containing chlorinated phases.

Scientists involved in the conservation domain have proposed other inhibitor compounds for copper-based artefacts. Faltermeier [19] has carried out tests to evaluate the effectiveness of 2-aminopyrimidine (AP), 2-amino-5-mercapto-1,3,4-thiadiazole (AMT), 5,6-dimethylbenzimidazole (DB), 2-mercaptopyrimidine (MP), 2-mercaptobenzimidazole (MBI), 2-mercaptobenzothiazole (MBT) and 2-mercaptobenzothiazole (MBO) on copper coupons covered with layers containing chloride. These tests were focused on the ability of those compounds to prevent the conversion of nantokite (CuCl) into paratacamite ($\text{Cu}(\text{OH})_3\text{Cl}$), which leads to major damage on archaeological artefacts. Considering the performance and various requirements like change in the visual appearance, MBT seems to be recommended for the preventive treatment of copper-based artefacts.

For other metallic surfaces, only a few inhibitor compounds have been tested. Some preliminary tests have been performed with 4,4-diaminodicyclohexylmethane for lead artefacts [20]. Recently, in the case of silver protection, EIS experiments have been performed on various tarnishing inhibitors in combination with waxes or varnish, and have shown that the best performances are observed with 2-mercaptobenzothiazole and 5-methylbenzotriazole [2]. The authors of these studies suggest that association of those inhibitors with varnish or wax could improve the efficiency of the protection.

For silver artefacts, some inhibitors such as volatile amines have also been tested during storage. They are generally applied by transport in the vapour phase in the atmosphere. These volatile inhibitors (VPI) were applied by Bradley *et al.* [22] to avoid tarnishing of silver artefacts, but some doubts remain concerning their efficiency [21].

For the protection of iron elements of the cultural heritage, tannins are the inhibitors most often used. They were applied after mechanical cleaning

during the restoration of the cast iron roof over Big Ben in London in the 1950s [23]. Nowadays they are employed as rust converters in the case of iron archaeological artefacts that are covered by corrosion products. But the important change in the visual appearance of the artefacts after application, due to the formation of a dense black tannate complex layer, is often a limiting factor for their use in the conservation–restoration domain. In a few cases, phosphate conversion coatings have also been applied after the electrolytic treatment of guns recovered from submarine wrecks.

From these different works, it appears that only a few inhibitor compounds are used in the conservation domain and that most need special care in application or disposal, due to their toxicity (benzotriazole, ethylenediamine). Through this overview concerning the application of coatings and inhibitor compounds for the protection of elements of the cultural heritage, it appears that among the various systems already studied none can combine reversibility, respect for visual appearance and exceptional protection properties. Today, without proper maintenance procedures, the performances of these coatings decrease rapidly. Moreover, for outdoor conservation purposes the coatings and inhibitor compounds require considerable maintenance to provide long-term protection of the metallic surfaces.

Development of new protection treatments is motivated mainly by requests from curators responsible for collections of metallic artefacts who wish to avoid the need for systematic and expensive restoration. There is insufficient capacity to store a large proportion of such metallic artefacts from the cultural heritage in air-conditioned display cabinets. Because many of the protection systems currently in use are hazardous to human health, such as benzotriazole, etc., a major advance would be reached in the conservation domain by the development of new environmentally friendly systems that could be easily applied without expensive restoration works. Thus new protective systems based on the principle of regular maintenance could be developed and easily applied and allied to regular monitoring at minimal cost.

18.3 New anti-corrosion formulations: sodium carboxylates

For several years, the Laboratoire de Chimie du Solide Minéral (LCSM) (UMR CNRS 7555) has been studying sodium carboxylates with linear carbon chains as corrosion inhibitors of many metals: copper, zinc, iron, magnesium alloys and lead. These compounds are non-toxic and derived from fatty acids extracted from vegetable oil (colza, sunflower and palm). Thus, several anti-corrosion formulations have been developed based on sodium carboxylates with formulae $\text{CH}_3(\text{CH}_2)_{n-2}\text{COONa}$, $7 \leq n \leq 11$, and are nowadays used in industry mainly as temporary protection during the storage or transport of metallic pieces. The second part of this chapter is therefore devoted to the

study of linear saturated carboxylates on metallic artefacts to temporarily protect such artefacts in atmospheric conditions. The efficiency of NaC_n solutions will be illustrated for three different metals and through application on two artefacts:

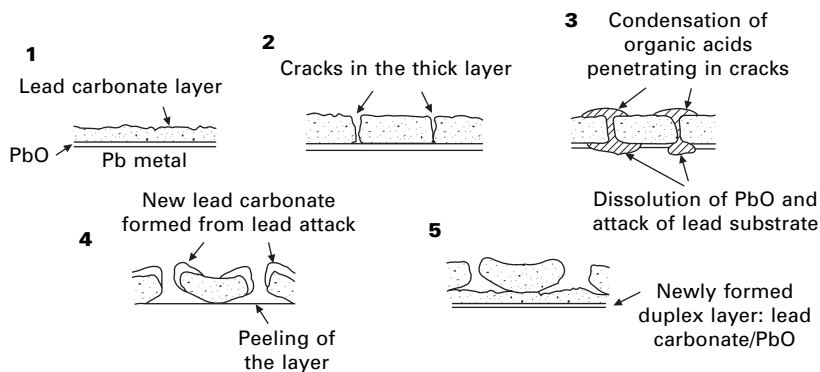
- a Gallo-Roman sarcophagus in lead
- a miner's lamp in copper alloy and iron (composite metallic artefact).

18.3.1 Inhibition treatment of lead artefacts by sodium decanoate: atmospheric conditions and acetic acid atmosphere

Many ancient lead artefacts are nowadays conserved in museums, because lead alloys were widely used in antiquity especially in water pipe networks, as weights for clocks or looms, and for sarcophagus or coin manufacture. Depending on the characteristics of the environment to which it is exposed, lead is quite reactive to common corrosive atmospheric compounds. It is naturally covered by anglesite (PbSO_4) and hydroxycarbonate compounds such as cerussite (PbCO_3), hydrocerussite ($\text{Pb}_3(\text{CO}_3)_2(\text{OH})_2$) or plumbonacrite ($\text{Pb}_{10}(\text{CO}_3)_6\text{O}(\text{OH})_6$) that do not cover sufficiently to be protective [24–27]. The presence of lead carbonate compounds is responsible for the anaesthetic white and powdery 'white rust' of lead, and can be localised on the surface in the form of pits, also called white 'lead flowers'.

Moreover, some lead artefacts are stored in small enclosures in museums, such as wooden displays or storage cabinets containing formic and/or acetic acid emissive materials such as wood or parchment paper [28]. These carboxylic acids provided by the cellulose hydrolysis are formic, propanoic, tannic and acetic acids. The latter is the major corrosive compound. So, after a long period of storage, lead surfaces can be converted into white and voluminous corrosion compounds, and in some cases the artefacts may be corroded in bulk through a progressive peeling of the corrosion layer [29, 30]. According to some authors [29–32], the fast corrosion phenomenon of lead induced by organic acid vapour is as described in Fig. 18.1.

In an atmospheric medium without SO_2 gas, the corrosion layer of lead is mainly composed of a lead carbonate layer and a thin underlayer of PbO . The organic acids are condensed in an aqueous surface film, and the lead carbonate compounds undergo an acid dissolution into soluble lead acetate or lead acetate oxide hydrate, $\text{Pb}_3(\text{CH}_3\text{CO}_2)_6\text{PbO}\cdot\text{H}_2\text{O}$. Then, the migration of this concentrated solution of acetate compounds into the cracks of the corrosion layer towards the metal surface leads to the dissolution of the PbO underlayer, the oxidation of lead, and then the peeling of the carbonate layer. These reactions allow the release of Pb^{2+} cations that are easily transformed into new carbonate compounds at the top of the layer, and a new lead carbonate



18.1 Schematic mechanism of lead corrosion by organic acid leading to a lamellar layer of lead carbonate compounds [29–32].

layer can be formed. Then a cyclic corrosion, caused by a concentrated acetate aqueous film, is initiated and leads to a porous and lamellar corrosion layer. This problem is commonly observed in many museums, especially for lead coins, on which surface details have completely disappeared.

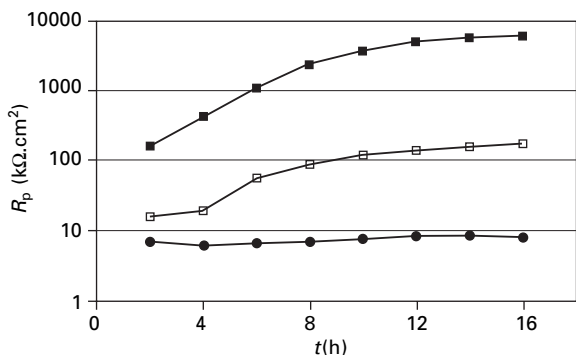
For lead protection, only a few inhibitors have been tested, including chromate, phosphate or amine compounds, but they are difficult for conservators to use and apply in practice [33–35]. Previous work has indicated that, for a constant concentration in solution, the greatest inhibition efficiency of lead corrosion by NaC_n compounds was obtained for the long carbon chains [36].

On lead artefacts, we focused our investigations on the action of sodium decanoate, $\text{CH}_3(\text{CH}_2)_8\text{COONa}$, denoted NaC_{10} . We studied the corrosion behaviour of lead coupons in a corrosive solution simulating the atmospheric corrosion (denoted ASTM water¹ [37]) and in a corrosive solution containing acetic acid. The corrosion rates and the electrochemical behaviour of lead were evaluated by using stationary electrochemical techniques. The inhibitor treatments were tested in a climatic chamber with either water or acetic acid vapour [38]. Then, we applied our results to parts of a Gallo-Roman lead sarcophagus to evaluate the treatment efficiency and the surface aspects of the artefact after treatment.

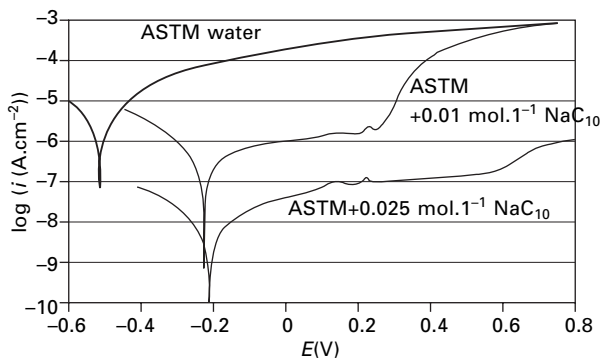
Inhibition efficiency in corrosive solution

In ASTM solution simulating atmospheric conditions, the polarisation resistance, R_p , of lead is shown in Fig. 18.2 versus the sodium decanoate concentration and the immersion time t . The lowest values of R_p were observed for the ASTM solution without inhibitor ($R_p < 10 \text{ k}\Omega\cdot\text{cm}^2$). In comparison

¹ ASTM D1384-87 water: $148 \text{ mg}\cdot\text{l}^{-1} \text{ Na}_2\text{SO}_4$, $138 \text{ mg}\cdot\text{l}^{-1} \text{ NaHCO}_3$, $165 \text{ mg}\cdot\text{l}^{-1} \text{ NaCl}$.



18.2 Effect of immersion time and NaC₁₀ concentration in the ASTM solution on the polarisation resistance R_p of lead: ● ASTM solution without inhibitor; □ ASTM solution with 0.01 mol.l⁻¹ NaC₁₀; ■ ASTM solution with 0.025 mol.l⁻¹ NaC₁₀.



18.3 Potentiodynamic curves of lead in ASTM solution containing 0.01 or 0.025 mol.l⁻¹ of NaC₁₀ after 24 hours of immersion.

with this result, a significant change in the R_p value is obtained even for low NaC₁₀ concentrations. For NaC₁₀ concentrations higher than 0.01 mol.l⁻¹, the R_p values drastically increase by about two to three orders of magnitude to reach a value of 9 MΩ.cm² for the 0.025 mol.l⁻¹ NaC₁₀ solution. It is interesting to note that a plateau is reached after 10–12 hours of immersion with these concentrations. The calculated inhibition coefficient

$\left(\theta = 1 - \frac{R_{p\text{without inhibitor}}}{R_{p\text{with inhibitor}}} \right)$ with the 0.025 mol.l⁻¹ NaC₁₀ solution is about 99.9% in these conditions.

The electrochemical behaviour of lead in NaC₁₀ solutions, especially the pitting sensitivity, was evaluated by recording the potentiodynamic curves after 24 h of immersion (Fig. 18.3). The addition of sodium decanoate induces a decrease of the corrosion current density and the passivation current density

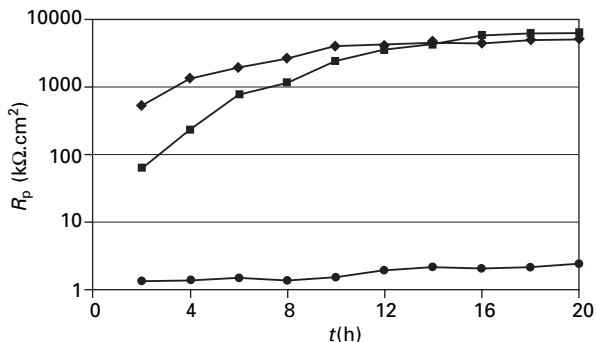
that is close to 10^{-7} A.cm⁻² at 0.25 V. These results are consistent with the R_p measurements. Moreover, a critical concentration above 10^{-2} mol.l⁻¹ seems to be necessary to avoid the pitting phenomenon, responsible for the white stain of lead carbonate on lead sheet.

Secondly, the NaC₁₀ concentration corresponding to the best results in the ASTM solution was tested in solutions simulating an acetic acid environment. Figure 18.4 shows the dependence of polarisation resistance time of lead in a solution containing an acetic acid/acetate mixture (composition 0.01 mol.l⁻¹ CH₃COOH + CH₃COONa at pH 7) with or without the addition of 0.025 and 0.05 mol.l⁻¹ NaC₁₀ at pH 7. For the acetic solution without inhibitor, the R_p values are slightly lower than the values in the ASTM solution. With 0.05 mol.l⁻¹ NaC₁₀ the polarisation resistance increases with time by about three orders of magnitude, reaching a value of 15 MΩ.cm² after 14 h of immersion.

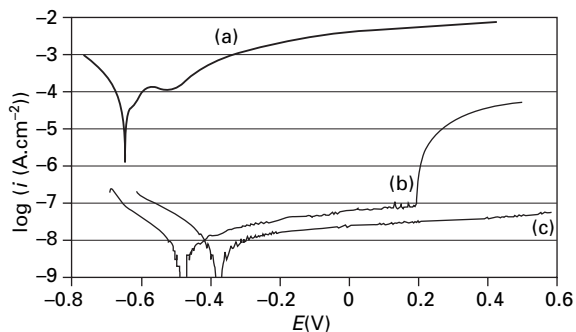
The potentiodynamic curves of lead recorded after 24 h of immersion in the acetic solution containing 0.025 or 0.05 mol.l⁻¹ of NaC₁₀ show that the addition of 0.025 mol.l⁻¹ of NaC₁₀ is sufficient to drastically decrease the corrosion current density of lead down to 10^{-8} A.cm⁻² (Fig. 18.5). Nevertheless, a concentration of 0.5 mol.l⁻¹ of NaC₁₀ is necessary to avoid the pitting phenomenon on lead in this medium. One can remark that the shift of the corrosion potential to higher values indicates that the anodic reaction of the corrosion is affected more by the presence of the inhibitor than the cathodic one.

Surface analysis

The lead surfaces after 24 hours' immersion in solution containing 0.05 mol.l⁻¹ of NaC₁₀ were observed by SEM, and the protective layers were analysed by X-ray diffraction. SEM observations revealed that the lead surface



18.4 Effect of immersion time and NaC₁₀ concentration in the acid acetic/acetate corrosive solution on the polarisation resistance R_p of lead: ● acid acetic/acetate solution without inhibitor; ■ with 0.025 mol.l⁻¹ NaC₁₀; ◆ with 0.05 mol.l⁻¹ NaC₁₀.



18.5 Potentiodynamic curves of lead in the acid acetic/acetate corrosive solution (a) containing 0.025 mol.l^{-1} of NaC_{10} , (b) containing 0.05 mol.l^{-1} of NaC_{10} , (c) after 24 hours of immersion.

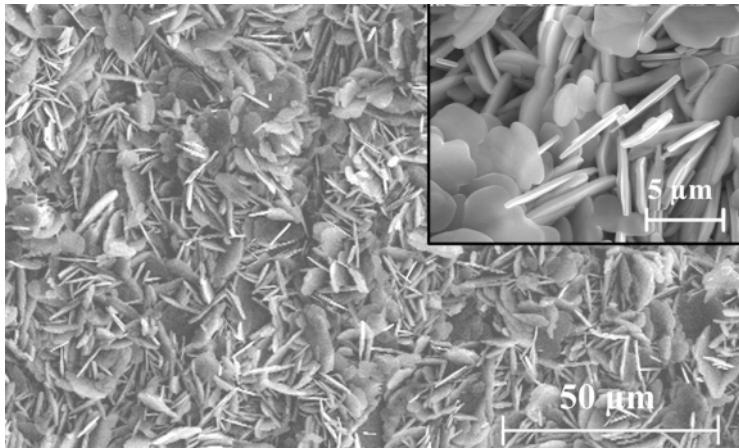
was very well covered by more or less tangled crystals which were flake-shaped (Fig. 18.6(a)). The XRD pattern of the passive layer after immersion corresponds to that of the synthetic lead decanoate (Fig. 18.6(b)). This lead soap, $\text{Pb}(\text{CH}_3(\text{CH}_2)_8\text{COO})_2$, denoted $\text{Pb}(\text{C}_{10})_2$, has been synthesised by precipitation after mixing a NaC_{10} solution and a lead nitrate solution, and studied in previous studies [39]. Its crystallographic structure has been determined [40].

Climatic chamber tests

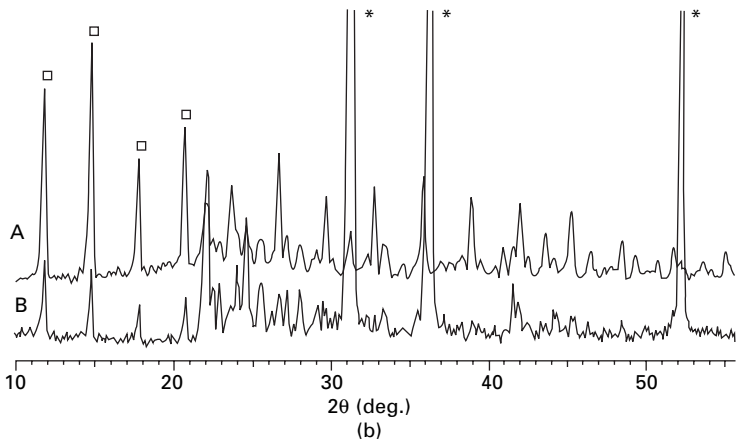
An immersion treatment of lead sheets in different NaC_{10} solutions was carried out for 24 hours, and they were placed in the climatic chamber to undergo the FKW cycles for three weeks² [38]. Table 18.1 presents the surface aspect and the qualitative corrosion state after this test. We can conclude that the treatments based on the immersion in the 0.005 and 0.01 mol.l^{-1} NaC_{10} solutions seem to be insufficient to form a protective passive layer. On these samples, the surface showed some parts covered by white powdery lead carbonates after three weeks of corrosion in the climatic chamber. These compounds were identified by X-ray diffraction as PbCO_3 , $\text{Pb}_3(\text{CO}_3)_2(\text{OH})_2$ and $\text{Pb}_{10}(\text{CO}_3)_6\text{O}(\text{OH})_6$.

The metallographic cross-section of the untreated lead sheet after the climatic chamber test, displayed in Fig. 18.7(a), confirms the presence of a thick layer of plates of lead carbonate. The treatments based on more concentrated NaC_{10} solutions (0.025 and 0.05 mol.l^{-1}) give good results and the lead sheets reveal an unchanged surface aspect. As displayed in Fig.

² Climatic chamber test: 8 hours at 100% humidity, using twice-distilled water heated to 40°C , then 16 hours under the room conditions.



(a)





(b)

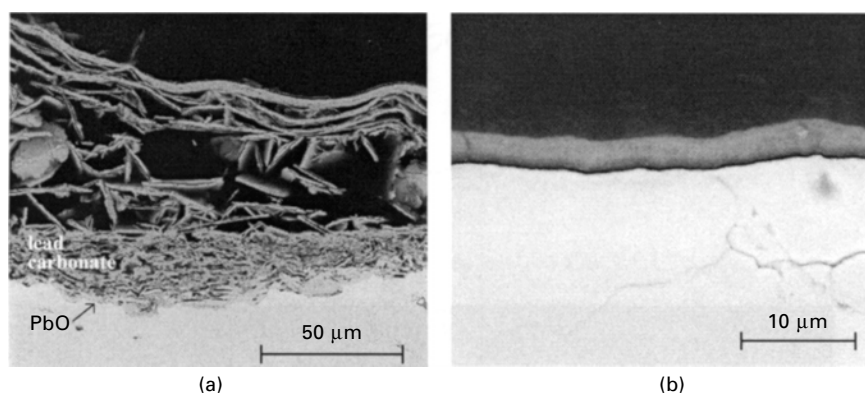
18.6 (a) SEM micrographs of lead sheets dipped for 24 hours in the $0.05 \text{ mol.l}^{-1} \text{ NaC}_{10}$ solution. (b) XRD patterns of (A) $\text{Pb(C}_{10}\text{)}_2$ powder, and (B) the coating formed on lead after immersion for 24 hours in the $0.05 \text{ mol.l}^{-1} \text{ NaC}_{10}$. *: peaks of lead substrate; □: characteristic peaks of the layered structure of $\text{Pb(C}_{10}\text{)}_2$.

18.7(b), the presence of the $\text{Pb(C}_{10}\text{)}_2$ layer on the lead surface seems to favour the formation of a dense covering layer, responsible for the good surface aspect of the sample. It is noteworthy that XRD analyses have shown that this passive layer is also constituted mainly of lead carbonates.

To characterise the effect of the inhibition treatment on the corrosion by organic acid vapour, a sample treated by immersion in the $0.05 \text{ mol.l}^{-1} \text{ NaC}_{10}$ solution for 24 hours and an untreated sample were exposed to the acetate-enriched climatic chamber test for three weeks. As can be observed in Fig. 18.8(a), the untreated sample shows very extensive corrosion: the

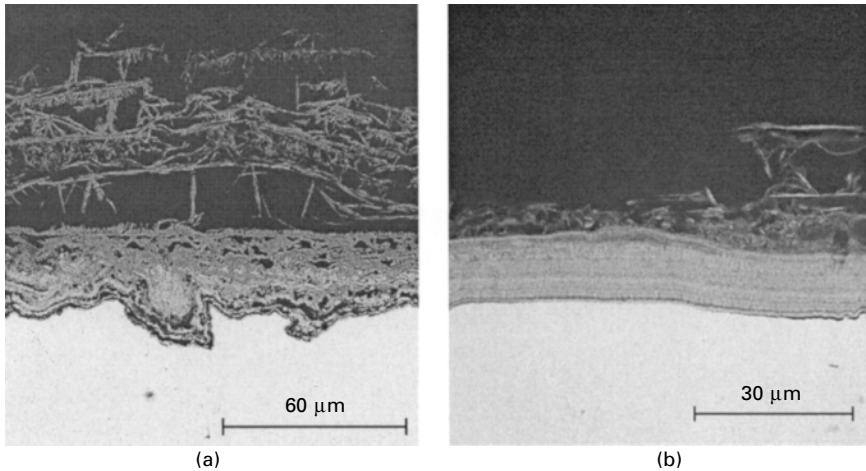
Table 18.1 Surface aspect and corrosion resistance after 3 weeks in climatic chamber in pure water environment of lead sheets treated for 24 hours in solutions containing different amounts of NaC_{10}

| NaC_{10} content (mol.l ⁻¹) | Surface aspect after 3 weeks in climatic chamber | | Corrosion Resistance |
|--|---|---|----------------------|
| Without treatment | Very corroded surface with an important powdery layer of lead carbonate |  | --- |
| 0.005 | Surface covered by powdery white lead carbonate | | --- |
| 0.01 | Some surface parts covered by white powdery compound | | + |
| 0.025 | Uniform and covering film on the surface |  | ++ |



18.7 Metallographic cross-sections after 3 weeks in climatic chamber in water environment of (a) untreated lead sheet, and (b) lead sheet treated in 0.05 mol.l⁻¹ NaC_{10} for 2 hours.

corrosion layer is very porous, lamellar and brittle, which is consistent with the brittleness of the corroded objects in museums. The lamellar character of the corrosion layer confirms that this climatic chamber test can simulate the corrosion mechanism described by some authors (Fig. 18.1, [30–32]). Contrary to the classic climatic chamber test (Fig. 18.7(b)), the treated sample shows a thicker and more lamellar corrosion layer (Fig. 18.8(b)), constituted mainly of lead carbonates according to XRD analyses. Nevertheless this layer is very compact and dense and inhibits the formation of large ‘lead flowers’ on



18.8 Metallographic cross-sections after 3 weeks in climatic chamber in acetic acid environment of (a) untreated lead sheet, and (b) lead sheet treated in $0.05 \text{ mol.l}^{-1} \text{ NaC}_{10}$ for 24 hours.

the surface and the progressive peeling of the carbonate layer.

Inhibition treatment on a part of a Gallo-Roman sarcophagus

Electrochemical tests with NaC_{10} were carried out on real archaeological surfaces of lead. Three fragments of approximately the same size (10 cm^2) were taken from a Gallo-Roman lead sarcophagus belonging to a French museum (Museum of Gallo-Roman Civilisation, Lyon), after restoration operations (Fig. 18.9(a)). The effect of an addition of $0.05 \text{ mol.l}^{-1} \text{ NaC}_{10}$ on the corrosion rate of the archaeological lead was measured during 14 hours on two different fragments. The polarisation curves show that the addition of corrosion inhibitor reduces the corrosion rate by a factor of 100 on this type of metal (Fig. 18.9(b)). So the inhibition efficiency is in the 99–99.8% range. This value is similar to that obtained on pure commercial lead.

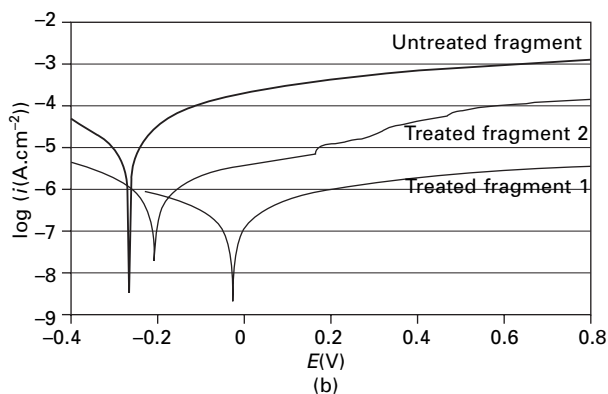
Also, inhibition treatment by immersion during 24 hours in $0.05 \text{ mol.l}^{-1} \text{ NaC}_{10}$ was performed on a large fragment of the sarcophagus. The resulting surface aspect was suitable for exposure in the museum, and the treatment can be easily removed by soft cleaning with ethanol.

Discussion

The electrochemical study has shown that sodium decanoate is a good candidate to inhibit the corrosion of lead in the two corrosive media: ASTM D1384-87 standard solution simulating atmospheric corrosion, and acetic acid-enriched



(a)



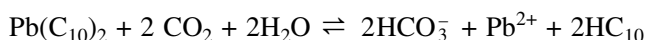
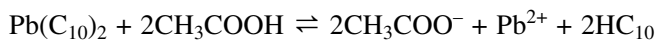
(b)

18.9 (a) Gallo-Roman lead sarcophagus. (b) Potentiodynamic curves of Gallo-Roman lead sarcophagus fragments in ASTM water containing $0.05 \text{ mol.l}^{-1} \text{ NaC}_{10}$ after 20 hours of immersion.

solutions simulating the atmosphere in the wooden displays. The best result was obtained with the addition of $0.05 \text{ mol.l}^{-1} \text{ NaC}_{10}$. The inhibitor efficiency was estimated as 99.9%. Moreover, the tests in the climatic chamber using water or the acetic acid environment have confirmed the good inhibition properties of NaC_{10} . The results have also shown that this inhibition treatment can be easily adapted to archaeological lead.

The mechanism of inhibition can be described as follows. Once a critical concentration of metallic cation is reached after an initial oxidation of the substrate by the oxygen dissolved in the aqueous solution, the protection of

metals by sodium carboxylates is due to the formation of a protective layer composed of the metallic soap, $\text{Pb}(\text{C}_{10})_2$. This micrometric lead soap layer induces a drastic decrease of the anodic current and an increase of the corrosion potential of the metal. $\text{Pb}(\text{C}_{10})_2$ is insoluble ($K_s = 10^{-12}$ [41]) and exhibits a hydrophobic character, which can explain the good resistance of NaC_{10} -treated samples during the climatic chamber tests. The metallographic studies of the lead sheets after these tests have clearly shown that the initial presence of the lead soap drastically changes the morphology of the corrosion layer. Indeed the NaC_{10} treatment provokes the formation of a dense covering layer of lead carbonate in comparison with that on the untreated sample. One can suppose that the presence of $\text{Pb}(\text{C}_{10})_2$ soap on the surface locally neutralises the acidity due to the condensation of acetic acid and/or CO_2 in the adsorbed water film, following the reactions



These reactions maintain a higher pH value in the superficial water film. The local acidification of the metal/corrosion interface leading to the dissolution of the metal (Fig. 18.1) is then greatly limited by the $\text{Pb}(\text{C}_{10})_2/\text{HC}_{10}$ equilibrium, which allows the stabilisation of a compact layer of lead carbonate.

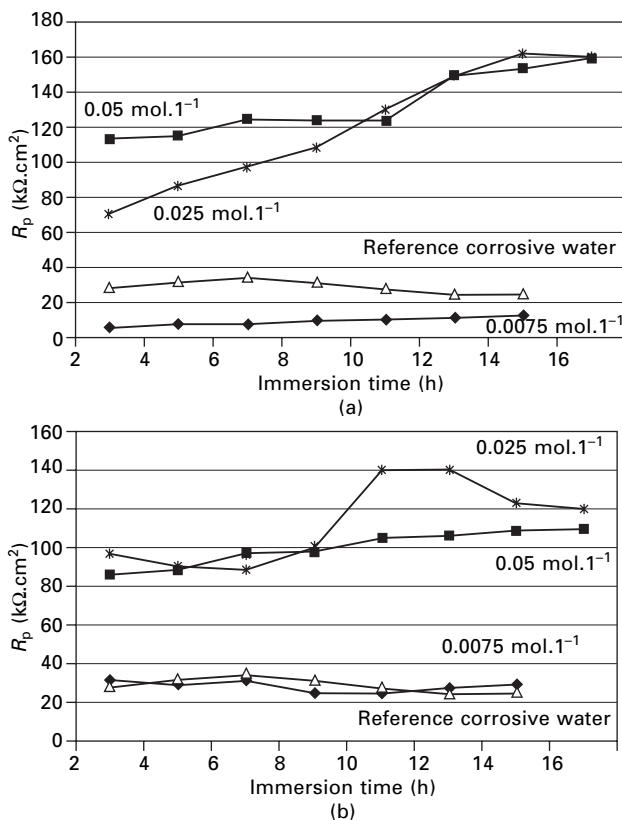
18.3.2 Inhibition treatment of bronze artefacts

Since the late 1960s, the main compounds used for protecting copper alloy artefacts have been azol compounds, especially benzotriazol. In this part of the chapter, we report the preliminary results obtained with sodium carboxylates for bronze protection. The effectiveness of heptanoate and decanoate have also been evaluated by both stationary electrochemical measurements and accelerated tests in a humidity chamber. Then the inhibitor solution was applied on parts of a miner's lamp in copper alloys and tested in a climatic chamber.

Inhibition efficiency on bronze coupons (20 wt% Sn)

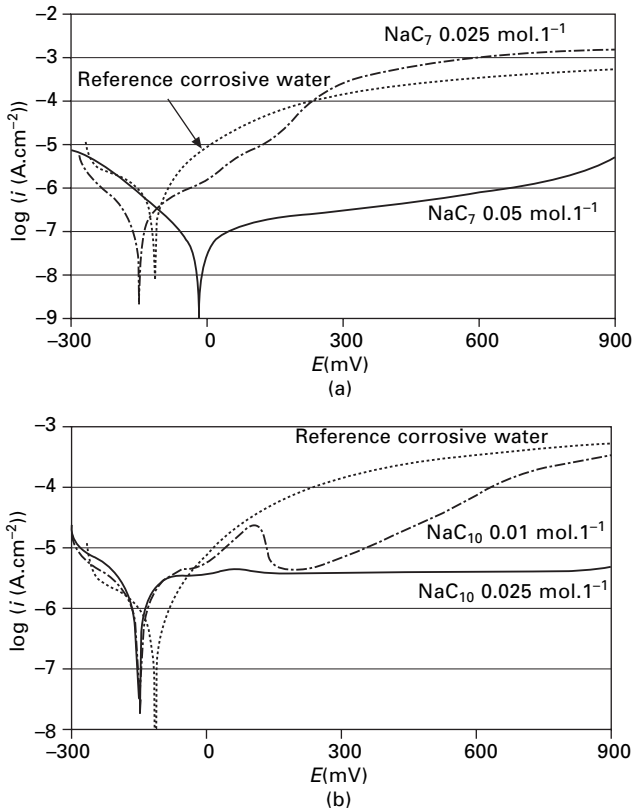
First, the inhibition efficiency on bronze coupons was evaluated. Figure 18.10 shows the evolution of the polarisation resistance of bronze in both reference corrosive water and the same electrolyte containing sodium carboxylates. For carboxylate concentrations higher than 0.075M, the R_p values reach 100–150 $\text{k}\Omega\cdot\text{cm}^2$, which corresponds to an inhibition coefficient of about 85%. It is noteworthy that the two carboxylates tested exhibit the same protection.

The polarisation curves recorded on the bronze soaked in ASTM D1384



18.10 Polarisation resistance versus immersion time of bronze in ASTM D1384 water containing different amounts of (a) sodium heptanoate (NaC_7) and (b) sodium decanoate (NaC_{10}).

water containing sodium carboxylates confirm their inhibiting character (Fig. 18.11). Indeed, the addition of 0.05M NaC_7 in the solution leads to the appearance of a passivation plateau on the I-E curves and lowers the corrosion current. For sodium decanoate, the limiting concentration is only 0.025M to obtain an efficient passivation plateau. Consequently, the sodium carboxylates with seven and ten carbons have a similar efficiency in inhibiting bronze corrosion, with a maximum inhibition coefficient of about 90%. Nevertheless, a long carbon chain is required to ensure sufficient protection against pitting. These electrochemical results are confirmed by the photograph of the bronze coupons after three weeks in the climatic chamber (Fig. 18.12). Indeed, the inhibited samples with sodium decanoate show a slightly tarnished surface, though the uninhibited samples present a thick dark corrosion layer with some pits.



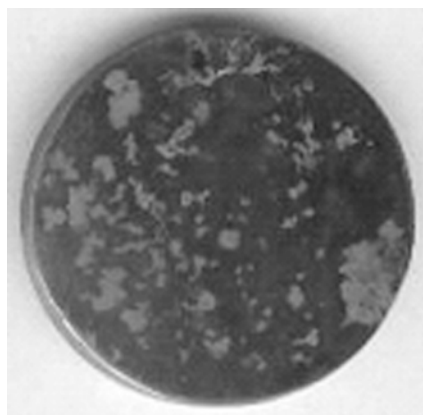
18.11 Polarisation curves of bronze after 24 h of immersion in ASTM D1384 water containing different amounts of (a) sodium heptanoate (NaC₇) and (b) sodium decanoate (NaC₁₀). Scan rate: 1 mV/s.

Applications, and efficiency of treatment on a miner's lamp

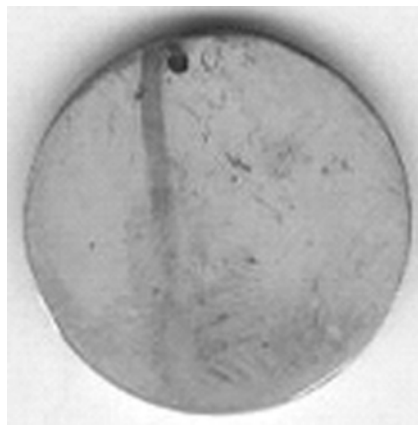
Finally, the NaC₇ compound was tested on the copper alloy part of a miner's lamp and aged in a climatic chamber (Fig. 18.13). After several months of exposure in a museum atmosphere, no visible corrosion was observed.

Summary

The inhibiting efficiency of sodium decanoate and heptanoate for bronze protection was evaluated. The best results were obtained with treatments based on NaC₇ for bronze samples. Contrary to lead, the corrosion inhibition of copper alloys by sodium carboxylates induces the formation of a nanometric layer of copper carboxylates Cu(C_n)₂, as previously observed by infra-red spectroscopy, XPS measurements and *in-situ* electrochemical AFM experiments [42–44].

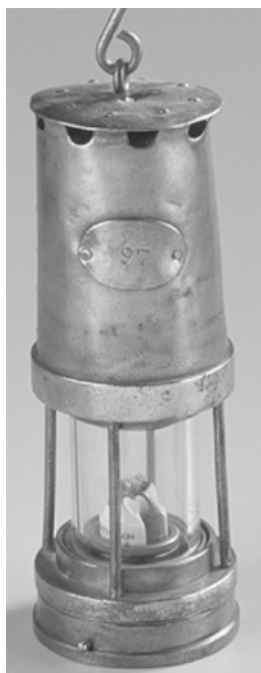


(a)



(b)

18.12 Photographs of bronze coupons after 21 days in the climatic chamber: (a) without inhibiting treatment, and (b) previously treated in a 0.05M sodium decanoate solution for 24 hours.



18.13 Miner's lamp in steel and bronze.

18.3.3 Inhibition treatment of iron artefacts by sodium carboxylates

Since a large proportion of the metallic artefacts from the cultural heritage are made of iron, this part of the chapter is devoted to the study of the efficiency of sodium carboxylates for iron protection. In the past, many treatments have been developed for iron protection, such as tannins or chromates. But most of them cannot be considered as non-toxic anti-corrosion treatments, and the effectiveness of tannins remains controversial. Moreover, significant changes in the visual aspect of artefacts after application are a limiting factor for the development of surface treatments on iron in the conservation–restoration domain.

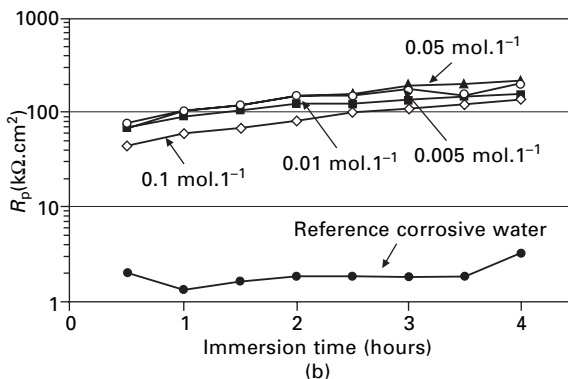
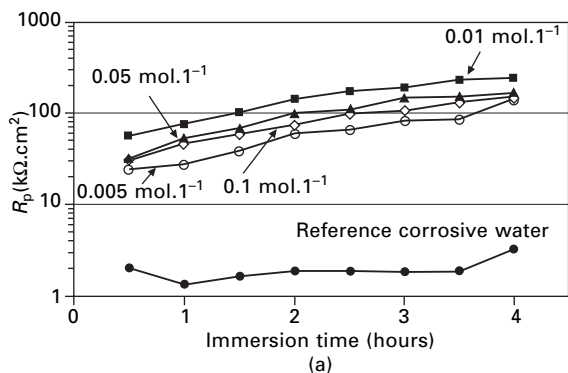
The results obtained with carboxylates on lead and copper alloys (see above) led us to examine this inhibitor family for the protection of iron surfaces. Therefore, the action of sodium heptanoate and decanoate was evaluated by stationary electrochemical techniques in a corrosive medium simulating the atmospheric corrosion. This experimental work allowed the determination of the best conditions of use (concentration, carbon chain length) for iron protection. Then, some tests on iron coupons and iron parts of a miner's lamp from the Centre Historique Minier (CHM), Lewarde, France, were carried out in a climatic chamber [38].

Inhibition efficiency on iron coupons

The performances of sodium carboxylates for iron protection were evaluated first by electrochemical measurements. The polarisation resistances were measured against immersion time in ASTM solution with different concentrations of sodium carboxylates, NaC_n . Figure 18.14 shows that for the NaC_7 and NaC_{10} solutions, an increase of R_p with immersion time was systematically observed. After 4 h of immersion the R_p values reached 150–250 $\text{k}\Omega\cdot\text{cm}^2$. These values are two orders of magnitude higher than those obtained in ASTM corrosive reference solution. For a specific carbon chain length, the influence of the concentration on the R_p values is not clearly revealed. In fact, for an immersion time of 4 h the R_p values measured for different concentrations reached the same order of magnitude. The addition of sodium carboxylates to the ASTM corrosive medium led to an increase of E_{corr} from -0.8 V to 0.2 – 0.3 V. This result is clearly underscored with the

calculation of the inhibition coefficient, $\theta = 1 - \frac{R_{p\text{without inhibitor}}}{R_{p\text{with inhibitor}}}$, after 4 h of immersion in ASTM solution containing carboxylates. In fact, for the different concentrations tested in this study, θ reaches values ranging from 96% to 98%.

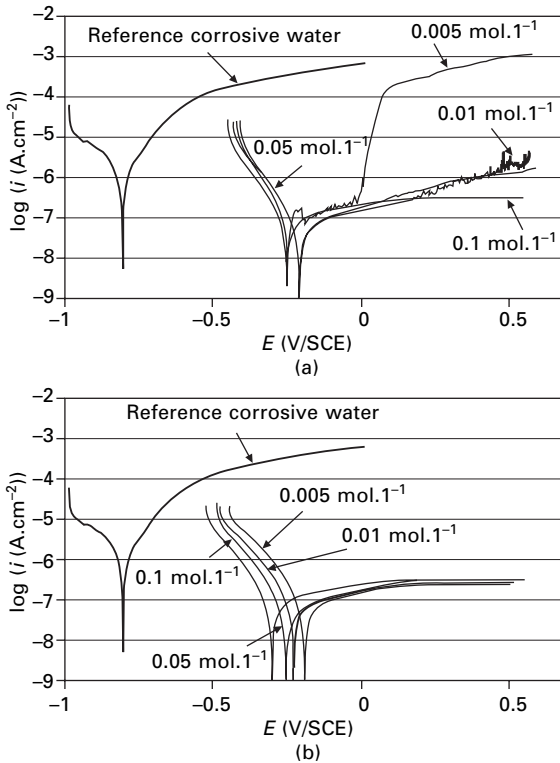
The influence of linear sodium carboxylates on the passivation behaviour



18.14 Influence of immersion duration on R_p of iron immersed in ASTM solutions containing different amounts of (a) NaC_7 and NaC_{10} .

and the resistance to pitting of steel were also determined. Comparison with the potentiodynamic curves corresponding to the inhibitor-free solution shows that carboxylate addition induced strong modification of the electrochemical behaviour (Fig. 18.15). A drastic shift of E_{corr} from -0.8 V to -0.2 V and a decrease of the corrosion current density were observed.

Unlike R_p measurements, $i = f(E)$ curves underline the influence of the concentration in the protection process. Indeed, for concentrations higher than 0.005M , the $i = f(E)$ curves display a passivation plateau with a low passive current density ($i_p = 5 \times 10^{-6}$ to 10^{-7} A/cm²). A different behaviour was observed for 0.005M NaC_7 solution because a pitting phenomenon occurs near 0.0 V (Fig. 18.15(a)). The passive current density measured for concentrations higher than 0.005M was about 5×10^{-6} A/cm². These results show a greater stability of the passive film with the highest carboxylate concentration. With sodium decanoate, NaC_{10} (Fig. 18.15(b)), the curves show a large passivation plateau without pitting phenomena, whatever the concentration (≥ 0.005 mol.l⁻¹). Comparison of the $i = f(E)$ curves obtained for NaC_7 and NaC_{10} shows that the increase of the carbon chain length of the

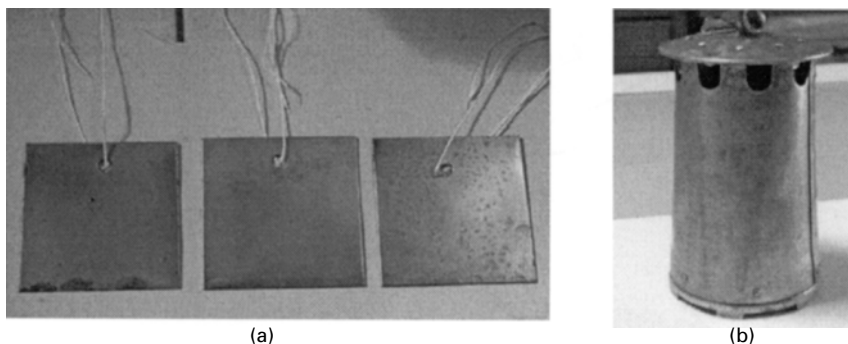


18.15 Potentiodynamic curves of iron in ASTM solution containing different amounts of (a) NaC_7 and (b) NaC_{10} after 5 h of immersion.

carboxylates allows the stabilisation of the passive layer on a larger potential domain even for low concentrations of inhibitor.

Climatic chamber tests

Mild steel sheets were immersed in 0.1M NaC_n sodium carboxylate solutions with $n = 7$ and $n = 10$ for 24 h. After the immersion treatment, the visual aspect of the metal was not modified. This result is of particular importance for application to the conservation domain. Figure 18.16(a) shows the different sheets after 10 days in the climatic chamber. For the untreated sample, pitting was clearly observed. In contrast, no red rust was observed for the samples treated in NaC_7 and NaC_{10} . The same tests were carried out on a safety lamp from the Centre Historique Minier shown in Fig. 18.16(b). In this experiment, the inhibiting treatments avoided the development of rust layers on the metallic surface of the lamp. Moreover, the application of sodium decanoate did not lead to change in the visual aspect of the iron artefact.



18.16 (a) Left to right: untreated sheet, NaC_7 treated sheet and NaC_{10} treated sheet. (b) Iron upper part of the miner's lamp after NaC_{10} treatment and 7 days in climatic chamber.

Summary

This study demonstrates that the sodium carboxylates NaC_7 and NaC_{10} are effective corrosion inhibitors for iron in a corrosive medium simulating atmospheric corrosion. When they are added to the ASTM corrosive medium, a significant decrease of the iron corrosion rate was systematically observed. The concentration and the carbon chain length of the carboxylate are not very important; even with addition at a low concentration (0.005 mol.l^{-1}), the corrosion rate is drastically reduced. Nevertheless, the concentration and the carboxylate type determine the resistance to the pitting phenomenon. The best performance was observed with the addition of NaC_{10} for which the passive current remains stable over large potential and concentration ranges. It seems that as in the case of copper, the inhibition of iron corrosion by sodium carboxylates is due to the formation of a nanometric layer of iron carboxylate. The stability of this passive layer is controlled by the solubility of the iron carboxylates which is strongly dependent on the carbon chain length of the carboxylate anion.

18.4 Conclusions

For more than 40 years, many scientists involved in the conservation of the cultural heritage have carried out research programmes based on the evaluation of the performance of anti-corrosion systems that are commonly used for the protection of metallic artefacts. Through these different studies, it appears that because of the variety of conservation conditions, most of the systems tested (waxes, varnish, inhibitors) cannot satisfy the various requirements encountered in the field of cultural heritage conservation. For that reason, the development of new protective systems for preserving metallic artefacts is of great interest.

In this context, for 10 years we have been studying a new corrosion inhibitor family for conservation purposes. This new family, based on sodium carboxylates with different carbon chain lengths extracted from vegetable oil, fulfils the main conditions of application laid down by the rules of conservation ethic. In fact, carboxylates are easily removable with solvents such as ethanol, allowing complete reversibility of the treatment. No visual aspect modification is observed on the samples and the artefacts treated in this work. Moreover, the non-toxic character of these corrosion inhibitors makes their handling easier in comparison with benzotriazol. Through our work, it appears that these inhibitors exhibit good anti-corrosion performance on a wide range of metallic surfaces.

To conclude, the use of sodium carboxylates as corrosion inhibitors in the context of restoration or conservation treatments seems very promising. This kind of treatment is of particular interest, especially for the preservation of technical and industrial cultural heritage elements conserved in museums located in old industrial buildings. The results of this study will be applied to the conservation of a collection of safety lamps from the Centre Historique Minier (CHM) at Lewarde in the north of France. This museum, which is located in an old colliery, exhibits a collection of 700 miners' lamps in a lamp room (Fig. 18.17). These lamps are made of iron and copper alloys which can easily be protected with sodium carboxylates. To avoid the development of corrosion layers on the iron surface, in agreement with the



18.17 View of the lamp room of the Centre Historique Minier of Lewarde.

curator we have proposed the use of sodium carboxylates within the framework of temporary conservation treatment, on the basis of the experimental results obtained in the present study. The application of these inhibitor compounds can finally be associated with a conservation procedure on real artefacts, to avoid long and expensive restoration work.

18.5 References

1. S. Keene, *IIC Conference: Adhesives and Consolidants* (1984), 104–106.
2. W. Mourey and E. Czerwinski, *ICOM-CC 10th Triennial Meeting*, Washington, DC (1993), 779–785.
3. S. Beale and R. Smith, in *Conservation of Metal Statuary and Architectural Decoration in Open-air Exposure*, Rome, ICCROM, 99–124.
4. P. Weil, *ICOM-CC 4th Triennial Meeting*, Venice (1975), 21–24.
5. D. Erhardt, W. Hopwood, T. Padfield and N. F. Veloz, *ICOM-CC 7th Triennial Meeting*, Copenhagen (1984), 1–3.
6. L.B. Brostoff and E.R. de la Rie, in *Metals 98*, James & James Ltd (1998), 320–328.
7. L.A. Ellingson, T.J. Shedlosky, G.P. Bierwagen, E.R. de la Rie and L.B. Brostoff, *Studies in Conservation*, 49 (2004), 53–62.
8. W. Mourey, in *Metals 95*, James & James Ltd (1996), 225–227.
9. C. Price, D. Hallam, G. Heath, D. Creagh and J. Ashton, in *Metals 95*, James & James Ltd (1996), 223–241.
10. V. Otieno-Alego, G. Neath, D. Hallam and D. Creagh, in *Metals 98*, James & James Ltd (1998), 309–314.
11. V. Otieno-Alego, D. Hallam, A. Viduka, G. Neath and D. Creagh, in *Metals 98*, James & James Ltd (1998), 315–319.
12. P. Weil, in *National Sculpture Review, 8th Annual Meeting of the American Institute for Conservation of Historic and Artistic Works*, San Francisco (1980), 129–140.
13. M. Pilz and H. Römich, in *Metals 95*, James & James Ltd (1997), 245–250.
14. S. Turgoose, in S. Keene, ed., *Corrosion Inhibitors in Conservation*, UKIC Occasional Paper 4, UK Institute for Conservation (1985), 13–17.
15. P.T. Wilthew, *ICOM-CC 6th Triennial Meeting*, Ottawa (1981), 183–189.
16. L.E. Merck, *Studies in Conservation*, 26 (1981), 73–76.
17. H.B. Madsen, *Studies in Conservation*, 12 (1967), 163–167.
18. L.B. Brostoff, in *Metals 95*, James & James Ltd (1996), 99–108.
19. R.B. Faltermeier, *Studies in Conservation*, 43 (1998), 121–128.
20. V.E. Griz, L.Ya. Milova, V.N. Kuchinskii, S.Z. Levin and V.P. Vinogradova, *Prot. Met.*, 12 (1976), 180–182.
21. L. Espié, N. Lacoudre, T. Beldjoudi and J. Dugot, *Techné*, 12 (2000), 19–27.
22. S.M. Bradley, in S. Keene, ed., *Corrosion Inhibitors in Conservation*, UKIC Occasional Paper 4, UK Institute for Conservation (1985), 21–22.
23. S.J. Turner, in S. Keene, ed., *Corrosion Inhibitors in Conservation*, UKIC Occasional Paper 4, UK Institute for Conservation (1985), 29–30.
24. A.M. Beccaria, E.D. Mor, G. Bruno and G. Poggi, *Br. Corros. J.*, 17 (1982), 87.
25. T.E. Graedel, *J. Electrochem. Soc.*, 141 (1984), 922.
26. V. Brusica, D.D. DiMilia and R. MacInnes, *Corrosion*, 47 (1991), 509.
27. E. A. Joerg and O.F. Devreux, *Corrosion*, 52 (1996), 953.
28. J. Tetrault, *J. IIC-CG*, 17 (1992), 17.

29. N.H. Tennent, J. Tate and L. Cannon, *SSCR J.*, 4 (1993), 8–11.
30. C. Degrigny, R. Le Gall and E. Guilminot, *ICOM Committee for Conservation 11th Triennial Meeting*, Edinburgh (1996), 865–869.
31. P.D. Donovan and J. Stringer, in N. E. Hammer, ed., *Proceedings of 4th International Congress on Metallic Corrosion*, NACE, Houston, TX (1972), 537–544.
32. S. Turgoose, in C.E. Miles and S.C. Pollard, eds, *Lead and Tin: Studies in Conservation and Technology* UKIC Occasional Paper 3, London (1985), 15–26.
33. S.A. Awad and Z.A. Elhady, *J. Electroanal. Chem. Interfacial Electrochem.*, 20(1) (1969), 79.
34. S.A. Awad, K.M. Kamel and A.R. Cook, *J. Electroanal. Chem. Interfacial Electrochem.*, 34(2) (1972), 431.
35. W.A. Badawy, M.M. Hefny and S.S. El-Egamy, *Corrosion* (Houston), 46(12) (1990), 978.
36. E. Rocca and J. Steinmetz, *Corrosion Science*, 43 (2001), 891.
37. ASTM Standard D1384-87 (1988).
38. AFNOR Standard NFT60-174, Dec. 1994.
39. E. Rocca, Thesis (1999), Nancy, France.
40. F. Lacouture, M. François, C. Didierjean, J.P. Rivera, E. Rocca and J. Steinmetz, *Acta Crystallographica C*, C57 (2001), 530.
41. K.A. Hunter and P.S. Liss, *J. Electroanal. Chem.*, 73 (1976), 347.
42. C. Rapin, P. Steinmetz and J. Steinmetz, *La Revue de Métallurgie*, 281, February 1996.
43. C. Rapin, P. Steinmetz and J. Steinmetz, *Corrosion* 98, Paper 211, February 1998.
44. E. Rocca, G. Bertrand, C. Rapin and J.C. Labrune, *J. Electroanal. Chem.*, 503 (2001), 133–140.

Surface characterisation of corrosion inhibitors on bronzes for artistic casting

A. GALTAYRIES, A. MONGIATTI and P. MARCUS
Ecole Nationale Supérieure de Chimie de Paris, France and
C. CHIAVARI Università di Ferrara, Italy

19.1 Introduction

In the field of conservation of outdoor metal artefacts, the use of protective films against corrosion is often required. Organic inhibitors usually produce very thin chemisorbed films that lead to a decrease of the corrosion rate due to the slowing down of one or both of the anodic and cathodic electrochemical reactions.

Prior to this study, d.c. and a.c. electrochemical measurements (Polarisation Curves and Electrochemical Impedance Spectroscopy, EIS) [1] had been performed in order to compare the inhibiting efficiency of a 1,2,3-benzotriazole (BTA) mixed with BTA derivative on two different bronzes: the traditionally used Cu–5Sn–5Zn–5Pb bronze alloy (wt%) and the novel Si-containing Cu–8Sn–3Si bronze. A preliminary evaluation of the protectiveness of BTA mixed with 5-hexyl-BTA (C6-BTA) on pure copper and on the two bronzes was deduced from the comparison of the polarisation curves and impedance spectra recorded after immersion for one hour in simulated acid rain [1]. On pure copper and on the CuSnZnPb bronze alloy, the inhibitor film reduces the anodic and cathodic current densities [2, 3], whereas on the CuSnSi bronze, the inhibiting action is weaker. On both bronzes, the organic film is stable down to a potential of approximately -0.3 V vs Ag|AgCl. Below this potential, the desorption of the organic compound, or the reduction of the copper oxidised species, to which the film is supposed to be bonded, probably takes place. The comparison of the polarisation resistance, measured by EIS, indicated that in the absence of corrosion inhibitors, CuSnZnPb is less resistant to corrosion (lower R_p after 1 hour, 24 hours and 168 hours) than CuSnSi, but after treatment by BTA + C6-BTA, it becomes more resistant than CuSnSi. The EIS spectra indicated the formation of a continuous and protective film on pure Cu, and a more defective one on CuSnZnPb [1–3]. In the case of CuSnSi, the EIS spectra are similar to those obtained for the unprotected alloy and the corrosion resistance is three orders of magnitude lower than for the inhibited CuSnZnPb alloy. The conclusion is that the organic film is probably incomplete.

The objective of this work was to analyse the surfaces of the two bronzes by means of X-Ray Photoelectron Spectroscopy (XPS) before and after immersion in a solution of corrosion inhibitors (BTA + C6-BTA), in order to understand the interaction of the inhibitor with the bronze surfaces. For comparison, the surfaces of pure metals (Cu, Sn, Pb, Zn and Si) were also analysed under the same experimental conditions.

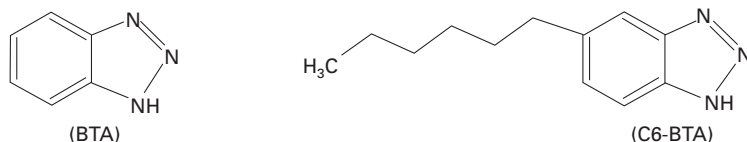
19.2 Experimental

19.2.1 Materials

Polycrystalline Cu, Pb, Sn and Zn were purchased from Goodfellow. Polycrystalline 85Cu–5Sn–5Zn–5Pb (wt%) and 89Cu–8Sn–3Si (wt%) alloys were supplied in the form of cast plates ($50 \times 50 \times 3 \text{ mm}^3$) by the Venturi Arte foundry (Bologna, Italy). All metallic samples were mechanically polished (SiC 1200 grit paper), rinsed in H_2SO_4 (10%), pure water and acetone, and dried in air. A Si (100) single crystal was provided by ACM (Application Couches Minces, France). It was degreased in ethanol and acetone and dried in air.

19.2.2 Corrosion inhibitors

1,2,3-benzotriazole (BTA) was purchased from Aldrich and 5-hexyl-1,2,3-benzotriazole (C6-BTA) was provided by the University of Ferrara (Dr Marco Fogagnolo). The inhibitor solution was a mixture of 50 vol% BTA at $1 \times 10^{-3} \text{ m}$ (0.0595 g.l^{-1}) and 50 vol% C6-BTA at $1 \times 10^{-4} \text{ m}$ (0.0203 g.l^{-1}), prepared at 70°C . The structural formulas of the molecules are as follows:



The pH of the aqueous solution of BTA is ~ 6 . The choice of adding C6-BTA to the BTA solution was based on earlier works [4] where it was stated that the hydrophobic character of the long alkyl chain contributed to make the organic film more impervious to the penetration of the electrolyte. The samples were immersed in the inhibitor solution at 75°C for 1 hour. After immersion, the samples were dried in air (without rinsing).

19.2.3 Surface characterisation

For the surface characterisation by XPS, the Cu 2p, Zn 2p, Si 2p, Pb 3d, Sn 3d, O 1s, and C 1s core level spectra and Cu LMM Auger lines were recorded

with a VG ESCALAB Mk II X-ray photoelectron spectrometer, with AlK_{α} radiation ($h\nu = 1486.6$ eV), at a pass energy of 20 eV. The spectrometer was calibrated against the reference binding energies (BEs) measured for clean Ni and Au samples (Ni $2p_{3/2}$ and Au $4f_{7/2}$ lines set at 852.8 eV and 84.0 eV, respectively). In these conditions, the binding energy of the C 1s core level for aliphatic carbon is 285.0 eV. The take-off angle of the photoelectrons was 90° , with respect to the sample surface. In the XPS spectrometer, the base pressure of the analysis chamber was 3×10^{-10} mbar (3×10^{-8} Pa). To process the XPS data, a commercial computer program (Eclipse, provided by VG) was used.

For semi-quantitative analysis, we have considered that the functional dependence on the kinetic energy (KE) of the electron mean free path (λ) and of the transmission factor of the analyser ($T(KE)$) compensate one another, i.e. $\lambda T \approx \text{constant}$. This is based on measurements performed previously in the laboratory showing that $T \approx (KE)^{-0.5}$ and the assumption that λ is proportional to $(KE)^{0.5}$ [5]. The calculation model assumes a homogeneous sample. In this model, the intensity is expressed as:

$$I_N^{M,\infty} = F \cdot T(E_c) \cdot D_N^M \cdot \sigma \lambda_N^M \sin \theta \quad 19.1$$

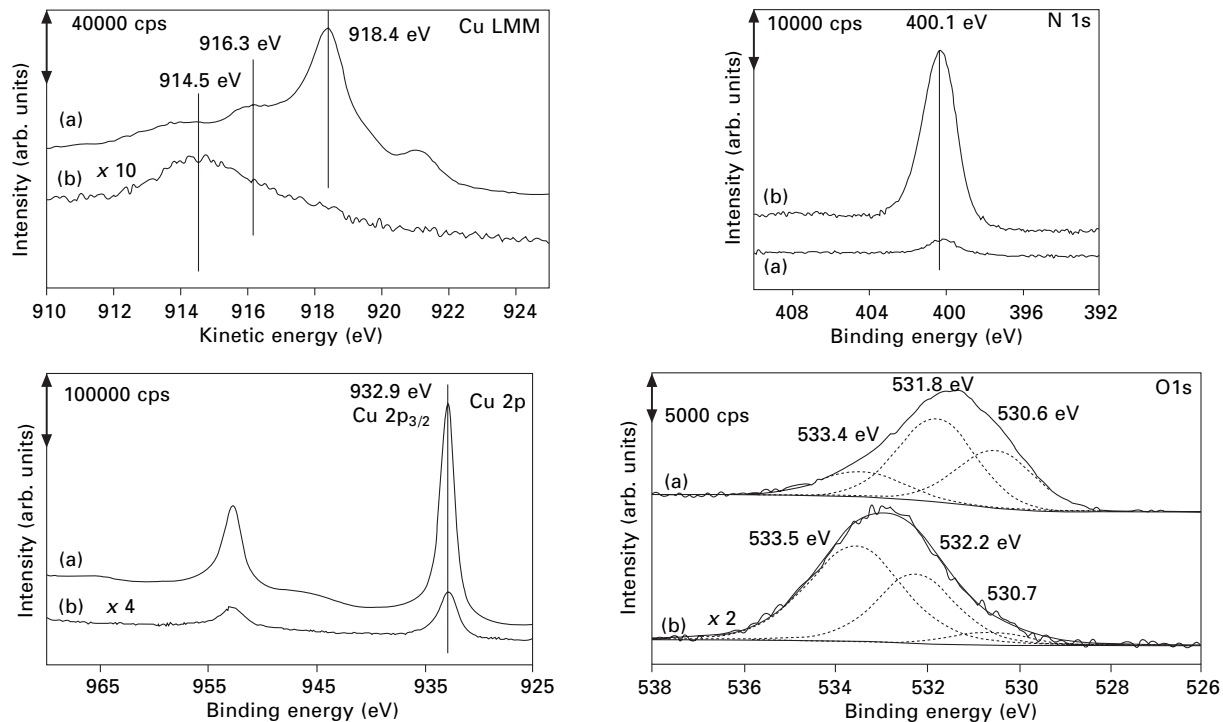
where F is the photon flux, $T(E_c)$ the transmission factor, D_N^M the atomic density of N (element) in the matrix M , σ the photo-ionisation cross-section, λ_N^M the photoelectron inelastic mean free path from N (element) in M (matrix), and θ the take-off angle. From this model, the atomic density ratio of two elements A and B $\left(\frac{D_A}{D_B}\right)$ can be obtained:

$$\frac{D_A}{D_B} = \frac{I_A}{I_B} \cdot \frac{\sigma^B}{\sigma^A} \quad 19.2$$

19.3 Results

19.3.1 Corrosion inhibitor treatment of pure Cu

After polishing, the Auger spectrum of copper (Cu $L_3M_{45}M_{45}$) presents a maximum in kinetic energy located at 918.4 ± 0.1 eV (Fig. 19.1), characteristic of metallic copper [5–7], and a smaller contribution at 916.3 ± 0.2 eV, attributed to Cu_2O [7]. The Cu 2p core level spectrum (Fig. 19.1), located at a binding energy (BE) of 932.9 ± 0.1 eV, does not present any satellite at higher binding energy, which proves the absence of Cu^{2+} in the outermost layers [7]. The spectra indicate the presence of an ultra-thin layer of Cu_2O on Cu. An estimation of the oxide thickness, assuming that the layer is continuous, gives 0.5 ± 0.1 nm. In addition to the systematic presence of carbon (C 1s core level peak), some surface contaminants are detected from the N 1s (BE



19.1 Cu LMM Auger lines and Cu 2p, N 1s and O 1s core level peaks for pure Cu (a) before and (b) after treatment in the corrosion inhibitor solution.

400.1 \pm 0.1 eV), O 1s (two additional peaks at BE 531.8 \pm 0.1 eV and 533.4 \pm 0.1 eV), and S 2p core level peaks (BE 168.6 \pm 0.1 eV, not shown here). The intensities from the contaminants are weak (except carbon), and may be attributed to copper nitrides (from the bulk), to adsorbed OH groups on copper oxide and/or to copper sulphates ((BE 531.8 eV), and to adsorbed water on OH groups (BE 533.4 eV).

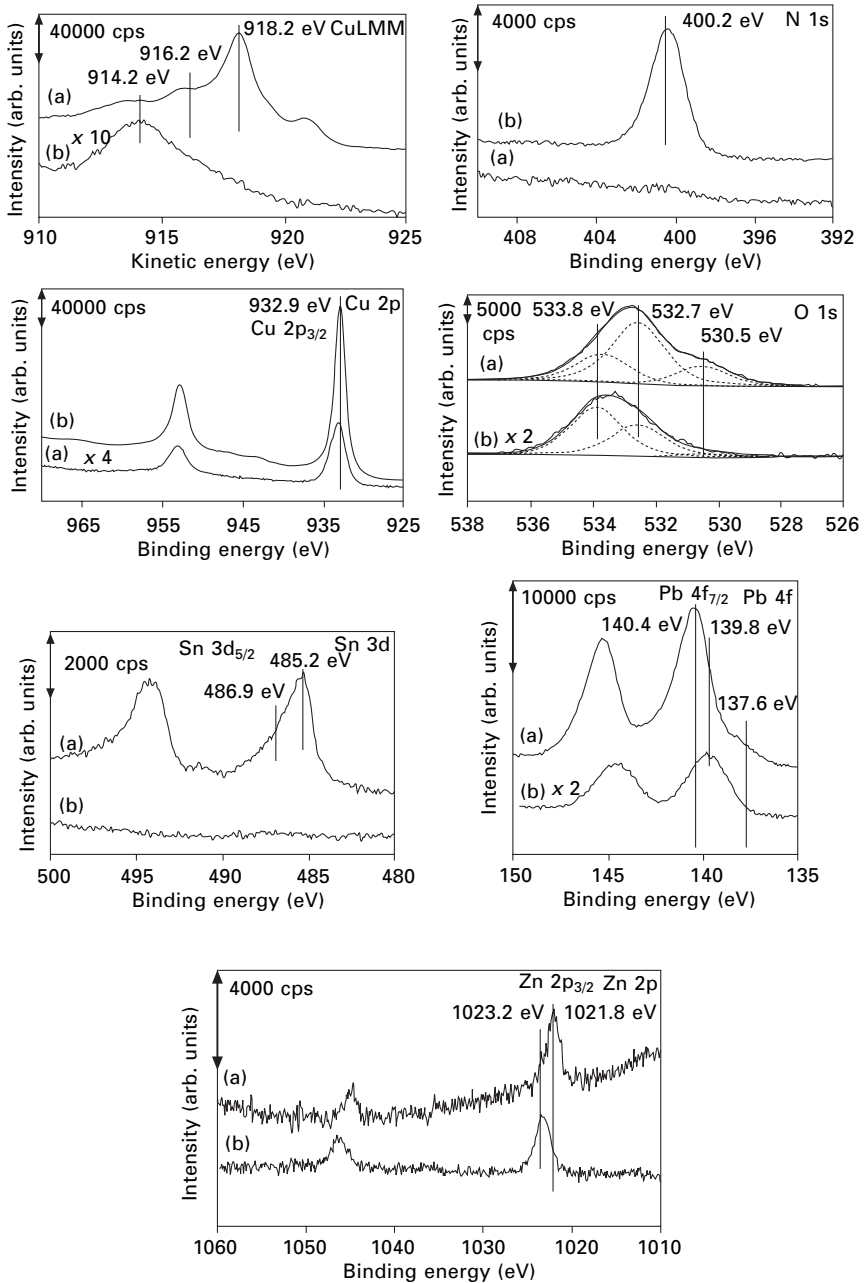
After treatment in the inhibitor solution, the XPS analyses present an intense N 1s core level peak (Fig. 19.1), located at a binding energy of 400.1 \pm 0.1 eV, which can be unambiguously attributed to the presence of adsorbed inhibitor on the surface. Complementary information is obtained from the examination of the Cu LMM Auger lines as well as the Cu 2p core level peak (Fig. 19.1). The Auger signal is both attenuated and modified, with a maximum in kinetic energy located at 914.5 \pm 0.2 eV. The position of this Auger line is in good agreement with published values, for BTA on copper surfaces [8, 9], attributed to the formation of a Cu(I)-inhibitor complex, adsorbed on oxidised copper (Cu₂O). The shape of the Cu 2p spectrum is unchanged (binding energy of 932.9 \pm 0.1 eV) but the intensity is markedly attenuated by the inhibitor layer.

The intensity and the shape of the O 1s peak are also significantly modified by the adsorption of BTA. Three peaks contribute to the experimental data: the main contribution is now located at higher binding energy (533.5 \pm 0.1 eV), another intense peak is located at BE 532.2 \pm 0.1 eV and a residual signal is detected at BE 530.7 \pm 0.1 eV, indicating that Cu₂O is probably still detected. The peaks at 532.2 \pm 0.1 eV and 533.5 \pm 0.1 eV can be attributed to external contamination by adsorbed CO, CO₂ occurring during transfer in air, as well as to water trapped in the inhibitor layer [8], respectively.

19.3.2 Corrosion inhibitor treatment on bronze alloys

CuSnPbZn

After polishing, the Cu LMM Auger spectra and Cu 2p core level (Fig. 19.2) are similar to those obtained for pure copper (main Auger line at 918.2 \pm 0.1 eV and shoulder at 916.2 \pm 0.2 eV, Cu 2p_{3/2} binding energy of 932.9 \pm 0.1 eV). The O 1s core level peak shape seems different from the one presented for pure copper. It has been decomposed using three components at similar binding energies: a main contribution at high binding energy (532.7 \pm 0.1 eV), a shoulder at low binding energy (530.5 \pm 0.1 eV), and a third peak at a binding energy of 533.8 \pm 0.1 eV. The peak attribution is discussed below. As regards the alloyed elements, the Sn 3d_{5/2} core level spectrum (Fig. 19.2) presents two contributions, the more intense one located at a binding energy of 485.2 \pm 0.1 eV (attributed to metallic Sn in the alloy, see e.g. [10, 11]) and a smaller one at 486.9 \pm 0.1 eV (attributed to Sn⁴⁺ in SnO₂ [6, 10–12]). The Pb 4f_{7/2} core level spectrum (Fig. 19.2) also presents two



19.2 Cu LMM Auger lines and Cu 2p, Sn 3d, Pb 4f, Zn 2p, N 1s and O 1s core level peaks for the CuSnPbZn bronze (a) before and (b) after treatment in the corrosion inhibitor solution.

contributions: a strong one at a binding energy of 140.4 ± 0.1 eV (attributed to lead sulphate [13]), and a small one at 137.6 ± 0.1 eV (attributed to PbO_2 [13]). The Zn $2p_{3/2}$ core level spectrum (Fig. 19.2) presents only one peak at 1021.8 ± 0.1 eV. The attribution of this binding energy will be discussed later. The surface contamination by sulphates is also detected from the examination of the S $2p$ core level peak (not shown here, BE 169.6 ± 0.1 eV), in agreement with the high binding energy feature in the $\text{Pb}4f_{7/2}$ peak. There is no nitrogen contamination on the surface of this sample (Fig. 19.2).

The surface composition of the alloy was determined using the XPS core level intensities (total intensity of each core level of the alloyed element). Table 19.1 presents the results. It indicates that before (and after immersion), the surface is enriched in Pb, and depleted in copper and zinc, compared to the bulk composition. As lead is insoluble in copper [14] and behaves as a separate phase, present as inclusions in the alloy (confirmed by EDS/XRD characterisations [1, 15]), lead enrichment on the surface may come from the mechanical polishing, where Pb from the inclusions is preferentially spread on the surface. During the chemical etching in H_2SO_4 , preferential dissolution of copper may occur.

Table 19.1 also indicates that copper is the main element on the surface. As regards the O $1s$ peak attribution, it can be proposed that the value of BE 530.5 eV is mainly due to copper oxide (Cu_2O) on the surface (lead oxide and zinc oxide are only weakly contributing, considering the low intensity of the Pb and Zn core level signals). Similarly to pure copper, the other contributions can be attributed to the presence of lead sulphates and/or OH groups adsorbed on the copper oxide layer (532.2 eV), and to adsorbed water on the hydroxylated copper oxide (533.8 eV).

After treatment in the solution of inhibitors, a strong N $1s$ core level signal is detected (BE 400.2 ± 0.1 eV), indicative of the presence of the adsorbed inhibitor film (Fig. 19.2). The data reported in Fig. 19.2 for the Cu LMM Auger lines, the Cu $2p_{3/2}$, Sn $3d_{5/2}$, Pb $4f_{7/2}$, Zn $2p_{3/2}$ and O $1s$ core level peaks, indicate that, after treatment:

Table 19.1 Surface composition of the alloy (at%) determined from the total XPS core level intensities (Cu $2p_{3/2}$, Sn $3d_{5/2}$, Zn $2p_{3/2}$, Pb $4f_{7/2}$) before and after treatment with the corrosion inhibitor solution

| | Cu | Sn | Zn | Pb |
|--|------------------|------------------|------------------|------------------|
| Bulk CuSnZnPb alloy | 91 (85.7 wt%) | 2.7 (4.8 wt%) | 4.5 (4.4 wt%) | 1.5 (4.7 wt%) |
| Before immersion in the inhibitor solution | 82 | 2.8 | 1.3 | 14 |
| After immersion in the inhibitor solution | 71 | 0.0 | 9.3 | 20 |

- the tin signal (Sn 3d) is not detected
- the lead signal presents a contribution at $139.8 \pm 0.2\text{eV}$, the intensity of which is significantly attenuated (by a factor of 5) compared to the lead intensity before treatment
- the position of the Cu $2p_{3/2}$ core level signal is unchanged at a binding energy of $932.9 \pm 0.1\text{ eV}$ but its intensity is attenuated (by a factor of 8.5) by the inhibitor layer
- the maximum of the Cu LMM Auger line is now located at a kinetic energy of $914.2 \pm 0.2\text{ eV}$
- the Zn $2p_{3/2}$ core level is now located at $1023.2 \pm 0.1\text{ eV}$ (similar intensities before and after treatment in the solution)
- the main signal in the O 1s core level is at a binding energy of 533.8 eV (trapped water in the organic film), but a very low intensity signal is still detected at $530.5 \pm 0.1\text{ eV}$, possibly due to the presence of copper oxide. The total intensity of oxygen has decreased by a factor 2.5.

No sulphur was detected in the S 2p core level region.

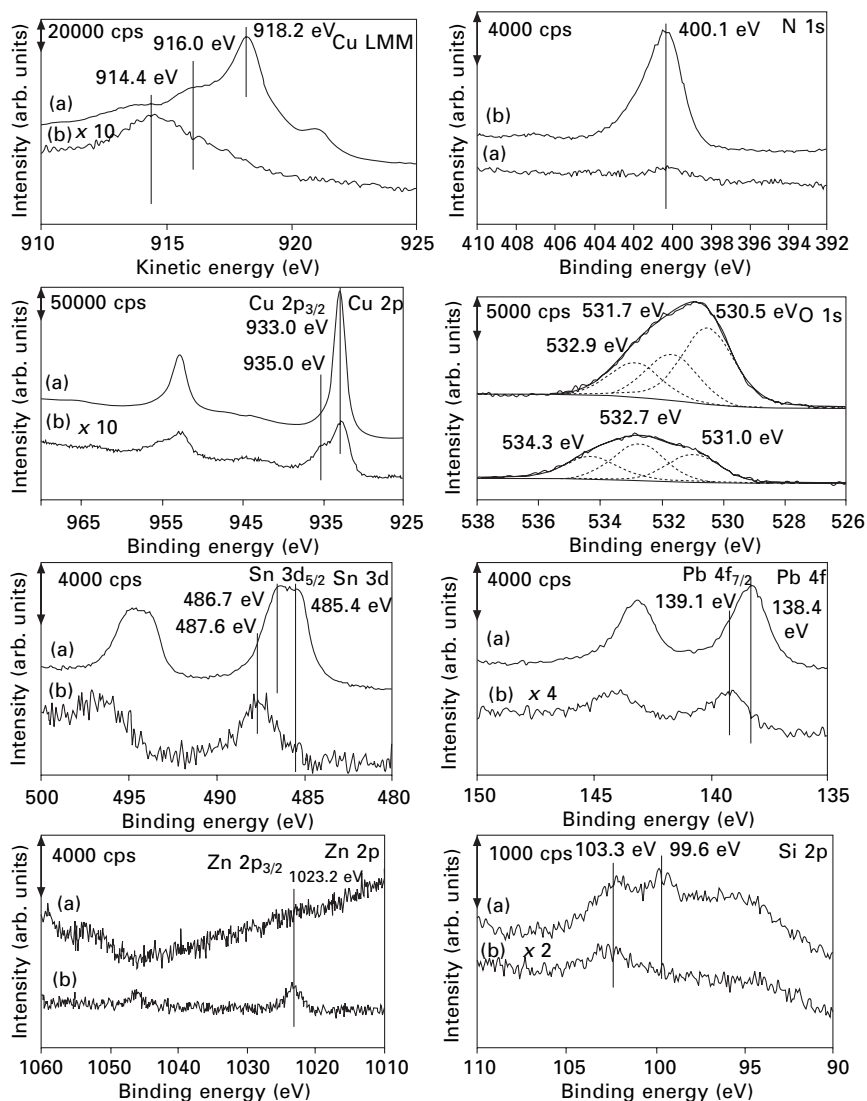
The direct conclusions from these observations are that tin does not react with the organic inhibitor and that copper and zinc are involved in the adsorption of the organic film. The behaviour of copper in the alloy is similar to that of pure copper. As regards quantitative aspects, Table 19.1 indicates that, after treatment, the surface concentrations of zinc (mainly) and lead have increased.

CuSnSi

After polishing, the XPS analyses (see Fig. 19.3 and Table 19.2) show the presence of Cu (Cu 2p), Sn (Sn 3d), Si (Si 2p) and also Pb (Pb 4f) (as an impurity in the sample). Zinc is not detected on the surface. The Cu $2p_{3/2}$ core level spectrum presents a peak at a binding energy of $933.0 \pm 0.1\text{ eV}$. The Cu LMM main peak is located at $918.2 \pm 0.1\text{ eV}$, with a shoulder at

Table 19.2 Surface composition (at%) of the CuSnSi (Zn, Pb) alloy determined from the total XPS core level intensities (Cu $2p_{3/2}$, Sn $3d_{5/2}$, Si 2p, Zn $2p_{3/2}$, Pb $4f_{7/2}$) before and after treatment with the corrosion inhibitor solution

| | Cu | Sn | Si | Zn | Pb |
|---|----------------|------------------|------------------|------------------|------------------|
| Bulk CuSnSi alloy | 89 (89 wt%) | 4.1 (7.6 wt%) | 6.4 (2.8 wt%) | 0.3 (0.3 wt%) | 0.1 (0.4 wt%) |
| Before immersion in the inhibitor (at%) | 72 | 6.2 | 18 | – | 3.3 |
| After immersion in the inhibitor (at%) | 57 | 3.7 | 27 | 8.9 | 4.0 |



19.3 Cu LMM Auger lines and Cu 2p, Sn 3d, Pb 4f, Zn 2p, Si 2p, N 1s and O 1s core level peaks for the CuSnSi bronze (a) before and (b) after treatment in the corrosion inhibitor solution.

916.0 ± 0.1 eV. Sulphates are not detected in the S 2p core level spectrum (not shown here).

The other alloyed elements present both metallic and oxidised components at binding energies of 485.4 ± 0.1 eV and 486.7 ± 0.2 eV for Sn 3d_{5/2}, and 99.6 ± 0.1 eV and 103.3 ± 0.2 eV for Si 2p (Fig. 19.3). It is worth noting that the Zn 3p and/or Sn 4p core levels overlap with Si 2p in the low binding

energy side (Fig. 19.3). As regards Pb $4f_{7/2}$, the only detected signal, at 138.4 ± 0.1 eV, corresponds to PbO₂. The surface is enriched in Si and Pb, compared to the bulk alloy (Table 19.2). The O 1s core level spectrum was also decomposed into three components at similar binding energies as for pure copper and the CuSnPbZn bronze (530.5, 531.7 and 532.9 eV). The lower binding energy value most probably corresponds to copper oxide (Cu₂O) on the surface, as for the previous case, the binding energy value of 531.7 eV may correspond to OH groups adsorbed on copper oxide as well as to tin and silicon oxides. The highest binding energy (533.9 eV) can be attributed to adsorbed water on the hydroxylated copper oxide, as mentioned previously.

After treatment in the solution of corrosion inhibitors, an intense N 1s signal is detected, centred at 400.1 ± 0.1 eV. Similarly to the case of the CuSnZnPb bronze sample:

- the maximum in kinetic energy in the Cu LMM Auger spectrum is located at 914.4 ± 0.2 eV
- a signal from Zn (Zn $2p_{3/2}$ core level) is now detected at a binding energy position of 1023.2 ± 0.1 eV
- the lead signal presents a contribution at 139.1 ± 0.1 eV, the intensity of which is significantly attenuated (by a factor of 9) compared to the lead intensity before treatment.

Compared to CuSnZnPb, some new features are observed:

- a very weak signal of tin (Sn 3d) is detected, with a dominant contribution from the oxide (487.6 ± 0.1 eV), and a very weak metallic signal (485.4 ± 0.1 eV) (total decrease in intensity by a factor 20 compared to before immersion)
- the signal of silicon in silicon oxide is detected
- the Cu $2p_{3/2}$ signal is still observed at a binding energy of 933.0 ± 0.1 eV but a new feature is detected at 935.3 ± 0.1 eV, corresponding to the presence of Cu²⁺ (with shake-up satellites [7] at 6–10 eV on the high binding energy side of the main peaks). The total copper intensity has decreased by a factor of 14
- the total intensity of the O 1s signal has decreased by a factor of 10. The core level signal is decomposed into three peaks at BE 531.0 ± 0.1 eV, 532.7 ± 0.1 eV and 534.3 ± 0.1 eV. The latter value is slightly above (+0.5 eV) the higher binding energy peak in the O 1s decomposition for CuSnZnPb, after treatment. This peak may still be attributed to adsorbed water. The other two binding energies are in good agreement with the O 1s peak decomposition for CuSnZnPb, attributed to oxygen in lead sulphates and/or in OH groups adsorbed on copper, zinc or tin oxides (532.7 eV) and oxygen in oxides (531.0 eV).

The direct conclusions from these observations are that copper and zinc

participate in the adsorption of the organic inhibitor film. Some copper is also oxidised into Cu^{2+} . Tin is hardly detected and probably does not participate in the organic inhibitor complex. Table 19.2 indicates also that, after immersion in the corrosion inhibitor solution, the surface concentrations of zinc and lead (impurities in the bulk alloy) have significantly increased. The silicon signal is significantly detected.

19.3.3 Inhibitor treatment of the other alloying elements (Sn, Pb, Zn, Si)

In this part of the work, the pure metals (Sn, Pb, Zn) as well as pure Si were treated in the same inhibitor solution, containing the BTA + C6-BTA mixture.

Tin

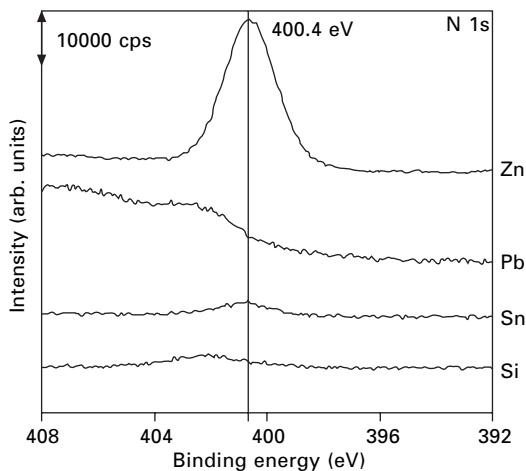
Before immersion in the corrosion inhibitor solution, the Sn $3d_{5/2}$ core level spectrum presented two signals corresponding to the metal at 485.0 ± 0.1 eV and to an SnO_2 oxide at 487.0 ± 0.1 eV [10–11]. The thickness of the layer has been estimated to be about 5.0 nm. After immersion in the solution, there was no signal detected in the N 1s core level region (Fig. 19.4). This clearly shows the absence of reactivity of tin towards this inhibitor. The intensity of the metallic signal had decreased by a factor of 5, in favour of the intensity of tin oxide.

Lead

Before immersion in the corrosion inhibitor solution, the surface of the lead sample was mainly composed of lead sulphates (Pb $4f_{7/2}$ binding energy of 139.0 ± 0.1 eV and S 2p binding energy of 168.5 ± 0.1 eV [13]), formed during etching in H_2SO_4 . A weak signal of metallic lead was also detected at 136.6 ± 0.1 eV [13] (about 10% of the intensity of the oxidised lead signal). After immersion, there was no signal detected in the N 1s core level region (Fig. 19.4); only a low intensity shoulder was detectable at about 402 eV, corresponding to the Pb 4d core level peak. This experiment reveals the absence of reactivity of lead towards the inhibitor.

Zinc

Before immersion, the zinc surface was oxidised (presence of an intense O 1s core level peak located at 531.9 ± 0.1 eV) and also slightly contaminated by nitrogen (N 1s core level peak located at 398.8 ± 0.2 eV). The binding energy of Zn $2p_{3/2}$ was 1022.3 ± 0.1 eV. After immersion, an intense N 1s core level peak was detected at 400.4 ± 0.1 eV (Fig. 19.4), showing the



19.4 Comparison of N 1s core level regions for pure Zn, Pb, Sn, and Si samples after treatment in the corrosion inhibitor solution.

presence of adsorbed inhibitor on the zinc surface. The binding energy of Zn $2p_{3/2}$ was slightly shifted to 1023.1 ± 0.1 eV, as in the case of the zinc-containing bronze alloy.

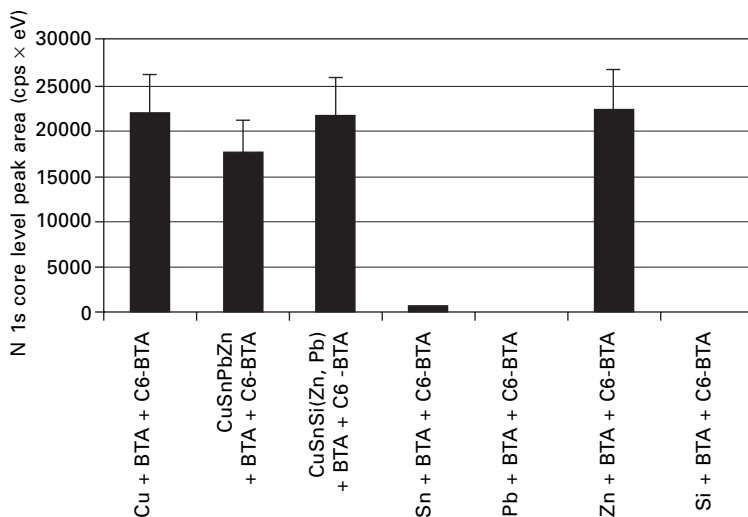
Silicon

Before immersion in the inhibitor solution, the silicon sample was covered by a thin layer of SiO_2 (binding energy of 102.9 ± 0.1 eV) passivating the silicon surface (binding energy of 98.8 ± 0.1 eV). The equivalent thickness of the silica thin layer has been estimated to be 0.5 nm. After immersion, there was no signal detected in the N 1s core level region (Fig. 19.4). The binding energies of silicon and silicon oxide were unchanged. The ratio of the intensities of silicon and silicon oxide remained similar. The surface was more contaminated (carbon and oxygen). The direct conclusion is that silica does not react with the inhibitor.

19.4 Discussion

19.4.1 Comparison of the N 1s intensity on the different surfaces

The N 1s core level peak intensity (area in counts per second \times eV), measured after BTA + C6-BTA treatment on all the different substrates are reported in Fig. 19.5, allowing a direct comparison of the substrates. The results indicate that there are no marked differences, within experimental errors, for the reactive substrates (Cu, Zn, and the two bronzes).



19.5 Comparison of the N 1s core level peak areas (cps × eV) for the different substrates, after treatment in the corrosion inhibitor solution.

19.4.2 Copper-inhibitor complex on reactive surfaces

On the reactive substrates, on which the presence of adsorbed BTA + C6-BTA was observed, the binding energy of the N 1s core level peak was 400.2 ± 0.2 eV. This value is not discussed much in the published data, but is in very good agreement with the value of 400.1 ± 0.1 eV reported by Tommesani *et al.* [8]. However, it has been made clear in many works that the presence of BTA is established by an intense N 1s peak (see e.g. [9]). In our experiments, the N 1s binding energy is not significantly dependent on the reactive surface, when copper is present, and is not significantly different on pure zinc.

The Cu 2p and Cu Auger signals for pure copper and for both bronzes are quite similar: BE of 932.8 ± 0.1 eV for Cu 2p_{3/2} and kinetic energy of 914.5 ± 0.2 eV for the Cu LMM Auger lines. This result is in very good agreement with the published data describing a Cu(I)-inhibitor complex, either on pure copper [8, 9, 16] or on copper-containing alloys such as brass [9, 16], copper-tin alloy [17], and copper-nickel alloy [9]. In such a complex, copper(I) is located not only at the interface, but also in the organic film [18, 19]. In addition to the formation of such a Cu(I)-inhibitor complex, the presence of Cu(II) was systematically detected on the CuSnSi bronze alloy. (Cu(II) represents about 50% of the total Cu 2p_{3/2} intensity). The presence of a small amount of Cu(II) has already been reported in the case of pure copper [9, 16], and it did not depend on the immersion time in the BTA solution. The extreme sensitivity of the BTA-treated copper surface to air was invoked to justify the oxidation of Cu(I) to Cu(II). This was evidenced by the increased

intensity of the Cu(II) contributions in the Cu 2p core level, for increasing exposure time to air after immersion [9]. The conclusion was that the Cu(I)-inhibitor was unstable in air. However, Tommesani *et al.* [8] do not mention this copper oxidation. The same oxidation of Cu(I) to Cu(II) was observed with BTA-protected copper-nickel alloys, and brass samples [9]. A BTA-Cu(II) complex has also been suggested [20], but its protective properties would be quite poor [18]. This Cu(II) complex was not observed for copper-*tin* after immersion in aerated seawater following a treatment of 1 g.l^{-1} of BTA [17]. By analogy with the previous observations of Cu(II) on BTA-protected samples, it is possible to attribute it to copper oxidation in air, during the short transfer of the sample to the spectrometer. From the absence of any signal located in the region of KE 918.5 eV in the CuLMM spectra, whatever the copper-containing sample, it can be deduced that metallic copper is not detected and that the inhibitor film is fairly thick (more than three times the electron inelastic mean free path λ in this film, estimated at 30 \AA in ref. [8]).

The formation of a surface BTA-inhibitor complex on pure Zn has not been studied in detail in other works. However, for Cu-30Zn [9], the authors concluded that zinc must be involved in the surface complex, and they confirmed that BTA adsorbed on zinc, but did not indicate any experimental data. Our experimental data on pure zinc confirm the surface reactivity of Zn towards BTA (+ C6-BTA) and the formation of a Zn(II)-inhibitor complex, characterised by a Zn $2p_{3/2}$ binding energy of $1023.1 \pm 0.1 \text{ eV}$ and a N 1s binding energy of $400.4 \pm 0.1 \text{ eV}$. According to the XPS data, the same complex seems to be formed with Zn on the surface of both bronze alloys (same Zn $2p_{3/2}$ and N 1s binding energies).

In this work, the O 1s core level peak fitting has systematically proved the presence of copper oxide (on pure copper and on both bronze alloys) before immersion in the inhibitor solution. Some authors have suggested that copper oxide is necessary for the formation of the surface complex [19, 21], involving an electrostatic interaction between the positively charged surface and the BTA anion. Other authors indicate that oxygen may play a role but is not necessary [16]. Tommesani *et al.* [8] performed a systematic O 1s peak fitting with two components, centred at $530.8 \pm 0.1 \text{ eV}$ and $533.1 \pm 0.1 \text{ eV}$, the former being attributed to oxygen in Cu_2O and the latter to either hydroxylated species or bound/trapped water in the organic film. The N/O intensity ratio was used to estimate the organic Cu(I)-inhibitor film thickness (the higher the N/O(Cu_2O) atomic ratio, the thicker the inhibitor film), and the amount of trapped water (N/O(trapped water) atomic ratio). The latter ratio was constant and equal to 1.0 ± 0.2 [8]. It was not possible in the present work to fit the O 1s spectrum with only two contributions. However, analogous intensity ratios were calculated, after O 1s peak fitting, for the high binding energy O 1s component, for pure copper (1.6 ± 0.2) as well as

for bronzes (1.4 ± 0.1 for CuSnPbZn and 5.0 ± 0.5 for CuSnSi). The values suggest that there is water in the organic inhibitor layer, and also that there is less water in the case of the film formed on CuSnSi (though the protective efficiency is worse, according to the electrochemical data [1]).

Additional information is deduced from the calculation of the C/N atomic ratio. Experimental results give values of 5.6 ± 0.5 , 6.9 ± 0.7 , 5.0 ± 0.5 and 4.7 ± 0.5 for Cu, CuSnPbZn, CuSnSi and Zn, respectively. These values are higher than the theoretical ratio of 3.4 expected from the concentrations of BTA + C6-BTA used in this work. One explanation could be that C6-BTA adsorbs preferentially on the surface ($C/N = 4.0$); the excess of carbon may be due to different attenuations of the C 1s and N 1s signals (N 1s being more attenuated than C 1s) and/or to surface contamination.

19.4.3 Comparison of protected bronzes

The combination of XPS data and previous electrochemical data [1] shows that there is no straightforward relationship between the amount of adsorbed inhibitor and its inhibiting efficiency. An explanation of the better corrosion behaviour of BTA + C6-BTA on CuSnPbZn as compared to BTA + C6-BTA on CuSnSi can be found from the comparison of the XPS data for the alloys and the pure metals.

On silicon and lead, no BTA + C6-BTA adsorption was observed, which seems to contradict previous published works. A recent paper dealing with the adsorption of BTA on lead samples [15] concludes that a protective layer of a lead-BTA complex is formed, on top of a PbO oxide layer. The difference in BTA concentration between the present work and the cited work [15] may explain such a difference, as well as the irreversible reaction of lead with H_2SO_4 , during the chemical etching performed prior to the inhibiting treatment. The same protocol was also used for the bronze samples, thus the same absence of reactivity of lead in bronzes towards BTA + C6-BTA is expected. In the case of silicon, a weak adsorption of BTA (0.25 mol.l^{-1}) was observed [16] (10 to 40 times lower than on copper, brass and iron). To get an idea of the surface coverage in silica, in this work the silicon oxide intensity in the bronze after treatment (Si 2p core level) was compared to the silicon oxide intensity in the pure silicon sample. This resulted in about 20% of the surface covered by silica. This value remains compatible with the experimental error in the estimation of the N 1s peak area, which was not significantly lower than for the other samples, after treatment. A significant surface coverage of silica, as estimated here, poorly reacting with BTA + C6-BTA, may explain the loss of efficiency of the organic inhibitor film, as observed in the previous electrochemical measurements. This would also be consistent with the presence of Cu^{2+} , indicating that, in the case of CuSnSi, the alloy is less protected.

For tin, no significant adsorption of BTA + C6-BTA was found on the

pure polished tin sample, and a very weak tin signal only was detected for the bronzes after treatment. Thus, our data show absence of reactivity of tin dioxide towards BTA + C6-BTA (and to our knowledge, no comparative data are available).

19.5 Conclusions

X-ray Photoelectron Spectroscopy (XPS) has been used to compare the surface reactivity of two bronzes, CuSnPbZn and CuSnSi, pure metals (Cu, Zn, Sn, Pb) and silicon towards 1,2,3-benzotriazole (BTA) mixed with 5-hexyl-BTA (C6-BTA).

Pure copper and zinc showed a marked surface reactivity towards BTA + C6-BTA. After immersion of polished copper in the BTA + C6-BTA inhibitor solution, the Cu LMM Auger lines were modified (KE 914.5 eV), and a N 1s signal at a binding energy of 400.1 ± 0.1 eV appeared, both characteristic of the formation of a Cu(I)-inhibitor complex. On polished zinc, the formation of a Zn(II)-inhibitor complex was characterised by a N 1s signal at a BE of 400.4 ± 0.1 eV, and a Zn 2p_{3/2} BE of 1023.1 ± 0.1 eV. Tin, lead and silicon did not react or reacted very weakly with BTA+C6-BTA.

After immersion of the bronzes in the inhibitor solution, the same Cu(I)-inhibitor and Zn(II)-inhibitor complexes as on pure copper and zinc were observed, as zinc is present on the surface as either an alloyed element or an impurity in the bronze sample. The C/N atomic ratios seem to indicate that C6-BTA adsorbs preferentially on the surface. Water was found to be trapped in the organic inhibitor film. A significant amount of silica was observed on the surface of CuSnSi. Silica being poorly reactive towards BTA + C6-BTA, this may explain the lower efficiency of the organic inhibitor film on this alloy observed previously by electrochemical measurements. It was confirmed in this work by the presence of Cu²⁺ on the surface of the CuSnSi alloy (and not on the Si-free bronze).

19.6 References

1. C. Chiavari, PhD Thesis, Politecnico of Milan, 2003.
2. G. Brunoro, A. Frignani, A. Colledan, C. Chiavari, *Corrosion Sci.*, 2003, vol. 45, 2219–2231.
3. C. Chiavari, A. Colledan, G. Brunoro, *Proceedings of the European Corrosion Congress*, paper no. 90 (CD-Rom), EUROCORR 2001, Riva del Garda, Italy, 2001.
4. G. Brunoro, F. Zucchi, L. Tommesani, G.L. Garagnani, *Sci. and Technol. for Cultural Heritage*, 1995, vol. 4, 1–11.
5. G. Deroubaix, P. Marcus, *Surf. Interface Anal.*, 1992, vol. 18, 39–46.
6. E. Paparazzo, L. Moretto, *Vacuum*, 1999, vol. 55, 59–70.
7. S.K. Chawla, N. Sankarraman, J.H. Payer, *J. Electron Spectrosc. Relat. Phenom.*, 1992, vol. 61, 1–18.

8. L. Tommesani, G. Brunoro, A. Frignani, C. Monticelli, M. Dal Colle, *Corrosion. Sci.*, 1997, vol. 39, 1221–1237.
9. D. Chadwick, T. Hashemi, *Corrosion Sci.*, 1978, vol. 18, 39–51.
10. G. Ingo, E. Angelini, T. De Caro, G. Bultrini, A. Mezzi, *Surf. Interf. Anal.*, 2004, vol. 36, 871–875.
11. D.N. Wang, A.C. Miller, M.R. Notis, *Surf. Interf. Anal.*, 1996, vol. 24, 127–132.
12. B. Gergely, C. Guimon, A. Gervasini, A. Auroux, *Surf. Interf. Anal.*, 2000, vol. 30, 61–64.
13. T.L. Barr, *J. Vac. Sci. Technol. A*, 1991, vol. 9, 1793–1805.
14. S. Chattopadhyay, S. Srikanth, *J. Phase Equilibria*, 1995, vol. 15, 553–557.
15. V.C. Sharma, U. Snakar Lal, T. Singh, *Studies in Conservation*, 2003, vol. 48, 203–209.
16. R. Combarieu, G. Dauchot, F. Delamare, *Proceedings of the International Conference on Metals Conservation, Metal '98*, W. Mourey and L. Robbiola (eds), James & James (Science Publishers) Ltd, UK, 1998, 223–228.
17. R. Walker, *Corrosion (NACE)*, 2000, vol. 56, 1211–1219.
18. J.B. Cotton, I.R. Scholes, *Br. Corrosion J.*, 1967, vol. 2, 1–5.
19. Y. Ling, Y. Guang, K.N. Han, *Corrosion*, 1995, vol. 51, 367–375.
20. R.F. Roberts, *J. Electron Spectrosc. Relat. Phenom.*, 1974, vol. 4, 273–291.
21. F. Mansfeld, T. Smith, *Corrosion*, 1973, vol. 29, 105–107.

Influence of microstructure and composition on corrosion of lead-rich organ pipes

C. CHIAVARI, C. DINOI, C. MARTINI and
D. PRANDSTRALLER, Università di Bologna, Italy
and G. POLI, Università di Modena, Italy

20.1 Introduction

The European heritage of the organ is preserved in numerous historical instruments. One major threat to this heritage is the indoor atmospheric corrosion of lead and lead–tin alloys of organ pipes. It is well known that wood emits organic vapours, including acetic acid, that are corrosive towards lead [1–4]. The action of these vapours emitted by the wooden structures of the instrument can be one of the main causes accountable for lead pipe corrosion but, to our knowledge, a systematic study has never been dedicated to the study of the factors responsible for the decay of the instruments.

In order to identify these factors and so to develop a conservation strategy, a research project (COLLAPSE, Corrosion of Lead and Lead Alloys of Organ Pipes in Europe; www.goart.gu.se/collapse), composed of both field studies and laboratory experiments, has been set up. Field studies include the selection and study of organs affected by corrosion to be compared with organs not affected by corrosion. As case studies, some historical pipe organs in different European countries (Germany, Italy, Belgium, the Netherlands) have been selected (reference organs). Also the instruments selected as non-corroded organs appeared to contain some corrosion.

The concentration of organic compounds in the atmosphere of the organs (church environment and organ wind supply) has been measured by the Department of Environmental Inorganic Chemistry, Chalmers University of Technology, Göteborg (Sweden). Information on the church environment and on the conditions of the organ (changes of the room heating system, organ restoration or rebuilding activities, materials used in the room and in the organ, etc.), collected by GoArt, Göteborg University (Sweden), have also been taken into account.

During field studies, samples were taken from selected pipes in the reference organs, with the aim of identifying the phase composition and morphology of corrosion products, as well as evaluating the influence of microstructure and composition of the pipe metal on the corrosion behaviour.

It is worth pointing out that most organ pipes were manufactured with a wide range of lead–tin alloys, from nearly pure lead to nearly pure tin with many other intermediate possibilities. A pipe organ may consist of hundreds of pipes, arranged in different stops (i.e. sets of pipes with similar tone quality) and each stop contains a number of pipes that corresponds to the notes on the keyboards and on the pedal keys. Such a high number of pipes requires an effective manufacturing process as well as the use of a material with good casting properties and good workability. The process used nowadays for manufacturing organ pipes still closely resembles the process described by Dom Bedos de Celles in 1766 [5]. The first step (Fig. 20.1(a)) in the construction of a pipe is the production of the metal sheet by casting molten metal on a flat bench covered with sand or cloth. The metal sheet is then hammered (Fig. 20.1(b)) or rolled or scraped to the desired thickness. The shape of the different parts of the pipe (foot, body and languid) are traced and cut from the sheet (Fig. 20.1(b)). In the final step the sheet is bent and soldered (Fig. 20.1(b)). Recycling scrap metal is a common organ building practice that leads to the production of sheets with slightly different compositions. Different sheets can be used for manufacturing different pipes in the same stop or different parts of the same pipe, therefore pipes constructed with different materials can be exposed to the same environment because they belong to the same organ: this situation is the ideal case for studying the influence of material parameters on corrosion behaviour.

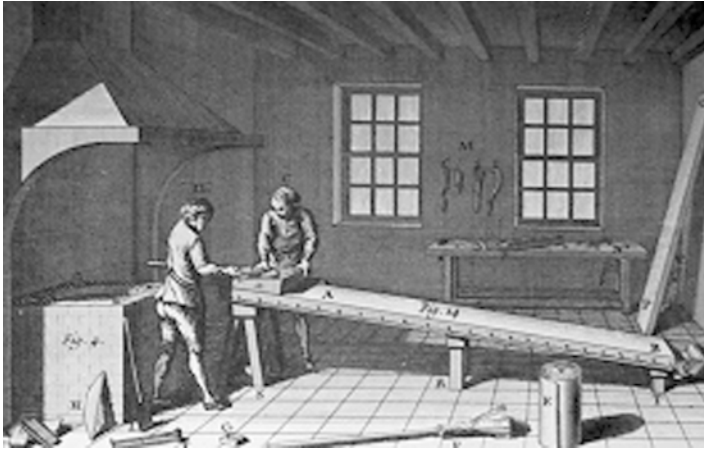
In the present chapter, the results of chemical and microstructural investigations on samples from (1) the organ in the Basilica di Collemaggio (L'Aquila, Italy), selected as a reference organ affected by corrosion, and (2) the organ in the Church of Madonna di Campagna (Ponte in Valtellina, Italy), selected as a reference for a 'healthy' situation, are reported.

20.2 Experimental

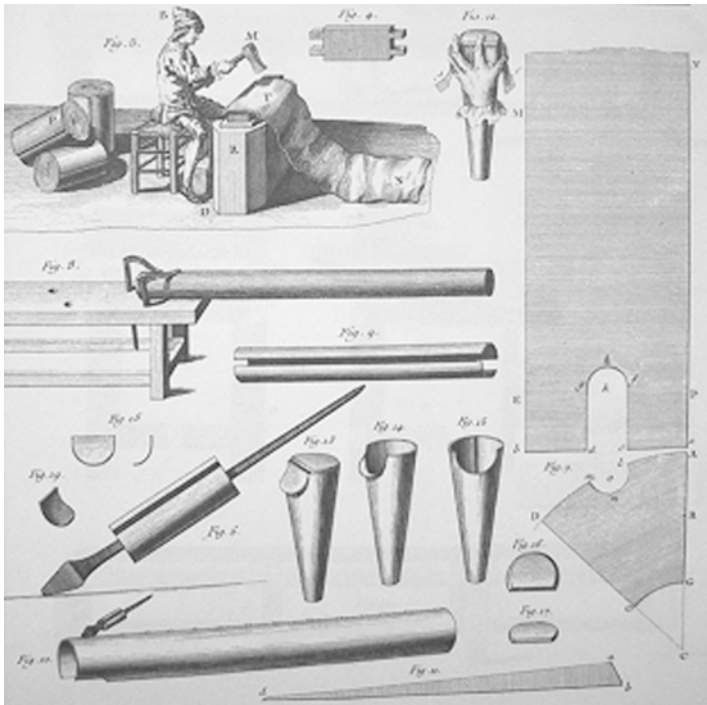
Pipe metal samples were taken from two historical reference organs:

- Corroded Italian organ, in the Basilica of S. Maria Maggiore di Collemaggio, L'Aquila, Italy; attributed to the organ builder Luca Neri da Leonessa, second half of the seventeenth century.
- Uncorroded Italian organ in the Church of Madonna di Campagna, Ponte in Valtellina, Italy; built by Bizzarri, 1518, Antegnati, 1589, Prati, 1657.

The methodology for taking samples has been designed so as to minimize both damage to the corroded pipe and alteration of the sample during cutting. Square samples (surface area $\sim 1\text{cm}^2$) were taken from the foot of the most representative pipes from a corrosion point of view. Where it was not possible to take square samples, samples were scraped from the pipe metal or from



(a)



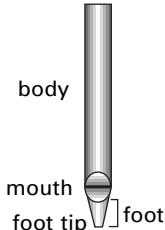
(b)

20.1 The construction of flue pipes: (a) casting; (b) hammering, tracing and soldering [5].

corrosion products. The samples are briefly described in Table 20.1 and the surfaces of square samples are shown in Fig. 20.2.

Sample P5VIIIft comes from the foot tip of a pipe composed of two different materials soldered together during restoration (Fig. 20.3). The lower

Table 20.1 Description of samples and schematic drawing of a flue pipe (the first letter indicates the location of the organ; the first arabic number indicates the pipe in the stop (stop: set of pipes with similar tone quality); the roman number indicates the stop; the last letters indicate the sampling zone: b = body, f = foot, ft = foot tip)

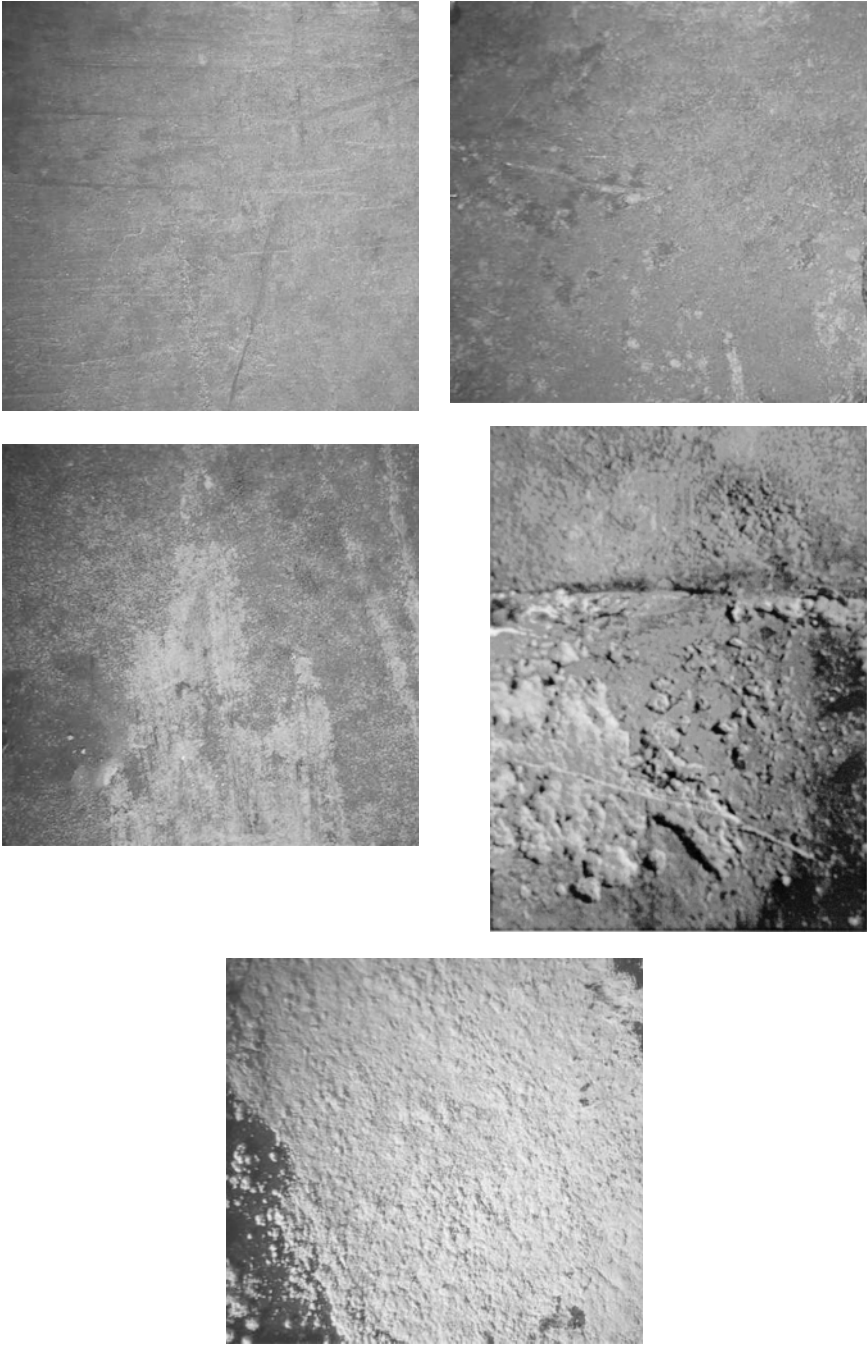
| Organ location | Sample | Description | |
|-------------------------|----------|---------------------------|--|
| L'Aquila (A) | A5XIIf | Square sample |  |
| | A5VIIIb | Metal shavings | |
| | A11XIIf | Metal shavings | |
| Ponte in Valtellina (P) | P5VIIIft | Section of the foot tip | |
| | P5VIIIIf | Square sample | |
| | P7VIIIIf | Square sample | |
| | P4XIIf | Square + scraped powder | |
| | P9VIIIIf | Shavings + scraped powder | |

part of the tip, (P5VIIIftn, 'new') was added in 1994 and consists of pure lead, whereas the upper part, (P5VIIIfto, 'old') is the original lead–tin alloy from the sixteenth century (Fig. 20.2(d)), i.e. the same alloy as sample P5VIIIIf that was taken from the foot of the same pipe.

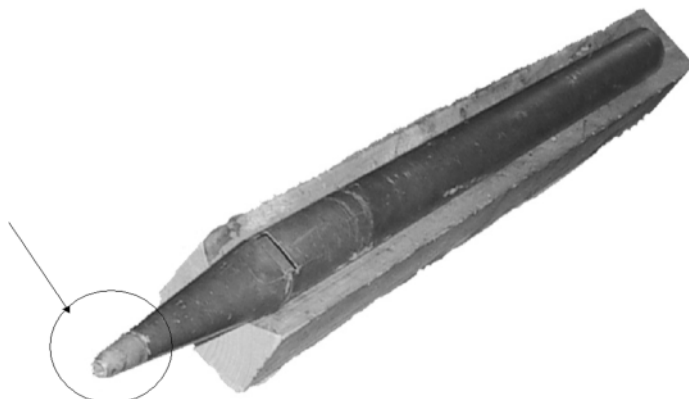
The surfaces of the pipe metal samples were observed by Stereo Microscopy (SM), Optical Microscopy (OM) in bright field/reflected polarized light, and Scanning Electronic Microscopy (SEM) with Energy Dispersive (EDS) microprobe. Corrosion products on square samples were analysed by X-Ray Diffractometry (XRD); localized qualitative analysis of corrosion products was carried out by IR micro-spectroscopy in Attenuated Total Reflectance (ATR) mode on square samples, whereas samples of corrosion products consisting of small amounts of scraped powders were analysed by Fourier Transform Infrared Spectroscopy (FTIR) after preparation of the conventional KBr tablet. Reference spectra for IR analyses were found in refs [6] and [7].

The samples for metallographic examination were sectioned transversely and longitudinally, cold-embedded in epossidic resin, mechanically ground with SiC paper up to 4000-grit, then polished with colloidal silica down to grade 0.05 μm . Afterwards, the surface was etched by three parts acetic acid (glacial) and one part H_2O_2 (30%), in order to examine the microstructure [8]. The grain size (expressed by the grain size number G) was determined in both the surface and the cross-section of etched samples by image analysis (Image Pro Plus) according to the ASTM E 1382 standard [9]. The maximum thickness of the corrosion layer was measured in the cross-section of unetched samples, observed in reflected polarized light.

In the case of corroded samples, the corrosion products on the surface of square samples were removed before chemical analysis of the alloy composition by Flame Atomic Absorption Spectroscopy (FAAS). The alloy was then dissolved by immersion in a 50% v/v aqueous solution of HNO_3 .



20.2 Inner surface of pipe metal samples: (a) P4XIIf; (b) P5VIIIIf; (c) P7VIIIIf; (d) P5VIIIIf; (e) A5XIIf.



20.3 General view of pipe P5VIII: note the foot tip replaced during restoration.

Table 20.2 Composition of pipe metal samples, wt% (FAAS)

| Organ location | Sample | Sn | Cu | Bi | Sb | Ag | As |
|----------------------------|-----------------------|------|------|------|------|------|----|
| L'Aquila (A) | A5XII _f | 0.17 | – | 0.04 | – | – | – |
| | A5XII _b | 0.24 | 0.03 | – | – | 0.01 | – |
| | A11XII _b | 0.22 | – | – | – | – | – |
| | P5VIII _{ftn} | – | 0.02 | – | 0.06 | – | – |
| Ponte in Valtellina (P) | P5VIII _f | 0.73 | 0.05 | – | 0.19 | 0.02 | – |
| | P7VIII _f | 0.63 | 0.21 | 0.06 | 0.18 | 0.03 | – |
| | P4XII _f | 1.51 | 0.25 | 0.05 | 0.11 | 0.02 | – |
| | P9VIII _{ft} | – | 0.03 | – | 0.07 | 0.01 | – |

20.3 Results

The main component of the alloy was lead, with a tin content ranging from 0 to 1.5 wt% and Cu, Bi, Sb and Ag as main impurities (Table 20.2). Pipes from the organ in L'Aquila were manufactured with lead-rich alloys containing very small amounts of impurities, whereas pipes from the organ in Ponte in Valtellina display a higher content of tin, copper and antimony. Within the same organ, the composition changed from pipe to pipe. The composition of the pipe A5XII slightly changed also with the sampling point (body or foot) (Table 20.2). In all cases, the corrosion process was concentrated in the inner surface of the pipe, namely in the foot tip. The morphology of corroded surfaces is shown in Fig. 20.2.

IR spectroscopy (IR) and X-Ray Diffractometry (XRD) showed that the corrosion products consist mainly of lead carbonates (hydrocerussite and cerussite), with traces of lead acetates and sulphates (Table 20.3). The presence of lead acetate (JCPDS-PDF 18-1740) cannot be confirmed by XRD because

Table 20.3 Products identified by XRD and IR analyses on the inner surface of corroded pipes (H = $\text{Pb}_3(\text{CO}_3)_2(\text{OH})_2$ hydrocerussite; C = PbCO_3 cerussite)

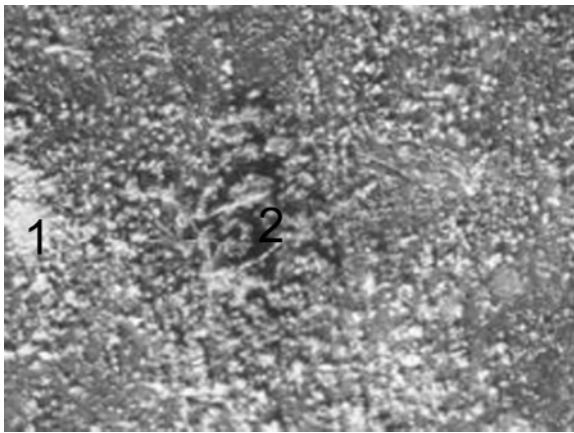
| Sample | XRD | IR |
|-----------|------|----------------------------|
| A5XIIIf | H, C | H, C |
| P5VIIIIf | H | H, C, acetates, sulphates* |
| P5VIIIftn | H | H, C |
| P7VIIIIf | H | H, C, acetates, sulphates* |
| P4XIIIf | H | H, C, acetates, sulphates* |
| P9VIIIIf | – | H, C, acetates, sulphates* |

* Traces of solder size (bole, proteinaceous ligants)

some of the main peaks are at a low diffraction angle ($<10^\circ 2\theta$) and other peaks overlap with those of hydrocerussite.

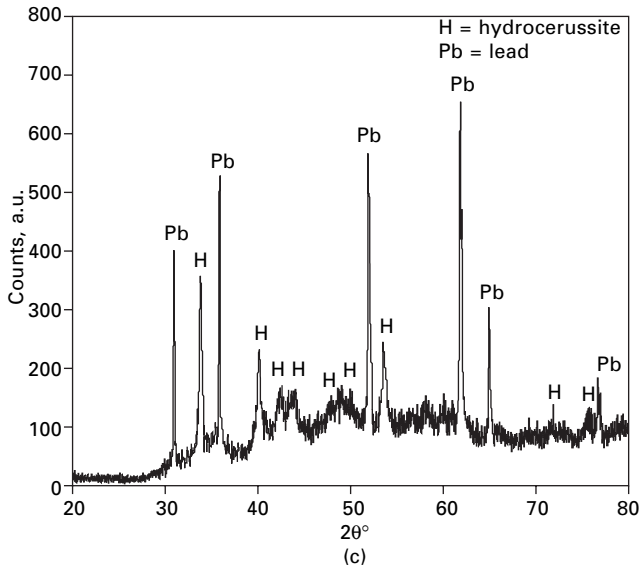
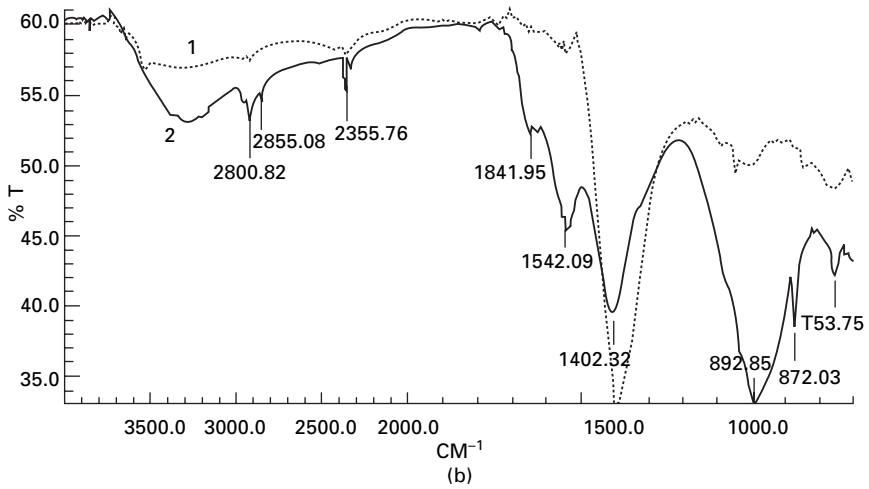
Traces of solder size, i.e. the mixture of proteinaceous ligants and ‘bole’ (calcium carbonate and aluminium silicates [10]) used for the preparation of the surface before soldering the lead sheet during the construction of the pipe, were also detected. An example of IR spectra recorded on the inner surface of the P7VIIIIf pipe, where traces of solder size besides lead corrosion products are clearly visible, is shown in Fig. 20.4.

The morphology of the corrosion products was observed by optical microscopy in reflected polarized light; the cross-sections of the square samples are shown in Fig. 20.5. The maximum thickness of the corrosion products is summarized in Fig. 20.6.



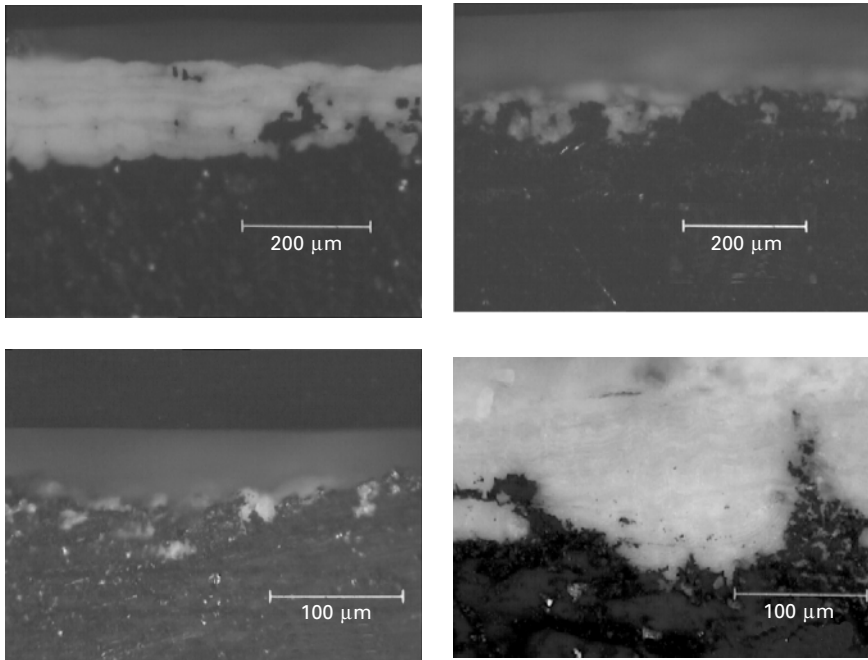
(a)

20.4 (a) Optical micrograph of sample P7VIIIIf with indication of different areas analysed by ATR-IR; (b) ATR spectra of bole traces and corrosion products; (c) XRD pattern of the whole area in micrograph (a).

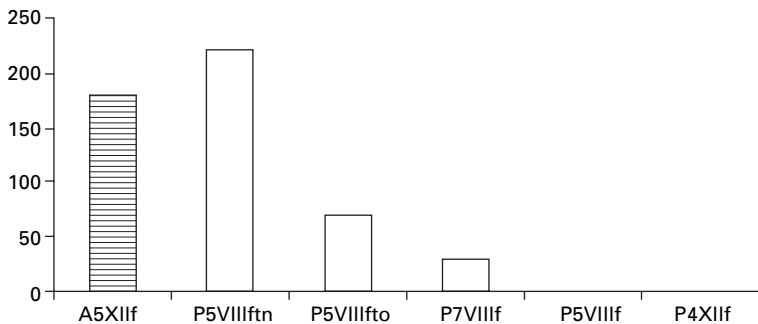


20.4 Continued

The new part of the foot tip of pipe P5VIII was covered with a continuous corrosion layer (sample P5VIIIftn, Fig. 20.5(a)), thicker than the one in the ancient part (sample P5VIIIfto, Fig. 20.5(b)). No corrosion products were visible in cross-section in the ancient part of the foot far from the solder seam (sample P5VIIIf, Fig. 20.6). Sample P7VIIIf (Fig. 20.5(c)) showed a localized and uneven growth of corrosion products, while sample A5XIIIf (Fig. 20.5(d)) was covered with a thick and extensive layer. No corrosion products were visible in the cross-section of sample P4XIIIf. Microstructural



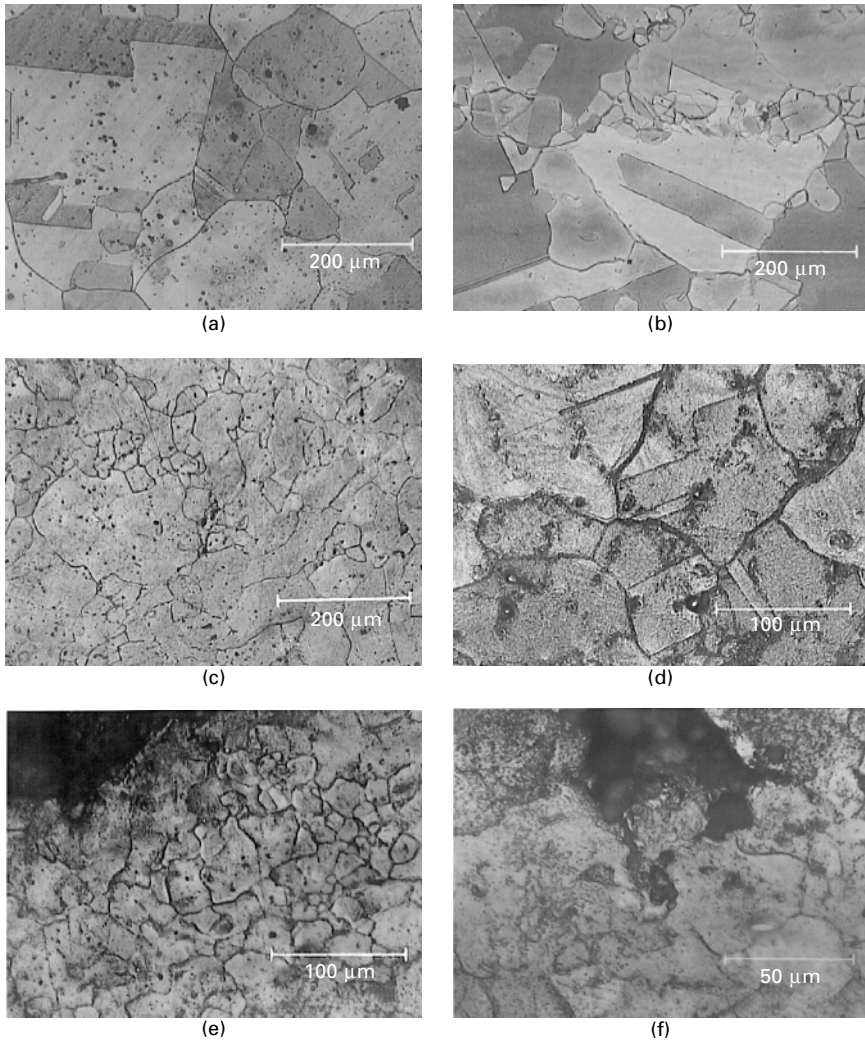
20.5 Cross-sections of corroded pipes in reflected polarized light: (a) P5VIIIftn, new part; (b) P5VIIIfto, old part; (c) P7VIIIIf; (d) A5XIIIf.



20.6 Maximum thickness (μm) of corrosion products in cross-section.

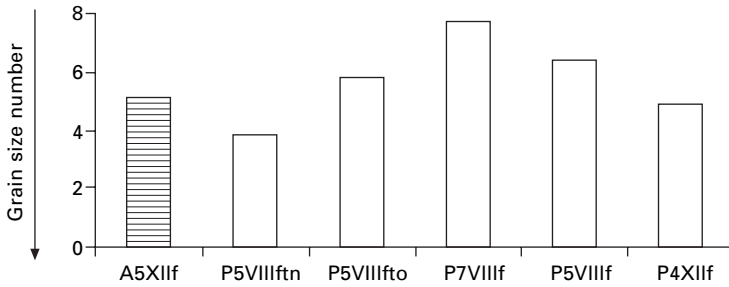
examination of the samples, both on the surface (SM) and in cross-section (CM), showed a completely recrystallized microstructure with equiaxed twinned grains (Fig. 20.7). In cross-section, the observation of the microstructure at the interface between metal and corrosion products revealed traces of highly localized attack in sample P7VIIIIf (Fig. 20.7(f)), in agreement with the results of the observation of corrosion products in Fig. 20.5(c).

In the histogram of Fig. 20.8, the grain size number values of pipe metal samples are compared (high values of the grain size number G correspond to



20.7 Optical micrographs of the samples: general views of the microstructures of (a) A5XIIf (SM), (b) P5VIIIftn (SM), (c) P5VIIIIf (SM) and (d) P4XIIf (CM); details of the interfaces between metal and corrosion layer in (e) P7VIIIIf (CM) and (f) P7VIIIIf (CM).

low values of grain size). The average grain size of these samples ranges from 30 to 80 μm . Pipe metal samples of rather pure lead-rich alloy (A5XIIf, P5VIIIftn, Table 20.2) displayed a coarse grain structure (Fig. 20.7(a) and (b) with low values of grain size number G (i.e. big grains). The grain size in the new part of pipe P5VIII (P5VIIIftn) was higher than in the ancient part of the same pipe (P5VIIIfto and P5VIIIIf) that consisted of a less pure alloy. The grain size of the two samples from the ancient part was comparable: it



20.8 Average size number G (ASTM E 1382) of crystalline grains measured in cross-section of pipe metal samples.

did not change significantly with the distance from the solder seam between 'old' and 'new' material.

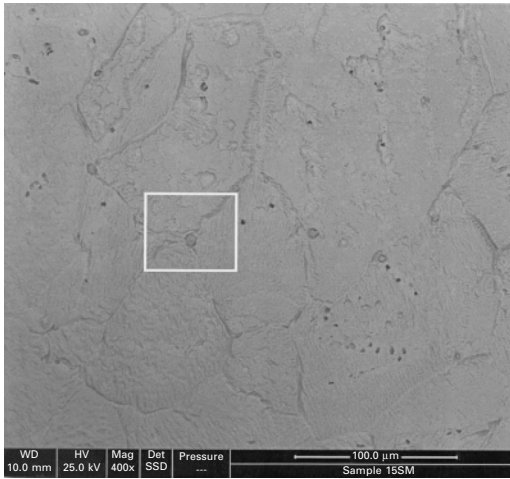
As far as the identification of phases in the microstructure is concerned, localized EDS analyses of pipe metal samples showed the presence of tin inclusions at grain boundaries (Fig. 20.9) in the lead-rich matrix of the samples with the highest tin content. Similarly, copper inclusions were detected in the samples with the highest copper content: Fig. 20.10 shows the cross-section of sample P7VIIIIf, with a copper-rich inclusion near the interface between metal and corrosion products. It is worth noting that this sample undergoes localized corrosion (Figs 20.5(c) and 20.7(f)).

20.4 Discussion

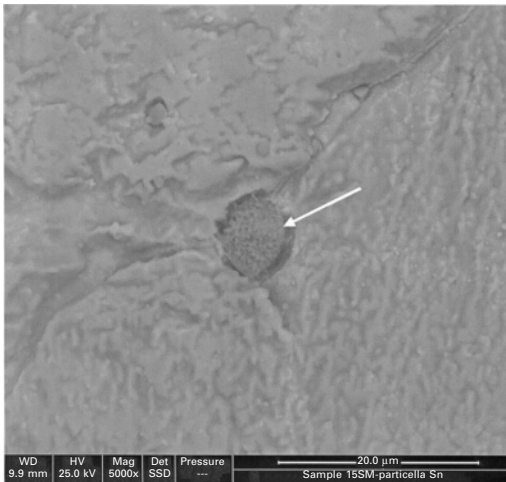
Corrosion mainly affects the inner surface of lead-rich pipes, therefore the degradation process becomes evident from the outside only when the pipe collapses because most of the pipe wall transforms into a whitish powder. Corrosion appears to start in the lower part of the foot and might extend up to the mouth of the pipe. Since the sound is generated in the mouth area and the tone quality is extremely sensitive to changes in the mouth area geometry and surface structure, it is important to detect the phenomenon and begin conservation procedures before the corrosion reaches the mouth area.

All the samples were covered mainly with lead carbonates, which are most commonly found as corrosion products on lead in atmospheres containing organic compounds [1, 11–13]. The extent of corrosion depends both on the concentration of organic compounds in the organ environment and on chemical and microstructural features of the pipe material.

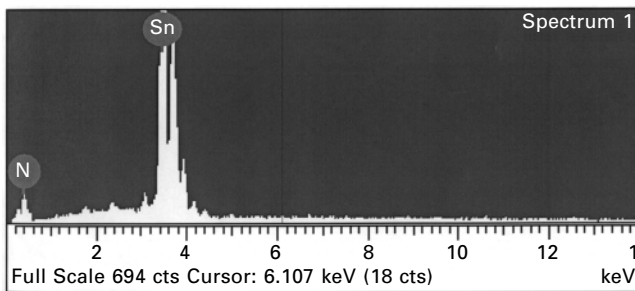
As regards the influence of environmental features on corrosion behaviour, the coverage and thickness of corrosion products was lower in samples from Ponte in Valtellina than in samples from L'Aquila (Figs 20.2, 20.5, 20.6). Measurements of the concentration of organic compounds in the atmosphere inside the organ detected a lower concentration of acid vapours (in particular



(a)



(b)



(c)

20.9 SEM image of sample P4XIIIf; (a) backscattered electrons image; (b) detail of (a), where the white arrow indicates an inclusion at grain boundary; (c) EDS spectrum of the inclusion in (b).

acetic and formic acid) in Ponte in Valtellina [14]. Therefore, corrosion and concentration of organic acids in the atmosphere inside the organs appear to be directly correlated.

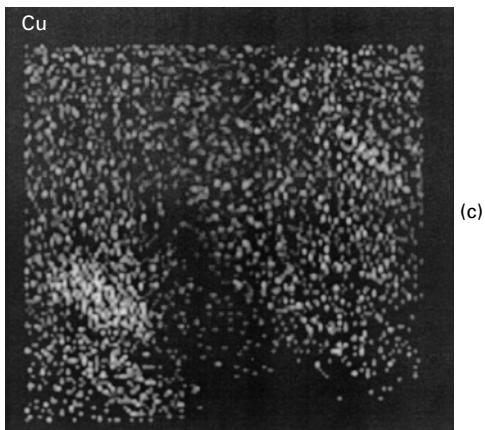
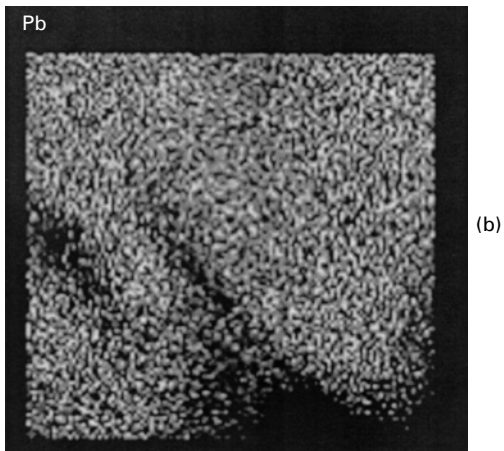
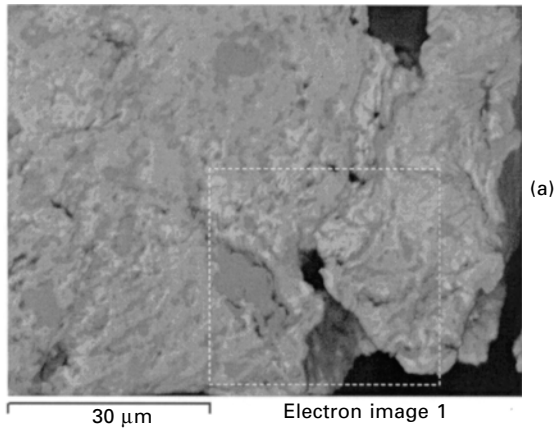
As regards the influence on corrosion behaviour of material features, the alloy composition was first considered. Tin as an alloying element is present in many samples: most of the samples from Ponte in Valtellina contain more tin than samples from L'Aquila (Table 20.2). In samples from Ponte in Valtellina, all exposed to the same atmosphere, the thickness and coverage of corrosion products on the surface appear to decrease with increasing tin content in the alloy (Table 20.2, Fig. 20.6). However, it is worth noting that in the case of different atmospheres and comparable tin content, environmental features are the dominant factor: only a very small amount of corrosion products was collected from the foot of pipe P9VIII, with no detectable amount of tin (Table 20.2), whereas the low-tin sample from L'Aquila was extensively corroded.

In samples with a comparable tin content, the corrosion resistance decreases with increasing copper content (trace level). For example, as shown in Fig. 20.2(b) and (c) Fig. 20.6, the sample P7VIII_f, with 0.21 wt% of copper in the alloy, was more corroded than P5VIII_f with a copper content of 0.05 wt%.

Sample P5VIII_f is a particular case: in this pipe the composition of the alloy in the restored foot tip is different from that of the original alloy. In the coupling of the two different materials the modern alloy, with a lower tin content and with no protective natural patina, corroded preferentially.

From a microstructural point of view, all the samples consist of lead-rich alloys that have been manufactured by plastic deformation (rolling, hammering) and therefore display a recrystallized microstructure with equiaxed twinned grains (Fig. 20.7), which is in agreement with the recrystallizing behaviour of lead [15]. This means that it is not possible to correlate the morphology of crystalline grains to the corrosion behaviour because the grains have the same morphology in all the samples. But, if we consider the inclusions in the grain structure, we might find an explanation for the influence of copper content on corrosion: copper inclusions (which precipitate at grain boundaries because of the low solubility of this element in the lead-rich matrix [16], as shown in Fig. 20.10) might promote localized corrosion [13] (Figs 20.5(c) and 20.7(f)).

A comparison between the graphs of Figs 20.6 and 20.8 does not point out any clear relationship between the grain size and the corrosion behaviour, probably because grain-boundary effects are of minor importance in the stress-free situation of a recrystallized, equiaxed structure, where the main microstructural factor influencing corrosion is likely to be intergranular precipitation [2, 17]. It must also be considered that factors such as (i) the content of elements with a low solubility in lead (e.g. Cu, Sb) and (ii) the degree of deformation, that in this case both vary from sample to sample,



20.10 Backscattered electron image (a) of sample P7VIII f (cross-section) and Energy Dispersive X-ray maps of lead (b) and copper (c) in the area surrounded by the dashed white line. The interface between metal and corrosion products is located in the lower part, right-hand side, of the image.

have an influence on the grain size [15]. For example, grain refinement with increasing copper content was observed in two pipes with a similar tin content, from the same stop of the same organ (Ponte in Valtellina) manufactured by the same organ builder (M. A. Bizzarri, 1518): P5VIII (ASTM grain size number $G = 6.3$) and P7VIII ($G = 7.7$, Fig. 20.8).

20.5 Conclusions

The results of the characterization of the samples taken from corroded pipes indicate that lead carbonates are the main corrosion products that form on the inner surface of the foot of the pipes. Samples from reference organs with a high concentration of organic acids in the environment (e.g. L' Aquila) are extensively corroded. One of the key material factors in influencing the corrosion behaviour of the pipes appears to be the tin content in the alloy, and also copper traces seem to play a significant role. Further work is needed to evaluate the influence of tin and copper content on corrosion.

20.6 Acknowledgements

The COLLAPSE project is a research project supported by the European Commission under the Fifth Framework Programme and contributing to the implementation of the Key Action 'The City of Tomorrow and Culture Heritage' within the Energy, Environment and Sustainable Development (contract no. EVK4-CT-2002-00088). The authors wish to thank the organ builders and restorers Marco Fratti (Campogalliano, Italy) and Riccardo Lorenzini (Montemurlo, Italy) for help and advice. Dr Andrea Tombesi of CIGS, University of Modena, is gratefully acknowledged for FTIR and micro-IR analyses.

20.7 References

1. T.E. Graedel, *J. Electrochem. Soc.*, 1994, vol. 141, 4, 922–927.
2. L.L. Shreir, R.A. Jarman, G.T. Burstein, *Corrosion*, Butterworth-Heinemann, Oxford, 1994.
3. J. Tetreault, J. Sirois, E. Stamatopoulou, *Studies in Conservation*, 1998, vol. 43, 17–32.
4. P.B. Hallebeek, Comparison of the corrosive properties of seven types of plywood, in: *Contributions of the Central Research Laboratory to the Field of Conservation and Restoration*, edited by H. Verschoor and J. Mosk, Amsterdam, 1994, 95–108.
5. Dom Bedos de Celles, *L'Art du Facteur d'Orgues*, Leonce Laget, Paris, 1976 (anastatic copy of the original edition of 1766).
6. K. Nakanishi, P.H. Salomon, *Infrared Absorption Spectroscopy*, Emerson Adams Press, 2000.
7. C. Degrigny, Nouvel examen des résultats d'analyses par diffraction R.X. et spectroscopie

- pie Infra-Rouge effectués à l'E.N.S.C.P. (1^{ère} tranche), Programme Plomb – Report, ARC' Antique, Nantes, France, 1995.
8. C. Di Martini, 'Lead and lead alloys: metallographic techniques and microstructures, in: *Metallography and Microstructures*, Vol. 9, ASM Handbook on CD-ROM, ASM International and The Dialog Corporation, 1999.
 9. Standard test methods for determining average grain size using semiautomatic and automatic image analysis, E1382-97, American Society for Testing and Materials, Annual Book of ASTM Standards, 1997.
 10. T. Grygar, J. Hradilová, D. Hradil, P. Bezdička, S. Bakardjieva, *Anal. Bioanal. Chem.*, 2003, vol. 375, 1154–1160.
 11. A.R. Cook, R. Smith, Atmospheric corrosion of lead and its alloys, in: *Atmospheric Corrosion*, edited by W.H. Ailor, John Wiley & Sons, London, 1982, 393–404.
 12. P. Mattias, G. Maura, G. Rinaldi, *Studies in Conservation*, 1984, vol. 29, 87–92.
 13. C. Degrigny, Etude de la dégradation des objets en plomb dans les collections publiques et des moyens de les stabiliser et de les conserver à long terme, Programme Plomb – Final Report, ARC' Antique, Nantes, France, 1997.
 14. A. Niklasson, S. Langer, K. Pointet, L. Rosell, J.-E. Svensson, to be published (2004).
 15. W. Hofmann, *Lead and Lead Alloys*, Springer Verlag, 1970.
 16. D.J. Chakrabarti, D.E. Laughlin, Copper–lead binary phase diagram, in: *Alloy Phase Diagrams*, Vol. 3, ASM Handbook on CD-ROM, ASM International and The Dialog Corporation, 1999.
 17. R.D. Prengaman, Structural control of non-antimonial lead alloys via alloy additions, heat treatment and cold working, in: *Pb80, Edited Proceedings of the 7th International Lead Conference*, Lead Development Association, London, 1980.

-
- abandonment period 32–3
abandonment phase 33–4, 35
abhurite 165
Access Research and Technology for the Conservation of the European Cultural Heritage (*ARTECH*) 3
acetic acid 315–24
acid etching 219
acid solution exfoliation measurements 146–8
acrylic varnishes 309–10
active corrosion 192
 see also reactivated corrosion
aerated soils 53–7
aerial binders 112
ageing tests
 atmospheric corrosion of iron 131, 139–44
 contemporary low-alloy steel 140–2
 environmental conditions and corrosion rate measurements 142–4
 experimental procedures 142, 143
 experimental results 146–8
 historical artefact 139–40, 141
 simulation of corrosion processes of buried bronze artefacts 205–6, 214–16, 217
air drying 166–7
akageneite 42, 50, 117, 199
 chlorine-containing phases 171–2, 177, 181–7
alloy composition, and corrosion of lead-rich organ pipes 357, 364
 α -FeOOH *see* goethite
anglesite 165, 315
anodic reaction 157
anodic sites, blocking of 137–8
apparent oxygen diffusion coefficient 101–4, 118
applied research 8–10
Archaeological Iron After Excavation (AIAE) 13
archaeometric studies 1
 research funding biased towards 2–6
artificial patinas 266–8
 study of behaviour in atmospheric conditions 268–70
ArtMatters 2
atacamite 182
atmospheric corrosion of iron 21–3, 24, 110, 111, 131–51
 description 132
 experimental ageing of historical artefacts 139–48
 mechanistic modelling 131, 132–9, 144–6
atmospheric testing of artificial patinas 268–70
attenuated total reflection Fourier transform infrared spectrometry (ATR-FTIR) 277
average corrosion rates 60–1, 71–3
 concrete-embedded iron 121–2, 127
 deduction of instantaneous corrosion rate from 105, 106
bacteria 155–6
 sulphate reducing 156, 164
‘battle for oxygen’ 156, 161, 162
benzotriazole (BTA) 312–13
 bronzes for artistic casting 335–51
Bertholon corrosion layers model 8–9, 35–9
binders 111–12, 115, 120–1
 porosities 120–1
binding energy (BE) 337–46
biofilms 155–6, 288
biological colonisation 155–6
bistoury handle 221–2, 224, 225, 226, 231, 234, 235

- black patinas 219–20, 235–6
 analysis 224–31
 ‘common’ 232–4, 235
 ‘uncommon’ 233–4, 235
 ‘black spots’ 9
 blistering 194, 197
 Bode plots 81, 84–6, 215, 216, 217
 bone 273, 280–1
 breaking up 194, 197–8
 brochantite 209, 265, 269
BROMECA 12
 bronzes/bronze artefacts
 corrosion structures 240–3
 inhibition treatment 324–7
 miner’s lamp 326, 327
 simulation of corrosion processes of
 buried bronze artefacts 203–18
 archaeological artefacts 207–9, 210, 211
 copper-based alloys and ageing tests
 205–6, 214–16, 217
 materials and methods 205–7
 soils from archaeological sites 209–14
 type 2 corrosion 241, 242, 252–9
 surface characterisation of corrosion
 inhibitors on bronzes for artistic
 casting 335–51
 tin and copper oxides 239–62
 characterisation of internal corrosion
 layers 244–54
 copper oxides 247, 248
 oxide areas containing both copper
 and tin 252–4, 255, 256, 257
 tin oxide, copper oxide and ‘type 2’
 corrosion 254–9
 tin oxides 247–51
see also copper-based alloys
 brown globules of liquid 194, 198, 199
 ‘brown spots’ 9
 bulk metal analysis 223–4, 225
 burial conditions, chronology of 163–4
 Butler–Volmer activation law 110
 calcite 24, 26
 carbon filter 297, 301
 cassiterite 165
 cast iron
 air drying 166
 corrosion in seawater 162–3
see also iron-based materials
 cathodic curve modelling 88–9
 cathodic reaction
 iron-based artefacts in seawater 158
 location of 98–100
 cellulose nitrate varnishes 309
 cementitious environments, corrosion in *see*
 concrete-embedded iron
 Centre Historique Minier (CHM), Lewarde
 332–3
 ceramics 258
 cerussite 165, 357–8
 chemical changes 194, 198–200
 chloride corrosion cycle 170
 chlorides 204
 intentional patination 227, 234, 235
 and pitting 194–5
 seawater 154, 156, 164, 165
 chlorine-containing phases 170–89
 corrosion products 176–87
 cross-section characterisation 174–6
 experimental corpus of archaeological
 artefacts 172–4
 chronoamperometry 78, 87–9, 90
CIMETAL research programme 109–10
 climatic chamber tests
 ageing tests 131, 139–44, 146–8
 corrosion inhibitors 319–21, 330–1
 clinoatacamite 227, 235
COLLAPSE project 7, 352
 colour zoning 245, 253
 complex impedance plane 84
 concrete-embedded iron 28, 109–30
 characterisation of corrosion layout
 111–22
 binder 111–12, 115, 120–1
 context and objectives 111–12
 dense product layer 115–19
 evaluation of average corrosion rates
 121–2, 127
 experimental corpus 112–13
 metallic substrate 114–15
 methodology 113–14
 transformed medium 115, 116,
 119–20, 122
 modelling approach 122–7
 oxygen reduction 123–7
 presentation 122–3
 concretion layers 157
 copper alloys 164
 ‘white’ metals 165
 conductivity of seawater 153–5
 conservation 1–17, 31
 artefact’s history and its material
 condition 31–4
 conservators’ pro-active responsibilities
 11–12
 fundamental and applied research 8–10

- in-situ* 6–8, 272–3
 - see also* Nydam
- necessity for research 6–10
- networking 3–4, 12–13
- research funding problems 2–6
- training in conservation science 10–11
- conservation protocols 4, 5
- constant phase element (CPE) 80
- copper 9, 251
 - copper-inhibitor complex 313, 347–9
 - corrosion inhibitor treatment of pure copper 337–9, 347, 350
 - lead-rich organ pipes 357, 364, 366
 - copper inclusions 362, 364, 365
 - on-line monitoring of indoor atmospheres 296, 297–306
- copper-based alloys 203–18
 - copper-tin-silicon bronze 335, 347–9
 - compared with copper-tin-lead-zinc bronze 349–50
 - corrosion inhibitor treatment 342–5, 347
 - copper-tin-zinc-lead bronze 335, 347–9
 - compared to copper-tin-silicon bronze 349–50
 - corrosion inhibitor treatment 339–42, 347
- inhibitors 312–13
- intentional patination *see* intentional patination
- marine corrosion 164, 166
- simulation of corrosion processes of buried bronze artefacts 203–18
 - see also* bronzes/bronze artefacts
- copper-benzotriazole complex 313, 347–9
- copper carbonate 164, 166, 209, 227, 228, 229
- copper chlorides 209
- copper monoxide 258
- copper oxides 239–62
 - copper-tin oxide mixtures 243, 252–4, 255, 256, 257, 258
 - ‘type 2’ corrosion 254–9
- copper roofs 263–71
 - corrosion damage and products in Prague 263–4
 - Queen Anna’s Summer Palace 264–70
- copper-II corrosion products 203, 207
- cornerstone 274, 275
- Corresponding to the Limitos Marker (C. Limitos Marker) 38–9
- corrosion depth
 - Nydam lance- and spearheads 276–7, 281–2, 289
 - on-line monitoring 303–5
 - corrosion film thickness from 297–8
 - from mass gain 298
 - resistance sensors 295
 - see also* corrosion rates
- corrosion film thickness 297–8
- corrosion inhibitors 308–34
 - new anti-corrosion formulations 314–31
 - bronze artefacts 324–7
 - iron artefacts 328–31
 - lead artefacts 315–24
 - state of the art 309–14
 - inhibitor compounds 312–14
 - varnish 309–10
 - waxes 310–12
 - surface characterisation of corrosion inhibitors on bronzes for artistic casting 335–51
 - comparison of N 1s intensity on different surfaces 346–7
 - comparison of protected bronzes 349–50
 - copper-inhibitor complex on reactive surfaces 347–9
 - Cu-Sn-Pb-Zn 339–42, 347
 - Cu-Sn-Si 342–5, 347
 - experimental 336–7
 - inhibitor treatment of the other alloying elements 345–6
 - treatment of pure copper 337–9
- corrosion layers
 - Bertholon model 8–9, 35–9
 - intentionally patinated artefacts 231–2
 - tin and copper oxides in bronzes 244–54, 255, 256, 257
 - World War I artefacts 78
 - advanced electrochemical study of internal corrosion layers 82–9, 90
 - specific electrochemical behaviour 80–1
- corrosion potential
 - free corrosion potential and corrosion by seawater 159, 160
 - monitoring 7
 - Nydam modern samples 278, 285–7
- corrosion products
 - analysis of 24–5
 - chlorine-containing phases 176–87
 - copper roofs and claddings 263–4
 - iron-based artefacts in seawater 157–64
 - cast iron 162–3
 - chronological parallelism between

- iron corrosion products and burial conditions 163–4
 - in-situ* growth 159–62
 - theoretical formation and growth 157–8
- iron in soil 48–51, 52, 53, 54
 - species transport in corrosion products 92–108
- lead-rich organ pipes 357–9, 360
- Nydam 277–8, 282–4, 286–7
- 'white' metals in seawater 165
- corrosion rates
 - atmospheric corrosion 135, 136–7, 145, 146–8
 - measurement 142–4
 - average *see* average corrosion rates
 - Glinet site 100–7
 - calculation of oxygen-18 quantity that precipitated into corrosion products 105
 - deduction from average corrosion rate 105, 106
 - hypothesis of oxygen transport control 100–4, 106
 - iron at Nydam 284–5, 287–8, 289–90
 - iron in seawater 156, 161
 - iron in soil 42–3, 59–73
 - average corrosion rates 71–3
 - minimal value 60–1
 - validation of maximal limit 61–71, 74
 - on-line monitoring of indoor atmospheres 295, 297–305, 306
- corrosion system
 - bronze 240–3
 - iron 92–3, 173–4
 - characterisation 44–53, 54, 55, 56
 - Glinet archaeological site artefacts 96–8, 99
 - iron embedded in old binders 111–22
- COST actions, EU 4, 6
- cracks/cracking 194, 195–6
 - chlorinated phases 186
 - concrete 109
 - concrete-embedded iron 115, 116
 - copper roof 265, 266
 - iron in soil 26, 48–50, 56, 59, 98, 106
- critical thickness 127
- cuprite 164, 269
 - crystals 215
 - intentional patination 227, 228, 229, 233, 235
 - layer on bronze artefacts 203, 207, 209
- cuprous oxide 39, 247, 248, 252–3, 254, 255, 256, 257–8, 259
- current intensity 144–6
- current overpotential curve 88–9
- dark-field optical microscopy (DFOM) 243–5, 246, 247, 249, 250, 258
- De Levie theory of porous electrodes 82–3
- dechlorination treatments 165, 166–7
- decuprification 245, 246, 253, 259
- degradation state *see* state of preservation
- dense product layer (DPL)
 - average corrosion rates 60–1
 - chlorinated phases on iron artefacts 174–87
 - concrete-embedded iron 115–19
 - mechanistic modelling 122–7
 - iron equivalent thickness 60
 - iron in soil 45, 48–51, 52
 - corrosion mechanisms 53–7
 - species transport in 92–108
 - analysed corpus and experimental methods 94–6
 - corrosion rates evaluation 100–7
 - corrosion system 96–8, 99
 - hypothesis of oxygen transport control 100–4, 106
 - location of cathodic reaction 98–100
 - porosity 98, 99
- depth of seawater 155
 - and burial chronology 163
- descriptive method 36–8
- diagnostic system 200, 201
- diffusion 56–7
 - apparent oxygen diffusion coefficient 101–4, 118
 - concrete-embedded iron 125–6
 - Fick's laws 103–4, 125, 136
 - oxygen transport control hypothesis 100–4, 106
 - zones 28
- dipwells 274, 275, 279–80
- distribution plant 297, 301–3
- double aegis and counterpoise 220, 221, 224, 225, 226, 231, 233, 235
- dry corrosion 21
- drying *see* wet-dry cycle
- dust 301
- E24 steel 159–62
- E36 steel 140–2, 147–8
- Efestus* project 203, 204
- Egyptian patinated artefacts 220–2, 223–36

- electrical resistance *see* resistance sensors
- electrochemical impedance spectroscopy (EIS) *see* impedance spectroscopy
- electrochemical techniques 9–10, 77–91
- advanced electrochemical study of internal corrosion layer 82–9, 90
 - artefacts 77–8
 - chronoamperometry 78, 87–9, 90
 - electrolyte 79–80
 - methods 78
 - sample preparation, electrochemical cell and electrodes 78–9
 - specific electrochemical behaviour depending on corrosion layers 80–1
- Electrochemical Techniques in Metal Conservation (ETIC) 13
- electrolyte 79–80
- conductivity and impedance diagram 82
 - thickness and modelling atmospheric corrosion 137
- electron probe microanalysis (EPMA) 44, 114, 174
- empirical envelope law 19–20
- energy dispersive spectrometry (EDS) 44, 94, 114, 174
- X-ray maps of chlorinated zones 176–7, 178, 179
- energy dispersive X-ray spectroscopy (EDXS) 243, 245, 246, 247, 249, 252, 258
- environmental monitoring
- indoor *see* on-line corrosion monitoring
 - Nydam 274–5, 279–81
- epoxy polymer systems 310
- equivalent thickness
- iron 60
 - solubility method for corrosion rate 62, 67–71
- Etruscan bronze artefacts 243–59
- European Network for Conservation/Restoration Education (ENCoRE) 11
- European Union (EU) research funding and programmes 1–17
- Evian water 79–80, 82, 84–9
- examination/investigation 1–17
- networking 12–13
 - research funding biased towards 2–6
- excavation condition 33
- experimental ageing *see* ageing tests
- external corrosion layer 78
- feasibility studies 272
- feminine statuette 220, 221, 224, 225, 226, 231, 233–4, 235
- ferric chloride 166
- ferric hydroxides 158
- ferric oxychloride 171–2
- ferrous hydroxide 158
- ferrous hydroxychloride 172, 179, 181–7,
- ferrous oxyhydroxides 158
- see also* akaganeite; goethite; lepidocrocite
- Fick's laws of diffusion 103–4, 125, 136
- field exposures 297
- commercial instruments, sensors and 301–3
- film thickness, corrosion 297–8
- flaking 194, 196–7
- fouling, macroscopic 156
- fundamental research 8–10
- galena 165
- Gallo-Roman lead sarcophagus 322, 323
- γ -FeOOH *see* lepidocrocite
- gangue 157
- ghost microstructures 245–6, 247, 249, 258–9
- Glinet archaeological site 6, 43, 51, 53, 54, 186
- corrosion mechanisms 58–9
 - species transport in corrosion products 92–108
- goethite 42, 111, 186, 199
- atmospheric corrosion 22, 23, 24
 - concrete-embedded iron 117, 118
- Glinet archaeological site 96–8
- corrosion mechanisms 58–9
- iron in soil 48, 49, 51, 53, 62
- corrosion mechanisms 53–7
- Marly viaduct rod 139–40, 141
- solubility 63–7, 68
 - and corrosion rate 71–2
- gold/gold artefacts 9
- intentional patination 233, 234, 235, 236
- grain boundaries 258–9
- grain size 360–2, 364
- graphitised corrosion products 162–3
- green rusts 42, 158
- Groupe des Méthodes Pluridisciplinaires Contribuant à l'Archéologie (GMPCA) 12
- Harpocrate figurine 220, 221, 224, 225, 226, 231, 233–4, 235
- history of artefact 31–4

- humidity 132, 298–301
 hydraulic binders 112
 hydrocerussite 165, 357–8, 359
 hydrogen chloride 166
 hypoeutectoid steels 45–7
 impedance spectroscopy
 bronze artefacts 215–16, 217
 copper-based alloys 206
 ageing 215, 216
 Nydam modern samples 279, 287–8
 World War I steel artefacts 78, 82–7, 90
 complex impedance plane 84
 corrected impedance diagrams 84–5
 fitting of the impedance diagrams 85–6
 porous electrode impedance modelling 82–4
 squared impedance plane 86–7
- in-situ* conservation/preservation 6–8, 272–3
 see also Nydam
- inclusions
 lead-rich organ pipes 362, 363, 364, 365
 slag inclusions 47, 48
- Inralac 310, 311
- indoor atmospheres *see* on-line corrosion monitoring
- Inferior Limitos Marker (I. Limitos Marker) 36
- informative potential 33–4
- inhibitor compounds 312–14
 see also corrosion inhibitors
- inkpot 221–2, 224, 225, 226, 231, 234, 235
- innovative conservation techniques 9–10
- intentional patination 219–38
 analysis of black patinas 224–31
 analysis of bulk metals 223–4, 225
 analysis of other surface layers 231–2
 artefacts 220–2
 instrumentation and methods for analysis 222–3
 types of patina found 232–5
- internal corrosion layer 78, 81
 advanced electrochemical study of 82–9, 90
- International Centre for the Study of the Preservation and Restoration of Cultural Property (ICCROM) 10–11
- International Council of Museums – Conservation Committee (ICOM–CC) Metal Working Group 8, 12–13
- investigation *see* examination/investigation
- iodine diffusion profile 96, 101–4, 118–19
- ion beam analysis (IBA) 222
- iron-based materials 8–9, 18–30
 atmospheric corrosion *see* atmospheric corrosion
 cast iron 162–3, 166
 chlorine-containing phases *see* chlorine-containing phases
 concrete-embedded iron *see* concrete-embedded iron
 corrosion by seawater 156–64
 corrosion in soil *see* soil, corrosion in electrochemical techniques and World War I artefacts 77–91
 inhibition treatment by sodium carboxylates 328–31
 inhibitors for iron 313–14
 marble-like patterns 26, 27, 96–8, 116, 117
 Nydam site *see* Nydam
 reactivated corrosion 190–202
 solubility of iron 62–7, 68
 uniform and localised corrosion 18–20
- iron equivalent thickness 60
- ISO 8044 201
- journals 2
- Karomama statue 234
- kinetic constant for oxygen reduction 124–5
- kinetic energy (KE) 337–45
- Laboratories on Science and Technology for the Conservation of the European Cultural Heritage (*Labs TECH*) 3
- laboratory exposures 297
 commercial instruments, sensors and 298–301
 prototype logger and laboratory manufactured sensors 303–5
- lanceheads 276–8, 281–4
- L'Aquila pipe organ 353–66
- laser cleaning 10
- laurionite 165
- lead/lead-based materials 7
 corrosion inhibition 345, 346, 347
 Cu-Sn-Zn-Pb alloy 335, 339–42, 347–50
 lead-BTA complex 349
 inhibition by sodium decanoate 315–24
 Gallo-Roman sarcophagus 322, 323
 'white' metals 164–5
- lead acetates 357–8

- lead carbonates 315–16, 319, 320–2
 - organ pipes 357–8, 362, 366
- lead hydroxycarbonate compounds 315
- lead oxides 165
- lead-rich organ pipes 7, 352–67
 - manufacture 353, 354
 - microstructure and composition 357–66
 - samples 353–7
- lead soap 319, 320, 323–4
- lead sulphates 357–8
- Leonardo CURRIC project 10–11
- lepidocrocite 42, 111, 133, 199
 - air drying of marine cast iron 166
 - atmospheric corrosion and reduction of
 - 21–3, 24, 134–5, 136–7, 144–6, 148, 149
 - concrete-embedded iron 117
 - Marly viaduct rod 139–40, 141
- limit of the original surface (limitos) 34–5
 - locating 35–9
- limiting step, identification of 126–7
- localised corrosion 18–20
- low-alloy steels 18–30
 - ageing experiment 140–2, 147–8
 - atmospheric corrosion 21–3
 - corrosion in cementitious environments 28
 - corrosion in soils 23–8
 - uniform corrosion and localised
 - corrosion 18–20
 - see also* iron-based materials
- low-carbon steel 41–76
 - average corrosion rate estimation 59–73
 - corrosion mechanisms 53–9
 - corrosion system characterisation 45–53
 - literature review 42–3
 - seawater 159–62
 - see also* iron-based materials
- maghemite 42, 48, 49
 - air drying of marine cast iron 166
 - concrete-embedded iron 117
 - Marly rod rust layer 139–40, 141
 - Nydam 283
- magnetite 42, 48, 49, 51, 53, 62, 111, 186
 - concrete-embedded iron 117
 - corrosion mechanisms and magnetite
 - veins in goethite 53–7
 - Glinet archaeological site 96–8
 - iron-based artefacts in seawater 158
 - Marly viaduct rod 139–40, 141
 - Nydam 283
 - solubility 63–7
 - and corrosion rate 71–2
 - magnetite-maghemite striations 26, 96–8
 - major symptoms 193, 194, 201
 - malachite 164, 166, 209, 227, 228, 229
 - marbling 26, 96–8, 116, 117
 - marine corrosion *see* seawater
 - markers for location of the OS (limitos
 - markers) 8–9, 38–9
 - Marly viaduct rod 139–44, 146–8
 - mass gain/loss
 - atmospheric corrosion 143–4, 146–8
 - corrosion depth from 298
 - modern samples in soil from Nydam
 - 278, 284–5
 - on-line monitoring 296, 301–2
 - mass transport 88–9
 - see also* diffusion
 - material condition of the artefact 31–4
 - maximal limit of corrosion rate 61–71, 74
 - mechanical twins 258–9
 - mechanistic modelling 19–20, 110
 - atmospheric corrosion 131, 132–9
 - results for climatic chamber ageing
 - tests 144–6
 - concrete-embedded iron 122–7
 - oxygen reduction 123–7
 - presentation of modelling approach
 - 122–3
 - Mediterranean basin 7–8
 - mercaptobenzothiazole (MBT) 313
 - mercury porosimetry 95, 98, 99
 - metal/oxide interface 48–51
 - metallic substrate
 - concrete-embedded iron 114–15
 - iron in soil 44–8, 92–3
 - metallurgical structures 38
 - method for describing corrosion 36–8
 - methylbenzotriazole 313
 - micro Raman spectroscopy (μ Raman) 3, 44, 114, 140
 - chlorinated phases 175, 181–2
 - intentional patination 223, 227, 229, 231
 - tin and copper oxides 249–51, 254, 256, 257, 258
 - micro X-ray absorption near edge structure (μ XANES) 44, 139–40, 141, 175–6, 182–4
 - micro X-ray diffraction (μ XRD) 3, 44, 114, 254, 255, 256
 - chlorinated phases 175, 177–81
 - intentional patination 223, 227, 228, 231
 - micro X-ray fluorescence (microXRF) 3
 - microcrystalline waxes 310
 - microporosities 98, 116

- microstructure of lead-rich organ pipes
 - 359–62, 364–6
- mineralisation 192–3, 201
- miners' lamps 326, 327, 330, 331, 332–3
- minimal corrosion rate 60–1
- minor symptoms 194, 201
- modern samples
 - experimental ageing and atmospheric corrosion 140–8
 - Nydam site 278–9, 284–8, 289–90
 - simulation of corrosion processes of buried bronze artefacts 203–18
- multidisciplinary teams 12
- N 1s core level peak intensity 338, 339, 341, 344, 346–7
- nanoporosities 98, 116
- nantokite 164, 227, 231, 235, 313
- networking 3–4, 12–13
- neutron diffraction 3
- neutron radiography 3
- nitrocellulose varnishes 309
- Nordic Green patina system 268–70
- nuclear waste storage 19, 41, 92, 109, 131
- Nydam site 6, 272–92
 - corrosion products 277–8, 282–4, 286–7
 - environmental monitoring 274–5, 279–81
 - modern samples 278–9, 284–8
 - nature of 272–3
 - research methodology 273–9
 - research results 279–88
 - state of preservation of artefacts 276–7, 281–2, 288–9
- Nyquist diagrams 80–1, 84
- on-line corrosion monitoring 293–307
 - experimental 293–7
 - field exposures 297
 - commercial instruments and sensors 301–3
 - laboratory exposures 297, 303–5
 - commercial instruments and sensors 298–301
 - prototype corrosion logger 296, 303–5, 306
 - QCM 293–4, 298–303, 306
 - reference methods 296, 303–5
 - resistance sensors 293, 294–6, 298–303, 306
 - results 297–305
- organ pipes, lead-rich 352–67
- organic acids
 - corrosion of lead 315–16
 - and lead-rich organ pipes 362–4
 - see also* acetic acid
- original surface (OS) 1, 8–9, 34–5
 - limit of (limitos) 34–5
 - locating 35–9
- Ormocer coatings 312
- oxide barrier 21, 24
- oxygen
 - accessibility in the internal corrosion strata 39
 - apparent oxygen diffusion coefficient 101–4, 118
 - 'battle' for 156, 161, 162
 - diffusion and corrosion mechanisms of low-carbon steels 56–7
 - dissolved in seawater 155, 162, 163–4
 - oxygen transport control hypothesis 100–4, 106
 - soils from Sardinian archaeological sites 210–11
 - ternary diagram for copper, tin and oxygen 252–3, 257–8
- oxygen-18 (¹⁸O)
 - calculation of ¹⁸O quantity that precipitated into corrosion products 105, 106
 - profile from Glinet site 98–100
 - saturated water 95–6
- oxygen reduction
 - atmospheric corrosion 144–6
 - modelling 135–7
 - concrete-embedded iron 123–7
- parabolic modelling 105, 106
- Paraloid B72 varnish 309, 313
- paratacamite 209, 313
- passivating alloys 19
- passive film 164–5
- patinas 203
 - bronzes 239, 240–3
 - copper roofs and claddings 263–4, 265
 - artificial patinas 267–8
 - reconstruction 266–7
 - study of behaviour of artificial patinas in atmospheric conditions 268–70
 - international patination *see* intentional patination
- peat 273, 280, 281
- periods of time 31–2
- pH 211
 - and corrosion rate 67–2
 - seawater 155
- phase angle 81, 84

- phases of time 31–2
- phosphates 63–5, 204
- phosphorus 45–7
- physical changes 194–8
- physico-chemical condition 32
- Pioloform 310
- pipe organs *see* lead-rich organ pipes
- pitting 19–20, 194–5
- plasma treatment 9, 10
- polarisation resistance
 - bronze 324, 325
 - iron 328, 329
 - lead 316–17, 318
- polyethylene waxes 310
- Ponte in Valtellina pipe organ 353–66
- pore impedance 83, 84
- porosity
 - concrete-embedded iron
 - binders 120–1
 - DPL 115–16, 117
 - Glinet site DPL 98, 99
- porous electrode impedance modelling 82–4
- posnjakite 269
- post-corrosion symptoms 193–200
 - chemical changes 198–200
 - physical changes 194–8
- potentiodynamic curves 159–60
 - bronze 324–5, 326
 - iron 329–30
 - lead 317–18, 319
- Pourbaix diagram 283–4
- powdery orange-brown corrosion products
 - 194, 198, 199–200
- premonitory symptoms 192–3
- Preventive Conservation of Metals in
 - Museums (PCMM) 13
- primary sources, artefacts as 32
- PROMET project 7–8
- protection systems *see* corrosion inhibitors
- proton-induced X-ray emission (PIXE) 3,
 - 224–7
- prototype corrosion logger 296, 303–5, 306
- pump room 297, 301–3
- Punic coin 209, 210, 214, 215

- quartz crystal microbalance (QCM) 293–4, 306
 - field exposures 301–3
 - laboratory exposures 298–301
- Queen Anna's Summer Palace copper roof
 - 264–70
 - artificial patinas 267–8
 - study of behaviour in atmospheric conditions 268–70
 - corrosion damage 264–5, 266
 - reconstruction 265–7
- Qumran Copper Scroll 39

- radioactive waste disposal 19, 41, 92, 109, 131
- Raman spectroscopy *see* micro Raman
 - spectroscopy (μ Raman)
- reactivated corrosion 190–202
 - defining 192
 - diagnostics 200
 - perspectives 200–1
 - post-corrosion symptoms 193–200
 - chemical changes 198–200
 - physical changes 194–8
 - premonitory symptoms 192–3
- Recherche du métal perdu* exhibition 4–5
- red-orange patination 232, 234, 235
- redox potential 67–2
- reference coupons 296, 303–5
- reinforced concrete *see* concrete-embedded iron
- relative humidity (RH) 132
- research 1–17
 - fundamental and applied 8–10
 - funding biased towards examination and archaeometric studies 2–6
 - necessity for 6–10
 - pro-active responsibilities for conservators 11–12
- resistance sensors 293, 294–6, 306
 - field exposures 301–3
 - laboratory exposures 298–301
 - Nydam 279, 287–8
- Rhodopas M 310
- Roman Empire patinated artefacts 221–2,
 - 223–36
- romarchite 165
- rust layer 22–3, 132
 - Marly viaduct rod 139
 - modelling 133
 - thickness measurement 147–8, 149
- Rutherford backscattering spectrometry (RBS) 223, 227, 230, 231

- salinity of seawater 153–5
- sand grains 38
- Sant'Antioco archaeological site 205, 207–9
 - soil 212–14
 - ageing tests 214–16, 217
- sarcophagus, lead 322, 323
- Sardinian archaeological sites 205, 207–9
 - soils 212–14
- Sauerbrey equation 294

- seawater 7, 152–69
 air drying 166–7
 corrosion of copper alloys 164
 corrosion of iron-based artefacts 156–64
 cast iron 162–3
 chronological parallelism between
 iron corrosion products and burial
 conditions 163–4
in-situ growth of corrosion products
 159–62
 theoretical formation and growth of
 corrosion products 157–8
 corrosion of ‘white’ metals 164–5
 description of seawater environment
 153–6
 knowledge of degradation state of
 metallic artefacts 165–7
- shape 32
- shells 280–1
- siderite 24, 25, 26, 42, 50, 62
 corrosion mechanisms at Glinet
 archaeological site 58–9, 186
 DPL 51, 53, 186
 Nydam iron artefacts 282–4, 287
 solubility 63–7, 68
 and corrosion rate 72
 and equivalent thickness 70, 71
- silicon
 corrosion inhibition 346, 347, 349
 Cu-Sn-Si bronze 335, 342–5, 347–50
- siloxane molecules 312
- SILPROT project 7
- silver/silver artefacts
in-situ conservation 7
 inhibitors 313
 intentional patination 233, 234, 235
 on-line monitoring 296, 297–306
- sintering 258
- slag inclusions 47, 48
- Sobek aegis and counterpoise 220, 221,
 224, 225, 226, 231, 233, 235
- sodium carboxylates 314–31, 332–3
 bronze artefacts 324–7
 iron artefacts 328–31
 lead artefacts 315–24
- sodium chloride 80, 82, 84–7
- sodium decanoate 315–31
 bronze artefacts 324–7
 iron artefacts 328–31
 lead artefacts 315–24
- sodium heptanoate 324–31
 bronze artefacts 324–7
 iron artefacts 328–31
- soil, corrosion in
 buried bronze artefacts 203–18
 soil analysis 206–7
 soil from Sardinian archaeological
 sites 209–14
 iron-based materials 23–8, 41–76, 111, 114
 average corrosion rate estimation
 59–73
 corrosion mechanisms 53–9
 corrosion system characterisation
 44–53, 54, 55, 56
 species transport in corrosion
 products 92–108
 parameters for archaeological sites 45, 46
- solder size 358
- solid solution heterogeneities 258–9
- solubility
 calculations 62–7
 validation of corrosion rate’s maximal
 limit 61–71
- spalling 148, 149
- spearheads 276–7, 281–2
- species transport in corrosion products
 92–108
- spectral mapping 101, 102
- spherical shells 176, 177
- squared impedance diagrams 86–7
- stabilisation treatments 166–7
- stable/unstable objects 192
- stainless steels 157
- stannic oxide 249–51, 252–3, 254, 255,
 256, 257–8, 259
- stannous oxide 249
- state of preservation
 knowledge of degradation state 165–7
 Nydam artefacts 276–7, 281–2, 288–9
- steels
 low-alloy *see* low-alloy steels
 low-carbon *see* low-carbon steel
 stainless 157
see also iron-based materials
- strata *see* corrosion layers
- strigil 221, 222, 224, 225, 226, 231, 235
 red-orange patination 232, 234, 235
- sulphate reducing bacteria (SRB) 156, 164
- sulphates 199, 211
- sulphides 42
- Superior Limitos Marker (S.Limitos
 Marker) 38
- surface appearance 32
- tannins 313–14
- Techné* 2

Technologische Studien 2

- temperature
 - on-line monitoring 298–9
 - seawater 155
- tenorite 164
- ternary diagram 252–3, 257–8
- tetrahydrate ferrous hydroxychloride 172
- Tharros archaeological site 205, 207–9
 - soil 212–14
 - ageing tests 214–16, 217
- thickness
 - chlorinated phases 177, 180
 - corrosion film 297–8
 - corrosion products in lead-rich organ pipes 359, 360
 - critical 127
 - DPL and TM for concrete-embedded iron 115, 116
 - measurement for rust layer 147–8, 149
 - minimal value of corrosion rate 60
 - solubility method for corrosion rate 62, 67–71
- thiosulphate reducing bacteria (TRB) 156
- thiourea 312
- time, periods and phases of 31–2
- tin/tin-based materials
 - corrosion inhibition 345, 346, 347, 349–50
 - Cu-Sn-Si alloy 335, 342–5, 347–50
 - Cu-Sn-Zn-Pb alloy 335, 339–42, 347–50
 - lead-rich organ pipes 353, 355, 357, 364, 366
 - tin inclusions 362, 363
 - ‘white’ metals 164–5
- tin oxides 239–62
 - mixtures of tin-copper oxide 243, 252–4, 255, 256, 257, 258
 - ‘type 2’ corrosion of bronze artefacts 254–9
- training in conservation science 10–11
- transformed medium (TM) 45, 51–2, 55, 92–3
 - average corrosion rates 60–1
 - concrete-embedded iron 115, 116, 119–20, 122
 - corrosion mechanisms 57
 - iron equivalent thickness 60
 - type 2 corrosion of bronzes 241, 242, 259
 - oxide areas containing both copper and tin 252–4
 - tin oxide, copper oxide and 254–9
- uniform corrosion 18–20
- unstable/stable objects 192
- valence inversions 26, 27
- varnish 309–10
- vinyl polymer varnishes 310
- vivianite 63–5, 68
- volatile amines 313
- water
 - environmental monitoring at Nydam 274–5, 279–81
 - seawater *see* seawater
 - water content of soils 209–10
 - water table 275, 279–80
 - waterlogged site *see* Nydam
 - wave turbulence 163
 - wavelength dispersive spectroscopy (WDS) 174
 - waxes 310–12
 - weight gain/loss *see* mass gain/loss
 - wet-dry cycle 21–3, 110, 132–9
 - drying stage 132, 137–8
 - experimental 142–3, 144–6
 - wet stage 132, 135–7
 - wetting stage 132, 133–5
 - ‘white’ metals 164–5
 - wood 352
 - World War I steel artefacts 77–91
- X-radiography 2–3, 276
- X-ray diffraction (XRD) *see* micro X-ray diffraction (μ XRD)
- X-ray photoelectron spectroscopy (XPS) 336–50
- ZARC circuit 80
- zinc
 - corrosion inhibition 345–6, 347, 348, 350
 - Cu-Sn-Pb-Zn alloy 335, 339–42, 347–50